Vol. 297, No. 1–2, October 31, 1994 ISSN 0003-2670

Special Issue

(Guest Editors: R.P.H. Garten and H.W. Werner)

ANALYTICA CHIMICA ACTA

An international journal devoted to all branches of analytical chemistry

Analysis of Thin Films, Interfaces and Surfaces

ELSEVIER

ANALYTICA CHIMICA ACTA

Scope. *Analytica Chimica Acta* publishes original papers, rapid publication letters and reviews dealing with every aspect of modern analytical chemistry. Reviews are normally written by invitation of the editors, who welcome suggestions for subjects. Letters can be published within **four months** of submission. For information on the Letters section, see inside back cover.

Submission of Papers

Americas

Prof. Harry L. Pardue
Department of Chemistry
1393 BRWN Bldg, Purdue University
West Lafayette, IN 47907–1393
USA

Tel:(+1-317) 494 5320
Fax:(+1-317) 496 1200

Computer Techniques

Prof. J.T. Clerc
Universität Bern
Pharmazeutisches Institut
Baltzerstrasse 5, CH-3012 Bern
Switzerland

Tel:(+41-31) 6314191
Fax:(+41-31) 6314198

Prof. Sarah C. Rutan
Department of Chemistry
Virginia Commonwealth University
P.O. Box 2006
Richmond, VA 23284-2006
USA
Tel:(+1-804) 367 7517
Fax:(+1-804) 367 8599

Other Papers

Prof. Alan Townshend
Department of Chemistry
The University
Hull HU6 7RX
Great Britain

Tel:(+44-482) 465027
Fax:(+44-482) 466410

Prof. Willem E. van der Linden
Laboratory for Chemical Analysis
Department of Chemical Technology
Twente University of Technology
P.O. Box 217, 7500 AE Enschede
The Netherlands
Tel:(+31-53) 892629
Fax:(+31-53) 356024

Prof. Paul Worsfold
Dept. of Environmental Sciences
University of Plymouth
Plymouth PL4 8AA
Great Britain

Tel:(+44-752) 233006
Fax:(+44-752) 233009

Submission of an article is understood to imply that the article is original and unpublished and is not being considered for publication elsewhere. *Anal. Chim. Acta* accepts papers in English only. There are no page charges. Manuscripts should conform in layout and style to the papers published in this issue. See inside back cover for "Information for Authors".

Publication. *Analytica Chimica Acta* appears in 18 volumes in 1995 (Vols. 297–314). *Vibrational Spectroscopy* appears in 2 volumes in 1995 (Vols. 8 and 9). Subscriptions are accepted on a prepaid basis only, unless different terms have been previously agreed upon. It is possible to order a combined subscription (*Anal. Chim. Acta* **and** *Vib. Spectrosc.*).
Our p.p.h. (postage, packing and handling) charge includes surface delivery of all issues, except to subscribers in the U.S.A., Canada, Australia, New Zealand, China, India, Israel, South Africa, Malaysia, Thailand, Singapore, South Korea, Taiwan, Pakistan, Hong Kong, Brazil, Argentina and Mexico, who receive all issues by air delivery (S.A.L.–Surface Air Lifted) at no extra cost. For Japan, air delivery requires 25% additional charge of the normal postage and handling charge; for all other countries airmail and S.A.L. charges are available upon request.

Subscription orders. Subscription prices are available upon request from the publisher. Subscription orders can be entered only by calendar year and should be sent to: Elsevier Science B.V., Journals Department, P.O. Box 211, 1000 AE Amsterdam, The Netherlands. Tel: (+31-20) 5803 642, Telex: 18582, Telefax: (+31-20) 5803598, to which requests for sample copies can also be sent. Claims for issues not received should be made within six months of publication of the issues. If not they cannot be honoured free of charge. Readers in the U.S.A. and Canada can contact the following address: Elsevier Science Inc., Journal Information Center, 655 Avenue of the Americas, New York, NY 10010, U.S.A. Tel: (+1-212) 633 3750, Telefax: (+1-212) 633 3990, for further information, or a free sample copy of this or any other Elsevier Science journal.
Advertisements. Advertisement rates are available from the publisher on request.

US mailing notice – Analytica Chimica Acta (ISSN 0003-2670) is published 3 times a month (total 54 issues) by Elsevier Science B.V. (Molenwerf 1, Postbus 211, 1000 AE Amsterdam). Annual subscription price in the USA US$ 3677.75 (valid in North, Central and South America), including air speed delivery. Second class postage paid at Jamaica, NY 11431. *USA Postmasters*: Send address changes to Anal. Chim. Acta, Publications Expediting, Inc., 200 Meacham Av., Elmont, NY 11003. Airfreight and mailing in the USA by Publication Expediting.

ANALYTICA CHIMICA ACTA

An international journal devoted to all branches of analytical chemistry

(Full texts are incorporated in CJELSEVIER, a file in the Chemical Journals Online database available on STN International; Abstracted, indexed in: Aluminum Abstracts; Anal. Abstr.; Biol. Abstr.; BIOSIS; Chem. Abstr.; Curr. Contents Phys. Chem. Earth Sci.; Engineered Materials Abstracts; Excerpta Medica; Index Med.; Life Sci.; Mass Spectrom. Bull.; Material Business Alerts; Metals Abstracts; Sci. Citation Index)

VOL. 297 NO. 1–2 CONTENTS OCTOBER 31, 1994

Special issue on the Analysis of Thin Films, Interfaces and Surfaces

Preface
(by R.P.H. Garten and H.W. Werner) 1

Trends in applications and strategies in the analysis of thin films, interfaces and surfaces (Review)
R.P.H. Garten (Dortmund, Germany) and H.W. Werner (Vienna, Austria) 3

Applications
Surface analysis of thin films and interfaces in commercial aluminium products
M. Textor and M. Amstutz (Neuhausen am Rheinfall, Switzerland) 15
Microanalysis of atmospheric particles and fibres by electron energy loss spectroscopy, electron spectroscopic imaging and scanning proton microscopy
P. Berghmans, J. Injuk, R. Van Grieken and F. Adams (Antwerp-Wilrijk, Belgium) 27
Surface analytical studies on metal surface and interface phenomena
H. Viefhaus (Düsseldorf, Germany) 43

Non-destructive Depth Profiling
High energy ion scattering and recoil spectrometry in applied materials science (Review)
L.J. Van IJzendoorn (Eindhoven, Netherlands) 55
Non-destructive analysis of materials and devices by means of scanning acoustic microscopy
J. Van den Berg, J. Van Oijen (Eindhoven, Netherlands) and H.W. Werner (Vienna, Austria) 73
Characterization of interfaces by photothermal methods
H.G. Walther (Jena, Germany) and W. Karpen (Stuttgart, Germany) 87

Electron Spectroscopic Methods Applied to Problem Solving
Chemistry of grain boundaries in calcia doped silicon nitride studied by spatially resolved electron energy-loss spectroscopy
J. Bruley (Bethlehem, PA, USA), I. Tanaka (Kyoto, Japan), H.-J. Kleebe (Bayreuth, Germany) and M. Rühle (Stuttgart, Germany) 97
Low energy electrons (LEED, STM and HREELS) in the microanalytical characterization of complex surface structures
W. Weiss, U. Starke and G.A. Somorjai (Berkeley, CA, USA) 109
Recent advances in x-ray photoelectron microscopy
K. Holldack and M. Grunze (Heidelberg, Germany) 125
Correlation of insulator properties with electron spectroscopic observations
C. Le Gressus (Bruyères-le-Chatel, France) and G. Blaise (Orsay, France) 139
Electron radiation-induced effects in Auger electron spectroscopic characterization of high-T_c superconductors
E.W. Seibt (Karlsruhe, Germany), A. Zalar (Ljubljana, Slovenia) and N. Roose (Brussels, Belgium) 153
Characterization of grain boundary segregation in an Fe–Si alloy
P. Lejček (Prague, Czech Republic) 165

(Continued overleaf)

Contents (continued)

X-ray photoelectron spectroscopic study of the oxidation of polycrystalline rhenium by exposure to O_2 and low energy O_2^+ ions
C. Morant, L. Galán and J.M. Sanz (Madrid, Spain) 179
Application of factor analysis in electron spectroscopic depth profiling on copper oxide
H. Bubert, M. Korte, R.P.H. Garten, E. Grallath (Dortmund, Germany) and M. Wielunski (Bochum, Germany) 187

SIMS, SNMS and TOF-SIMS – Trends and Applications
Spatially multidimensional secondary ion mass spectrometry analysis (Review)
F.G. Rüdenauer (Seibersdorf, Austria) 197
Optimization of secondary ion mass spectrometry for quantitative trace analysis (Review)
G. Stingeder (Vienna, Austria) 231
Characterization of sharp interfaces and delta doped layers in semiconductors using secondary ion mass spectrometry (Review)
M.G. Dowsett and R.D. Barlow (Coventry, UK) 253
Secondary-neutral and secondary-ion mass spectrometry analysis of TiN-based hard coatings: an assessment of quantification procedures
W. Bock, H. Gnaser and H. Oechsner (Kaiserslautern, Germany) 277
Plasma secondary-neutral and secondary-ion mass spectrometry investigations on ceramic / copper powder pellets
H. Jenett (Dortmund, Germany), M. Luczak (Steinfurt, Germany) and O. Dessenne (Voreppe, France) 285
Time-of-flight secondary ion mass spectrometry of poly(alkyl acrylates): comparison with poly(alkyl methacrylates)
P.A. Zimmerman and D.M. Hercules (Pittsburgh, PA, USA) 301

ANALYTICA CHIMICA ACTA
VOL. 297 (1994)

ANALYTICA CHIMICA ACTA

An international journal devoted to all branches of analytical chemistry
Revue internationale consacrée à tous les domaines de la chimie analytique
Internationale Zeitschrift für alle Gebiete der analytischen Chemie

Anal. Chim. Acta, Vol. 297 (1994)

ELSEVIER

Amsterdam – Lausanne – New York – Oxford – Shannon – Tokyo

0003-2670/94/$07.00

SPECIAL ISSUE

ANALYSIS OF THIN FILMS, INTERFACES AND SURFACES

ELSEVIER

Analytica Chimica Acta 297 (1994) 1

ANALYTICA CHIMICA ACTA

PREFACE

Analytical chemistry today, the general subject of this journal, is becoming increasingly involved in close cooperation between numerous disciplines and branches of science and technology; this will allow a variety of complex problems to be solved in various fields of our modern technological evolution, to ensure the continuity, security and advancement of our quality of life and social development. Analytical chemistry is concerned wherever significant contributions are linked to the composition of matter, its purity and its uniformity. In all these respects, analytical chemistry is steadily evolving into characterization at levels that have not been accessible before, not only trace concentrations and materials purity, but also local micro-dimensions, and micro-dimensional interfaces and thin-film layers, in particular. Therefore, it was decided to produce a topical issue of this journal on the fascinating facet of thin-film analysis.

With regard to the widespread interests of the readers of this journal, covering all branches of analytical science, we wish to emphasize in this topical issue the broad fields of applications and the important aspects of methodical advances. We have collected papers from different areas with a wide scope of surface analytical applications and with some recent methodical trends in order to present a reasonable impression of the state of their development. Some emphasis is placed on techniques for the in situ characterization of interfaces — techniques that overcome the limitations derived from the former requirement for ultra-high-vacuum conditions during the inspection of surfaces.

Numerous important and interesting results, techniques and strategies were disregarded or sacrificed in this issue to obtain, in our opinion, a balanced view of a very broad and diversified field, scrutinized by numerous highly sophisticated approaches and methods. This balance, of course, is based on the subjective experience of the Guest Editors. Equally, it could have been shifted somewhat into other directions.

After having read the large number of papers, we are convinced that the reader will have an interesting and informative survey of a number of currently very important topics from very different parts of the overall field of applications, presented in highly qualified and up-to-date contributions by well recognized experts, and that the reader will enjoy this up-to-date conception of the "state-of-the-art" of thin-film, interface and surface analysis.

R.P.H. Garten
Dortmund

H.W. Werner
Vienna

SSDI 0003-2670(94)00057-S

ELSEVIER

Analytica Chimica Acta 297 (1994) 3–14

ANALYTICA CHIMICA ACTA

Review

Trends in applications and strategies in the analysis of thin films, interfaces and surfaces

R.P.H. Garten

Max-Planck-Institut für Metallforschung, Stuttgart, Laboratorium für Reinststoffanalytik, Bunsen-Kirchhoff-Str. 13, D-44139 Dortmund 1 (Germany)

H.W. Werner

Institut für Allgemeine Physik der Technischen Universität Wien, Wiedener Hauptstr. 8, A-1040 Vienna (Austria)

Received 11th August 1993

Abstract

Prominent aims and general aspects of the analysis of thin films, interfaces and surfaces are reviewed. The terminology is presented, and a limited sketch displays the major techniques important in this field. Some topical subjects in thin film analysis are identified, starting from its application for support of technology. This leads to reflections upon some trends concerning both optimization and application.

Keywords: Surface techniques; Thin films; Surface analysis

1. Aims in optimizing microanalytical information

Analytical product support and analytical development take important positions in technology development, promoting the speed of the development and the quality achieved [1]. Chemical analysis is steadily developing into characterization at levels which have not been accessible before, for example analysis of molecular structures, detection of element traces, purity of materials, study of local interfaces and thin film layers with micro-dimensions and nanometre resolution.

Developments and improvements of thin-film analysis, as a specialized field of micro- and microtrace-analysis, are basically directed to the optimization of analytical economy, power of detection, reliability, selectivity of information from different local sites and from different chemical species of the same element, see Fig. 1. In the optimization process, all these different characteristic features of micro-analysis are closely interconnected with each other, often in a very complicated way (as is exemplified in the review paper on multi-dimensional SIMS by F.G. Rüdenauer in this issue). Improvements of either of these features will generally require a sacrifice in the performance of one or some of the other

Correspondence to: R.P.H. Garten, Max-Planck-Institut für Metallforschung, Stuttgart, Laboratorium für Reinststoffanalytik, Bunsen-Kirchhoff-Str. 13, D-44139 Dortmund 1 (Germany).

SSDI 0003-2670(93)E0520-H

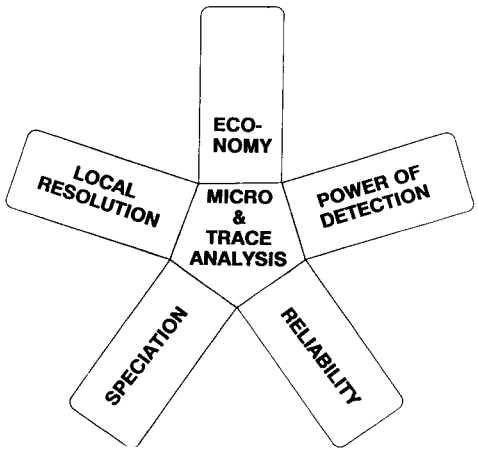

Fig. 1. Improvements of criteria in micro and trace analysis.

characteristics [2]. Thus, optimization requires a sophisticated treatment of the methodical approaches used in thin-film and interface analysis. The optimization procedure is time-consuming and expensive, so it influences analytical economy, of course. However, it is the only way to achieve analytical reliability, and without reliability, there is no economy at all. In the general analytical routine, the importance of accuracy is often readily appreciated by the customer [3].

Further, optimization has to be performed for each particular problem and material individually, so a survey of the whole field in an application-oriented sense would make up an extensive array of sophisticated methods investigating highly specialized tasks, materials and devices. Hence, it is beyond the scope of this special issue, to present today's state of the art from all the various fields of thin film and interface analysis.

Importance of thin-film analysis

The analytical characterization of clean and covered surfaces of solid matter takes a very important position in the field of microanalysis and local microdistributional analysis, because a number of physical and chemical properties of solids are defined by the specific properties of the near-surface layer [4–6].

Such properties contribute to, or even govern numerous chemical reactions, so they are effective in phenomena of adsorption, corrosion, passivation, weathering, electrical polarization, etc. Properties of the surface layer also strongly affect mechanical characteristics (friction, adhesion, wear, lubrication, bonding), general electronic properties (work function, photoelectric and electrochemical properties) and optical characteristics. Specific thin-film technologies are applied in the production of modern protective coatings [7–9] and of electronic devices [10–19]. Such technologies are utilized to prepare components with very strong changes of the material's properties between directly adjacent layers. The local distance of such layers is steadily decreasing with the progressive miniaturization of technology. Thus, the analytical assistance in technology, viz. the examination, characterization and optimization of such components requires methods capable of determining the spatial distributions in one (depth profile; line scan), two (surface map), and three dimensions (combined map/depth profile; see the review by F.G. Rüdenauer).

To start with, we shall present some general aspects and terminology, and then display a limited sketch of the major techniques important in this field, including references to appropriate reviews.

Definition of the problem

Thin film analysis methods make it possible to determine the chemical and physical structures of thin films and interface layers. They refer to the (compositional and structural) characterization of layers of a thickness from a few nanometres up to micrometers. The general goal is to determine the in-depth distribution with a layer-by-layer depth resolution from a tenth up to some hundred nanometres, depending on the analytical problem under study.

In this context, the microdimensional chemical structure refers to the spatial distribution of chemical species (elements, compounds, bond types) in a specimen, and physical structure means the spatial distribution of physical characteristics, particularly the crystallographic arrangement of atoms, its imperfections, as well as the topography of the specimen [5]. These methods include, among others: AES, SIMS, ESCA, RBS, EPMA, analytical STEM. The conventional acronyms

used in thin-film analysis are listed in Table 1. A number of significant analytical features for chemical interface and thin film analysis are presented in Table 2.

2. Major methods for thin film analysis

Modern methods of major importance in thin-film and interface analysis are based on the physical interaction of primary (exciting) particles or quanta with the thin-film matter to be analyzed, and the detection of secondary particles or quanta emitted from this interaction processes. Therefore, these methods are adequately arranged according to the nature of the exciting and the emitted particles relevant in those interactions. Table 3 gives an abridged survey of the basic processes of major importance as well as an indication of the main methods thus formed. Typical performance parameters of the major methods are compared in Table 4.

From the view of practical analytical application, the most relevant are the electron spectroscopic methods AES and XPS and the ion spectroscopic method SIMS/SNMS. These techniques probe surfaces by a primary exciting beam (Fig. 2, cf. Table 3), and analyze the energy distribution of emitted electrons (AES, XPS) or the mass distribution of sputtered secondary ions/post-ionized neutrals. However, these secondary particles can in turn interact with atoms of the surface layer. The interaction of these information-carrying secondary particles with matter is so intense that collisions between these particles and an atom of the solid will result in a loss of the characteristic information carried (viz. kinetic energy, momentum, state of charge); the probability of such a loss is between 0.15 and 1 per every atomic layer traversed. Only those information carriers remain undisturbed, which

Table 1
Conventional acronyms of the different methods

AES	Auger electron spectrometry
AFM	atomic force microscopy
ATR-IR	attenuated total reflection-infrared spectrometry
CPAA	charged particle activation analysis
EELS	electron energy-loss spectrometry
EPXMA	electron probe x-ray microanalysis
EDX	energy-dispersive x-ray analysis
ERD	elastic recoil detection
ESCA	electron spectroscopy for chemical analysis (= XPS)
EXAFS	extended x-ray absorption fine structure
FT-IR	Fourier transform infrared spectrometry
GDMS	glow discharge mass spectrometry
ISS	ion scattering spectrometry
LEED	low-energy electron diffraction
LMS	laser mass spectrometry
NAA	neutron activation analysis
NRA	nuclear reaction analysis
PIXE	proton-induced x-ray emission
RBS	Rutherford back-scattering spectrometry
SAM	scanning Auger microprobe
SCAM	scanning acoustic microscopy
SEM	scanning electron microscopy
SIMS	secondary-ion mass spectrometry
SNMS	sputtered neutrals mass spectrometry
STEM	scanning transmission electron microscopy
STM	scanning tunneling microscopy
TDS	thermal desorption spectrometry
TEELS	transmission electron energy-loss spectrometry
TEM	transmission electron microscopy
TOF	time-of-flight (mass spectrometer)
TXRF	total reflection x-ray fluorescene analysis
UPS	ultraviolet photoelectron spectrometry
XPS	x-ray photoelectron spectrometry
XRD	x-ray diffraction
XRFA	x-ray fluorescence spectrometric analysis

Table 2
Selected analytical features for chemical characterization of structures in thin films, interfaces and surfaces and related techniques (adapted from [26])

Elemental range
Limit of detection
Quantification
Spatial resolution in 1, 2 and 3 dimensions:
lateral resolution
depth resolution
(spectroscopic information depth)
Chemical compound information
Time
Cost: man power needed
instrumentation, automation
Destructiveness
Consumptiveness
Sample preparation
Flexibility

have not undergone such interactions, i.e., which have been ejected from a few outermost atomic layers. Consequently, the signal obtained from a solid surface is characteristic selectively of the outermost atomic layers (see Table 4 for magnitudes).

The most important prerequisite in getting a signal from the surface layer of the actual specimen is to keep it under clean surface conditions. Adsorption of reactive constituents from the ambient gas atmosphere results in covering of a clean surface at a rate of one monolayer per second at a partial pressure of $p \approx 10^{-4}$ Pa of this constituent. To maintain a clean surface for an analysis period of some minutes will require ultra-high vacuum conditions ($p \leqslant 10^{-7}$ Pa) in any surface analytical instrument. Clean surfaces and interfaces are prepared or exposed by use of in situ or ex situ techniques [20–25].

Electron spectrometry

In XPS, monochromatic x-rays from the exiting beam are absorbed by an atom. The atom will emit a photoelectron with a kinetic energy characteristic of the respective element via the photoelectric effect. Altered atomic energy levels due to chemical binding effects and different molecular environments result in chemical shifts up to

Table 3
Abridged matrix of interaction processes (in italics) between primary beams and solid matter emitting secondary particles, and (steep) indication of main methods for thin film analysis. The conventional acronyms for the methods are listed in Table 1 (reduced from [5]).

Excitation	Emission (= detection)			
	Photons	Electrons	Ions	Neutrals
Photons	*Fluorescence, reflection,* XRFA Raman scattering ellipsometry	*Photo- and Auger electron emission* XPS	*Photodesorption and local heating*	
Electrons	*Electron-induced photon emission* EPMA SEM-EDX TEM-EDX	*secondary electrons, back-scattered and Auger electrons* AES	*Electron stimulated desorption*	
Ions	*Ion-induced photon emission* PIXE	*Ion-induced electron emission*	*secondary ion emission* SIMS GDMS *Ion scattering* ISS RBS, ERD *intrinsically inelastic:* NRA	*Emission (sputtering) of neutrals* SNMS
Neutrals	*Particle-induced photon emission*	*Particle-induced electron emission*	*Particle induced ion emission* FAB-MS	*Sputtering*
Heat	*Thermal radiation*	*Thermionic emission*	*Thermal ion desorption*	*Thermal evaporation*
Electric field Stylus techniques	STM, AFM	*Field electron emission*	*Field ion emission*	

Table 4
Selected analytical features of different thin film and selvage methods (revised from [5]).

	Performance indicator		XPS	AES	SIMS/SNMS dynamic	SIMS/SNMS static	ISS	RBS	TEM	EPMA/SEM	LMS	GDMS
Infomation depth	+	1 μm						+	+	+	+	
	++	< 100 nm						++	++	++		++
	+++	⩽ 3 nm	+++	+++	(+++)	+++	+++	+++				
Depth resolution	+	1 μm						+		+	+	
	++	< 100 nm			++			++		++		++
	+++	⩽ 3 nm	+++	+++	(+++)			(+++)	+++			
	++++	monolayers				++++	++++					
Lateral resolution	(+)	20 μm	(+)			(+)	(+)				(+)	–
	+	1 μm				+		+		+	+	
	++	100 nm		++	++							
	+++	2 nm						+++				
Elemental range	+	> Li					+	+	+	+		
	++	> He	++	++								
	++	H...U			+++	+++		(+++)			+++	+++
Limit of detection	+	⩾ 0.1%	+	+		+	+	+	+	+		
	++	ppm				(++)	(++)	(++)			++	++
	+++	ppb			+++							(+++)
Chemical species information	+	small		+								
	++	available	++	(++)	++							
	P	physical structure			(P)		P	P				
Specimen damage	–	considerable			–				–	+	–	–
	+	moderate		+								
	++	small	++	(++)		++	++	++				
Difficulties in quantitation	+	high			+							
	++	moderate	++	++		++	++	++	++		++	++
	+++	low	(+++)	(+++)			(+++)	(+++)	+++			(+++)
Flexibility	+	moderate										
	++	good		++		++	++	++	++			++
	+++	excellent	+++		+++					+++	+++	
Existing data available	+	moderate				+	+	+	+		+	+
	++	many	++	++	++					++		

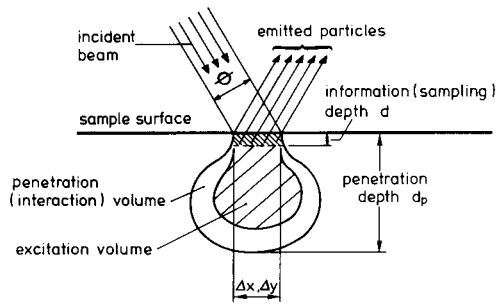

Fig. 2. Penetration depth and information depth in relation to lateral resolution $\Delta(x \times y)$. For numerical examples of lateral resolution and contributing depth intervals see Fig. 3 (from [5]).

several electron volts. These shifts indicate its chemical states.

In AES, an electron beam is utilized for atomic inner-shell ionization. The atomic de-excitation process can result in emission of Auger electrons from all atoms except H and He. The kinetic energy of these electrons is characteristic of the three electronic levels involved, so it is characteristic of the respective element. Chemical shifts in the Auger lines likewise appear, and are often greater than in XPS, but their interpretation is less straightforward, due to three altered energy levels involved. Even more informative on the chemical state is often the Auger lineshape, which reflects the share of valence electron density in the Auger process.

Emitted electrons are monitored as a function of their kinetic energy by means of electrostatic analyzers, of either the concentric hemispherical analyzer type or the cylindrical mirror analyzer type.

Ion spectrometry

In SIMS and SNMS, energetic (keV) ions of the primary beam knock out neutrals, and charged atoms and clusters by transfer of their energy through collision cascades [26–28].

By selection of the appropriate ions, energies and impact geometry, secondary particles and molecules are emitted solely from the top few atomic layers, or even from the outermost molecular layer of the solid specimen [84], because the only collisions that can cause secondary particle emission (sputtering) are those that occur in the outermost layer, bringing sufficient momentum – pointing outwards – to an atom. Sputtered ions (atomic or molecular; SIMS) are identified by mass spectrometry. Types of mass spectrometers in use are quadrupole, magnetic double focusing, and time-of-flight instruments.

Post-ionization of the sputtered neutrals (SNMS) converts the major part of the secondary neutral particles flux into ions for their successive mass spectrometric determination. Therefore, the most obstructive drawback of SIMS, viz. its strong matrix effects due to differences in the ionization probabilities during direct ion emission is removed in SNMS by the decoupling of the particle ablation from the ionization step. Further, primary ions can be used at optimized low energies (0.3 keV) to improve depth resolution (ca. 20 Å) in depth profiling analysis (see below) at high beam-current densities.

Ion scattering spectrometries are based on energy analysis of the fraction of the primary ions that are reflected as ions into a well defined solid angle. The mass of the scattering target atom is determined from the energy of the scattered primaries by the collisional kinematics. Sputtering is virtually absent due to the low stopping cross-section at low primary energy (ISS) or at high primary energy (RBS).

In ISS, the probability of reflected primaries to survive in the ionic state after a collision is very low (ca. 10^{-3}), so contribution is made only from single collisions. The information depth is therefore a single atomic layer. Electrostatic energy analyzers are applied to monitor the spectra of ions in this energy range.

In high-energy (MeV region) ion-induced spectroscopies (RBS, NRA, PIXE), the scattering cross-section (RBS) and the cross-sections for production (NRA, PIXE) of the detected species decrease with decreasing primary energy. Cross-sections become practically zero below a certain depth in each case due to the energy loss of the primary ions in traversing the target. The information depths depend on the detected species, the irradiated specimen and experimental parameters, ranging from a few nanometres up to sev-

eral micrometres. Based on this energy dependence of the cross-sections, non-consumptive depth profiling is feasible using these methods. In RBS, depth information in the $1-10^3$ nm range is superimposed on the elemental information comprised in the energy spectra likewise as in ISS. Applying appropriate alignment conditions of a single crystalline specimen lattice with respect to the primary ion beam, additional structural information can be gained, and foreign atoms on lattice positions can be distinguished from those on interstitial positions. Solid state (surface barrier Si) detectors are used for spectroscopy of high energy ions in RBS; solid state Si(-Li) X-ray detectors and intrinsic Ge γ-ray detectors are applied in PIXE and NRA.

Depth profiling analysis

A combination of the mentioned methods of surface analysis with successive erosion of the atomic surface layers by ion sputtering presents a universally applicable approach for depth profiling analysis. Sputtering is a destructive method of bombardment with, e.g., Ar^+ ions of an energy of 0.2–5 keV. The eroded surface atoms can be simultaneously utilized for SIMS/SNMS analysis. In AES or XPS the residual surface is in situ analyzed. Application of ion sputtering enables the composition of the specimen to be uncovered layer-by-layer on an atomic scale. Combined sputtering/thin-film analysis directly produces a measured sputtering profile. It presents the measured signal-intensity I from an element i as a function of sputtering time t under well defined constant sputtering conditions $I = I(t)$. This should be converted into a quantitative composition–depth profile $c = c(z)$ [29,30]. The main task in quantifying a measured sputtering profile is to generate the original distribution, from an accurate calibration of the depth scale $z = z(t)$, and another accurate calibration of the concentration scale $c = c(I)$. Even in the case of ideal erosion conditions, the compositional variation with depth as well as the altered rate of erosion with varied composition have to be taken into account when establishing either calibration. Moreover, in a second step, the effect of the sputtering process on the composition and on the structure (microroughening) of the specimen surface has to be considered, besides some further detrimental instrumental effects. In particular these deviations from the "ideal" erosion process cause broadening of measured depth profiles, i.e., deterioration of the depth resolution. In extreme cases even a complete distortion of the original true profile may be found [14,15,29–39].

The process of surface erosion by sputtering is very complex. It is the subject of a specialized

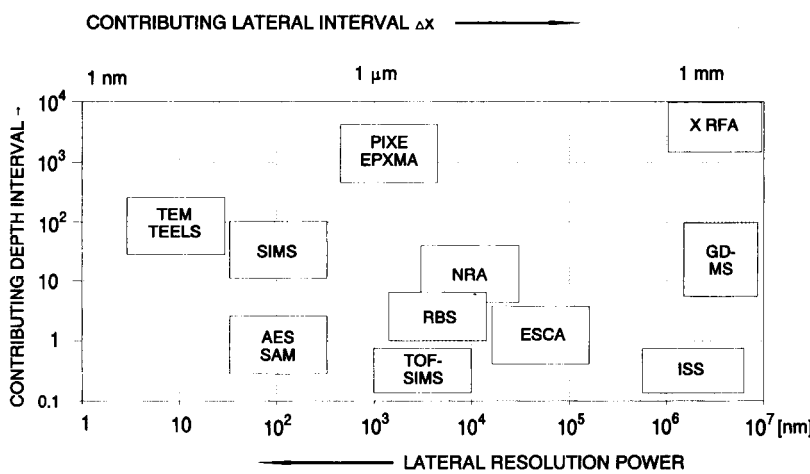

Fig. 3. Typical ranges of the lateral and depth intervals contributing to an analysis in the various methods. Acronyms are given in Table 3, updated from [5].

field of research [40]. For its application in depth profiling analysis, the crucial fact is that surface atoms (or clusters) are abraded from the specimen by the energy transferred in the ion impact. The actual rate of erosion depends on various parameters (ion species and energy, angle of impact, mass and binding energy of specimen atoms, its crystal structure and orientation, etc.). Alteration of the specimen is caused by primary-ion implantation, displacement from collision cascades, stimulated diffusion, non-uniform selective sputtering, and adsorption of species from the vacuum system. All these effects contribute to a deviation of the measured depth profile from the original true profile and to a deterioration of the accuracy of a depth profile analysis.

Laterally resolved analysis

Since primary excitation is generally performed by means of particle beams, it is possible to form a laterally resolved excitation spot by adjusting focus and/or diaphragms, according to the resolving power of the beam-defining optics ("scanning" or "probe" methods). Beam optical imaging ("microscopy" of charged secondary particles – as the information carriers – is another concept successfully applied in TEM, SIMS and XPS (see articles by F.G. Rüdenauer and by K. Holldack and M. Grunze in this issue). Limitations of either approach are set by suffering from intensity losses, and by imaging imperfections. Typical ranges of lateral and depth intervals probed by the various methods are compared in Fig. 3.

3. Thin film analytical support in technology

In this issue, we have focused on a selection of thin film analytical application papers from intentionally rather different fields, to emphasize today's practical usefulness in actual analytical problem solving, and to exemplify the wide scope of thin-film analytical application to different branches of science and technology. The importance of analytical assistance in the development of advanced technology and materials is impressively exemplified in the field of microelectronics, which probably demonstrates today's highest degree of high-tech advancement in the sense of integration of *analytical* support into the *development and production* processes [11,42,43]. It is obvious, that the technological success of this approach will become increasingly significant also in other branches [e.g., 44–50], in the extent as the trends to miniaturization, high package density, high performance per unit mass, high degree of purity as well as of compositional definition or smaller accepted variability of properties (e.g., critical temperature of superconductors) are driven to their extreme performances. Further representative branches addressed by the papers of this topical issue are metallic and ceramic interfaces, friction and wear, oxidation, catalysts, superconductor materials and sensor devices, analysis of significant biological and environmental matter. Further important applications *not* covered here are organic polymers [51–54] and adhesive strength of coatings [55–58], modifications of organic materials surfaces by ion beams, insulating glassy advanced material [59], electrochemical phenomena [60,61], corrosion research [58,62–64], tribology and lubrication [65,66] optical, electro- and magneto-optical and magnetic materials.

4. Topical developments and techniques

Typical different methodological approaches were additionally considered in this issue's selection to convey a glance into the "analytical toolbox" of methods at hand for thin film applications today. Review papers are dedicated to highly topical methodical developments in three-dimensional imaging analysis, quantitative work in SIMS, application of RBS and ERD, and advancement in TOF-SIMS. Further methods addressed in more detail are XPS microscopy, use of low energy electrons, STEM, and scanning acoustic microscopy, SNMS, AES, XPS and EELS. Last but not least, a synergetic approach is demonstrated to be particularly fruitful in a variety of applications, reflecting an up-to-date im-

pression of its practical importance. It is based on the application of different analytical techniques to obtain results superior to those obtained with each technique applied separately.

The presentation also includes recent important techniques, principles and artifacts studied, viz. non-destructive analysis, high molecular weight compounds, sharp interfaces (spikes or delta-layers), selvage layer analysis, chemical speciation, use of factor analysis in electron spectrometry, and characterization of charging effects as well as electron radiation induced effects. Missing prime aspects are covered in review papers elsewhere, viz. studies of artefacts in depth profiling [67], specimen preparation to enhance performance characteristics of instrumental methods for interface analysis [13,25,48,68], spectroscopic ellipsometry for the characterization of surface layers [66], STM [69–71], laser ablation for microanalysis [72,73], TXRFA [74,75], Raman and FTIR spectrometry in thin film characterization [61,76,77] and others.

Particularly important topics for the advancement of thin film analysis are in the development of theoretical concepts for the understanding of basic physical processes, e.g., in the sputtering process [78], in the emission of atomic and cluster ions from surfaces, in post-ionization plasma diagnostics [39,79], in the electron depth distribution function [80], and in the electronic band structure diagnostics [81]. These aspects were deliberately omitted, as were instrumental inventions and technological engineering which are necessary to put analytical procedures into the industrial real life of analytical assistance [21].

Of course, this selection is incomplete as well as biased from our personal prospects. Nevertheless, it does represent a compendium of actual research papers from a wide variety of problem solutions and progress in thin film and interface analysis. Some emphasis is placed on the techniques for in situ characterization of interfaces, viz. techniques that cross over the limitations derived from the former requirements for ultra-high vacuum in the analytical specimen's inspection.

Table 5
Topical trends to information enhancement

	Information enhancement
Contrast	spectral resolution chemical selectivity intensity (dynamic range) signal-to-noise ratio spatial resolution depth (sputter conditions) lateral imaging capabilities (smaller beam diameter, "image" processing)
Quantification	data banks standard reference materials standard procedures, traceability
Sample maintainance	low damage
Analytical flexibility	samples types

5. Trends in thin film analysis

A number of topical improvements in thin film analysis is aimed at the enhancement of the information obtained. In Table 5, primary fields of such information enhancement are identified. These fields focus on enhancement of the analytical contrast, of the spatial resolution, and on improved quantification. To increase the reliability of the information from delicate specimens, a treatment as preservative as possible must be guaranteed. To enhance universal applicability of the information, methods and procedures should be used more flexibly with an increased variety of samples, like non-conductive materials, organic substances, biological cells, etc.

Although main emphasis of practical application is undoubtedly in the field of electron spectroscopies, a clear trend is to be seen in the ion spectroscopies to overcome the most important limitations in the features addressed in Fig. 1:

(1) Significantly improve the reliability of SIMS-related techniques (see review by G. Stingeder) and
(2) Enhance the efficiency of sputtered particles detection (see [84] and papers on SNMS in this issue),

(3) Push forward the performance concerning local selectivity, analytical information yield and data processing in three dimensional SIMS (see review by F.G. Rüdenauer)
(4) Get accessible information about the chemical status of the surface composition "as it was before analysis started" by use of sputtered particles, because they carry information about the surface composition *before* their removal. It is essential to remove only 10^{-4} per analysis from the surface monolayer so that every impinging primary ion on the average hits an undisturbed spot on the surface [84], and
(5) Profit from the potential for high accurate determination procedures via the combined use of corroborating methods [11,12,64,82] including high energy ion scattering spectrometry (see review by L.J. van IJzendoorn).

Very important and promising topics are (a) the development and validation of the basic theory for the physical processes involved in AES, XPS, SIMS, SNMS and (b) the preparation and characterization of suitable reference materials and reference data [22,33,38,83].

6. Trends to interface analysis

Interfaces are becoming more and more important, as technology turns to steadily decreasing dimensions in microstructures of components. A similar trend holds for the interest in ever decreasing dimensions of parts of systems analyzed in biological, medical, and environmental studies reaching from cell components to single particles in fine aerosols. Such interfaces cover a manifold extending by far over the domain of surfaces, which just represent the special case of an interface between the gas (or vacuum) phase and a condensed phase. During last years, however, an increasing interest is spent to the structure, composition and properties of interfaces between adjacent condensed phases, and an increasing demand exists to develop techniques adjusted to the characterization of those interfaces, too. Therefore, considering the analytical characterization of interfaces, in general, the term "surface analysis", established for the past two decades in commercially applied analytical work, was chosen to be changed into "analysis of thin films, interfaces and surfaces" for the title of this issue. In this way, we accommodate to the research trend aimed at studies of transition phases in junctions in condensed matter.

Mostly, this aim is tackled today in different ways, viz. adapting and optimizing the existing strategies and techniques from surfaces analysis to the modified tasks in characterizing such transition phases, i.e., by converting the initial *interface* analytical task into a *surface* analytical job, by means of exposing the interface region (or the transition phase) to vacuum, either by ion-sputtering, by mechanical means (peeling, cracking, scribing), or by chemical agents (etching, anodization). On the other hand, increasing efforts exist in developing in situ techniques to characterize "buried" structures and thin films. Techniques have to be used, that are completely new to this field of thin film analytical applications, including synchrotron radiation sources as well as coincidence spectrometry resolving very short pulse times. At the surface layers, electron spectroscopies are used to probe the electronic density distribution, to get information about the states of energy of the binding electrons, and thus to conclude about the chemical species present. From buried layers, however, highly sophisticated variants of molecular spectroscopies have to be used to get any information about the chemical states. The information carrier species have to be maintained during traversing much greater depths. One problem now, in interface analysis, is how to define exactly the probed depth in the specimen. One typical approach to solve this problem is to allow for slowing down the primary particle of a given energy E_{PO}, but to utilize an excitation/information-emitting process that shows a distinct resonance quality at a characteristic energy $E_{Res} < E_{PO}$. A second approach is to unfold, by tomography, the excitation/information-emitting profile from the measured response integrated over layers at different depth. Applications to practical analysis in this field are still very hand-picked. Acoustic microscopy and descendants offer a very interesting potential in

that respect. Further important methods include RBS, NRA, ATR-IR.

7. Trends to in-line diagnostic techniques

In technological development, every step in the product line from research to development and to the product needs a specific kind of analytical methodology. These different phases of analytical investigations can be subdivided into [1]

(1) properties of materials and phenomena in processes,
(2) functional verification of devices,
(3) parameters relevant for device breakdown, failures or low yield in production output, and
(4) processing parameters monitoring; optimization of process output as a function of multiple parameters.

These four phases analytically support four phases of technological development, which are characterized as

(1) research in materials and processes,
(2) development of a product design,
(3) development of processing design, and
(4) production stage.

There exists an increasing demand for methods qualified for in-line diagnostics of devices for non-destructive monitoring of process parameters.

To meet this demand, methods are favoured that are capable merely to measure some indicative selected information, fast and reliably, instead of a comprehensive analytical characterization of the device. Thus, in-line diagnostics can be used as a relevant information carrier in the transfer of scientific insight based on analytical data into successful modern technological processing.

In this way, thin film analysis is contributing to improved product quality, increased productivity, and preservation of materials resources, helping also in solving society-relevant problems. To be successful, this approach requires close contact and interdisciplinary partnership of the analyst with the technological engineer, in this application, or with other relevant scientific branches, in numerous other analytical applications.

References

[1] H.W. Werner and M. Grasserbauer, in M. Grasserbauer and H.W. Werner (Eds.), Analysis of Microelectronic Materials and Devices, Wiley, Chichester, 1991, pp. XVI–XLI.
[2] G. Tölg, Analyst, 112 (1987) 365.
[3] R. Fischbach, Nachr. Chem. Tech. Lab., 41 (1993) 54.
[4] M.P. Seah and D. Briggs, in D. Briggs and M.P. Seah (Eds.), Practical Surface Analysis, Vol. 1, Auger and X-Ray Photoelectron Spectroscopy, Wiley, Chichester, 2nd edn., 1990, p. 1.
[5] H.W. Werner and R.P.H. Garten, Rep. Progr. Phys., 47 (1984) 221.
[6] G.A. Somorjai, Surf. Interface Anal., 19 (1992) 493.
[7] F. Garbassi and E. Ochiello, Anal. Chim. Acta, 197 (1987) 1.
[8] A.J. Kinloch, J. Mater. Sci., 15 (1980) 2141.
[9] C. Boiziau and G. Lecayon, Surf. Interface Anal., 12 (1988) 475.
[10] C.R. Brundle, Fresenius' Z. Anal. Chem., 324 (1986) 426.
[11] M. Grasserbauer and H.W. Werner (Eds.), Analysis of Microelectronic Materials and Devices, Wiley, Chichester, 1991.
[12] P. Alnot, A.M. Huber and J. Olivier, Surf. Interface Anal., 9 (1986) 283.
[13] M.P.A. Viegers, A.F. De Jong and M.R. Leys, Spectrochim. Acta, 40B (1985) 835.
[14] P.R. Boudewijn, M.R. Leys and F. Roozeboom, Surf. Interface Anal., 9 (1986) 303.
[15] M. Gauneau, R. Chaplain, A. Regreni, M. Salvi, G. Guillemot, R. Azoulay and N. Duhamel, Surf. Interface Anal., 11 (1988) 545.
[16] K. Ploog, Surf. Interface Anal., 12 (1988) 279.
[17] W.D. Chen, H. Bender, A. Demesmaeker, W. Vandervorst and H.E. Maes, Surf. Interface Anal., 12 (1988) 156.
[18] M. Meuris, W. Vandervorst and H.E. Maes, Surf. Interface Anal., 12 (1988) 339.
[19] R. v. Criegern, H. Zeininger and S. Röhl, Proceedings of the Sixth International Conference on Secondary Ion Mass Spectrometry, SIMS VI, Versailles, 1987, A Benninghoven, A.M. Huber and H.W. Werner (Eds.), Secondary Ion Mass Spectrometry SIMS VI, Wiley, Chichester, 1988, pp. 419–422.
[20] R.G. Musket, W. McLean, C.A. Colmenares, S.M. Makowieck and W.J. Sieckhaus, Appl. Surf. Sci., 10 (1982) 143.
[21] J.C. Riviere, Surface Analytical Techniques, Oxford University Press, Oxford, 1990.
[22] M. Schmidt, E. te Kaat, H. Bubert and R.P.H. Garten, Fresenius' Z. Anal. Chem., 319 (1984) 616.
[23] J.M. Walls, D.D. Hall and D.E. Sykes, Surf. Interface Anal., 1 (1979) 204.

[24] S. Hofmann, Scanning Microscopy, 1 (1987) 989.
[25] R. v. Criegern, R. Lange-Gieseler and H. Zeininger, Fresenius' J. Anal. Chem., 341 (1991) 60.
[26] H.W. Werner and R.P.H. Garten, Trends Anal. Chem., 4 (1985) 11.
[27] R. Behrisch (Ed.), Sputtering by Particle Bombardment, Vols. I and II, Topics in Appl. Phys. Vols. 47, 52, Springer Verlag, Berlin, 1981, 1983
[28] A. Benninghoven, F.G. Rüdenauer and H.W. Werner, Secondary Ion Mass Spectrometry, Chemical Analysis Vol. 86, Wiley, New York, 1987.
[29] S. Hofmann, Surf. Interface Anal., 2 (1980) 148.
[30] H.W. Werner, Acta Electronica, 19 (1976) 53.
[31] H. Oechsner (Ed.), Thin Film and Depth Profile Analysis, Topics in Current Phys. Vol. 37, Springer Verlag, Berlin, 1984.
[32] S. Storp, Spectrochim. Acta, 40B (1985) 745.
[33] A. Zalar and S. Hofmann, Surf. Interface Anal., 2 (1980) 183.
[34] M.P. Seah and C.P. Hunt, Surf. Interface Anal., 5 (1983) 33.
[35] H.W. Werner, Surf. Interface Anal., 4 (1982) 1.
[36] J. Fine and B. Navinsek, J. Vac. Sci. Technol., A3 (1985) 1408.
[37] J. Fine, P.A. Lindfors, M.E. Gorman, R.L. Gerlach, B. Navinsek, D.F. Mitchell and G.P. Chambers, J. Vac. Sci Technol., A3 (1985) 1413.
[38] A. Zalar and S. Hofmann, J. Vac. Sci. Technol., A5 (1987) 1209.
[39] P. Beckmann, M. Kopnarski and H. Oechsner, Mikrochim. Acta, Suppl. 11 (1985) 79.
[40] N.Q. Lam, Surf. Interface Anal., 12 (1988) 65.
[41] B.O. Kolbesen and W. Pamler, Fresenius' Z. Anal. Chem., 333 (1989) 561.
[42] M.G. Dowsett, Fresenius' J. Anal. Chem., 341 (1991) 224.
[43] A. van der Wijk and H.W. Werner, Surf. Interface Anal., 16 (1990) 253.
[44] M. Amstutz and M. Textor, Surf. Interface Anal., 19 (1992) 595.
[45] P. Wilhartitz and H.M. Ortner, Fresenius' J. Anal. Chem., 341 (1991) 224.
[46] H. Puderbach, H. Bubert, A. Quentmeier, R.P.H. Garten and S. Storp, Mikrochim. Acta, Suppl. 11 (1985) 103.
[47] M. Rühle, Mikrochim. Acta, Suppl. 12 (1992) 75.
[48] W. Mader, Z. Metallkd., 83 (1992) 478.
[49] S. Oswald, L. Siegert and G. Große, Fresenius' J. Anal. Chem., 341 (1991) 180.
[50] G. Ziegler, Fresenius' Z. Anal. Chem., 333 (1989) 360.
[51] G. Marletta, S.M. Catalano and S. Pignataro, Surf. Interface Anal., 16 (1990) 407.
[52] L. Sabbatini and P.G. Zambonin (Eds.), Surface Characterization of Advanced Polymers, Verlag Chemie, Weinheim, 1993.
[53] D. Briggs, in D. Briggs and M.P. Seah, Practical Surface Analysis, Vol. 1, Auger and X-Ray Photoelectron Spectroscopy, Wiley, Chichester, 2nd edn., 1990, Chap. 9, pp. 359–396.
[54] W. Knoll, W. Hickel, M. Sawodny, J. Stumpe and H. Knobloch, Fresenius' J. Anal. Chem., 341 (1991) 272.
[55] J.W. Severin, Thesis, Technical University Eindhoven, 1993.
[56] W.J. van Ooij and A. Sabata, Surf. Interface Anal., 19 (1992) 101.
[57] W.L. Baun, Appl. Surf. Sci, 4 (1980) 291 and 374.
[58] H. Nickel, Spectrochim. Acta, 47B (1992) 27.
[59] K. Miethe, poster C23 presented at the 7th Arbeitstagung Angewandte Oberflächenanalytik, Jülich, June 1992, Abstracts, p. 129.
[60] P. Marcus and I. Olefjord, Surf. Interface Anal., 11 (1988) 569.
[61] R. Kellner and G. Götzinger, Fresenius' Z. Anal. Chem., 319 (1987) 837; B. Mizaikoff, K. Taga and R. Kellner, Fresenius' J. Anal. Chem., 346 (1993) 355.
[62] J.E. Castle, Surf. Interface Anal., 9 (1986) 345.
[63] H. Fischmeister, Fresenius' Z. Anal. Chem., 322 (1988) 421.
[64] R. Holm, D. Holtkamp, R. Kleinstück, H.-J. Rother and S. Storp, Fresenius' Z. Anal. Chem., 333 (1989) 546.
[65] H.J. Mathieu, D. Landolt and R. Schuhmacher, Surf. Interface Anal., 9 (1986) 477.
[66] A. Röseler, Fresenius' J. Anal. Chem., 346 (1993) 358.
[67] S. Hofmann, Progr. Surf. Sci., 36 (1991) 35.
[68] M. Rühle, Fresenius' J. Anal. Chem., 341 (1991) 369.
[69] G.K. Binning and H. Rohrer, Rev. Mod. Phys., 59 (1987) 615.
[70] K. Besocke, Fresenius' Z. Anal. Chem., 333 (1989) 312.
[71] G. Friedbacher, P.K. Hansma, D. Schwarzenbach, M. Grasserbauer and H. Nickel, Anal. Chem., 64 (1992) 1760.
[72] L. Moenke-Blankenburg, in J.D. Winefordner (Ed.), Laser Microanalysis, Chemical Analysis, Vol. 105, Wiley, New York, 1989, p. 288.
[73] A. Ciocan, J. Uebbing and K. Niemax, Spectrochim. Acta, 47B (1992) 611.
[74] V. Penka and W. Hub, Spectrochim. Acta, 44B (1989) 483.
[75] W.W. van den Hoogenhof and D.K.G. de Boer, Spectrochim. Acta, 48B (1993) 277.
[76] J. Oelichmann, Fresenius' Z. Anal. Chem., 333 (1989) 353.
[77] G. Kolb, Th. Salbert and G. Abstreiter, Fresenius' J. Anal. Chem., 341 (1991) 166.
[78] P. Sigmund, in R. Behrisch (Ed.), Sputtering by Particle Bombardement, Vol. I, Topics in Appl. Phys. 47, Springer Verlag, Berlin, 1981, pp. 9–72.
[79] H. Oechsner, Z. Phys., 261 (1978) 37.
[80] W.S.M. Werner, Surf. Interface Anal., 18 (1992) 217.
[81] R. Weissmann and K. Müller, Surf. Sci. Rep., 105 (1981) 251.
[82] M. Grasserbauer, presented at the 12th Int. Symp. Microchemical Techniques, Sept. 7–12, 1992, Córdoba.
[83] R.P.H. Garten, H. Bubert and L. Palmetshofer, Anal. Chem., 64 (1992) 1100.
[84] E. Niehuis, in preparation.

ELSEVIER

Analytica Chimica Acta 297 (1994) 15–26

ANALYTICA CHIMICA ACTA

Surface analysis of thin films and interfaces in commercial aluminium products

M. Textor [a], M. Amstutz

Alusuisse-Lonza Services Ltd., Research and Development, 8212 Neuhausen am Rheinfall (Switzerland)

Received 11th June 1993; revised manuscript received 29th September 1993

Abstract

Interfaces in commercial aluminium-based products like surface coated sheet and extrusions, laminates and metal matrix composites are of decisive importance to the producer and customer as regards product performance and long term quality. The application of surface-sensitive techniques [x-ray photoelectron spectroscopy (XPS), secondary ion mass spectrometry (SIMS), secondary neutral mass spectrometry (SNMS), x-ray fluorescence spectroscopy (XRF), transmission electron microscopy (TEM)] to study and control the composition and structure of oxide layers and conversion coatings, which become the interface in aluminium-polymer products, is discussed. Quantitative evaluation of surface enrichment processes of alkali and earth alkaline metals during aluminium foil annealing allows the producer to establish quality relevant upper limits for the concentration of these impurity elements. Two further examples are related to solid–liquid interfaces and cover the influence of oxide films on the etchability of high purity aluminium for electrolytic capacitors and the surface composition of aluminium–gallium (AlGa) alloys during alkaline etching with Ga surface enrichment having a large influence on the electrochemical potential of this battery anode material.

Keywords: Surface techniques; Thin films; Aluminium; Laminates; Metal matrix composites

An increasing proportion of commercial aluminium-based products is either surface coated or composed of different materials. Examples are pretreated and lacquered car body sheet, structural aluminium–polymer–aluminium laminates for light weight architectural applications, particle and fibre reinforced metal matrix composites, lacquered foil and thin laminates for the packaging industry. In all these cases interface structure and composition is of decisive importance to the properties and quality of the products. Failure during service life is often related to interfacial reactions reducing the integrity of the multimaterial products or the adhesion of surface coatings; although a problem related in many cases to decorative rather than to functional aspects, the damage is potentially very large.

Interfaces in commercial aluminium-based products are in many cases related to one of the following general cases.

Correspondence to: M. Textor, Alusuisse-Lonza Services Ltd., Research and Development, 8212 Neuhausen am Rheinfall (Switzerland).

SSDI 0003-2670(93)E0550-Q

Al(metal)–aluminium oxide–lacquer or polymer interface

The interface is either a natural oxide film typically 3–10 nm thick grown during aluminium fabrication (e.g., rolling, annealing) or an artificially reinforced oxide layer of 0.1–5 μm thickness (e.g., via anodization, chemical or plasma oxidation). The first case is typical for lacquered or laminated thin foil which cannot be treated by wet-chemical methods. The main factors governing interfacial properties are metal composition, rolling lubricant quality and annealing conditions since these will primarily determine the composition of the oxide film and of the local oxide–X interface with X being a lacquer or polymer. The second case of artificially reinforced oxide films is commercially important for thin strip and thicker gauged material that can be coil anodized (continuous anodising of aluminium strip) and where higher requirements regarding the corrosion resistance of the interface have to be met, e.g., for architectural sheet and extrusions or for lithographic sheet. The main factors influencing the structure and composition of anodic oxide films are the type and temperature of the electrolyte and the bath parameters (current density, voltage, time of treatment).

Al(metal)–conversion coating–lacquer or polymer interface

Conversion coatings produced by wet-chemical immersion processes are the most important interfaces where highest requirements regarding the corrosion resistance of lacquered or painted aluminium surfaces have to be met, e.g., in automotive and architectural applications. Chromate, chromium phosphate and zinc phosphate showed the best performance, but environmentally more acceptable alternatives based on titanium and zirconium compounds have been developed and are used for applications where less severe corrosion situations have to be dealt with, e.g., in packaging application like aluminium cans. X is generally a lacquer, paint, adhesive or polymer foil. The factors of importance are primarily type and conditions of the conversion process and to a lower degree type and microstructure of the underlying alloy.

Al(metal)–metal B–metal C

Electroplating of aluminium needs special pretreatment processes in order to establish a sound bonding between the substrate and the electroplated layer. The natural oxide film on aluminium has to be removed and replaced by a metallic film forming a stable bond to the electroplated metal layer. The metallic film is generally zinc (often modified with other metals like iron and manganese to reduce the tendency of critical galvanic element formation) or tin which forms during treatment in alkaline zincate and stannate bath processes respectively. The oxide film is removed in these processes and zinc or tin deposited on the aluminium surface via a redox process.

Surface-analytical techniques and electron microscopy are important tools to study and better understand the chemistry and the factors of influence related to interfacial reactions [1]. Four examples have been chosen to illustrate the application of surface-sensitive methods, two are related to solid–solid, two to solid–liquid interfaces:

(1) preferential migration of alkali and alkaline earth elements in lacquered or laminated aluminium foil during annealing, a potential cause of interfacial corrosion and undermining under corrosive conditions;

(2) control of thickness and composition of conversion coatings as a pretreatment before application of organic coatings for automotive car body sheet, architectural sheet and thin strip for packaging applications;

(3) surface oxide films influencing the formation of etch structures during electrolytic etching of high purity aluminium foil for electrolytic capacitors;

(4) interfacial enrichment of gallium in aluminium during caustic soda etching affecting the corrosion potential and the use of 'active' aluminium alloys as battery anodes.

1. Experimental

X-ray photoelectron (XP) spectra were obtained with a Leybold LH 10 instrument equipped

with an Al x-ray source, secondary ion mass (SIM) spectra with the same instrument using a Leybold IQE 12/38 ion source (3 kV Ar^+ or O_2^+ primary ions) and a Balzers QMG 511 quadrupole mass spectrometer. The typical back pressure is 5×10^{-9} mbar.

Secondary neutral mass spectrometry (SNMS) was used in a separate instrument, the Leybold INA 3. Typical measuring conditions were: target potential 375–400 V, RF power 170–180 W, plasma pressure $(3–4) \times 10^{-3}$ mbar.

For transmission electron studies surface oxide films were detached from the aluminium substrate by dissolving the metal by either the bromine–methanol or mercury chloride–methanol technique. The oxide films were washed with methanol and mounted on conventional TEM grids.

Chromate films were analysed for chromium by x-ray fluorescence (XRF) spectroscopy using either a Philips PW 1400 instrument and an Sc/Mo double-anode x-ray source or a Portaspec 2501 portable non-vacuum instrument and a W x-ray source. Absolute chromium coverage was determined by dissolving the chromate layer in 2 M NaOH, neutralizing the NaOH solution with HNO_3 and analysing the chromium concentration in an inductively coupled plasma (ICP) spectrometer.

2. Results and discussion

Oxide film properties on annealed aluminium foils

The thickness and composition of oxide films on aluminium alloys depend on both metal composition and fabrication conditions (rolling, thermal treatment, surface treatment). Since the surface quality of the final product related for example to corrosion resistance or adhesion strength in composite materials depends upon the properties of the oxide film, it is crucial to have an improved understanding of the (quantitative) relationship between surface composition and product surface properties. This is particularly true for aluminium foil, for which high standards have to be met with regard to surface cleanliness, wettability of lacquers, etc. X-ray photoelectron

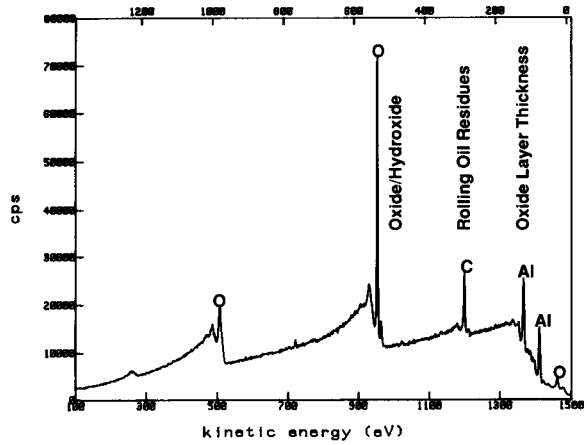

Fig. 1. XP spectrum (Al $K\alpha$ radiation) of an annealed Al 99.2 foil surface.

spectroscopy (XPS) is particularly suited for studying the average thickness and composition of oxide films on foil surfaces. The XP spectrum of a typical annealed Al 99.2 foil surface is shown in Fig. 1. Typically three spectral regions are of particular interest.

(1) Al 2s and Al 2p: the relative intensities of metal and oxide peaks (chemical shift typically 2.9 eV) allow calculation of the oxide film thickness with high reproducibility [2–4].

(2) The C 1s peak area carries information on the presence and concentration of hydrocarbon, alkoxy and carboxylate residues from lubricants used during the cold-rolling process [3,5].

(3) The O 1s region can give information on the relative proportion of oxide and hydroxide surface species. Early stages of oxide hydration and surface corrosion processes can easily be followed, as shown in Fig. 2. For the case of an unstable oxide film, which – as a function of time in humid air – is converted to a thickened hydroxide layer, the Al 2p (metal) signal diminishes while at the same time a second O 1s emission at a binding energy of 534 eV appears which is typical of hydroxide. During the history of this sample the atomic stoichiometry (calculated from relative XPS sensitivity factors) changes from 1.55 (near 1.5 corresponding to Al_2O_3) to 2.80 (near $Al(OH)_3$ stoichiometry).

The reason for a reduced chemical stability of

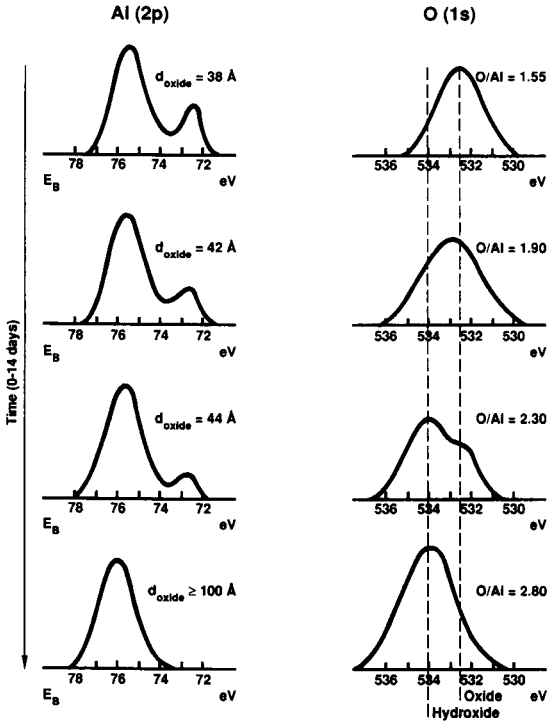

Fig. 2. Al 2p and 0 1s XP spectra of an unstable oxide film on aluminium foil as a function of time (in total ca. 14 days) in air of relative humidity > 60%.

oxide films cannot always be defined by an XPS investigation owing to the relatively low sensitivity of this method. Surface analysis and depth profiling using the generally much more sensitive SIMS technique often give valuable additional information. Examples are the massive surface enrichment of lithium and magnesium (present as low-level impurities in commercial aluminium) during the degreasing annealing process which is used to remove the volatile organic rolling oil residues from the foil surface [3,6]. Fig. 3 is a SIMS spectrum (positive ions) of an aluminium foil annealed at 280°C. Despite the low concentration of lithium (3 ppm) and magnesium (12 ppm) in the aluminium metal, high intensities of $^{7}Li^{+}$ and $^{24}Mg^{+}$ in the surface (oxide) SIMS spectrum point to substantial surface enrichment of these two impurity elements in annealed aluminium foil. Fig. 4 proves that the observed surface enrichment is a thermally activated process. During the annealing, Na, Mg and particularly Li are en-

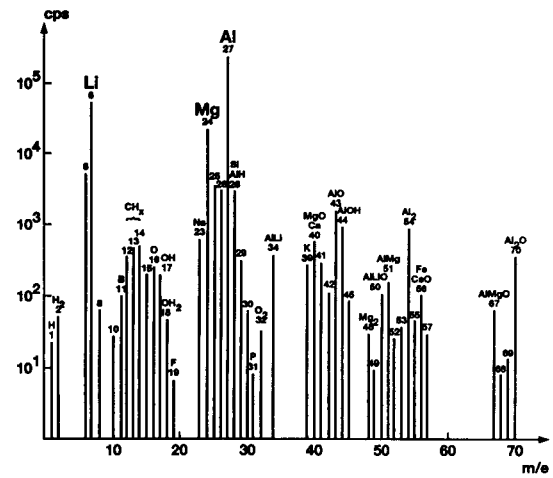

Fig. 3. Positive SIMS spectrum of the oxide film on aluminium foil annealed at 280°C. High intensities of $^{7}Li^{+}$ and $^{24}Mg^{+}$ point to massive surface enrichment of these two impurity elements in the oxide film.

riched in the surface oxide film by 2–4 orders of magnitude compared to their bulk concentration and reduce the chemical stability of the oxide

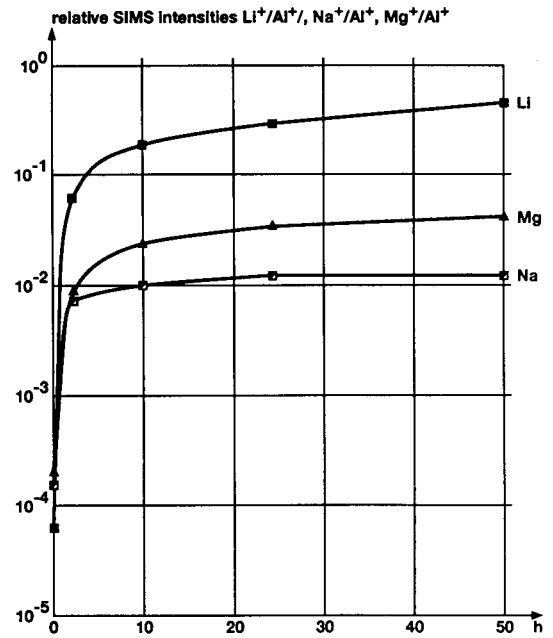

Fig. 4. Relative SIMS intensities $^{7}Li^{+}/^{27}Al^{+}$, $^{23}Na^{+}/^{27}Al^{+}$ and $^{24}Mg^{+}/^{27}Al^{+}$ for electropolished (0 h) aluminium foil and as a function of annealing time up to 50 h at 280°C. Foil quality: Al 99.2, 3 ppm Li, 8 ppm Na, 12 ppm Mg, foil gauge: 8 μm.

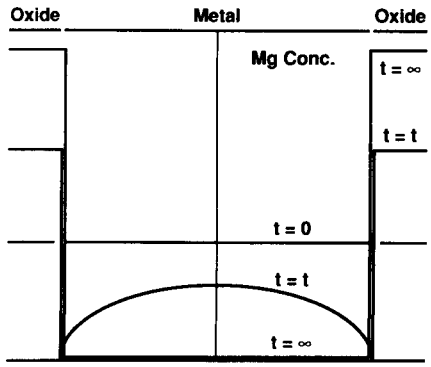

Fig. 5. Schematic drawing of the magnesium concentration across an aluminium foil assuming a model of thermally induced surface enrichment and diffusion of magnesium to the aluminium oxide interfaces as the rate determining step.

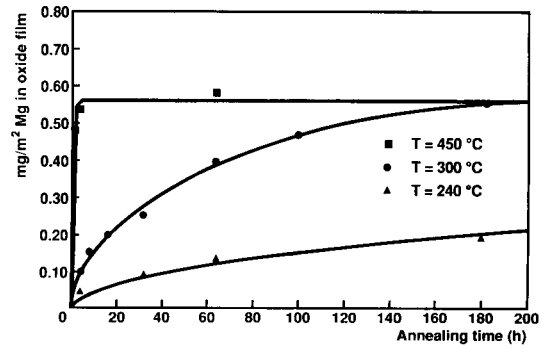

Fig. 6. Magnesium surface concentration determined by integration of quantitative SIMS depth profiles as a function of annealing time at temperatures of 240, 300 and 450°C. Commercial Al 99.2 foil, 40 μm thick, bulk Mg concentration 11 ppm. Symbols refer to experimental values, solid lines to calculated curves (see text and Ref. 8).

film (Fig. 2). Therefore these trace elements with a high negative free energy for oxide formation and a high diffusion coefficient in aluminium metal have to be carefully controlled in foil alloys in order to guarantee a high corrosion resistance and good adhesion stability of lacquered aluminium foil for packaging applications.

In the case of magnesium impurity levels the surface enrichment during annealing can be described by a simple model (Fig. 5) with the diffusion of magnesium to the surface as the rate-determining step followed by rapid oxidation and incorporation into the oxide film [7,8]. The diffusion coefficient was adjusted to fit the experimental magnesium surface concentrations, which were determined through a quantification of SIMS intensities, integration of the depth profiles and conversion to quantitative surface coverage values (mg m^{-2}). Fig. 6 demonstrates in the case of a 40-μm Al 99.2 foil with a magnesium impurity level in the metal of 11 ppm the excellent match achieved between the calculated curve of magnesium surface coverage as a function of annealing time for 240, 300 and 450°C annealing temperature and the experimentally determined values. At long enough annealing times the surface coverage approaches an upper limit corresponding to the situation where all magnesium has segregated to the two surfaces of the foil. Six different commercial alloys used for foil production were systematically analysed. The diffusion coefficient adjusted to best fit the experimental values turned out to be mainly dependent on grain size (Fig. 7). This observation points to grain boundary diffusion as an important mechanism in magnesium surface segregation, at least at the relatively low temperature studied here. Knowing the alloy grain-size-dependent diffusion coefficient, it is then possible to predict the magnesium surface concentration for a specific combination of parameters, i.e., magnesium concentration in the metal, foil gauge, annealing temperature and an-

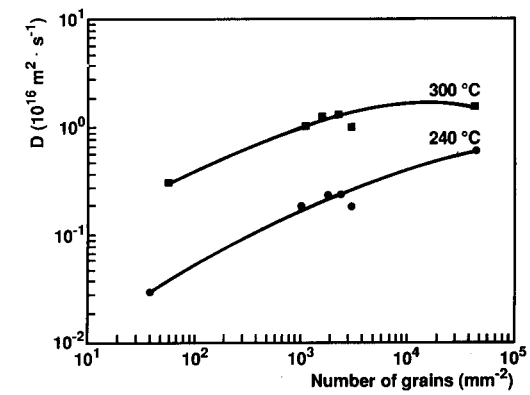

Fig. 7. Diffusion coefficient of magnesium in different commercial aluminium foil qualities as a function of grain size (number of grains per mm^2) in the aluminium foil at temperatures of 240 and 300°C.

nealing time. Since an upper limit of surface magnesium concentration must not be exceeded for specific foil products, the model provides production supervision with a much more precise tool for control of potential magnesium-induced surface problems, for example interfacial corrosion or loss of lacquer adhesion in converted packaging foils.

The experimental evidence gained by XPS and SIMS analysis points to the following surface reactions taking place during the annealing process:

(i) reduction of the physisorbed rolling oil lubricant film;

(ii) increase of oxide film thickness;

(iii) enrichment of alkali and earth alkaline trace elements due to the reaction with either oxygen and/or the aluminium oxide film.

Lacquered foils with increased concentrations of these elements at the oxidic interface are more susceptible to loss of lacquer adhesion during use in corrosive situations (e.g., sterilizing, fruit juice packaging, etc.). Both alkaline undermining and blister formation by osmosis have been shown to cause magnesium oxide induced delamination. Our view of the surface reactions taking place is schematically illustrated in Fig. 8.

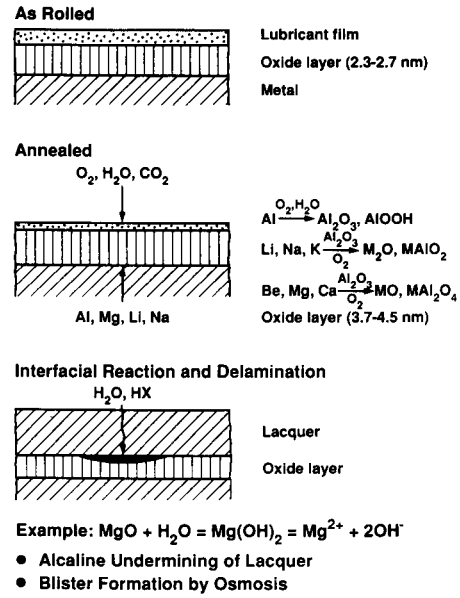

Fig. 8. Schematic drawing of the surface composition of as rolled and annealed aluminium foil and the chemical reactions taking place during annealing of foil and for alkali and alkaline earth element induced interfacial reactions and delamination of lacquer.

Conversion coatings

High requirements regarding the long-term stability of aluminium–lacquer interfaces have to be satisfied to meet external architectural requirements (e.g., facades) and also to satisfy the needs of the automotive industry (e.g., for car body sheet). Chromate, chromium phosphate and zinc phosphate conversion coatings are particularly effective pretreatment techniques before applying organic coats. Film formation reactions and composition of these coatings are shown in

Table 1
Filmforming reactions and composition of conversion coatings: chromate, chromium phosphate and zinc phosphate

Chromating		
Etch (acid):	$Al + 3H^+ \rightarrow Al^{3+} + 3H$	
Coating composition:	Chromium phosphate (Cr III):	
	$CrPO_4$, $AlPO_4$	
	Chromate (Cr VI):	
	$Cr(OH)_2 \cdot HCrO_4$, $Al(OH)_3$, $Cr(OH)_3$, $CrFe(CN)_6$	
Phosphating		
Etch (alkaline):	$Al + 3H_2O + 6F^- \rightarrow AlF_6^{3-} + 3H + 3OH^-$	
Coating formation:	20–50 ppm $F^- \rightarrow$	No coating formed on Al
	400-600 ppm $F^- \rightarrow$	Coating created on Al
		$AlPO_4$
		$Zn_3(PO_4)_2 \cdot xH_2O$ (Hopeit)
		$Zn_2M(PO_4)_2 \cdot xH_2O$ (M = Ni, Mn)

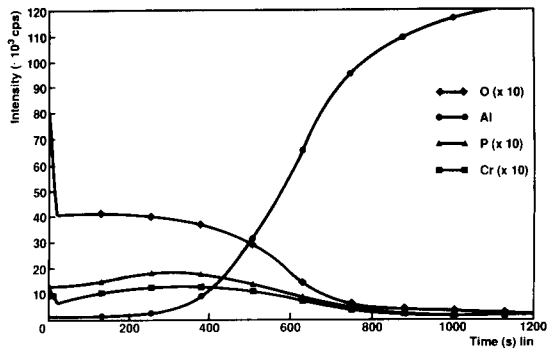

Fig. 9. SNMS depth profile (intensities as a function of sputtering time) of a chromium phosphate conversion layer on aluminium. Surface coverage is 140 mg m^{-2} Cr, corresponding to an approximate layer thickness of 280 nm.

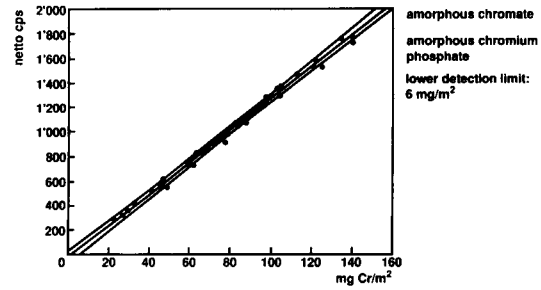

Fig. 11. Cr $K\alpha$ intensities (background substracted) measured with a portable XRF spectrometer as a function of absolute chromium surface coverage for chromate and chromium phosphate conversion coatings on AlMg1 sheet samples. The three solid lines refer to the best fit curve and the 95% confidence limits respectively. Lower detection limit 6 mg m^{-2} Cr.

Table 1. Both the stoichiometry and film thickness are important quality factors and depth profiling using the SNMS technique is a particularly effective means of gathering the relevant information quickly. Fig. 9 shows the SNMS depth profiles using 375 eV Ar^+ ion bombardment through a chromium phosphate conversion layer. Provided that suitable standards are available, the SNMS intensities can be quantified and integrated intensities along the depth profiles can be correlated with absolute coverage, e.g., mg m^{-2} Cr as shown in Fig. 10. Deviation from thickness and/or stoichiometry, established using ideal standards, can therefore be easily detected.

In production, however, it is generally sufficient and much more cost-effective simply to control the thickness of the conversion coating. This

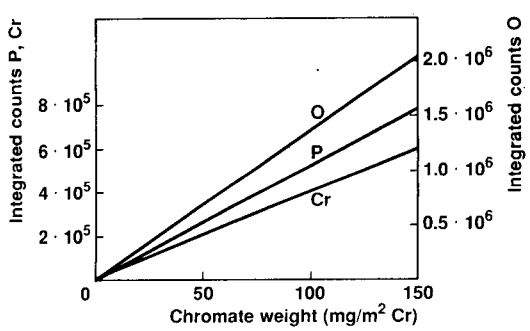

Fig. 10. Integrated SNMS intensities along the depth profile through chromium phosphate conversion coatings on aluminium as a function of chromium surface coverage.

can easily be established using the XRF technique, and portable spectrometers working under atmospheric pressure are sufficiently sensitive and accurate to determine chromium surface coverage in a reliable way (Fig. 11). The typical detection limit is 6 mg m^{-2} Cr, corresponding to a coating thickness of ca. 12 nm.

Surface properties affecting etchability

An important application of high-purity aluminium foil (typically Al 99.99, 50–150 μm thick) is for electrolytic capacitors. The foil is etched in chloride electrolytes, generally by electrochemical techniques, to increase the specific surface area and hence the electrical capacitance. Following the etching procedure the foil is anodized in barrier-type-forming electrolytes to the desired voltage (Fig. 12).

In the case of anode foil for high-voltage applications (up to 600 V) a tunnel-like etch structure is particularly effective. Fig. 13 shows a typical crystallographically oriented etch structure with high tunnel density; the tunnels have diameters which can be adjusted from 0.2 μm to several microns and extend typically from 20 to 60 μm into the material. High tunnel densities are essential for achieving high capacitance values. During potentiostatic etching in chloride electrolytes three subsequent stages in the current i vs. time t diagram are observed experimentally (Fig. 14): (1) oxide dissolution and chloride-in-

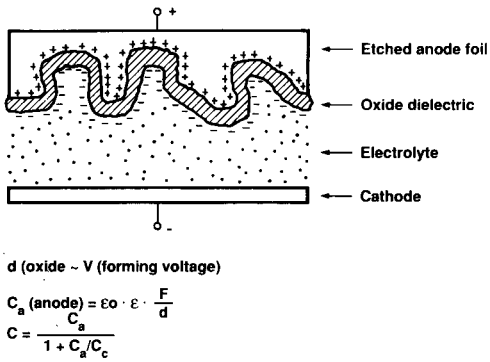

Fig. 12. Schematic drawing of a capacitor with an etched anode foil of high specific surface F, anodically oxidized to form a dielectric oxide layer thickness d and a total capacitance C.

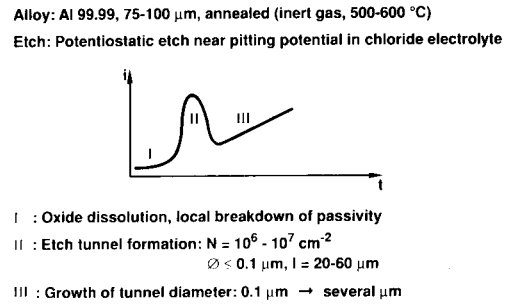

Fig. 14. Potentiostatic etching of high purity aluminium foil in chloride electrolyte with three distinct phases in the current i vs. time t plot. N = Tunnel density, l = tunnel length.

duced local breakdown of the oxide film; (2) formation of etch tunnels with a density N of 10^6–10^7 cm^{-2} and final length l; (3) increase of tunnel diameter due to dissolution of the tunnel walls.

Tunnel initiation is dependent on several factors. The most important single factor is the chemical nature of the oxide film that forms during a high-temperature final annealing cycle (500–600°C) of the as-rolled foil and forms the initial interface between the aluminium metal foil and the aqueous etching electrolyte. Many different laboratory-annealed samples have been surface analysed by XPS and TEM of detached oxide films to establish the relationship between oxide film properties and etch response, particularly etch tunnel density. Fig. 15 demonstrates three different situations.

(1) XPS shows the oxide layer to be primarily composed of Al and O with small amounts of Si, Ca and N (as ammonium; the N 1s binding energy equals 401 eV). The oxide layer is amorphous (no electron diffraction pattern), but some

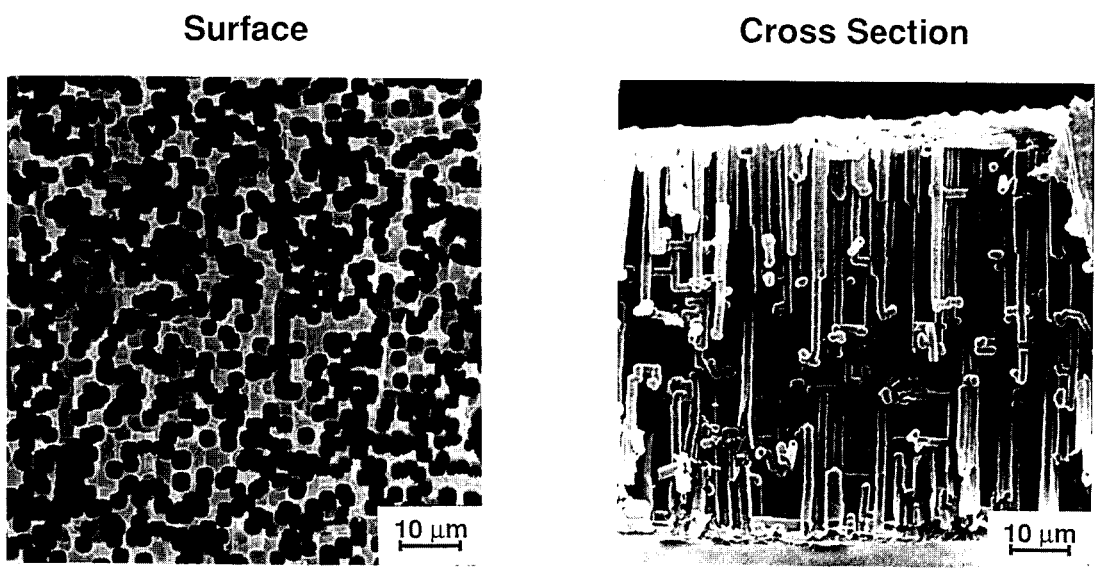

Fig. 13. Tunnel etch structure of an Al 99.99 anode foil used for electrolytic capacitors. Left: SEM image of the surface. Right: cross-section with three-dimensional view of the tunnel structure. Sample preparation: oxidation of pore walls (barrier oxide layer) and dissolution of the metal to show the oxide replica.

local thickening of the oxide film is observed. This is probably a precursor to crystalline γ-Al_2O_3 formation and is likely to influence the local breakdown of passivity in chloride electrolytes, which is the first step in the localized tunnel formation mechanism.

(2) In the second case the XPS analysis does not give significantly different results compared to case (1). However, the surface behaves passively under electrochemical conditions that would normally provide etching attack. The reason is a substantial amount of γ-Al_2O_3 crystallites that have formed below the amorphous oxide film [9]. The consequence is far too low a tunnel density after a standard etch test.

(3) This case corresponds to a situation where instead of tunnel formation most of the etch current density causes pitting with little gain in specific surface area. XPS shows the surface of the foil (before etching) to contain a nitrogen

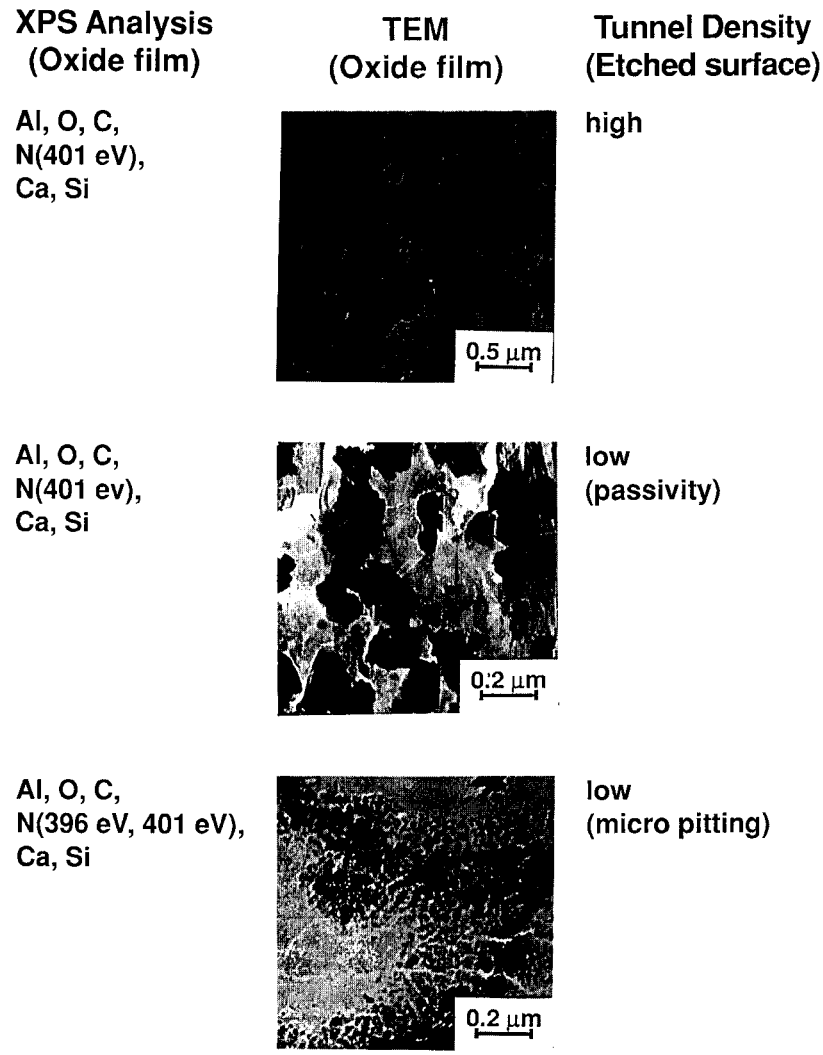

Fig. 15. Results of surface film characterization of an annealed Al 99.99 foil for electrolytic capacitor application using XPS and TEM of detached surface films. The three cases represent different fabrication (particularly annealing) conditions for the foil and show large differences in etch response (etch tunnel density).

species with an N 1s binding energy (BE) of 397 eV. The view that this is a nitride variant is clearly substantiated by the TEM investigation which shows the surface film to be partly composed of a fine-grained crystalline phase whose electron diffraction pattern could easily be indexed as the aluminium nitride (AlN) phase. AlN can form on aluminium during annealing in nitrogen with very low oxygen contents and at high temperatures ($\geqslant$ 590°C) [10].

Although the variations in fabrication conditions in the three above-mentioned cases were relatively small, significant effects can result in terms of surface film composition and, as a consequence, etching response during the electrochemical etch in chloride electrolytes.

Gallium-related surface effects during alkaline etching of AlGa alloys

Aluminium has an interesting potential as anode material for batteries. However, the inherent passivation properties have to be overcome without adversely affecting the self-corrosion rate in the chosen electrolyte. Aluminium–air batteries are available on the market, e.g., as emergency power supplies for remote areas. The electrolyte used is usually based on alkaline sodium hydroxide solution. Generally high-purity aluminium-based alloys are used with specific elements such as zinc, tin, indium or gallium being added to modify the electrochemical properties (activation and anode potential) [11,12].

An alloy of type Al 99.9–Mg 0.5 with a Ga content of 85 ppm (corresponding to a typical natural impurity level) was studied by electrochemical and surface-analytical techniques as a function of caustic soda treatment in 12% NaOH at 45°C. The starting material did not show any particularly significant surface properties. However, as a function of alkaline etching time, substantial amounts of gallium were detected. In general the gallium could only be measured after some slight ion bombardment to thin or remove the oxide film. Table 2 shows the results of the XPS study for a sample treated for 2 min in the NaOH solution. The positions of the Ga 2p photoelectron and Ga Auger peaks clearly show the gallium to be present in metallic form. The development of Ga XPS emission intensities as a function of ion bombardment and of the corresponding SIMS depth profiles (Fig. 16) leave no doubt that the gallium is enriched in a thin film just below the oxide film, probably in the form of a thin metallic AlGa alloy layer with a much higher gallium concentration (order of 2–8 atom%) than the base alloy (85 ppm Ga).

The development of this subsurface gallium concentration as a function of etching time in

Table 2
Results of XPS study on an Al 99.9–Mg 0.5–Ga 85 ppm alloy after etching in 12% NaOH at 45°C for 2 min. Depth profile was run using 3 kV Ar^+ ion bombardment

Sputter depth (nm)	XPS intensities (cps. eV)				Atomic ratio Ga/Al
	Al (2p) oxide	Al (2p) metal	Ga ($2p_{3/2}$)	Ga (Auger)	
0	2140	1200	–	–	–
2.5	2360	2060	466	275	0.0048
5.0	1390	3130	2920	396	0.020
7.5	1000	4030	2720	324	0.014
	XPS Binding energies (eV)				
	Ga (2p)	Ga (Auger) (KLL)			
Exp. b.e.	1116.2	1068.5			
Ga (metal, ref.)	1116.1	1068.3			
Ga (oxide, ref.)	1118.1	1062.8			

b.e. = XPS binding energy.

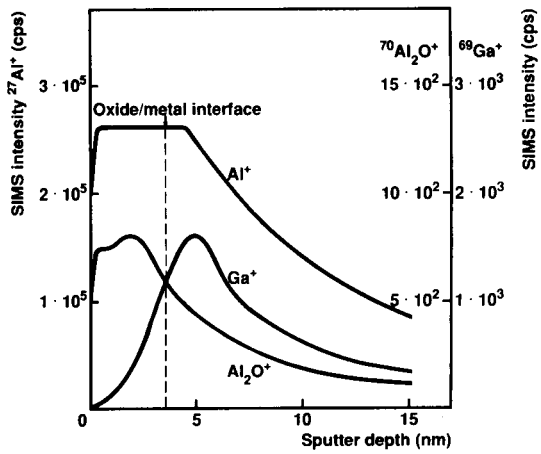

Fig. 16. SIMS depth profiles of an Al 99.9–Mg 0.5–Ga 85 ppm alloy etched in 12% NaOH at a temperature of 45°C for 2 min, showing gallium enrichment below the (natural) oxide film. Sputter conditions: 3 kV Ar^+ ions.

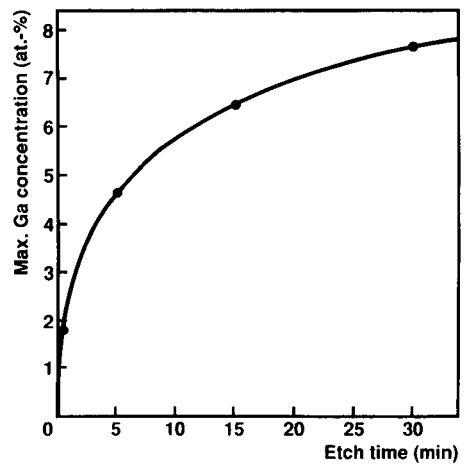

Fig. 17. Gallium concentration corresponding to maximum in SIMS depth profile as a function of etch time in 12% NaOH at 45°C. The curve was fitted to a theoretical model described in the text.

NaOH solution can be simply described assuming the etch rate for aluminium and gallium to be proportional to the corresponding surface concentration C_s at time t:

$$\text{dissolution rate of Ga:} \frac{dC(\text{Ga})}{dt} = k(\text{Ga})C_s^{\text{Ga}}(t)$$

$$\text{dissolution rate of Al:} \frac{dC(\text{Al})}{dt} = k(\text{Al})C_s^{\text{Al}}(t)$$

If the etch rate constant k is different for the two metals, the one with the lower etch rate constant (Ga) will be enriched at the surface until a steady state is achieved. This is exactly what is observed and a good fit to the experimental curve is possible assuming

$$\frac{k(\text{Ga})}{k(\text{Al})} = 9 \times 10^{-4}$$

The experimental values and fitted curve are shown in Fig. 17.

The electrochemical potential (measured in 1 M NaCl electrolyte) clearly shows a strong dependence on the surface composition, and as the gallium surface concentration reaches the maximum value, the potential approaches the 'free potential' of an active aluminium anode (Table 3). The role of gallium in aluminium alloys of high purity for anodes in alkaline batteries can be better understood by taking into account the highly different composition of the metal in a thin surface film which forms during the early (running-in) operation of the battery.

Conclusions

Modern surface-analytical techniques like XPS, SIMS and SNMS combined with more conventional electron microscopy (TEM) are powerful tools to study surfaces and interfaces. In commercial aluminium-based packaging foil a natural oxide film often forms the interface between the metal substrate and a polymer or lacquer. The

Table 3
Results of quantitative SIMS study on Al 99.9–Mg 0.5–Ga 85 ppm etched in 12% NaOH at 45°C for 0–30 min and corrosion potential values measured in 1 M NaCl vs. the saturated calomel electrode (SCE)

Etch time (min)	Max. Ga conc. at oxide–metal interface (atom-%)	Corrosion potential vs. SCE (mV)
0	< 0.05	−780
0.5	1.7	−810
5	4.6	−1050
15	6.5	−1090
30	7.8	−1100

composition of the oxide layer is dependent on the fabrication condition (particularly annealing) and chemical composition of the aluminium metal, and can substantially differ from the expected Al_2O_3 stoichiometry, e.g., due to the preferred surface migration of alkali and alkaline earth elements. Oxide films rich in lithium or magnesium are much more reactive towards water penetrating through lacquers and can cause interfacial corrosion reactions leading to delamination in lacquered or laminated products.

SNMS is particularly suited to study conversion coatings like chromate and phosphate layers used as a pretreatment in architectural and automotive applications. Their thickness and composition have to be carefully controlled in order to guarantee the required long-term interfacial stability under severe corrosive conditions.

Electrochemical etching of high purity aluminium foil for high voltage electrolytic capacitors requires the formation of etch tunnels. The oxide film which initially separates the metal and the electrolyte during the etching process is primarily responsible for etch tunnel formation; in order to understand the relevant factors of influence both analytical and structural (XPS, TEM, electron diffraction) methods have to be applied.

Aluminium alloys used as anode material for alkaline aluminium/air batteries contain specific alloying elements to improve the electrical performance. In the case of AlGa alloys it could be shown that the alloy surface is likely to have a different composition compared to the bulk metal. Significant gallium surface enrichment during alkaline dissolution is observed and a clear relation between gallium surface concentration and electrochemical potential could be established.

References

[1] M. Amstutz and M. Textor, Surf. Interface Anal., 19 (1992) 595.
[2] B.R. Strohmeier, Surf. Interface Anal., 15 (1990) 51.
[3] M. Textor and R. Grauer, Corros. Sci., 23 (1983) 41.
[4] I. Olefjord, H.J. Mathieu and P. Marcus, Surf. Interface Anal., 15 (1990) 681.
[5] J.A. Treverton and M.P. Thomas, Int. J. Adhes. Adhes., 9 (1989) 211.
[6] N.C. Davies and J.A. Treverton, Proc. 63rd Conf. Jpn. Inst. Light Metals, November, Inst. Light Metals, Tokyo, 1982, p. 161.
[7] A. Csanàdy and D. Marton, Proc. Int. Light Metal Congr. Leoben-Vienna, Aluminium Verlag GmbH, 1981, pp. 218-219.
[8] K. Rüegg. M. Textor and M. Amstutz, ECASIA 1985 (Poster No. 128).
[9] A.F. Beck, M.A. Heine, E.J. Caule and M.H. Pryor, Corros. Sci., 7 (1967) 1.
[10] W. Meierhoefer, Dissertation, Universität Zürich, 1972.
[11] A.R. Despic, M.A. Drazik, M.M. Purenovic and N. Cikovic, J. Appl. Electrochem., 6 (1976) 527.
[12] G.M. Scamans, W.B. O'Callaghan, N.P. Fitzpatrick and R.P. Hamlen, in T. Reily and B.W. Baxter (Eds.), Proc. 15th Int. Power Sources Symp., Brighton, 1986.

ELSEVIER

Analytica Chimica Acta 297 (1994) 27–42

ANALYTICA CHIMICA ACTA

Microanalysis of atmospheric particles and fibres by electron energy loss spectroscopy, electron spectroscopic imaging and scanning proton microscopy

Patrick Berghmans, Jasna Injuk, Rene Van Grieken and Freddy Adams

Department of Chemistry, University of Antwerp (UIA), Universiteitsplein 1, B-2610 Antwerp-Wilrijk (Belgium)

Received 23rd April 1993, revised manuscript received 8th July 1993

Abstract

Some aspects of micro- and surface-analytical beam techniques for studies of individual airborne particulates are reviewed. Applications of the microanalysis techniques of electron spectroscopic imaging, secondary ion imaging and proton induced x-ray-micro analysis (micro-PIXE) for the characterization of individual particles in environmental samples and chemically modified asbestos fibres are discussed.

Keywords: Asbestos fibres; Atmospheric particles; Electron spectroscopic imaging; Secondary ion imaging; Micro-PIXE

The present drive for analytical developments enabling spatial, depth, point and bulk analysis methods for surface elements can be credited to their increasing importance in many areas of science and technology. In environmental chemistry, microscopical surface characterization is particularly relevant. The composition and structure of microscopically sized environmental particles are important parameters for their persistence and fate in the environment, their toxicology and for inferring the assignment of particles to specific sources of pollution. Chemical analysis has also shown the presence of unique surface layers on environmental particles. In addition, elemental concentration levels in individual particles often show substantial variations from the average, even if the particles are morphologically similar. This indicates that various particles, even within a narrow size range, may be derived from different emission sources or formation mechanisms. Micro-analysis can reveal whether a specific element or compound is uniformly distributed over all the particles of a population or whether it is a component of only a specific group of particles. In rare cases the lateral and depth distribution of elements within one particle has been inferred. With such data, one can more easily interpret, pinpoint and eventually control sources of particulate pollution, and more refined information about source mechanisms and heterogeneous surface reactions can be derived.

Correspondence to: F. Adams, Department of Chemistry, University of Antwerp (UIA), Universiteitsplein 1, B-2610 Antwerp-Wilrijk (Belgium).

SSDI 0003-2670(93)E0401-R

Microscopical particle characterization is nowadays one of the more challenging aspects of microbeam analysis because it requires microprobe capabilities, which enable the generation of compositional maps that establish the lateral distribution of an element. Many of the available microscopic techniques permit analysis of microscopic particles or individual fibres, but have the disadvantages of sampling error problems, they suffer from excessive lengths of time required to obtain the data and require extensive sample preparation. Little research has been done, however, on the direct characterization of the microscopic variation of element concentrations, including trace species, within individual particles. Quantitative analysis is often difficult because of the uncertainty in defining a precise analytical volume. Also, with techniques involving energetic beam interactions, the sample may be altered because of chemical reactions, selective volatilization of elements or migration in the solid. Finally, the analytical signals often depend in a complex way on the instrumental and sample parameters.

Several analytical techniques have been used to study surface layers and/or to analyze elemental concentrations as a function of depth for a collection of particles without lateral spatial resolution. These techniques include x-ray photoelectron spectroscopy (XPS), Auger electron spectroscopy (AES), photoacoustic spectroscopy (PAS), and conventional secondary ion mass spectroscopy (SIMS).

In order to reduce the effects of the intrinsic limitations associated with some techniques (such as reduced sensitivity for some classes of substances, owing to the very small analytical vol-

Table 1
Methods for surface analysis used in studies of microparticulate solids

Probe	Analytical signal	Technique	Acronym	Resolution	
				Lateral	Surface
Electrons	Electrons	Auger electron spectroscopy	AES	50 nm	1–2 nm
	Electrons	Electron energy loss spectroscopy	EELS	10 nm	thin sample
	X-rays	Energy dispersive x-ray spectrometry	EDXRS	0.2 μm	2 μm
X-ray photons	Electrons	X-ray photoelectron spectroscopy	XPS	10 μm (tube)	nm
	Electrons	X-ray absorption near edge spectroscopy	XANES	1 μm (synchrotron)	nm
Low energy ions	Ions	Ion scattering spectrometry	ISS	none	nm
keV ions	Ions	Secondary ion mass spectroscopy (dynamic)	SIMS	0.1 μm	3 nm
	Ions	Secondary ion mass spectroscopy (static)	SSIMS	1 μm	nm
IR photons	Photons	Fourier transform infrared spectroscopy	FTIR	20 μm	μm
UV photons (laser)	Ions	Laser microprobe mass analysis/Fourier transform laser microprobe mass spectrometry	LAMMA/ FT-LMMS	1–5 μm	50 nm
X-rays (synchrotron)	X-rays	Fluorescence x-rays	SRXRF	1 μm	none
Protons	X-rays	Micro-proton induced x-ray micro-analysis	micro-PIXE	1–10 μm	thin sample

umes sampled), the combined use of different analytical and visualization techniques is necessary. This allows a much more complete and detailed study of individual particles. For example, the morphological resolution and the large depth of focus associated with scanning electron microscopy (SEM) is useful in morphological analysis, while SIMS is useful in the determination of the chemical composition, because of its high sensitivity. The techniques are complementary and are very powerful when used together.

Some aspects of micro- and surface-analytical techniques for environmental studies as well as microanalysis applied to individual environmental particles have previously been reviewed [1–3]. Table 1 gives an overview of the main analytical features of some micro- and surface-analytical beam techniques for the characterization and analysis of environmental particles. The techniques are classified by the type of probe used to obtain the observed analytical signal and also the limitations in surface and lateral resolution of each type are summarized.

Heterogeneities in the composition in single particles are frequently observed from site to site, and SIMS offers special capabilities for particulate analysis. The inherent depth profiling capabilities of SIMS, along with its high sensitivity and full periodic table elemental coverage, its capability to measure isotope ratios and finally its ion imaging potential of specific constituents, make it uniquely suited to the study of intraparticle trace element concentration gradients. For studies of the depth distribution of trace elements, SIMS can be successfully applied to individual particles [4]; yet, irregular topography of particles can degrade the depth resolution considerably. When the imaging capabilities of a secondary ion microprobe or microscope are employed, an image depth profile can be generated which yields information on three-dimensional elemental distributions within single, micrometer-sized particles [5,6]. With an ion microscope, such information can be acquired simultaneously for a group of individual particles present in an image field typically on the order of 100 μm in diameter. The limiting lateral resolution is about 0.5 μm for the ion microscope and less than 0.1 μm for the scanning ion microprobe. When molecular information of particles is needed, both laser microprobe mass spectrometry (LMMS) [7,8] and SIMS can be used since they exhibit qualitatively the same positive ions. The speciation capabilities of LMMS and time of flight (TOF) LMMS have been exploited successfully, e.g., in the study of polyaromatic compounds in particulate samples [9,10].

SEM has allowed the compositional analysis of particles down to μm diameters using energy dispersive x-ray analysis (EDX). However, it is unsuitable in the majority of cases for the analysis of smaller particles. The scanning transmission electron microscope (STEM) extends the size range of EDX analysis to the nm region, as a fine electron probe and thin specimens lead to increased spatial resolution. However the low collection rate of x-rays from small sample volumes becomes a limiting factor, leading to long data acquisition times. An alternative analytical method in the STEM is electron energy loss spectroscopy (EELS). EELS seems to have promising potential as an analytical technique in the chemical characterization of airborne particulates, but thus far few applications to single particle analysis have been reported. Combined with EDX for heavy element quantification, and with electron diffraction, where appropriate, the STEM seems highly suited to aerosol analysis.

Whereas Auger electron spectroscopy (AES), x-ray emission spectroscopy, and many other techniques are concerned with the analysis of the several possible processes induced by the de-excitation of the atom which received the energy lost by the incident electron, EELS deals with the energy loss (ΔE) distribution of the electron probe at the exit surface of the thin specimen. It is beyond the scope of this paper to give a complete review of these techniques and of their applications to chemical analysis of particulate and fibrous material; several hundreds of articles are published every year in various journals or conference proceedings. In order of glance through some recent publications, we have only selected a few papers dealing with EELS [11–13], AES [14,15], x-ray emission spectroscopy [16]. A brief discussion of applications of AES and x-ray

photoelectron spectroscopy (XPS) to single particle analysis is given by Powel [17]. Cox III and Linton [18] already discussed extensively the aspects of environmental applications of XPS involving airborne particle chemistry. Small et al. [19] and Gordon et al. [20] reported on the use of Fourier transform infrared spectroscopy (FTIR) to study atmospheric pollutants and to characterize organic substances in aerosols.

The use of focused MeV ion microprobes for studies of materials samples has increased rapidly during the last decade. Today, about 40 available nuclear microprobes are used around the world for material analysis. The scanning proton microprobe (SPM) utilises a well-focused beam of high energy protons (1 to 3 MeV) or other light ions, to scan a specimen. In its operation, it is similar to the SEM. After the incident MeV ion beam enters the target, most of the particles penetrate the specimen and roughly retain their incident directions. Part of the energy transferred to the target as the impinging ions decelerate produce many types of radiation, each of them containing information about the atoms and nuclei in the matrix. A variety of signals that can be collected and processed are used to obtain unique information on the composition of the sample. It uses PIXE (proton induced x-ray emission), RBS (Rutherford backscattering) or RFS (Rutherford forward scattering) and NRA (nuclear reaction analysis) for elemental or isotopic analysis.

In what follows we will illustrate the potential of microscopical characterization of fibrous and environmental particles with two examples from recent laboratory experience. First we give examples of the characterization of surface modified asbestos particles using SIMS and EELS. Then we treat the application of the SPM for the characterization of the North Sea aerosol.

1. Surface characterization of chrysotile asbestos fibres

In order to reduce the cytotoxic and long term haemolytic activity of asbestos fibres, there have been many efforts to modify the surface reactivity. The use of $TiCl_3$ as a modifier provokes a modification of the surface properties specific to the mineral concerned [21,22]. Also, the gas phase reaction of chrysotile with organosilane compounds has led to thermally and chemically stabilized asbestos fibres [23]. For a better understanding of specific surface structures and reactivity of the modified fibres, in relation to their biological reactivity, knowledge about the spatial distribution of reaction products is necessary. The inhomogeneity on the microscopical level of the composition of the asbestos fibres and the small fibre size require the use of highly sensitive microanalytical techniques providing high lateral resolution. Given these constraints, EELS, in conjunction with electron spectroscopic imaging (ESI), is a very suitable analytical method to address this problem. As will be demonstrated, these techniques offer the possibility of detecting differences in surface composition and mapping the reaction products on the modified chrysotile surfaces down to the sub-micrometer level.

The elemental distributions measured with ESI are processed with a commercial digital image-processing unit (IBAS 2000, Zeiss/Kontron, Eching, Germany), operated at an image size of 512 $\times$ 512 pixels and a 8 bit grey value resolution. The images as acquired from a TV camera (SIT 66, Dage-MTI) are automatically analyzed. The EELS instrument (ZEISS EM 902, Oberkochen, Germany) is used nearly in the original version completed by a digital control of the photomultiplier detector with the computer (IEEE 488) interface system and an image-processing system with some special image processing programs (Zeiss/Kontron). The analyses were performed at electron optical magnifications of 50 000 to 140 000, corresponding to a selected area of approximately 200–100 nm in diameter (with the filter entrance aperture of 100 μm acting as a selected-area aperture). The optimal signal-to-noise ratios of the elements of interest were obtained with an objective aperture of 60 μm. In all cases, the energy-selecting slit was set to a width of 10 eV.

One of the severest limitations of the usual procedures for processing energy-filtered images is the difficulty in obtaining accurate data on the net elemental intensity. First, it is necessary to

define an analytical model for the background estimation. The background intensity usually decreases smoothly with energy loss ΔE, approximating to the power-law form $I_b = A\Delta E^{-R}$, where A and R are constants which can be determined by examining the energy dependence of I_b at energy losses just below the ionization threshold. Unfortunately, both A and R may vary across the specimen as a result of local changes in thickness and chemical composition, both of which affect background intensity and its energy dependence. Therefore the background estimation procedure must be performed separately for every pixel point of the image. Generally a three-image procedure is used, where two images are taken before the charateristic edge and one image at the specific edge, but in some critical situations the application of this procedure does not yield reliable results. Indeed, for high-resolution mapping of elements with relatively low concentration, the signal-to-background ratio is generally quit low, putting severe constraints on procedures which rely on the extrapolation of the background using two measurements in the vicinity of the edge.

A perforated supporting film of polyvinyl formaldehyde (Formvar) on 700 mesh electron microscope grids is used to mount the modified fibres. The deposited fibres become electrostatically attached to the supporting film. To avoid measuring carbon from the support material, only the portion of the asbestos fibres that are not lying directly on the support material are selected and analyzed.

For obtaining cross sectional information, the fibres are embedded in a Spurr (epoxy) resin and thin sections (ca. 35–45 nm thick) are cut across the fibre axis using an ultramicrotome (LKB Ultrotome III, LKB-Products AB, Bromma, Sweden). The cross-sectioned samples appear to yield more insights into morphological details, and offer the ability to obtain spatial information on the submicroscopical level with recognition of fine structure.

ESI of organosilane coated chrysotile

The first step in the analysis procedure is the recording of energy loss spectra to survey the possible elements of interest. Fig. 1 shows a typical EEL spectrum of a chrysotile fibre treated with trimethyl chlorosilane. The characteristic carbon K-edge is located at $\Delta E = 284$ eV. The observed carbon jump ratio (peak-to-background) ratios range between 1.1 and 1.3.

ESI of carbon distributions are carried out with serial ESI acquisition, which means that the different energy-filtered images are acquired successively, using the three-window method, to re-

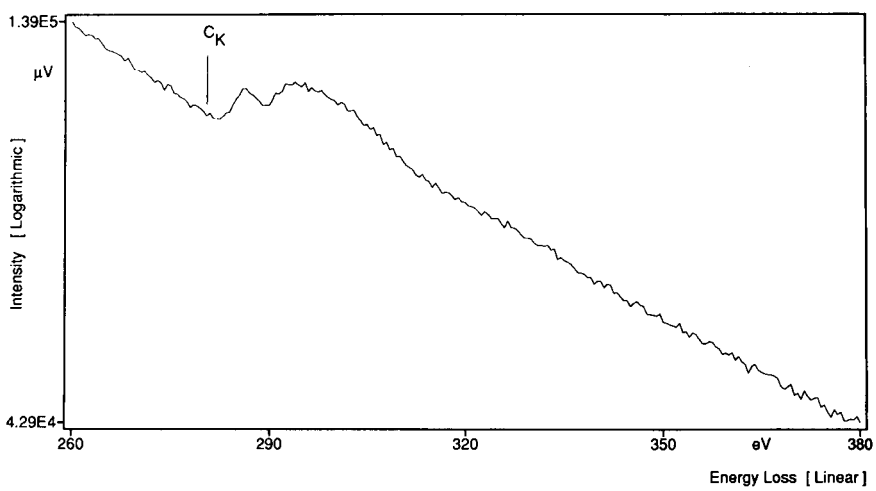

Fig. 1. Electron energy loss spectrum of asbestos fibres treated with organosilane taken between 260 and 380 eV energy loss showing the carbon K-edge at 284 eV.

move the background contribution from the image recorded above the ionisation edge, at the maximum signal intensity. This is performed as follows: two background images are obtained with a SIT Vidicon camera just prior to the ionisation edge ($\Delta E = 250$ and 270 eV) and one image at the ionisation edge (energy loss $\Delta E = 300$ eV) and recorded with a Kontron SEM/IPS image processing unit. The processed images were segmented interactively by expanding the grey values of the processed images over the whole grey range and raising the threshold until all background noise was cut off, in order to minimize the signals present in structures other than the specimen.

Initially, the power law background extrapolation procedure is evaluated for its effectiveness as a background correction, by inspecting the region below the carbon edge in the ESI mode. Therefore, the validity of the image processing is verified for a set of "ghost" images from and around a hypothetical edge, with the third image taken at an enery loss position just below the characteristic edge. The non-characteristic signal, observed in the net distribution, results from extrapolation errors and camera artifacts, and is used as a cut-off threshold for subtracting the noise contribution in order to obtain a more statistically valuable net image. No filtering techniques are employed in the image processing in order to avoid these supplementary, non-controllable artifacts. Only contrast enhancement is performed on the low contrast net images by expanding the set of grey values to the full range available.

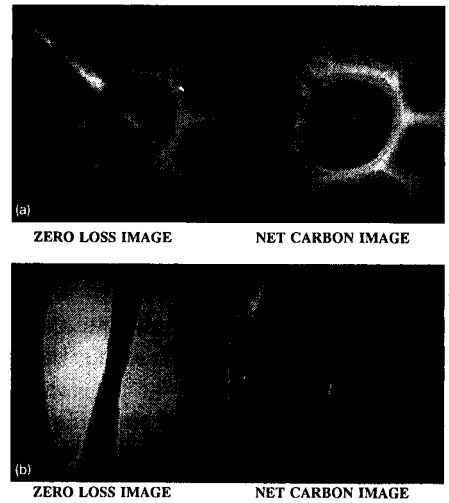

Fig. 2. Carbon mapping of organosilane treated chrysotile fibres, mounted on a perforated carbon foil, with the zero-loss image (left) and the net carbon-image (right).

ESI images for carbon in trimethyl chlorosilane modified chrysotile, supported on a perforated carbon foil are depicted in Fig. 2, with the net carbon distribution image (right) and the con-

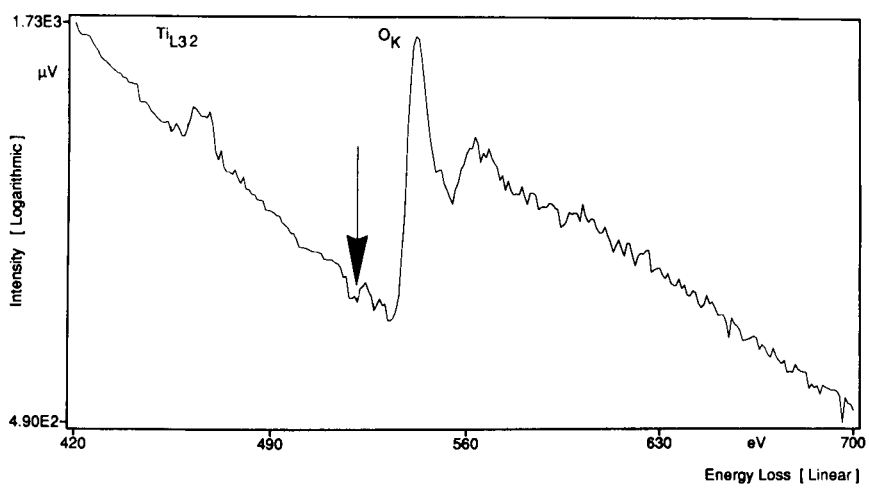

Fig. 3. EELS of a Ti-treated chrysotile fibres section, embedded in a Spurr resin, showing the Ti-$L_{3,2}$ edge at 455 eV and the O-K edge at 530 eV.

ventional zero-loss image (left), respectively. All images were acquired with a magnification of 50 000 ×. The use of a conducting perforated carbon foil is advantageous since the stability of such electrically insulating asbestos fibres under the electron beam is increased. This allows the operation of the electron microscope at greater magnifications without sacrificing beam intensity.

From such carbon maps it could be concluded that the organosilane coating is not homogeneously distributed over the fibres. Some fibres do not seem to have been affected by the organosilane treatment, which indicates that the carbon layer does not completely encompasses each and every fibre. This means that the surface modification is only partially effective.

EELS and ESI study of $TiCl_3$-treated chrysotile

In the following example we have investigated the asbestos fibres' condition after their chemical modification process with $TiCl_3$, especially in view of a possible penetration of titanium in the first layer and a localised built-up of species of the modification reaction inside the tubes of the fibres.

Before performing chemical mapping, the extended area of interest of the section was examined by recording a typical energy-loss spectrum. A part of one of these EEL spectra from an area (250 nm × 200 nm) within the chrysotile fibril of the modified asbestos is shown in Fig. 3, and it reveals the presence of titanium with the Ti-$L_{2,3}$ edge at 455 eV. The Ti $L_{3,2}$ threshold peak shows two dissimilar peaks with multiplet structures at both L_3 and L_2. The sharpness of these peaks makes the Ti edge easily recognizable even at low Ti contents. The pre-edge, preceding the oxygen edge, is assigned to a manifestation of the bond between oxygen and titanium, arising from transitions to the $2t_{2g}$ and $3e_g$ anti-bonding orbitals of the Ti–O bonds [24]. The appearance of this shoulder at the onset of the oxygen edge is an indication that the titanium chloride has chemically reacted with the chrysotile fibres and is not chemisorbed.

While for EELS analysis a relatively large area of an ultrathin fibre section is selected, the localization of titanium is possible with ESI in very small areas, restricted only by the spatial resolution of the electron microscope. Taking into account that the jump ratio for Ti is sufficiently high for imaging, first the three-image method was used for the collection of the electron spectroscopic images.

Lateral elemental Ti maps (magnification of 140 000 ×) obtained with ESI analysis of the cross-sectioned treated fibres demonstrate unambiguously the presence of titanium inside the

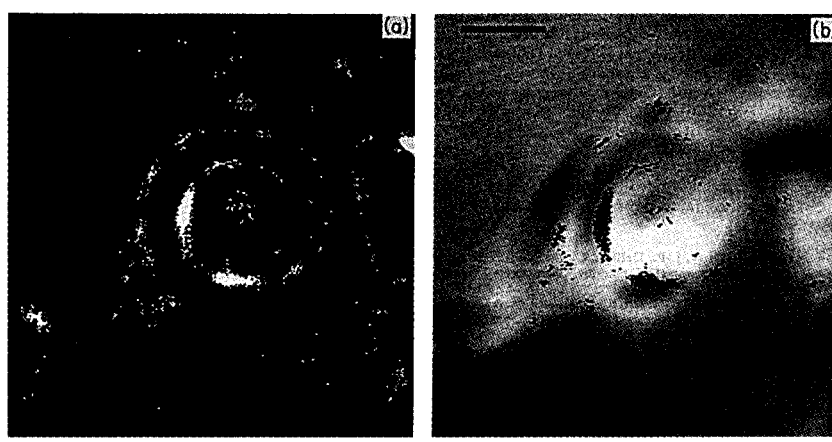

Fig. 4. Elemental mapping of Ti in a cross section of a $TiCl_3$-treated fibre embedded in a Spurr resin. (a) The net-titanium image is obtained by subtracting an extrapolated image at 460 eV (calculated from the 435 eV and 445 eV images) from the 460 eV image, (b) combination of binary titanium distribution image (black) and the grey reference electron specific image at 435 eV (Scale bar = 25 nm).

hollow tubes of the fibres as well as on the external surface of the fibres, which shows that the Ti distribution forms a non-complete encapsulation around the material. The superposition of the titanium map (in black) on the grey reference area depicted in Fig. 4 indicates that the

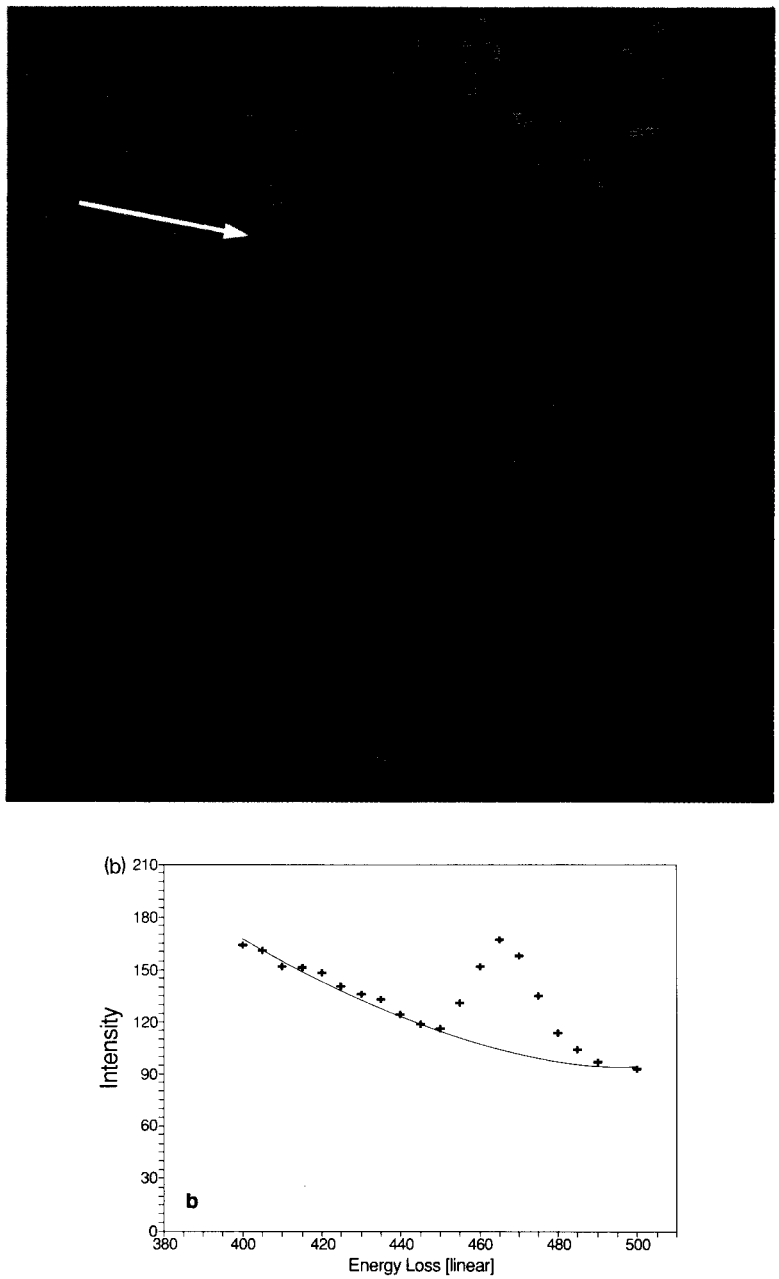

Fig. 5. Zero-loss image of a cross section of $TiCl_3$-treated chrysotile fibres embedded in a Spurr resin (full picture is 200 nm) showing the Ti-signal in overlay (a); Datapoints (+) of a selected part of the EEL spectrum generated from the images, at one pixel location near the surface of fibril. The background curve was modelled by fitting the 10 pre-edge points (+) to the power law curve (b).

modification follows the spiral curvature of the chrysotile asbestos.

In addition to the inaccuracies which are obtained using the three-image procedure, statistical noise plays an important role in the background estimation. Hence, in this typical situation, it is difficult to distinguish the true characteristic signal from background and noise. Therefore we investigated the use of a point-by-point processing of the spectrum through increasing the number of images before and after the edge, attempting a significant progress in accuracy for the restoration of the net image from the three-dimensional data set, by taking into account the local thickness variations and increasing the accuracy in the A and R determination. To calculate the background counts beneath the characteristic core edge, a least-squares fitting procedure, using a data-analysis program, PV ~ WAVE (Precision Visuals, Colorado), is performed in parallel for all pixels in the series of images.

This multi-image procedure can be easily modified to take the statistical uncertainty on the intensities in the original images into account, in order to differentiate between variations due to noise limitations or real elemental data. In this way, next to the net image, also a corresponding uncertainty image can be calculated which allows the identification of the area in the image with a net intensity significantly different from zero. At different locations in the net image, the EEL-spectrum, its background and the intensity distributions across the X and Y directions through the net image at those locations can be interactively inspected.

The WAVE processing routine allows the operator to display an EEL spectrum at each selected pixel position in the image. The number of

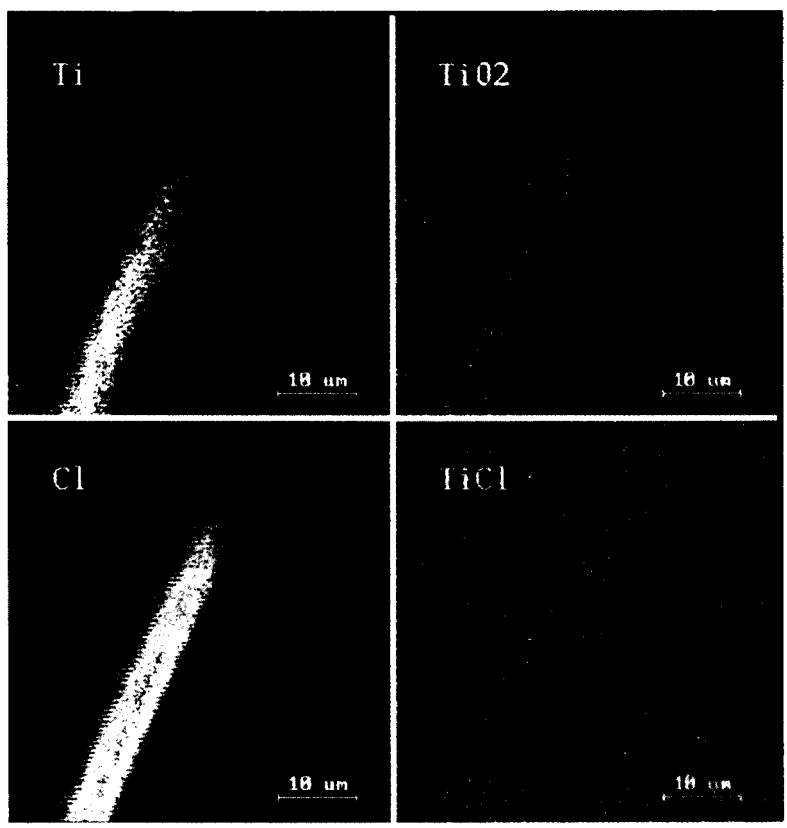

Fig. 6. Negative secondary ion images for Ti^-, TiO_2^-, Cl^- and $TiCl^-$ of $TiCl_3$-treated chrysotile fibres deposited on a GaAs wafer. The diameter of the imaged area is 25 μm.

data points selected for construction of this spectrum corresponds to the number of images collected (in this case 20). The resulting statistically significant net-distributing of titanium is presented in Fig. 5a, showing the Ti-signal in overlay. The image spectrum for one pixel position located on the fibre section, as indicated by the arrow, is presented in Fig. 5b, showing a clear edge of Ti-$L_{2,3}$ above the extrapolated background.

The use of a multi-image ESI procedure at different electron energies, for processing the net-element distribution, has demonstrated its utility in cases where low element concentrations are analyzed. In general, one has to be aware that the multi-image method is very sensitive to radiation damage and specimen drift occuring during the image collection. These effects, arising from the high intensity level of the electron beam required for high magnification electron microscopy, mostly can be avoided by using cryo-cooling in order to stabilize the sample prior to image collection. In comparison with the three-image method, significant increase for the yield in characteristic net-signal is obtained, while the statistical uncertainty on the intensities for every pixel position decreases. The calculation with the use of the WAVE procedure ensures that the images represent a true Ti distribution and not mass thickness variations.

Secondary ion imaging of titanium coated fibres

An ion microprobe (CAMECA IMS 4F) was used for the SIMS measurements. The lateral resolution of this equipment is limited to about 0.2 μm. The achieved primary beam current densities are kept rather low to make feasible three-dimensional distribution analysis in a reasonable time. Therefore we mainly deal with the two-dimensional lateral distribution analysis. For this purpose the CAMECA 4F was furnished with a SEM-box which controls the deflection raster plates of the primary beam and collects synchronously the signal from the electron multiplier to send it to an image-processing unit, an IBAS 2000 unit, described above.

In order to reach sufficiently high counting rates, a primary beam of mass filtered Cs^+ ions at a net 10.0 kV and approximately 100 pA is rastered over a 5 μm $\times$ 5 μm area. Ion images (25 μm^2 imaged field), mass spectra and energy distributions of negative secondary ions are obtained. Because of the drastic deterioration of the electrical parameters of the asbestos, the samples are prepared from a suspension in hexane that had been spotted on an ultra-pure GaAs-wafer. This resulted in clumps of fibres dried on the GaAs-wafer. The energy distributions that are obtained for each sample dried on a GaAs-wafer show that no significant amount of electrical charge had accumulated within the area of analysis.

The lateral elemental maps of the major secondary ion species present, Ti^-, TiO_2^-, Cl^-, and $TiCl^-$ are shown in Fig. 6. The diameter of the imaged area is 25 μm in all the elemental maps. A pixel time of $t_d = 0.5$ or 1 ms was used for collection of these images, having 256 $\times$ 256 pixels.

It is clear that the secondary ion images of Ti and TiO may be used to selectively indicate the contour of the asbestos fibre. The titanium ion images show that, within the lateral resolution of the ion microprobe, the titanium has reacted fairly evenly over the selected area of the chrysotile surface, and no evidence of any significant built up of localized titanium containing compounds is observed. The $TiCl^-$ map does not show any contribution, hence we assume the absence of $TiCl_x$ species on the $TiCl_3$-treated fibres. This is an extra indication that $TiCl_3$ has reacted fully with the chrysotile structure. Microstructures on these fibres, however, cannot be studied with the ion micro-probe image-processing combination using a Cs^+ primary ion beam, as the dimension of these structures are ca. 0.1 μm or smaller and so below the limit of resolution of this technique.

2. Characterization of the north sea aerosols by spm

Atmospheric transport and deposition of pollutants over long distances have received attention, particularly in connection with the acid rain

problem, the photochemical oxidants and ozone formation, and, more recently, the global climatic effects. Though the pollution of the oceans is not a new phenomenon, the question of how important a role the atmosphere plays in this was addressed only a decade ago [25]. A number of studies conducted at the end of the 1970s and the beginning of the 1980s (e.g., [26–28]) revealed direct deposition from the atmosphere as a potentially major input source for contaminants.

Due to a large number of limitations, direct measurements of pollutant fluxes over the sea are scarce [29]. In order to overcome this problem, several authors have proposed, as an alternative, the use of mathematical models to predict the atmospheric input of particulate matter to the large water surfaces [30] or to calculate deposition indirectly, based on measured airborne concentrations and kinematic parameters which control the rate of mass transfer [31].

Regarding to the pollution of coastal and shelf systems of the North Sea, there has been a growing concern especially since Weichart in 1973 concluded that the southern North Sea is one of the most heavily polluted areas [32]. Because of its relevance, since quite some years our laboratory has studied the North Sea environment intensively; we focused our efforts primarily on the heavy metal deposition and concentrations, and physical and chemical characterization of individual North Sea particles responsible for this flux. Previous studies showed that some 95% of the total deposition is explained by fluxes of particles with a diameter larger than 4 μm i.e. the so-called "giant particles"; this emphasizes the accuracy of size-determinations of large particles as the limiting factor in the estimation of total fluxes. The following example gives a quantitative idea on how important relatively large particles are in the whole deposition process. Since the gravitational settling velocity is roughly proportional to the square of the particle diameter and the particle mass is proportional to the cube of the particle diameter, the deposited mass is a function of diameter to the 5th power. Therefore one single 10 μm particle contributes as much to the total deposited mass as 100 000 particles of 1 μm.

In the above-stated context, an attempt was made to demonstrate the potential usefulness of the flexible SPM system in a quite novel approach: to estimate quantitatively from field measurements the atmospheric input of heavy metals into the North Sea and to evaluate the nature of aerosol particles, especially the "giant" particles, responsible for this flux. The basic reason for the use of a focused proton beam is the high sensitivity of PIXE in a small sample mass allowing the determination of fingerprinting trace elements, and the potential for elemental concentration mapping over spatial intervals of a few microns permitting studies of the internal heterogeneity of giant aerosol particles.

The aerosol samples were taken in the frame of EUROTRAC Air-Sea Exchange experiment, on the research platform "Nordsee" (54°10′, 7°53′E). As a follow-up of previous experiments on the North Sea [33], isokinetic collection of size-segregated aerosols on Nuclepore filters (0.4 μm pore size) was carried out in a continuous forced air flow within a wind tunnel, which directs itself continuously towards the wind with a wind-vane. The major problem in all previous aerosol deposition studies over the North Sea in the past, was that the giant aerosols have not been adequately assessed, because of difficulties in sampling these particles in a representative way. Indeed, the linear velocity of the particles in the air should exactly be the same as the inlet speed in the sampling device. By taking samples with the means of a wind tunnel, this problem is overcome since it allows quantitative collection of giant particles without problems of a variable cut-off with wind direction and wind speed.

The micro-PIXE measurements were done at the Central Bureau for Nuclear Measurements (CBNM) in Geel, Belgium [34]. The microbeam line is mounted in the target hall of the KN-3.7 MV vertical single stage Van de Graaff accelerator. The accelerator is equipped with a radio-frequency ion source used to produce H^+ or He^+ ions. The energy spread of the accelerator is about $\pm 0.07\%$, a typical value for single ended machines, while the brightness has been measured on the beam line to be 3.5 pA/(mrad^2 μm^2) at a proton energy of 2 MeV. The distance from the object slits to the target position is 425

cm. The entire beam line is resting on a 420 cm long and 500 kg heavy granite bench carried by four active pneumatic vibration insulators. The beam line is equipped with the two pairs of stainless steel "Heidelberg"-type slits, which are electrically insulated and equipped with cable connections to enable monitoring of the beam current striking each individual slit. This option has proven useful during the start-up procedure. As the beam focusing element, a magnetic quadrupole lens doublet is chosen. The lenses are mounted on the granite bench beam line support, in direct contact with the chamber. Therefore, the lenses cannot be moved relative to the chamber, what requires a very precise beam line alignment. The copper-grid shadow pattern was used to facilitate the focusing and the size of the ion beam. A lateral resolution of 2.5×2.5 μm^2 was routinely achieved at a beam current of 100 pA. In the Geel SPM, a flexible front computer is used together with a powerful host computer. A VMEbus system acts as a front-end computer which controls the beam scanning and the acquisition of data from a maximum of four detectors and from the beam charge monitor. The host computer is a MicroVax-II, equipped with a Nuclear Data ND9900 multiparameter MCA system.

The aerosol samples were analyzed by scanning the beam over a fairly large square region, mostly of 128×128 μm^2 in a 64×64 pixels scanning pattern. The x-rays induced by the proton beam were continuously recorded and sorted by the data acquisition system, producing x-ray intensity images of selected elements on a graphics terminal. From these maps, clusters of particles deposited on the backing were located. The time of analysis varied between 30 and 60 min, depending on the elements present and their respective amounts. Elements ranging from S to Ca

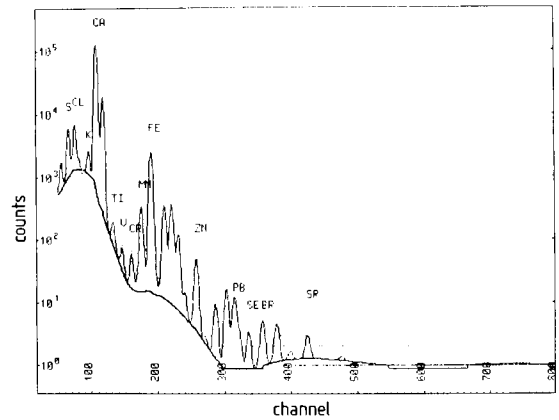

Fig. 7. PIXE spectrum obtained from from the analysis of a single aerosol particle-summed spectrum from all 4096 irradiated pixels in the scanning frame.

normally yield high x-ray count rates and were detected within a short counting time. Higher-Z elements have lower x-ray production cross sections and consequently require longer irradiation times for adequate detection.

The off-line spectrum analysis was performed by using a linear least-squares fitting procedure and the corresponding mass of the trace elements was then calculated from a calibration library. A PIXE spectrum obtained from the analysis of one single aerosol particle is given in Fig. 7.

By using the scanning proton beam, it was possible to reveal elemental distributions within a single aerosol particle structure. Detected total amounts for S, Cl, K, Ca, Ti, V, Cr, Fe, Ni and Zn were in the range of 0.01 (Zn) to 390 (Cl) pg, and these would have been difficult to quantify using other microprobe techniques (Table 2). The accuracy is estimated to be around 10%.

The elemental distributions on the individual particle level have demonstrated the heteroge-

Table 2
The range of elemental concentrations (pg) for the two representative particle groups found in the North Sea troposphere

Group	S	Cl	K	Ca	Ti	V	Cr	Fe	Ni	Zn
Marine aerosols	10–33	20–390	5–17	1–4	–	–	–	–	–	–
Agglomerated aerosols	2–20	8–100	1–16	1–7	0.1–3.8	0.1–0.3	0.2–2.6	0.2–1.1	0.01–0.08	0.01–0.52

neous structure of marine aerosols (Fig. 8). Especially in the case of agglomerates of particles, a distinct difference in elemental composition was found. Commonly in the presence of a high load of airborne sea-salt particles, a large fraction of the heavy metal rich particles were found to be

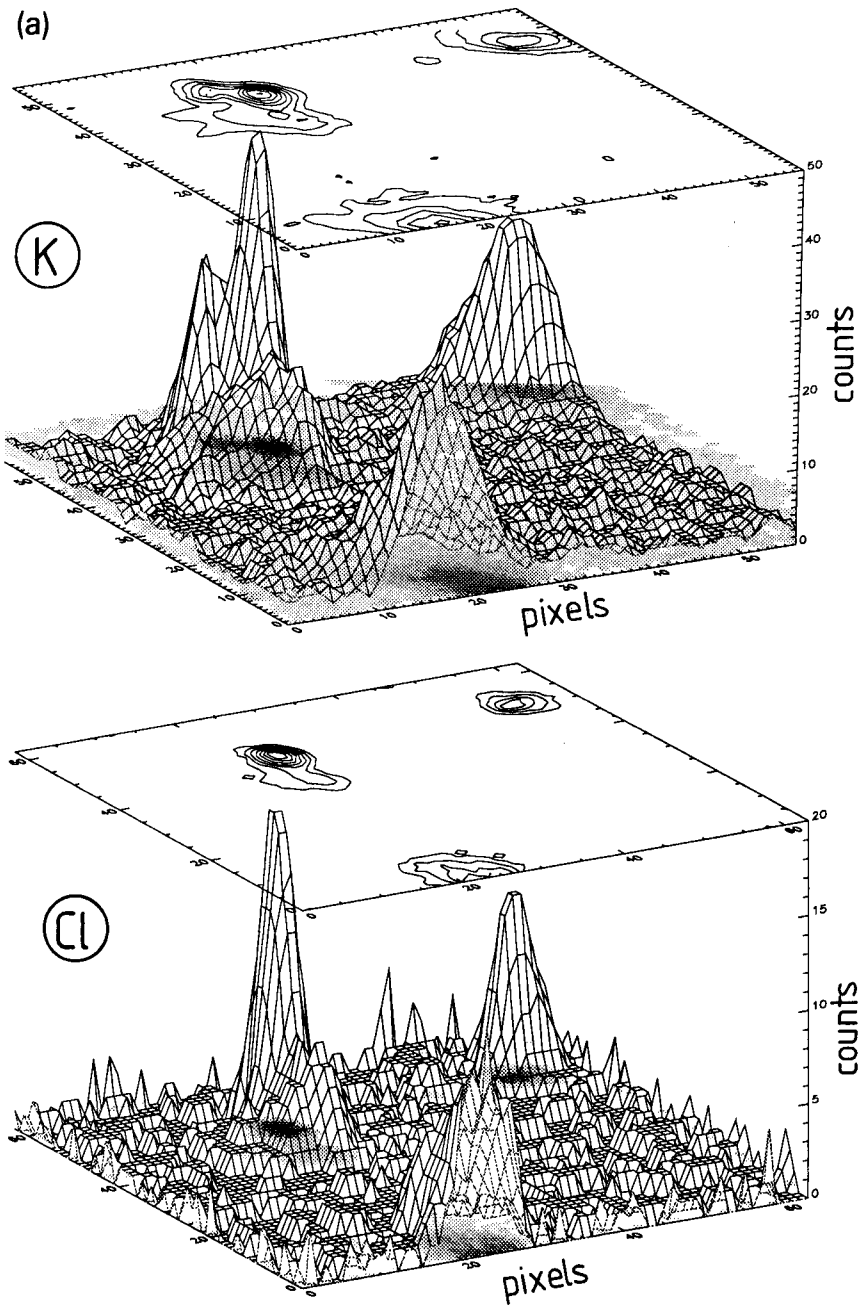

Fig. 8. Elemental mapping of Cl, K, Ca and Ti, obtained from the analysis of North Sea aerosol particles. The heterogeneous structure of the marine particles is evident. The total scanning area is about $64 \times 46\ \mu m^2$.

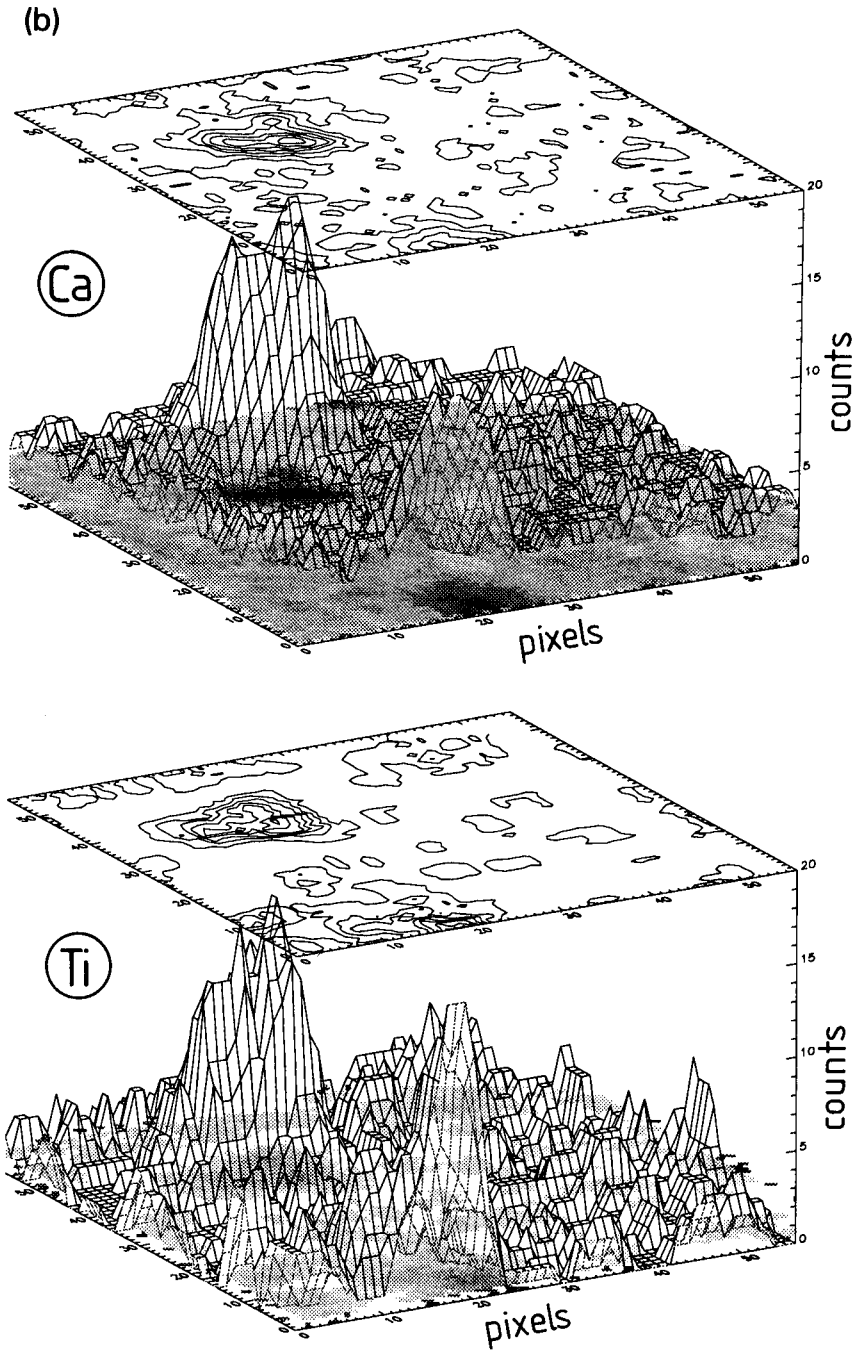

Fig. 8 (continued).

internally mixed, forming the coarse marine aerosol fraction with diameter above 5 μm. Hence, while elements like V, Cr, Ni, Zn are usually more abundant in the sub-micrometer size range in polluted air, it was demonstrated that these particles can coagulate with the sea-salt

aerosols and reach super-micrometer dimensions. Elemental maps taken during the scanning analysis of a few aerosol particles are shown in Fig. 8.

From an environmental prospect, it was also of interest to relate the elemental aerosol compositions to their sources, i.e., to identify source profiles of the North Sea aerosols. Therefore we have analyzed the variability of the 10 elemental concentrations. The principal sources for most particulate trace elements in the marine troposphere of the North Sea appear to be sea-salt generation (oceanic source) and a variety of mainly high-temperature combustion processes (anthropogenic sources). The predominant particle groups were particles with a high loading of marine elements (Cl, S, K) and agglomerated particles containing simultaneously sea-salt and trace elements ascribable mostly to anthropogenic processes (Ti, V, Cr, Fe, Ni, Zn).

This work was sponsored by NFWO/FNRS Brussels, Belgium and by the Belgian Prime Minister's Service for the Programmation of Science Policy under the Programme Interuniversity Attraction Poles (IUAP), the Eurotrac Project EU7/08 and the Impulse Programme on Marine Sciences (contract MS/06/050). We thank Dr. U. Wätjen and Ing. L. Braitenbach, from the CEC-JRC, Central Bureau for Nuclear Measurements, Geel, for the micro-PIXE analyses.

References

[1] M. Grasserbauer, Mikrochim. Acta, III (1983) 415.
[2] R. Van Grieken and C. Xhoffer, J. Anal. Atom. Spectrom., 7 (1992) 81.
[3] C. Xhoffer, L. Wouters, P. Artaxo, A. Van Put and R. Van Grieken, in J. Buffle and H.P. Van Leeuwen (Eds.), Environmental Particles, Vol. I, Lewis Publishers, Boca Raton, FL, 1992, 107.
[4] M. Van Craen, D.F.S. Natusch and F. Adams, Anal. Chem., 54 (1982) 1786.
[5] G. Morrison and G. Slodzian, Anal. Chem., 47 (1975) 932A.
[6] X.B. Cox III, S.R. Bryan and R.W. Linton, Anal. Chem., 59 (1987) 2018.
[7] E. Denoyer, R. Van Grieken, F. Adams and D.F.S Natusch, Anal. Chem., 54 (1982) 26a.
[8] L. Van Vaeck and R. Gijbels, Fresenius' J. Anal. Chem., 337 (1990) 743.
[9] T. Mauney and F. Adams, Sci. Total Environ., 36 (1984) 215.
[10] Ro Chul-Un, I.H. Musselman, R.W. Linton, in P.E. Russel (Ed.), Microbeam analysis-1989, San Francisco Press, San Francisco, CA, 1989, 293.
[11] A.D. Maynard and L.M. Brown, J. Aerosol Sci., 23 (1992) 433.
[12] C. Xhoffer, P. Berghmans, I. Muir, W. Jacob, R. Van Grieken and F. Adams, J. Microsc., 162 (1991) 179.
[13] C. Colliex, J.L. Maurice and D. Ugarte, Ultramicroscopy, 29 (1989) 31.
[14] J. Chazelas, J. Cazaux, G. Gillmann, J. Linch and R. Szymanski, Surface Interface Anal., 12 (1988) 45.
[15] A. Erdemir and C.C. Cheng, Ultramicroscopy, 29 (1989) 266.
[16] P. Dravid, C.E. Lymam, M.R. Notis and A. Revcolevschi, Ultramicroscopy, 29 (1989) 60.
[17] C.J. Powell, in K. Heinrich (Ed.), Characterization of Particles, Proc. of the Particle Analysis Session of the 13th Int. Conf. of Microbeam Analysis Society, Ann Arbor, MI, 1980, p. 131.
[18] X.B. Cox III and R.W. Linton, in K.R. Spurny (Ed.), Physical and Chemical Characterization of Individual Airborne Particles, Wiley Sons, New York, 1986, p. 341.
[19] G. Small, R. Kroutil, J. Ditillo and W. Loerop, Anal. Chem., 60 (1988) 264.
[20] R. Gordon, N. Trivedi and B. Singh, Environ. Sci. Technol., 22 (1988) 672.
[21] D. Cozak, C. Barbeau, F. Gauvin, J.-P. Barry, C. DeBlois, R. De Wolf and F. Kimmerle, Can. J. Chem., 61 (1983) 2753.
[22] F.M. Kimmerle and P. Roberge, Titanium Coated Asbestos Fiber, U.S. Pat., 4,388,149 (1983).
[23] A. Van Meerbeek and E. Ruiz-Hitzky, Coll. Polym. Sci., 257 (1979) 178.
[24] L.A. Grunes, R.D. Leapman, C.N. Wilker, R. Hoffmann and A.B. Kunz, Phys. Rev. B, 25 (1982) 7157.
[25] NAS, The Tropospheric Transport of Pollutants and Other Substances to the Oceans, National Academy of Sciences Press, Washington, DC, 1978, p. 194.
[26] NAS, The Tropospheric Transport of Pollutants and Other Substances to the Oceans, National Academy of Sciences Press, Washington, DC, 1978, p. 243.
[27] R.M. Van Aalst, R.A.M. Van Ardenne, J.F. de Kreuk and Th. Lems, Pollution of the North Sea from the Atmosphere, TNO Report CL 82/152, Organization for Applied Scientific Research, Netherlands, 1982, p. 124.
[28] H. Rodhe, R. Soederlund and J. Ekstedt, Ambio, 9 (1980) 168.
[29] R.M. Van Aalst, in Schneider et al., (Eds.), Dry Deposition of Aerosol Particles: Aerosols, Lewis Publishers, Chelsea, MI, 1986.
[30] J.A. Van Jaarsveld, R.M. Van Aalst and D. Onderdelinden, Deposition of Metals from the Atmosphere into the

North Sea: Model Calculations, Report RIVM 842015002, Bilthoven, Netherlands, 1986, p. 21.
[31] S.A. Slinn and W.G.N. Slinn, Atmos. Environ., 14 (1980) 1013.
[32] G. Weichart, Ambio, 2 (1973) 99.
[33] J. Injuk, Ph. Otten, R. Laane, W. Maenhaut and R. Van Grieken, Atmos. Environ., 26A (1992) 2499.
[34] N.E.G. Lovestam, E. Swietlicki, U. Wätjen, E. Louwerix, A. Perujo and P. Rietveld, Nuclear Instrum. Meth., B69 (1992) 463.

ELSEVIER

Analytica Chimica Acta 297 (1994) 43–53

ANALYTICA CHIMICA ACTA

Surface analytical studies on metal surface and interface phenomena

H. Viefhaus

Max-Planck-Institut für Eisenforschung GmbH, Max Planck Str. 1, D-40237 Düsseldorf (Germany)

Received 13th July 1993; revised manuscript received 29th September 1993

Abstract

Surface and interface segregation phenomena on metals can influence many material properties. From equilibrium surface segregation studies on binary model systems (single crystals), thermodynamic data for the segregation systems can be derived and may be used to explain phenomena on more complex systems. Equilibrium surface segregation is normally limited to occur within one atomic surface layer, but phosphorus segregation is an exception. By interaction with crystal defects, P atoms may also be enriched in subsurface layers. This was confirmed by Auger electron-spectroscopy, x-ray excited photoelectron spectroscopy, depth profiling and atom probe studies on surface and grain boundary segregation for several iron base alloys. The influence of segregation phenomena on some material properties is demonstrated by the results of surface analytical investigations.

Keywords: Surface techniques; Metal interfaces, Metal surfaces, Segregation

Many processes, such as gas–metal reactions, corrosion, catalysis, surface diffusion, sintering, recrystallization, adhesion, friction and wear, are decisively determined by the atomic composition of surfaces of metals. In addition, the atomic composition of internal interfaces, such as grain boundaries, is of great importance as it affects the mechanical properties and corrosion behaviour of metals. At 300 K the outer interfaces will normally be covered by impurity atoms from the ambient gas atmosphere. For materials to be applied at high temperatures, the composition of all interfaces may be drastically changed by segregation phenomena, i.e., by the enrichment of dissolved atoms diffusing from the bulk to surfaces or grain boundaries.

At this institute, the surface segregation

$$\text{atoms(dissolved)} \rightleftharpoons \text{atoms(segregated)}$$

has been investigated for binary alloy systems of composition Fe–X, with X = C, N, P, O, S, Si, Sn, Sb, Al..., by surface analytical methods [1–7]. The concentration of segregated elements on the surfaces could be determined by Auger electron spectroscopy (AES) as a function of bulk concentration of the element X and of temperature. Binding states of the segregated atoms were characterized by x-ray excited photoelectron spectroscopy (XPS) [8–11]. For model systems such as

Correspondence to: H. Viefhaus, Max-Planck-Institut für Eisenforschung GmbH, Max Planck Str. 1, D-40237 Düsseldorf (Germany).

SSDI 0003-2670(93)E0548-L

single crystals of composition Fe–X, additional surface structure information was derived from low-energy electron diffraction (LEED) investigations.

For alloy embrittlement of polycrystalline samples by segregated atoms at grain boundaries, well prepared samples were fractured within the AES system and the grain boundary faces were analysed by AES. Embrittlement decreases the cohesion of grain boundaries and the fracture is mainly along grain boundaries (intergranular). The grain boundary composition with respect to enrichment phenomena may be determined by comparing the Auger electron spectra of trans- and intergranular regions.

The thermodynamics of equilibrium segregation at interfaces (surfaces and grain boundaries) are described by the Langmuir–McLean eq. [12]:

$$\frac{\Theta_i}{1-\Theta} = x_i \exp - \left(\frac{\Delta G_i^0}{RT}\right) \tag{1}$$

where Θ_i is the occupancy of the interface sites with the segregated element and x_i is the mole fraction in the bulk. The free energy of segregation is

$$\Delta G_i^0 = \Delta H_i^0 - T\Delta S_i^{xs} \tag{2}$$

where ΔH_i^0 is the enthalpy of segregation and ΔS_i^{xs} the excess entropy of segregation.

If the temperature- and bulk concentration-dependent equilibrium surface (or grain boundary) coverage of the segregated elements is determined by AES, then according to

$$\ln\left(\frac{\Theta_i}{1-\Theta_i}\right) = -\frac{\Delta H_i^0}{RT} + \frac{\Delta S_i^{xs}}{R} + \ln x_i \tag{3}$$

a plot of the left-hand side of Eq. 3 versus reciprocal temperature should give straight lines, from which the segregation enthalpy and excess entropy can be derived. Fig. 1 shows such a plot for Si surface segregation on a (100) oriented Fe–3%Si single crystal [3]. From this plot a segregation enthalpy $\Delta H_s^0 = -48$ kJ mol^{-1} and an excess entropy $\Delta S_{Si}^0 = -15$ J mol^{-1} K^{-1} were determined.

1. Surface segregation

Equilibrium surface segregation was observed for several (100) oriented Fe–X systems and evaluation of the AES results according to the Langmuir–McLean formalism led to the following results for the binary systems: for silicon $\Delta H_{Si}^0 = -48$, for carbon $\Delta H_C^0 = -85$ and for phosphorus $\Delta H_P^0 = -160$ kJ mol^{-1}. All three elements were present within a (100) oriented single crystal sample of Fe–3%Si, with 90 ppm P and 35 ppm C as bulk impurities (typical transformer steel composition). For the binary systems Fe–X mentioned above, all segregated elements were present at half a monolayer surface coverage ($\Theta = 0.5$) for saturation equilibrium.

Fig. 2 shows the segregation kinetics followed by AES for the (100) oriented Fe–3%Si sample during an increase in sample temperature from 300 to 1173 K. A complex behaviour is observed. The observed segregation kinetics may be explained if one considers the results which were derived from AES studies on surface segregation on the binary systems and if additional information on the diffusivity of the individual components is available. The bulk diffusion coefficient D_X^v for the elements X may be determined from systematic investigations on surface segregation kinetics [13]. For the segregation enthalpies it is known that $\Delta H_{Si}^0 < \Delta H_C^0 < \Delta H_P^0$ and for the diffusivities: $D_v^C \gg D_v^{Si}$; D_v^P. Knowing these data, the segregation kinetics of C, Si and P in Fig. 2 may be discussed. In spite of the low bulk concentra-

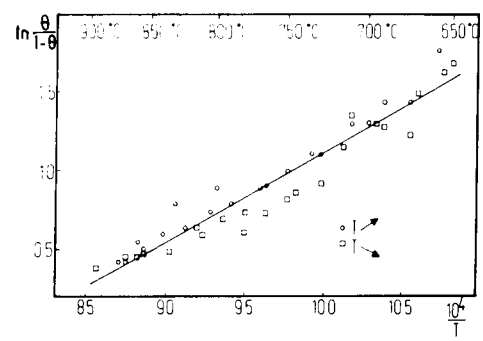

Fig. 1. Langmuir plot for Si equilibrium surface segregation on a (100) oriented Fe–3 wt.% Si single crystal [3].

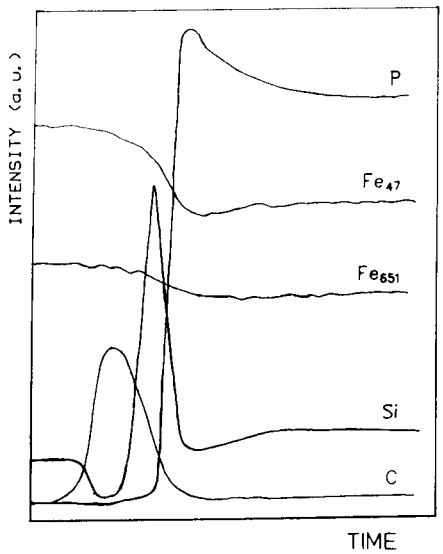

Fig. 2. Surface segregation kinetics of C, Si and P on a (100) oriented Fe–3 wt.% Si–90 ppm (w/w) P–10 ppm (w/w) C single crystal during a temperature increase from 300 to 1173 K.

tion, but because of the large diffusivity, carbon segregates at lower temperatures (> 600 K) to the surface and is enriched within a $c(2\times 2)$ surface structure having $\Theta = 0.5$ at saturation level. Because of the well known strong repulsive interaction between carbon and silicon atoms, the latter atoms are displaced from the surface region at the maximum C segregation level. Even the bulk concentration of 3% Si is no longer present in the outermost layers, as indicated by the complete disappearance of the Si Auger signal. With increasing temperature carbon atoms are dissolved within the bulk and the free surface sites within the $c(2\times 2)$ structure are occupied at least partly by segregating Si atoms. Si is the next element to be enriched because of its high bulk concentration and its diffusivity being comparable to that of P. However, as soon as enough P atoms have diffused to the surface they displace the Si atoms present because of a higher segregation enthalpy for the P atoms. In the final stage, some of the segregated P atoms are dissolved within the bulk and again the free surface sites are occupied partly by Si atoms.

AES studies on equilibrium surface segregation were performed for the same single crystal. During the displacement of segregated Si atoms by P atoms a repulsive interaction between these two atoms was indicated. For the case of an interaction between two segregating species A and B, the segregation enthalpies of the two elements, ΔG^0_A and ΔG^0_B, will depend on the surface coverage Θ. For this case an interaction term is added to the segregation enthalpy (similar to the procedure of changing from the Langmuir adsorption isotherm to the Fowler isotherm), giving:

$$\Delta G_A = \Delta G^0_A + \alpha'_{AB}\left(\Theta^s_B - x^b_B\right) \quad (4a)$$

and

$$\Delta G_B = \Delta G^0_B + \alpha'_{AB}\left(\Theta^s_A - x^b_A\right) \quad (4b)$$

where ΔG^0_X is the free segregation enthalpy for the binary systems and α'_{AB} represents the excess energy which results if a couple AB is formed with respect to the interaction within the bulk. Negative values of α'_{AB} mean an attractive interaction and lead to cosegregation and/or to the formation of surface compounds of the two cosegregating species [14]. For $\alpha'_{AB} > 0$ the degree of segregation should be decreased for both species. Depending on the bulk concentration and the ΔG^0 values, complete desegregation of one species can be observed, which is demonstrated by Fig. 3 for C and Si surface segregation

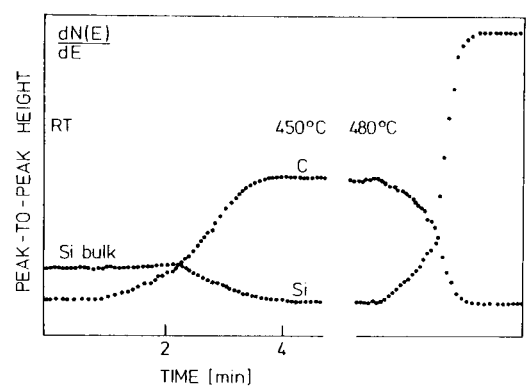

Fig. 3. C and Si surface segregation and displacement reaction on a (100) Fe–3 wt% Si single crystal with carbon as bulk impurity.

on (100)Fe–3%Si with carbon as an impurity. At the carbon saturation level no further AES signal of Si could be detected.

Fig. 4 shows that during the displacement of segregated Si atoms by also segregating P atoms on the (100) surface, the total surface coverage passes through a temperature-dependent minimum, which is caused by a repulsive interaction between the two segregating atoms. What was true for the segregation system Si and C is also observed for the system Si and P, namely that at higher temperature a complete disappearance of Si atoms occurs for a high coverage of P atoms. On increasing the temperature further, Si atoms may appear again to occupy surface sites which have become free by the dissolution of P atoms. At about 1100 K the Si concentration corresponds again to the bulk concentration observed without any segregated atoms. If only the bulk concentration is present, ΔG_{Si} should be zero at this temperature. According to Eqs. 4a and b and considering the thermodynamic data for the binary systems (ΔG^0_{Si}) at 1100 K, the interaction coefficient α'_{SiP} may be evaluated:

$$\Delta G_{Si} = \Delta G^0_{Si} + \alpha'_{SiP}\Theta^s_P = 0$$

Θ^s_P can be derived from the fact that the maximum P coverage corresponds to $\Theta = 0.5$ on the (100) surface. A high interaction coefficient of 84 kJ mol^{-1} results.

From the temperature dependence of the P equilibrium segregation coverage according to the Langmuir plot in Fig. 5, the values $\Delta H_P = -180$ kJ mol^{-1} and $\Delta S_P/R = -8.4$ are obtained.

For nearly all the (100) oriented Fe–X systems studied so far, even at the segregation saturation level the enrichment by segregated atoms is observed to be within a monolayer on the surface. The segregation of P (and possibly also of sulphur) can be different, as will be demonstrated by the following experimental studies and their interpretation.

During P surface segregation on a (100) oriented Fe surface, LEED measurements indicate a $c(2 \times 2)$ structure which leads to half a monolayer coverage at saturation level. At the P surface saturation level for a (100) Fe–1.8%P sample, Egert and Panzner [8] observed by XPS measurements two binding states for the P $2p$ elec-

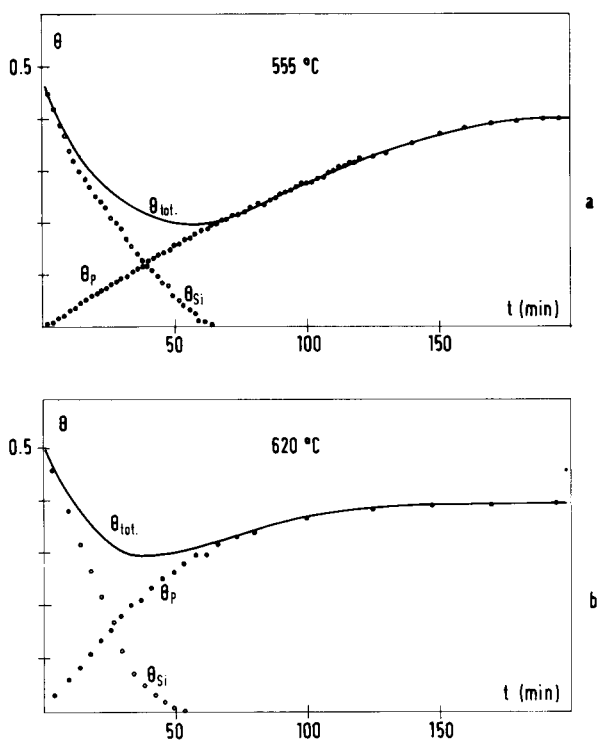

Fig. 4. Displacement of segregated Si atoms by also segregating P atoms on a (100) oriented surface of a single crystal. Composition as in Fig. 2. (a) At 555°C; (b) at 620°C.

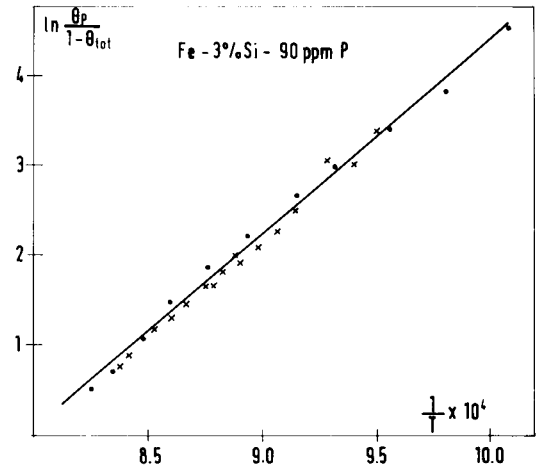

Fig. 5. Langmuir plot of the P equilibrium surface segregation on a (100) single crystal surface. Sample composition as in Fig. 2.

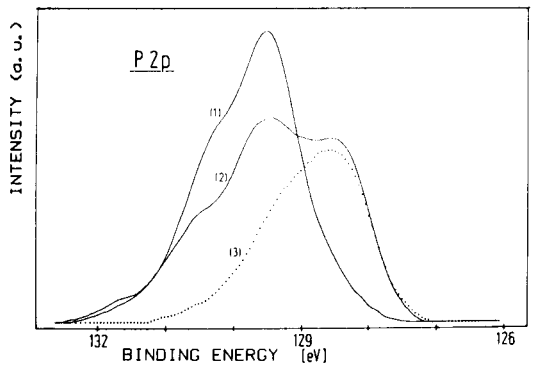

Fig. 6. XPS spectra for the phosphorus $2p$ core level [8]. (1) For Fe_3P; (2) for a (100) oriented Fe–1.8 wt.% P single crystal, P at segregation saturation level; (3) same as (2) but only P surface coverage.

tron level. This is reproduced by spectrum (2) in Fig. 6. This spectrum looks very similar to the P $2p$ spectrum (1) of Fe_3P in Fig. 6. However, the formation of Fe_3P for the case of P segregation may be ruled out as the LEED pattern shows only the $c(2 \times 2)$ structure and Fe_3P should yield a complex LEED pattern because of its complicated crystallographic structure.

By a more detailed AES analysis of the P segregation process [5], it was recognized that after establishing surface saturation with segregated P atoms on the (100) surface, which is confirmed by the well developed $c(2 \times 2)$ LEED pattern, a further increase in the P Auger signal at 120 eV energy was recorded if the sample was held at higher temperature (Fig. 7). No change in the observed LEED pattern could be detected during this additional increase in P Auger intensity.

To explain all these observations, it was assumed that after establishing surface saturation with segregated P atoms, further enrichment of diffusing P atoms in subsurface layers occurs. Additional studies were performed to confirm this assumption. An Auger spectrum of P is characterized by two main signals, one at a low energy of 120 eV and a second one at a high energy of 1860 eV. Because of the large energy difference for the two corresponding Auger electrons, the information depth for the two P signals is quite different. Whereas the low-energy signal is very

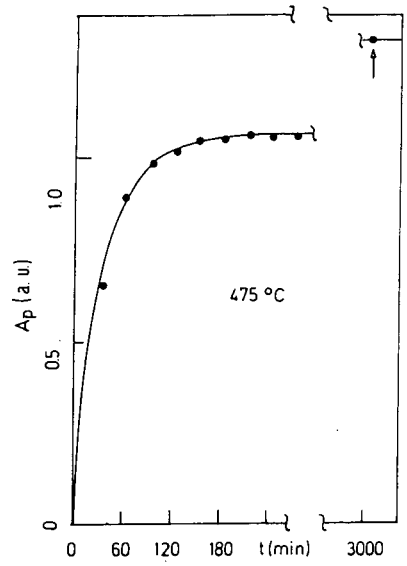

Fig. 7. P enrichment kinetics on (100) oriented surface of a Fe–1 wt.% P single crystal at 475°C [5].

surface sensitive, the signal at 1860 eV energy reveals information for about 50 atomic layers. Having reached P surface saturation enrichment, further enrichment in subsurface layers should therefore mainly influence the high-energy P signal. A plot of the high-energy signal A_H^p of P against the low-energy signal A_L^p (Fig. 8) confirms this as it shows that after some time only an increase in the high energy signal is measurable.

Having obtained by these studies a first confirmation of subsurface enrichment for P, further

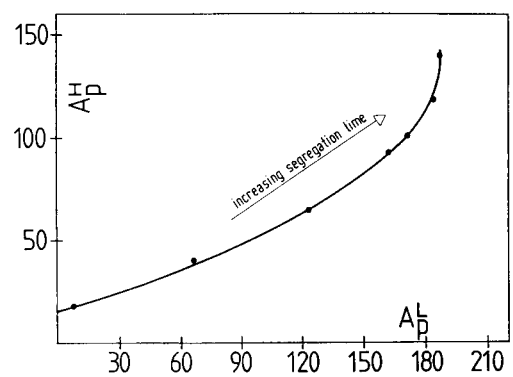

Fig. 8. Plot of the P Auger signal at high energy, A_p^H, versus P Auger signal at low energy, A_p^L, for a P segregation cycle from a clean surface to the saturation state.

confirmation was derived from AES depth profiles recorded for different P segregation levels of the (100) oriented sample.

After establishing different segregation levels for the P atoms, AES depth profiles were recorded for the following conditions: (1) at 300 K and only surface saturation with P atoms; (2) at 300 K and after prolonged enrichment of P; (3) at 773 K and only surface saturation; and (4) at 773 K and with the assumed subsurface enrichment of P. The results of the different AES depth profiles recorded for 3 keV Ar^+ ions and a 1 μA cm^{-2} ion beam current density are summarized in Fig. 9. For the depth profiles recorded at 773 K the final state corresponds nearly to a steady-state condition between P atom removal by Ar^+ ions and segregation of P atoms by diffusion from the bulk. Because of subsurface enrichment of P in case 4 the replacement of sputtered P atoms is initially so fast that a nearly constant surface concentration results. After this initial period the sputter profile corresponds approximately to that of case 3.

Having now confirmed the subsurface enrichment of P, the question arises of what the reason for this additional segregation of P atoms is. An explanation could be an interaction of P atoms with crystal defects, such as dislocations, which move to the surface at higher temperatures. Indications of such an interaction were derived from the observation that after repeated P segregation and sputter removal cycles, the additional enrichment of P disappeared more and more and finally only surface saturation could be observed.

If an interaction of P atoms with dislocations exists there should be an influence of the number of dislocations on P diffusion and segregation. The density of dislocations within a sample may be increased by deformation of the sample and stabilizing the dislocation density by alloying molybdenum.

The P segregation kinetics for such a deformed polycrystalline Fe–Mo–P alloy (Fig. 10), demonstrate a pronounced further increase in P Auger intensity after the surface has been saturated. The influence of dislocation density on P diffusion is illustrated in Fig. 11. The diffusivity for P was determined by tracer methods for non-deformed and deformed Fe–Mo alloys. A marked increase in the diffusivity for the deformed samples can be recognized.

The possible interaction between dislocations

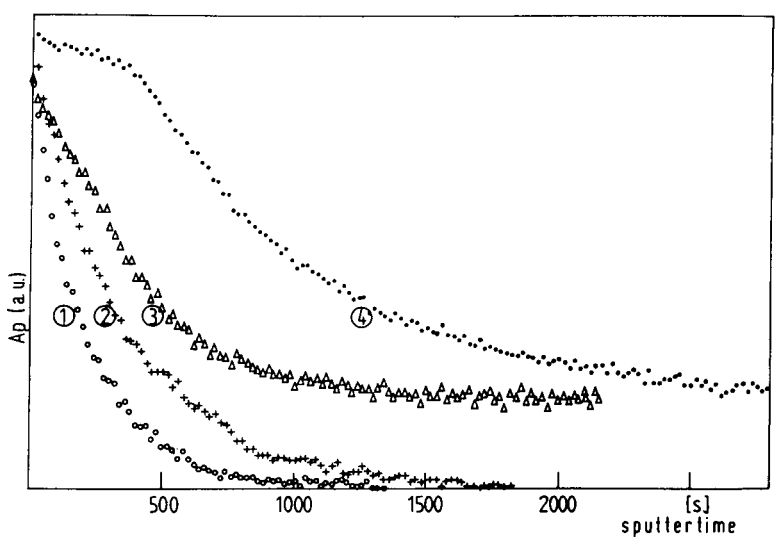

Fig. 9. AES sputter profiles for a (100) oriented Fe–1 wt.% P sample and P at different segregation levels (see text). (1) At 300 K and surface saturation level; (2) at 300 K and surface saturation and subsurface enrichment of P; (3) at 500°C and same as (1); (4) at 500°C and same as (2). Sputter conditions: Ar^+ ions of 3 keV energy and 1 μA cm^{-2} beam current density.

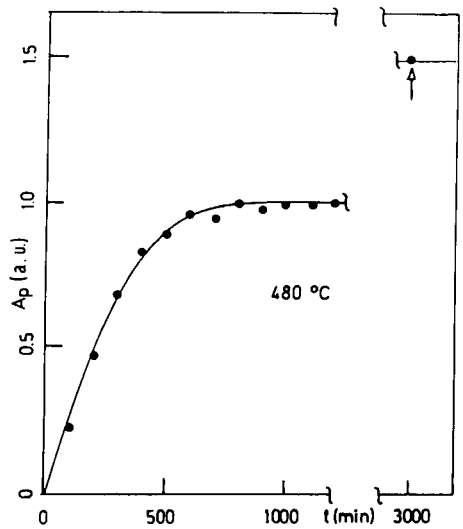

Fig. 10. P enrichment kinetics on an Fe–0.55 wt.% Mo–250 ppm (w/w) P sample at 480°C.

and dissolved P atoms will be discussed later again in connection with grain boundary segregation studies.

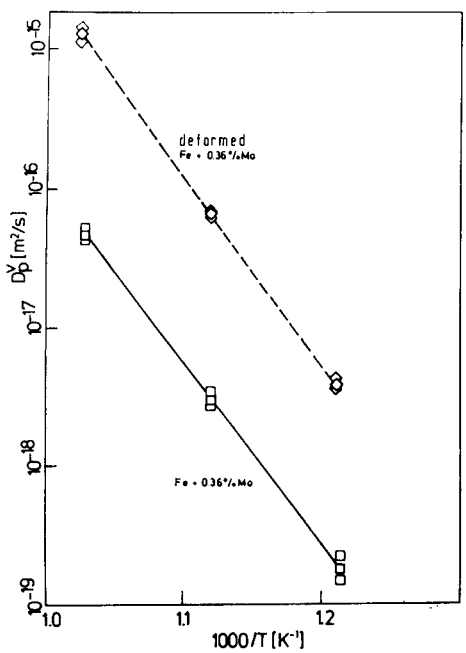

Fig. 11. Diffusivities for P volume diffusion in non-deformed and deformed Fe–Mo alloys (composition as in Fig. 10) determined by tracer methods [5].

2. Grain boundary segregation

The very surface-active elements S and P also show a strong tendency for enrichment at grain boundaries of metals and cause the well known phenomenon of temper embrittlement of steels. Problems with grain boundary segregation of S may be solved by adding some Mn to the alloy and with MnS formation there are no further mobile (dissolved) S atoms for segregation. No similar solution was found for dissolved P atoms and the avoidance of pronounced grain boundary segregation of P is of great importance for steels which are applied at higher temperatures.

For Fe–P alloys with bulk concentrations of P in the range 0.003–0.3% the grain boundary segregation equilibrium

P (in the bulk) ⇌ P (at the grain boundary)

established in the temperature range 673–1073 K was studied by AES for fractured samples [15]. Sample fracture was performed within the surface analytical system and AES was applied to determine the P grain boundary concentration.

The results of the temperature dependence for the equilibrium P grain boundary concentration could again be described by the Langmuir–McLean Eq. 1 and Fig. 12 gives the corresponding Langmuir plot and the derived thermodynamic data for P grain boundary segregation.

Similar studies on the influence of P grain boundary segregation on temper embrittlement were performed on steel samples with additional

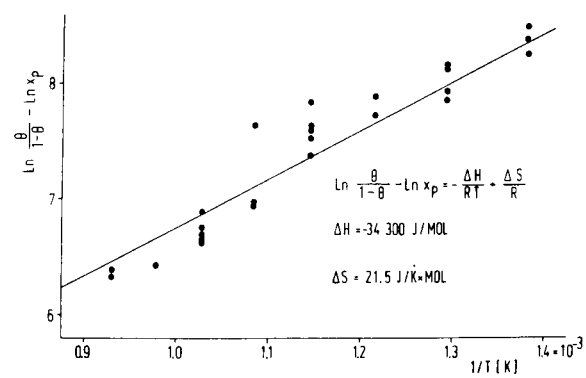

Fig. 12. Langmuir plot for P equilibrium grain boundary segregation in Fe–P alloys [15].

metal alloy components [16]. The beneficial effect of molybdenum on the temper embrittlement of steels is well known [17], but there was no satisfactory explanation for the influence of Mo. As Mo has only a small effect on the amount of P segregated at grain boundaries in carbon-free iron alloys [18], it is likely that Mo has to be present in the form of carbides to be able to scavenge the P. During nucleation and growth of precipitates such as carbides, dislocations are formed surrounding the precipitates. A possible explanation for the influence of Mo carbides could therefore be that by interaction with dislocations a trapping effect for P atoms in some region around the Mo carbides occurs.

To confirm this assumption, a field ion microscopy (FIM)/atom probe was used to measure the concentration of P within the Mo carbides and in some region surrounding the precipitates [19].

Fig. 13 shows a plot of data which were obtained from a 3 nm diameter carbide particle formed during 380 h of annealing at 873 K. The plot shows 20 atoms per line, which was estimated to be approximately equal to the number of atoms collected from each evaporated layer of 0.4 Å thickness. No P atoms were observed within the carbide and no marked enrichment of P at the carbide/matrix interface, but an enhanced P concentration of about 2% was observed within a region ca. 15 nm wide surrounding the carbide. This enrichment is probably caused by the dislocations being present there and again an indication of P atom interaction with dislocation obtained.

Precipitates may also be present at grain boundaries of steels in the form of carbides, nitrides or sulphides. Their influence on P grain boundary segregation and possible correlations with dislocation formation and interaction are the main topic of current research in this area of interface analysis.

If the discussion is not restricted to equilibrium segregation at surfaces and grain boundaries and the segregation behaviour of further impurity or alloying elements is considered a lot of additionally observed phenomena which may occur at interfaces could be presented. Only a few additional examples demonstrating the influence of segregation effects on material properties and the possibilities of surface analytical methods will be presented here.

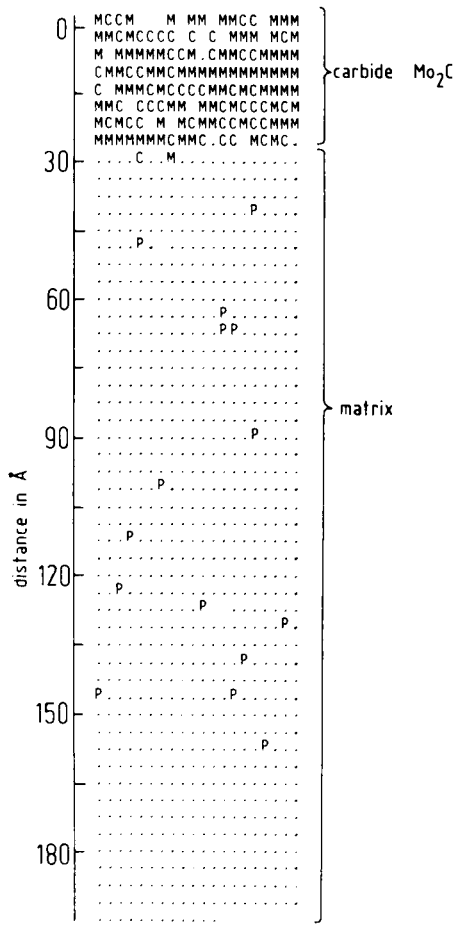

Fig. 13. Field evaporation sequence through carbide and region surrounding it. M = molybdenum; C = carbon, dots = iron and P = phosphorus [19].

Corrosion-protecting layers are of special importance for the application of high-temperature materials. The formation of slow-growing, dense and well adherent oxide layers would be desirable. Al_2O_3 would be a good candidate because of its thermodynamic stability under all practical conditions. Alumina layers, however, often exhibit bad adherence, leading to spalling off for the oxide layer, especially during thermal cycling. To improve the adherence of alumina layers,

several model alloys were studied, of which the alloy Fe–6Al containing 0.1–1% Ti showed very good results. In order to obtain information on the reason for the improved adherence properties, sputter profiles were recorded for the oxide layers which had been formed on this model alloy. A typical sputter profile is presented in Fig. 14. The most important feature of the profile is the simultaneous enrichment of C and Ti at the oxide/matrix interface, indicating the formation of a TiC or Ti(C, O) layer at the interface by segregation of C and Ti. The formation of this TiC layer was studied systematically with AES and LEED on surfaces of single crystals having the same composition and different orientations [20]. It was shown that this TiC layer grows epitaxially on the low-indexed faces of this alloy and during the initial stages of oxidation also the Al_2O_3 layer grows epitaxially on top of the TiC layer. The good adherence of the TiC layer was also indicated by a very low sputter rate for Ti and C in comparison with sputter rates for oxide films. With respect to Fig. 14, this means that only a very thin layer was present, but because of the low sputter rate for Ti and C the profile is broadened.

This example shows that the adherence of corrosion layers may be improved by segregating elements forming a thin intermediate layer between the oxide and matrix. The influence of segregating elements on the adherence of oxide layers on high-temperature materials may not always be positive as will be seen from the next example. For several years it has been discussed in the literature that sulphur may segregate to the oxide/matrix interface, leading to reduced adherence of the oxide layer. In order to obtain information on the composition of the oxide/matrix interface, it would be desirable to analyse the interface by surface analytical methods. Thin foils of typical high-temperature materials were oxidized and small slices of the oxidized foil were fixed at one end on a sample holder for the scanning Auger system. After introducing the sample into the ultra-high vacuum (UHV) system, the free end of the foil could be bent by a wobble stick in order to induce at least partly oxide removal from the substrate. Those parts exhibiting the oxide/matrix interface could be analysed by AES with high lateral resolution.

To elucidate this kind of experiment, as an example results of a scanning electron microscope (SEM) and AES study on an Fe–18Cr–12Al alloy will be described. The SEM image in Fig. 15 shows some areas where the oxide layer has been removed, but at some other regions the oxide is still present. The oxide areas appear bright if the oxide is still adhering to the metal matrix and

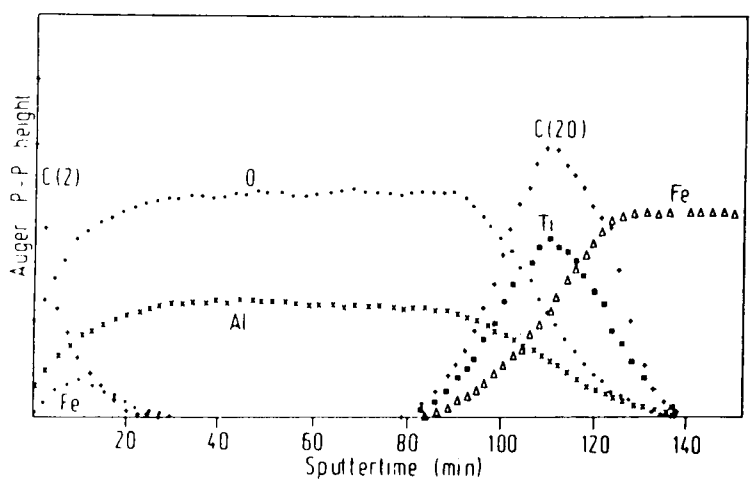

Fig. 14. AES depth profile of an oxidized Fe–6Al–0.5Ti–0.01C sample, oxidized at 1273 K in an oxygen atmosphere of 10^{-19} bar for 30 min [20].

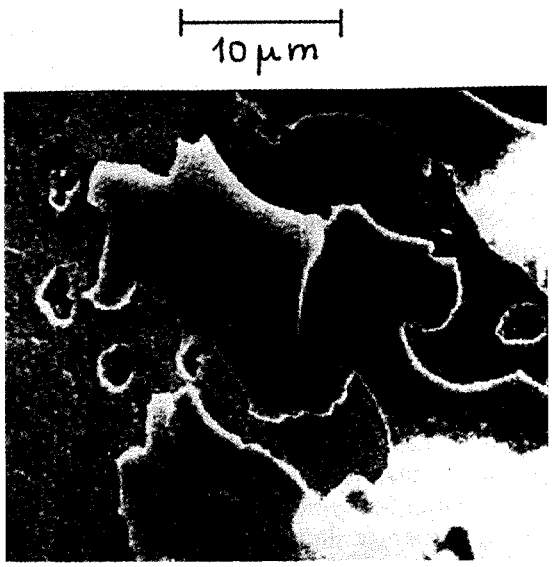

Fig. 15. SEM image of an oxidized Fe–18Cr–12Al sample. The oxide is partly removed within the UHV system.

dark corresponding to parts of the oxide layer where contact with the matrix has been lost. For the interface regions a pronounced roughness can be recognized and several voids may be detected. Fig. 16 gives a more detailed SEM image of the rough matrix and of several voids. Again, the bright area corresponds to a small part of still adhering oxide layer. An elemental map for sulphur on the same area as in Fig. 16 is depicted in Fig. 17. It illustrates that sulphur is strongly en-

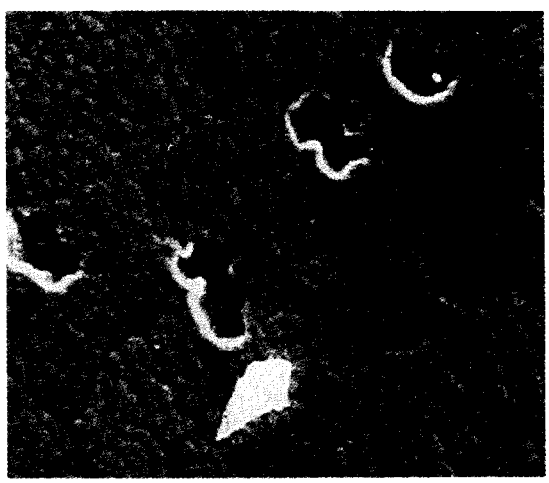

Fig. 16. SEM image exhibiting the interface between oxide and matrix. Dark areas are voids and the bright area corresponds to some part of still adhering oxide.

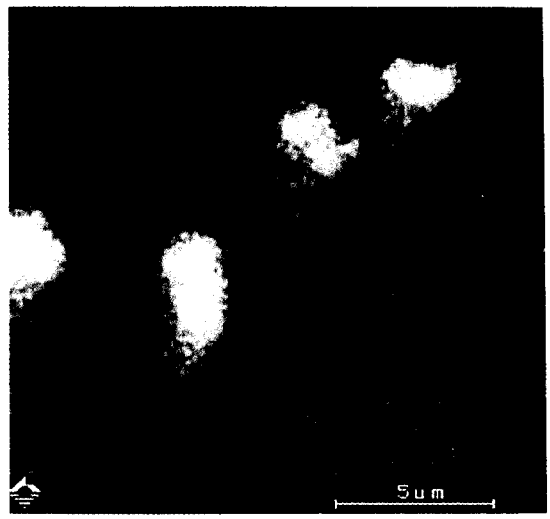

Fig. 17. Sulphur elemental map of the same area as in Fig. 16. Bright areas correspond to enhanced S signal intensity.

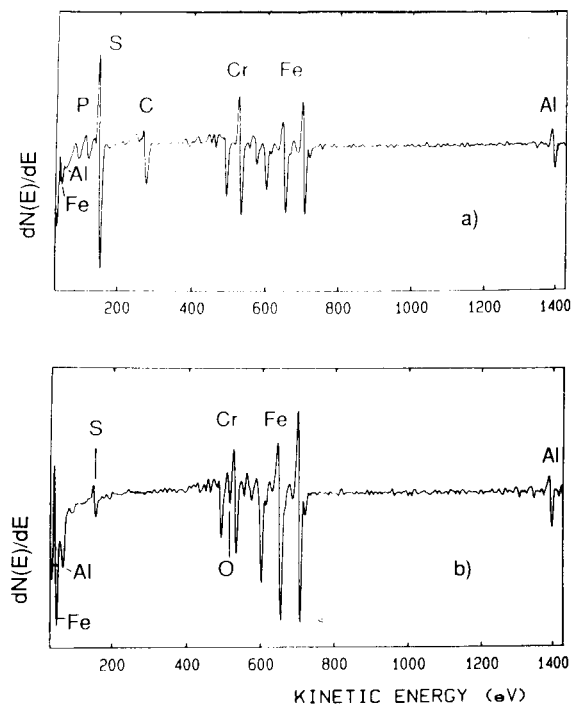

Fig. 18. AES point spectra recorded (a) within the voids and (b) on the matrix (cf., Fig. 17).

Fig. 19. SEM image of a grain boundary on a fractured sample.

riched within the voids. Auger electron spectra recorded within the voids and on the matrix are reproduced in Fig. 18. The small amount of S to be detected on matrix regions may be caused by already existing micro voids.

Hence the main influence of sulphur segregation seems to be that it favours the formation of voids because of a pronounced decrease in surface energy. This effect also results in a decrease in layer adherence.

Voids or pores may also be present at grain boundaries, as will be seen in the next example. On the SEM image in Fig. 19 of a fractured Ni–Fe–Al–Cr sample exhibiting part of a grain boundary, the existence of voids or pores can clearly be seen. Again, a sulphur map was recorded for the same area and is shown in Fig. 20. Sulphur enrichment within the voids or pores is illustrated. Unexpectedly, for this case no sulphur could be detected on the grain boundary.

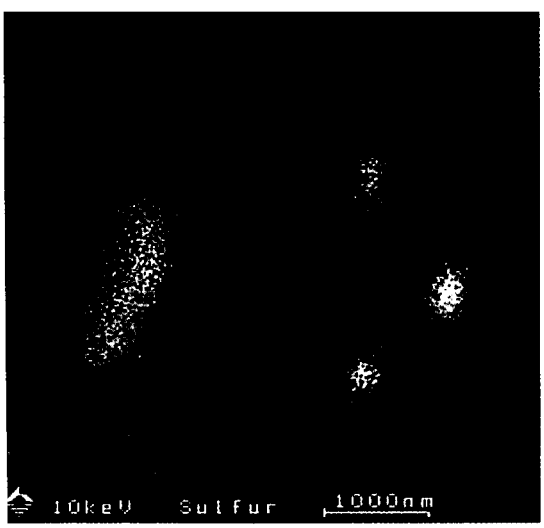

Fig. 20. Sulphur elemental map of the same sample area as shown in Fig. 19.

References

[1] H.J. Grabke, H. Viefhaus, G Tauber and W. Paulitschke, Surf. Sci., 63 (1977) 391.
[2] H. Viefhaus and H.J. Grabke, Surf. Sci., 109 (1981) 1.
[3] H. de Rugy and H. Viefhaus, Surf. Sci., 173 (1986) 418.
[4] H. Viefhaus and M. Rüsenberg, Surf. Sci., 159 (1985) 1.
[5] H. Viefhaus, J. Wittig and K. Hennesen, Nichtmetalle in Metallen, DGM, Oberursel, 1988, p. 245.
[6] M. Rüsenberg and H. Viefhaus, Surf. Sci., 172 (1986) 615.
[7] M. Rüsenberg, PhD Thesis, University of Dortmund, Dortmund, 1986.
[8] B. Egert and G. Panzner, Surf. Sci., 118 (1982) 345.
[9] G. Panzner and W. Diekmann, Surf. Sci., 160 (1985) 253.
[10] G. Panzner and B. Egert, Surf. Sci., 144 (1984) 651.
[11] W. Diekmann, G. Panzner and H.J. Grabke, Surf. Sci., 218 (1989) 507.
[12] H.J. Grabke and H. Viefhaus, in H.J. Gabke (Ed.), Oberflächenanalytik in der Metallkunde, DGM, Oberursel, 1983, p. 93; and in P.A. Dowlen an A. Miller (Eds.), Surface Segregation Phenomena, CRC Press, Boca Raton, FL, 1990, p. 207.
[13] K. Hennesen, H. Keller and H. Viefhaus, Scr. Met., 18 (1984) 1319.
[14] Ch. Uebing and H. Viefhaus, in Surface Segregation Phenomena, CRC Press, Boca Raton, FL, 1990, p. 241.
[15] H. Erhart and H.J. Grabke, Met. Sci. 15 (1981) 401.
[16] H.J. Grabke, Surf. Interface Anal., 14 (1989) 686.
[17] J. Yu and C.J. McMahon, Metall. Trans., 11A (1980) 277.
[18] D.Y. Lee, E.V. Barrera, J.P. Stark and H.L. Marcus Metall. Trans., 15A (1984) 1415.
[19] R. Möller, S.S. Brenner and H.J. Grabke, J. Phys. (Paris) C2, 3 (1986) 277.
[20] H. Viefhaus, J. Peters and H.J. Grabke, Surf. Interface Anal., 10 (1987) 280.

ELSEVIER

Analytica Chimica Acta 297 (1994) 55–72

ANALYTICA CHIMICA ACTA

Review

High energy ion scattering and recoil spectrometry in applied materials science

L.J. van IJzendoorn

Cyclotron Laboratory, Eindhoven University of Technology, P.O. Box 513, 5600 MB Eindhoven, Netherlands

(Received 23rd July 1993, revised manuscript received 28th January 1994)

Abstract

The fundamentals of high energy ion scattering and recoil spectrometry (possibly combined with channelling) are discussed in relation to the accuracies required for materials science studies and in relation to characteristics of competing surface analysis techniques. The extreme versatility of ion scattering techniques is demonstrated by a survey through many application areas in materials science ranging from plastics to oxidic insulators, semiconductors and metals.

Keywords: Surface techniques; High energy ion scattering; Recoil spectrometry; Materials science

1. Introduction

During the past three decades ion scattering evolved as a mature analytical technique in the field of materials science. Among a large number of techniques which are specifically sensitive to surfaces such as Auger electron spectroscopy (AES), x-ray photo-electron spectroscopy (XPS) and electron microprobe analysis, ion scattering became well established mainly because of its reliable quantitative character and the possibility of depth profiling without the use of sputtering.

Several analytical techniques can be distinguished based on differences in the energy of the incident ions. After a tour through the basics of ion scattering, this review will primarily handle incident ion energies above 1 MeV and the corresponding techniques classified under high energy ion scattering (HEIS). Among these, Rutherford backscattering spectrometry (RBS) is the most important exponent. The use of these high incident ion energies also enables the possibility to detect the recoiled particle of each individual scattering event which corresponds to techniques named by recoil spectrometry (usually denoted as elastic recoil detection analysis (ERDA)). The phenomenon of ion channelling basically applicable to all ion scattering techniques will also be addressed.

An exhaustive treatment of the details of RBS and channelling can be found in several excellent reviews [1,2]. This paper makes an attempt to discuss the most important application areas of HEIS by selecting a large number of examples ranging from the research on thin layers in semiconductor industry towards the analysis of catalysts in surface chemistry. In the first part of the paper the basic principles of ion scattering will be addressed with an emphasis put on the specific merits and disadvantages in order to stress the

SSDI 0003-2670(94)00055-Q

importance of selecting the analysis techniques most ideally suited to study a specific problem in materials science.

2. Fundamentals

2.1. Element identification

All ion scattering techniques rely on the detection of energy transfer in a binary collision between the incident ion and a nucleus of the target. This binary collision can be of an elastic as well as an inelastic nature. In most cases elastic scattering occurs. Only for low mass incident ions and energies above ~ 3 MeV the Coulomb repulsion is overcome and the target nucleus can be excited.

The energy of both the scattered ion and the recoiled nucleus can be calculated accurately from the laws of conservation of energy and momentum and are usually expressed in the so called kinematic factors:

$$K_1 = \frac{E_1}{E_0} = \left\{ \frac{\cos\theta + \sqrt{\cos^2\theta - (1+\mu)(1-\mu+\mu Q/E_0)}}{1+\mu} \right\}^2 \quad (1)$$

and

$$K_2 = \frac{E_2}{E_0}$$

$$= \frac{\mu}{(1+\mu)^2}\cos^2\phi \left\{ 1 \pm \sqrt{1 - \frac{(\mu+1)Q}{\mu E_0 \cos^2\phi}} \right\}^2 \quad (2)$$

The energy of the incident ion is E_0 while E_1 represents the energy of the incident ion after scattering at an angle θ with the direction of the incident beam. E_2 is the energy of the nucleus recoiled under an angle ϕ (see Fig. 1). The mass ratio of the recoiled and incident particle (M_2/M_1) is represented by μ and Q is the kinetic energy lost in case of an inelastic collision. Excitation of the nucleus is an endothermic reaction, which implies a positive quantity for Q. For elastic collisions $Q = 0$. The unique relation between K_1 (or K_2) and M_2 (via μ) allows the identification of the target nucleus by measuring the energy of the scattered or recoiled particle.

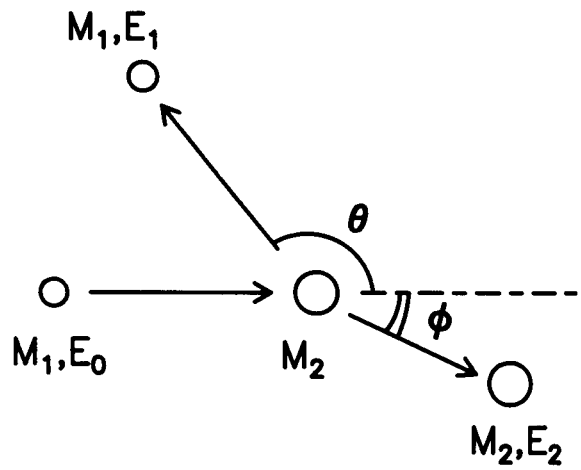

Fig. 1. The basic scattering geometry and definition of scattering parameters in the laboratory frame of reference.

The energy resolution of the detection system, which is, throughout this paper, assumed to be the commonly used solid state surface barrier detector with an energy resolution of ~ 15 keV, thus directly limits the mass resolution and therefore also a reliable element identification. Optimum mass resolution is obtained for backscattering angles near 170°. Nevertheless, RBS with 2 MeV He ions and a scattering angle of 170° is not capable of distinguishing individual isotopes with a mass-difference of 1 atomic mass unit (amu) for $M_2 \geqslant 40$. For target nuclei with masses around 200 amu the mass resolution is about 20 amu which implies that, e.g., Pb and W cannot be distinguished. A better mass resolution is obtained when the ratio M_1/M_2 ($=\mu^{-1}$) approaches unity, e.g., when scattering or recoil experiments are carried out with heavy projectiles.

2.2. Depth profiling

The penetration of fast projectiles in a solid allows not only scattering to occur at the surface of a sample but also at depth. Particles scattered at depth loose energy due to scattering kinemat-

ics but also by interaction with the atoms along their trajectory in the solid. The projected range or penetration depth strongly depends on the energy and charge of the projectile nucleus Z and is connected with the analysable depth. The global separation between low energy ion scattering (LEIS) or ion scattering spectroscopy (ISS) ($E_0 \leqslant 10$ keV), medium energy ion scattering (MEIS) (10 keV $\leqslant E_0 \leqslant$ 500 keV) and high energy ion scattering (HEIS) ($E_0 \geqslant 500$ keV) is mostly concerned with this analysable depth range and with the cross section of the scattering process. In general, LEIS and MEIS obtain information from the outermost surface layer and the first ~ 10 nm respectively and only HEIS techniques facilitate depth profiling over hundreds of nanometres. The projected range of 2 MeV He^+ ions (used in RBS) is ~ 5–10 μm and scattered ions from a depth of ~ 1–2 μm are still detectable.

Basically, two energy loss mechanisms can be distinguished: at first ionisation and excitation of the electrons in the solid called electronic stopping and secondly energy loss by many small angle collisions with the nuclei in the solid called nuclear stopping. For HEIS techniques electronic energy loss is approximately a factor 10^3 higher than nuclear energy loss. An important consequence is that the sputter yield of MeV light ions (H and He) is very low ($\leqslant 10^{-3}$) which implies negligible sample erosion during a typical scattering experiment. The possibility of non-destructive depth profiling (i.e., depth profiling without sputtering also denoted as non-consumptive) can thus be achieved and is one of the strong advantages of depth profiling by ion scattering techniques.

The measurement of the energy of the scattered or recoiled particles thus serves both the purpose of element identification and to calculate the depth at which scattering occurred. For multi-layered samples containing several elements this can lead to ambiguities between the mass of target atom and its depth in the sample. The energy loss of ions per unit length ($\mathrm{d}E/\mathrm{d}x$) is usually represented by the stopping power cross-section ϵ defined as $\mathrm{d}E/N\mathrm{d}x$ in units of eV cm^2 (N represents the atomic density of the material). For the entire process, describing energy loss on both ingoing and outgoing paths and the collision with an atom A in a compound of composition AB, the energy loss factor is defined as:

$$\epsilon_{\mathrm{A}}^{\mathrm{AB}} = \frac{K_{\mathrm{A}}\epsilon^{\mathrm{AB}}(E_0)}{\cos\theta_1} + \frac{\epsilon^{\mathrm{AB}}(K_{\mathrm{A}}E_0)}{\cos\theta_2} \qquad (3)$$

θ_1 and θ_2 are the angle between the incoming beam with the sample normal and the outgoing beam with the sample normal respectively. This relation allows to relate the detected ion energy with the depth at which scattering occurred. The stopping power of the projectile is assumed to be constant along the ingoing path $\epsilon(E_0)$ (the so-called surface approximation) justified by the slow variation of ϵ with E. The same holds for the particle along the outgoing path $\epsilon(K_{\mathrm{A}}E_0)$. Using grazing incidence or a grazing exit angle (either θ_1 or θ_2 approaches 90 degrees), the energy loss can be increased for scattering at a specific depth and the depth resolution can be increased.

The depth resolution which can be achieved is directly coupled to the magnitude of the electronic stopping which is tabulated for H and He ions in all elements by Ziegler et al. [3]. A semi-empirical fitting procedure through many experimental data points results in an estimated accuracy of 5–10% in the values of the stopping power for He in every individual element. Concerning recoil spectrometry, scaling laws also allow estimates for stopping powers of heavy projectiles but the scarce experimental data limits the accuracy of these stopping powers to ~ 20–30%.

The stopping power in compounds can be calculated using Bragg's rule which postulates that the stopping power is a linear combination of the elements in the compound weighted by their abundance. This approximation which is found to introduce errors less than 5% for alloys, usually produces uncertainties of 10–20% for compounds of which at least one element is volatile in atomic form.

Generally, the stopping power has a maximum value near an energy of the projectile of ~ 100–300 keV/amu and is gradually decreasing with increasing energy above 300 keV/amu. An increase in the energy of the projectile then results

in a decrease in depth resolution. The typical depth resolution for RBS (2 MeV He^+, $\theta = 170°$, normal incidence) is ~ 20 nm while increasing the energy to ~ 9 MeV decreases the depth resolution to ~ 50 nm. In specific examples of very flat samples with grazing angle techniques, the depth resolution for RBS can be as good as 1–2 nm near the surface of the sample [4].

Apart from the magnitude of the stopping power and the scattering geometry also the resolution of the detection system plays a decisive role in the depth resolution. Fundamental limits to the depth resolution are posed by the statistical nature of the interaction of the throughpassing ions with the electrons (energy straggling) and multiple scattering which cause a deteriorating depth resolution with increasing depth. Boerma et al. [5] discussed the ultimate resolution for both RBS and recoil spectrometry in conjunction with the design of a magnetic spectrograph.

Concluding, it should be pointed out that the depth resolution of RBS as such, is definitely not superior to the depth resolution which can be achieved using sputtering in combination with surface sensitive techniques like secondary ion mass spectrometry (SIMS), AES or XPS. A major advantage of ion scattering techniques however is the fact that sputtering is unnecessary. Awkward problems involving differences in sputtering speed when crossing a layered structure and differences in preferential sputtering yields are avoided.

2.3. Sensitivity, accuracy and detection limits

As was already indicated by the possible inelastic nature of the collision, an important choice in the design of a scattering experiment concerns the energy of the incident ion beam. Traditionally the most popular (and useful) energy interval which allows a straightforward quantification of the results concerns the situation when the incident energy is too low to induce inelastic collisions or nuclear reactions and too high to require corrections on the scattering cross-sections due to screening of the nuclei by electrons. In this energy domain the differential scattering (or recoil) cross-sections can be calculated analytically using only Coulomb repulsion between the two nuclei:

$$\frac{d\sigma}{d\Omega} = \left(\frac{Z_1 Z_2 e^2}{4E}\right)^2 \frac{4}{\sin^4\theta} \times \frac{\left\{\sqrt{1-\left(\mu^{-1}\sin\theta\right)^2} + \cos\theta\right\}^2}{\left\{\sqrt{1-\left(\mu^{-1}\sin\theta\right)^2}\right\}} \quad (4)$$

In this formula, originally derived in a slightly different form by Ernest Rutherford in 1911 [6], Z_1 represents the charge of the incident ion and Z_2 the charge of the target nucleus. This expression shows directly the increasing sensitivity of ion scattering techniques with the atomic number of the target nucleus. For RBS this implies a detection limit for surface impurities on a Si wafer of $\sim 3 \times 10^{14}$ at./cm^2 for Cl and even $\sim 3 \times 10^{11}$ at./cm^2 (10^{-4} monolayer) for Au! This detection limit can be improved by increasing the mass of the incident ion or lowering the incident energy. Recently, this was demonstrated by Doyle and co-workers [7,8] who advertised the heavy ion backscattering spectrometry (HIBS) technique using 200–400 keV C^+ ions bringing detection limits down to $\sim 10^{10}$ at./cm^2 for Fe on Si and $\sim 8 \times 10^8$ at./cm^2 for Au on Si.

For the materials scientist, one of the most important advantages of ion scattering techniques is the quantitative nature without the use of external standards. This quantitative nature is solely based on the accuracy of the Rutherford formula. It is therefore of prime importance to indicate the energy regime in which this formula is valid. At the high energy end, the thresholds of non-Rutherford nuclear cross-sections have been successfully derived by Bozoian and co-workers [9–11] for $Z_1 = 1$, 2 and 3 projectiles using a Yukawa-like perturbation to the Coulomb potential. These thresholds are in agreement with a substantial amount of experimental data and the underlying analytical theory is claimed to be applicable for heavy projectiles such as C and O. As an example, Table 1 shows the threshold energies defined as the energy at which the cross-sections deviates 4% from the Rutherford value, for backscattering experiments ($\theta = 170°$) with H, He

Table 1
Energy thresholds in MeV for non-Rutherford scattering (the threshold is defined as the energy at which the scattering cross-section deviates 4% from the value calculated with Eq. 4. For projectile energy values higher than the tabulated values, cross-section measurements have to be performed)

Z_2 (target nucleus)	$Z_1 = 1$ (H)	$Z_1 = 2$ (He)	$Z_1 = 6$ (C)
8 (O)	0.890	2.500	15.240
14 (Si)	1.450	3.950	23.500
26 (Fe)	2.530	6.900	44.200
79 (Au)	7.870	24.970	71.900

and C projectiles on O, Si, Fe and Au target atoms.

At low energies, deviations from the Rutherford cross-sections occur as a result of screening of the field of the target nucleus by the surrounding electrons. L'Ecuyer et al. [12] derived an expression to calculate the correction on the Rutherford cross-section which is found to be independent of the scattering angle. Table 2 reports the energies at which the experimental cross-section is expected to deviate 4% of the Rutherford value.

Tables 1 and 2 elucidate why RBS using incident He ions with an energy of 1–2 MeV is most popular and widely spread as a reliable quantitative analysis technique. It also shows that the ultra-sensitive HIBS techniques requires screening corrections. The use of He projectiles with energy values above the threshold for non-Rutherford scattering (usually referred to as HEBS, i.e., high energy backscattering spectrometry) requires external calibrations but can nevertheless be a fruitful exercise since the non-Rutherford cross-sections for the light elements (C, N, O) can be significantly enhanced compared to the $1/E^2$ decrease of the Rutherford cross-sections of possible heavy target nuclei in the same experiment [13]. For recoil spectrometry (ERDA) which is most often carried out with heavy projectiles like 35 MeV Cl or 30 MeV Si, the energy interval in which Rutherford cross-sections are accurate is less clearly founded. In spite of the fact that as a rule of thumb an energy of ~ 1–2 MeV/amu is considered to meet the required Rutherford scattering, the use of external standards in recoil spectrometry is of common practice.

Table 2
Energy thresholds in MeV for screening corrections (the threshold is defined as the energy at which the cross section deviates 4% from the value calculated with Eq. 4. When the projectile energy is below the tabulated values screening corrections have to be carried out for calculating the scattering cross-section

Z_2(target nucleus)	$Z_1 = 1$ (H)	$Z_1 = 2$ (He)	$Z_1 = 6$ (C)
8 (O)	0.02	0.04	0.12
14 (Si)	0.03	0.07	0.20
26 (Fe)	0.09	0.19	0.57
79 (Au)	0.42	0.83	2.49

Concluding it should be pointed out that the sensitivity of ion scattering techniques for heavy surface impurities on a light substrate is usually superior to that of AES or XPS. Pushing the limits using HIBS results in detection limits comparable to that of static SIMS and total reflection x-ray fluorescence [7].

An indication of the detection limits for bulk impurities in Si is 5.10^{18} As/cm^3 and 1.10^{18} Au/cm^3. ERDA experiments reach typically detection limits down to 10^{-1} at.% although recently the use of ΔE–E telescopes for the detection of the recoils lowered the detection limits to 10^{-2} at.% [14]. It should be noted that the dynamic range of SIMS down to bulk concentrations of ppm cannot be reached by ion scattering techniques. The destructive nature of the sputtering process is however limiting the versatility of sputtering based analysis techniques. Due to preferential sputtering and unknown ionisation efficiencies reference samples very similar in nature to the particular sample under study are required. In contrary ion scattering techniques do not require standards and the reliable knowledge of the scattering cross-sections allows a much wider application area without the need of external standards and moreover without a loss of accuracy in quantification. This is undoubtedly one of the major advantages of ion scattering techniques.

2.4. Structure information

Apart from measuring atomic concentrations, ion scattering techniques are also able to provide

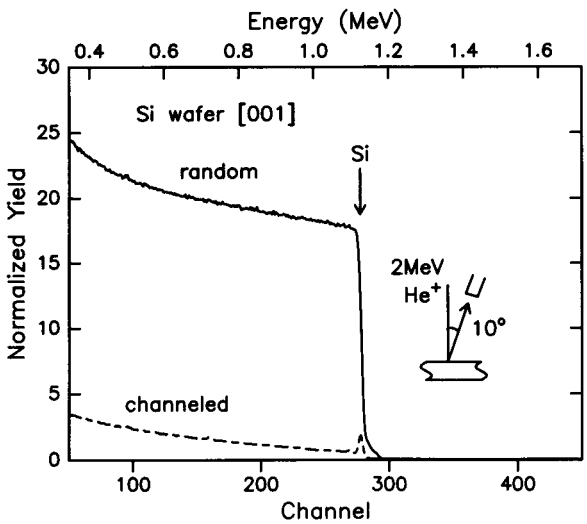

Fig. 2. Random and channelled RBS spectra of a clean Si wafer. The arrow represents the energy of He ions scattered at the surface. The continuum represents scattering at various depths in the substrate.

information on the crystal structure of a sample. Basically the incident ion beam can be aligned with one of the major crystal axes or planes of the crystal. In this case the atoms in the crystal are oriented along rows or in planes with respect to the incoming ion beam and the near surface atoms shield atoms embedded in the bulk of the crystal. This so-called channelling effect reduces the scattering yield from the bulk of the crystal by a factor of ~ 30. The ratio of the lowest achievable yield and the yield measured in a "random" direction is often referred to as the minimum yield: $\chi_{\min.}$ and is different for each particular axis or plane. Fig. 2 shows axial channelling along the $\langle 100 \rangle$ axis in a Si wafer; $\chi_{\min} = 2.7\%$.

Since atoms displaced from their lattice position will no longer be shielded and have a high scattering yield compared to the substitutional atoms, channelling provides the possibility to, e.g., investigate the crystal quality of epitaxially deposited films or the possibility to study damage profiles after ion implantation. More detailed information on the location of impurities embedded in the crystal can be obtained by studying the angular dependence of their scattering yield. Naturally the exact angular differences between major crystal axes of deformed epitaxial layers and the bulk crystal can be determined in a similar manner and can serve to obtain information on, e.g., lattice deformation.

Important requirements for channelling experiments are an incident ion beam with a divergence $\leqslant 0.1\psi_c$ (ψ_c is the maximum angular deviation between beam direction and crystal axis which allows the channelling effect to occur) and a crystal with a size $\geqslant$ beam spot (typically 1 mm^2). In common practice only single crystalline materials or epitaxial layers deposited on these crystals are investigated.

Most of the channelling work is carried out at medium or high ion energies using RBS [2,15]. The alignment procedure becomes tedious for high incident ion energies since the critical angle for channelling ψ_c is proportional to $(Z_1 Z_2/E)^{1/2}$.

Applications of recoil spectrometry combined with channelling are scarce [16] mostly due to the limited freedom in scattering geometry and the relatively high degree of sample damage introduced by heavy projectiles.

Channelling techniques in ion scattering have to be put in perspective by comparison with x-ray diffraction techniques (XRD) and transmission electron microscopy (TEM). The sensitivity for bulk crystal defects in channelling is limited due to the decrease of only a factor of 30 in yield as result of the channelling effect. Areal densities of point defects of $\sim 1 \times 10^{15}/\text{cm}^2$ can be measured [17] when located in a limited depth interval. However, problems arise with the quantification of extended defects such as screw dislocations or line dislocations. The accuracy is limited due to uncertainties in the effective scattering cross-section of such complexes and the complicated (non-random) flux distribution in the bulk of the crystal [2]. Although TEM is not able to resolve point defects, the sensitivity for extended defects is $\sim 10^2/\text{cm}^2$, far superior to RBS. The accuracy of channelling in deducing the lattice constants of deformed epitaxial layers from angular positions ($\sim 10^{-3}$) is not generally as good as the accuracy of lattice constants determined by high resolution x-ray diffraction ($\sim 10^{-4}$). However, compared to XRD ion channelling has the extra option to select a depth interval in which

the lattice constants can be determined. Channelling is particularly useful in determining crystal quality over a relatively large area equal to the beam spot size of ~ 3 mm^2. In that respect the very local information that high resolution TEM provides and the extreme sensitivity of XRD should be interpreted with care when good crystal quality over large areas are required.

3. Applications

In order to gain some insight in the numerous applications of RBS and ERDA, a rather artificial separation is put forward in the types of analysis which are carried out. At first, some examples of true surface characterisation will be discussed. Secondly the largest application area, i.e., depth profiling will be visited. Examples involving only atomic depth distributions as well as examples involving depth profiling of defects will be shown. Several application areas are discussed: semiconductor process control, semiconductor research, research on ceramic materials as well as research on coatings. Thirdly, some specific applications of ion channelling will be visited, where structure information is the main goal of the analysis.

Before starting off with the applications, it is useful to discuss some of the elementary numerical procedures to extract information from measured ion scattering spectra. At first,the areal density of element X, N_X is extracted from a peak area A_X through:

$$N_X = \frac{A_X \sin \alpha}{Q\left(\frac{d\sigma}{d\Omega}\right)_X \Omega} \tag{5}$$

Q represents the dose of incident ions and Ω the solid angle of the detector. The angle between the incoming beam and the plane of the surface of the sample is α. The accuracy of the areal density obtained is directly coupled to the accuracy of the applied ion dose Q. The latter can be measured directly on an insulated target holder when secondary electron suppressors are applied. More flexible is the use of a chopper or transmission Faraday cup in the beam line which does not pose restrictions on the scattering geometry. A recent review on current measurements is found in [18]. The use of an "internal standard", i.e., the deposition of a thin layer of a known thickness and composition on each sample is quite elaborate and moreover only replacing the dose calibration problem by uncertainties regarding the quantification of the deposition method. Quite often the experimental demands required to obtain an accurate dose measurement are circumvented by using the "random height" method. In this procedure the peak A_X is divided by the signal height of the substrate, Y_s:

$$Y_s = Q\left(\frac{d\sigma}{d\Omega}\right)_s \Omega \frac{\delta E}{\epsilon_s^s \sin \alpha} \tag{6}$$

In this formula δE represents the energy width of a channel in the spectrum. The "random height" method implies that channelling (lowering the scattering yield) has to be avoided carefully using, e.g., continuous spinning of the sample around the sample normal during the experiment, acquiring a "true random" spectrum. It should be noted that by evaluating the ratio A_X/Y_s (Q and Ω vanish from this ratio) the experimental problem of an accurate dose measurement is replaced by the uncertainties in the energy loss factor which have been discussed before.

In order to obtain the concentration profile of element A the signal yield Y_A in a channel of the multi-channel analyser (corresponding to an energy interval δE) has to be converted into an atomic concentration by:

$$\frac{N_A}{N_s} = \frac{Y_A}{Y_s} \frac{\left(\frac{d\delta}{d\Omega}\right)_s}{\left(\frac{d\sigma}{d\Omega}\right)_A} \frac{\epsilon_A^s}{\epsilon_s^s} \tag{7}$$

N_A is the atomic density of element A in cm^{-3} in the substrate with an atomic density N_s.

Apart from the classical interpretation of scattering spectra using the generally applicable formula mentioned above, nowadays powerful computer simulation programs (of which RUMP [19] is most widely spread) are used for the interpre-

tation of RBS spectra. An expert eye on the RBS spectrum is usually required to suggest an artificial layer structure of which the program calculates a synthetical spectrum. Automatic optimisation procedures are not always successful due to the mass-depth ambiguity in most RBS spectra and therefore optimisation is often done manually.

4. Surface impurities

The analysis of surface impurities with a mass higher than the substrate is routinely carried out with RBS and usually aimed to quantification. Applications can be found in semiconductor industry where, e.g., surface contaminations can be introduced during wet chemical etch procedures or during sputter cleaning treatments. RBS is applied on a routine basis to tune these processes. With the ever continuing miniaturisation in IC manufacturing the relevant surface contamination levels drop down below the detection limits of ordinary RBS (2 MeV He^+ ions, $\theta = 170°$) and this development stimulated the exploration of the HIBS technique. A detailed comparison of the detection limits of several surface analysis techniques in IC manufacturing is given by Diebold et al [20].

An entirely different application concerns the study of model catalysts in surface chemistry. Commercial catalysts are usually in powder form which limits possible investigations by surface analysis techniques. The use of model catalysts which consist of a flat Si or aluminium carrier with a thin oxide layer circumvents this problem. (Sub)monolayer coverage with catalytically active metals can be achieved by the same wet chemical deposition methods used for commercial powder catalysts. Although LEIS is most widely used in this research area [21] also RBS can contribute to this field. An example is the preparation of the MoS_x/SiO_2 catalysts which are commercially applied for the dehydrosulfurization of oil fractions. The deposition of MoO_3 by wetting with a MoO_2Cl_2–ethanol solution as well as the sulfidation with H_2S on a SiO_2/Si model support can be quantified with RBS. Typical, Mo loading

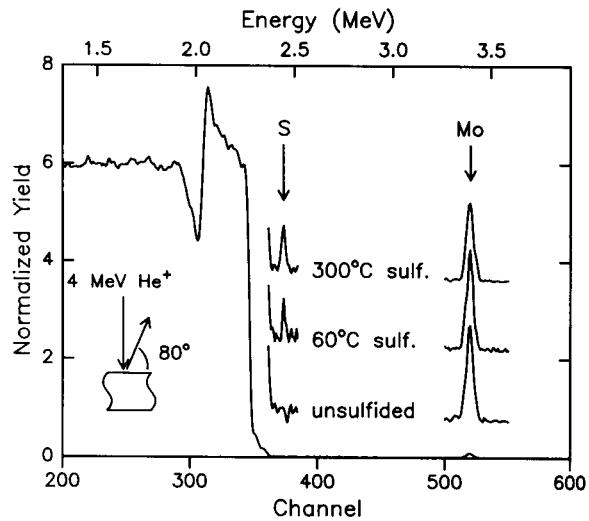

Fig. 3. Preparation and sulfidation of a MoS_x model catalyst. The arrows indicate the energies of He ions scattered on Mo and S atoms located at the surface.

could be tuned to $\sim 1 \times 10^{15}$ at./cm^2 and sulfidation to MoS_2 was proved to occur as shown in Fig. 3. Combining this information with static SIMS and XPS allowed to unravel the detailed sulfidation mechanism of MoO_3 to MoS_2 through MoO_xS_y intermediates [22]. It is interesting to note that recently also several attempts have been reported to apply RBS on non-flat surfaces [23] which would allow direct analysis of catalyst powders.

An unconventional example which also emphasizes the technological possibilities of RBS concerns the analysis of the black deposit inside old incandescent light tubes as shown in Fig. 4. Although RBS is not restricted, like most other surface analysis techniques using charged particles, to (semi)conducting samples, the tube fragment was covered with a ~ 200 Å carbon layer in order to prevent the glass from charging. The glass composition is reflected by the edges of Na, Si, K or Ca and Ba in the spectrum. A distinct peak corresponding to 3.8×10^{15} Hg/cm^2 deposited from the plasma inside the incandescent tube is found in the spectrum. Extensive studies proved the operating characteristics of the tubes to be correlated to the Hg deposition.

5. Depth profiling

5.1. Semiconductor process control

Traditionally, the most important application area for depth profiling with HEIS is found in semiconductor process control and research. Semiconductor device fabrication requires generally several important material deposition or modification steps. This includes ion implantation, deposition of thin films by chemical vapour deposition or sputtering and several annealing procedures. Most of these steps can be monitored and/or tuned with RBS or ERDA. It should be noted that although RBS is generally referred to as a non destructive or non consumptive technique the latter only implies that no sputtering during analysis is required. The implantation of ions which accompanies the analysis modifies both structure and composition of the ultrapure monocrystalline silicon wafers and therefore ion scattering techniques can not be used for on-line process monitoring in contrary to optical analysis techniques.

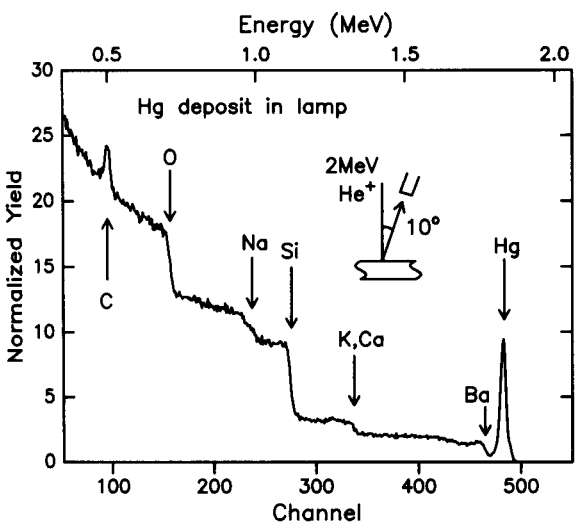

Fig. 4. RBS analysis of a black spot inside an incandescent light tube. Energies of He ions scattered at the surface are indicated for most of the constituents. The Hg deposit amounts to 3.8×10^{15} at/cm^2 while the overall glass composition was found to be $Na_{20}Si_{44}(Ca+K)_4Ba_{0.5}O_{120}$.

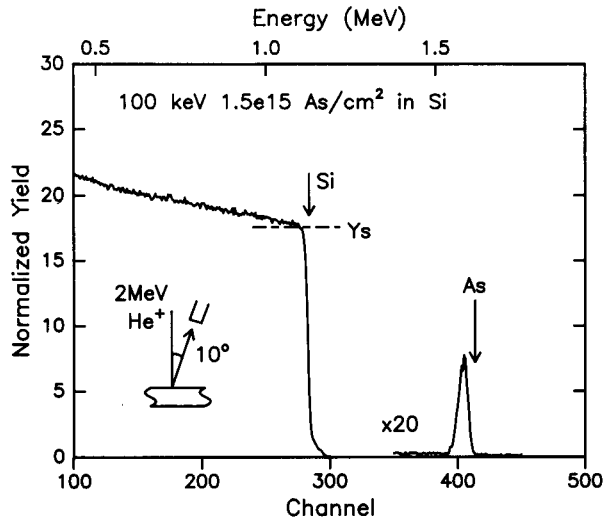

Fig. 5. Calibration of an ion implanter using RBS. In order to apply the "random height" method, a 'true' random Si signal was obtained by rotating the substrate during the measurement around the sample normal while the angle of the incoming beam with respect to the sample normal was fixed at 7°.

The first classical example concerns the dose calibration of ion implanters. Fig. 5 shows a 100-keV As^+ implantation with a dose of 1.5 10^{15} at./cm^2. Dose calibration was carried out by applying the "random height" method. In order to minimize possible errors in the stopping power and scattering yield of the crystalline Si substrate by accidental channelling, the angle between the incoming beam and the sample normal (the ⟨100⟩ axis) was taken 7 degrees and moreover the sample was rotated around the sample normal during the measurement.

The second example which specifically shows the versatility of RBS in multilayered structures concerns the fabrication of a so-called "strap". A strap serves as an interconnect over an insulating oxide region in an integrated circuit. This interconnect can consist of a $TiSi_2$ layer which is formed by a reaction of a thin film of titanium and a thin film of amorphous silicon both deposited by sputtering. The reaction between Ti and α-Si, e.g., occurs during annealing around 500°C which forms the C49 crystalline phase of $TiSi_2$. An additional anneal at ~850°C serves to convert the $TiSi_2$ to the more stable and defect

free C54 phase. The areal densities of the deposited α-Si and Ti layers have to be tuned precisely in order to obtain the $TiSi_2$ compound with the desired properties. Fig. 6 shows the RBS spectrum of an as deposited α-Si/Ti/SiO_2/Si layered structure. The quantitative nature of RBS serves here to obtain quite accurately the areal densities of α-Si and Ti by integration of the two peaks.

Apart from the silicides, also diffusion barriers such as TiN and TiW (N) are routinely characterised with RBS. Determining the stoichiometry of these layers is usually more difficult since it requires the evaluation of the nitrogen peak which is located on the continuum of the Si substrate. Using the Ti and/or W signal yields in combination with Eq. 7 introduces errors up to 10–20%.

Another example of depth profiling with RBS in semiconductor technology is shown in Fig. 7 which illustrates the analysis of a conductive Al layer with 1 at.% silicon and 0.5 at.% Cu incorporated. The traces of Si and Cu are added to suppress diffusion of Si into the Al and to suppress electro-migration effects respectively. Artefacts during the deposition of the layers by sputtering cause a non-homogeneous depth distribution of Cu throughout the Al and additional annealing treatment is required to obtain a homogeneous depth distribution.

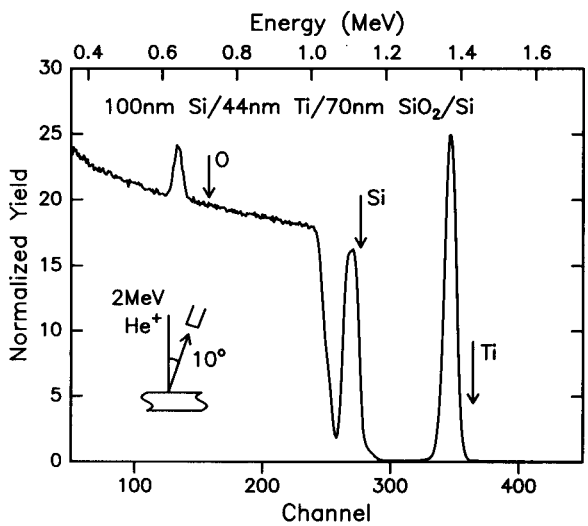

Fig. 6. RBS spectrum of a layer stack Ti/α-Si/SiO_2/Si required for the production of a strap in semiconductor technology. Accurate areal densities of α-Si and Ti can be extracted in order to control the $TiSi_2$ stoichiometry. Note the shifts of the Ti and O peaks with respect to the surface scattering positions due to electronic energy loss.

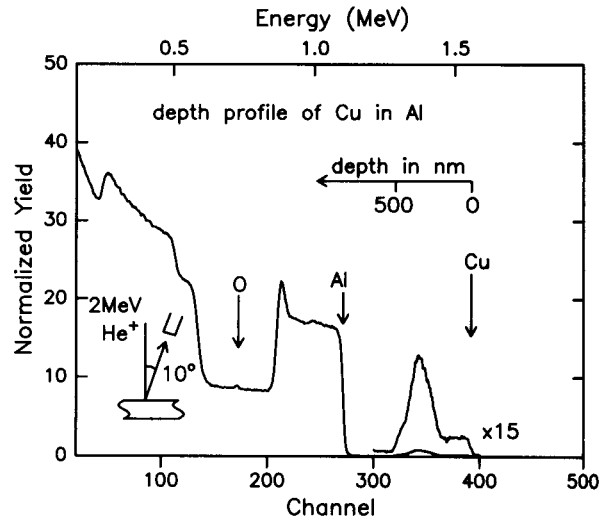

Fig. 7. Analysis of a Cu doped Al contact 'wire' on a Si wafer. The Cu depth profile is obtained by conversion of the energy of the scattered He ions to a depth scale using the energy loss factor.

5.2. *Semiconductor research*

Research in semiconductor materials is oriented towards the development of new materials and accompanying deposition methods which allow applications on large 6 or 8 inch silicon wafers. The formation of almost all refractory metal silicides has been subject of extensive research [24]. Commonly deposition of the metal by sputtering or e-beam evaporation is employed with a subsequent annealing step. Quite fashionable is also the formation of epitaxial buried silicides by high dose ion implantation and subsequent annealing in order to produce a metal base transistor [25–27]. The same technique of high dose implantation was explored to form buried SiO_2 layers which isolates the substrate from a still monocrystalline surface layer in which devices can be fabricated. In many studies RBS is used to measure layer composition and thickness

and sometimes detailed aspects of the kinetics of the reaction processes are extracted by evaluating depth profiles quantitatively (see, e.g., [28,29]).

During the last decade also advanced deposition techniques such as molecular beam epitaxy (MBE) became available and allowed the fabrication of epitaxial metastable compounds and superlattices. An important example is the SiGe system. Monocrystalline $Si_{1-x}Ge_x$ layers can be fabricated in every possible composition ($x = 0$ up to $x = 1$) and epitaxy on Si occurs, up to a critical layer thickness (which depends on x) where epitaxy breaks down. An example of the RBS spectrum of a SiGe layer grown by MBE is shown in Fig. 8. The random spectrum enables to measure both x accurately (in the present example $x = 0.08$) and the thickness of the layer. The channelled spectrum shows a low minimum yield for the epitaxial layer which indicates that the critical layer thickness is not yet reached.

MBE can also be used to deposit layered structures which show the fundamental limitations of ion scattering. Fig. 9 shows a superlattice of five periods of (20 nm $Si_{0.78}Ge_{0.22}$/20 nm Si) on a silicon substrate. The spectrum was measured with a grazing incident and exit angle as

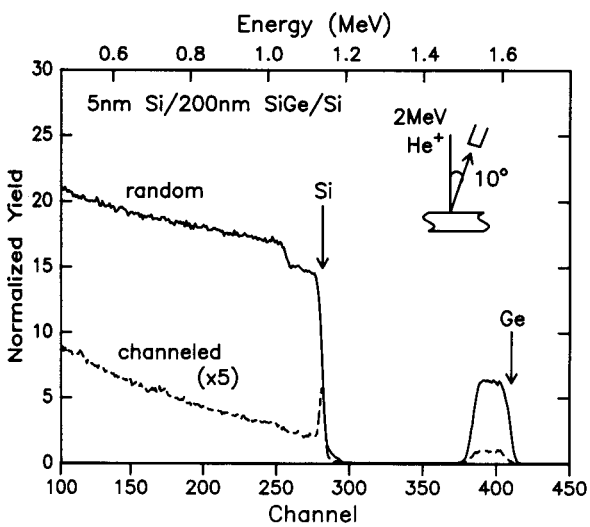

Fig. 8. Large area epitaxial growth measured with RBS-chanelling. Additionally layer thickness and stoichiometry can be evaluated by measuring the Ge signal area and the Si and Ge signal heights.

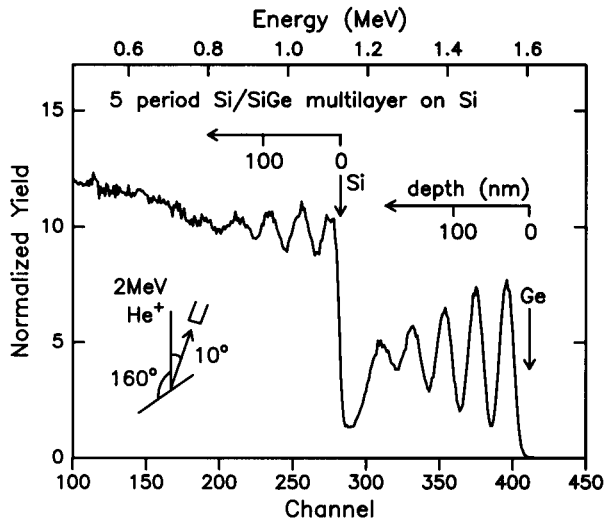

Fig. 9. Limits to the depth resolution in RBS spectra demonstrated by a 5-period Si/SiGe multi-layered structure. Note that the depth scales for Si and Ge start at different positions on the energy scale.

shown in the insert. Although the depth resolution in the Si top layer is approximately 4 nm, a degradation of the depth resolution is observed with increasing depth which can be attributed to energy straggling and multiple scattering. When the individual superlattice periods decrease in thickness, RBS fails to unravel the individual layers but usually the total areal density of a well-defined number of periods can be obtained and thus overall deposition parameters can still be measured. Finally, it has to be noted that MBE is not limited to the SiGe system. The III–V semiconductors based on GaAs are also extensively studied and many elegant ion scattering studies are reported in literature (see, e.g., [30,31]).

With the ongoing miniaturisation in IC industry, standard lithography and wet chemical etching of photoresists fails to produce sharp images when submicron dimensions are approached. An interesting alternative is the use of a dry developable resist system which is based on the selective incorporation of Si from the gas phase in an UV-exposed part of the photoresist. Subsequent bombardment with an anisotropic oxygen plasma produces sharp side walls while creating a protec-

tive SiO_2 coating on UV-exposed areas of the resist while unexposed areas are removed. The kinetics of the incorporation of Si from the gas phase in the photoresists was measured with RBS and is an application in polymeric species of direct importance for research in Si technology [32]. An example of the Si incorporation is shown in Fig. 10. The application of RBS and ERDA on polymeric species is usually hampered by sample degradation but can still lead to interesting results. The quantification of inorganic metals in polymers is usually achieved without problems since during polymer degradation non-volatile metal oxides or carbides are formed and the areal density of the metals is preserved [33]. ERD or RBS studies in pure polymeric systems, e.g., diffusion of deuterated polymers into hydrogenated polymers is usually carried at low temperatures in a cryostat in order to suppress degradation effects [34].

Applications of ERDA in semiconductor research are oriented towards the detection of light elements. ERDA using 2 MeV He projectiles in a standard RBS facility is easily carried out and used for the detection of H in various materials, e.g., amorphous Si or silicon(oxy)nitrides, deposited from a plasma or by CVD [35]. The differential cross-section for recoiling H is non-Rutherford and therefore usually standards are applied. Fig. 11 shows the example of a H profile in a 80-nm Si_3N_4 film deposited by CVD. The application of ERDA with heavy ion beams in order to detect C, N or O has been applied for research on the kinetics of oxidation of (oxy)nitrides [36] and the use of an ΔE–E telescope facilitated to measure low oxygen concentrations (10^{-2} at.%) in polysilicon layers. Recently, also high energy He beams were found to prove successful in profiling C, N and O in thin films [37]. An example is shown in Fig. 12 where an oxygen profile in a plasma deposited amorphous silicon layer is depicted.

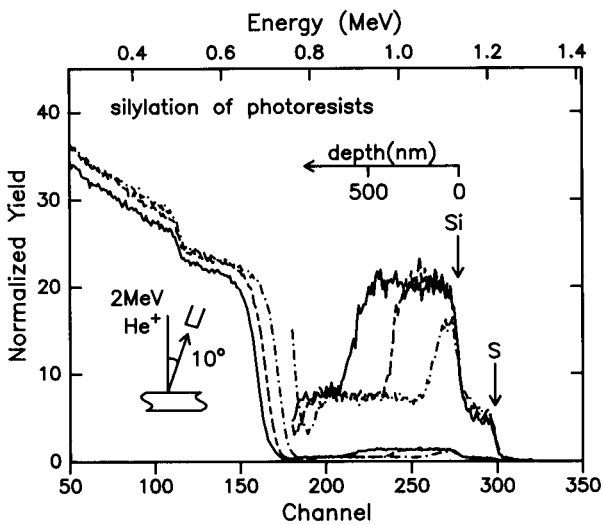

Fig. 10. Si depth profiles in photoresists. The non-exposed photoresist was treated with hexamethyldisilazane (HMDS) at 140° during 5 (dashed line), 10 (dash–dotted line) and 15 (solid line) min, respectively.

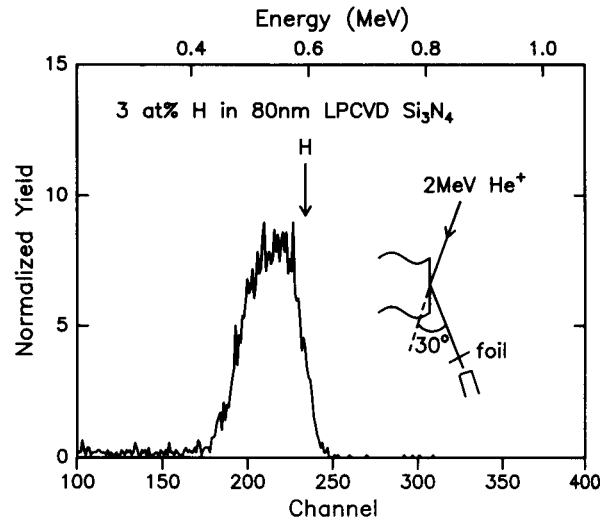

Fig. 11. Elastic recoil detection analysis with 2 MeV He ions. The detector is shielded from the forwardly scattered projectiles by a 9.8-μm Mylar foil. Only hydrogen recoils reach the solid state detector.

5.3. More examples from materials science

Ceramic materials have been studied quite extensively during the last decade. Ferro-electric materials, promising for large storage media, as well as the discovery of high T_c superconductors, stimulated the application of RBS in this area. Possibilities for the fabrication of thin films were immediately explored in order to meet the re-

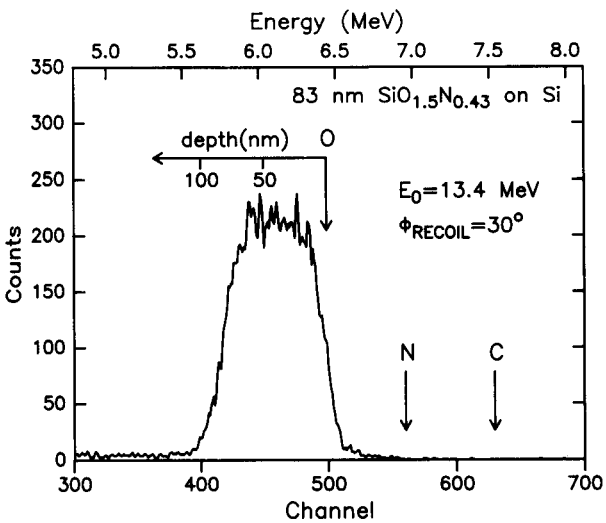

Fig. 12. Detection of oxygen in a siliconoxynitride using 13.4 MeV He ions and a 5-μm thin film detector which selectively stops the recoils. The incident energy of 13.4 MeV is chosen to use a broad cross section resonance for recoiling oxygen.

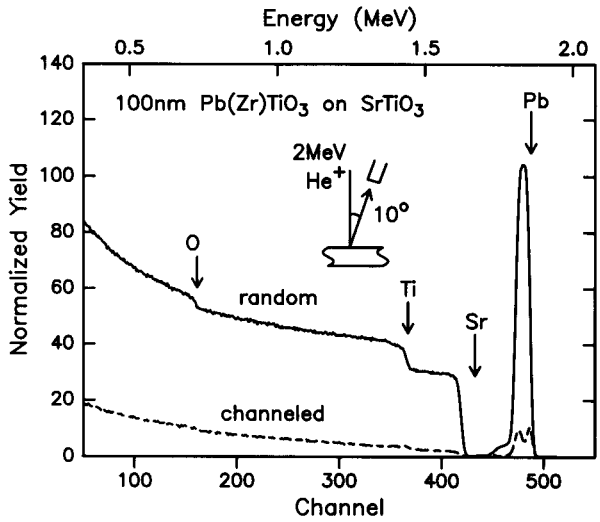

Fig. 13. Random and channelled RBS spectra of Pb(Zr)TiO_3 (PZT) deposited by laser ablation on a $SrTiO_3$ substrate.

quirements for applications in IC technology. Again sputtering, e-beam evaporation and, for pilot studies, laser ablation have been tried. Fig. 13 shows an RBS spectrum of a Pb(Zr)TiO_3(PZT) on a $SrTiO_3$ substrate deposited by laser ablation. Control of the layer thickness (100 nm) and the stoichiometry (Pb/Ti = 1) were obtained with help of RBS. The channelled spectrum in Fig. 13 also shows a high degree of epitaxy on the crystalline substrate but the channelled scattering intensity profile reveals a large defect density

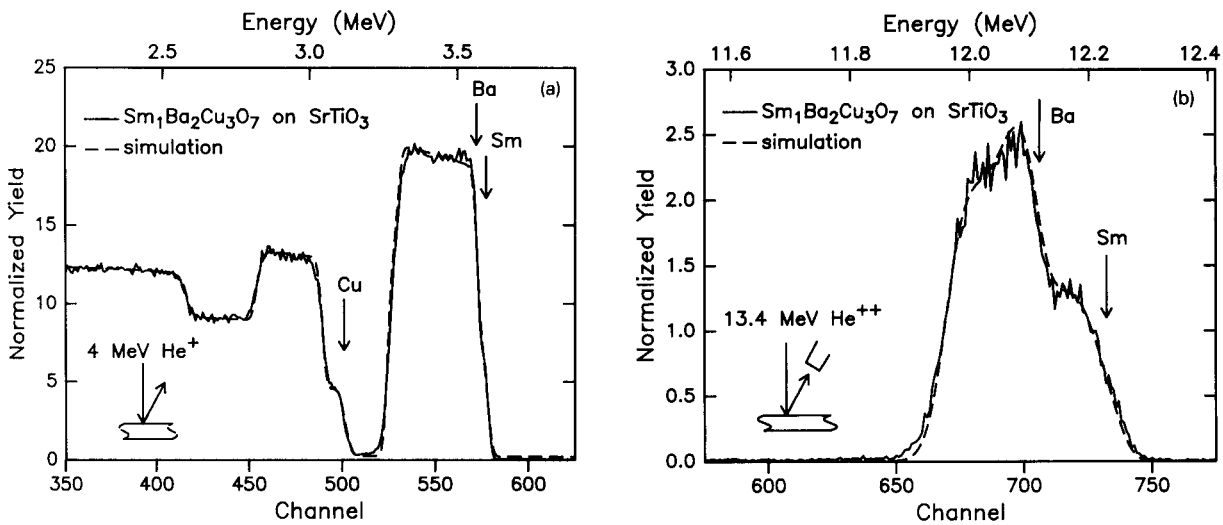

Fig. 14. (a) RBS spectrum with 4 MeV He ions of a $Sm_1Ba_2Cu_3O_7$ superconductor deposited with a e-beam MBE system on a $SrTiO_3$ substrate. The dotted line represents a simulation with RUMP. (b) Kinematic separation of the Sm and Ba signals using 13.4 MeV He ions. At this energy the scattering of He on Sm and Ba is still accurately evaluated using Rutherford cross sections. The simulated spectrum has been calculated for a layer of $Sm_1Ba_2Cu_3O_7$ with a thickness of 3600×10^{15} at./cm^2.

near the PZT/$SrTiO_3$ interface. Similar spectra of thin films of superconductors like $Y_1Ba_2Cu_3O_7$ on $SrTiO_3$ are reported in the literature. By investigating the angular dependence of the scattering yield near axial channels the mosaic spread, a measure of the quality of epitaxy, was determined [38].

Due to the huge background of the $SrTiO_3$ substrates, the oxygen content of both the superconductor and PZT layers can only be determined with errors up to 20% using RBS. Methods to circumvent this problem are either the use of ERDA or the use of high energy backscattering spectrometry (HE-BS)[13].

Oxygen measurements of samples from the family of $Y_1Ba_2Cu_3O_7$ compounds have to be interpreted with some care due to the dependence of the oxygen concentration on both the temperature of the material and the partial oxygen pressure. Applying ion scattering in a vacuum chamber with possible temperature rise due to beam heating requires the use of low beam currents (below $\sim$ 10 nA) and limits the accuracy to at best 5% in the atomic oxygen concentration which is not sufficient to study subtle differences in the value of T_c with oxygen content.

The $Sm_{1+x}Ba_{2-x}Cu_3O_7$ system is of particular interest for the fabrication of Josephson junctions since superconduction vanishes when x is increased from 0 to 0.5. Due to the large number of stable isotopes of Sm and Ba and the small differences in kinematic factors, RBS with 4 MeV He^+ is not able to measure the Sm/Ba ratio (see Fig. 14a). Only heavy incident projectiles or high energy He beams will enable the quantification of this ratio. Fig. 14b shows an RBS spectrum of a 0.5 μm thick layer of $Sm_1Ba_2Cu_3O_7$ measured with 13.4 MeV He ions. The threshold for non-Rutherford scattering is 15.3 MeV for Ba and 17.6 MeV for Sm using a scattering angle of 165°. A straightforward interpretation using the simulation package RUMP as depicted in Fig. 14b, yields the Sm/Ba ratio of 0.5. Finally, it is worth noting that elegant studies have been performed in the $Y_1Ba_2Cu_3O_7$ system using channelling. The temperature dependence of the full-width-half-maximum (FWHM) of angular scans was monitored and showed a sudden change of width near T_c, demonstrating the phonon anomaly in the CuO plane [39].

Other areas of thin film research which benefit indirectly from quantification with RBS are the deposition of metallic magnetic multilayers (e.g., Co/Pd, Co/Pt or Co/Cu, Fe/Cu) and the deposition of x-ray mirrors (W/C or Mo/Si). Both research areas have been initiated due to the tremendous control of the deposition of thin films originally developed for semiconductor technology. Both applications, however, usually require the analysis of superlattices with numerous periods with individual layer thicknesses of the elements of interest of approximately 5–20 Å. As noted before RBS does not provide enough depth resolution to study every individual layer but can still give the overall areal density of the metals involved for a well-defined number of periods.

Finally, an area of growing technological interest should be mentioned: the deposition of superhard, wear resistant coatings (general structure formula: $M–B_xN_yZ_z:H$, M is the metal, e.g., SiC, CrN, TiN, ZrN) and the deposition of lubrication films (MoS_2 or graphitic carbon). Again RBS is able to quantify layer thickness and composition. For the analysis of coatings consisting of light elements such as BN or BNC, ERDA is the obvious technique to apply. The production of wear resistant tools can also be achieved by high dose ion implantation in steels. RBS serves to determine the stoichiometry of the chemical compounds formed which are often very similar to compounds in the aforementioned coatings only with a superior adhesion to the substrate [40].

6. Structure analysis with channelling

Channelling is used in many elegant studies both to investigate the detailed structural properties of materials and also to illustrate the potential of the ion channelling technique. This paragraph will primarily emphasize the most important applications of channelling directly linked to technological applications.

The most widely used application of channelling is a quick investigation of the degree of epitaxy of thin films on monocrystalline sub-

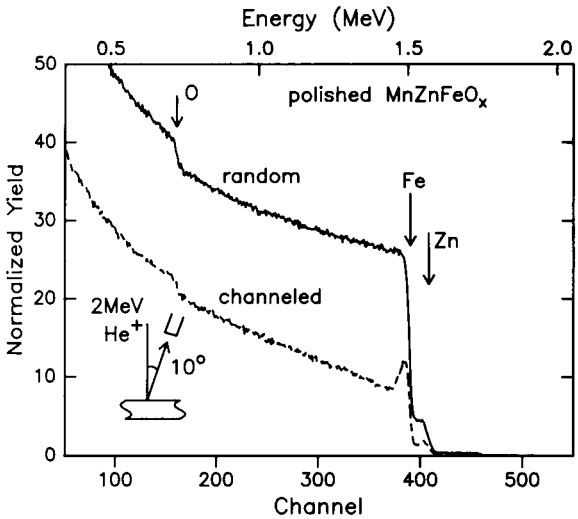

Fig. 15. Crystal damage introduced near the surface of a $MnZnFeO_x$ ferrimagnet by polishing measured with RBS changeling.

strates. Examples have already been depicted in Figs. 8 and 13. The scattering yield in the channelled spectrum is used as a measure for quality of crystalline epitaxy and is operated as a probe to optimize deposition conditions and additional thermal treatment for new film/substrate combinations. When the minimum yield is found close to 3% further tuning occurs with other techniques, e.g., TEM or XRD which are able to detect much lower defect densities.

A strongly related feature with independent significance is the application of damage depth profiling. The scattering yield in a channelled spectrum as a function of depth can identify defects near interfaces [17] or defect profiles after ion implantation. This method is quite often applied in the monitoring of recrystallisation processes, e.g., with the fabrication of buried epitaxial silicides [27] or the production of delta doping layers with solid phase epitaxy. Another more technological oriented application is the measurement of crystal damage near surfaces due to cleaning by sputtering or polishing procedures. An example is depicted in Fig. 15 which shows a ferrite doped with Mn and Zn used for recording purposes. Since the long range magnetic properties of the crystal vanish in the amorphized near surface region, the damage profile in the channelled RBS spectrum was used to select the final polishing procedure which minimizes the amorphous layer thickness.

A third application area concerns the check for incorporation of (artificially introduced) impurities in a host lattice. The location of impurities at interstitial sites can be revealed by measuring the angular dependent scattering yield of the impurity which should reach a maximum at the angular position which corresponds to the minimum yield of the substrate. Flux peaking of the ion beam in the channels can cause an increase in yield above the value for a randomly oriented incoming beam (the yield is dependent on the product of ion flux and scattering cross-section). A classical example concerns the location of Yb in Si [41]. Similar studies using more subtle differences in the shape of the angular scans have been performed on many systems such as the location of clusters of boron in Si and the location of Hf in cubic Al, Cu or Ag hosts [42,43]. Another interesting example concerns the study of planar waveguides which are developed to

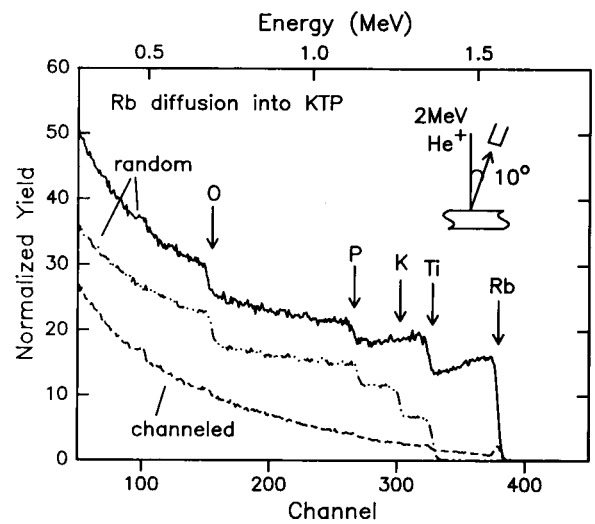

Fig. 16. Diffusion of Rb into KTP in order to produce a waveguide. The dashed line represents the original KTP material while the solid line represents the RBS spectrum after Rb indiffusion; the K at the surface is replaced by Rb. The dash–dotted line shows the channelled spectrum of the Rb containing waveguide and shows preservation of the crystal structure.

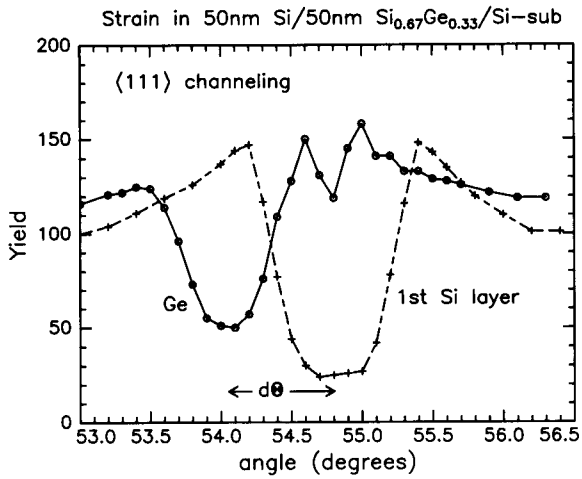

Fig. 17. Angular scans revealing strain in a Si/SiGe/Si multilayered structure. The angular scan of the strained Si/Ge layer was obtained by integrating the Ge peak in the spectrum for each specific angle between the incoming beam and the substrate normal. The angular scan of the first Si layer was obtained similarly by evaluating the Si signal corresponding to the first layer in the spectra. The resulting dΘ is a measure of the tetragonal distortion in the SiGe layer.

fabricate solid state optical switches or amplifiers. Fig. 16 shows the spectrum of a monocrystalline $KTiPO_4$ substrate before and after indiffusion of Rb. The substitution of K by Rb alters the index of refraction without destructing the crystal. The random spectrum after indiffusion clearly shows the replacement of K by Rb while the channelled spectrum of the Rb(K)$TiPO_4$ shows the preservation of the lattice.

The last application of channelling which is primarily used in semiconductor research is the measurement of lattice deformation in epitaxially strained metastable alloys or silicides. The angular position of the non-normal axes of the distorted films can be measured and are displaced with respect to the cubic unit cell. Many examples of the analysis of MBE deposited films in the III–V system have been reported in the literature, e.g., $In_xGa_{1-x}As$ on a GaAs substrate or GaP_xAs_{1-x} on a GaAs or InP substrate [30,44]. An example from the SiGe system is shown in Fig. 17. The investigated sample concerns the following stack: 50 nm Si/50 nm $Si_{0.67}Ge_{0.33}$/Si substrate. The angular scan through the ⟨111⟩ axis measured in the (110) plane of the integrated Ge signal is displaced by dΘ with respect to the position of the ⟨111⟩ axis of the Si top layer or the Si substrate. The fine structure in the angular scans was reproduced by Monte Carlo trajectory calculations of the channelled ions. The lattice constant perpendicular to the substrate was found to be 0.5537 ± 0.0005 Å in agreement with XRD measurements [45,46]. More elegant analysis methods were developed for the analysis of strained layer superlattices by planar channelling [30].

It should be noted, that analyses based on angular scans are experimentally tedious and require usually careful interpretation often with time consuming Monte Carlo simulations. In practice often XRD is used as a quick routine tool to determine perpendicular lattice constants in tetragonally distorted films and ion channelling comes into play when the depth distribution of the strain has to be determined.

7. Conclusions

High energy ion scattering, in particular RBS, proves to be an invaluable tool in materials science. The most important distinguishing marks are the quantitative nature without the need of standards and the ability for non-destructive depth profiling. The sensitivity for surface impurities on a low-Z substrate (i.e., $Z_{imp} > Z_{substrate}$) is usually better than the commonly applied surface analysis techniques and the ultra-sensitive HIBS technique is among the most sensitive surface characterisation techniques available at present. The analysis of elements with $Z < 10$ on a heavy substrate can be achieved with elastic recoil detection techniques or by using high energy He ions taking advantage of broad resonances in the scattering cross-section. The ultimate depth resolution in non-destructive depth profiling will always be limited by the fundamental restriction of energy straggling and multiple scattering. Although typical depth resolutions of 10–20 nm can be obtained routinely in ion scattering the ulti-

mate resolution of surface analysis techniques combined with sputtering cannot be met.

The channelling technique is very useful for the analysis of epitaxial layers and enables defect depth profiling. Apart from these widely applied features more elegant and elaborate channelling studies allow studies on the lattice location of bulk impurities as well as the analysis of lattice deformation in, e.g., strained layered systems.

Most of all, ion scattering techniques are characterised by their extreme versatile character. Virtually all materials ranging from plastics to oxidic insulators, semiconductors and metals can be analysed without loss of accuracy and with great ease.

References

[1] W.K. Chu, J.W. Mayer and M.A. Nicolet, Backscattering Spectrometry, Academic Press, New York, 1978.

[2] L.C. Feldman, J.W. Mayer and S.T. Picraux, Materials Analysis by Ion Channeling, Academic Press, New York, 1982.

[3] J.F. Ziegler, Helium: Stopping Powers and Ranges in All Elemental Matter, Volumes 3 and 4 of The Stopping and Ranges of Ions in Matter, Pergamon, New York, 1977.

[4] Y. Tamminga, M.F.C. Willemsen, F.H.P.M. Habraken and A.E.T. Kuiper, Nucl. Instrum. Methods, 200 (1982) 499.

[5] D.O. Boerma, F. Labohm and J.A. Reinders, Nucl. Instrum. Methods, B50 (1990) 291.

[6] E. Rutherford, Philos. Mag., 21 (1911) 669.

[7] B.L. Doyle, J.A. Knapp and D.L. Buller, Nucl. Instrum. Methods, B42 (1989) 295.

[8] J.A. Knapp and B.L. Doyle, Nucl. Instrum. Methods, B45 (1990) 143.

[9] M. Bozoian, Nucl. Instrum. Methods, B56/57 (1991) 740.

[10] M. Bozoian, Nucl. Instrum. Methods, B58 (1992) 127.

[11] K.M. Hubbard, J.R. Tesmer, M. Nastasi and M. Bozoian, Nucl. Instrum. Methods, B58 (1992) 121.

[12] J. L'Ecuyer, J.A. Davies and N. Matsunami, Nucl. Instrum. Methods, 160 (1979) 337.

[13] J.C. Barbour, B.L. Doyle and S.M. Myers, Phys. Rev. B, 38 (1988) 7005.

[14] W.M. Arnold Bik, C.T.A.M. de Laat and F.H.P.M. Habraken, Nucl. Instrum. Methods, B64 (1990) 832.

[15] J.F. van der Veen, Surface Science Reports, 5 (1985) 199.

[16] C. Janicki, P.F. Hinrichsen, S.C. Gujrathi, J. Brebner and J.P. Martin, Nucl. Instrum. Methods, B34 (1988) 483.

[17] A.T. Vink, P.J. Roksnoer, J.W.F.M. Maes, C.J. Vriezema, L.J. van IJzendoorn and P.C. Zalm, Jpn. J. Appl. Phys., 29 (1990) L2307.

[18] F. Pászti, A. Manuaba, C. Hajdu, A.A. Melo and M.F. da Silva, Nucl. Instrum. Methods, B47 (1990) 187.

[19] L.R. Doolittle, Nucl. Instrum. Methods, B9 (1985) 344.

[20] A.C. Diebold, P. Maillot, M. Gordon, J. Baylis, J. Chacon, R. Witowski, H.F. Arlinghaus, J.A. Knapp and B.L. Doyle, J. Vac. Sci. Technol., A10 (1992) 2945.

[21] H. Niehus, W. Heiland and E. Taglauer, Surface Science Reports, 17 (1993) 252.

[22] A.M. de Jong, H.J. Borg, L.J. van IJzendoorn, V.G.F.M. Soudant, V.H.J. de Beer, J.A.R. van Veen and J.W. Niemantsverdriet, J. Phys. Chem., 97 (1993) 6477.

[23] P.R. Berning and A. Niiler, Nucl. Instrum. Methods, B73 (1993) 178.

[24] S.P. Murarka, Silicides for VLSI applications, Academic Press, New York, 1983.

[25] J.C. Hensel, A.F.J. Levi, R.T. Tung and J.M. Gibson, Appl. Phys. Lett., 47 (1985) 151.

[26] A.E. White. K.T. Short, R.C. Dynes, J.P. Garno and J.M. Gibson, Appl. Phys. Lett., 50 (1987) 95.

[27] A.H. van Ommen, J.J.M. Ottenheim, A.M.L. Theunissen and A.G. Mouwen, Appl. Phys. Lett., 53 (1988) 669.

[28] I.J.M.M. Raaymakers, L.J. van IJzendoorn, A.M.L. Theunissen and K.B. Kim, Mat. Res. Soc. Symp. Proc., 146 (1989) 267.

[29] L.S. Hung, J. Gyulai, J.W. Mayer, S.S. Lau and M.A. Nicolet, J. Appl. Phys., 54 (1983) 5076.

[30] S.T. Picraux, W.K. Chu, W.R. Allen and J.A. Ellison, Nucl. Instrum. Methods, B15 (1986) 306.

[31] W.K. Chu, W.R. Allen, S.T. Picraux and J.A. Ellison, Phys. Rev. B, 42 (1990) 5923.

[32] R.J. Visser, J.P.W. Schellekens, M.E. Reuhman-Huisken and L.J. van IJzendoorn, Proc. SPIE, 771 (1987) 111.

[33] L.J. van IJzendoorn and J.P.W. Schellekens, Nucl. Instrum. Methods, B40/41 (1989) 806; J. Appl. Phys., 65 (1989) 799.

[34] P.J. Mills, C.J. Palmstrøm and E.J. Kramer, J. Mater. Sci., 21 (1986) 1479.

[35] M.F.C. Willemsen, A.E.T Kuiper, L.J. van IJzendoorn and B. Faatz, in J.R. Tesmer and J.C. Barbour (Eds.), Proc. Conf. Heavy Ion Beams, Materials Research Society, 1990, p. 103.

[36] A.E.T. Kuiper, M.F.C. Willemsen, A.M.L. Theunissen, W.M. van de Wijgert, F.H.P.M. Habraken, R.H.G. Tijhaar, W.F. van der Weg and J.T. Chen, J. Appl. Phys., 59 (1986) 2765.

[37] L.J. van IJzendoorn, H.A. Rijken, S.S. Klein and M.J.A. de Voigt, Appl. Surf. Sci., 70/71 (1993) 58.

[38] O. Meyer, J. Geerk, Q. Li, G. Linker and X.X. Xi, Nucl. Instrum. Methods, B45 (1990) 483.

[39] R.P. Sharma, L.E. Rehn, P.M. Baldo and J.Z. Liu, Phys. Rev Lett., 62 (1989) 2869.

[40] K. Kobs, H. Dimigen, C.J.M. Denissen, E. Gerritsen, J. Politiek, L.J. van IJzendoorn, R. Oechsner, A. Kluge and H. Rijssel, Appl. Phys. Lett., 57 (1990) 1622.

[41] J.U. Andersen, O. Andreason, J.A. Davies and E. Uggerhøj, Rad. Eff., 7 (1971) 25.

[42] P.J.M. Smulders, D.O. Boerma, B. Bech Nielsen and M.L. Swanson, Nucl. Instrum. Methods, B45 (1990) 438.
[43] M.B. Kurup, K.G. Prassat, R.P. Sharma and D.O. Boerma, Nucl. Instrum. Meth. B13 (1986) 68.
[44] R. Flagmeyer, Nucl. Instrum. Methods, B68 (1992) 190.
[45] L.J. van IJzendoorn, G.F.A. van de Walle, A.A. van Gorkum, A.M.L. Theunissen, R.A. van den Heuvel and J.H. Barrett, Nucl. Instrum. Methods, B50 (1990) 127.
[46] G.F.A. v.d. Walle, C.W. Fredriksz, A.A. van Gorkum, R.A. van den Heuvel, C.W.T. Bulle-Lieuwma and L.J. van IJzendoorn, Philips J. Res., 44 (1989) 141.

ELSEVIER

Analytica Chimica Acta 297 (1994) 73–86

ANALYTICA CHIMICA ACTA

Non-destructive analysis of materials and devices by means of scanning acoustic microscopy

J. van den Berg [a,*], J. van Oijen [a], H.W. Werner [b]

[a] *3A NDT Company, J. van Heelustraat 66, 5615 NE Eindhoven, Netherlands,*
[b] *Institut für Allgemeine Physik, Technical University Vienna, Vienna, Austria*

(Received 20th August 1993; revised manuscript received 15th October 1993)

Abstract

The position of scanning acoustic microscopy (SCAM) in the context of destructive versus non-destructive analytical techniques is discussed. The principle of SCAM is touched briefly to a level which will allow an understanding of the various examples of application presented in this article. Examples of SCAM applications will be reported (a) on different types of non-destructive analysis such as: detection of delaminations, voids and microcracks, grain structures, geometrical multilayer composition, strain detection and surface roughness and (b) samples from different fields of material science and technology: IC technology, metals, plastics and advanced materials (glass fibre reinforced composites). The message of this contribution is to focus attention on SCAM as a non-destructive, fast technique which can be used with success in selected cases, where additional information about the sample is present. However, theory of SCAM and hence interpretation of SCAM images is not straightforward and needs expert knowledge.

Keywords: Acoustic methods; Surface techniques; Microscopy; Scanning acoustic microscopy

1. Introduction: destructive versus non-destructive analysis

In principle, every physical or chemical analysis changes the system under investigation and is therefore destructive in the strict sense [1]. The different types of destruction are listed in Table 1. However, the destructivity, R_d, which is the rate of destruction per impinging particle i.e. number of induced "changes" (e.g., displaced atoms, excited electrons) per cm^3 and s, and the total degree of destruction $n_d = R_d \times$ flux (total number of particles that have penetrated 1 cm^2 of the sample during an analysis) can vary from sample to sample, and from method to method. Destructivity in general decreases, when going from keV ions to electrons, x-rays, light and acoustic waves respectively. When keeping the flux constant one will find that "all methods are destructive, but there are some that are more destructive than others." In practice one speaks of a non-destructive method, nevertheless, when the degree of destruction is below a given threshold value.

* Corresponding author.

SSDI 0003-2670(93)E0709-G

Table 1 [1]
Types of destruction

Bond breaking, bond formation
Contamination
– Implanted ions (substitutional, interstitial) or electrons
– Trapping of charges e^-, 1^-, 1^+
Target particle transport
– Displacement within lattice (defects, dislocations)
– Ejection of particles from the lattice [a]
– thermal based: evaporation (laser)
– sputter based [b]: (i) static SIMS (1 monolayer/1 h)
(ii) dynamic SIMS (30 Å/1 h)
Sample size reduction, sample preparation
– Cutting a 6 in. wafer into 1 cm^2 pieces
– Thinning (cross-section)

ESCA: measure the remaining surface composition.
[a] Consumption of the sample.
[b] SIMS: the sputtered particle carries information about the situation before the sputtering.

Non-destructive methods in this sense are: x-ray techniques [x-ray fluorescence (XRF) and x-ray diffraction (XRD)]; electron spectroscopic methods [Auger electron spectroscopy (AES), electron probe micro analysis (EPMA) and x-ray induced proton spectroscopy (XPS)]; scanning electron microscopy (SEM), Rutherford backscattering (RBS) and scanning acoustic microscopy (SCAM). The spectroscopic technique SIMS (secondary ion mass spectrometry) is intrinsically destructive because it always needs removal of target material (consumptive technique [1,2]). Note that (a) the "non-destructive methods" AES and XPS, when applying sputter erosion for depth profiling are consumptive techniques too, (b) RBS is the only technique that gives a useful depth profile without needing to recourse to sputtering [3].

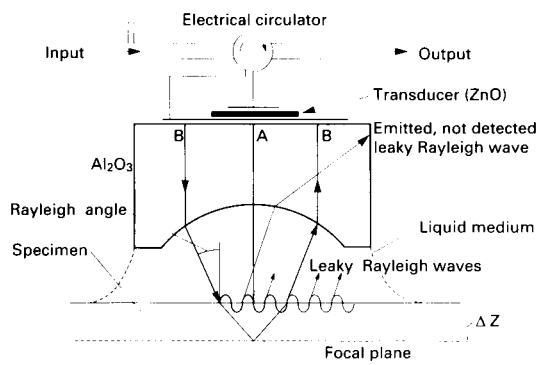

Fig. 1. Arrangement (schematic) of source (= detector) and the lens for acoustic waves in relation to specimen. Only the rays which enter the specimen under the Rayleigh angle are collected by the detector, after reflection.

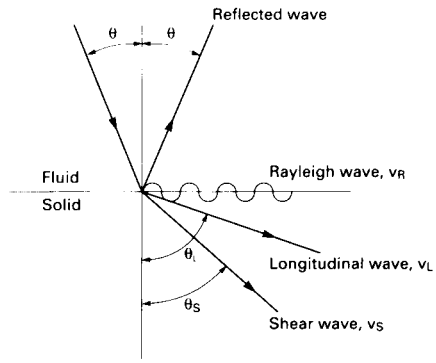

Fig. 2. Types of waves [longitudinal, transversal (shear) and Rayleigh waves (combination of longitudinal and shear waves at the surface)] occuring in a SCAM. The velocity of Rayleigh, longitudinal and shear waves are indicated with v_R, v_l and v_s respectively. From Briggs [4].

Apart from the destructivity of a method in itself, the degree of destruction also depends on the kind of sample preparation. SCAM, the topic of this article, is the least destructive method in itself, although even with SCAM certain samples may undergo changes. Moreover, it needs no sample preparation and the lateral sample size is unlimited: samples can be very large (up to hundreds of centimetres) and can easily be inspected non-destructively with SCAM. In the following we shall describe the principle and applications of SCAM as a non-destructive and depth profiling imaging technique.

Table 2
Lateral resolution, R_l, and penetration depth, R_p, as a function of SCAM frequency in iron [b,c]

Mode	Frequency range (MHz)	Lateral resolution [a] R_l (μm)	Penetration depth [b,c] R_p (μm)
Low frequency	25– 100	48–12	< 6000– < 600
High frequency	100–2000	12– 0.6	< 400– < 10

[a] R_l (μm) = $1.2/f$ (GHz).
[b] R_p is a function of $1/f^2$ and focus length.
[c] R_p also depends on material, here given for iron.

2. Principle of the SCAM

2.1. Two-dimensional (2D) imaging in the x,y-plane (C-scan)

A piezoelectric crystal (ZnO) is the source for acoustic waves in a scanning acoustic microscope: when it is excited with an alternating electric rf field (frequency, f) it generates acoustic waves. These acoustic waves are focused by a spherical lens (Al_2O_3) into one spot at e.g. a depth Δt below the surface of the specimen (Fig. 1). The types of waves occurring in a SCAM system are depicted in Fig. 2: longitudinal waves, transverse (shear) waves and Rayleigh waves (combination of shear waves and longitudinal waves at the sample surface).

Source and lens (= transducer) are mechanically integrated for optimum transfer of the acoustic energy. A coupling fluid (usually water) is used between lens and specimen, in order to lower the attenuation of acoustic energy to the specimen. An image of the specimen in a plane at a depth z below the surface is obtained in principle, when the transducer is scanned across this plane (surface coordinates x,y; depth coordinate z, Fig. 3a). In the geometry depicted in Fig. 1, the piezoelectric crystal (transducer) is source and detector of the acoustic waves, one after the other; the circulator and the mode of excitation (see below) allow to separate outgoing and incoming acoustic waves, respectively.

Owing in particular to the strong absorption of high frequency waves, high acoustic frequency analysis operates in a burst mode and low acoustic frequency analysis in a pulse mode. Reflections at the surface and possibly at underlying layers appear with delayed time (up to μs) after generating the acoustic source signal (Fig. 3a and b). Hence, abrupt changes in elastic properties in the sample, which have a difference in acoustic velocity and/or density, will result in a change in reflection R_t. The intensity of the reflection depends on the differences in the acoustic impedance Z (Z = acoustic velocity × density of the material) inside the specimen, according to

$$R_t = \frac{Z_2 - Z_1}{Z_2 + Z_1}$$

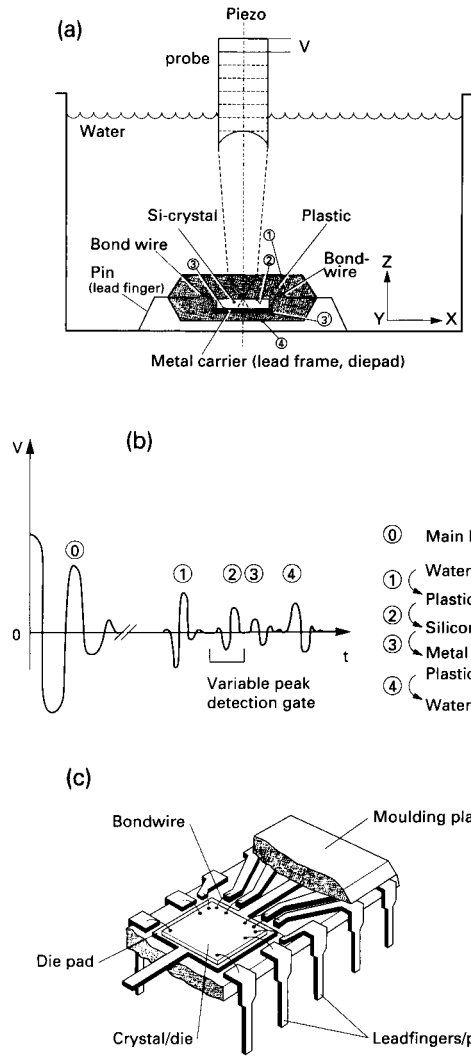

Fig. 3. (a) Signals, $V(t) = V(z)$, obtained from a multilayer structure, in this case a completely packaged IC. (b, c) Si mounted on a metal lead frame and encapsulated in plastic which can be analysed in the SCAM without any further sample preparation.

where Z_1 and Z_2 are the acoustic impedances of two different materials respectively. A large difference between Z_1 and Z_2 will gain a strong reflection and vice versa.

The lateral resolution R_l (see 2.3.1) obtained with a scanning acoustic microscope in the diffraction limited case depends on the smallest obtainable acoustic beam diameter. The diameter

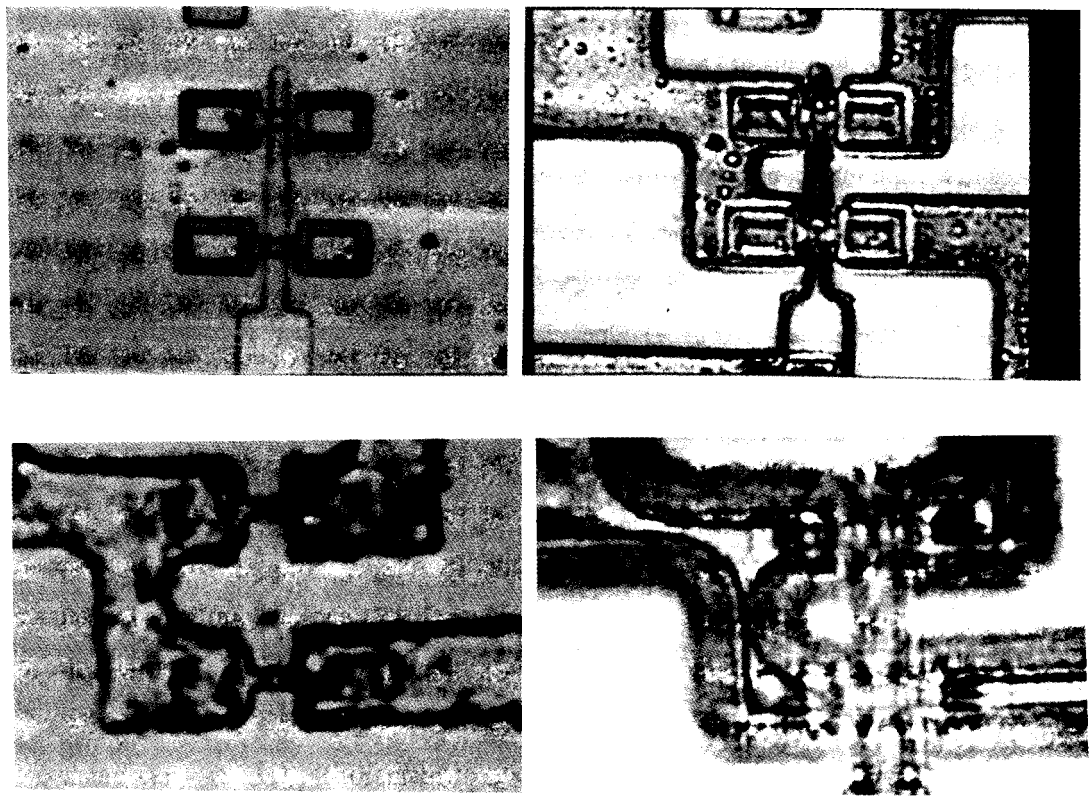

Fig. 4. SCAM micrographs (2.0 GHz) of aluminium lines on a structure of an integrated circuit. Top: good adhesion of the Al-lines shown as the broad white-grey lines in the left picture; left: SCAM micrograph at the surface ($z = 0$); right: SCAM micrograph below the surface ($z = -0.5$ μm). Bottom: bad adhesion of the Al-lines shown as the broad dark lines; Left: SCAM micrograph at the surface ($z = 0$); right: SCAM micrograph below the surface ($z = -0.5$ μm).

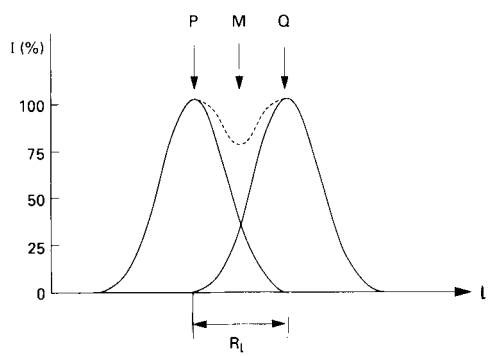

Fig. 5. Rayleigh criterium for resolution. Intensity distribution (solid curves) of diffraction disks (main maxima shown only of two point objects P and Q). Superposition of the peaks given by dashed line. The two peaks are considered to be resolved, when the height of the valley of the superposition curve (position M) is 75% of the maximum peak height.

in turn decreases with increasing frequency (cf. 2.3). In the so-called low frequency mode with frequencies f up to 100 MHz the beam focus-point and hence R_I is about 12 μm. In the high frequency mode, frequencies up to 2 GHz are used. Values for R_I of about 0.6 μm can then be achieved.

2.2. Non-destructive depth analysis

2.2.1. Non-destructive acoustic microscopic analysis in the low frequency mode

In the low frequency (lf) mode, at time $t = 0$, one single acoustic pulse (main bang) of duration $T_0 = 20$ ns is sent into the specimen (Fig. 3a). This pulse is reflected at discontinuities of the acoustic impedances (interfaces, e.g., water–plas-

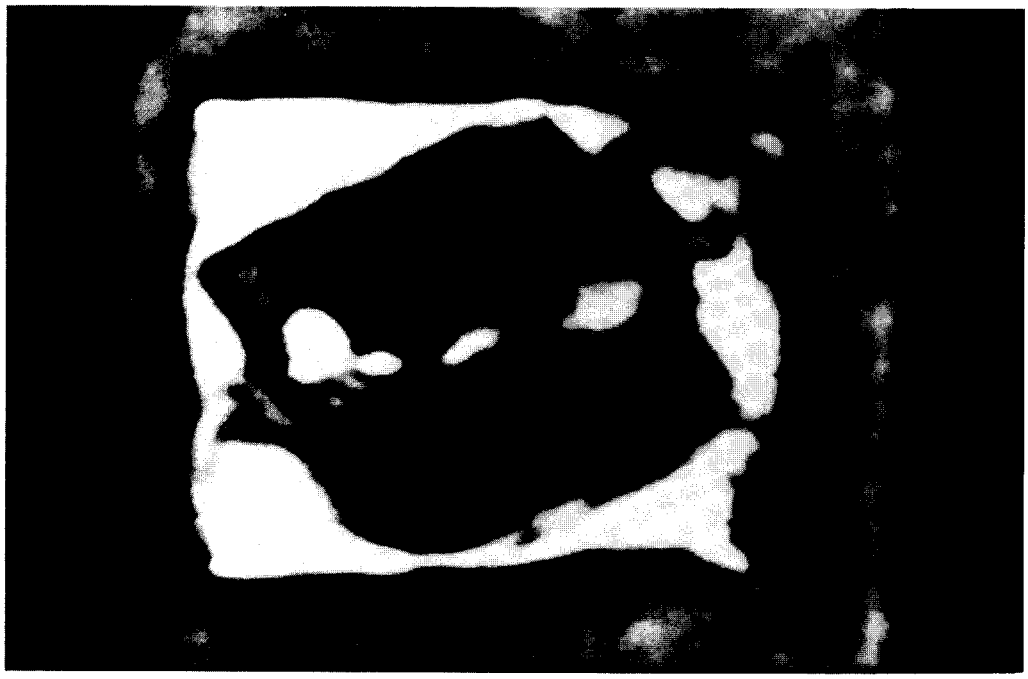

Fig. 6. Low frequency SCAM image (50 MHz) showing details of a small power transistor (dimensions 15×15 mm^2) with insufficient adhesion. The position of the silicon crystal is not oblique in the white square. Underneath the crystal delamination shows up as white. This is a problem due to the conductivity of heat dissipated by the transistor.

Table 3
Guide to acoustic imaging

Frequency	1 MHz.....10 MHz.....30 MHz.....100 MHz.....200 MHz.....500 MHz.....1 GHz
	- medical ultrasound -
	- conventional ultrasonic NDT -
	- coarse grain metals: defect detection -
	- cracks in plastic ensulated IC devices -
	- composite materials -
	- cracks in ceramis IC packages -
	- spot welds -
	- heat sealing of food pouches -
	- ceramic chip capacitors : delaminations & cracks -
	- hermetic seal reliability -
	- polymer-foil package lamination -
	- integrated cirquit die-attach -
	- thick film adhesion and porosity -
	- laser spot welds -
	- fine ceramics: defect detection -
	- fine grain metals : defect detection -
	- seam welds on tin cans -
	- lead bonds on hybrid cirquits -
	- ceramic substrate porosity & cracks -
	- cracks in silicon wafers -
	- thin film adhesion -
	- grain structure determination -
	- fine line inspection on silicon -
Wavelength : 1.5 mm	15 microns 1,5 microns

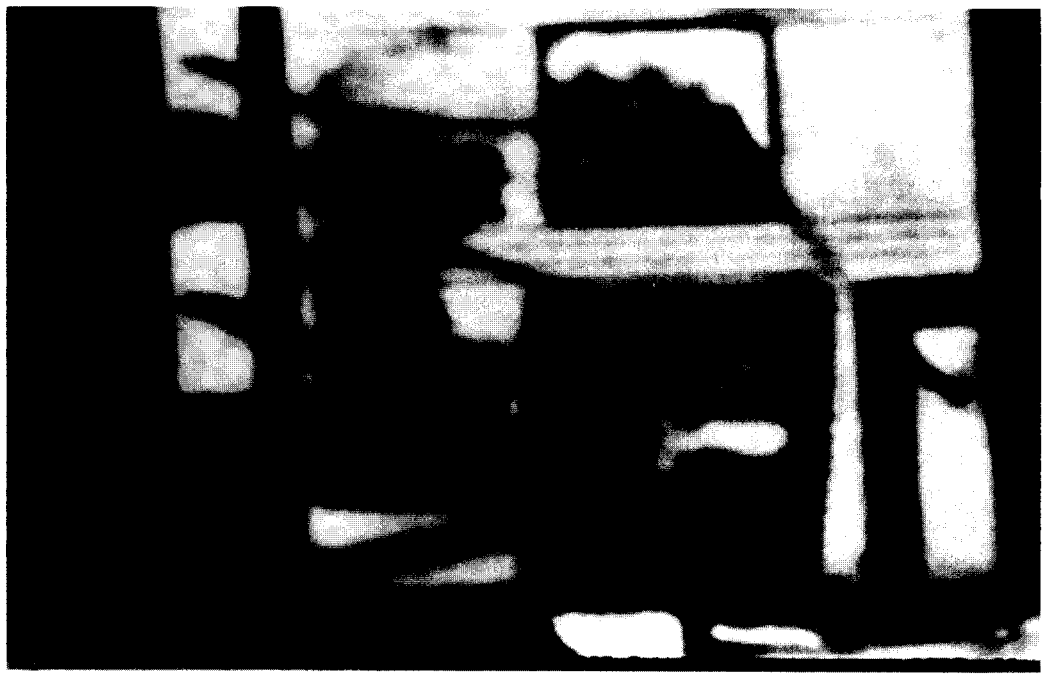

Fig. 7. Low frequency SCAM image (30 MHz) of a power transistor. Large delaminated areas (marked) underneath the silicon crystal inside the plastic encapsulation can be clearly seen. The crystal on top is a fairly loosened from the lead frame (seen as white), whereas the crystal has one bad bonded area (also seen as white). Due to scattering of the acoustic waves the image shows bondwires from the two silicon crystals to the connectors at the side of the image.

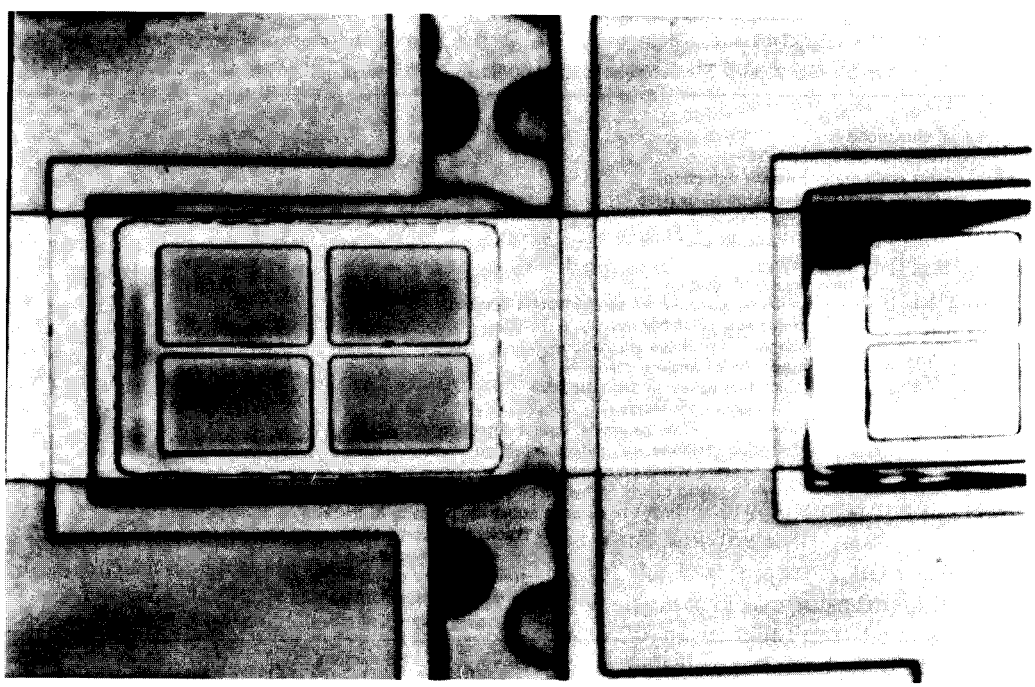

Fig. 8. Acoustic image of a newer kind of display shows a bad bonded Al-line (0.5 μm underneath the surface) on silicon substrate. The image is made using a frequency of 1.3 GHz. Unlike low frequency SCAM the bad bonded areas show up as blackened half circles in the vertical lines in the image. This is because the transducer of the high frequency SCAM generates also Rayleigh waves which needs another (often complex) interpretation of the image.

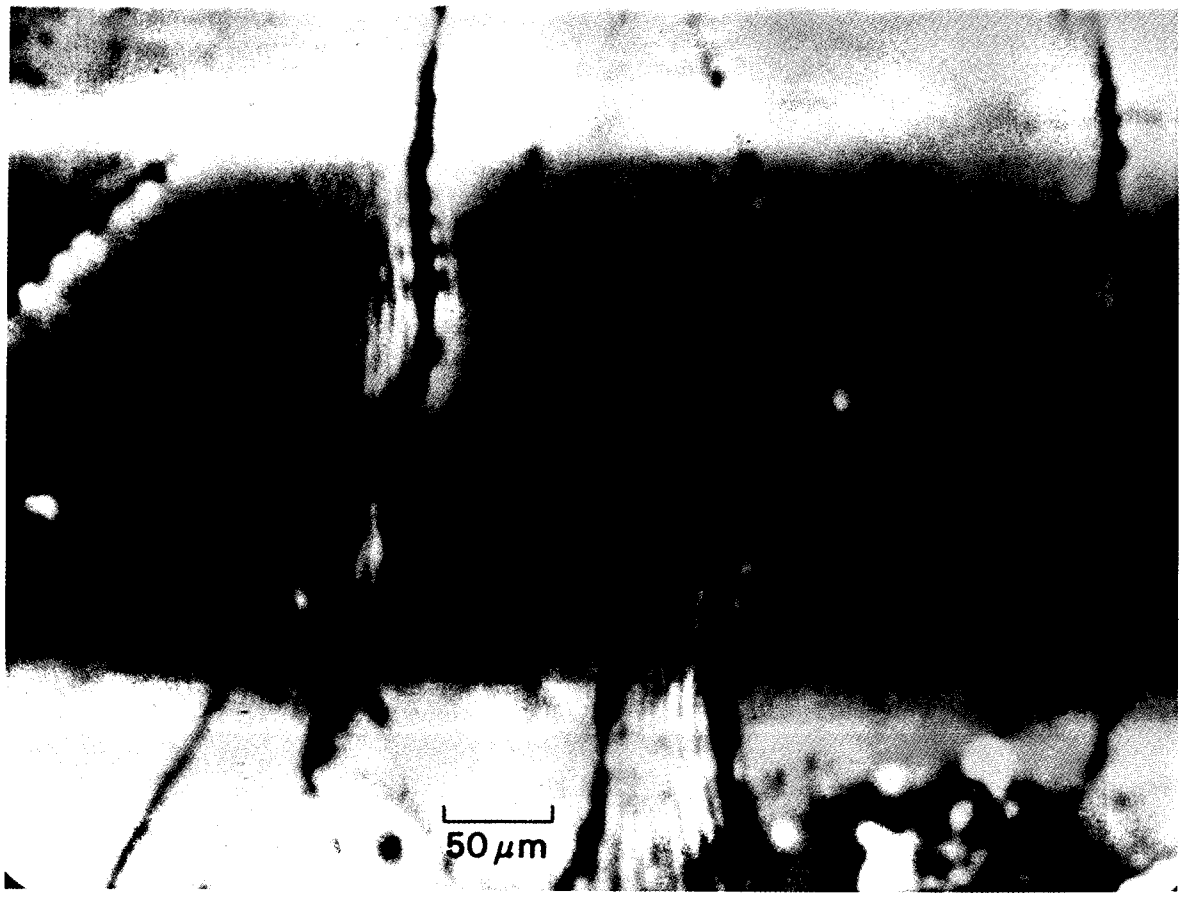

Fig. 9. Microcracks: part of the grain of quartz in granite. SCAM micrograph obtained with $f = 0.73$ GHz. The cracks that generate acoustic fringes run obliquely to the surface. From Briggs [4].

tic; Fig. 3b) present at different depths z_i. Due to its finite velocity of propagation the acoustic pulse will reach these interfaces at times $t_i = z_i/v$, where v is the velocity of the acoustic wave. The reflected waves will hence appear at the detector at the corresponding times t_i one after the other. By putting a time gate at the detector, say at time t_1, only the signals from the interface at depth z_1 (water–plastic) are detected. By keeping the time gate fixed (say at time z_1) and making a scan (x,y-rasterlike) of that plane, (see 2.1) every reflection in the x,y-position is put into a digital framestore to obtain an image of the plane at depth z_1. The lateral resolution in this low frequency mode will be about 12 μm at the most using water as a coupling medium (Table 2). The main feature of the low frequency SCAM is, that an internal x,y-image can be made having a relatively high resolution and a high penetration. Non-destructive analysis of multilayer structures can be achieved by shifting the position of the time gate: one interface after the other can be detected.

2.2.2. Non-destructive acoustic microscopic analysis in the high frequency mode

In the low frequency mode, as discussed above, one single pulse (repetition frequency 10 kHz) is enough to give a reflected signal with sufficient signal-to-noise ratio. In the high frequency mode, the attenuation is much larger (proportional to f^2); therefore the reflected signals will be much

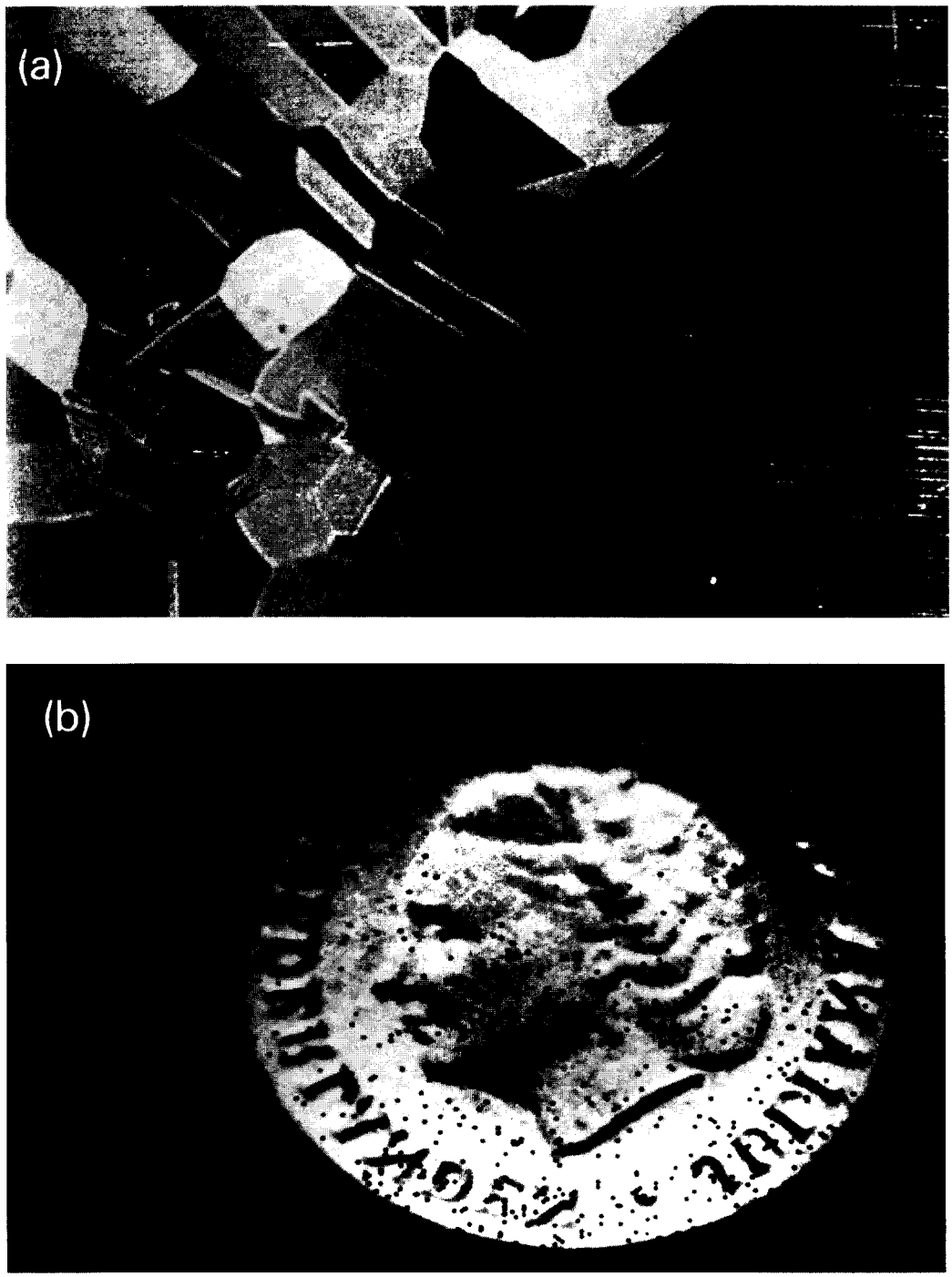

Fig. 10. (a) Different metallurgical phases Ni, Fe and Cr in a Dutch coin detected using a high frequency SCAM (1.6 GHz, about 0.2 μm underneath the surface). The phases were detected due to the Rayleigh waves, which are generated by the transducer used. (b) The same Dutch coin (thickness of 2 mm) viewed from the backside using low frequency SCAM of 50 MHz. The low frequency SCAM does not generate these Rayleigh waves, therefore no phases can be detected.

weaker and hence the signal-to-noise ratio is worse. In order to improve this situation a series of n-pulses (burst) are fired into the specimen. By integration of the respective signals, the signal to noise ratio is improved.

In the low frequency mode, a pulse of duration $T_0 = \Delta t$ corresponds to a bandwidth in frequency space of $\Delta f = 1/\Delta t$. When we want to use a given frequency f_1 the detector is tuned for passing only this frequency. In the high frequency mode, when the pulse-train (wavelength λ_0 and frequency f_0) is sufficiently long, the corresponding image in frequency space is restricted to a very sharp peak around frequency f_0. An A-scan and an x,y scan (C-scan) is obtained in the same way as in the low frequency mode; the lateral resolution is large (Table 2). Fig. 4 shows images of an integrated circuit at the surface ($z = 0$) and at a depth $z = -0.5$ μm, field of view 200×200 μm, $R_l = 0.6$ μm.

2.3. Frequency dependence of lateral resolution R_l and penetration depth R_p

2.3.1. Lateral resolution R_l

The lateral resolution is defined as the minimum distance between two features in the image that can be seen just separated. In a diffraction limited system the image of one point on the object is a diffraction disk (main maximum) surrounded by concentric rings of bright (maxima) and dark (minima) zones. According to the Rayleigh criterium two points are considered to be resolved when the height of the valley of the superimposed intensities is 75% of the individual peak heights (Fig. 5).

In the case of SCAM where we neglect broadening of the beam in the specimen, R_l is determined by the beam diameter d_b. In the diffraction limited case $d_b \approx \lambda$, where λ = wavelength of the acoustic wave. Considering that $\lambda = v/f$, we

Fig. 11. Steel grains with SCAM (1.1 GHz; image width 1 mm). The differences in grey level are caused by the direction dependence of the acoustic waves (i.e., Rayleigh) velocity. The grain boundaries represent a disturbance for the propagation of the acoustic waves. From [5].

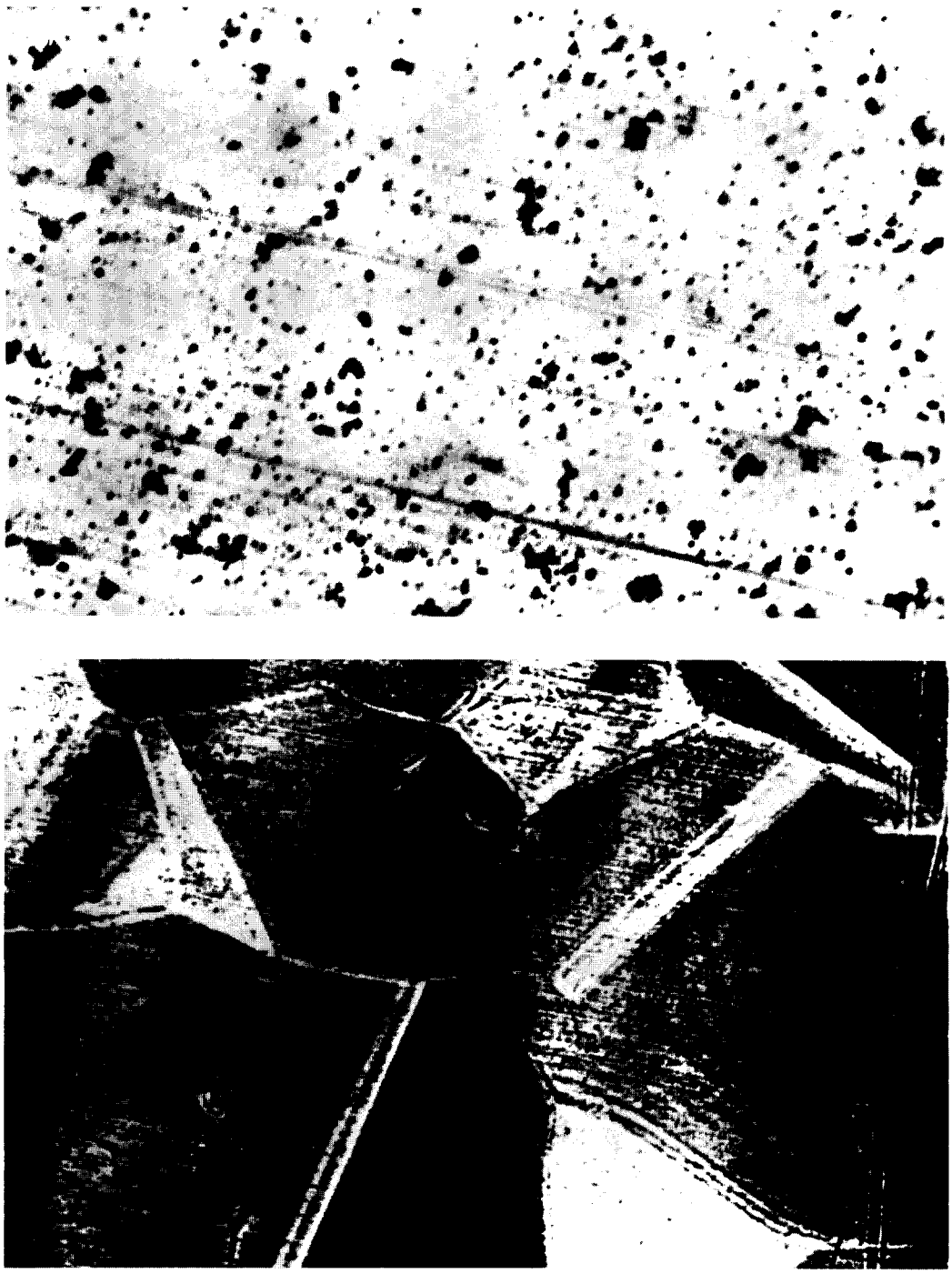

Fig. 12. (a) Conventional optical micrograph of a polished ferrite surface. (b) SCAM micrograph (1.0 GHz) of the same surface region showing the crystallite structure under a thin superficial contamination layer, smeared out during polishing. From [6].

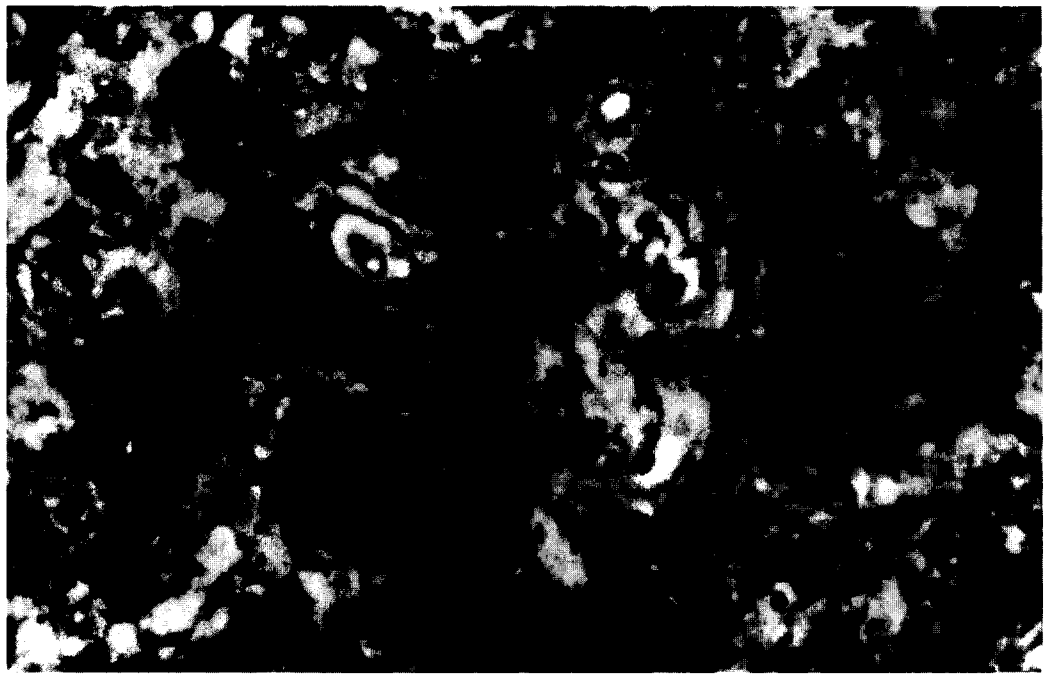

Fig. 13. Acoustic image (100 MHz) of a rough surface of a paint layer. Inclusions and pores show up due to the differences in acoustic impedance and scattering of the acoustic waves. From [5].

obtain $R_l = d_b = \lambda \propto 1/f$. This means that the resolution is the better (i.e., two points that need to be resolved can be positioned closer to each other) the larger the frequency. Table 2 illustrates this frequency dependence. As a rule of thumb we can use the relation $R_l = 1.2/f$ (GHz). With a frequency of 2 GHz in the case of high frequency mode, one obtains $R_l = 0.6$ μm. This value is comparable to the lateral resolution obtainable in conventional optical and scanning optical microscopes.

2.3.2. Penetration depth R_p and attenuation of acoustic waves

When a beam of acoustic waves passes through matter, it looses energy by interactions with atoms of the sample (beam attenuation or absorption). The trajectory of the beam will end at a point where the whole beam energy has been transferred to the specimen. This depth, where the beam trajectory comes to an end is called penetration depth. Analogous to the stopping power (energy loss, $\Delta E/\Delta z$ per cm; E = energy, z = depth) of matter for an ion beam, we use $\Delta W/\Delta z$ for the attenuation (W = power contained in the beam). When W_0 is the total power of the beam approaching the specimen, the penetration depth R_p is defined through the relation: $W_0 = (\Delta W/\Delta z)R_p$ or $R_p = W_0/(\Delta W/\Delta z)$. Note that R_p depends on $\Delta W/\Delta z$, where $\Delta W/\Delta z$ is material dependent. We must take into account that $\Delta W/\Delta z$ may depend on the frequency. Briggs [4] has reported that the attenuation, i.e., $\Delta W/\Delta z$ of acoustic waves propagating through matter is proportional to f^2. Using this frequency dependence in the above relation we find that R_p is proportional to $1/f^2$ for one and the same sample. Table 2 shows values for R_p for different frequencies in iron. It is clear therefrom that high lateral resolution in material science is only possible in the reflection mode, since the penetration depth is only a fraction of a micron. Table 3 shows fields of application for acoustic imaging ranging from medicine to IC inspection. Note

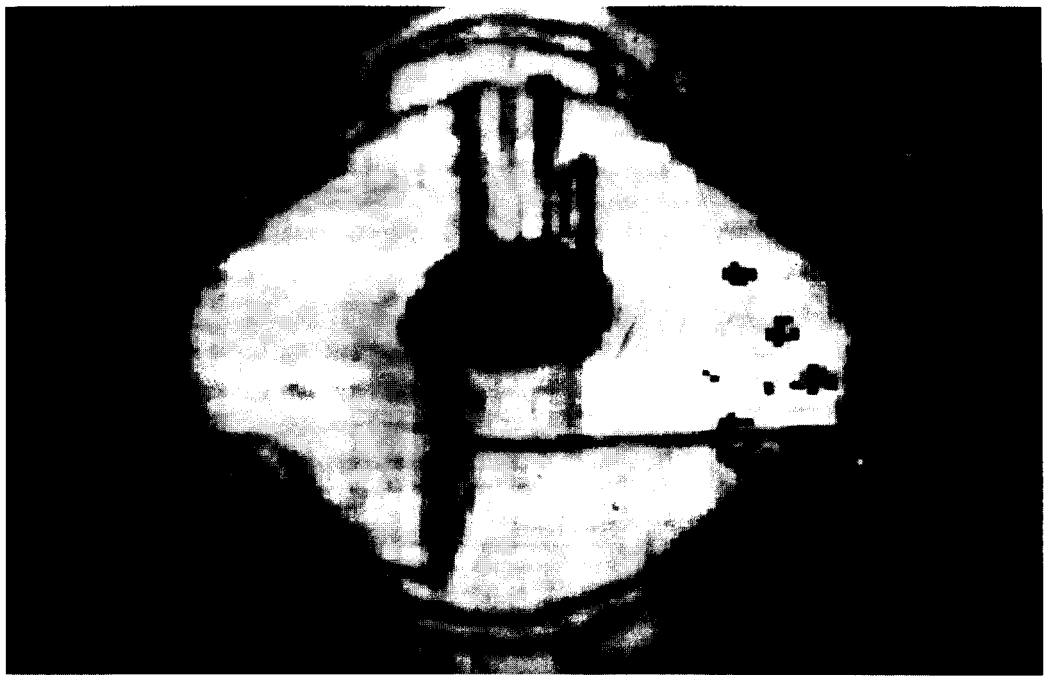

Fig. 14. Low frequency SCAM image (30 MHz) made by scanning through all 6 delaminated layers of a fibre reinforced composite sample. The gate is set very wide in order to collect all reflected signals from the 6 layers in the sample.

that the penetration depth in organic (light element) tissue for medical application is much larger (up to some tens of cm) than in iron.

2.4. Improvement of the understanding of SCAM

The theory of SCAM is complex and beyond the scope of this paper. For a more profound treatment of the theory, in particular for an accurate interpretation of images from different types of samples see [4].

3. Application of SCAM to various materials, devices and problems

3.1. Detection of voids and inclusions

Voids can occur when air bubbles or gas bubbles are generated or gas is occluded in the material. Such voids can be detected by means of the contrast that is due to difference in elastic properties (attenuation, velocity of propagation and reflection) of the substrate and the air (gas) in the sample. Although a void is different in origin from a small delaminated zone, they are physically the same and cannot be distinguished from each other. Fig. 6 shows small delaminated zones inside a power transistor. Inclusions can be considered as voids filled with (solid) matter.

3.2. Delaminations

They give the same SCAM image as voids with large area extension; however, they are caused by a different mechanism: they are due to bad adhesion of two layers onto each other (Fig. 6). Fig. 7 shows a power transistor with large delaminated areas. Fig. 8 shows a delaminated Al-line on a silicon substrate.

3.3. Microcracks

Surface oblique cracks can be detected in SCAM by way of the interference fringes which they generate (see Fig. 9).

3.4. Different (metallurgical) phases in alloys

Different phases in alloys can be detected because of the variations in elastic properties. Fig. 10a shows several phases in an alloy of a Dutch coin ($f = 1.6$ GHz). Fig. 10b shows the penetrating power of SCAM ($f = 50$ MHz): the former Queen is seen "through" the coin, resulting in a side-inverted (mirrored) image.

3.5. Grain structures

Grains of polycrystalline material have identical elastic properties. The origin of contrast here is that the stiffness tensor changes its orientation according to the crystallographic orientation of each grain. Fig. 11 shows the structure of a polished and cleaned steel sample. Note that the SCAM image has been obtained without etching the sample! Fig. 12 is another illustration of the non-destructive character of a SCAM analysis: Fig. 12a is a conventional optical micrograph of a polished (not cleaned afterwards) ferrite sample; a structureless image is found with some pits and stripes. In a SCAM micrograph (Fig. 12b) of the same sample, the grain boundaries can be detected. This is due to the transducer. The transducer has a high-angled lens and therefore it generates Rayleigh waves at the surface of the sample. These reflected Rayleigh waves interfere with the normal reflected acoustic waves. The result is an image which has a high contrast. The interpretation, however, of this kind of images can be difficult.

3.6. Multilayer structures

The geometrical composition/structure of these layers can be investigated by means of several C-scans (see 2.2.1), i.e., shifting the time gate to the different interfaces (cf. Fig. 3).

3.7. Strain detection

Strain detection can be achieved via the differences in elastic properties between a strained and

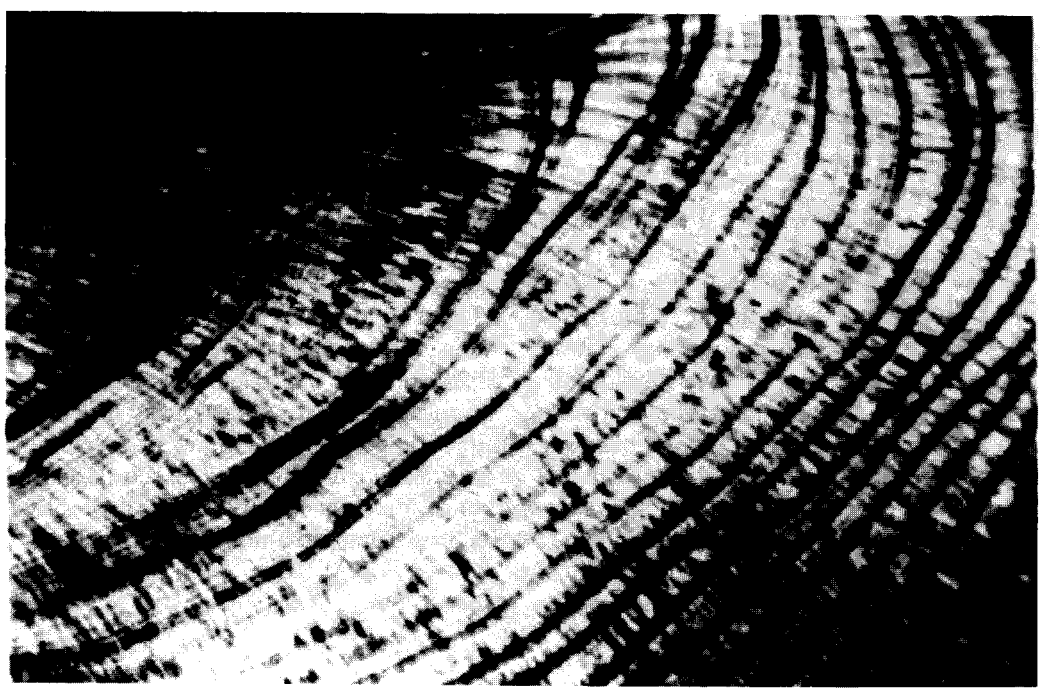

Fig. 15. High frequency SCAM image clearly shows the yearrings of bones in the ear of a fish (1.0 GHz). The sample had to be polished in order to get a flat surface.

an unstrained layer, which results in the respective brightness (contrast).

3.8. Surface roughness

Fig. 13 shows the surface of a paint layer with inclusions and pores. They are visible by their different brightness (grey level).

3.9. Fibre reinforced composite

The sample consists of a number of carbon layers (thicknesses 0.5 mm) each reinforced with glass fibres of small dimensions (up to 50 μm). Such materials are used to make bullet-proof jackets. Quality control is carried out by means of bullet tests and SCAM analysis: when the bullet has hit the multilayer ensemble, the energy released is expected to be dispersed across the point of impact without causing cracks or delaminations between the different layers. By choosing a "broad" time gate (cf. Fig. 3) the layers can be inspected (quasi) simultaneously. Fig. 14 shows such a micrograph. One can see 6 layers and the area of the bullet impact. It clearly shows a delamination of each of these 6 layers.

3.10. Bones in the ear of a fish

The SCAM micrograph (Fig. 15) shows the yearrings of bones in the ear of a fish.

4. References

[1] H.W. Werner and A. Torrisi, Fresenius' J. Anal. Chem, 337 (1990) 337.
[2] H.W. Werner, A.G. Fitzgerald, B.E. Storey, D. Tabian, NATO Advanced Study Institute, Institute of Physics Publishing Ltd., Bristol, Quantitive Microbeam Analysis, Proceedings 40th Scottish Universities Summer School, Physics, Dundee, August 1992.
[3] L.C. Feldman and J.W. Mayer, Fundamentals of Surface and Thin Film Analysis, North Holland, Amsterdam, 1986.
[4] A. Briggs, An Introduction to Scanning Acoustic Microscopy, Oxford University Press, Royal Microscopical Society, London, 1985.
[5] Courtesy LEICA Mikroskopie und Systeme; unpublished 1993.
[6] H.W. Werner, in R.A. Levy (Ed.), Microelectronic Materials and Processes, NATO ASI Series E: Applied Science, Vol. 164, 1989, Kluwer, Dordrecht.

ELSEVIER

Analytica Chimica Acta 297 (1994) 87–96

ANALYTICA CHIMICA ACTA

Characterization of interfaces by photothermal methods

H.G. Walther

Institut für Optik und Quantenelektronik, Max-Wien-Platz 1, D-07743 Jena (Germany)

W. Karpen

Institut für Kunststoffprüfung und Kunststoffkunde, Pfaffenwaldring 32, D-70569 Stuttgart (Germany)

Received 1st April 1993; revised manuscript received 20th July 1993

Abstract

An overview is given of the ability of photothermal techniques to detect hidden interfaces in solid-state samples. The photothermal signal behaviour for horizontal, vertical and randomly distributed interfaces is described. Methods for imaging buried thermal inhomogeneities are discussed. Selected applications are given which demonstrate the potential of the photothermal approach to measuring layer thickness and coating adhesion, to tracing cracks and pores and to evaluating microstructured or crystalline specimens.

Keywords: Surface techniques; Interfaces; Photothermal methods

Many applications in solid-state physics, especially in thin-film physics, are based on the physical behaviour of interfaces. These interfaces are characterized by a more or less abrupt change of material properties. The interfaces that are considered are either produced on purpose (e.g., lateral or depth structuring) or may occur as defect boundaries, unwanted inhomogeneities and imperfections. Interfaces can appear on a macroscopic scale with typical dimensions of a few millimetres. The aim of non-destructive evaluation methods is to investigate the interfaces. Interfaces on a microscopic scale of micrometre size can be grain boundaries, microstructured patterns, microflaws or defects in crystal growth.

In this paper, interfaces that are optically invisible because they are embedded in opaque, strongly absorbing or light-scattering material are considered. As optical methods fail one can use neutron diffraction to detect interfaces up to extensions of about 0.1 μm. Magnetic resonance techniques, microwave attenuation or ultrasonic diagnostics can "see" patterns above the millimetre scale. The intermediate mesoscopic range from micrometres to millimetres can be made accessible by photothermal techniques, a recent approach which has been used extensively for interface investigations during the last decade [1].

Correspondence to: H.G. Walther, Institut für Optik und Quantenelektronik, Max-Wien-Platz 1, D-07743 Jena (Germany).

SSDI 0003-2670(93)E0484-0

1. Principle of photothermal measurements

During photothermal measurement, a change in sample temperature is generated by energy deposition (e.g., by laser illumination). There are different possibilities of time variation of the heat generation, typically periodic, pulsed or step-like heating. As each of them can be considered to be composed of sinusoidal components with different frequencies, consideration here is restricted to the case of periodic heating. For this case the solutions of the heat diffusion equation are strongly damped temperature waves called "thermal waves" (TW) propagating across the sample [2]. During an experiment the amplitudes of the TW and their phase shift with repect to the periodic sample illumination can be measured. An important parameter is the thermal diffusion length $\mu = (k/\pi f \rho c)^{1/2}$ depending on the sample properties thermal conductivity k, specific heat capacity c, density ρ and modulation frequency f. For a plane thermal wave the quantity μ is the distance where the wave amplitude has decreased to $1/e$ of its initial value while its phase has shifted by 1 rad.

2. Theoretical description of thermal wave propagation at interfaces

At an interface between different media the material properties are changing and the TW are partly reflected. The thermal reflection coefficient describing the portion of the incident TW that is reflected depends on the thermal impedance mismatch between the two materials. First, interfaces that are oriented parallel to the sample surface are considered, then those perpendicular to it and finally disordered or statistically distributed internal interfaces.

Horizontal interfaces

Infinitely extended boundaries that are parallel to the sample surface, e.g., layered structures, are considered. For a step-like depth profile in thermal impedance, and for ideal thermal contact, both temperature and heat flux are continuous across the interface. The thermal reflection coefficient R is defined by a combination of thermal effusivities $e = \sqrt{k\rho c}$ of the layer and the substrate, $R = (e_1 - e_2)/(e_1 + e_2)$ [3]. R is real and independent of frequency. If the thermal contact is not ideal, a temperature difference across the interface results. In this event a thermal contact resistance has to be introduced, modifying the thermal reflectivity accordingly [4]. Now R becomes both complex and frequency-dependent. Fig. 1 shows calculated phase frequency curves for a one-layer system. There, extrema and zero crossings appear in the phase scans, allowing estimation of the layer thickness. These extrema are shifted to higher modulation frequencies with increasing contact resistance. In addition to the case of an abrupt change in material properties, a continuous transition between them may be possible. Such a smeared transition is an indication of interdiffusion or chemisorption. The TW reflection from such an interface is modified significantly, as illustrated by the calculations in Fig. 2. For decreasing slope of the transition and negative thermal reflectance, the phase extrema are shifted to higher frequencies [5].

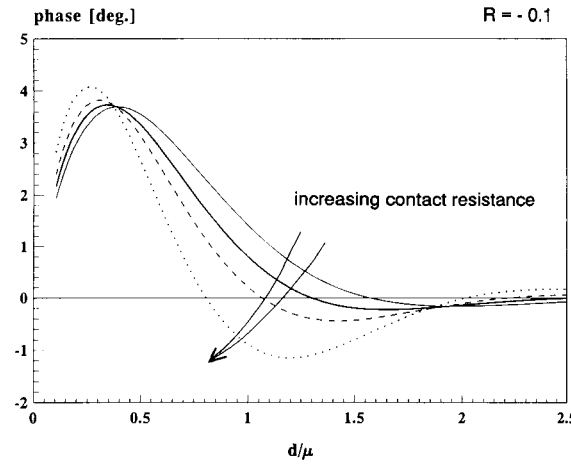

Fig. 1. Calculated phase deviations versus normalized layer thickness at different thermal contact resistances.

Vertical interfaces

Vertical interface detection requires the observation of lateral heat flow [6]. At thermally isolat-

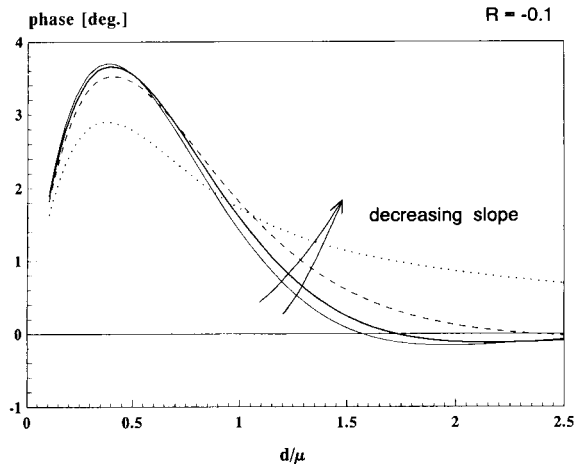

Fig. 2. Calculated phase deviations versus normalized layer thickness for different slopes of the material transition.

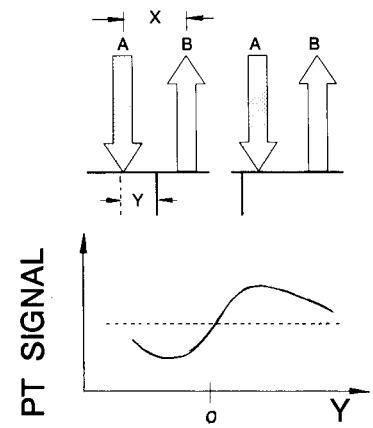

Fig. 3. Scan over a vertical crack, whereby a fixed offset X between heating beam position A and probe beam position B is used. The photothermal signal amplitude will be decreased if the crack is between A and B, whereas it will be increased if A and B are near and on the same side of the crack.

ing interfaces or edges the heat flux dams up. This can be probed by photothermal techniques with a lateral offset between the heating spot and probe spot. The signal obtained depends very sensitively on the thermal impedance along the sample surface. This situation is shown schematically in Fig. 3. If both the heating spot and probe spot are on the same side of the interface, an increase in signal amplitude is expected, but if the interface is between them, then a decrease will be observed.

Randomly distributed interfaces

Some materials of technical relevance are characterized by interfaces between different statistically distributed phases. Examples are porous materials, ceramics, microcrystalline structures such as alloys or minerals, mixtures, short-fibre reinforced plastics, evaporated layers with columnar growth and samples with rough surfaces. The essential feature is that internal interfaces affect TW propagation in a way depending on the size

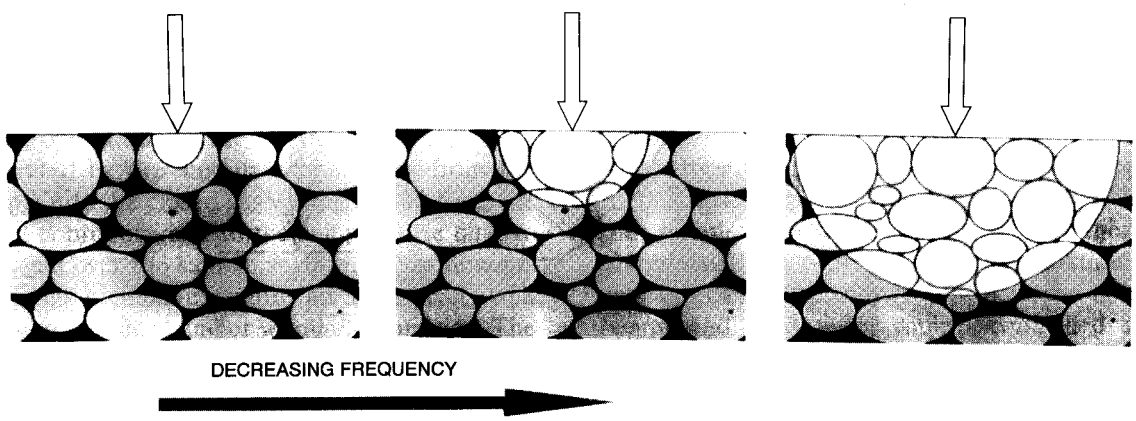

Fig. 4. Schematic representation of thermal wave propagation within a multi-phase material at different modulation frequencies f. With decreasing f the thermal diffusion length increases and more internal interfaces will be probed by thermal waves. The bright area denotes the volume being penetrated by thermal waves.

of the separated microhomogeneous areas related to the thermal diffusion length. This is depicted schematically in Fig. 4. At very high modulation frequencies the thermal diffusion length is smaller than the mean grain size of the multi-phase sample. Consequently, the thermal waves propagate undisturbed as in a homogeneous material. If the modulation frequency is decreased and the thermal diffusion length correspondingly increased, the thermal waves start to penetrate individual interfaces and will be scattered from them. At sufficiently low modulation frequencies many arbitrarily oriented interfaces are passed by the thermal waves. In this case they will average the individual interfaces and "see" a homogeneous material with effective-medium properties. As a result, one observes a fractal behaviour of heat diffusion which causes deviations in the frequency-dependent magnitude and phase of photothermal signals [7]. From this behaviour mean size parameters, e.g., grain size diameter or porosity, can be derived.

3. Photothermal measuring techniques

Owing to periodic illumination of the sample followed by absorption or by other kinds of non-elastic interaction, an oscillating heating of the surface is induced around the illuminated spot. This leads to a characteristic time and local variation of the surface temperature, which can be measured either directly or indirectly. Various photothermal techniques have been developed to detect sensitively the heating or post-heating effects. An overview on this topic has been given recently [8–10]. Fig. 5 shows a schematic representation of the commonly used photothermal measuring techniques for studying solid-state samples.

Photothermal radiation (PTR) measurement provides direct detection of the surface temperature. Here the quantity under investigation is the change in thermal radiation emitted from a surface element of the sample. The advantage of this technique is the fact that the signal is obtained in

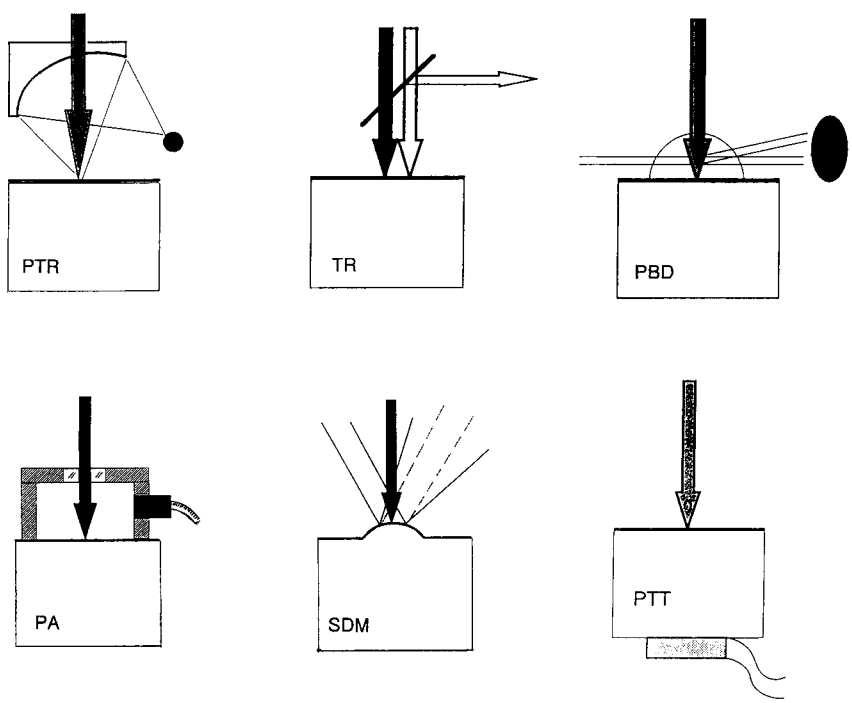

Fig. 5. Photothermal methods to investigate solid samples: PTR = photothermal radiation measurement; TR = thermoreflectometry; PBD = photothermal beam deflection; PA = gas cell technique; SDM = surface displacement measurement; PTT = piezoelectric transducer technique.

a remote way. The shape of the objects can be arbitrary, but one has to make sure that the quality of imaging a sample spot on the detector is constantly good. Signal evaluation may be complicated if the sample is transparent or reflective in the IR spectral range.

An appropriate technique for the investigation of conducting samples is thermoreflectometry (TR). It includes several effects where surface illumination modifies the reflectivity of a probe beam. Reasons can be both the temperature dependence of the dielectric function of the medium and the photoinduced generation of charge carriers, preferentially in semiconductors [11]. The former is the thermal part and the latter is the plasma part of thermoreflectance. As the time dependence is different for them, they can be separated.

The surface temperature can be detected indirectly by probing the temperature of the surrounding gas in the immediate neighbourhood of the illumination spot. The locally illuminated and hence heated sample shares its energy with the adjacent gas where a thermal lens is generated due to the temperature-dependent refractive index. In the "mirage effect" or photothermal beam deflection (PBD) technique, a probe beam propagating along the path parallel to the surface is deflected in this thermal lens along the direction of the gas temperature gradient. Generally the deflection has components perpendicular and parallel to the sample surface. Offset measurements using the transverse mirage effect are sensitive indicators of perturbations in the heat flow along the sample surface.

With the photoacoustic (PA) gas cell technique, one measures the gas pressure oscillations generated by the modulated heat flux from the sample into the closed gas volume. Therefore, the signal is proportional to the temperature change averaged over the sample surface. Measurements using this technique require an acoustically well shielded sample chamber with minimum size. The detection of photothermally generated gas pressure changes is achieved with microphones or piezoelectric foils.

The locally and modulated irradiated sample expands owing to thermoelastic interaction of the heated region, resulting in surface deformation and acoustic vibrations. The surface deformation can be determined very sensitively from the change in direction of a reflected probe beam. This is the approach of surface displacement measurement (SDM). At sufficiently high modulation frequencies photothermally induced stress and strain in the sample itself can be detected appropriately by adapted piezoelectric transducers (PTT).

4. Problems of photothermal imaging

Different photothermal techniques exist to provide spatially resolved information about structured or inhomogeneous samples. Commonly used are scanning techniques [12]. Here the sample under test is scanned by a laser beam, which is intensity modulated at suitable frequencies. At each step the signal is recorded and fed into a lock-in amplifier. This is a time-consuming procedure but allows for high signal-to-noise ratios. When using a continuous-wave laser the unmodulated focused heating beam is directed along the sample surface, being followed by the detection spot at a certain fixed distance from it corresponding to the time lag between heating and detection. This flying spot method [13] is sensitive to lateral distortions of heat flux resulting from vertical interfaces. Using thermographic techniques [14] the whole sample surface is irradiated by an extended heating beam. Then, by means of thermoreflectance or IR radiation measurement, the sample is imaged on a matrix detector. By appropriately synchronizing the periodic illumination with the camera frame rate or by appropriately gating the camera with respect to the heating pulses, depth information about the sample can be achieved. These thermographic methods provide a lot of information in a very short time, but they require powerful heating beams and expensive computer-controlled cameras.

A combination of both scanning and thermographic techniques was reported recently by Busse et al. [15], allowing for a considerable decrease in measuring time without the neccessity of using

expensive IR cameras. The sample under test is periodically illuminated and simultaneously the emitted IR radiation flux is scanned at a four times higher rate. The output signals are analysed pixel by pixel by a computer to provide both the signal amplitude and phase for each surface element.

On evaluating and interpreting photothermal images one has to consider the imaging properties of the photothermal techniques concerning resolution and contrast. Generally it must be borne in mind that one always "sees" photothermally an invisible interface or pattern as being convoluted with both the heating beam profile and a function describing the heat diffusion followed by the specific signal formation. The latter, called "photothermal point spread function" (PSF), was derived in [16] to describe the blurred image of a buried point-like thermal defect. From this PSF it is possible to derive signal amplitude and phase contrast and the definition of photothermal imaging. One must expect extrema of the "visibility" curve of a hidden defect, depending on its depth and on the thermal diffusion length. Photothermal contrast arises from both local variations in thermal density and thermal conductivity. Usually, the second contribution, which is closely connected to the microscopic material structure, dominates. The signal contrast, moreover, depends on the modulation frequency and defect depth, as shown by Patel et al. [17]. At certain frequencies a thermal inhomogeneity becomes invisible for photothermal inspection.

Because photothermal imaging is near-field imaging, its resolution is given by defect depth rather than by thermal wavelength (presuming the depth is smaller than the diffusion length). This behaviour affects the detectability of size-limited interfaces because their images are blurred owing to the diffusive TW propagation. Roughly, the thermal diffusion length limits the observation depth of any material. For commonly used frequencies between 1 Hz and 1 MHz one covers a range from about 3 mm to 3 μm for metals and semiconductors and from about 0.2 mm to 0.2 μm for plastics. Fig. 6 shows calculated phase scans over two buried neighbouring defects illustrating the dependence of photothermal contrast and resolution on modulation frequency.

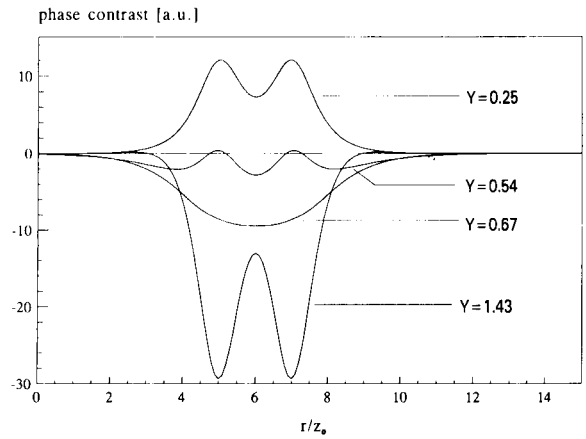

Fig. 6. Calculated phase contrast scans from two neighbouring point defects at various modulation frequencies. Parameter $Y = \mu / z_0$. The defects are located at depth z_0 and separated by twice z_0.

5. Selected applications

Layers and cracks on a macro- and mesoscopic scale

By measuring the superposition of thermal waves reflected at horizontal interfaces one can estimate the thickness of layers or coatings on substrates. The thickness accuracy depends on the thermal reflectivity R between layer and substrate, which determines the signal contrast [18]. Table 1 shows selected values of both R and maximum phase deviation from the bulk signal $\Delta\phi_{max}$. A satisfactory accuracy of about 1% error

Table 1
Thermal reflection coefficient, R, and maximum phase deviation, $\Delta\phi_{max}$

Layer/substrate	R	$\Delta\phi_{max}$ (°)
Paint/steel	−0.9	40
Ceramic/steel	−0.5	20
Titanium/steel	−0.3	12
Nickel/brass	−0.01	0.5
Paint/polymer	±0.2	±7.5
Metal/polymer	0.9	−40

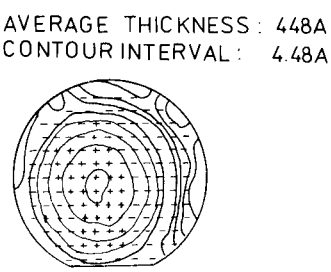

Fig. 7. Titanium thickness uniformity map. Contour lines each represent a change of 1% in the average thickness, or 0.5 nm. The plus and minus signs denote positive and negative deviations from the average thickness (from [19]).

in thickness can be achieved if insulators on metals or semiconductors are investigated. This quality of measurement requires appropriately adapting the thermal diffusion length to film thickness by tuning the modulation frequency. As an example, Fig. 7 shows thickness measurements for titanium on a silicon wafer, demonstrating the sensitivity of the TW method [19].

Photothermal techniques, in contrast to ultrasonic, eddy current or magnetoinductive techniques, allow the thickness determination of insulating layers on insulators. A relevant example is paint layers on polymers. Here, because of similar effusivities, the photothermal contrast is small and the errors in paint thickness estimation will be about 10%. Some difficulties arise in comparing experimental results with theoretical models because of the 3D situation, layer translucency and uncertain thermal properties. In these cases it is more appropriate to compare the measurements with results obtained from well known reference samples. It is worth pointing out that photothermal thickness measurements are also applicable to layers that are either sticky or wet [20].

Theoretically, it should be possible to estimate simultaneously partial thicknesses of a multi-layer system, if the signal can be interpreted unambiguously. The first attempts have been made to characterize a double layer, but so far the success of such an approach has been restricted by the poor measuring accuracy [21].

In addition to the depth of an interface, the width of the transition zone can also be probed. At soft or smeared transitions the TW will suffer a modified reflection compared with abrupt transitions [22]. Such soft transitions occur when layers are fabricated by phase transition, ion implanting, interdiffusion or some kinds of glueing.

If the mechanical contact between coating and substrate is not ideal (because of partial or local delamination), then the thermal contact resistance increases, resulting in an increase in thermal reflectance. Often such an increased thermal contact resistance correlates with a reduced mechanical layer adhesion, allowing for a quantitative

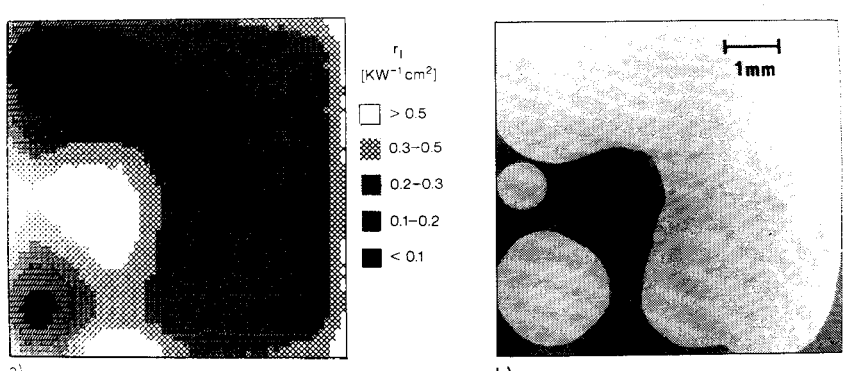

Fig. 8. Inspection of the thermal coupling of a chip bonding by photothermal (left) and x-ray techniques (right). A silicon chip is glued by a silver-containing adhesive to a substrate. The grey scale on the left quantifies the thermal contact resistance. Bright spots mean poor adhesion because of missing adhesive. These spots are characterized as dark areas identified in the x-ray image (from [23]).

sticking estimation and the detection of adhesion defects. An impressive example was given by Beyfuss et al. [23], who reported the photothermal evaluation of bondings of silicon chips to heat sinks compared with x-ray imaging. A typical result is shown in Fig. 8. Another example of characterizing the contact quality was given by Heuret et al. [24], who investigated the air gap thickness arising on crimping metal rings on metal pipes.

Photothermal techniques are appropriate for measuring the influence of substrate pretreatment on layer adhesion. This is important for paints on polymers [25], electrochemically induced deposits or plasma-sprayed coatings [26,27]. The attenuation of thermal waves in inhomogeneous layers is much lower compared with ultrasonic attenuation. Therefore, they are suited to probing these coatings and their interfaces.

An application-related example of photothermal detection of vertical interfaces is the quality control of welding seams, using the mirage technique [28] or radiation measurement [29]. In addition to the detection of hidden defects such as flaws or voids, the distribution and homogeneity of the welding material can be observed. The reason is the reduced heat conductivity of the welding material. Moreover, the edges of the heat-influenced zone in the modified microstructure will become detectable.

Microstructured semiconductors

Photothermal methods are unique techniques for the determination of structure-related electronic properties of semiconductor materials and devices both in laboratories and for on-line inspection. In semiconductors the periodic light absorption drives both thermal and plasma waves, each having its specific time behaviour. At the surface and internal interfaces an increased recombination velocity of the free carriers occurs and results in typical photothermal signal changes that indicate the possibility of interfacial lattice damage [30].

The well established method of phase-sensitive detection of probe beam modulation, which is sensitive down to $\Delta R/R = 10^{-7}$, can be combined with micrometre spot size probing and MHz excitation frequencies. Hence it becomes possible to detect individual defects in crystal growth (*e.g.*, dislocations or stacking faults), as has been reported for silicon and GaAs wafers [31–34]. The detection and interpretation methods are sensitive enough to resolve various levels of lattice strain associated with different types of dislocations.

Photothermal reflectometry allows for monitoring both dose (ranging from 10^{10} to 10^{16} ions cm^{-2}) and uniformity of ion implantation in silicon and GaAs wafers [35,36]. The thermoreflective signal from doped samples is correlated with peak carrier concentration of the concentration profiles, as was revealed by comparative measurements [37]. A further important advantage of TW techniques is their ability to measure the implantation dose through overlayers such as screens or gate oxides.

Photothermal techniques can be successfully applied to control the fabrication process of dielectric overlayers such as silicon dioxide or silicon oxynitride on silicon that are used in very large scale integration (VLSI) technology. Film thicknesses from 25 to 150 nm can be estimated with a reproducibility of about 1 nm. Metallization layers have also been studied by modulated thermoreflectance. As shown by Rosencwaig [38] micrometre resolution images of voids and microcracks in fine aluminium lines on silicon could be recorded without stripping the passivation or cap metal layers. Similar results could be obtained by non-photothermal techniques only at the expense of about a two orders of magnitude longer analysis time and/or destruction of the sample.

Microstructure and crystallography

Grain structures in single- and multi-phase metals and alloys show up very clearly in thermal wave images. As an example, in contrast to scanning electron microscopic images, grain interfaces can be detected also for multi-phase materials with only small differences in atomic numbers between the grains, and for single-phase materials. No preliminary etching is required as the grain boundaries represent local areas of strongly pertubated lattice structure and therefore of considerably changed thermal conductivity. The thermal conductivity of electrical insulators and semi-

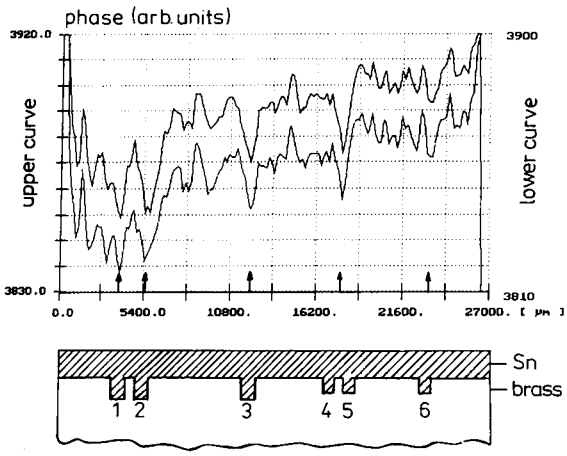

Fig. 9. Measured phase scans over a tinned brass plate at two modulation frequencies (tin thickness ca. 0.3 mm) (from [16]).

conductors is determined by two main factors, the harmonic and anharmonic phonon–phonon interaction and the scattering of the phonons by the crystal boundaries. The phonon–phonon interaction dominates at high temperatures whereas the scattering of phonons by the crystal boundaries leads to a size-dependent thermal conductivity at low temperatures. Sample temperature has to be referred to its Debye temperature [39].

Grain boundary effects were first demonstrated by Rosencwaig [38] using two-dimensional thermoreflectance. In Fig. 9 a radiation measurement scan over a tinned brass plate is presented, showing fluctuations in photothermal signals which are caused by individual grains within the tin layer. Grain boundaries of nanometre thickness decrease heat conduction, which can be expressed as increased thermal contact resistance. From the standard deviation of the photothermal signal amplitude, Meyer-Berg et al. [40] estimated the thermal contact resistance between sputter-deposited Al grains in the range of about 10^{-2} K cm W^{-1}. The correlation between microstructure and thermal diffusivity could be confirmed by a variety of investigations on polycrystalline samples (e.g., Peralta et al. [41] studied the diffusivity variation of high-purity Al as a result of different recrystallization processes). Phase transformation in steel caused by case hardening could be detected photothermally [42]. The well established relationship between hardness and thermal conductivity provides a non-destructive tool for measuring both surface hardness and hardened layer thickness. By comparing photothermal results with those obtained from reference samples, it should be possible to determine the crystallographic composition of unknown films.

The strong dependence of thermal wave propagation on microstructure allows for the estimation of material porosity [43,44]. Thus, for instance, Inglehart et al. [44] performed measurements on porous model samples made from glass-bonded alumina to establish the dependence of thermal properties on particle size.

Conclusions

Photothermal techniques provide a powerful tool for the investigation of interfaces that are not accessible by optical measurements. Thermal wave methods are applicable to a variety of different materials ranging from metals and semiconductors to ceramics and polymers. The determination of layer thicknesses and coating adhesion becomes possible in single- and, to some extent, in multi-layer systems with an accuracy depending on the material properties. Photothermal imaging also allows for the detection of buried inhomogeneities such as subsurface defects and cracks. The close correlation between microstructure and thermal conductivity allows for the evaluation of microstructure dimensions in term of grains and pores. The previous disadvantage of long measuring times required for imaging by scanning techniques can be overcome by new developed multiplex lock-in thermography. The examples presented above show the capability of photothermal methods to characterize both macro- and microscopic interfaces.

The authors are indebted to G. Busse and J. Pelzl for helpful discussions and useful advice, to U. Seidel for performing numerical calculations and to J. Burt for critical comments on the text. H.G.W. is grateful to the Deutsche Forschungsgemeinschaft for financial support of the photothermal investigations.

References

[1] G. Busse and H.G. Walther, in A. Mandelis (Ed.), Principles and Perspectives of Photothermal and Photoacoustic Phenomena, Elsevier, New York, 1992, p. 205.

[2] A. Rosencwaig and A. Gersho, J. Appl. Phys., 47 (1976) 64.

[3] C.A. Bennett and R.R. Patty, Appl. Opt., 20 (1981) A60.

[4] J. Jaarinen, Acta Polytech. Scand., Appl. Phys. Ser., 162 (1988) 162.

[5] H.G. Walther, K. Friedrich, U. Seidel, W. Karpen and G. Busse, in D. Bicanic (Ed.), Photoacoustic and Photothermal Phenomena III (Springer Series in Optical Sciences, Vol. 69), Springer, Berlin, Heidelberg, 1992, p. 669.

[6] L.C. Aamodt and J.C. Murphy, J. Appl. Phys., 54 (1983) 581.

[7] D. Fournier and A.C. Boccara, Physica C, 157 (1989) 587.

[8] A.C. Tam, Rev. Mod. Phys., 58 (1986) 381.

[9] J.C. Murphy, L.C. Aamodt and J.W.M. Spicer, in A. Mandelis (Ed.), Principles and Perspectives of Photothermal and Photoacoustic Phenomena, Elsevier, New York, 1992, p. 43.

[10] F.A. McDonald and G.C. Groover, Phys. Acoust., 18 (1988) 167.

[11] R.E. Wagner and A. Mandelis, J. Phys. Chem. Solids, 52 (1991) 1061.

[12] G. Busse and A. Ograbek, J. Appl. Phys., 51 (1980) 3576.

[13] Y.Q. Wang, P.K. Kuo, L.D. Favro and R.L. Thomas, in J.C. Murphy, J.W.M. Spicer, L.C. Aamodt and B.S.H. Royce (Eds.), Photoacoustic and Photothermal Phenomena II (Springer Series in Optical Sciences, Vol. 62), Springer, Berlin, Heidelberg, 1990, p. 24.

[14] J.M. Lloyd, Thermal Imaging Systems, Plenum Press, New York, 1975.

[15] G. Busse, D. Wu and W. Karpen, J. Appl. Phys., 71 (1992) 3962.

[16] K. Friedrich, K. Haupt, U. Seidel and H.G. Walther, J. Appl. Phys., 72 (1992) 3759.

[17] P.M. Patel, D.P. Almond and H. Reiter, Appl. Phys., B43 (1987) 9.

[18] H. Petry, Laser Praxis, 6 (1990) 60.

[19] A. Rosencwaig, in D.O. Thompson and D.E. Chimenti (Eds.), Review of Progress in Quantitative Nondestructive Evaluation, Vol. 9, Plenum Press, New York, 1990, p. 2031.

[20] G. Busse, D. Vergne and B. Wetzel, in P. Hess and J. Pelzl (Eds.), Photoacoustic and Photothermal Phenomena, Springer, Berlin, Heidelberg, 1988, p. 427.

[21] W. Karpen, A. Bohnacker, H.G. Walther, K. Friedrich, U. Seidel and G. Busse, in D. Bicanic (Ed.), Photoacoustic and Photothermal Phenomena III (Springer Series in Optical Sciences, Vol. 69), Springer, Berlin, Heidelberg, 1992 p. 248.

[22] H.G. Walther, K. Friedrich, U. Seidel, G. Busse and W. Karpen, in D. Bicanic (Ed.), Photoacoustic and Photothermal Phenomena III (Springer Series in Optical Sciences, Vol. 69), Springer, Berlin, Heidelberg, 1992, p. 669.

[23] M. Beyfuss, J. Baumann and R. Tilgner, in J.C. Murphy, J.W.M. Spices, L.C. Aamodt and B.S.H. Royce (Eds.), Photoacoustic and Photothermal Phenomena II (Springer Series in Optical Sciences, Vol. 62), Springer, Berlin, Heidelberg, 1990, p. 17.

[24] M. Heuret, F. van Scheel, M. Egee and R. Danjoux, Mater. Sci. Eng., B5 (1990) 119.

[25] H.G. Walther, W. Karpen, in D. Balegeas, G. Busse and G.M. Carlomagno (Eds.), Quantitative Infrared Thermography, QIRT 92, Editions Europeenes Thermic et Industrie, Paris, 1992, p. 388.

[26] J. Hartikainen, Appl. Phys. Lett., 55 (1989) 1188.

[27] P.M. Patel and D.P. Almond, J. Mater. Sci., 20 (1985) 955.

[28] F. Lepoutre, D. Fournier and A.C. Boccara, J. Appl. Phys., 57 (1985) 1009.

[29] G. Busse, R. Rief and P. Eyerer, Can. J. Phys., 64 (1986) 1195.

[30] I. Little, G.M. Crean and S.J. Sheard, Mater. Sci. Eng. B, Solid State Adv. Technol., B5 (1990) 89.

[31] B. Witowski, W. Lee Smith and D. Willenborg, Appl. Phys. Lett. 52 (1988) 640.

[32] A. Bivas, W. Lee Smith, R.R. Kola, Z.R. Radzimski and G.A. Rozgonyi, J. Cryst. Growth, 103 (1990) 200.

[33] L.J. Inglehart, A. Broniatowski, D. Fournier, A.C. Boccara and F. Lepoutre, Appl. Phys. Lett., 56 (1990) 1749.

[34] H. Nakamura, K. Tsubouchi, N. Mikoshiba and T. Fukuda, Jpn. J. Appl. Phys., 24 (1985) L876.

[35] D. Fournier and A.C. Boccara, Mater. Sci. Eng. B, Solid State Adv. Technol., B5 (1990) 83.

[36] Application Note 150.01, Therma Wave, Fremont, CA, 1986.

[37] N. Uchitomi, H. Mikami, N. Toyoda and R. Nii, Appl. Phys. Lett., 21 (1988) 30.

[38] A. Rosencwaig, in N.G. Einspruch (Ed.), Microstructure Science, Vol. 9, Academic Press, Orlando, 1985, p. 227.

[39] A.K. Collins, M.A. Pickering and P.L. Taylor, J. Appl. Phys., 68 (1990) 6510.

[40] G. Meyer-Berg, R. Osiander, P. Korpiun, P. Kakoschke and H. Joswig, Photoacoustic and Photothermal Phenomena III (Springer Series in Optical Sciences, Vol. 69), Springer, Berlin, Heidelberg, 1992, p. 711.

[41] S.B. Peralta, S.C. Ellis, C. Christofides, A. Mandelis, H. Sang and B. Farahbakhsh, Res. Nondestruct. Eval., 3 (1991) 69.

[42] J. Jaarinen and M. Luukkala, J. Phys. (Paris) Colloq., 44 (1983) p. 503.

[43] J.R. Banavar, D.L. Johnson and S.R. Nagel, Phys. Rev. Lett., 61 (1988) 2748.

[44] L.I. Inglehart, R.A. Haber and J.B. Wachtmann, in Proc. Fall Meeting Materials Research Society USA, Boston, 1989.

ELSEVIER

Analytica Chimica Acta 297 (1994) 97–108

ANALYTICA CHIMICA ACTA

Chemistry of grain boundaries in calcia doped silicon nitride studied by spatially resolved electron energy-loss spectroscopy

John Bruley *[,b], I. Tanaka [c], H.-J. Kleebe [d], M. Rühle [a]

[a] *Max-Planck-Institut für Metallforschung, 70174 Stuttgart, Germany*
[b] *Department of Materials Science, Lehigh University, Bethlehem, PA 18015, USA*
[c] *Department of Metallurgy, Kyoto University, Kyoto 606, Japan*
[d] *Universität Bayreuth, Institut für Materialforschung, 95440 Bayreuth, Germany*

(Received 7th October 1993; revised manuscript received 11th February 1994)

Abstract

Spatially resolved electron energy-loss spectroscopy has been used to interrogate the chemistry and bonding at grain boundaries in hot isostatically pressed (HIPed) high purity silicon nitride ceramics nominally doped with either 0, 100, 300 or 500 at. ppm calcium. Analysis of the nanometer thick glassy films between grains, shows that there is a monotonic increase in impurity segregation with dopant concentration. The predominant constituents of the grain boundary films are Si, O and N, forming a silicon oxynitride phase ranging in composition from SiO_2 to Si_2N_2O. The energy-loss near-edge structure indicates the structure of the glass is composed predominantly of tetrahedra but also suggests the presence of a small concentration of molecular N_2, possibly as sub-microscopic bubbles. There is still no data on the composition gradients on a sub-nanometer level, though it is shown that in the detection limit set by counting statistics, near single atom sensitivity with a spatial resolution of 0.22 nm is achievable.

Keywords: Electron energy-loss spectroscopy; Calcia; Ceramics; Grain boundaries; Silicon nitride

1. Introduction

An electron energy-loss spectrum of a finely focused swift electron beam (of sub-nanometer lateral dimension) after transmission through a thin foil, contains local information on the chemical and electronic structure of the foil. The technique is known as spatially resolved electron energy-loss spectroscopy (SREELS). Our concern in this work is the examination of grain boundaries in high temperature silicon nitride structural ceramics by SREELS.

Previous microstructural characterization of a wide range of Si_3N_4 materials with many different liquid phase sintering additives has revealed that except for some "special boundaries" there exists an amorphous film wetting two grain boundary junctions and filling the triple grain junctions. Furthermore, the grain boundary film is found to have an equilibrium thickness, the

* Corresponding author.

SSDI 0003-2670(94)00056-R

magnitude of which depends upon the amount and type of dopant in the system [1–8]. A model, proposed to account for the equilibrium thickness, is based on the balance between repulsive disjoining forces (due to mesoscopic structural ordering) and attractive van der Waals dispersion forces [9]. The balance is expected to depend on local chemical composition and distribution of charge density. To correctly estimate the magnitudes of the forces, experimental data on the local chemistry and atomic structure is required.

Previous studies have confirmed that the glassy phase is oxygen rich and includes the cation impurities [1–3,10] but to date there has been no accurate determination of the amount of oxygen present, nor the degree of impurity segregation. The importance of these boundaries stems from their direct influence on properties at high temperatures, such as strength and creep behaviour [11–14]. Recently, SREELS and transmission electron microscopy observations (TEM) were made on liquid phase sintered silicon nitride ceramics with ytterbia added as a sintering aid and small amounts of calcia to mimic the influence of contamination [15]. The work focused on the effects of cation co-segregation and the influence of heat treatments designed to crystallize the glassy phases. The grain boundary thickness was observed to vary by up to 0.4 nm with the glass composition, and in particular to the CaO content.

In the present work experiments are conducted on a series of hot isostatically pressed (HIPed) high-purity Si_3N_4 samples doped with various amounts (up to 500 ppm) of CaO. These studies were designed to investigate the effects of well-controlled dopant concentrations on the boundary structure of purer materials than previously examined, and thereby attempt to elucidate the role of cations on the grain boundary chemistry. Chemical profiling of the oxygen and nitrogen is carried out across the nanometer thick glassy films, and a study is made on the local structure using SREELS. Lastly, the counting statistics of the data are analyzed to discover the current "realistic" limits of sensitivity for SREELS in the silicon nitride system.

Table 1
Incident dose (for a ten second experiment) for different probe sizes with the FEG-STEM (data taken from [18,19])

Mode	Current (nA)	$d_\perp$ (nm)	D ($\times 10^{10}$ e$^-$ nm^{-2})
Spot	0.01	0.22	1.6
Spot	0.2	0.60	4.4
Spot	1.0	1.00	8.0
Spot	6.0	3.50	3.9
Area scan (4.5 by 3.5 nm)	1.00	3.50	0.4

2. Materials and methods

Four sets of high-purity Si_3N_4 samples, initially containing less than 50 at. ppm total cation impurities, were processed by hot isostatic pressing using commercially available high purity α-Si_3N_4 (SN-E10 powder from Ube Ind.), with controlled amounts (0, 100, 300 and 500 at. ppm) of CaO additions. The actual calcium content was measured by inductively coupled plasma atomic emission spectrometry to be 0, 80, 220 and 450 at. ppm in the four samples, respectively. Surface oxide pre-existing on the silicon nitride powder provides enough oxygen to form a siliceous glassy film at the grain boundaries. Full details of the processing techniques have been described previously [14,16,17]. Densities of the processed materials were more than 99.5% of theoretical density. All the specimens used in this study were thinned to electron transparency in the conventional method of polishing, dimpling followed by ion milling to electron transparency. To avoid the specimen charging under the electron beam, they were coated in a thin carbon layer.

The SREELS experiments were carried out using a VG Microscopes' HB501 dedicated scanning transmission electron microscope (STEM) operating at 100 keV, fitted with a Gatan's Model 666 parallel electron energy loss spectrometer (PEELS). With the high brightness cold field emission electron source it is routine to form a probe 0.5 nm in diameter (fwhm) having a beam current of about 0.2 nA, Table 1 [18]. An ultra-high-resolution objective pole piece having spher-

ical aberration coefficient $C_s = 1.3$ mm, enables a probe size with more than 90% of the 0.01 nA beam current contained within two parallel planes separated by 0.22 nm [19]. A spectral resolution of 0.5–0.7 eV is obtained with the spectrometer entrance semi-angle limited to about 8 mrad. The incident beam convergence is similarly about 8 mrad. The microscope is operated under ultra-high vacuum with 10^{-9} mbar in the specimen chamber, which minimizes specimen contamination.

With the development of parallel detection spectrometers, SREELS has become a valuable tool for materials characterization. However, to cope with the intrinsically low signal-to-background, data processing is almost always required. The simplest process is to subtract a smooth power law background, fitted in the region prior to the edge. Curve fitting adds uncertainty to the signal intensity. This reduces the detection sensitivity which is limited by the signal-to-noise ratio [20]. The parallel detection devices introduce extra noise, which is expressed as a reduction in the detective quantum efficiency (DQE), such as photo diode read-out noise and channel-to-channel gain variations. To minimize the influence of read-out noise high count rates must be used and to circumvent the difficult gain calibration procedure necessary to correct for gain variations, data acquisition using the first (or second) energy difference mode is often implemented [21,22]. The first-difference spectrum is the numerical difference between two identical spectra but displaced on the photodiode by a small energy shift. Both the slowly varying background and gain variations are suppressed and the sharp slope changes at edges are accentuated. Energy difference is most useful for edges with "white-line" features at the edge threshold. For broader structures or edges that grossly overlap giving rise to an energy dependent background, the "spatial difference" method offers several advantages. The interface sensitivity near-edge structure is exposed by subtracting a scaled standard spectrum, typically recorded a few nanometers away from the first spectrum. The scaling is chosen to remove as much of the bulk contribution as possible. The signal-to-noise may be maximized by integrating the edge over a wide energy range. Interpretation of the edge structures is often more straightforward than energy difference, and quantification using the ratio technique and experimental standard or calculated cross-sections is possible. No a priori information of spectral shapes and widths is necessary with the spatial difference.

The energy-loss near-edge structures (ELNES) within the first 30 eV of the threshold contain information of the electronic and atomic structure. Often ELNES from well-known compounds can be used as chemical "fingerprints" to identify the coordination environments of atoms in unknown sites [23]. According to single electron theory, the transition strength at the edge is proportional the "dipole-allowed" local density of unoccupied states. A recent review on the theory of near-edge structures can be found in [24].

The spatial resolution achievable with SREELS has received much attention in the literature. A fundamental limit is set by the ionization impact parameter, which scales as the inverse of energy loss. For edges over 200 eV and using a convergent focused probe and finite collection angle, the impact parameter is certainly less than typical interplanar spacings. Thus, in principle, the goal of column-by-column analysis is possible if the probe can be focused and maintained at small enough dimensions throughout the foil. Batson [25] has recently discussed and reviewed the factors that contribute to the spatial resolution in electron scattering experiments. Beam broadening resulting from high angle scattering events is of limited concern since the majority of high angle electrons are not collected by the spectrometer and therefore do not contribute to the signal. For thin films and small collection apertures, the practical limit of spatial resolution is the instrumental probe size, which is 0.22 nm or smaller depending on the pole-piece and operating voltage. Recently it has been shown that when crystalline samples are aligned on a zone axis, electron channelling tends to focus the beam intensity onto the atom columns, limiting the spread of the beam [27,28]. Often, the requirement to provide adequate counting statistics by increasing probe current (and consequently probe size) or

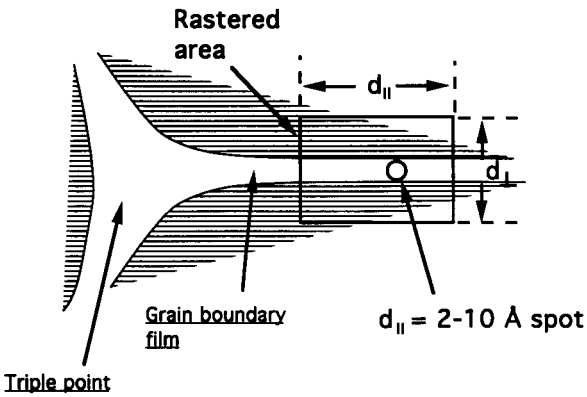

Fig. 1. Schematic of SREELS analysis. The probe can be focused to a spot or scanned across a prescribed area of incorporating the projected image of the boundary. The probe size parallel and perpendicular to the interface affect the elemental detection sensitivity.

the need to limit dose or dose rate onto radiation sensitive materials controls the spatial resolution [29].

The following procedures for the SREELS experiments are adopted. EELS data are acquired and processed using Gatan's EL/P software. Composition line profiles are acquired using a custom function called "Spectre-Image" [30]. With the function, several hundred spectra may be automatically acquired and up to 4 separate edges processed using an E^{-r} background fitting and removal routine. The elemental intensity ratios are converted to atomic ratios using the ratio technique by dividing by the relative cross-section ratio, calculated using SIGMAK and SIGMAL routines [20] running within the EL/P program.

The interface plane is tilted parallel to the incident beam direction. Spectra are recorded either with a stationary probe on the interface or with the beam scanning over an area of 3.5 nm by 4.5 nm. This edge-on geometry of a silicon nitride sample is schematically illustrated in Fig. 1. For the "spatial difference" method two spectra are necessary, one with the interface placed in the center of the spot or rastered zone and a second with it placed just outside this region. The difference between the two spectra contains the interface sensitive components to the ELNES. Normalization is typically required so that the reference spectrum correctly matches the background intensity. The normalization factor can often be chosen by trial and error with sufficient accuracy to leave little of no trace of the background spectrum. Thickness variations lead to an energy dependency in the background (i.e., due to multiple plasmon scattering) which will become apparent in the spatial difference but for small beam displacements and broad plasmon features this effect is often much smaller than the structure from an overlapping edge due to the bulk matrix.

Wherever possible, edges were recorded with dispersions of 0.1 eV per channel. When this provides insufficient signal intensity, a greater dispersion, such as 0.2 or 0.3 eV per channel, is chosen. The data presented here are typically the sum of 2 or 3 spectra, each being of between 10 and 30 s acquisition time per photodiode readout.

3. Results and discussion

The boundary widths of this set of samples were previously measured to range from 0.7 to 1.5 nm, the value being dependent upon the dopant concentration [31]. The unexpected but reproducible result was that a 0.3 nm reduction in boundary thickness was observed when less than 100 ppm of CaO is added. Fig. 2 illustrates this thickness data (open symbols) as a function of the

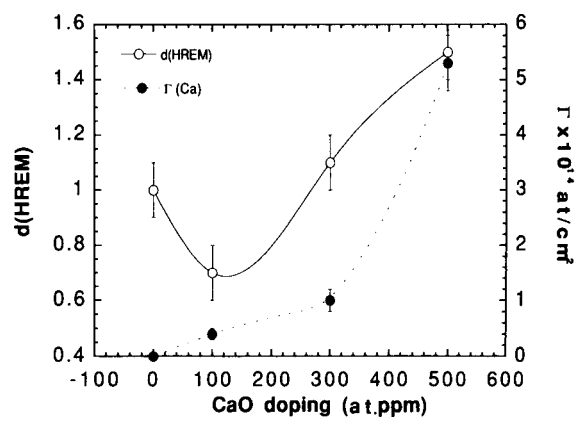

Fig. 2. Plot of grain boundary thickness measured by HREM [31] (open symbols) and grain boundary CaO coverage measured by SREELS (filled symbols) versus the total CaO dopant concentration.

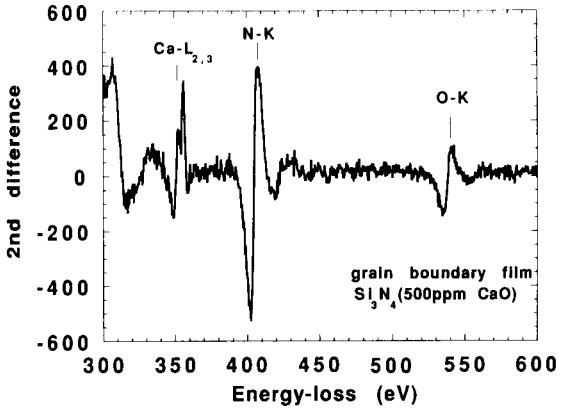

Fig. 3. Second-difference spectrum recorded at a grain boundary film in the 500 at. ppm doped Si_3N_4 highlighting the presence of oxygen and calcium.

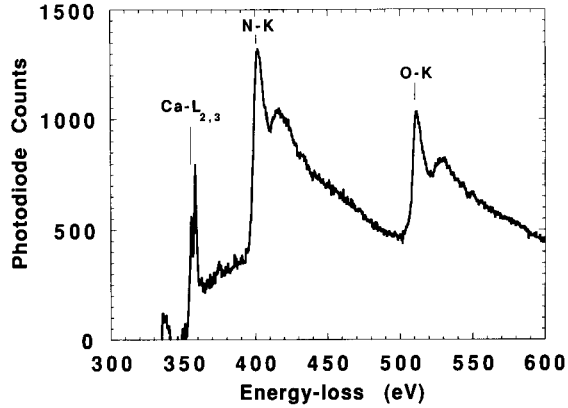

Fig. 4. Spatial difference spectrum of the grain boundary film. The near-edge structures of the nitrogen, oxygen and calcium are retained in this mode. These can be used to extract bonding information within the boundary.

dopant CaO concentration. The thicknesses are determined with an accuracy of ± 0.1 nm by measurement from several high-resolution electron micrographs (HREM).

It is estimated that if all the CaO were to segregate to the boundaries in these samples, one might expect about monolayer coverage with additions of 500 ppm or more. To identify the presence of Ca using EELS at the sub-monolayer levels a difference mode is necessary because of the small signal-to-background. Fig. 3 shows a typical second energy difference spectrum that was recorded with an energy shift of ± 8 eV. The Ca $L_{2,3}$ edge is visible at 350 eV along with the K edges of nitrogen at 400 eV and oxygen at 530 eV. The overlayer of carbon due to coating and extra carbon contamination contributes to the background at the Ca edge (The carbon K-edge threshold is at 285 eV). This overlayer limits the detection sensitivity of Ca. Assuming the probe samples only the glass, the simplest interpretation of the spectra shown in Fig. 3 is that the boundary contains nitrogen, oxygen and calcium. Silicon is additionally present but its $L_{2,3}$ edge (100 eV) is not visible in the energy loss range shown in Fig. 3. A spatial difference spectrum of the grain boundary film is illustrated in Fig. 4. The scaling was chosen to provide zero background beneath the Ca edge. In this case the resultant nitrogen and oxygen intensities will not correctly reflect the true grain boundary film composition. It clearly exhibits the double white line feature of the Ca edge and the O and N K-edges. The O and N ELNES are similar. However, data from a single spot location does not unambiguously prove the existence of nitrogen or oxygen in the glassy phase because of the possibility of beam overlap into neighbouring silicon nitride grains and the presence of a surface oxide. Chemical profiling (or mapping) and close scrutiny of the nitrogen ELNES provides greater certainty and enables determination of the glass composition.

Fig. 5 demonstrates an oxygen-to-nitrogen chemical profile across a boundary of the 300 at.

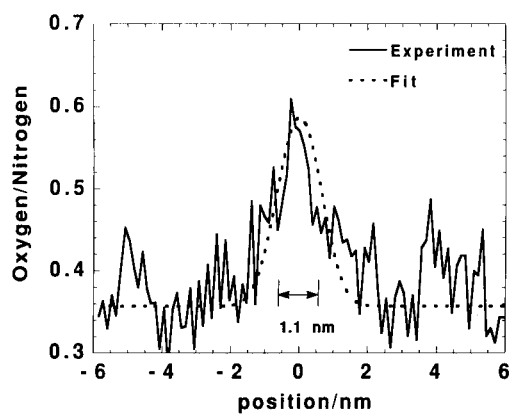

Fig. 5. Oxygen to nitrogen concentration profile across a boundary in the 300 at. ppm doped Si_3N_4.

ppm CaO doped material. One hundred spectra, with an acquisition time of 1 s per spectrum, were used to generate this figure. The increase in the oxygen content at the grain boundary is clearly seen. The full-width-half-maximum of this distribution equals 2.4 nm and is somewhat wider than the structural width observed by HREM equal to 1.1 nm. A fit to the data is provided by convoluting a Gaussean curve (to model the incident beam profile and beam broadening) with a step function (to model a thin film of uniform composition) of width 1.1 nm. The discrepancy between chemical and structural width may be systematic, i.e., due to either beam overlap with the neighbouring Si_3N_4 grains or boundary tilt. Alternatively it could represent real chemical diffusivity across the boundary, as a result non-planar boundary facets (such as pits or islands) or solubility of oxygen in the nitride. An upper estimate of the beam broadening in an amorphous 50 nm thick SiO_2 film is ca. 4 nm (using the single scattering model due to Goldstein et al. [32]). The finite collection angle (20 mrad) samples just about 1 nm of this broadened probe for a 50 nm thick foil. Achieving better spatial resolution requires either thinner foils or smaller collection apertures-both of which reduce the counting statistics. Quantification of the chemical profile in Fig. 5 appears to confirm that a beam broadened profile is correct. By assuming the intensity profile approximates to the model Gaussean, it is deduced that if all the oxygen contained within the film at the grain boundary constituted an SiO_2 layer, the boundary width would be only 0.6 nm (assuming the density of SiO_2 to be 2.2 g/cm^3). This width is only 60% of its structural width of 1.1 nm as measured by HREM. If, on the other hand, nitrogen were present within in the glassy phase, for example as an Si_2N_2O layer, the film would be ca. 1.2 nm thick, assuming a similar molar volume, which is in much better agreement with the structural width. It is considered improbable that the amorphous film is a single phase of uniform composition. More likely, the glass is an oxynitride, compositionally graded from nitrogen rich at the glass crystal interface to oxygen rich in the central portion of the film. Significant oxygen solubility in the solid silicon nitride grains is not expected. In Table 2, the data extracted from the chemical profiles for the set of doped materials has been compiled. Despite different widths, the profiles provide a consistent picture of nitrogen being dissolved in the glass. The film composition may be estimated by comparing the ratio $\delta(SiO_2)/d(HREM)$. A ratio of 1 indicates pure SiO_2 and a ratio of 0.5 indicates Si_2N_2O. The films appear to range from SiO_2 to Si_2N_2O with a greater tendency towards the nitrogen-rich side. Brinker et al. [33] have studied the formation and thermodynamics of oxynitride mixtures in liquid melts for temperatures exceeding 1600°C. It has been noted that increasing concentrations of Si_3N_4 or oxygen partial pressures leads to the exothermic decomposition of such liquids with the evolution of N_2 and SiO gases according to the reaction:

$$Si_3N_4 + SiO_2(l) + O_2(g) \longrightarrow 4SiO(g) + 2N_2(g)$$

$$\Delta G^\circ(1980\ K) = -80.3\ kcal\ mol^{-1}$$

The ELNES of the nitrogen edge at the boundary and the spatial difference is shown in Fig. 6. The spatial difference highlights changes to the chemical and structural environment of the nitrogen atoms in the boundary. Only the edge components that are due to nitrogen in bonding environments like bulk silicon nitride are removed. Such alterations might be localized either within the glass itself or at the interface between the glass and the Si_3N_4 grain. The presence of similar ELNES components in the bulk glass

Table 2
The chemical widths, d(CHEM) (measured at full-width-half-height of the line profile) and the peak oxygen to nitrogen concentration ratios as a function of dopant concentration (the value of $\delta(SiO_2)$ would be the width of a pure amorphous SiO_2 layer and d(HREM) is the boundary thickness measured by HREM [31])

CaO (ppm)	d(CHEM) (nm)	[O]/[N]	$\delta(SiO_2)$ (nm)	d(HREM) (nm)
0	7.8	0.07	0.7	1.0
0	9.6	0.05	0.6	1.0
0	3.6	0.11	0.5	1.0
100	3.7	0.07	0.3	0.7
300	3.0	0.40	1.0	1.1
300	2.4	0.25	0.6	1.1

pockets within the regions between three grain triple points suggests the former is most likely. The white line indicates nitrogen forms double or triple bonds similar to molecular N_2 gas. This might be an indication of bubble formation. Bubbles have not yet been observed in any samples by HREM even after heat treatment where one might anticipate coalescence. Such bubble formation is a well-known phenomenon in liquid melts and causes frothing [33]. Alternatively, it may be the result of radiation damage to the beam sensitive grain boundary film. The oxygen ELNES is the same as for SiO_2 and is similar to the N edge in the nitride indicating it is 2-coordinated within a tetrahedral network. The lack of white line features on the O–K ELNES indicates insignificant amounts of O–O or O–N bonding. There is no evidence for the presence of O_2 bubbles. This may be due to sublimation of SiO. No chemical shifts in either the N or O K-edges have been observed suggesting mostly covalent bonding. The presence of pure SiO_2 might be signalled by a small upward chemical shift in the edge position due to charge transfer. One way to view the grain boundary film is as a solid solution of SiO_2 and Si_3N_4 with mixed tetrahedra. There may also exist sub-microscopic bubbles of nitrogen gas held under high pressure. A similar edge structure is observed in nitrogen bubbles in diamond [34]. This would be the first reported evidence for gas bubbles within the grain boundary films of hot pressed silicon nitride.

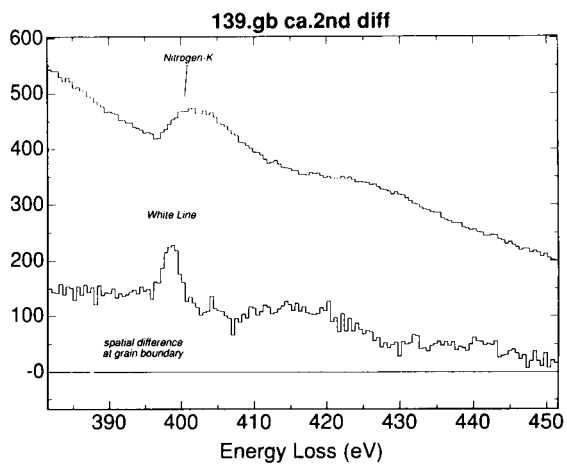

Fig. 6. N–K ELNES at grain boundary and the spatial difference to the neighbouring grain. The white line feature at the edge threshold suggests some degree of double bonding of nitrogen in the boundary region. This structure may not represent the nitrogen as it appears in its unirradiated state, since it may have been induced by beam damage. Nevertheless, it does confirm the presence of nitrogen in the glassy phase.

The spatial resolution of the data is inadequate to enable comment on the form of oxygen-to-nitrogen gradients within the films. As seen in Fig. 5, there is a finite oxygen-to-nitrogen ratio equal to 0.3 on the nitride grains away from the glassy film indicating an approximately 6 nm thick surface oxide. This layer is due to oxidation after ion milling and adds to the background, degrading optimum sensitivity and resolution.

Determining the Ca/O ratios from the second difference spectra and assuming a Si_2N_2O grain boundary film gives the CaO content. In total, over 60 spectra of many boundaries in each of the four different samples were recorded and quantified. There was never any Ca detected in the material with no added CaO. In the other three materials, the nominal CaO content (given in Table 3) is determined as follows. For each material the measured ratio of Ca/O was plotted as a function of O/N (Fig. 7). The measured O/N ratio is proportional to the probe size. A straight line was fitted to the data and its intersection with the ordinate at zero O/N was taken as the effective grain boundary Ca/O content. The reasoning behind using this method is based on the assumption that for larger probe sizes, the ratio is less sensitive to details of the probe shape, composition gradients and radiation damage. We observed a monotonic increase of this intercept with CaO doping. The coverage of Ca in the film, Γ, is given by the measured bulk Ca concentration multiplied by the boundary thickness. A monolayer of CaO corresponds to a coverage of about 1.1×10^{15} molecules/cm^2.

The coverage has been plotted in Fig. 2. It demonstrates the increase in CaO segregated to the boundary with doping. This contrasts with the HREM data which indicates a modest decrease in the boundary thickness for about 80 at. ppm CaO. It was suggested that a small concentration

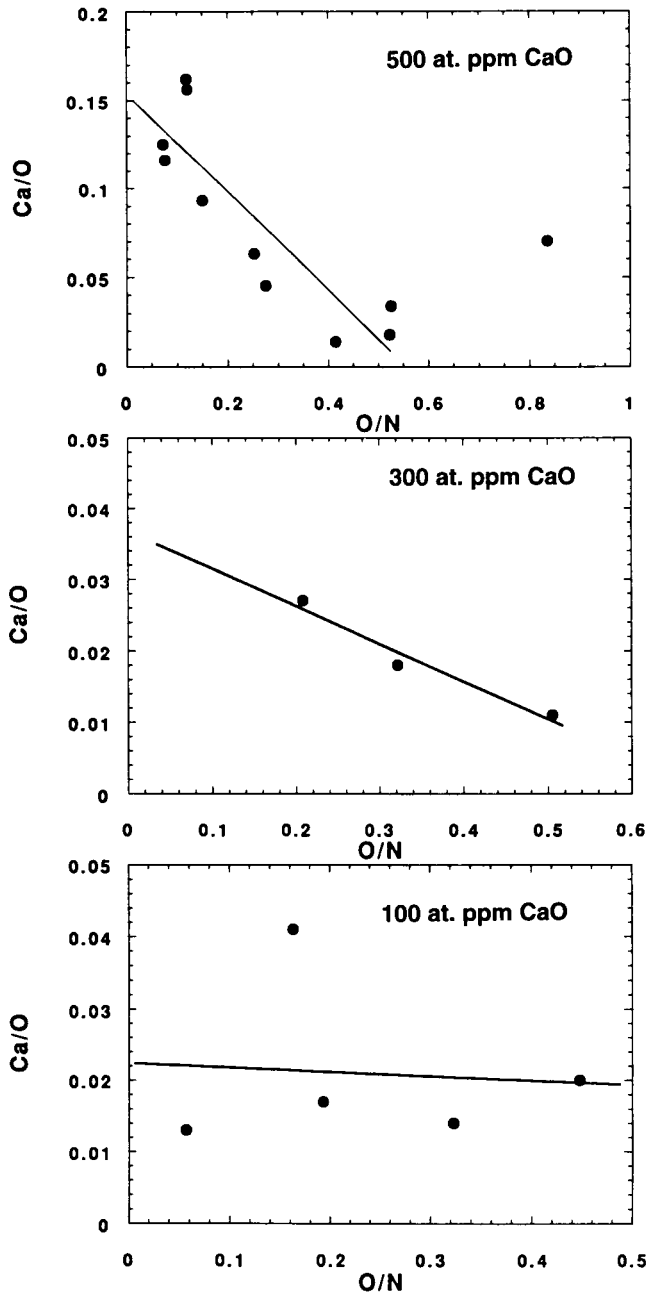

Fig. 7. The Ca/O atomic ratio plotted as a function of the O/N ratio. The data was extracted from the intensities of the 2nd difference spectra. The intercept at low oxygen corresponds to larger beam sizes or increased N solubility with Ca content. The Ca content at this intercept provides the data for the plot in Fig. 2. Effects due to radiation damage are minimized using larger probe sizes.

Table 3
Calcium content of grain boundary film (Ca/O ratio given by intercept of C/O versus O/N plot. Bracketed values in the Ca/O column refer to the extrema of Ca/O values. The coverage (measured in Ca atoms per unit area) is derived assuming normal molar volumes and the Ca is contained within a film composed of Si_2N_2O. Θ_{Ca} is the fractional coverage of possible Ca sites in monolayers)

CaO (ppm)	[Ca]/[O]	d(HREM) (nm)	Γ_{Ca} ($\times 10^{14}$) (atoms/cm^2)	Θ_{Ca} monolayer
0	None	1.0±0.1	–	–
100	0.023±0.004 (0.003–0.090)	0.7±0.1	0.4±0.1	0.03±0.01
300	0.037±0.004 (0.030)	1.1±0.1	1.0±0.2	0.09±0.02
500	0.151±0.004 (0.030–0.213)	1.5±0.1	5.3±0.5	0.42±0.04 (0.08–0.6)

of cations (less than a monolayer) would modify the correlation length in glass network structure thereby destroying order across the boundary and reducing slightly the net repulsive force [31]. With the highest doping, the amount of CaO segregated in the glass film corresponds to about one half monolayer. This level of coverage accounts for most of the CaO added to the system. The remainder resides in the glassy pockets where Ca has also been detected. There is some evidence to suggest that the concentration of Ca is slightly reduced in glassy pockets, though more work is required to statistically validate this. The energy-loss data suggests a similar content of nitrogen, i.e., SiN_2O, in the amorphous triple points. Measurements of composition along an individual boundary or across triple points indicate no significant variability. There is still no information concerning the distribution of the cations across the thin film. Future experiments using smaller probes are planned to interrogate the cation's segregation profile, attempting to ascertain if the Si_3N_4 surface is covered by Ca or whether there exists a thin charged central layer. The Ca cation distribution and its associated space charge will affect the strength of the electrostatic forces at the boundaries.

It may be noteworthy that on a micron length scale (micron), the CaO content in each sample appears to be inhomogeneously distributed. This effect is particularly marked with the 500 at. ppm doped material, where the Ca/O ratio is seen to range from 0.03 to 0.2. The source of such large scale fluctuations is still unknown, though it seems unlikely that systematic errors alone could account for them. Grain boundary misorientation, surface oxidation and beam spreading would certainly give rise to variations but these would be much less than that observed. Inhomogeneities due to poor mixing can not be ruled out without more detailed investigation. The observed inhomogeneity would not contradict the results of earlier reports of uniform Ca distributions since those studies had less chemical sensitivity and spatial resolution than achieved here. Radiation damage can lead to very significant changes in composition. The fact that grain boundary thickness was not observed to vary to the same extent [31] raises a point of concern since the model proposed to account for an equilibrium thickness implies an equilibrium film composition. Clearly these observations will have important implications on the modelling if they can be verified by further study.

4. Detection sensitivity and chemical profiling

The above spectra represent the routine performance that can be achieved with relative ease using commercial instrumentation. This data is used to furnish "realistic" estimates of the limits of detection. The signal-to-noise ratio (SNR) provides the ultimate limit to detection sensitivity. A common approach is to determine first the SNR for a known concentration and then to calculate that concentration necessary to yield a pre-specified SNR (For 98% confidence of detection the SNR should be greater than 3) [32]. The appeal of this approach is its simplicity. As long as similar experimental conditions are chosen, the effects of multiple scattering and beam broadening are included in the estimate. The following analysis follows the conventional approach to minimum detection sensitivities. For a perfect detection system (i.e., DQE ≈ 1) noise obeys

Poisson statistics, and the measured SNR is given by

$$\mathrm{SNR} = \frac{I_x}{\sqrt{2I_B}} \quad (1)$$

where I_x is the integrated signal intensity and I_B is the background beneath I_x, both in counts. Such an approach is reasonable for "difference" techniques that automatically reduce channel-to-channel gain variations in the spectrum. The factor of 2 within the square root accounts for the independent statistical error in the background spectrum. Here, we ignore the systematic error introduced by the background fitting, since this error is not expected to be large using spatial difference or energy difference. For interface segregation, the surface coverage of element x per unit area, Γ_x, is the important thermodynamic parameter. The measured signal I_x is proportional to the dose D (the charge of electrons incident per unit area) and coverage via,

$$I_x = Dd_{\parallel} t\Gamma_x \sigma_x(\Delta, E_x). \quad (2)$$

where $\sigma_x(\Delta, E_x)$ is the partial ionization cross section integrated over a window Δ and with threshold at E_x. The area of interface sampled by the illumination is given by the product $d_{\parallel} t$. assuming the foil thickness is t and the probe size parallel to the interface is $d_{\parallel}$. We suppose all the segregant is located within $d_{\perp}$ of the interface where $d_{\perp}$ is the dimension perpendicular to the interface. It should be noted that segregation of charged defects in the space charge region at the ceramic boundary may extend up to a Debye length, which can be several tens of nanometers in non-stoichiometric materials. The background signal is due to the whole illuminated volume, $V = d_{\perp} d_{\parallel} t$, and is given by

$$I_x = Dd_{\perp} d_{\parallel} t\rho_B \sigma_B(\Delta, E_x). \quad (3)$$

where ρ_B is the atomic density of the matrix and $\sigma_B(\Delta, E_x)$ is the scattering cross section into the chosen energy loss region. Combining expressions 1, 2 and 3 gives the minimum detectable coverage:

$$\Gamma_{\min} = 3\sqrt{2}\,\frac{\sqrt{\sigma_B}}{\sigma_x} \cdot \sqrt{\frac{d_{\perp}\rho_B}{d_{\parallel} tD}} \quad (4)$$

Note that for both fixed dose D and probe shape (i.e., constant $d_{\perp}/d_{\parallel}$), Γ is independent of absolute probe size, $d_{\parallel}$. Some enhancement to detection sensitivity can be achieved using an elongated (or astigmatic) probe shape such that $d_{\perp}/d_{\parallel} < 1$. In general D and $d_{\parallel}$ are not independent for typical microscope operating conditions. Elastic and inelastic scattering reduces the value of I_x and I_B by the same factor and would increase Γ only by a small amount for thin foils.

Table 1 gives the beam currents and approximate dose for 10 second exposure and different probe sizes using a V.G. HB 501 microscope (data taken from [18,19]). The 5-fold reduction in the dose for the very small spot sizes translates to a $1/\sqrt{5}$ (or 55%) reduction in the optimum detection sensitivity for interface segregation. Scanning the beam over a fixed area with a constant beam current during spectrum acquisition reduces the dose relative to the fixed beam. In this case the sensitivity scales with the size of the raster (or magnification). Table 4 highlights the minimum coverage detectable for oxygen and calcium in the silicon nitride system, using values for the signal intensity and noise extracted directly from the data.

For the Si_3N_4 system, the data indicates that for 1 nm resolution the optimum sensitivity for Ca coverage is about 3×10^{12} cations/cm^2. Assuming normal densities, this coverage is equivalent to about 0.003 monolayers. If 0.22 nm resolution was desired, about 7×10^{12} CaO molecules/cm^2 (or ca. 0.007 monolayer) would be detectable at the grain boundary. This amounts to the detec-

Table 4
Experimental values of signal, noise, SNR and the measured atomic concentrations of Ca and O (minimum detectable coverage is estimated for an SNR equal to 3. The bulk concentration [X] is converted to surface coverage, Γ, by multiplying by $d_{\perp}$)

Signal	Matrix	Signal (counts)	Noise (counts)	SNR	X at.%	$\Gamma_{\min}$ [a] (atoms/cm^{-2})
Ca–L_{23}	Si_2ON_2	4.19×10^5	1.9×10^3	217	1.9	3.1×10^{12}
O–K	Si_3N_4	3.43×10^5	1.9×10^3	177	13.0	4.8×10^{13}

[a] Assuming a probe size of 1 nm.

tion of one or two calcium atoms on an individual atomic column for a foil of thickness 50 nm. A similar estimate of the sensitivity to oxygen detection in silicon nitride indicates that for 0.22 nm resolution a coverage of 10^{14} atoms/cm^2 is observable. This is equivalent to about one tenth of a monolayer of silicon dioxide. This a degree of sensitivity and spatial resolution is obviously desirable if the theoretical models, implying chemical gradients and charged double layers, are to be adequately tested. The dopant concentrations used in this set of the materials are typical of the impurity levels in sintered silicon nitrides.

5. Conclusions

The grain boundaries in HIPed high-purity silicon nitride material are separated by amorphous oxygen-rich films with equilibrium thickness. Doping with CaO changes the thickness and the amount of Ca segregation within the film increases with dopant concentration. In the 500 at. ppm doped sample, there is up to 1 monolayer of CaO and 3 to 4 layers of silicon oxynitride. An important observation concerns the compositional variations seen amongst boundaries within a given material. The boundary films are predominantly composed of silicon, oxygen and nitrogen, ranging in composition from SiO_2 to Si_2N_2O. There is evidence to suggest the formation of sub-microscopic gas bubbles of N_2 within the thin film glass. This would result from a decomposition of the oxynitride melt during the processing. Further sub-nanometer scale experiments are necessary to ascertain the presence of local chemical gradients and to identify the source of these inhomogeneities. These measurements indicate that 0.01 monolayer of Ca, with a spatial resolution of 0.22 nm, is within detection range.

6. Acknowledgements

The funding for purchase of the PEELS instrumentation was provided by a grant from the Volkswagen Stiftung. Thanks go to Dr. C. Colliex and Dr. M. Tencé for permission to use the VG STEM at the Université Paris Sud (Orsay, France) for some of this work. Discussions with Professor D. Clark at the University of California (Santa Barbara, CA), Dr. R.M. Cannon at Lawrence Berkeley Laboratory, Berkeley, Ca., Dr. M.K. Cinibulk, at Air Force Research Center (Dayton, OH) and Dr. S. Bhandarker at AT&T (Murrey Hill, NJ) are gratefully acknowledged.

7. References

[1] H.-J. Kleebe, M.K. Cinibulk and M. Rühle, J. Mater. Sci. Lett., 12 (1993) 70.
[2] H.-J. Kleebe, M.J. Hoffman and M. Rühle, Z. Metallkunde, 83 (1993) 610.
[3] D.R. Clarke, N.J. Zaluzec and R.W. Carpenter, J. Am. Ceram., 64 (1981) 601.
[4] O.L. Krivanek, T.M. Shaw and G. Thomas, J. Appl. Phys., 50 (1979) 4223.
[5] M.K. Cinibulk, H.-J. Kleebe and M. Rühle, J. Am. Ceram. Soc., 76 (1993) 426.
[6] H.-J. Kleebe, J. Eur. Ceram. Soc., 10 (1992) 151.
[7] D.R. Clarke, Ultramicroscopy, 4 (1979) 33.
[8] H.-J. Kleebe and M. Rühle, Mater. Res. Soc. Symp. Proc., 238 (1992) 859.
[9] D.R. Clarke, J. Am. Ceram. Soc., 70 (1987) 15.
[10] H.-J. Kleebe, J.S. Vetrano, J. Bruley and M. Rühle, Proc. 49th Annual EMSA Meeting, August 4–9, San Jose, CA, 1991, p. 930.
[11] R.L. Tsai and R. Raj, J. Am. Ceram. Soc., 63 (1980) 513.
[12] R. Raj, J. Geophys. Rev., B87 (1982) 4731.
[13] C.J. Hwang and J. Wei Chen, J. Am. Ceram. Soc., 73 (1990) 1626.
[14] I. Tanaka, K. Igashira, T. Okamoto, K. Niihara and R.M. Cannon, J.Am. Ceram. Soc., (1993) submitted for publication.
[15] H.-J. Kleebe, J. Bruley and M. Rühle, J. Eur. Ceram. Soc., (1994) in press.
[16] I. Tanaka, G. Pezzotti, T. Okamoto, Y. Miyamoto and M. Koizumi, J. Am. Ceram. Soc., 72 (1989) 1656.
[17] J. Zeng, I. Tanaka, O. Yameda, Y. Miyamoto and K. Niihara, J. Am. Ceram. Soc., 75 (1992) 148.
[18] C. Colliex, in M.M. Disko, C.C. Ahn and B. Fultz (Eds.), Transmission Electron Energy Loss Spectrometry in Materials Science, The Minerals, Metals and Materials Society, Warrendale, PA, 1992, Chap. 4
[19] N.D. Browning and S.J. Pennycook, Microbeam Analysis, 2 (1993) 81.
[20] R.F. Egerton, Electron Energy Loss Spectroscopy in the Electron Microscope, Plenum Press, New York, 1986.
[21] H. Shumann and P. Kruit, Rev. Sci. Int., 56 (1985) 231.
[22] M. Kundmann and O.J. Krivanek, Microsc. Microanal. Microstruct., 2 (1991) 245.
[23] R. Brydson, H. Sauer and W. Engel, in M.M. Disko, C.C.

Ahn and B. Fultz (Eds.), Transmission Electron Energy Loss Spectrometry in Materials Science, The Minerals, Metals and Materials Society, Warrendale, PA, 1992, Chap. 6.
[24] P. Rez, in M.M. Disko, C.C. Ahn and B. Fultz (Eds.), Transmission Electron Energy Loss Spectrometry in Materials Science, The Minerals, Metals and Materials Society, Warrendale, PA, 1992, Chap. 4.
[25] P.E. Batson, Ultramicroscopy, 47 (1992) 133.
[26] D.B. Williams, J.R. Michael, J.I. Goldstein and A.D. Romig Jr., Ultramicroscopy, 47 (1992) 121.
[27] R.F. Loane, E.J. Kirkland and J. Silcox, Acta Crystallogr., A44 (1988) 912.
[28] S.J. Pennycook and D.E. Jesson, Phys. Rev. Lett., 64 (1990) 938.
[29] J.K. Weiss and R.W. Carpenter, Ultramicroscopy, 40 (1992) 339.
[30] M. Tencé, Spectre-Image EL/P Custum Function, Laboratoire de Physique des Solides, Université Paris Sud, Orsay.
[31] H.J. Kleebe, M.K. Cinibulk, I. Tanaka, J. Bruley, R.M. Cannon, D.R. Clarke, M.J. Hoffman and M. Rühle, Proc. MRS Fall Meeting 1993, Boston, MA.
[32] J.I. Goldstein, D.B. Williams and G. Cliff, in D.C. Joy, A.D. Romig Jr. and J.I. Goldstein (Eds.), Principles of Analytical Electron Microscopy, Plenum Press, New York, 1986, Chap. 5.
[33] C.J. Brinker, D.M. Haaland and R.E. Loehman, J. Non Cryst. Solids, 56 (1983) 179.
[34] J. Bruley and L.M. Brown, Philos. Mag., A59 (1989) 247.

ELSEVIER

Analytica Chimica Acta 297 (1994) 109–124

ANALYTICA CHIMICA ACTA

Low energy electrons (LEED, STM and HREELS) in the microanalytical characterization of complex surface structures

W. Weiss, U. Starke, G.A. Somorjai

Department of Chemistry and Materials Sciences Division, Lawrence Berkeley Laboratory, University of California, Berkeley, CA 94720 (USA)

Received 11th June 1993; revised manuscript received 29th September 1993

Abstract

The use of surface analytical techniques has created a broad knowledge of the geometric structures of even complex single-crystal surfaces and surface–adsorbate systems; which is essential to the understanding of their physical and chemical properties. Four techniques that use low-energy electrons as a probe are reviewed in this paper. These are low-energy electron diffraction (LEED), low-energy electron microscopy (LEEM), scanning tunneling microscopy (STM) and high-resolution electron energy loss spectroscopy (HREELS). Their experimental principles, theoretical backgrounds and specific capabilities in surface science studies are discussed. Recent examples of these techniques for structure determination of complex clean surfaces and complex adsorbate molecular systems are presented, with an emphasis on organic adsorbate molecules.

Keywords: Surface techniques; Low energy electrons; Microanalytical characterization

During the past twenty years there has been a revolution in surface chemical analysis. This was brought about by the development of new techniques in ever increasing numbers that permit surface analysis on the molecular scale. Electrons, ions and photons are being used as surface probes to provide surface structure and surface composition with continually improving spatial resolution, time resolution and energy resolution.

This review focuses on the use of low energy electrons for the characterization of surfaces and adsorbed molecules with complex structures. We shall discuss the use of low-energy electron diffraction (LEED)-surface crystallography that provided most of the quantitative information (bond distances, bond angles) about these structures. Low-energy electron microscopy (LEEM) and scanning tunneling microscopy (STM) are contributing increasingly to surface structure determination. These techniques will also be reviewed. Finally, high-resolution electron energy loss spectroscopy (HREELS), that yields the vibrational spectra of surfaces and adsorbed

Correspondence to: G.A. Somorjai, Materials Sciences Division, Lawrence Berkeley Laboratory, University of California, Berkeley, CA 94720 (USA).

SSDI 0003-2670(93)E0549-M

molecules, will be discussed with emphasis on the structure of adsorbed organic molecules of considerable complexity that were studied using this technique.

As is usual in modern surface science studies, the combined use of these and other surface analysis techniques can provide a detailed picture of the surface chemical bond and the structural rearrangement for a given adsorbate–substrate system as the experimental variables (substrate surface structure, adsorbate coverage, temperature and pressure) are altered.

1. LEED

LEED has become the most widespread technique for structural characterization of single crystal surfaces. A complete surface structure determination can be performed by applying multiple scattering theory to compute the variation of the diffracted beam intensities I, with electron kinetic energy eV for an assumed arrangement of surface atoms and adsorbed molecules and by comparing the results to the I–eV curves obtained by experiments. The LEED pattern can be used to routinely check the preparation of ordered surfaces or to monitor surface structure changes after different sample treatments such as heating to elevated temperatures, adsorption of gases and so forth. This can be performed by inspection of the LEED pattern, and the size and symmetry of the surface unit cell can be determined by applying kinematic diffraction theory.

Experimental principle and instrument types

The principle of an LEED experiment is shown schematically in Fig. 1. A monoenergetic and parallel electron beam is created in an electron gun. It consists of a heated cathode biased on a negative potential V, which is located within a Wehnelt cylinder and emits the electrons. These are collimated by a lens system and finally leave the drift tube with the desired kinetic energy eV, which typically lies between 20 and 300 eV. The drift tube is on the same potential as the sample, so that the electrons traverse a field free space to the sample surface from where they are scattered back. The elastically backscattered electrons form the diffraction pattern which can be detected in several ways.

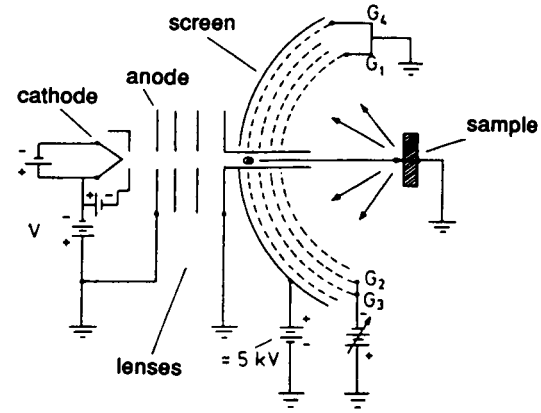

Fig. 1. Schematic representation of the principle of a LEED experiment with a "display-type" LEED instrument.

The most common type of instrument is the "display-type" shown in Fig. 1. Here the backscattered electrons pass a system of hemispherical concentric grids. The first one is grounded, and the second one is on a more negative "retarding" potential so that the energy difference is slightly smaller than the primary electron energy, and only elastically scattered electrons can pass through. The third grid is grounded again and finally the electrons are accelerated to several keV onto a fluorescent screen, where the LEED pattern can be observed visually. From there it can be stored by photographic techniques or with a video camera. Full computer-controlled video camera LEED systems have been developed for data acquisition [1]. In a back-view LEED instrument the LEED pattern on the fluorescent screen is observed from the backside where the electron gun is located. It displays a much larger part of the diffraction pattern as compared to conventional display-type LEED system [2]. Another type of instrument is the so-called "diffuse LEED system", where the scattered electrons pass the same sequence of grids as in a display-type instrument and are then detected by a two-dimensional array of channel plates [3]. Because of the high sensitivity of the channel plates very low intensities can be de-

tected, and much lower incident electron beam currents (pA instead of mA) are necessary compared to conventional LEED systems of the display type. For a typical *I–eV* curve data aquisition the electron dose is less then one electron per 100 unit cells. Therefore electron beam sensitive structures can be investigated without damaging them. It is also possible to analyze the diffuse background between the diffraction spots which makes disordered systems accessible. Another type of LEED instrument (spot profile analysis LEED system) has been designed for measuring LEED beam profiles [4]. Here a set of electrostatic octupol plates placed between the sample and a channeltron detector can deflect the backscattered electrons and scan them over the aperture in front of a channeltron detector. Again a sequence of grids in front of the detector only allow the elastically scattered electrons to pass through. In this way LEED beam profiles can be measured very accurately, as well as the entire LEED pattern.

Theory

According to the wave nature of matter postulated by de Broglie in 1924, electrons with the velocity v and mass m have a wavelength of

$$\lambda = h/mv$$

h being the Planck constant. The wavelength of 150 eV electrons is about 0.1 nm, which corresponds to atomic distances in solids. Because of their small mean free path the low energy electrons can penetrate only a few atomic layers into the solid, and a diffraction pattern will be formed by the outermost atomic layers of the sample. Within two-dimensional geometrical diffraction theory the interaction of electrons with the surface is treated as elastic scattering of waves by a two-dimensional lattice, which means that the finite penetration of the electrons into the solid is neglected. The reciprocal lattice is defined by

$$\mathbf{a}_i \mathbf{a}_j^* = 2\pi\delta_{ij}$$

where $\mathbf{a}_i$ are the real space unit cell vectors and $\mathbf{a}_j^*$ the reciprocal space unit cell vectors. Because there is no diffraction condition perpendicular to the two-dimensional surface lattice, the corresponding reciprocal lattice forms rods of infinite length perpendicular to the surface plane and intersecting this plane at the reciprocal lattice points defined by $h\mathbf{a}_1^* + k\mathbf{a}_2^*$ (h and k are integers). In Fig. 2 the diffraction pattern formation is shown by using the Ewald construction. According to the Laue equations, constructive interference occurs when $\mathbf{K} = \mathbf{K}_{hk} - \mathbf{K}_0 = \mathbf{G}$, where $\mathbf{K}$ is the electron scattering vector, and $\mathbf{K}_0$ and $\mathbf{K}_{hk}$ are the wave vectors representing the incoming and backscattered electrons, respectively. $\mathbf{G}$ is a reciprocal lacttice vector represented by the rods labeled hk in Fig. 2. It can be seen that the LEED pattern is a projection of this reciprocal lattice onto the screen (at normal incidence). Therefore the size and symmetry of the two-dimensional surface unit cell can be determined straightforward from the LEED beam positions.

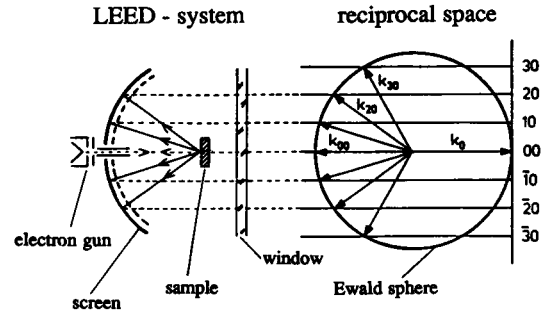

Fig. 2. Ewald construction for a LEED experiment (right side) and a schematic representation of the diffraction pattern formation in the LEED system (left side). Further explanation in the text.

Like in x-ray crystallography, the intensities of the diffracted beams have to be analyzed for a complete surface structure determination, since they contain the information about the atomic positions within the unit cell and in the deeper layers. In surface crystallography one measures the LEED beam intensities as a function of the electron energy (intensity–voltage curves) and compares them to calculated intensity–voltage curves for a given structure model. In a search the atomic coordinates in the structure model are varied until the best fit between experimental and theoretical intensities is obtained. Because of the strong interaction of the electrons with the atoms in the solid, multiple scattering takes place.

Therefore the LEED beam intensities have to be calculated within multiple scattering theory. These dynamical LEED calculations are complex and time consuming, which sets limits for the maximum number of atoms within a unit cell of structures to be solved [5]. A new development in this field is automated Tensor LEED, which considerably reduces the computation time for LEED calculations and allows us to handle more complex surface structures [6]. With this technique structures that contain up to 10 atoms within the two-dimensional surface unit cell can be determined. It also became possible with this technique to detect adsorbate induced reconstructions on substrate surfaces, which means that the substrate surface atoms change their positions due to interaction with the adsorbate molecules. Examples are O/Pt(111) [7] and ethylidyne on Pt(111) [8]. Also, surfaces of more complex compounds like metal oxides have become accessible for structure studies. Thin films of iron oxide grown epitaxially onto Pt(111) substrates have been identified recently as magnetite Fe_3O_4, and their (111) surface structure was determined by applying automated Tensor LEED [9].

Examples of complex surface structure analysis by LEED crystallography

Reconstructed metal surface. The (110) crystal face of platinum [10]. The atomic geometry of the (1 × 2) and (1 × 3) structures of the Pt(110) surface has been determined from low energy electron diffraction intensity analysis. Both structures are found to be of the missing row type, consisting of (111) microfacets and with relaxations in the top and in the subsurface layers. In both reconstructions the top layer spacing d_{12} is contracted by ca. 20% together with a buckling of $\Delta\delta \approx 0.17$ Å in the third layer and a small lateral shift of ca. 0.04 Å in the second layer. Further relaxations down to the fourth layer were detectable. The surface relaxations correspond to a variation of interatomic distances ranging from −7% to +4% where, in general, a contraction of ca. 3% for the distances parallel to the surface

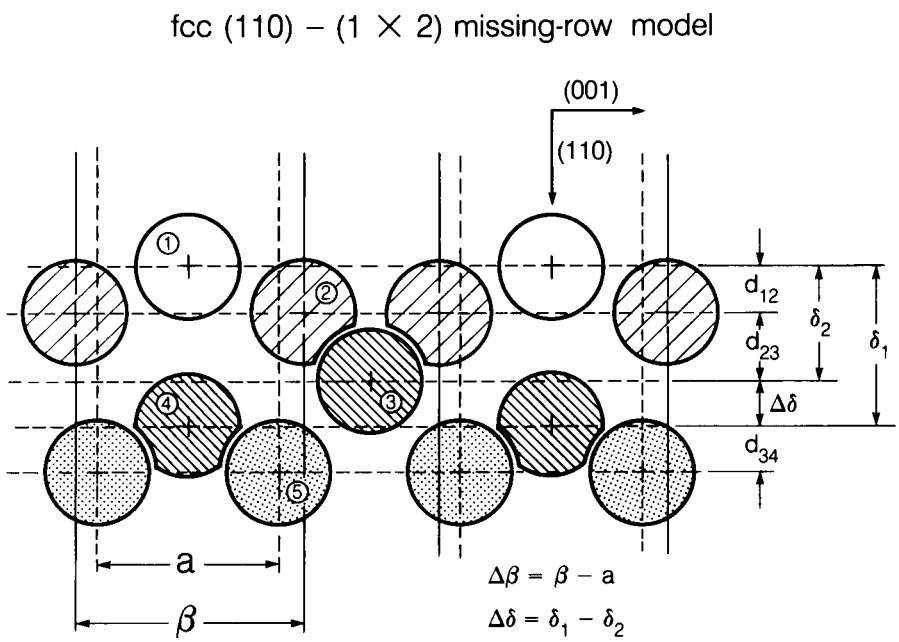

Fig. 3. Side view of the (1 × 2) reconstructed Pt(110) surface. The top layer spacing d_{12} and the buckling in the third layer $\Delta\delta$ are indicated.

occurs. The model of the (1 × 2) structure is shown in Fig. 3. It can be converted to the (1 × 3) structure on the Pt(110) surface by heating in oxygen at 1200 K for 30 min. Both reconstructed surfaces are clean within the detection limits of the Auger spectrometer. The adsorption of CO lifts the reconstruction in both structures. After desorption of CO at 500 K the initial structures appear again.

Adsorbate induced reconstruction. The surface structure of ethylene on the Pt(111) crystal face [8]. The adsorption of ethylene on the Pt(111) crystal face at 300 K produces an ethylidyne molecule (C_2H_3) with its C–C axis perpendicular to the surface. The top methyl group is away from the surface and the C atom bound to the surface fits into a threefold hollow fcc site. (There is no Pt atom in the second layer directly under the threefold site.) The structure is shown in Fig. 4. The C–C bond distance is 1.49 Å, and the C–Pt bond length is 1.91 Å. A buckling within the top two substrate layers is detected, which corresponds to a local expansion of the first to second layer distance underneath the adsorbate by 0.08 Å as compared to the bulk value. The three substrate atoms forming the hollow site are closer to one another than in the bulk structure by 0.11 Å. A tilt of the C–C bond by 6 degrees seems to occur, and could be indicative of a wagging vibration of this bond. The H atoms do not contribute to the diffraction that yields the ordered pattern, as indicated by the absence of H related features in the experimental *I–V* curves, suggesting relatively free rotation of the methyl group about the C–C axis.

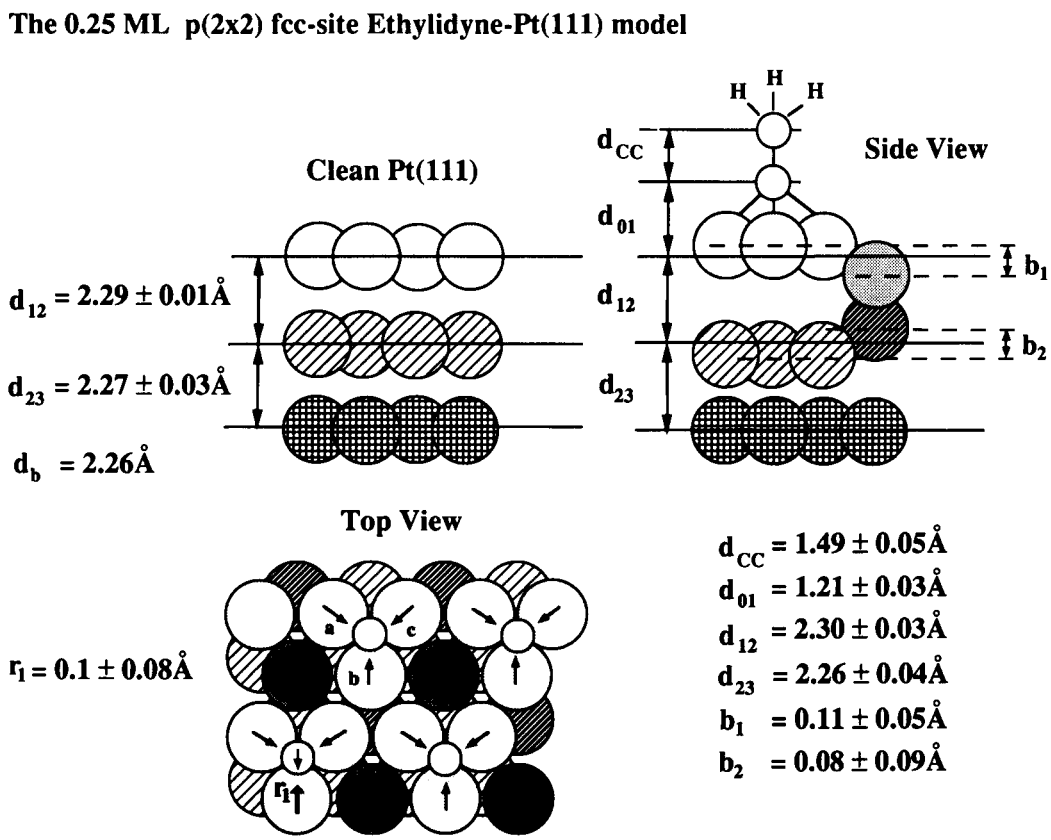

Fig. 4. Structure model for the ethylidyne–Pt(111) surface-adsorbate system forming a p(2 × 2) superstructure. Some structural parameters are indicated. For comparison a side view of the clean Pt(111) surface is shown also.

This ethylidyne structure on Pt(111) clearly indicates that the adsorption of a molecule that forms a chemisorption bond between the adsorbate and the substrate atoms restructures both the molecule as well as the substrate metal atoms to form a cluster with well defined geometry. Both lateral and perpendicular displacements of metal atoms around the adsorption sites are clearly detectable.

Surface structure of ordered iron oxide, Fe_3O_4, thin films [9]. A detailed surface structure determination is reported for an iron oxide film grown on a foreign metal substrate. Up to 10 monolayers of well-ordered iron oxide films were grown onto Pt(111) substrates. By applying automated Tensor low energy electron diffraction to many possible bulk and surface structures, the films were identified to be magnetite, Fe_3O_4. They form an unreconstructed polar (111) surface termination that exposes one quarter monolayer of iron ions over a distorted hexagonal close packed oxygen layer and minimizes the number of dangling bonds. This structure is shown in Fig. 5, and is characterized by the $\Delta = 0.42$ Å upward displacement of the oxygen atoms labeled A with respect to the oxygen atoms labeled B. This relaxation may be driven by electrostatic forces since it reduces the surface dipole of this polar surface. Another feature is the 30% contraction (with respect to the bulk value) of the spacing d_{12} between the plane defined by the equivalent B oxygens and the second iron layer, as well as the 20% expansion of the spacing d_{23} between the second iron layer and the oxygen layer below it. The same structure is found for the (111) surface of a sputtered and annealed α-Fe_2O_3 (111) single crystal, which has therefore been reduced to Fe_3O_4.

Real space structure analysis techniques

The LEED techniques discussed so far provide information about surface structures via their diffraction intensitities in reciprocal space. In recent years experimental techniques have been developed, that can provide direct images of the surface structure on an atomic scale. Field ion microscopy and high energy electron microscopy are well established in that respect, but they will not be discussed in detail in the present context due to the nature of their probes, i.e. ions and electrons with energies in the keV range, respectively. Low-energy electrons are utilized in two rather new experimental techniques: The low-energy electron microscope (LEEM) which was developed by Telieps and Bauer [11–15] which will

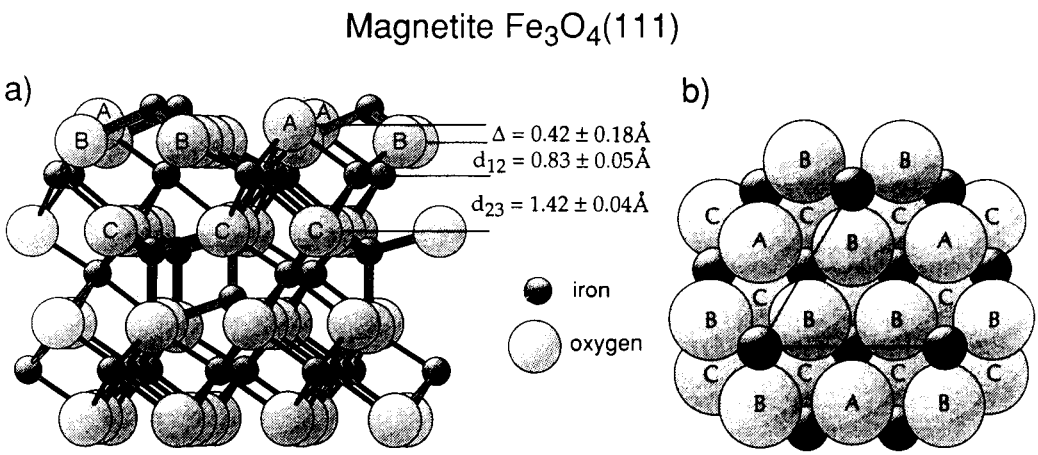

Fig. 5. (a) Perspective side view of the Fe_3O_4(111) surface structure (surface is on top). Relaxed layer spacings in the surface region are indicated. The corresponding bulk values are $\Delta = -0.04$ Å, $d_{12} = d_{23} = 1.19$ Å. Bonds formed by tetrahedral and octahedral iron atoms are drawn thick and thin, respectively. Tetrahedral sites are occupied by Fe^{3+} ions, octahedral sites are occupied randomly by 50% Fe^{2+} and 50% F^{3+} ions. The ionic sizes are reduced by a factor of 0.5. (b) Top view onto the Fe_3O_4(111) surface with the full ionic sizes. The lattice vectors of the (2×2) unit cell are also indicated.

be discussed first, and the scanning tunneling microscope (STM) [16] that has greatly accelerated the development of surface structure determination. Whereas LEED always averages over a sample surface area of several square millimeters, STM can image local atomic features and provide information about non-periodically arranged adsorbate adatoms, vacancies and steps. When used together, these techniques can complement each other very efficiently in characterizing surface structures.

2. LEEM

The LEEM instrument requires a sophisticated electron optical imaging system. The electrons are kept at rather high energies (20 keV) in the lens system and then are decelerated down to energies between 25–200 eV before they hit the surface. Therefore, penetration depth and interaction with the surface is very similar to LEED. For the electron optical projection the elastically backscattered electrons are accelerated once again to about 20 keV. In LEEM either the specular beam ("bright field mode") or a higher order diffraction beam ("dark field mode") can be used for imaging. The resolution in lateral direction obtained so far is about 15 nm. Monoatomic steps can be resolved using the dark field mode when adjacent terraces contribute to different higher order diffraction beams (e.g. (5 × 1)-Au(100) [14,15,17]), but also the specular beam can be used in tilted incidence geometry to resolve atomic steps (e.g., (2 × 1)-Si(100) [14,15,18]). The LEEM images are displayed on a fluorescent screen, aided by a multichannel plate array and can be recorded by a TV camera. This provides real time capability and makes this instrument particularly suitable to investigate dynamic processes like phase transition, epitaxial growth, etc. The first extensive study in this respect was concerned with the phase transition of the Si(111)-(7 × 7) to the Si(111)-(1 × 1) structure which takes place at $T = 870°C$ [14,15,18]. The nature of this phase transition was determined to be of first order. The preparation procedure was shown to have a strong influence on supercooling of the (1 × 1) phase and the nucleation behavior of the (7 × 7) phase [14,15,18,19]. Depending on the duration of heat treatment the temperature range where the phase transition occurs can be different. After a brief flash, a narrow range of 3–6 K is observed, and after long annealing the supercooling temperature of the (1 × 1) phase can locally be as large as 100 K. The phase transition appears then to be of second order when studied with LEED or other laterally averaging techniques [18–20]. A second example of real time observation with LEEM is the epitaxial growth of Cu or Au on Mo(110) or Si(111), respectively [21]. Growth modes, nucleation centers and phase transitions have been studied for these systems [22–25]. For details the reader is referred to the quoted publications.

3. STM, experimental principles

While the LEEM requires the use of sophisticated electron optics, the STM is based on a relatively simple design principle. Microscopes as small as 1 cm^3 have been built [26–28], and ultrahigh vacuum (UHV) compatible microscopes fitted on a 2 inch outer diameter flange (CF 38) are available commercially [26,27]. Many other designs for operation in air or vacuum have been developed and are commercially available in some cases. In the following we describe the basic principle of the STM and some typical designs that have been used in UHV. The tip of a metal wire is brought in close proximity of an electrically conducting sample (Fig. 6). When the distance between tip and surface is sufficiently small (1–10 Å), the gap in between can be viewed as a quantum mechanical potential well [29]. If a bias is applied between tip and sample a tunneling current may flow through the gap [30]. In a first approximation the vacuum levels of tip and sample are connected by a linear potential line which forms a trapezoidal potential well according to the bias applied. For a more simplified evaluation of the tunneling current, a square well with an effective barrier height may be assumed. Under these assumptions the current depends exponentially on the distance between tip and sample.

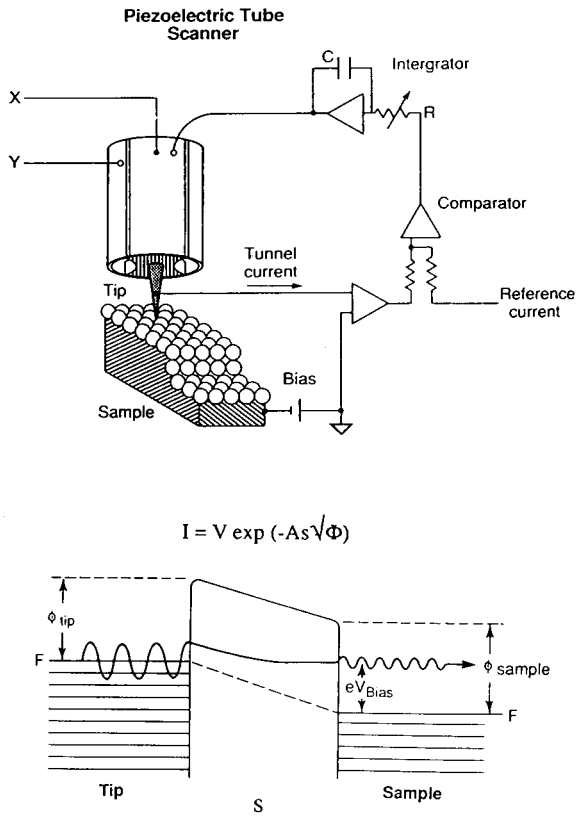

Fig. 6. Experimental principle of the scanning tunneling microscope (upper part). In the lower part the potential energy diagram is shown when a bias voltage is applied between tip and sample.

This picture is sufficient for a qualitative discussion of STM images, but its limitations are obvious. For a thorough theoretical discussion see, e.g., the review by Hansma and Tersoff [31] or Ogletree and Salmeron [32] and references therein. In reality, the tunneling current depends on the density of states in tip and sample and the gap distance, which is typically in the Å range. The density of states varies across the surface unit cell as well as the atomic height on different terraces seperated by steps. Thus, the interesting feature to observe is the variation of the tunneling current with the lateral position of the tip above the surface. The position of individual atoms (or rather their related electronic states) may be resolved in small area scans, and large area scans of the step structure of the sample can be imaged as a result of the current change with the changing gap distance. Actually instead of monitoring the current change, the tip is often repositioned to maintain a constant current and the motion of the tip is monitored. This measurement mode is called constant current mode. It was used in the original design by Binnig et al. [16] and in most of the early experiments. Maintaining the z position of the tip and monitoring the current is called constant height mode, and is common nowadays for fast scanning on flat samples.

The reliable positioning and movement of the tip is realized with piezoelectrical ceramics. This can be done with three separate piezoelements for each dimension [16] or with a single tube scanner as in later designs [26,27,33,35]. A difficult problem is to move the tip over a large area on the sample that exceeds the range of a piezoelectric element (usually 1000–10000 Å), and to approach the tip to the sample from macroscopic

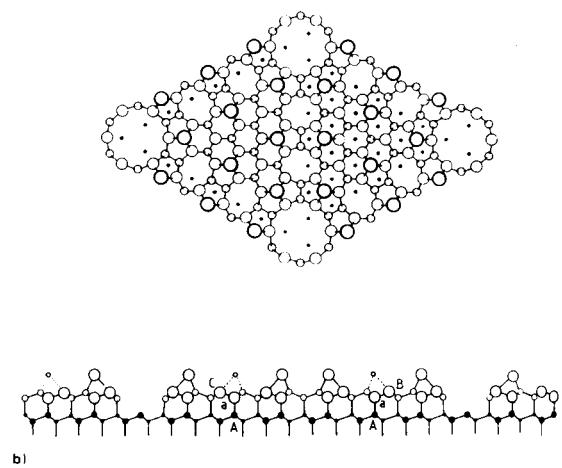

Fig. 7. Atomic structural model, DAS model, of the Si(111)-(7 ×7) structure. (a) Top view. Atoms located nearer to the surface are illustrated with the larger circles. Open circles represent atoms in the reconstructed layer and solid circles, in the bulk lattice. The model contains (1) dimers (small open circles along the sides of triangular subunits of the 7×7 unit cell), (2) a stacking fault layer (medium open circles) in the left triangular subunit, and (3) adatoms (large open circles) on the top layer. (b) Side view. Atoms on the (10-1) lattice plane along the long diagonal of the 7×7 unit cell are shown with the larger circles than those behind them.

distance into tunneling range. Several scanning designs have been tried [16,33–37] and many variations of STM have been introduced using motor drives or other mechanical approach devices, where the motion has to be transmitted into the vacuum [38].

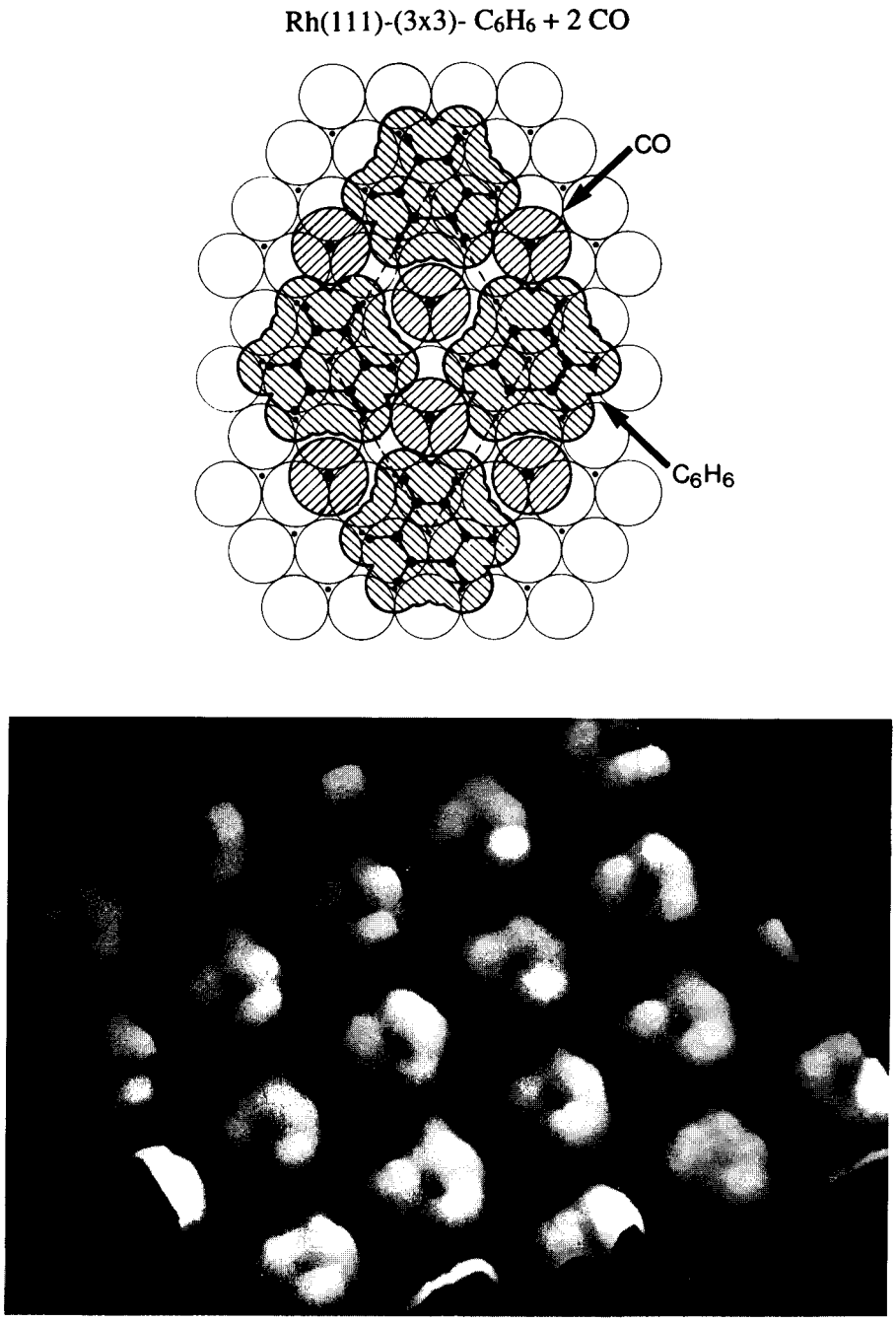

Fig. 8. STM image (lower part) and a schematic representation obtained from a LEED intensity analysis (upper part) of the structure formed by benzene and CO coadsorbed on Rh(111).

Examples of complex surface structure analysis by STM

Reconstructed Si(111)-(7 × 7) surface structure [39–44]. Only with the help of the scanning tunneling microscope has it become possible to solve the complex (7 × 7) reconstructed Si(111) surface structure that contains 49 atoms within its unit cell. STM images revealed 12 maxima per unit cell that were attributed to adatoms, which form an additional incomplete surface layer. The best model that fits the STM pictures is a dimer adatom stacking fault model. In this detailed model, the registry of half the adatoms is changed with respect to the deeper layers under the surface. The large minimum reflects a vacancy in the first regular surface layer. The electronic density of states around atoms with different stacking in relation to the bulk is different, and thus the maxima in the two halves have different intensities under certain bias conditions. In the model that is at present accepted for the (7 × 7) surface

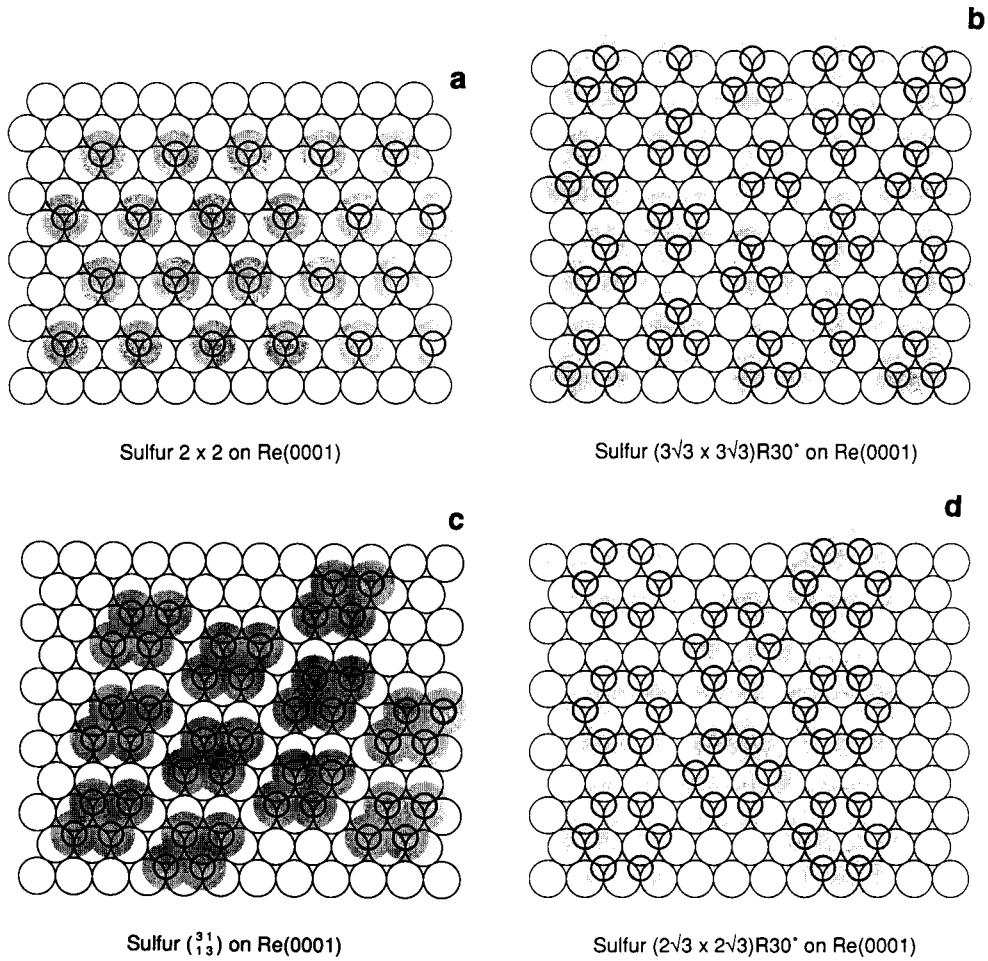

Fig. 9. Coverage dependent structures formed by sulfur adsorbed on Re(0001): (a) monomer (2 × 2) structure at 1/4 of a monolayer; (b) trimer $(3\sqrt{3} \times 3\sqrt{3})R30°$ structure at 1/3 of a monolayer; (c) tetramer structure with a periodicity indicated by the matrix notation at 1/2 of a monolayer; (d) hexamer $(2\sqrt{3} \times 2\sqrt{3})R30°$ structure at coverages above 1/2 of a monolayer.

structure, the number of dangling bonds per unit cell is reduced from 49 to 19. It is shown in Fig. 7 [40].

Structure of benzene on Rh(111) [45,46]. The center of the benzene molecule occupies a three-fold hollow site when adsorbed on the Rh(111) crystal face. When coadsorbed with CO, its π-ring is oriented parallel with the surface, and the C–C bonds are expanded with respect to the C–C bonds in the gas phase molecule. The ordered (3×3) surface structure could be imaged by the scanning tunneling microscope (Fig. 8). The STM picture indicates an ordered array of benzene molecules, confirming many of the findings of LEED surface crystallography. CO is not visible in the STM picture, and the reasons for its difficult detection is not clear at present. Nevertheless, this clearly demonstrates the possibility of imaging complex molecules with STM. It is hoped that by direct comparison with LEED crystallography data one can convert the qualitative information obtained from the STM pictures into quantitative data, that is, bond distances and bond angles. The theory of STM is under rapid development at present. It is hoped that theoretical analysis of data like this, in terms of structural parameters, will be possible in the near future.

Coverage dependent structures of sulfur monolayers on Re(0001) [47,48]. The structures formed by S on the Re(0001) surface as a function of coverage have been studied by STM. Up to a coverage of 1/4 of a monolayer the (2×2) structure shown in Fig. 9a is formed, which is due to S–S repulsive first neighbour interactions. As the coverage is increased to 1/3 of a monolayer, the sulfur atoms coalesce into trimers, forming a $(3\sqrt{3} \times 3\sqrt{3})R30°$ superlattice, first near domain boundaries and then at all regions. In these trimers each S atom sits in the same three-fold hollow site as in the low coverage monomer structures, as shown in Fig. 9b. When the coverage is increased ca. 1/2 monolayer, the trimers rearrange to form tetramers with a periodicity as indicated by the matrix notation in Fig. 9c. The highest coverage structure that was obtained upon further dosing with S shows the formation of sulfur hexamers, forming the $(2\sqrt{3} \times 2\sqrt{3})R30°$ periodicity shown in Fig. 9d. Heating this hexameric structure to higher temperatures removes some of the sulfur, and all the lower coverage structures (tetramers, trimers, monomers) can be regenerated. The clustering of S presumably is due to attractive interactions between S atoms at higher coverages. Only STM could image these most interesting structures formed by S on Re(0001) single crystal surfaces.

4. HREELS [49,50]

Experimental principles

In HREELS a monochromatized electron beam of 5–20 eV (ca. 10^{-19} J) energy strikes a solid surface. The back reflected electron's energies are measured with an energy resolution of ca. 5 meV, which is about an order of magnitude better than the energy resolution used in other electron spectroscopy techniques (this is the reason for the name, although photon spectroscopies have much higher energy resolutions). This highly

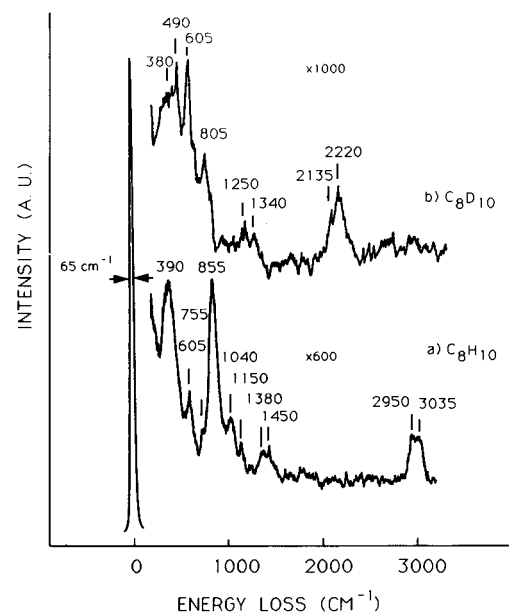

Fig. 10. HREELS spectra of the *ortho*-xylene molecules (a) C_8H_{10} and (b) C_8D_{10} adsorbed on Pt(111). Notice the differences in the spectra due to the different masses of H and D.

monochromatic beam upon incidence excites the various chemical bonds within the substrate lattice and the adsorbed molecules as well as bonds formed between substrate and adsorbate. The frequency modes of these chemical bonds are in the 500–2500 cm^{-1} range. A typical vibrational spectrum of the organic molecule *ortho*-xylene on the Pt(111) crystal face is shown in Fig. 10, where the electron energy loss is depicted on the x-axis. The electrons are back reflected from the surface with energies equal to $E_{reflected} = E_{incident} - E_{vibration}$ and they are detected by a suitable energy analyzer. Using HREELS, not only is H readily detectable at coverages much lower than a monolayer, but also isotope shifts due to different masses of H and D can be observed. Due to selection rules, adsorbed species with chemical bonds perpendicular to the surface are more readily detectable than adsorbed species with chemical bonds parallel to the surface. The sensitivity of this surface vibrational spectroscopy technique is so high (ca. 1% of a monolayer) that the structure of the molecules adsorbed at the different adsorption sites can be monitored as they fill up the various sites with increasing coverages. An HREELS spectrometer that is used most frequently by investigators is shown in Fig. 11.

Theory of HREELS

The physical origins of the intensities for the inelastic scattering processes that occur in HREELS include dipole scattering and impact scattering. Dipole scattering is similar in nature to the vibrational excitation mechanism in infrared (IR) vibrational spectroscopy. The long range Coulomb field of the incident electrons interacts with the dynamic dipole of vibrating substrate and adsorbate atoms, just as the electric field of the incident photons in IR spectroscopy interacts with the dynamic dipole of the molecule. This coupling enables the electrons to loose a quantum of energy by exciting higher vibrational modes of the substrate and adsorbate molecules. An important characteristic of dipole scattering arises from the physical nature of the Coulomb field of the incident electron at the metal surface. Electric fields can only have a component perpendicular to the metal surface, since parallel components are compensated by the image dipole in the metal. Therefore, only the component of the dynamic dipole moment perpendicular to the surface can couple with incoming electrons. This results in what is usually called the surface dipole selection rule, which states that only vibrations with dynamic dipole moments perpendicular to the surface can scatter electrons via the dipole

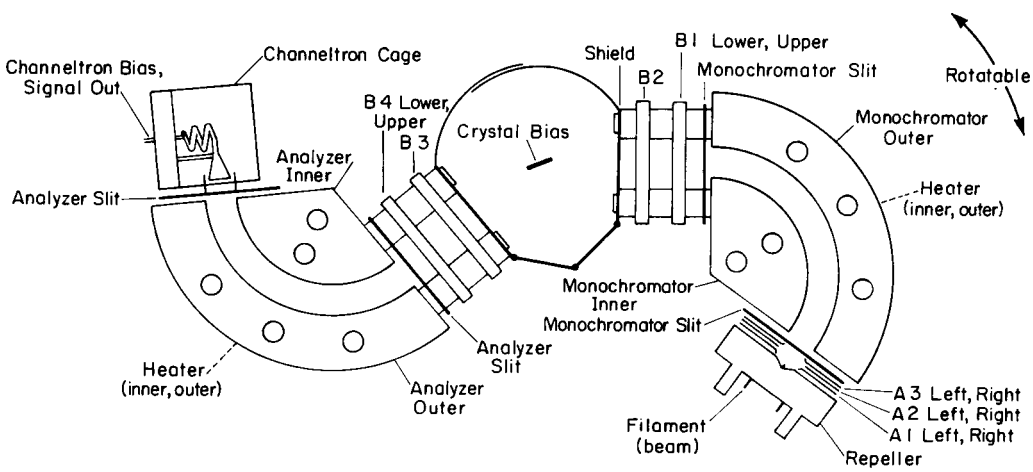

Fig. 11. Schematics of a HREELS spectrometer with a single-pass electron monochromator and a single-pass electron analyzer.

scattering process. Another characteristic of dipole scattering, which enables the discrimination between dipole and impact scattering processes, is the angular dependence of the scattering intensity. The dipole scattering intensity falls off rapidly for scattering angles away from the specular direction. The angular half width of the dipole scattering cone is on the order of $(\hbar\omega_0/2E_i)$, where ω_0 is the vibration frequency and E_i is the incident electron energy. In typical HREELS experiments, the dipole scattered electrons are concentrated within a couple of degrees of the specular beam.

During the impact scattering process the incident electrons loose energy by interacting directly with the atomic potentials while the electrons are within a few Å of the surface. During this short range interaction, the electrons essentially become impacted in the surface atoms for a short period of time, allowing vibrational modes oriented both parallel and perpendicular to the surface to be excited by the electrons. The short range impact scattering mechanism is physically a more complicated process than the long range dipole scattering process. The impact scattered electrons have a broad angular distribution, unlike the narrow angular distribution of dipole or quadrupole scattered electrons. Quite large scattering cross-sections can be observed for impact scattering when the energy of the incident electron is in resonance with an unoccupied electron state localized near the surface. This resonant impact scattering is analogous to resonant electron scattering from gas phase atoms and molecules where the incident electron is temporarily captured to form a short-lived negative ion. For impact scattering, several selection rules have been derived:

(1) The inelastic scattering intensity vanishes for a vibration that is odd with respect to a mirror plane symmetry, if the trajectories of both the incident and scattered electrons lie within this symmetry plane.

(2) The inelastic scattering intensity vanishes in the specular direction for a vibration that is odd with respect to a mirror plane symmetry if the plane containing the trajectories of the incident and scattered electrons is perpendicular to the mirror plane and the surface.

(3) The inelastic scattering intensity vanishes in the specular direction for a vibration that is odd with respect to a two-fold rotation symmetry.

To fully exploit the selection rules for impact scattering one needs to rotate the sample in the azimuthal direction. While most of the dipole scattering appears near the specularly reflected electron beam, the intensities that appear at larger angles usually are used to study impact scattering from adsorbed molecules.

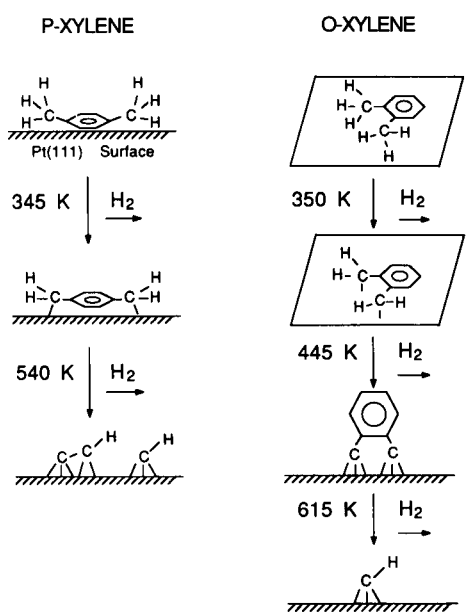

Fig. 12. Bonding, geometries and thermal decomposition pathways of *para*- and *ortho*-xylene adsorbed on Pt(111) at $T = 245$ K.

Examples of complex surface structures studied by high resolution electron energy loss spectroscopy

Structure and thermal decomposition of para- and ortho-xylene on Pt(111) [51]. HREELS combined with temperature programmed desorption (TPD) and LEED was used to investigate the low temperature adsorption structure and subsequent thermal decomposition fragments of *para*- and *ortho*-xylene on the Pt(111) crystal face. Both xylenes adsorb intact on Pt(111) at 245 K with the aromatic ring oriented parallel to the surface.

These structures are shown in Fig. 12. As derived from TPD and HREELS, both *para*- and *ortho*-xylene start to decompose thermally at 350 K by partial dehydrogenation of the methyl groups. Further decomposition pathways are markedly different for the two xylenes. For *para*-xylene, the remaining aliphatic and aromatic C–H bonds break at about 550 K leaving CH and C_2H species on the surface as shown in Fig. 12. By contrast, the aliphatic groups of *ortho*-xylene completely dehydrogenate at about 440 K, leaving a fragment with the aromatic ring oriented nearly perpendicular to the surface (Fig. 12).

Vibrational spectra and thermal decomposition of methylamine (CH_3NH_2) and ethylamine ($C_2H_5NH_2$) on the Ni(111) crystal face [52]. The bonding and geometry of methylamine (CH_3NH2) and ethylamine ($CH_3CH_2NH_2$) adsorbed on Ni(111) have been investigated by high resolution electron energy loss vibrational spectroscopy. Both amines adsorb molecularly at 150 K through

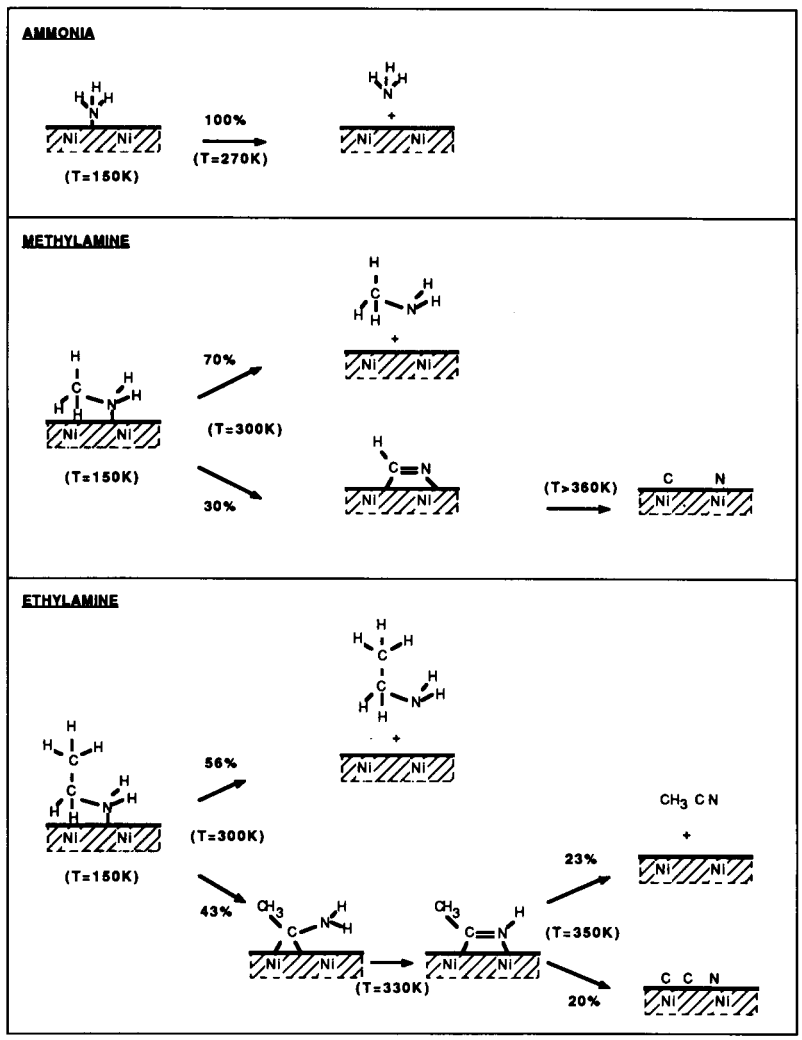

Fig. 13. Bonding, geometries and thermal decomposition pathways of ammonia, methylamine and ethylamine adsorbed on Ni(111) at $T = 150$ K.

the N lone pair. Significant metal–H interactions in the alkyl chain were indicated by softened C–H stretching modes with frequencies shifted from 2660 to 2680 cm^{-1}. TPD and HREELS were used to monitor their desorption and thermal decomposition on the Ni(111) surface. Both methylamine and ethylamine are dehydrogenated in the temperature range 300–400 K. Methylamine is dehydrogenated to HCN at ca. 330 K, which further decomposes above 300 K. Ethylamine is dehydrogenated to CH_3CN initially by αC–H bond scission, leading to desorption of that molecule at 350 K. Based on the vibrational spectra, a mechanism for the dehydrogenation process can be proposed. The sequential dehydrogenation of species that form with increasing temperature are shown in Fig. 13.

This work was supported by the Director, Office of Energy Research, Office of Basic Energy Science, Materials Science Division, of the US Department of Energy under contract No. DE-AC03-76SF00098. U. Starke and W. Weiss acknowledge support through a postdoctoral fellowship by the Deutsche Forschungsgemeinschaft (DFG).

References

[1] E. Lang, P. Heilmann, G. Hanke, K. Heinz and K. Mueller, Appl. Phys., 19 (1979) 287.
[2] L. de Bersuder, Rev. Sci. Instrum., 45 (1974) 1569.
[3] U. Starke, K. Heinz, N. Materer, A. Wander, M. Michl, R. Doell, M.A. Van Hove and G.A. Somorjai, J. Vac. Sci. Technol. A 10 (1992) 2521. D.F. Olgetree, G.S. Blackman, R.Q. Hwang, U. Starke, G.A. Somorjai and J.E. Katz, Rev. Sci. Instrum., 63 (1992) 104.
[4] U. Scheithauer, G. Meyer and M. Henzler, Surf. Sci., 178 (1986) 441.
[5] M.A. Van Hove, W.H. Weinberg and C.-M. Chang, in G. Ertl and R. Gomer (Eds.), Low Energy Electron Diffraction, Springer Verlag, Berlin, 1986.
[6] P.J. Rous and J.B. Pendry, Surf. Sci., 219 (1989) 355.
[7] U. Starke, N. Materer, A. Barbieri, R. Doell, M. Michl, K. Heinz, M.A. Van Hove and G.A. Somorjai, Surf. Sci., 287–288 (1993) 432.
[8] U. Starke, A. Barbieri, N. Materer, M.A. Van Hove and G.A. Somorjai, Surf. Sci., 286 (1993) 1.
[9] W. Weiss, A. Barbieri, M.A. Van Hove and G.A. Somorjai, Phys. Rev. Lett., 71 (1993) 1884.
[10] P. Fery, W. Moritz and D. Wolf, Phys. Rev. B, 38 (1988) 7275.
[11] E. Bauer and W. Telieps, Scanning Microsc. Suppl. 1 (1987) 99.
[12] E. Bauer and W. Telieps, Study of Surfaces and Interfaces by Electron Optical Techniques, Plenum, New York, 1988.
[13] E. Bauer, Electron Microscopy, Academic Press, New York, 1962.
[14] W. Telieps and E. Bauer, Ultramicroscopy, 17 (1985) 57.
[15] W. Telieps, Appl. Phys. A, 44 (1987) 55.
[16] G. Binnig, H. Rohrer, Ch. Gerber and E. Weibel, Phys. Rev. Lett., 49 (1982) 57.
[17] W. Telieps, M. Mundschau and E. Bauer, Optik, 77 (1987) 93.
[18] W. Telieps and E. Bauer, Surf. Sci. 162 (1985) 163.
[19] W. Telieps and E. Bauer, The Structure of Surfaces, Springer, Berlin, 1988 p. 53.
[20] E. Bauer, M. Mundschau, W. Swiech and W. Telieps, Vacuum, 41 (1990) 5.
[21] M. Mundschau, E. Bauer, W. Telieps and W. Swiech, Surf. Sci., 213 (1989) 381.
[22] M. Mundschau, E. Bauer and S. Swiech, J. Appl. Phys., 65 (1989) 581.
[23] M. Tikhov, M. Stolzenberg and E. Bauer, Phys. Rev. B, 36 (1987) 8719.
[24] M. Mundschau, E. Bauer, W. Telieps and W. Swiech, J. Appl. Phys., 65 (1989) 4747.
[25] M. Mundschau, E. Bauer and W. Swiech, Catal. Lett., 1 (1988) 405.
[26] K. Besocke, Surf. Sci., 181 (1987) 145.
[27] J. Frohn, J.F. Wolf, K. Besocke and M. Teske, Rev. Sci. Instrum., 60 (1989) 1200.
[28] S. Kleinkiek and K.H. Herrman, Rev. Sci. Instrum., (1993) in press.
[29] A. Messiah, in Quantum Mechanics, Wiley, New York, 1958.
[30] G. Binnig, H. Rohrer, Ch. Gerber and E. Weibel, Appl. Phys. Lett., 40 (1982) 178.
[31] P.K. Hansma and J. Tersoff, J. Appl. Phys., 61 (1987) R1.
[32] F. Ogletree and M. Salmeron, Progress in Solid State Chemistry, Pergamon Press, Oxford, 1991.
[33] G. Binnig and D.P.E. Smith, Rev. Sci. Instrum., 57 (1986) 1688.
[34] G.E. Poirier and J.M. White, Rev. Sci. Instrum., 60 (1989) 3113.
[35] D.M. Zeglinski, D.F. Ogletree, Jr., T.P. Beebe, R.Q. Hwang, G.A. Somorjai and M.B. Salmeron, Rev. Sci. Instrum., 61 (1990) 3769.
[36] G. Binnig and H. Rohrer, Rev. Mod. Phys., 59 (1987) 615.
[37] G. Binnig and H. Rohrer, Physica, 127B (1984) 37.
[38] S.-I. Park and C.F. Quate, Rev. Sci. Instrum., 58 (1987) 2011.
[39] G. Binnig, H. Rohrer, Ch. Gerber and E. Weibel, Phys. Rev. Lett., 50 (1983) 120.

[40] K. Takayanagi, Y. Tanishiro, M. Takahashi and S. Takahashi, J. Vac. Sci. Technol. A, 3 (1985) 1502.
[41] R.J. Hamers, R.M. Tromp and J.E. Demuth, Phys. Rev. Lett., 56 (1986) 1972.
[42] R.J. Hamers, R.M. Tromp and J.E. Demuth, Surf. Sci., 181 (1987) 346.
[43] R.S. Becker, J.A. Golovchenko, D.R. Hamann and B.S. Swartzentruber, Phys. Rev. Lett., 55 (1985) 2032.
[44] Ph. Avouris and R. Wolkow, Phys. Rev. B, 39 (1989) 5091.
[45] A. Wander, M.A. Van Hove and G.A. Somorjai, Phys. Rev. Lett., 67 (1991) 626.
[46] S. Chiang, R.J. Wilson, C.M. Mate and H. Ohtani, Vacuum, 41 (1990) 118.
[47] R.Q. Hwang, D.M. Zeglinski, A. Lopez Vazquez-de-Parga, C. Ocal, D.F. Ogletree, M.B. Salmeron and G.A. Somorjai, Phys. Rev. B, 44 (1991) 1914.
[48] M.B. Salmeron and G.A. Somorjai, in Y.W. Chung, A.M. Homola and G.B. Street (Eds.), Surface Science Investigations in Tribology, ACS Symposium Series 485, ACS, Washington, DC, 1992.
[49] B.E. Koel, J.E. Crowell and C.M. Mate, J. Phys. Chem., 88 (1984) 1988.
[50] H. Ibach and D.L. Mills, in Electron Energy Loss Spectroscopy and Surface Vibration, Academic Press, New York, 1982.
[51] D.E. Wilk, C.D. Stanners, Y.R. Shen and G.A. Somorjai, Surf. Sci., 280 (1993) 298.
[52] D.E. Gardin and G.A. Somorjai, J. Phys. Chem., 96 (1992) 9424.

ELSEVIER

Analytica Chimica Acta 297 (1994) 125–138

ANALYTICA CHIMICA ACTA

Recent advances in x-ray photoelectron microscopy

K. Holldack [1], M. Grunze

Angewandte Physikalische Chemie, Universität Heidelberg, Im Neuenheimer Feld 253, D-69120 Heidelberg (Germany)

Received 8th June 1993

Abstract

A short discussion is first presented of x-ray photoelectron microscopes operated with laboratory x-ray sources. With typical laboratory sources, the spectroscopic contrast in the images is based on differences in binding energy for the various chemical species, differential charging or photoelectron diffraction effects. Using synchrotron radiation, the initial and final states of the photoemission process can be defined and used to enhance chemical state information and contrast in laterally resolved images. Some recent examples from the authors group using synchrotron radiation in connection with a commercial x-ray photoelectron microscope (ESCASCOPE) to image lateral inhomogeneities in organic films and magnetic domains on magnetized substrates are discussed.

Keywords: Surface techniques; Electron spectroscopy for chemical analysis; x-ray photoelectron microscopy

The methods for laterally resolved chemical analysis of surfaces can be separated into scanning methods and imaging methods. In the former, a highly focused probe (electron beam, photon beam or ion beam) is scanned over the surface (or the surface is moved beneath the probe), in order to obtain a two-dimensional image of the chemical composition of the surface by energy-dispersive analysis of the secondary electrons or ions. This class of instruments includes the scanning ion microscope [1], scanning Auger microscope [2], small-spot electron spectrometry for chemical analysis (ESCA) systems [3] and the photon-induced scanning Auger microscope developed by Wuestenhagen et al. [4] utilizing synchrotron radiation. In addition, several groups are working on zone plates to focus synchrotron radiation to a beam of less than 1 μm in diameter in order to obtain laterally resolved images [5,6].

An alternative method to obtain lateral resolution in x-ray photoelectron spectroscopy (XPS) is to incorporate an aperture in the lens system of the analyser and to magnify the image [7]. This method was realised in imaging x-ray photoelectron spectrometers, where the probed area has a diameter of 100–150 μm and a lateral resolution of approximately 20 μm can be achieved. By lateral translation of the sample or by scanning the imaged area by means of electrostatic deflection plates in the analyser, these instruments produce a two-dimensional image of the elemental distribution on the surface. However, as the im-

Correspondence to: M. Grunze, Angewandte Physikalische Chemie, Universität Heidelberg, Im Neuenheimer Feld 253, D-69120 Heidelberg (Germany)

[1] Present address: BESSY GmbH, Lentzeallee 100, 1000 Berlin 33, Germany.

SSDI 0003-2670(93)E0521-8

age in any scanning method is created by a point-by-point analysis of the surface, data accumulation is time consuming, which can have detrimental effects if the samples are sensitive to radiation.

Incorporating a magnetic lens in the instrument enhances the collection efficiency and hence data accumulation, as has been shown by Drummond et al. [8]. Improvements are also achieved by a one-dimensional projection of the image through a narrow entrance slit on to a two-dimensional position-sensitive detector in the image plane of the analyser. A two-dimensional picture can be generated by sequential line scans [9].

A real photoelectron microscope, i.e. simultaneous position-sensitive detection of photoelectrons of a defined kinetic energy from a defined area from the surface, was realized by Beamson et al. [10], but only for low kinetic energies. The

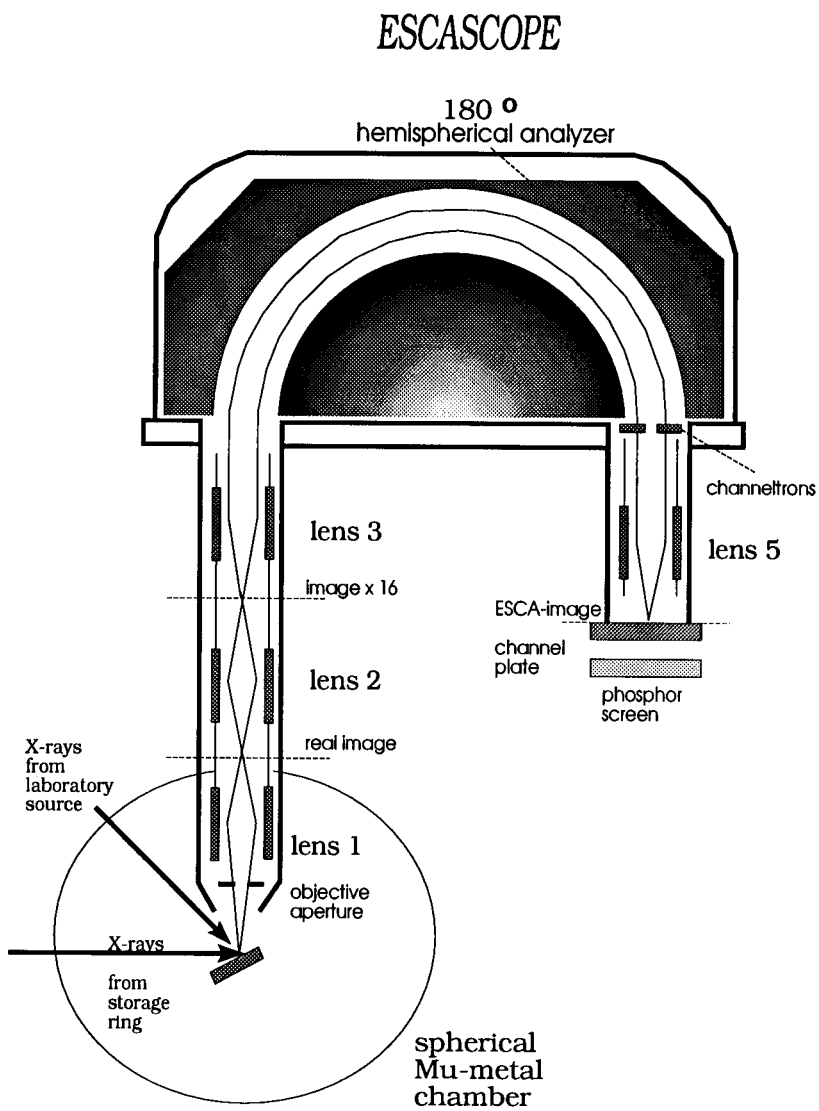

Fig. 1. Schematic diagram of the ESCASCOPE vacuum chamber and the analyser input and output lens system (see text).

principle is to localize the sample inside a strong magnetic field, such that the photoelectron trajectories are determined by the field gradient. As a consequence, photoelectrons emitted from the sample are confined to spiral orbits about the magnetic flux lines at the point of emission and travel along these lines to weaker field regions, where the divergent field projects the photoelectron distribution from the sample on to a detector plane. The area magnification is given by the ratio of the field strengths at the sample and the detector. This concept was further developed by Waddill et al. [11] in a photoelectron microscope utilizing a tunable synchrotron radiation photon source.

The only true imaging x-ray photoelectron microscope operated with a fixed-energy laboratory source is that developed and described by Coxon et al. [12]. This instrument (ESCASCOPE, Fisons Instruments) was used in the studies described here (see Fig. 1). It allows the identification of the distribution of elements on a sample surface with a lateral resolution of approximately 10 μm.

A schematic diagram of the ESCASCOPE analyser is shown in Fig. 1. A field aperture allows the selection of 50-, 150- and 880-μm diameter fields of view and the photoelectrons with a particular binding energy are detected in parallel on a channel plate detector. The parallel detection mode decreases the data collection time by several orders of magnitude compared with conventional small-spot ESCA where either the sample or the focused x-ray spot is translated to obtain a two-dimensional image. The image on the channel plate detector in the ESCASCOPE is obtained by a three-lens input objective with the third lens (lens 3) performing a Fourier transform of the surface image. Electrons leaving a particular point on the sample surface within a given range of angles pass into the analyser as an essentially parallel beam inclined at a particular angle to the plane, and those leaving at a different point on the surface will enter the analyzer with a different angle. The hemispherical analyser forms an image of this diffraction plane in its own image plane and acts as an energy filter. A further lens (lens 5) positioned at a distance from the exit plane of the analyser invert the transformation process and creates a real two-dimensional energy-filtered photoelectron image of the sample surface on the channel plate detector. For each element two images are acquired, one for the peak energy chosen and the other for the background recorded at a binding energy at least 10 eV lower than the peak so that a background-corrected image can be obtained. In the difference spectra intensity variations caused by surface roughness and topological features can be suppressed or even eliminated, when the asymmetry corrected image is displayed (see below).

The energy-filtered electron microscopic images of the sample surface can be generated with a lateral resolution of 10 μm for electron kinetic energies ranging from 30 to 3 keV. At lower kinetic energies the images are distorted by the astigmatism of the lenses. Also there are dichrotic image distortions due to stray magnetic fields. The resolution is limited by the astigmatic distortion of the lenses and the analyser. In addition, the image plane is bent such that the intensity decreases at the edge of the field of view by approximately 20% owing to sensitivity variations of the channel plate and the phosphorus screen.

However, these image distortions can be compensated for by a background subtraction procedure, which defines the asymmetry-corrected image I_{AS} of the measured photoelectron peak and the background:

$$I_{AS} = \frac{\alpha(x)\beta(x)(I_A - I_B)}{\alpha(x)\beta(x)(I_A + I_B)} \quad (1)$$

where I_A is the peak intensity, and I_B the background intensity. The chemical information is contained in $I_A - I_B$, but is still modulated by the system function (including lens aberrations) $\alpha(x)$ and a topography function $\beta(x)$. However, in the asymmetry function $\alpha(x)$ and $\beta(x)$ are eliminated, whereas they would still be contained in the simple difference image.

The field of view for imaging is identical with that in the spectroscopy mode, and similarly the energy resolution and the full widths at half maximum (FWHMs) of the peaks are the same. Hence, the imaging facility can be used to locate features of interest on the surface and the field apertures

in the electron input lens system can be used to isolate that feature for spectroscopic analysis. The sample surface can also be viewed by imaging elastically scattered electrons from a 500 eV flood gun and by an optical microscope [12,13]. Both the x-ray photoelectron images and the spectra are obtained with a conventional Mg Kα and Al Kα twin-anode x-ray source.

The ESCASCOPE used in the studies described below has additional facilities for cleaning the sample surfaces by ion bombardment and to compensate for charging effects in dielectric substrates with a flood gun. In addition, an optical microscope with a CCD camera having the same magnification as the electron energy analyser can be used to locate areas of interest on the sample. Sample holders can be heated to 600°C and cooled to liquid nitrogen temperatures. Sample transfer is achieved via a preparation chamber with an automated sample transfer mechanism. The system is pumped with an ion pump and has a base pressure of about 1×10^{-10} mbar. A detailed description of the ESCASCOPE is given elsewhere [12,13].

1. Contrast mechanisms in x-ray photoelectron microscopy using a laboratory x-ray source

In the following different mechanisms by which a contrast can be generated in an x-ray photoelectron image of a solid surface are discussed. First, the "normal" chemical contrast in imaging XPS is discussed, then contrasts due to different crystallographic orientations in polycrystalline samples, and finally contrast generated by differential charging of the sample surface. Several examples of the application of x-ray photoelectron microscopy utilizing a chemical contrast have been reported [12–15].

Chemical contrast

Here the capabilities of photoelectron microscopy as a tool in applied research are demonstrated and the results obtained from test structures prepared by a process called LIGA are discussed. Briefly, in the LIGA process a photosensitive polymer is coated on a substrate, exposed to white synchrotron light through a mask and subsequently developed [16]. By this process, structures with a very high aspect ratio can be prepared, which can subsequently be used as templates for micromechanical structures. In the particular experiment discussed here, a photosensitive polymer of thickness 100 μm was spin coated on to a metal oxide substrate surface. Subsequently, structures with different width and shape (e.g., columns) were fabricated. Some of the columns produced, however, delaminated easily from the substrate and the question arose of whether the failure was adhesive or cohesive. With an optical microscope, one cannot easily distinguish whether a polymer residue is left on the substrate (cohesive failure) or whether failure occurs at the metal oxide/polymer interphase.

These samples were transferred into the ESCASCOPE and studied with the laboratory source (Al Kα, 15 keV, 34 mA, incidence angle 45° with respect to the surface normal). Fig. 2a shows the C 1*s* image measured at $E_B = 284$ eV binding energy. The bright areas indicate a high carbon concentration, whereas the dark areas show a depletion of carbon. One can clearly see the columns evident from the circular dots along the diagonal in Fig. 2a. In addition, the columns cause an x-ray shadow seen as dark stripes which can be used to determine the actual height of the columns remaining on the surface, and hence to calculate where cohesive rupture in these columns occurred. Note that there are also white dots at the end of the shadows, which also correspond to failed columns, yet without any evidence of shadow formation. This indicates that these columns actually failed close to the polymer/metal oxide interphase. In Fig. 2b the image taken from the background at $E_B = 280$ eV is displayed. The bright areas are due to a high secondary electron background from the metal oxide substrate. (The picture obtained at the background energy of $E_B = 280$ eV is, in terms of its contrast, identical with that obtained directly on the substrate metal peaks). This image also contains the topographical contrast shown in Fig. 2a. Fig. 2c displays the difference between the peak and the background, where three different

grey scales can be distinguished, which can be identified as carboneous material from failed columns (bright spots), grey (metal background) and black (topographic contrast). The conclusion from this analysis was that a mixed mode of failure occurs in the columns, some delaminate close to the polymer substrate interface ("adhesive failure"), whereas some of the polymer structures actually break somewhere in the polymer ("cohesive failure").

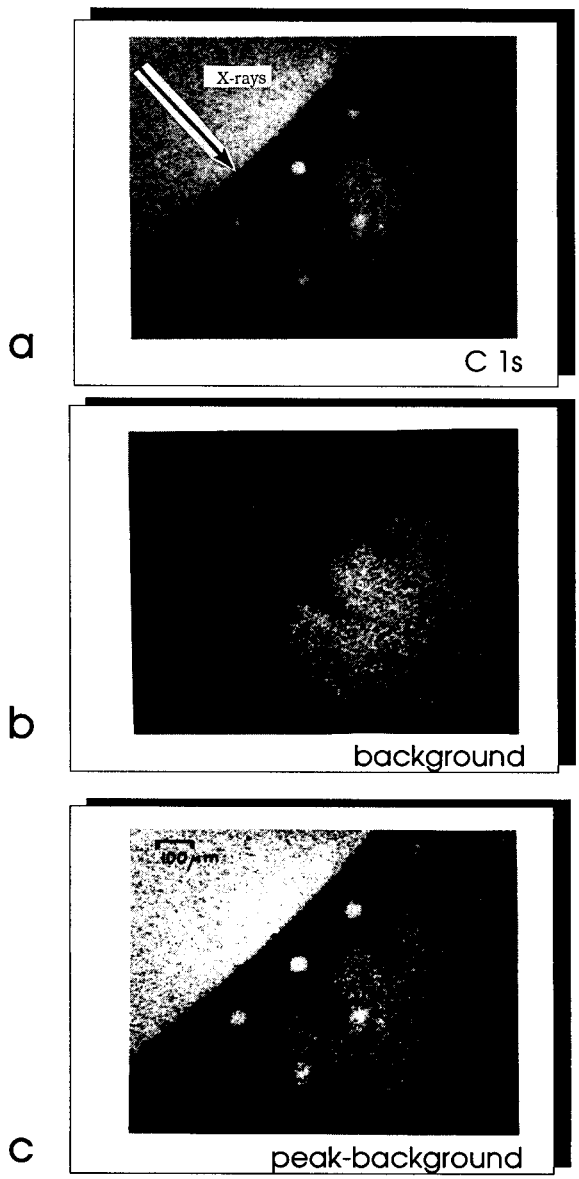

Fig. 2. ESCA images of failed polymer columns made by the LIGA technique. Two contrast mechanisms contribute to the images: (a) chemical contrast and (b) topographical contrast. (c) Difference image between (a) and (b).

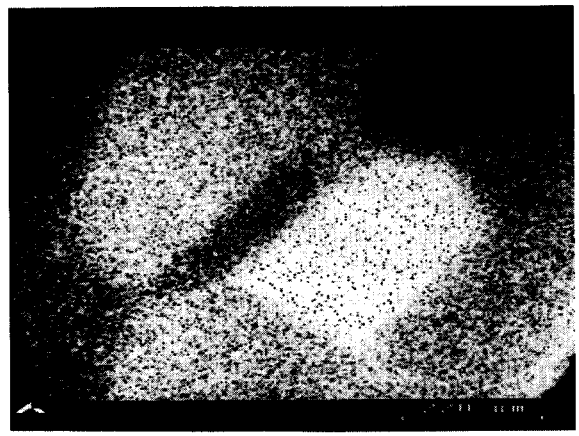

Fig. 3. ESCA image of a polycrystalline Ni foil measured on the Ni $2p_{3/2}$ photoemission peak excited with the Al source. The contrast between different crystallites arises from photoelectron diffraction (see text).

Crystallographic contrast

Fig. 3 shows the Ni $2p_{3/2}$ photoelectron image of a clean polycrystalline nickel foil, which was recrystallized in order to grow large crystallites [17] (the recrystallized films were prepared and provided to us by Dr. G. Hörz, Max-Planck-Institut für Metallforschung, Stuttgart, Germany). In the image a clear contrast due to photoelectron diffraction effects can be seen. It is well known that the wavefunctions of photoelectrons emitted from core levels of surface atoms interfere with the partial waves scattered from neighbouring atoms. This results in an angular distribution of emitted photoelectrons which can be interpreted at a surface hologram of the sample [18], reflecting the local crystal structure at the surface. The electron analyser having a fixed solid angle of 1×10^{-2} sr accepts only part of the angular pattern caused by the diffraction of photoelectrons. Changing the angle between the surface normal of the crystallites and the analyser results in an intensity variation. This intensity variation allows one to identify specific crystallites which appear as bright or dark regions in the

image as shown in Fig. 3. Hence the crystallographic contrast in the photoelectron images can be used to study the adsorption of gases on different crystallographic orientations of a specific material in one experiment [17].

Charging contrast

Differential charging on the surface will also lead to a contrast in the ESCA images provided that the differentially charged areas are sufficiently large to be lateral resolved and that the amount of charging is large enough to result in separated peaks in the spectrum. Charging contrast is demonstrated in Fig. 4. The spectra displayed in Fig. 4a show the C 1*s* signal of a nine-monolayer thick Langmuir–Blodgett film of cadmium arachidate deposited on an Si(100) surface. Subsequently, a copper mesh with a 100-μm mesh width was placed on top on the Langmuir–Blodgett multilayer and the sample was irradiated with 5 keV argon ions with a dose of 1×10^{16} cm^{-2}. The ion current was 1 μA and the time of bombardment was 20 s. The bombardment and unbombarded areas can be distinguished by optical inspection under a microscope for large ion doses. Subsequently, the C 1s signal was measured and it was observed that the irradiated area exhibited a C 1*s* peak at about 2.3 eV lower binding energy than the virgin film. In the lateral unresolved C 1*s* overview ESCA spectrum taken after removing the mesh, two clearly distinguishable bands are observed which, however, are not

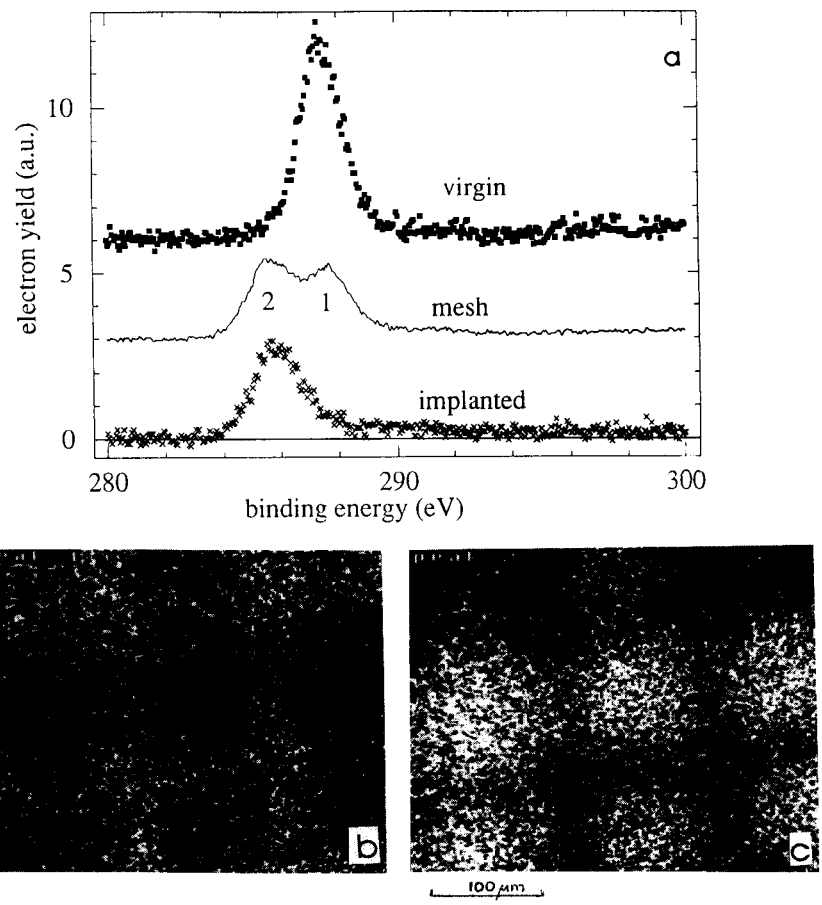

Fig. 4. (a) XP spectra excited with Al Kα radiation of the C 1*s* region from an Ar^+ implanted nine-layer Langmuir–Blodgett film of Cd arachidate, and the corresponding images taken at (b) 288.5 eV (peak 1) and (c) 285 eV (peak 2) after removal of the mesh.

due to different chemical species but primarily to different local charging. Fig. 4b displays the images taken on the peak numbered 1 at 288.5 eV for the non-irradiated areas, and in Fig. 4c the image taken at 284.5 eV for the argon ion-irradiated film. In the resulting image in Fig. 4b, the non-irradiated areas appear bright, whereas in Fig. 4c the irradiated areas give the higher signal. Both images were processed by subtracting the background at 280 eV binding energy.

The reason for associating the two peaks with differential charging rather than with a chemical modification of the cadmium arachidate multilayers is that the bombarded area shifts to lower binding energies compared with the non-bombarded film. As the virgin peak is due to aliphatic hydrocarbons in the long alkyl chains in cadmium arachidate, any chemical changes such as the formation of double bonds due to hydrogen abstraction should result in a binding energy shift to higher binding energies. Further, the shift in the peaks was observed to depend on the argon ion dose: at higher doses (5-min sputtering under same conditions) the C 1*s* peak in the implanted areas disappears completely. Using lower ion energies (500 eV), only a decrease in the intensity of the virgin peak, but no shift, was observed. Also, by adjusting the flood gun, peak 1 can be made to shift to lower binding energies and to overlap with peak 2.

Hence differential charging can be used to utilize contrasts in structurally modified polymer films. In the ESCA image, all information with respect to a changing chemical composition is hidden in the charging shift and is not detectable. This has to be considered when polymer films exposed to energetic radiation are analysed. The effect, however, can be used to study polymer films modified by lithographic techniques.

2. X-ray photoelectron microscopy using synchrotron radiation

In Fig. 5 a schematic diagram of the photoemission processes that can be used to distinguish between different chemical species on a surface is presented. Core-level photoemission (1), photoemission from valence states (2) and Auger electron emission (3) are processes which are non-resonant and can be excited by a constant-energy laboratory source. The non-resonant processes can, of course, also be excited with synchrotron radiation, but would only provide an advantage over a laboratory source when used at energies not available with the latter or if a higher photon flux is available. The Auger processes labelled 4 and 5, i.e., spectator autoionization emission and participant autoionization emission, require a tunable excitation source, in this particular case synchrotron radiation. Core-level electrons are resonantly excited into empty valence states and relaxation of the atom occurs via an autoionization cascade where the intermittent population inversion can decay via different channels. The basic difference from the non-resonant Auger process is that the excited electron remains in the potential of the excited atom and the emission process leads only to a singly charged final state, in contrast to the doubly charged final state in the non-resonant Auger process. One of the main

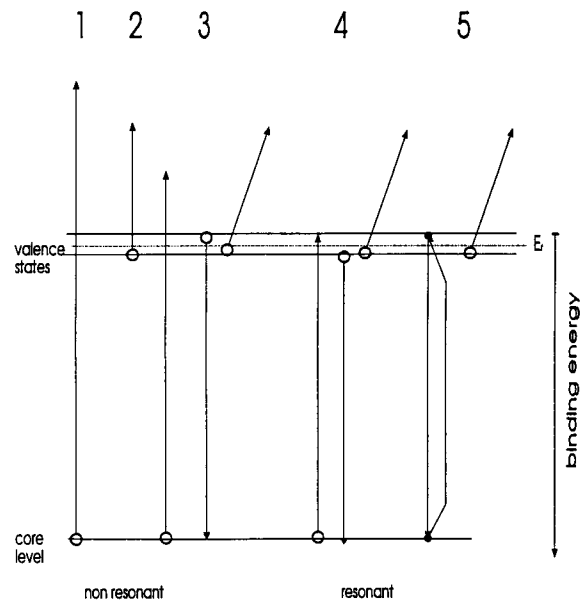

Fig. 5. Electron emission mechanisms that can be used to generate an image contrast in x-ray photoelectron microscopy. 1 = Core-level photoemission; 2 = photoemission from valence states; 3 = Auger emission; 4 = spectator autoionization emission; 5 = participant autoionization emission.

decay channels is spectator emission where, in analogy to Auger emission, the primary excited electron does not participate in the decay of the excited atom. In contrast, in the participant emission process the excited electron itself decays to the core level and an Auger electron is emitted from a valence state [19,20].

In the following it will be demonstrated that with resonant photoemission a much higher contrast in x-ray photoelectron microscopy is obtained compared with non-resonant processes. First, results obtained on a nine-monolayer Langmuir–Blodgett film of cadmium arachidate on Si(100), which in this case was bombarded with protons (300 keV kinetic energy and a dose of 10^{12}–10^{16} cm^{-2}) through a mesh in analogy to the argon ion implantation experiments described in the previous section are discussed. In the ESCA measurements using Al Kα radiation, only a single C 1s peak was observed before and after proton implantation. Hence there is no chemical contrast in the XPS data which could be used to image the lateral inhomogeneous structure caused by proton bombardment. However, in the near-edge absorption fine structure (NEXAFS) spectrum [21] displayed in Fig. 6a a drastic change in the spectrum is observed before and after implantation. This spectrum was obtained with p-polarized light at a incidence angle of 45° with respect to the surface normal. The CH resonance at 289 eV, which dominates the spectrum of the virgin Langmuir–Blodgett multilayer, is drastically reduced and a new resonance at 286 eV appears after proton implantation. This pre-edge resonance can be identified to arise from C–C double bonds (π^* resonance). Saturation of this new peak is obtained after a dose of 10^{16} H^+ cm^{-2} as shown in Fig. 6a. The NEXAFS data were obtained by measuring the 260-eV kinetic energy carbon Auger yield as a function of incident photon energy. Note that NEXAFS spectra are insensitive to charging effects.

Obviously, in contrast to the XPS data where both the aliphatic carbon and alkyl carbon have very similar binding energies and hence cannot be distinguished in the XPS spectrum, NEXAFS provides a high contrast for lateral imaging of the bombarded and non-bombarded areas of the

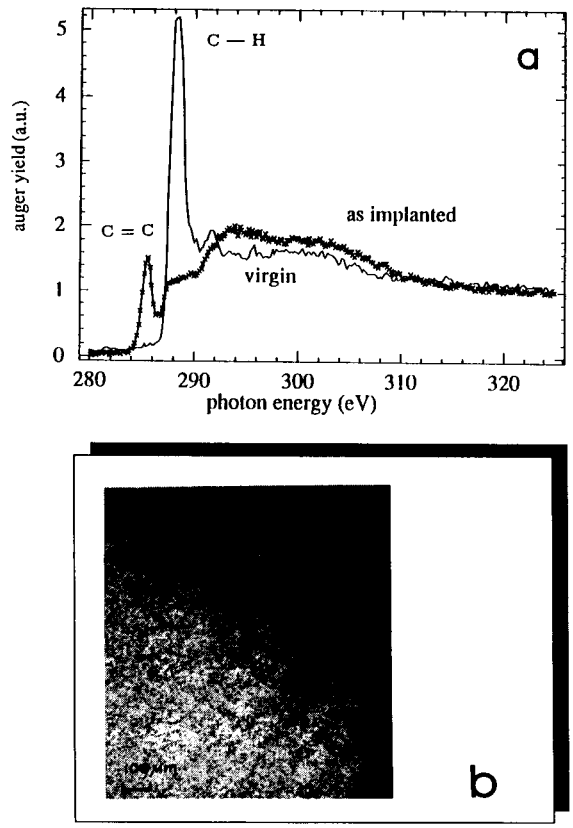

Fig. 6. (a) NEXAFS spectra taken in Auger yield mode (260 eV kinetic energy, C–KLL–Auger) for a 300-keV proton-bombarded Langmuir–Blodgett film of nine monolayers of Cd arachidate and (b) the image of the mesh structure detected on the C=C π^* resonance at 286 eV photon energy.

sample. In order to obtain an image of the surface (Fig. 6b), the monochromator was tuned to the maximum of the π^* resonance and images were accumulated over 60 min. The implanted areas appear bright. The contrast in the image is limited by the photon flux from the monochromator (the SX 700-III monochromator [22] used in these experiments has a low flux in this energy range) and by the lateral resolution, which was set to 20 μm to achieve a higher count rate. If the monochromator is tuned to the CH σ^* resonance at 286 eV of the non-implanted areas, the contrast in the images is weaker because the signal-to-background ratio is less favourable than in the case of the π^* resonance.

Protons with an energy of 300 keV have a

penetration depth in silicon of approximately 2 μm. The energy deposited in nuclear elastic recoils is concentrated in the substrate, whereas the inelastic electronic losses deposit energy also in the Langmuir–Blodgett film covering the silicon surface [23]. The observation that the irradiated areas contain C–C double bonds reveals that some of the hydrogen is dissociated from the alkyl chains and intra- or intermolecular double bonds are formed. The almost complete disappearance of the CH resonance is attributed partly to fragmentation of the alkyl chains, but also to the creation of a large number of *gauche* defects which will decrease the intensity of the CH resonance [21,24].

The utilization of NEXAFS on the carbon K edge to obtain laterally resolved images in polymer blends and in DNA was reported by Ade et al. [25]. In their work, the scanning transmission x-ray microscope at the National Synchrotron Light Source in Brookhaven was used to record spectra and lateral images with a resolution of 55 nm by measuring the transmitted x-rays as a function of incident photon energy.

The final example is intended to show that the photoelectron microscope offers unique possibili-

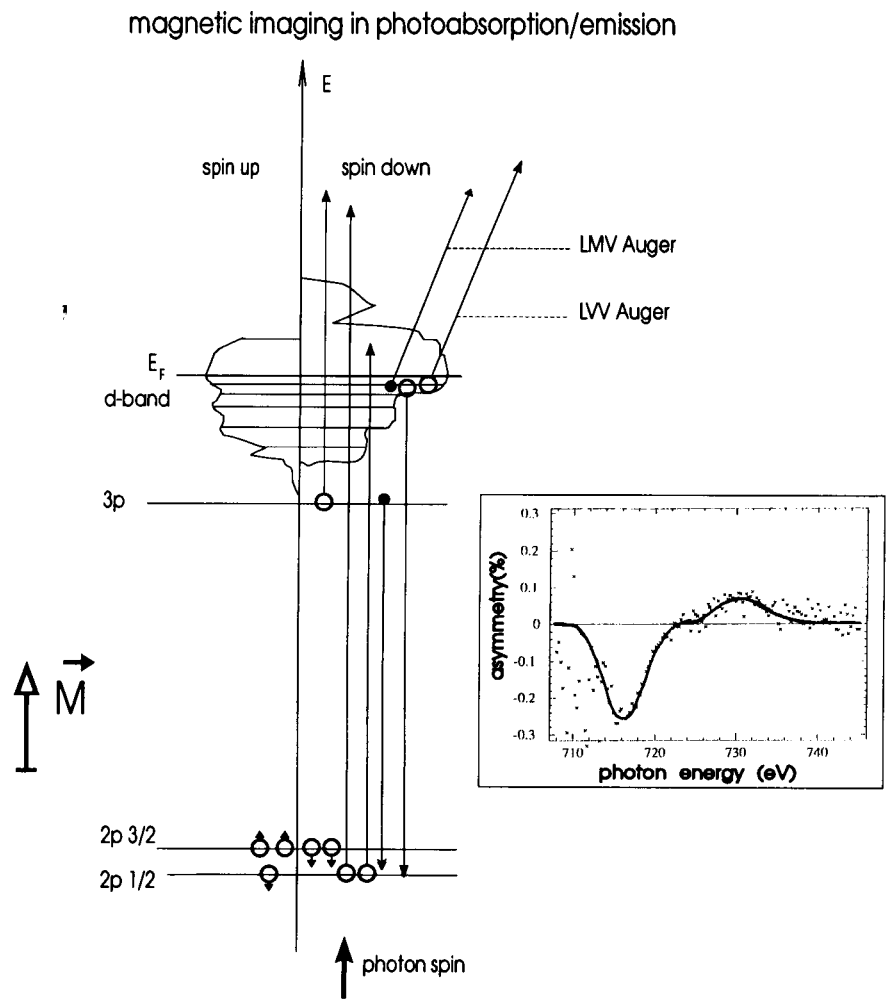

Fig. 7. Principle of magnetic imaging in photoabsorption and photoemission using circular polarized light. The inset shows the magnetic asymmetry measured in Auger yield mode (LVV) on the L-resonance lines of Fe.

ties in combination with circular polarized synchrotron radiation at the SX 700-III monochromator at BESSY and allows the imaging of magnetic domains or magnetized materials [26]. The effect used for imaging is the same as observed by Schütz et al. [27] in x-ray absorption, i.e., magnetic x-ray circular dichroism (MCXD). The basic process is shown in Fig. 7. In an external magnetic field (M) or in magnetized areas of the surface the valence states of the surface atoms are polarized, such that the density of states above the Fermi level is different for the two electron spins. The asymmetry in the *d*-states essentially acts as an internal spin detector in the atom, because excite core electrons with different spin can only populate final states, if the angular momentum of the photon (determined by the helicity of the circular polarized light), the spin of the core-level electron and the total angular momentum in the final state conserve the total angular momentum of the system. Because the density of empty states for spin-up and spin-down electrons is different, the excitation cross-section for a resonant excitation depends on the helicity of the incident radiation. In first approximation, the change in helicity and the change in magnetiza-

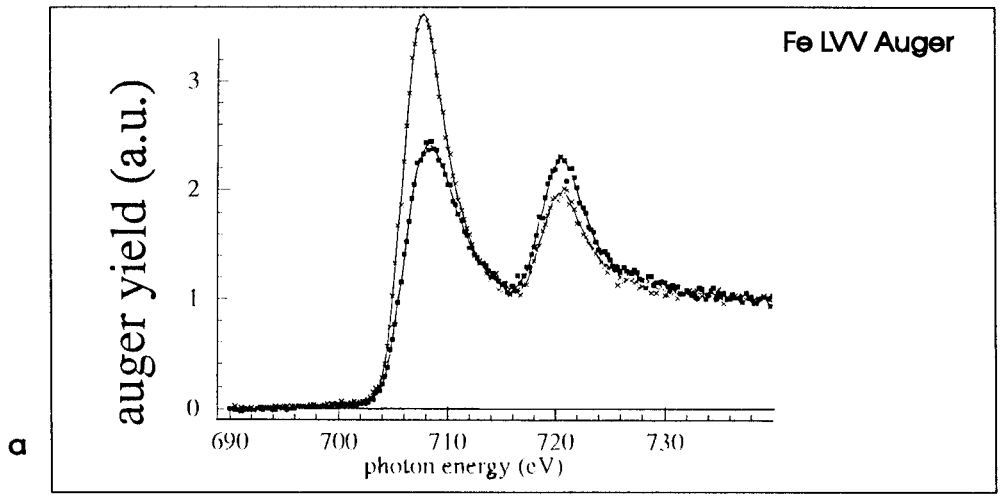

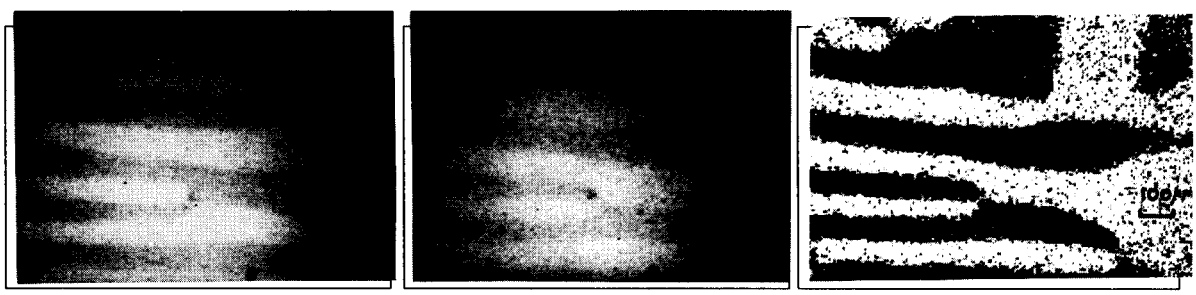

Fig. 8. (a) NEXAFS spectra in Auger yield mode (Fe LVV, 703 eV) from different magnetic domains on Fe (100). × = Magnetization parallel to the photon spin; ■ = magnetization antiparallel to the photon spin. The measurements were taken with right circular polarized light with 70% polarization. (b) Domain structure imaged with 708-eV photon energy and (c) domains imaged with 720-eV photon energy. (d) Asymmetry from images (b) and (c) according to Eq. 1.

tion are equivalent, since the cross-section for resonant excitation of these p–d resonances is proportional to the final state density.

Stöhr et al. [28] imaged magnetic domains by using the low-binding-energy secondary electrons as a detector for the absorption cross-section. The elemental resolution is achieved by resonant excitation of the L-edge of the element of interest. The disadvantage of this technique is, however, that it is practically a total yield method, in which secondary electrons created by inelastic collisions of the primary photoelectrons are also detected. This results in an unfavourable signal-to-background ratio.

If not the secondary electrons but the Auger electrons of the respective species of interest (Fe, Co, etc.) are detected, a second element specificity is added to the technique [29]. The mechanism, which allows one to discriminate magnetic domains by Auger electron detection, is, in a first approximation, the same as with total yield MCXD. The magnetic asymmetry is contained in the excitation and is revealed by the emitted Auger electron, because the emission cross-section for Auger electrons is proportional to the x-ray absorption cross-section. Hence an equivalent signal is obtained by detecting x-ray fluorescence. As will be shown below, by resonant excitation and Auger detection a signal-to-background ratio for imaging magnetic domains of 100 : 1 can be achieved. Magnetic multi-component systems can also be analysed, because the photoelectrons of magnetic elements show a circular dichroism effect by themselves, which, however, cannot be separated from a secondary electron signal. Further, it is possible to obtain a

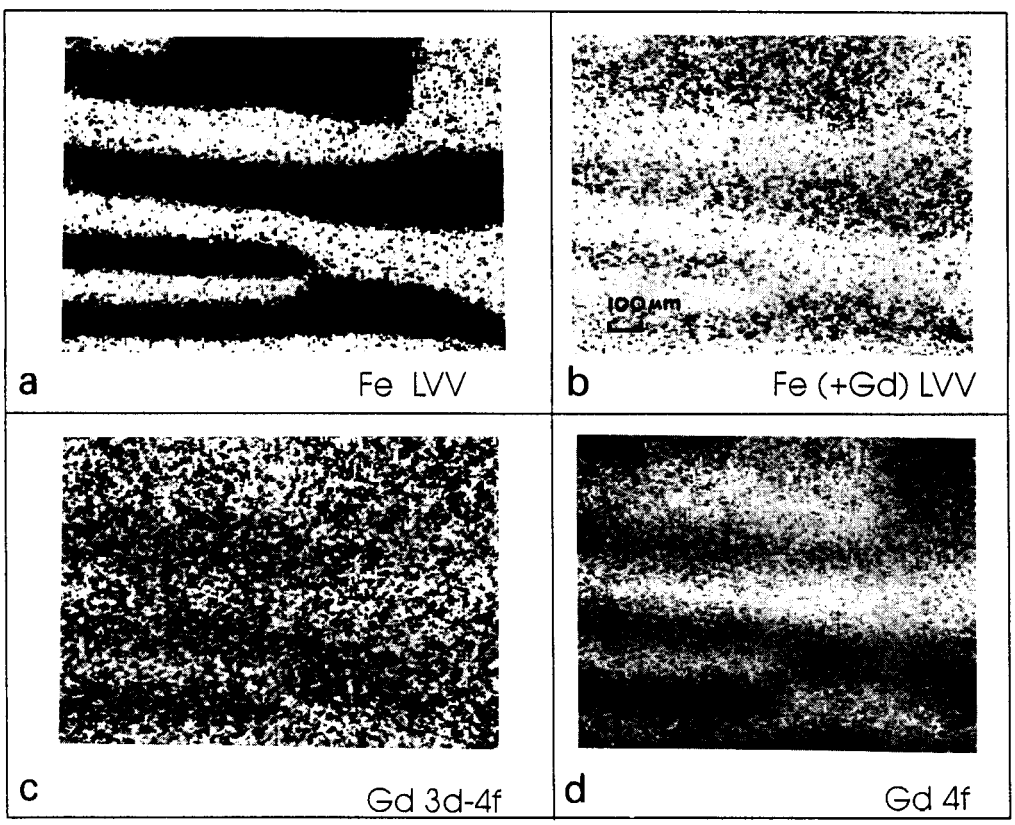

Fig. 9. Antiferromagnetic coupling of a Gd monolayer to magnetic domains on an Fe (100) crystal. (a) Pure Fe domains; (b) Fe domains observed through the magnetic cap layer of Gd; (c) Gd domains in photoabsorption; (d) Gd domains in $4f$ photoemission.

depth resolution by detection of Auger electrons created by inelastic losses, i.e., it is possible to image through magnetic layers.

With the imaging photoelectron microscope (ESCASCOPE) it was possible for the first time to image magnetic domains in the Auger yield mode and in direct photoemission [29]. The maximum magnetic asymmetry on the Auger LVV transition (inset in Fig. 7) is 30%. In a first approximation, all Auger transitions of the LMM triplet of the transition elements show the same asymmetry, i.e., the magnetic sensitivity is given by the excitation asymmetry rather than by the spin effects in the Auger emission process itself.

Fig. 8 shows the magnetic domains on an Fe(100) frame crystal. The crystal was sputtered for 5 min with 5-keV argon ions with the surface clean as checked by XPS. Subsequently, the crystal was magnetized which should, in principle, result in a homogeneous magnetization over the whole crystal. Owing to dislocations, however, different magnetic domains can be detected on the edge of the crystal. The magnetic crystallographic domains were imaged via the LVV Auger transition at 703 eV kinetic energy. In Fig. 8a the spectrum for the LVV Auger transitions obtained by scanning the photon energy through the $2p_{3/2}$, $2p_{1/2}$ resonances is displayed and shows the spectral contrast due to the different magnetization. The spectra were taken in the small-spot mode on differently magnetized large domains. The whole field of view was imaged (Fig. 8b) by setting the photon energy to the $2p_{3/2}$ resonance at 708 eV. The light was 70% σ^- polarized and already after a 3-min acquisition the domain structure can be clearly recognized. Areas where the magnetic moment is parallel to the photon spin appear bright, whereas areas where the magnetisation is antiparallel to the photon spin appear dark. Fig. 8c was taken on the $2p_{1/2}$ resonance at 720 eV. An image with a smaller but inserted contrast as compared to Fig. 8b is obtained (as expected from the NEXAFS spectrum in Fig. 8a). As in both peaks complementary information on the direction of the magnetization is obtained, the asymmetry-corrected image (Eq. 1) eliminates the topographical contrast and the distortions in the detector. The resulting image, obtained with the asymmetry function, is displayed in Fig. 8d. Note that the images were recorded in only 15 min at a pass energy of 176 eV.

Fig. 9 shows an experiment where one monolayer of gadolinium was evaporated on to the magnetic domains shown in Fig. 8. The magnetic domains on the clean Fe(100) crystal are represented in Fig 9a. Subsequently, a monolayer of Gd was deposited. The thickness of the layer was determined using the intensity of the Gd $4f$ photoemission peak excited with 70-eV photon energy. The XP spectrum after deposition shows the spectral features of Gd and the attenuated Fe signals.

The same procedure as used before on the Fe Auger electrons was applied to image the Fe domains through the Gd cap layer. The result is shown in Fig. 9b. One can easily recognize the domain structure, which is noisier because of the inelastic scattering of the Fe LVV Auger electrons in the Gd layer. In order to image the magnetic domains in Gd, we used an analogous spectral detection process as for Fe. Because the photon energy range as determined by the monochromator is limited to 2 keV, the Gd $2p$ levels are not accessible. However, the $3d$ resonances of Gd at 1189 ($3d_{3/2}$) and 1221 ($3d_{1/2}$) eV, respectively, can be used to image the magnetic domains in photoabsorption because these levels have the same spin polarization as the L3 and L2 resonances of Fe, except that the spin–orbit splitting is 32 eV for Gd compared with 12 eV for Fe. The Auger yield image in Fig. 9c was measured on the MNN Auger transitions of Gd at 879 eV kinetic energy. As described above, the images taken at 1197 and 1227 eV were used to obtain the asymmetry image according to Eq. (1). The image in Fig. 9c is noisy because the intensity from the Gd monolayer is smaller than that from the iron bulk material and the primary flux from the monochromator is reduced by a factor of 3 at this energy. Further, the magnetic asymmetry on the Gd $3d$ levels is only 6%. However, one can recognize that the domain structure is inverted compared with the Fe domains (Fig. 9a and b). Using magnetic circular dichroism in photoemission on the Gd $4f$ resonance [30], the count rate

can be enhanced (see Fig. 9d) and the antiferromagnetic coupling of Gd to the Fe domains underneath becomes evident. Here, the Gd $4f$ electrons were excited with 152 eV and the images were taken at 140.5 and 142 eV electron energy. The asymmetry image in Fig. 9d was obtained according to Eqn. 1. Multi-layer systems of different magnetic components were investigated with respect to their magnetism in a layer by layer fashion as described by Schneider et al. [26] using resonant Auger detection and by secondary electron detection as described by Stöhr et al. [28].

3. Discussion

X-ray photoelectron imaging in combination with synchrotron radiation can give new information about structural and chemical changes at surfaces that is more detailed than is possible with laboratory sources. However, the integral photon flux from an SX 700 monochromator (1×10^{10} photons s^{-1} at 100 mA ring current) is not higher than for a standard laboratory source. Especially at the carbon K-edge, where most of the monochromators show an absorption dip, the count rate prohibits the application of the method to monolayer adsorbate systems. The main advantage of excitation with monochromatic synchrotron radiation is the possibility of continuous variation of the photon energy which opens up access to the whole field of resonant effects. Hence also the increasing emission cross-section due to resonant excitation can be used to overcome the flux problems (see Fig. 9d taken at the giant $4f$ resonance of Gd at 152 eV).

Using elliptical polarized light, the photon spin can give access to magnetic information. The Auger yield technique developed with the present instrument allows the investigation of micromagnetism in composite or multi-layer systems, respectively.

4. Outlook

With the restrictions mentioned above, other contrast mechanisms can also be utilized such as circular dichroism effects in chiral molecules (CDAD [31]) or orientation domains in polymers on surfaces [23]. These effects provide image contrasts due to domains which distinguish themselves from each other only by their symmetry. The flux problems are expected to be overcome in the future at a wiggler/undulator beam line providing elliptically polarized light in combination with a wide energy-range monochromator.

We are indebted to Dr. H. Kerkow of Humboldt University for performing the proton implantation on the Langmuir–Blodgett films. We acknowledge and appreciate the cooperation with C.M. Schneider, K. Meinel, J. Kirschner (Halle), M. Kinzler, A. Weichert, M. Hofmann, A. Gölzhäuser, Ch. Wöll (Heidelberg), H.P. Oepen (Jülich), C.R. Brundle (IBM), T. Kachel, M. Willman and H. Petersen (BESSY). This work was supported by the Bundesminister für Forschung und Technologie through grant No. FKZ 055 VHFX1.

References

[1] P. Humphrey, J.C. Vikerman, A. Brown and N.M. Reed (Eds.), Secondary Ion Mass Spectrometry, Clarendon Press, Oxford, 1989, pp. 244–271.
[2] J.A. Venables, A.P. Janssen, C.J. Harland and B.A. Jouce, Philos. Mag., 34 (1976) 495.
[3] M.P. Seah and G.C. Smith, Surf. Interface Anal., 11 (1988) 69.
[4] V. Wuestenhagen, M. Schneider, J. Taborski, W. Weiss and E. Umbach, Vacuum, 41 (1990) 1577.
[5] F. Lodders, V. Persch, A. Goldmann, D. Rudolph and G. Schmahl, BESSY Annual Report, 1991, p. 486.
[6] H.W. Ade, J. Kirz, S.L. Hulbert, E. Johnsson, D. Anderson and D. Kern, Appl. Phys. Lett., 5 (1990) 1841.
[7] K. Yates and R.H. West, Surf. Interface Analysis, 5 (1983) 217.
[8] I.W. Drummond, F.J. Street, L.P. Odgen and D.J. Surman, Scanning, 13 (1991) 149.
[9] N. Gurker, M.F. Ebel and H. Ebel, Surf. Interface Analysis, 5 (1983) 13.
[10] G. Beamson, H.Q. Porter and D. Turner, Nature, 290 (1981) 556.
[11] G.D. Waddill, T. Komeda, P.J. Bennig and J.H. Weaver, J. Vac. Sci. Technol., A9 (1991) 1434.
[12] P. Coxon, J. Krizek, M. Humphersson and I.R.M. Wardell, J. Electron. Spectrosc. Rel. Phenom., 51/52 (1990) 263.

[13] E. Adem, R. Champaneria and P. Coxon, Vacuum, 41 (1990) 1695.
[14] M. Kinzler, M. Grunze, N. Blank, H. Schenkel and I. Scheffler, J. Vac. Sci. Technol., A10 (1992) 2691.
[15] M. Kinzler, M. Grunze, N. Blank, H. Schenkel and I. Scheffler, J. Adhes., (1993) in press.
[16] A. Heuberger, in Proceedings of SPIE Conference on Electron Beam, X-Ray and Ion Beam Technology: Submicrometer Lithographies VIII, San Jose, March 1989, p. 1089.
[17] A. Weichert, Diplomarbeit, Universität Heidelberg, Heidelberg, 1992.
[18] C.S. Fadley, in R. Bachrach (Ed.), Synchrotron Radiation Research: Advances in Surface and Interface Science, Pergamon, New York, 1992.
[19] W. Wurth, C. Schneider, R. Treichler, E. Umbach and D. Menzel, Phys. Rev. B, 35 (1987) 7741.
[20] T. Porwol, Phys. Scr., T41 (1992) 197.
[21] G. Hähner, M. Kinzler, Ch. Wöll, M. Grunze, M.K. Scheller and L.S. Cederbaum, Phys. Rev. Lett., 67 (1991) 851.
[22] M. Willmann, H. Petersen, F. Schäfers, M. Mast, B.R. Müller and W. Gudat, BESSY Annual Report, 1991, p. 466.
[23] Burenkov, et al., Range Tables of Ions in Matter, Energoatomizdet, Moscow, 1986.
[24] G. Hähner, Ch. Wöll, M. Buck and M. Grunze, Langmuir, 9 (1993) 1955.
[25] H. Ade, X. Zhang, C. Cameron, C. Castello, J. Kirz and S. Williams, Science, 258 (1992) 972.
[26] C.M. Schneider, K. Meinel, J. Kirschner, K. Holldack, M. Kinzler, M. Grunze, J. Appl. Phys., submitted for publication; BESSY Annual Report, 1992, p. 211.
[27] G. Schütz, et al., Phys. Rev. Lett., 58 (1987) 737.
[28] J. Stöhr, Y. Wu, M.G. Sarmant, B.D. Hermsmeier, G. Harp, S. Koranda, D. Dunham and B.P. Tonner, Science, 259 (1993) 658.
[29] C.M. Schneider, K. Meinel, J. Kirschner, H.P. Oepen and M. Grunze, in Proc. MRS Conf. 1993, in press.
[30] K. Starke, E. Navas, L. Baumgarten and G. Kaindl, Phys. Rev. Lett., submitted for publication; BESSY Annual Report, 1992, p. 360.
[31] J. Bansmann, Ch. Ostertag, G. Schönhense, F. Fegel, C. Westphal, M. Getzlaff, F. Schäfers and H. Petersen, Phys. Rev. B, 46 (1992) 13496.
[32] T. Kachel, W. Gudat, K. Holldack and M. Grunze, in preparation.

ELSEVIER

Analytica Chimica Acta 297 (1994) 139–152

ANALYTICA CHIMICA ACTA

Correlation of insulator properties with electron spectroscopic observations

C. Le Gressus

Centre d'Etudes de Bruyères-le-Chatel, B.P. 12, 91680 Bruyères-le-Chatel (France)

G. Blaise

Laboratoire de Physique des Solides, Bat. 510, Université Paris-Sud, 91405 Orsay (France)

Received 7th May 1993, revised manuscript received 10th August 1993

Abstract

Research of correlations between insulator macroscopic properties (electric strength, mechanical toughness, friction, radiation damage sensitivity, etc.) has shown that parameters related to polarization and energy dissipation processes are relevant for these properties. The investigation of the charging effect under an ionizing beam could be a way of characterizing polarization and relaxation processes leading to breakdown, fracture, etc. The physical basis which allows to understand the degree of insulator charging phenomena is reviewed. A universal concept of trapping as well as the nature of the energy which is stored in a charged dielectric are recalled. Basic principles of charging and detrapping were verified on well defined materials. It was observed that the relaxation of the mechanical energy consecutive to an abrupt variation of the polarization is a major cause of defect generation leading to failures. Results achieved by electron spectroscopy are reviewed. It is shown that there exist spectroscopic observations which can be related to parameters governing electric and mechanical strengths.

Keywords: Electron spectroscopy; Insulators

Insulators belong to a class of widespread materials: cables, capacitors, vacuum tubes, interruptors, adhesives, optical fibres, automotive industry, space, biomaterials, nuclear waste, etc. Technical problems dealing with insulators are related to electrical breakdown, mechanical fracture, loss of adhesion, etc. One of the most severe limiting factors in their application is the unpredictability of their response to a stress. Therefore insulators are characterized by a Weibull modulus indicating the probability of failure as a function of the applied stress. Much attention has been paid to the investigation of structure and chemical composition, and of their macroscopic electrical and mechanical properties but it is still difficult to link structure and properties. The unpredictability has been attributed to the presence of defects (point defects, dislocations, etc.) but there is no way to quantify the relative impor-

Correspondence to: C. Le Gressus, Centre d'Etudes de Bruyères-le-Chatel, B.P. 12, 91680 Bruyères-le-Chatel (France).

SSDI 0003-2670(93)E0481-L

tance of various defects on macroscopic properties.

An insulator subjected to a stress of whatever nature (electrical, mechanical, thermal, radiation) becomes polarized. The polarization can be the result of dipole orientations, of ion displacements, of electron motions and of charge trapping. Stress induced polarization is the essential phenomenon which governs the properties. This is why a correlation has been found between the relative permittivity ϵ_r and almost all properties: for example, the lower ϵ_r the higher the breakdown voltage, the higher the hardness, etc.

In the field of electrical engineering, mechanical engineering and tribology, charging has been recognized as being important to the response of the material against stress. Numerous techniques have been developed for space charge characterization (optical techniques, electrostatic techniques). However, results remain difficult to interpret because there is still a lack of understanding of charging–discharging phenomena and a lack of investigation of the charging effect on thermodynamical variables (free energy, entropy, etc.).

Electron spectroscopic methods [high resolution electron energy loss spectroscopy (HREELS), energy loss spectroscopy (ELS), secondary electron spectroscopy (SES), Auger electron spectroscopy (AES), electron spectroscopy for chemical analysis (ESCA)] applied to insulator characterization are hampered by charging effects and ionizing beam induced damage. Studies have been made how to neutralize or to compensate charging. However, no study was done to clarify the origin of the charging and to investigate what information could be extracted from it. It has been recently shown that the investigation of charging is an elegant way to characterize the reaction of an insulator subjected to a space charge stress field [1,2].

Because an analogy exists between electrical and mechanical properties and because both properties are related to the polarization [3], the characterization of charging appears as a way to clarify relationships between defects, polarization and any macroscopic property. However, the point which needs attention is the way how to introduce the notion of defects and of stress induced polarization in equations used to describe the crack or the breakdown propagations [4,5]. Basic problems to be solved are: what is a trap? What is the nature and the quantity of energy stored in a charged dielectric? How does the presence of traps modify the insulator free energy? What are energy relaxation processes? What technique is adapted to defect characterization?

This report will present (i) a review of polarization effects on insulator properties, (ii) a review of recent developments of the space charge physics which allows to understand relationships between polarization and macroscopic properties, and (iii) a review of electron spectroscopic observations related to dielectric polarization–relaxation processes and therefore to insulator properties.

1. Insulator properties related to defects and to stress induced polarization

The points of interest to deal with, regarding phenomena related to wear, adhesion, dielectric breakdown, etc., are the nature of surface and interface effects, the origin of exo-emission and the formation of the space charge under stress applications.

Surfaces and interfaces are zones where defects are concentrated, and also zones where failures are preferentially initiated.

Exo-emission appears during failures or even just when a stress is applied on dielectrics whatever its nature may be. Exo-emission is indicative of a dielectric relaxation process and a general interpretation of this emission has been proposed recently [6].

Triboelectrification or remanent electrification after poling (application of an electric field) are well known effects [7] and subject of an increasing number of studies.

Breakdown

For a long time the origin of electric breakdown has been considered to be different at the surface or in the bulk of insulators. Bulk breakdown has been described by the model derived

from Frölich's work in which electrons are accelerated in a high electric field, forming an electron cascade [8]. But a major contribution showing the physical limits of this model was obtained recently by electron spectroscopies [9,10]: electron scattering processes do not allow an electron to gain enough energy to ionize valence band levels in order to initiate a cascade process, unless the accelerating field exceeds several MV/cm which is far beyond the breakdown field in most practical situations.

Surface breakdown (flashover) has also been attributed to an electron cascade initiated at the insulator–metal–vacuum interface (triple point) and developing along the surface [11]. Arguments supporting the model are: (i) the correlation between the secondary electron yield δ and the breakdown voltage V_b: the higher δ the lower V_b, (ii) the existence of positive charges trapped at the surface after the breakdown propagation, and (iii) the actual importance of the triple point. Moreover we have to keep in mind that the breakdown voltage is a function of the insulator permittivity ϵ: the lower ϵ, the higher V_b.

The electron cascade model of surface breakdown is a matter of controversy. The purpose is not here to present arguments for and against but to emphasize that a recent simulation of the insulator secondary electron emission has shown [12] the role of defects and charging on the yield. Therefore it becomes obvious that secondary electron spectroscopy carries relevant information about insulator breakdown.

In fact, the two ionization cascade models have been less attractive since it has been recognized that aging and breakdown of insulators are both correlated with the formation of a space charge [13]. Since that time a very important effort has been conducted to develop space charge characterization techniques [7].

In the new approach of breakdown proposed recently [13], two waves are considered: an electromagnetic wave indicating that a trapped charge distribution is collapsing and then, some ns to ms later, a shock wave produced by the relaxation of the mechanical energy stored in the lattice left out of equilibrium after charge detrapping. These two waves are accompanied by various emissions: photons [3], electrons and ions. Ion emission by a polymer subjected to an electric field is a matter of increasing interest [14].

Friction and wear

The role of defects in the tribological behaviour of insulators has been demonstrated very recently [2]. Experiments have been achieved on a single alumina crystal in contact with another sapphire of same origin. It has been shown that friction generates defects which are not only concentrated in the friction area but are distributed over the whole sample. Because of the dielectric properties of materials in contact, the friction coefficient results from dipole movements and displacement of electric charges. The space charge formation is of course well observed when asymmetrical materials are in contact (mica and silica for example) and after contact sparks can be observed if the two materials are pulled.

Fracture mechanics

The analogy between mechanical and electrical properties of insulators is recognized since many years. For example, it was observed that Weibull's modulus is the same for mechanical and electrical strength failures. It has often been proposed to describe this analogy on the basis of the Griffith's criterion for crack growth, given by $G - W \geqslant 0$, where G is the energy release rate and W is the energy required for crack growth.

However, neither G nor W have been expressed in a dielectric polarized by a space charge. Very recent results [15] have shown that carrier trapping modifies the free energy of insulators and that detrapping may occur either via a reversible second order phase transition or via irreversible processes giving rise to breakdown with formation of cracks.

It has been shown that after polarization under an applied electric field the fracture toughness is decreased by about 50% [16]. Also, under an applied electric field cracks can be annealed or on the contrary can increase [17]. Crack annealing has been attributed to ion electromigration producing an activation of bondings at the surface of cracks. These results pose the problem

to investigate to what extent a space charge can change adsorption and segregation at surfaces, contributing therefore to modify thermodynamical equilibrium at the crack tip.

Because any catastrophic event such as breakdown, fracture and wear is related to energy dissipation and defect generation, an interesting question is to evaluate to what extent studies dealing with irradiation damage could help us to make progress in the understanding of electrical and mechanical insulator properties.

Irradiation effects

Investigation of defects produced by irradiation is of technological importance because ionizing irradiation modifies electric and mechanical strengths of insulators.

Two types of irradiation effects have been investigated in insulators: *formation of defects* and *electromigration*.

The formation of defects is usually attributed to stimulated desorption but we will see that there also exists another damage mechanism related to the dielectric relaxation process mentioned in the *Breakdown* section. The sensitivity of an insulator to beam damage could therefore be correlated with its dielectric properties.

Electromigration of alkali is a well known effect [18,19]. The diffusion occurs after an "incubation time" which is temperature dependent: the lower the temperature, the longer the incubation time. Probably this incubation time is connected to the internal electric field which is quickly attained under electron irradiation [12] and to the density of defects generated by incomming electrons. As it will be shown later, successive trapping–detrapping during irradiation is also a cause of sample heating. Moreover, considering that the sample enthalpy is modified by charge trapping, the alkali ion diffusion could be treated as a segregation effect in charged dielectrics.

Because practical difficulties are encountered when analyzing insulators with ionizing particles, various "tricks" for charge compensation–neutralization have been tried. Whereas it is now well accepted that there is no satisfactory neutralization technique which can be always successfully applied to any type of insulator, this way to approach the insulator characterization has hidden interesting physical aspects from which important applications may follow. The consequence is that the contribution of electron spectroscopic methods to the knowledge of dielectric properties is still low. Hopefully recent developments in space charge physics and improvements on space charge measurements can help further applications of these techniques to insulators.

2. Space charge physics

The space charge physics (SCP) is related to mechanisms of formation, migration and relaxation of charges. Main achievements of the SCP are: (i) to propose a universal description of the trapping site, (ii) to clarify the nature of the energy stored in a charged dielectric, and (iii) to link detrapping processes with the occurrence of breakdown.

Trapping site: polarizability defect

Blaise [20] has proposed an approach to charge trapping based on the concept of polaron used by Austin and Mott [21] to describe the conduction properties of insulators.

The consequence of the variation of the dielectric constant with distance from a mobile charge is the presence of a polarization charge. If the mobile charge is localized in an orbital of spherical symmetry, the field $E(r)$ at a distance r from the centre of the orbital has been calculated taking into account the polarization charge $Q_p(r)$ contained in a sphere of radius r. The potential energy between charge q and polarization charge contained within two spheres of radii a and b is:

$$W = \frac{q}{4\pi\epsilon_0}\int_a^b \frac{\mathrm{d}Q_p(r)}{r}$$

As a first approximation the polarization charge is supposed to be localized on a sphere of radius r_p so that:

$$\epsilon(r) = \epsilon(\infty) \quad r < r_p$$

$$\epsilon(r) = \epsilon(0) \quad r > r_p$$

$\epsilon(\infty)$ being the electronic dielectric constant and $\epsilon(0)$ the static constant.

Using this approximation W is given by:

$$W = -2\epsilon_0 E_R \left[\frac{1}{\epsilon(\infty)} - \frac{1}{\epsilon(0)}\right]\frac{a_0}{r_p} \quad (1)$$

where $E_r = 13.56$ eV is the Rydberg energy and a_0 the Bohr radius. As $\epsilon(\infty) < \epsilon(0)$ always applies, W is negative and a binding effect is expected from Eq. 1.

The quasi particle formed by the bound charge surrounded by the polarization charge is called a polaron. The distance r_p defines the radius of the polaron and $1/\epsilon_p = 1/\epsilon(\infty) - 1/\epsilon(0)$ characterizes the variation with distance of the dielectric response of the medium to the field of the charge.

In a medium of uniform polarizability the binding energy W is the same on all polaron sites and we can use the classical description of conduction proposed by Austin and Mott [21], where the charge carrying its polarization with it behaves like a heavy particle moving by the usual band mechanism at low temperature or by jumping at high temperature. Trapping takes place on specific polaron sites where the electronic dielectric constant $\epsilon(\infty)$ is lower than the surrounding medium [22]. Such sites are polarizability defects.

Trapping energy is expected to vary from a few hundredths to a few tenths of eV.

The concept of polarizability defects, responsible for charge trapping, is not in conflict with the well accepted idea that trapping is due to defects but it gives a clear insight into the nature of these defects that were not well understood.

Energy stored in a dielectric

The energy stored in a dielectric polarized by a static applied field comprises two terms.

(a) A *mechanical energy* which corresponds to ion and electron displacements under the influence of the applied field, that is to *the mechanical deformation of the structure* due to polarization.

(B) An *electromagnetic energy* which is the consequence of the dipoles formed by the displacement of charges.

Electromagnetic energy. The electromagnetic energy per unit volume stored in a medium of dielectric constant ϵ is given by:

$$w_{em} = 1/2\epsilon_0 E_a^2 - 1/2PE_a \quad (2)$$

where E_a is the applied field, and P the polarization.

Expression 2 is quite general [23]. The first term represents the electromagnetic energy due to the applied field in vacuum, the second term is associated with the polarization. The negative sign in the second term indicates that *the system (medium plus sources producing E_a) is more stable when it is polarized than when it is not*.

Mechanical energy. A dipole is formed by the action of the local field against internal forces. Under static conditions the mechanical potential energy, w_p, stored in the medium per unit volume is, assuming elastic forces:

$$w_p = 1/2PE_{loc} \quad (3)$$

E_{loc} being the local internal electric field.

Attention is drawn to the possible confusion between the term $1/2PE_a$ and $1/2PE_{loc}$ in Eqs. 2 and 3. In both cases the field to be considered is different.

Preliminary calculations indicate that the energy contained in Eq. 3 can largely exceed the 5 eV per trapped unit charge and therefore a non-negligible quantity of mechanical energy is stored around a charge.

It is well known that polymers subjected to an electric field recrystallize. A similar effect has been observed in ceramics [13]. This indicates a variation of the free energy of the material which is also of mechanical origin (atomic rearrangement). The variation of the free energy with polarization has only been calculated for ferroelectrics [24].

Detrapping and breakdown process

When charges are trapped in an insulator, they form a space charge whose equilibrium can be static or dynamic. It will be static if for example, the distribution is stable as function of time when the injection of charges is stopped. The equilibrium will be dynamic when, during injection, an

equal number of charges are trapped and detrapped per unit time; the detrapped charges being drawn away from the injection point. The parameters controlling the charge equilibrium are the temperature and the internal space charge field: charge spreading occurs when the temperature is raised and when the space charge field reaches a *critical* value which is a characteristic of the trap energy. When charges are detrapped they spread out into other surrounding traps. The distance over which a carrier drifts in the direction of the electric field before it disappears by trapping is the *schubweg* and the reciprocal schubweg is called *trapping rate*.

Many factors can upset the equilibrium of a space charge: a temperature increase, a small positive or negative increment of the external field, the distortion of the lattice produced by a mechanical strain and a phase transition.

In all these cases of perturbation of a space charge, the consequence of charge spreading is a lattice relaxation at the sites of detrapped charges, producing breakdown when a critical amount of energy density is released. The consequence is that the relaxation of the mechanical energy related to a charge trapping–detrapping process appears to be also an important cause of damage. This is a problem probably easy to clarify because the various damage processes have very different characteristic times.

In summary, parameters determining insulator macroscopic laws are listed in Table 1. The point of interest is now to discuss which of these parameters are accessible to electron spectroscopic methods.

Table 1
Parameters determining insulator macroscopic laws

Weibull modulus
Nature of defects
Electronic polarizability
Secondary electron yield
Trap energy distribution
Trap spatial distribution
Schubweg
Energy stored in a polarized sample
Dielectric relaxation time
Temperature increase related to trapping–detrapping process
Free energy variation as function of the polarization
Structural stability in the polarized state

3. Experimental verification of the space charge physics principles

When the first incoming electrons of high energy penetrate the insulator, they form first a negative space charge localized in depth. Then, a negative potential builds up, slowing down further incomming electrons and defocussing the beam. The consequence is that additional trapping of electrons occurs in less deep layers whereas positive charges appear at the surface layers, due to the secondary electron emission. As the secondary electron yield δ increases when the energy of primary electrons is decreasing, the amount of positive charges increases in proportion until δ becomes equal to unity. A double layer is formed with negative charges in depth and positive ones in outermost layers. The balance of the double layer results from a recombination process whose rate is depending on the value of the critical detrapping field.

To complete this brief description of the formation of a space charge we must mention that its equilibrium depends on the temperature and on the diffusion of ionized species. The double layer forms the origin of the stabilization of the surface potential. If the amount of positive charges is increased, the stabilization of the surface potential occurs at a lower value. This is what is obtained by using an additional ionizing beam produced by a flood gun operating at appropriate energy and grazing angle of incidence. In principle, it is possible to obtain a stabilized surface potential close to ground potential whatever the nature and the energy of the analyzing beam may be.

Assuming the sample and the electron microscope chamber form a plate capacitor as represented in Fig. 1, fields due to the double layer of thickness r and respective surface densities σ^+ and σ^-, are calculated.

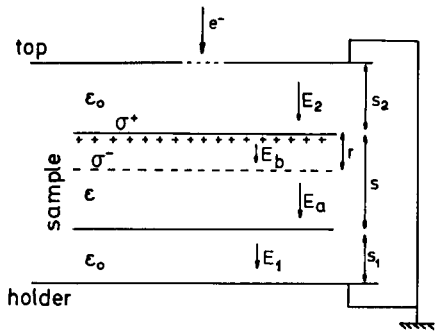

Fig. 1. Arrangement of a charged dielectric, gaps and electrodes in a scanning electron microscope: s, s_1, s_2 are the thicknesses, r the thickness of the double layer where charges are implanted, σ^+, σ^- are the charge densities. Fields in the various regions are denoted E_2, E_b, E_a, E_1.

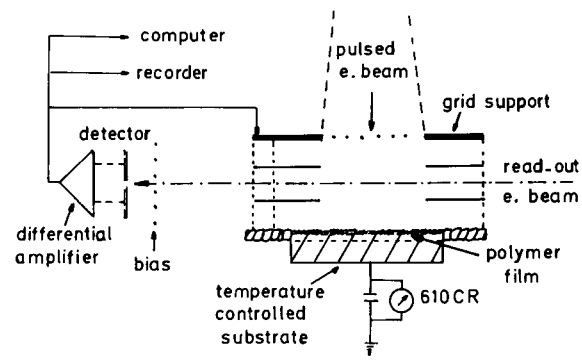

Fig. 2. "Two electron beams" apparatus showing the incidence of the two electron beams with respect to the sample surface. Experiments have been achieved on a polymer sample (12 μm thick, 2×10^{-7} C/pulse, temperature 110°C, sample surface 9 cm^2) [25].

With the notations of Fig. 1 we have:

Field between the top of the microscope chamber and the sample surface:

$$E_2 = \frac{r\sigma^- - \left[s + s_1\frac{\epsilon}{\epsilon_0}\right][\sigma^+ + \sigma^-]}{s\epsilon_0 + [s_1 + s_2]\epsilon} \quad (4)$$

Field between the double layer:

$$E_b = \frac{s_2\sigma^+ - \left[s_1 + (s-r)\frac{\epsilon_0}{\epsilon}\right]\sigma^-}{s\epsilon_0 + [s_1 + s_2]\epsilon} \quad (5)$$

Field in the sample below the negative charge

$$E_a = \frac{s_2[\sigma^+ + \sigma^-] + r\frac{\epsilon_0}{\epsilon}\sigma^-}{s\epsilon_0 + [s_1 + s_2]\epsilon} \quad (6)$$

Field between the bottom of the sample and the grounded holder:

$$E_1 = \frac{r\sigma^- + s_2\frac{\epsilon}{\epsilon_0}[\sigma^+ + \sigma^-]}{s\epsilon_0 + [s_1 + s_2]\epsilon} \quad (7)$$

The recombination rate is a function of E_b (Eq. 5); the secondary electron yield is dependent on E_2 and E_b (Eqs. 4 and 5); the transport of negative charge across the sample is in relation with the field E_a (Eq. 6). Electron spectroscopy signals will be affected by fields E_2 and E_b.

Much information can be drawn from Eqs. 4 to 7, depending on the sample environment. Let us consider for example a common practical situa-

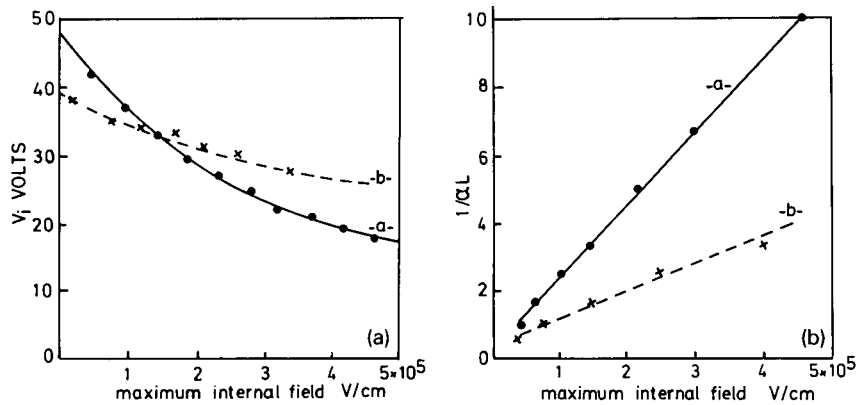

Fig. 3. (a) Incremental surface potential V_i vs. maximum internal field derived from Eq. 6. (b) Reciprocal trapping parameter $1/\alpha L$ vs. maximum internal field. αL can be calculated from V_i by using the equation $V_i = V_0[1 - \alpha L^{-1} \times \{1 - \exp - aL\}] = V_0 F(\alpha L)$ where V_0 is the incremental surface potential if all charges are trapped at $x = L$, where L is the sample thickness.

tion such as $r \ll s$ and $s_2 \gg s$. If the ground holder touches the sample ($s_1 = 0$) $E_b = \sigma^+/\epsilon$, whereas if $s_1 \gg s_2$ we have $E_b = \sigma^-/\epsilon$.

Space charge characterization techniques

Most of the parameters listed in Table I have been measured by using several different space charge characterization techniques. Among them two appear to be very performant: a "two electron beams technique" [25] and the "mirror method" [26,27].

Two electron beams technique. In this technique, two electron beams are used, each of 2.2 keV (Figure 2). A writing beam injects electrons into the free surface of the sample and a read out beam monitors the surface potential. The writing beam scans a raster over few cm^2 area of the sample and is automatically switched off when the required amount of charges has been injected into the sample. Charging times typically range from 50 to 200 ms. The read-out beam passes between the sample surface and a reference grid situated above the area of the sample. This beam is collected on a split detector, connected via a differential electrometer to a high gain amplifier whose output is fed back to the reference grid. The feed-back loop holds the read-out beam near its null position on the collector electrode and in so doing maintains the reference grid at the same potential as the sample surface. The grid potential is recorded and thus one obtains a direct reading of the incremental surface potential of the sample as a function of the incremental charging.

This technique has shown interesting possibilities for measuring the schubweg λ (Fig. 3) which is given by $\lambda = \mu\tau E$, where μ is the mobility, τ the relaxation time between two collisional events and E the applied electric field.

Mirror method. The method is simple and samples of different shapes and sizes can be investigated. The idea was to use the electron beam of an SEM at different energies to first charge the sample and then to work with it as an electrostatic probe to measure the potential distribution around the charge. With the electron source of the SEM at a voltage $-V_0$ ($V_0 > 0$), negative charges are implanted by using a beam of high energy $eV_0 \sim 30$ keV. Then the charged sample is scanned with the same beam after lowering its energy to $eV_1 < eV_0$. In the Gaussian approximation equipotential $-V_1$ produced by the implanted charges acts as a convex electrostatic mirror which forms a virtual image source S' of the objective lens aperture (Fig. 4). This is why the method is called mirror method.

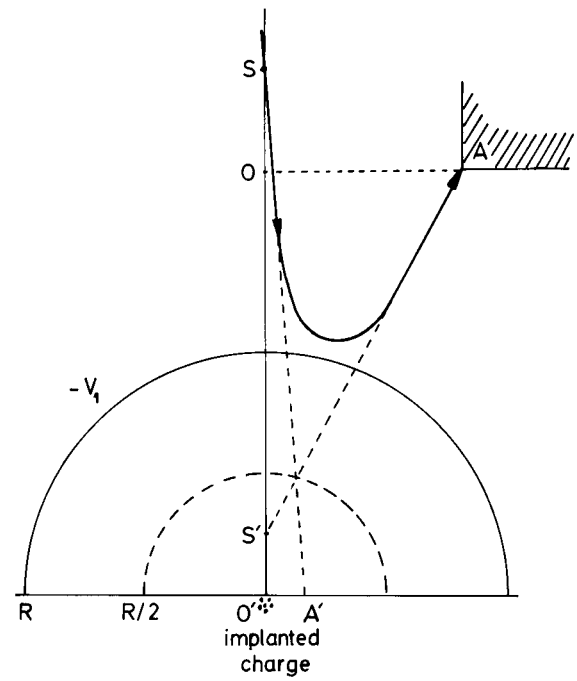

Fig. 4. Mirror effect due to a negative charge implanted with an electron beam of high energy eV_0 and observed with an electron beam of lower energy eV_1. Equipotential $-V_1$ formed by the implanted charge acts on the electron beam as a convex electrostatic mirror. In the Gaussian approximation the mirror (dashed circle) gives a virtual image S' of the objective lens apperture S. S' appears as the virtual electron source forming the image of the microscope chamber. For a quasi-punctual implanted charge the radius R of equipotential $-V_1$ is deduced from the objective lens image by the relation: $R = 4O'S \cdot O'A'/OA$ [28].

At a low scanning angle the beam, reflected on equipotential $-V_1$, impacts surrounding objects located in its trajectory and the electrons gener-

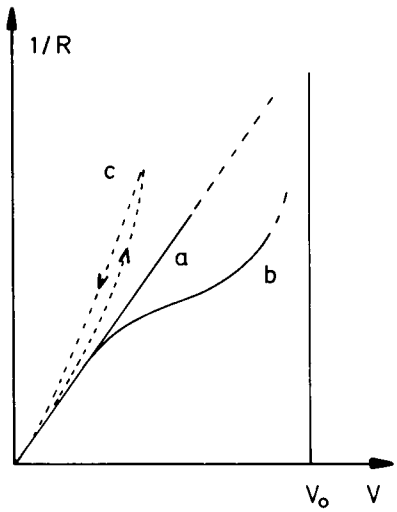

Fig. 5. Various types of $1/R = f(V)$ curves: (a) corresponding to a stable point charge; (b) to a stable charge spread parallel to the surface and (c) to a charge moving during the experimental investigation. V_0 is the voltage corresponding to implantation.

ated are collected by the secondary electron image detector of the microscope, forming the image of the microscope chamber.

At larger scanning angles the beam impinges upon the sample surface at a grazing incidence and there exists a positively charged zone which is the result of a combination of the local beam density and of the energy and angular dependence of the secondary electron yield.

Electrostatic calculations taking into account the sample permittivity and microscope chamber geometry have been carried out [28]. Experimentally, an equipotential V is characterized by its polar radius R in the direction perpendicular to the sample surface. R is deduced from the magnitude of the image of the objective lens aperture by a linear relationship. The curve $1/R = f(V)$ is then plotted. Three types of curves have been observed (Fig. 5).

(a) A linear variation with the curve passing through the origin: this corresponds to a point charge distribution with spherical equipotentials for which Coulomb's law applies. It should be mentioned that the slope of the curve $Q/R = f(V)$, where Q is the implanted charge has the dimension of a *permittivity*, the higher the permittivity, the lower the trap energy from Eq. 1, the lower the trapping rate and therefore the larger the charged volume.

(b) A linear variation followed by a plateau which tends to become parallel to the V axis. This behaviour corresponds to spherical equipotentials at large distance which transform progressively into oblate ellipsoid equipotentials as the distance to the surface becomes smaller and smaller. This transformation of the shape of equipotentials is due to the spreading of the charge in the surface plane.

(c) A linear variation followed by a steep increase along the $1/R$ axis. This variation which corresponds to a charge decay is still under investigation.

Charging is related to the spatial and energy distributions of traps and to the space charge field intensity. From the measurement of the potential around trapped charges various parameters influencing charge spreading have been investigated.

Effect of the electron dose

Three types of curves $V = f(\text{dose})$ are observed (Fig. 6).

(a) The potential at a given distance from the surface is varying in proportion to the dose until the maximum value equal to the implanting beam potential is reached (curve 1).

(b) The potential reaches a saturation value (curve 2). In this case a steady state leakage current is established. The variation of this current as a function of time is related to various parameters: (1) stability of the dielectric structure under the stress of the space charge, (2) temperature increase due to successive trapping–detrapping, (3) electrodiffusion of ionic species.

(c) The potential goes through several maxima before reaching a saturation value (curve 3). This means that the space charge collapses suddenly at critical doses before the steady state leakage current is established. The origin of this phenomenon is still under investigation.

Piezoelectric effect

In piezoelectric α-quartz, cut orthogonal to the Z optical axis, the charge distribution is

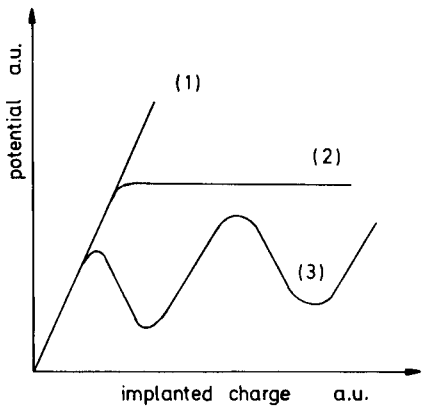

Fig. 6. Variation of the potential of the charged area at a given distance from the surface as a function of implanted dose: (1) linear variation, (2) steady state leakage current, (3) successive collapsing of the space charge before the steady state leakage current is established.

isotrope in the (0001) plane whereas, in X cut sample, charges spread preferentially along the Z axis. This anisotropy in the charge distribution means that charges move more easily in the Z direction than in others. In other words, the detrapping energy is anisotropic. This is in relation with the polarizability which is also anisotropic in this material. This experiment illustrates very well the influence of the polarizability on charge trapping [29].

Temperature effect

The variation of the potential of a piezoelectric α-SiO_2 has been observed from room temperature up to 500°C. The dielectric constant is almost constant ($\epsilon_r = 4$) from room temperature to about 300°C and then increases to 10 before the Curie point (573°C) is reached. Gradual decay of the potential from 300°C to 573°C and then charge disappearance at 573°C occurs.

The mirror method has also been used to study dielectric relaxation related to heating when the steady state current is reached. A transient time which depends on the experimental conditions has been observed, the relaxation law follows a power law as usual in such a phenomenon [30].

Role of polarizability defects

(a) Non-charging sensitive insulators. Stoichiometric MgO single crystals cleaned in ultra high vacuum and annealed at high temperature (1200°C for example) does not charge at room temperature until extrinsic defects are created. Nothing in the structure of MgO (if the presence of impurities or dislocations are ignored) suggests the existence of trapping sites. Consequently it is normal that charging does not occur.

(b) Charging sensitive insulators. Charging appears on MgO after the surface is coated with a very low coverage layer of metallic atoms (10^{10} per cm^2) [31]. When atoms are deposited on the surface new polaron sites appear at MgO–metal interfaces, leading to trapping.

A stoichiometric α-Al_2O_3 single crystal has a hexagonal structure with two different Al–O distances in the unit cell [32]. The presence of intrinsic local variation in atomic polarizability causes charging to occur at an appropriate temperature. This is well confirmed: cleaned crystal does not charge significantly (more than a few tens of volt) under ionizing beam at room temperature, but it does at −100°C [2]. Cr doped crystals no longer charge even at −200°C. Crystals doped with Cu or Ag charge at room temperature and the charge is dependent on the dopant.

Both MgO and Y_2O_3 are cubic and have a close band gap (5–6 eV). It is interesting to compare their charging behaviours. Stoichiometric Y_2O_3 oxide charges at room temperature. This is attributed to the presence of an interstitial space in the lattice (lack of oxygen atom) causing two types of yttrium environment. The minority type having a lower electronic polarizability is a trapping center [22].

Non stoichiometric polycrystalline Y_2O_3 which has oxygen vacancy enriched grain boundaries has a trapped charge distribution which depends on the electron dose [33].

Polymers of low dielectric constant are among the most sensitive materials to heavy charging. But the nature of the polarizability defects responsible for charging have not yet been characterized.

All of these results illustrate very well the role of local variation of polarizability on trapping.

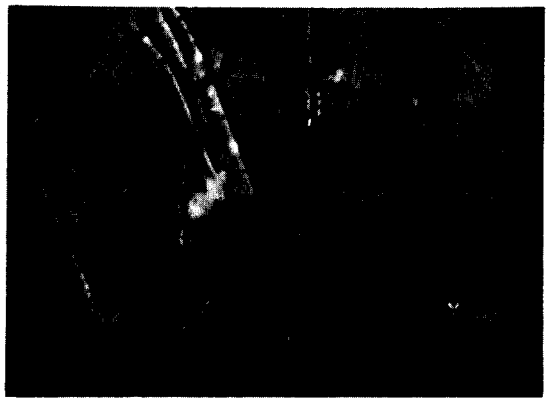

Fig. 7. Treeing tracks left by flashover on the surface of a polycrystalline stoichiometric Y_2O_3 freshly annealed (1200°C) [13].

(c) Damage related to trapping–detrapping phenomena. After the sample has been charged, any external perturbation can detrap charges on the edge of the charge distribution because here is the region where the space charge field is maximum. In case of detrapping of edge charges, which produce a local increase of the space charge field, inner charges can also be detrapped under the action of the field and thus the detrapping process becomes self accelerated. This is the mechanism leading to an electric wave propagation prior to breakdown occurrence. After the passage of this wave the mechanical relaxation of the lattice occurs, leading to breakdown when critical conditions are satisfied (Fig. 7).

Damage related to charge detrapping has been investigated with the mirror method applied in a scanning Auger microscope [13] (Fig. 8).

(d) Size factor. The electric strength is not an intrinsic material parameter because it depends on the material size. To demonstrate the relationship between charging and electric strength it is mandatory to demonstrate that charge characteristics are also a function of the sample size. The sample being mounted as shown in Fig. 9, when V_0 is increased, the potential V_s which varies linearly first reaches a saturation value V_c. When the potential saturates at V_c, the steady state leakage current is established thus, the quantity $2V_c/\Phi$ where Φ is the diameter of the grounded

Fig. 8. Scanning Auger image of the carbon contamination layer obtained after flashover on a quartz (the sample is tilted by 50° and the picture is taken at 1.3 kV). The dark area corresponds to the carbon contaminated layer which was outgassed by flashover(sample is 20 μm thick, it is charged with a 25 kV electron beam and breakdown is produced at 2 kV). Published with Courtesy of Geller Microanalytical Laboratory, Peabody, MA, USA) [31].

metallic ring can be considered as representative of the critical detrapping field. V_c/Φ is found to be a power law function of Φ whose exponent depends on the nature of the sample [34]. The exponent of this function characterizes the size factor. It must be mentioned that neither the power law function nor the exponent are universal [35].

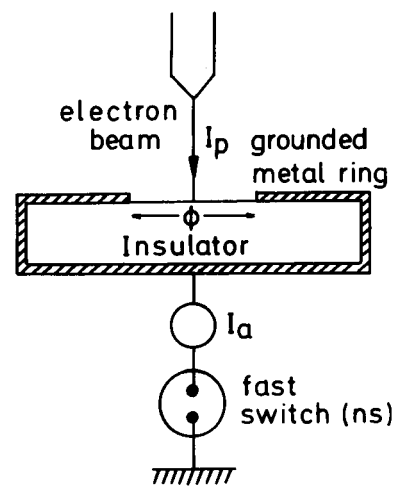

Fig. 9. Mounting of the sample with a grounded metallic ring of diameter Φ to measure the critical leakage potential $V_c(\Phi)$.

4. Correlation of insulator properties with electron spectroscopic observations

In this section a recapitulation is presented of studies which have been done to investigate insulator electrical and mechanical properties by using electron spectroscopy techniques. This attempt is focused on the search for observations related to parameters listed in Table 1.

Weibull modulus

The Weibull modulus is related to the presence of defects. Defects have been extensively investigated by ELS but, to our knowledge, it has not been established that the observed loss peaks are really related to the modulus.

Nature of defects

Most ELS works deal with deep defects located in the band gap. It has not been established that such defect levels are related to charging and consistent with the discharging temperature observed. Discharging occurs at low temperatures (a few hundreds of degrees for SiO_2) which is not compatible with E' centers located at 2 eV below the conduction band.

Electronic polarizability

An interesting attempt has been made on Y_2O_3 to correlate the charging characteristics measured by the pressure wave method [36], the electronic polarizability variation deduced from the measurement of the Auger parameter, the fracture toughness and the breakdown strength [37] as a function of oxygen concentration. In non stoichiometric samples, grain boundaries enriched in oxygen vacancies, are liable to fix charges differently than in bulk in correlation with the fact that they form preferential paths of fracture (Fig. 10).

Another interesting study deals with the modification of the electron state density (DOS) of quartz subjected to a compressive or tensile mechanical stress [38]. A significant DOS modification has been observed and the modification tendency is in agreement with band structure calculations. This behaviour implies certainly a change of polarizability which affects the trap energy and consequently the trapping rate and the space charge extension.

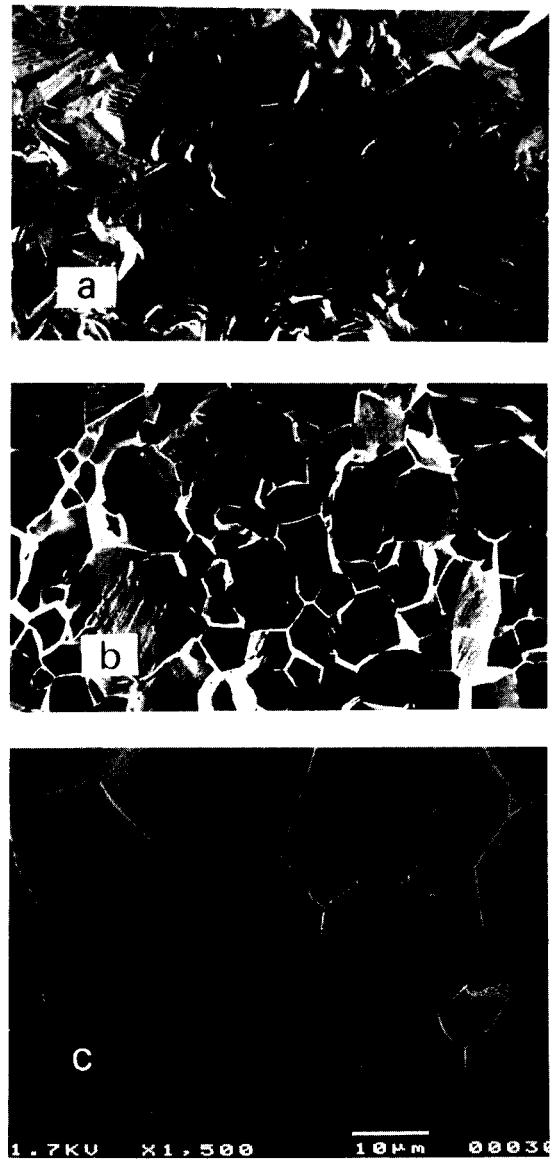

Fig. 10. (a) SEI after fracture of a stoichiometric Y_2O_3. The fracture is transgranular. (b) SEI after fracture of a non stoichiometric Y_2O_3. The fracture propagates along grain boundaries and is mostly of intergranular type SEM. (c) Secondary electron image of a polycrystalline non stoichiometric Y_2O_3 observed at $V_0 = 1.7$ kV. Grain boundaries where charges are preferentially trapped appear bright.

Another way to produce a strong perturbation of the lattice polarization is found in experiments

dealing with ion bombardment of insulators. Characteristic transitions have been observed in the energy distribution of electrons emitted from ion bombarded sodium halides [39,40]. It should be interesting to investigate to what extent the electron emission is related to the complex permittivity of the material and therefore to its mechanical and electrical properties.

Temperature increase related to trapping–detrapping process

The temperature increase related to charge detrapping is clearly demonstrated in Fig. 8. This result illustrates how a sudden variation of polarization may cause damage. Investigation of charging in AES has shown [41] that the surface potential decreases as a function of electron irradiation time. This decease can be interpreted as due to a charge detrapping related to a temperature increase or to a neutralization process due to ion electromigration.

The increase of the surface temperature of insulator bombarded by a neutralizing beam during analysis has been also observed in HREELS [42]. It is believed that successive trapping–detrapping is at the origin of the temperature increase observed from the ratio of energy loss to energy gain peaks, each one being on each side of the elastic peak.

Low energy electron emission

The influence of defects (energy and spatial distributions, trapping rate) and the influence of the electric field in the double layer have been introduced in the simulation of the insulator secondary electron yield [12]. The simulation has exhibited the important result that it is the direction of the field in the double layer which determines the escape depth of secondaries, not only the presence of positive surface charges as usually believed.

Internal photoemission techniques have been applied to measure absolute energy dependent electron–phonon scattering rates in SiO_2 [11,12]. These rates are used as input parameters in Monte Carlo transport simulations to calculate the hot electron dynamics at high electric fields. Quantities such as average electron energies, high field hot electron energy distributions, electron–hole pair generation by impact ionization and charge build up due to trapping and annihilation of the holes have been explained quantitatively. The hot electron dynamics allows to investigate the high field degradation in SiO_2 films. It has been shown that hot electrons cannot gain enough energy to ionize the valence band levels and it has been suggested that hot electrons can enter in a defect formation mechanism [9,10]. Although it is not in the frame of this work to discuss the figure of merit of these works we shall only notice that they do not take into account energetic aspects related to trapping and detrapping and they do not take into account the possible structural modification under high field.

Field electron emission from dielectric media has gained increasing attention due to its potential technological applications [43,44]. Cold electron emission that limits the performance of high voltage vacuum devices originate from particular microstructures having an associated dielectric medium. An electron spectrometer facility, incorporating an energy selective emission imaging capability, has been developed for making detailed investigations of individual microscopic emission processes. It has been possible to show that the emission mechanism is "non-metallic" in origin.

Conclusion

Research of correlation between insulator properties and spectroscopic observation is still at an early stage of development. However, recent progresses in the understanding of trapping–detrapping mechanisms and development of the space charge physics open up new perspectives. Much attention has been paid to quantitative surface analysis but little attention has been paid to link spectroscopic observations with thermodynamical variables of insulators and to find a relationship with the polarization. It is believed that surface science techniques are important tools to find a relationship between structure and macroscopic properties of insulators provided that the scientist accepts that the charging effect contains a physical message.

References

[1] C. Le Gressus and G. Blaise, IEEE Trans. Electr. Insul., 27 (1992) 472.

[2] S. Fayeulle, H. Berrough, B. Hamzaoui, D. Treheux and C. Le Gressus, Wear, 162–164 (1993) 906.

[3] A.K. Jonscher, Dielectric Relaxation in Solids, Chelsea Dielectrics, London, 1983.

[4] A.A. Griffith, Philos. Trans. Roy. Soc. A, 221 (1921) 163.

[5] J.C. Fothergill, IEEE Trans. Electr. Insul., 26 (1991) 1124.

[6] G. Blaise and C. Le Gressus, C.R. Acad. Sci. Paris, t. 314, Série II (1992) 1017.

[7] G.M. Sessler, in G.M. Sessler (Ed.), Electrets, Springer Verlag, London, 1979, p. 55.

[8] J.J. O'Dwyer, The Theory of Electrical Conduction and Breakdown in Solid Dielectrics, Clarendon Press, Oxford, 1973, p. 235.

[9] E. Cartier and P. Pfluger, Appl. Phys. A, 44 (1987) 43.

[10] E. Cartier, D. Arnold and M.F. McFreely, Interdisciplinary Conf. on Dielectrics, Supl. Revue "Le Vide, les Couches Minces", 260 (1992) 260.

[11] H. Boersch, H. Hamisch and W. Ehrlich, Z. Angew. Phys., 15 (1963) 518.

[12] J.P. Ganachaud and A. Mokrani, Conf. on Electrical Insul. and Dielectric Phenomena, IEEE Service Center, Piscataway, NJ, p. 233.

[13] C. Le Gressus and G. Blaise, IEEE Trans. Electr. Insul., 27 (1992) 472.

[14] M. Selle, G. Eberle, B. Gompf and W. Eisenmenger, CEIDP Annual Report, 1992, p. 876.

[15] G. Moya, D. Moya and C. Le Gressus, as Ref. 12, p. 104.

[16] K. Liang, M. Orange, G. Fantozzi, M. Gautier, J.P. Duraud and C. Le Gressus, in G. de With, R.A. Terpstra and R. Metselaar (Eds.), Euro-Ceramics, Maastricht, Vol. 2, 1989, p. 2151.

[17] G.B. Caso, M.G. Schwabel and V.D. frechette, J. Am. Ceram. Soc., 73 (1990) 41.

[18] F. Ohuchi, M. Ogino, P. Holloway and C.G. Pantano, Surf. Int. Anal., 2 (1980) 85.

[19] A. Miotello, Phys. Lett. A, 103 (1984) 279.

[20] G.Blaise, Microscopic and Macroscopic Description of the Polarization of Dielectric Materials. The Concept of Polaron Applied to the Conduction and Trapping of Charges, Interdisciplinary Conf. on Dielectrics, Supl. Revue "Le Vide, les Couches Minces", 260 (1992) 1.

[21] I.G. Austin and N.F. Mott, Polarons in Crystalline and Non-Crystalline Materials, Advances in Physics, Academic Press, New York, Vol. 18, 71 (1969) 41.

[22] G. Blaise, as Ref. 12, p. 98.

[23] L. Landau and E. Lifchitz, Electrodynamique des Milieux Continus, Mir, Moscow, 1969, p. 76.

[24] C.Kittel, Introduction to Solid State Physics, Wiley, London 1970.

[25] P.K. Watson, F.W. Schmidlin and R.V. Ladonna, IEEE Trans. Electr. Insul., 27 (1992) 680.

[26] C. Le Gressus, M. Gautier and J.P. Duraud, Revue Scientifique et Technique de la Défense, 2^{ième} trimestre, 1990, p. 67.

[27] C. Le Gressus, F. Valin, M. Henriot, M. Gautier, J.P. Duraud, T.S. Sudarshan, R.G. Bommakanti and G. Blaise, J. Appl. Phys., 69 (1991) 6325.

[28] B. Vallayer et al, in preparation.

[29] H. Gong, C. Le Gressus, K.H. Oh, X.Z. Ding, C.K. Ong and B.T.G. Tan, J. Appl. Phys., 74 (1993) 1944.

[30] K.H. Oh, C. Le Gressus, H. Gong, C.K. Ong B.T.G. Tan and X.Z. Ding, J. Appl. Phys., 74 (1993) 1250.

[31] J. Möller and J.W. He, Nucl. Inst. Methods Phys. Res., 13 (1986).

[32] R. Wyckoff, Crystal Structures, Interscience, New York, 1951.

[33] C. Le Gressus and G. Blaise, J. Electron Spectrosc. Relat. Phenom., 59 (1992) 73.

[34] K.H. Oh, C, Le Gressus, C.K. Ong B.T.G. Tan and G. Blaise, J. Appl. Phys., 74 (1993) 1960.

[35] R. Bartnikas and R.M. Eichhorn, Engineering Dielectrics, ASTM Special Technical Publication 783, IIA, Chap. 5, p. 500.

[36] C. Le Gressus, unpublished results.

[37] M. Gautier, F. Jollet, J.P. Duraud and C. Le Gressus, Non Stoechiometrie de Y_2O_3-Propriétés induites et Modifications de Structure, Revue Scientifique et Technique de la Défense, 2^{ième} trimestre, 1990.

[38] F. Jollet, Rapport CEA-R-5517, CEN-SACLAY, Gif-sur-Yvette, 1990.

[39] J. Fine, M. Szymonski, J. Kolodiziej, M. Yoshitake and K. Franzreb, in G. Betz and P. Valga (Eds.), Proc. Symp. Surface Science, Univ. of Vienna, 1993.

[40] J. Fine, M. Szymonski, J. Kolodiziej, M. Yoshitake and K. Franzreb, Phys. Rev. Lett., 71 (1993) 3585.

[41] S. Hofmann, private communication.

[42] M. Liehr, P.A. Thiry, J.J. Pireaux and R. Caudano, Phys. Rev. B, 33 (1986) 5682.

[43] K.H. Bayliss and R.V. Latham, Proc. Roy. Soc. A, 403 (1986) 285.

[44] N.K. Allen and R.V. Latham, Inst. Phys. Conf. Ser. 99, Section 6 (1989) 57.

ELSEVIER

Analytica Chimica Acta 297 (1994) 153–164

ANALYTICA CHIMICA ACTA

Electron radiation-induced effects in Auger electron spectroscopic characterization of high-T_c superconductors

E.W. Seibt

Kernforschungszentrum Karlsruhe, Institut für Technische Physik, Postfach 3640, D-76021 Karlsruhe (Germany)

A. Zalar

Institute for Electronics and Vacuum Technique, Teslova 30, 61000 Ljubljana (Slovenia)

N. Roose

Vrije Universiteit Brussel, Dienst Metallurgie, Elektrochemie en Materialenkennis, Pleinlaan 2, 1050 Brussels (Belgium)

Received 1st April 1993; revised manuscript received 19th July 1993

Abstract

The effect of radiation-induced changes on the surface and bulk compositions of high-T_c Bi–Pb–Sr–Ca–Cu–O and Y–Ba–Cu–O superconducting systems produced by electron-beam irradiation at room temperature was studied by means of high-resolution Auger electron spectroscopy (AES). Electrons of energies between 5 and 15 keV were used to investigate energy-dependent decomposition phenomena for a wide range of electron radiation doses up to about 10^{28} electrons m^{-2}. In addition, irradiations with scanned 10-keV electron beams were performed on $YBa_2Cu_3O_{6.8}$ single-crystal superconductors in order to investigate the radiation-induced effects on stoichiometric concentrations for oxygen and other elemental constituents using AES multiplex and sputter depth profiling techniques. The results indicate that there are significant changes in both the surface and the bulk compositions of the silver-sheathed $Bi_{1.7}Pb_{0.3}Sr_2Ca_2Cu_3O_{10.2}$–10 wt.% Ag tape samples, e.g., up to surface concentrations of about 10 at.% for oxygen and about 12 and 15 at.% for calcium and copper, respectively, whereas only small radiation-induced decomposition effects are observed for epitaxially grown $YBa_2Cu_3O_{7-x}$–$SrTiO_3$ thin-film superconductors. $YBa_2Cu_3O_{6.8}$ single crystals show relatively strong changes in surface composition in the low radiation dose range, but also a damage recovery effect stimulated at higher electron radiation doses.

Keywords: Surface techniques; Auger electron spectroscopy; Decomposition effects; Electron irradiation; High-T_c superconductors; Superconductors

The structural and electrical properties of ceramic superconductors in the Bi–Pb–Sr–Ca–Cu–O and Y–Ba–Cu–O families are influenced in different ways by irradiation processes depending

Correspondence to: E.W. Seibt, Kernforschungszentrum Karlsruhe, Institut für Technische Physik, Postfach 3640, D-76021 Karlsruhe (Germany).

SSDI 0003-2670(93)E0483-N

on the kinds of projectiles, e.g., neutral [1,2] and charged particles [3,4], and x-rays [5], with kinetic energies less than 0.1 MeV to several GeV and on details of the irradiation procedures. As these ceramic superconducting materials have a certain potential for application in electronics and radiation environments (e.g., as superconducting magnets or shieldings in high-energy accelerators or fusion reactors), the superconducting properties (transition temperature, T_c, critical current density, j_c) of such new superconductors should include a relatively high resistance to damage due to electron and ion beams and neutron or x-ray irradiation. For most combinations of bombarding particles and their energies, the radiation-induced damage mechanism acting between the incident projectiles and the material lattices involves ionization and/or electronic excitations of lattice atoms and also atomic knock-on displacement damage, provided that the transferred energies are above a material-dependent displacement threshold. The main purpose of most reported irradiation measurements has been the interpretation of disordering effects resulting in one-dimensional Cu–O chains and irradiation-induced lattice defects in high-T_c superconductors which lead to degradations [6] in both T_c and j_c, and in some instances also to j_c improvements [7], by using particle radiation-induced pinning centres.

Much of the early irradiation work was done on samples that contained foreign or multiple phases and that had poorly defined microstructures. For example, the effects of stoichiometry, structural transformations and metal-to-insulator transitions contribute to some of the radiation effects observed, making the true radiation behaviour of the ceramic superconductors difficult to interpret. Therefore, the demand for precise surface and bulk analytical investigations, e.g., performed with widely used Auger electron spectroscopy (AES) or other spectroscopic techniques [energy-dispersive x-ray (EDX) analysis, electron energy loss spectroscopy (EELS), etc.], is necessary to study the decomposition phenomena of this new class of oxide superconductors before and after irradiation. Recent investigations of these superconductors employing high-energy electron irradiation ($E_{El} > 100$ keV) have shown that these materials are very sensitive to electron irradiation, which produces changes in the structural and electrical properties [8,9]. In order to study the influence of the radiation of low-energy beam electrons comparable to AES primary electron excitation energies ($E_{El} < 15$ keV), irradiations of Bi–Pb–Sr–Ca–Cu–O and Y–Ba–Cu–O superconducting systems were performed at room temperature for a wide range of electron doses up to maximum 3.2×10^{28} electrons m^{-2} using electron energies between 5 and 15 keV.

Table 1
Typical data for silver-sheathed $Bi_{1.7}Pb_{0.3}Sr_2Ca_2Cu_3O_{10.2}$–10 wt.% Ag tapes (sample 1), $YBa_2Cu_3O_{7-x}$–$SrTiO_3$ thin films (sample 2) and $YBa_2Cu_3O_{6.8}$ single crystals (sample 3)

Superconductor type	Superconducting properties		Material properties		
	j_c(0 T, 77 K) (A m^{-2})	T_c (mid-point) (K)	ρ_{SC} (g cm^{-3})	$T_{melting}$ (°C)	$\lambda_{heat\ conduct.}$ (300 K) (W m^{-1} K^{-1})
$Bi_{1.7}Pb_{0.3}Sr_2Ca_2Cu_3O_{10.2}$–10 wt.% Ag silver-sheathed tape (sample 1)	$(3.3 \pm 0.2) \times 10^8$	110 ± 3	4.1 (6.13) [a]	~ 945 (in air)	5–6
$YBa_2Cu_3O_{7-x}$–$SrTiO_3$ thin film (sample 2)	2.5×10^8	88 ± 2	6.1 (6.38) [a]	~ 1015 (in air)	4–5
$YBa_2Cu_3O_{6.8}$ single crystal (sample 3)	$\sim 1 \times 10^9$	90 ± 2	6.30	990–1015 (in air)	4–5

[a] Theoretical values of material density ρ_{SC}.

The electron irradiation measurements presented here were concentrated on the radiation-induced compositional changes of surface and bulk high-T_c superconductors that occur after exposure to (i) increased electron-beam radiation doses and (ii) various primary electron energies. The samples of silver-sheathed $Bi_{1.7}Pb_{0.3}Sr_2Ca_2Cu_3O_{10.2}$–10 wt.% Ag tapes and $YBa_2Cu_3O_{7-x}$–$SrTiO_3$ thin films used in this study are promising representatives with relatively high transport-current carrying capabilities.

Another important parameter is the oxygen content of the irradiated samples. Previous work has shown that relatively small deviations of oxygen stoichiometry lead to significant decreases in both superconducting properties, j_c and T_c [10]. Thus, investigations of well defined $YBa_2Cu_3O_{6.8}$ single crystals were performed to observe the behaviour of the oxygen content after increasing electron radiation doses.

1. Experimental

Sample preparation

All three types of high-T_c superconducting samples used in these electron irradiation measurements were prepared using standard methods. The selected samples are of relatively high homogeneous quality in composition and structure. Several sample data for all three types are summarized in Table 1.

Silver-sheathed $Bi_{1.7}Pb_{0.3}Sr_2Ca_2Cu_3O_{10.2}$–10 wt.% Ag tapes (sample type No. 1). In view of the development of superconducting tapes or wires for magnets, Ag-sheathed $Bi_{1.7}Pb_{0.3}Sr_2Ca_2Cu_3O_{10.2}$–10 wt.% Ag composite tapes with relatively high critical current densities [j_c(0 T, 77 K) = 3.3×10^8 A m^{-2}] were prepared by the standard method of sintering finely ground stoichiometric amounts of the precursors Bi_2O_3 + PbO + $SrCO_3$ + $CaCO_3$ + CuO + Ag using the "powder-in-tube" method [11,12]. Before being filled into Ag tubes, the precursors were calcined several times, with intermediate grinding before each calcination step (24 h at 800°C in air). Quantitative high-resolution scanning Auger electron spectroscopy (AES) was used to determine the elemental distribution within the Bi(2223) phase. Typical grain sizes were between 5 and 10 μm, observed by scanning electron microscopy (SEM). At the grain boundaries foreign phases and a considerable amount of carbon were detected, the latter originating from the carbonate precursors. The average carbon content of the inside of the superconducting layer was found to decrease from 10 to about 1 at.% for j_c (0 T, 77 K) values going from 1.5×10^7 to a maximum of 3.3×10^8 A m^{-2} [13]. After cold working into silver-sheathed tapes (see Fig. 1) and reaction between 845 and 847°C in air to become a Bi(2223) phase with intermediate pressing cycles at 2.5 GPa, several annealing steps at 780–800°C were performed to optimize the critical current density in texturized tape materials. The transition temperature was determined by resistivity measurements to be T_c (mid-point) = 110 K.

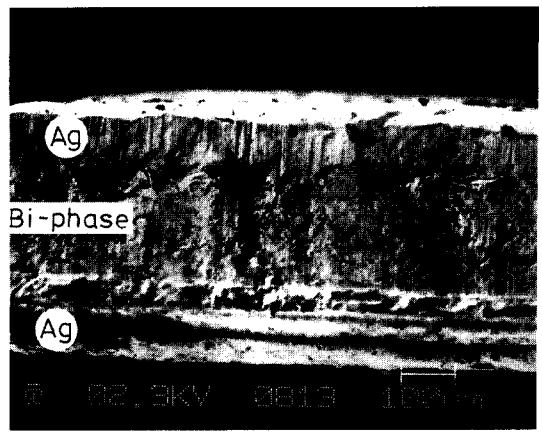

Fig. 1. Silver-sheathed high-j_c $Bi_{1.7}Pb_{0.3}Sr_2Ca_2Cu_3O_{10.2}$–10 wt.% Ag superconducting tape (length section).

$YBa_2Cu_3O_{7-x}$–$SrTiO_3$ thin films (sample type No. 2). Thin films of (123)-phase Y–Ba–Cu–O were grown epitaxially on single-crystalline (100)-oriented $SrTiO_3$ substrates using laser ablation. Typical film thicknesses were between 1.5 and 2 μm and grain sizes ca. 0.1 μm. Some thin film samples were reannealed in an oxygen atmosphere at about 550°C to promote the tetragonal to orthorhombic transformation. Resistive T_c measurements yielded values between 86 and 90 K.

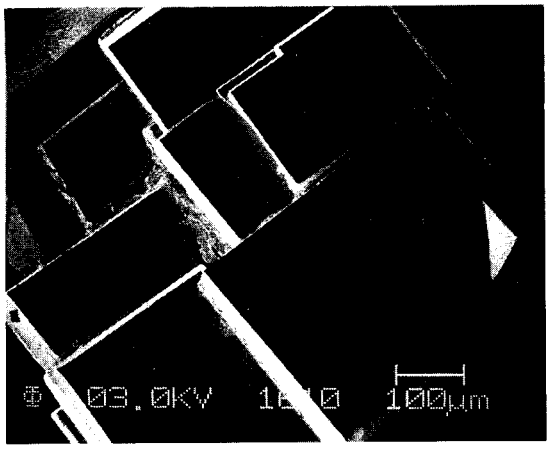

Fig. 2. Growth of 1–2–3 phase $YBa_2Cu_3O_{7-x}$ single crystal forming thin crystallites at a cooling rate of 0.1°C h^{-1}.

$YBa_2Cu_3O_{7-x}$ single crystals (sample type No. 3). $YBa_2Cu_3O_{7-x}$ single crystals with nominal molar compositions were produced by a self-flux method using the starting materials of Y_2O_3, $BaCO_3$ and CuO powders for (123)-phase samples (see Fig. 2). Typical heat treatments were applied between 990 and 1015°C in air. Slow cooling rates of ca. 0.1°C h^{-1} were used in order to obtain more extended crystals (maximum $5 \times 5 \times 2$ mm^3) [14]. The stoichiometric structure of the single crystals used as internal standards was generally determined by x-ray powder diffraction and EDX measurements. Typical compositions for $YBa_2Cu_3O_{7-x}$ single crystals with $x = 0.2$ were selected for the irradiation measurements.

Apparatus and method

In this work the criterion of electron radiation damage was the observation of changes in the elemental surface and bulk compositions of the superconducting samples irradiated with increasing electron doses. Because of the relatively small surface structures, e.g., grains, grain boundaries and precipitations, it is necessary to use an analytical technique with a sufficiently high local resolution. Therefore, the irradiation and analytical experiments were performed by use of a Perkin-Elmer PHI 600 scanning Auger multiprobe with an energy resolution of about 0.5% and a practical lateral resolution of less than 250 nm ($I_{EI} \approx 10$ nA).

Electron irradiation measurements were carried out starting at room temperature and using the electron beam of the same multiprobe in both scanning (raster size 10×8 μm^2) and focused stationary spot irradiation modes. In order to vary the electron radiation doses, the electron-beam current was increased step by step from 100 to a maximum of 2200 nA over constant irradiation times of 10 min. This procedure implies a change in beam diameter between about 0.5 and 1.3 μm. The electron beam was incident at an angle of 0° with respect to the sample surface normal. For single-crystal measurements the scanning irradiation mode was only used with the same raster size of 10×8 μm^2. After each irradiation period at a constant irradiation time of 10 min, the changes in surface composition were measured by the AES multiplex technique with a scanning electron-beam current of 100 nA (raster size 7×5 μm^2), which corresponds to an additive electron radiation dose of 1.2×10^{25} electrons m^{-2}. In these AES measurements no charging effects influenced the analytical results.

To study the energy-dependent damage of high-T_c superconducting samples, irradiation experiments were performed with electron energies of 5, 10 and 15 keV. All samples subjected to electron-beam irradiation were attached to stainless steel using conductive silver paste and partly also to copper sample carriers (for single-crystal samples) with large thermal masses in order to have good heat transition contacts.

Especially for quantitative AES measurements, both multiplex (for surface information) and sputter depth profiling techniques (for bulk information) were applied in combination with a small-spot duoplasmatron ion source (Perkin-Elmer) for 5- and 6-keV argon ions. The corresponding relative Auger sensitivity factors are related to internal standards of $YBa_2Cu_3O_{6.8}$ and $Bi_{1.8}Pb_{0.2}Sr_2Ca_1Cu_2O_{8.2}$ single crystals [15,16]. The main experimental parameters used for Ar^+ sputtering were 7 and 10 A m^{-2}, an angle of incidence of 41° and typical sputter rates of about 130 and 185 nm min^{-1}, respectively. Argon sputter rates were calibrated by Rutherford backscattering (RBS) measurements of thin films. After local bake-out of the vacuum system, a base pres-

sure of about 6×10^{-10} mbar was achieved for irradiation measurements and AES analysis. During Ar^+ sputtering the operating pressure with differential pumping rises by 1×10^{-8}–3×10^{-8} mbar.

Electron irradiation procedure

For the present irradiation measurements and AES analysis, the primary energy of the beam electrons, E_{El}, ranged between 5 and 15 keV. During their ionization and stopping processes caused by Coulomb interactions in the high-T_c material, the beam electrons of energies low enough to avoid knock-on displacement damage ($E_{El} \ll 120$ keV) produce different types of excitation, e.g., excited atoms and phonons. The range of the incident beam electrons (R_{El}) depends mainly on the electron energy (E_{El}) and the material density (ρ_{SC}) of the irradiated superconducting material according to the approximate empirical expression [17]

$$R_{El} \approx 1.03 \times 10^{-5} E_{El}^{1.5} / \rho_{SC} \quad (1)$$

for electron energies between 3 and 20 keV and material densities between 3 and 10 g cm^{-3}, where R_{El} is in cm when E_{El} is in keV and ρ_{SC} in g cm^{-3}. For example, for a silver-sheathed Bi(2223)-phase system (sample type No. 1) with a measured ρ_{SC} value of about 4.1 g cm^{-3} (the theoretical value is 6.13 g cm^{-3}), R_{El} can be estimated by Eq. 1 to take a value of about 0.8 μm for 10-keV electrons.

The electron-beam currents I_{El} used in irradiation measurements were varied over the range 5×10^{-8}–2.2×10^{-6} A (in some instances up to 3.5×10^{-6} A), resulting in an effective electron-beam power (P_{El}^*) which is defined by

$$P_{El}^* = f U_{El} I_{El} \quad (2)$$

The function f (in the present experiments $f \approx 0.7$) describes the fraction of those electrons which do not leave the sample surface as secondary or backscattered electrons and produce heat in the irradiated material.

Most of the radiation-induced excitation processes along the electron trajectories will finally result in the production of phonons. The electron-beam induced temperature rise, $\Delta T_{irrad.}$, of a plane sample surface related to ambient temperature can be estimated by assuming that the effective electron-beam power (P_{El}^*) is homogeneously dissipated inside a hemisphere of radius $R_{El}/2$ (using the thermal conduction relationship $P_{El}^* = -\lambda F_{surface} \times dT/dr$) and leads to the following expression [17]:

$$\Delta T_{irrad.} = 3 P_{El}^* / 2\pi\lambda R_{El} \quad (3)$$

where λ is the heat conductivity of superconducting materials in W m^{-1} K^{-1} and $F_{surface}$ is the irradiated surface area $= r^2\pi$ (r = radius of the beam spot).

If we consider, for example, 10-keV spot-focused electrons with an intensity of typically 1 μA (beam diameter ca. 0.9 μm) in a Bi(2223)-phase material using the values $R_{EL} \approx 1$ μm and $\lambda \approx 5.5$ W m^{-1} K^{-1}, then we find according to Eqs. 2 and 3 estimated $\Delta T_{irrad.}$ values of about 800°C. In order to demonstrate the electron radiation-induced surface effects, Fig. 3a and b show SEM pictures of a representative Bi(2223)-phase single grain (sample type No. 1) before and after electron irradiation. A typical change in the crystal structure at the Bi(2223)-system surface is indicated (see Fig. 3b) after a spot-focused electron-beam exposure to a radiation dose of 3.2×10^{28} electrons m^{-2}. The melting zones of the Bi(2223) surface (melting temperature $\approx$ 945°C in air) shown in Fig. 3b indicate that the estimation of radiation-induced rising temperatures $\Delta T_{irrad.}$ given above seems to be a reasonable approximation. To reduce this relatively high local heat production on the sample surfaces (irradiated area ≤ 1.3 μm^2), most of the present irradiation measurements, in particular for single crystals, were performed in the scanning irradiation mode with raster sizes of typically 10×8 μm^2.

2. Results and discussion

Electron-beam induced radiation damage

Electron radiation effects induced by 10-keV electrons starting at room temperature were studied as a function of the electron radiation doses which correspond to a successively increased

electron-beam current, to clarify the role of the electron beam in inducing changes in surface and bulk compositions in two typical Bi–Pb–Sr–Ca–Cu–O and Y–Ba–Cu–O superconducting compounds selected as examples for applications.

Silver-sheathed Bi (2223)-phase tapes. Spot-focused electron irradiations were performed on single grains of Ag-sheathed $Bi_{1.7}Pb_{0.3}Sr_2Ca_2Cu_3O_{10.2}$–10 wt.% Ag tape samples (sample type No. 1) to detect radiation-induced changes in the stoichiometric composition which occurs locally at the surface and in the bulk of superconducting grains. Representative SEM images of a freshly broken Bi(2223)-phase sample before and after

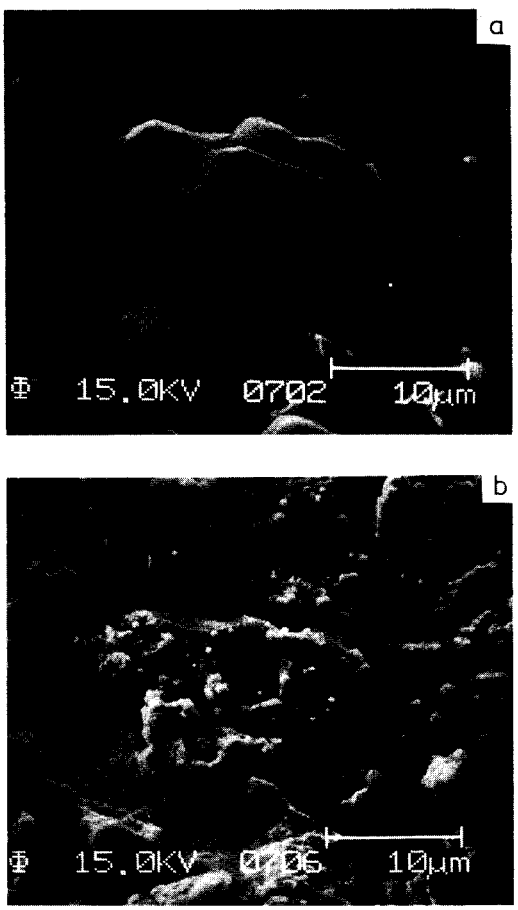

Fig. 3. Scanning electron micrographs of a Bi(2223)-phase single grain (a) before electron irradiation and (b) after spot-focused electron-beam exposure to a maximum radiation dose of 3.2×10^{28} electrons m^{-2}.

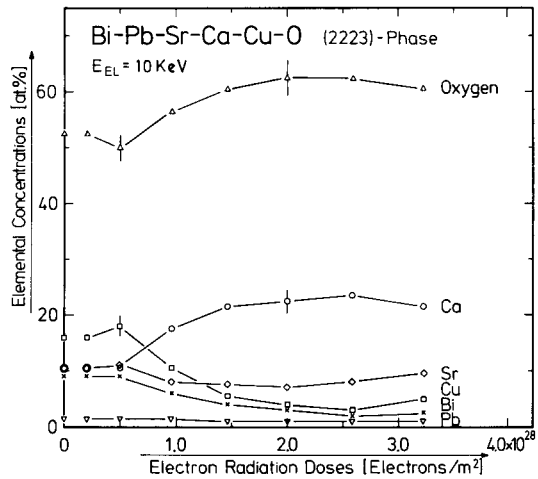

Fig. 4. Surface elemental concentrations of Bi(2223)-phase grains vs. electron-beam radiation doses for 10-keV electrons.

electron irradiation are displayed in Fig. 3a and b, respectively. The process of modification of the irradiated surface was observed in situ by detection of specific Auger electrons for each element of the Bi composite. No significant irradiation-induced decomposition effects were found up to a critical electron radiation dose of less than 5×10^{27} electrons m^{-2}. For higher electron radiation doses (ca. 1×10^{28} electrons m^{-2}), relatively strong decomposition effects at the surface were measured, e.g., the copper Auger intensity of the Bi(2223) system decreases with increasing electron radiation dose.

In Fig. 4, the elemental surface decomposition effects of the Bi(2223)-phase sample are summarized and represented as a function of electron radiation dose. In the low-radiation dose range ($\geqslant 5\times10^{27}$ electrons m^{-2}), oxygen exhibits a small deficiency peak which is in agreement with the results of Matsui et al. [18]. This indicates that the electron-beam stimulated oxygen desorption of the Bi(2223) phase [unirradiated Bi(2223) surface is enriched in oxygen by adsorption during the final annealing processes in an oxygen atmosphere] occurs within the range of damage due to electromigration or beam heating. However, at higher radiation doses the oxygen concentration increases and reaches saturation damage after irradiation of about 2×10^{28} electrons

m^{-2}, including a maximum effect of change in concentration of about 10 at.% (see explanation given for Fig. 5). The other components of the Bi(2223) phase show different decomposition effects. Thus, the Ca concentration is increased by about 12 at.% whereas the Cu and Bi concentrations are decreased by about 15 and 8 at.%, respectively. Only Sr and Pb show small decomposition effects between 1 and 3 at.%. It should be noted that all components of the Bi(2223) phase reach the threshold of saturation damage at $(2–3) \times 10^{28}$ electrons m^{-2}. It is also remarkable that some components show a slight recovery effect at a maximum electron radiation dose of 3.2×10^{28} electrons m^{-2}, especially for Cu and Sr.

The local evolution of the 10-keV electron-beam induced decomposition effects from the surface to the bulk material of a Bi(2223)-phase single-grain irradiation up to about 1.4×10^{28} electrons m^{-2} was monitored by AES depth profiling involving continuous sputtering with 6-keV argon ions. The results of the investigation of bulk decomposition effects are displayed in Fig. 5 and show a distinct peak behaviour inside the Bi(2223) grain, in particular for oxygen, copper and calcium. Copper exhibits the strongest decomposition effect of about 5 at.% at the surface (start for depth profiling), and up to 25 at.% in a depth of about 1 μm inside the grain, i.e., in total a ca. 20 at.% change in copper concentration. On the other hand, the oxygen content decreases in the same grain volume. This indicates in the case of electron radiation-induced damage that Cu–O bonds are broken in the whole radiation range of the 10-keV electrons, followed by oxygen diffusion out of the irradiated grain volume within a distance of about 1 μm to the surface. This behaviour results in an enrichment of oxygen at the surface up to a maximum concentration of about 60 at.%. The observations indicated by Fig. 5 are in agreement with the estimation of the 10-keV electron range according to Eq. 1.

Calcium, however, shows a segregation effect

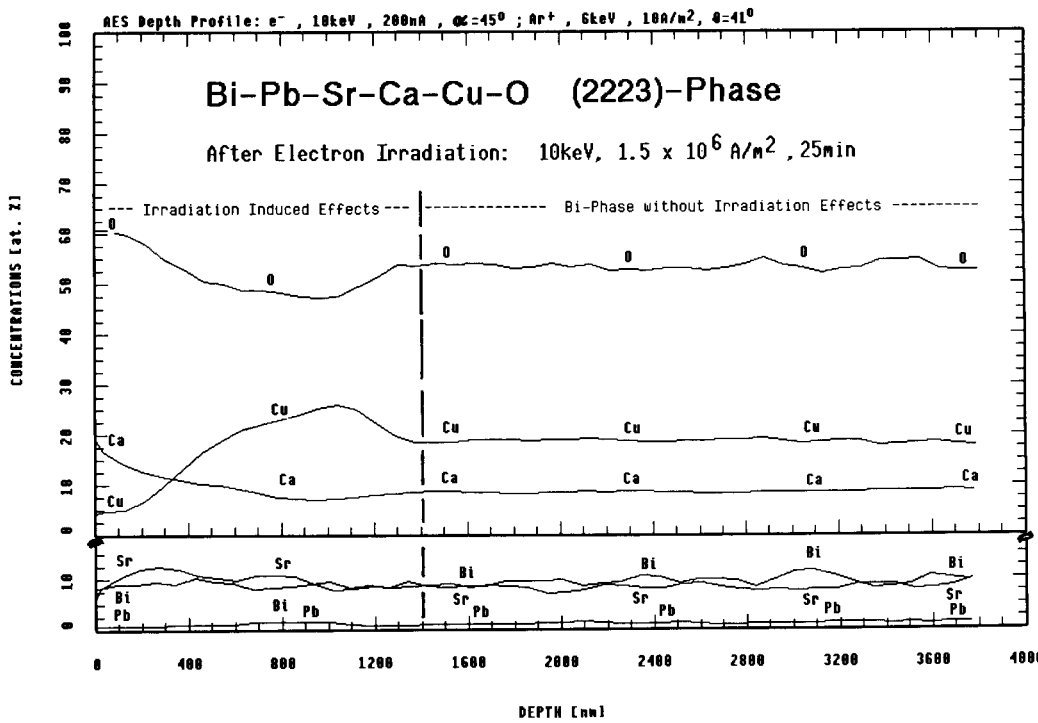

Fig. 5. Bulk decomposition effects of Bi(2223)-phase grains after 10-keV electron-beam irradiation of about 1.4×10^{28} electrons m^{-2} as a function of grain depth.

at the grain surface, with an excess in concentration of about 10 at.% compared with the initial composition values as indicated in the AES depth profiles in Fig. 5. This effect leads to the formation of non-superconducting phases at the superconductor surface, such as insulating Ca–O compounds. CaO and also BaO are the most stable of the oxides in high-T_c superconductors, with extremely low oxygen partial pressures in comparison with copper oxides. For Sr, Bi and Pb only small bulk decomposition effects of 1–3 at.% are observed inside the Bi(2223) grain.

$YBa_2Cu_3O_{7-x}$–$SrTiO_3$ thin films. The electron-beam induced decomposition effects of $YBa_2Cu_3O_{7-x}$–$SrTiO_3$ thin-film samples (sample type No. 2) was due to successive high-current irradiations in spot-focused and scanned electron-beam modes (raster size 10×8 μm^2) under the same conditions as for the Bi(2223)-phase samples. The results of 10-keV electron irradiation as shown in Fig. 6 surprisingly indicate a less efficient surface damage behaviour than for Bi–Pb–Sr–Ca–Cu–O superconductors. Thus, the epitaxially grown $YBa_2Cu_3O_{7-x}$–$SrTiO_3$ thin films are nearly radiation resistant to 10-keV electrons up to a maximum radiation dose of 3.2×10^{28} electrons m^{-2}. However, an exception is Ba, which at the very beginning of irradiation

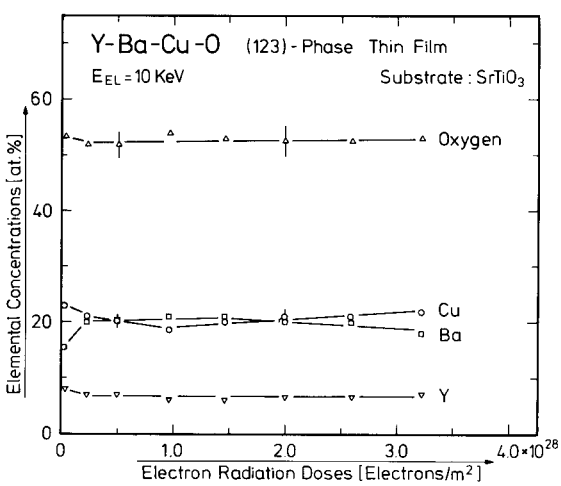

Fig. 6. Surface elemental concentrations of a $YBa_2Cu_3O_{7-x}$–$SrTiO_3$ thin film vs. electron-beam radiation doses for 10-keV electrons.

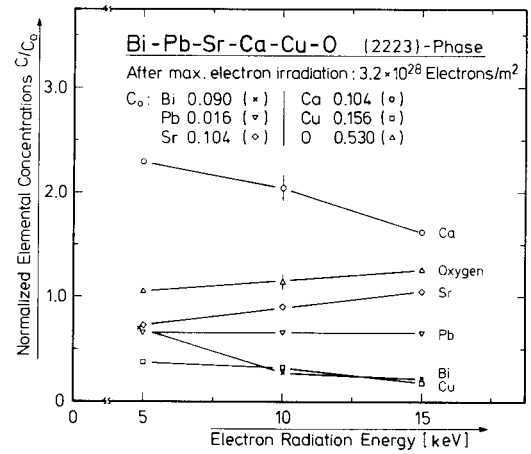

Fig. 7. Normalized surface elemental concentration values, C/C_0, of Bi(2223)-phase grains vs. electron radiation energy after exposure to a maximum radiation dose of 3.2×10^{28} electrons m^{-2} (C_0 is defined as the preirradiation value).

(after 2.5×10^{27} electrons m^{-2}) undergoes a jump in concentration from 16 at.% to a nearly constant level of about 20 at.%. The elemental concentration values measured before and after irradiation are representative within an experimental error of about ±5%. Corresponding bulk composition measurements by depth profiling also show no significant decomposition effects inside the irradiated Y–Ba–Cu–O thin film samples.

Electron energy-dependent radiation damage

To study the surface decomposition effects as a function of the electron energy, electron-beam irradiations of silver-sheathed Bi(2223)-phase tape and $YBa_2Cu_3O_{7-x}$–$SrTiO_3$ thin-film samples were performed using electron energies of 5, 10 and 15 keV. The measuring procedure for 5- and 15-keV electrons was the same as for 10-keV electron irradiations. The results for a maximum electron irradiation of 3.2×10^{28} electrons m^{-2} of a Bi(2223) sample are shown in Fig. 7. The changes in elemental concentrations at the grain surfaces are normalized here to preirradiation values. It can be concluded that the degree of electron-beam induced decomposition effects is dependent on the electron energy for Bi, Ca, Sr and O only, whereas the other components such as Cu and Pb show a fairly energy-independent damage behaviour. It is noteworthy that only for

Ca does the damaging effect decrease by about 30% with increasing electron energy. However, the reason for this unexpected radiation-induced damage behaviour is not known.

Comparison of the results for 5-, 10- and 15-keV electron irradiations of $YBa_2Cu_3O_{7-x}$–$SrTiO_3$ thin-film and $YBa_2Cu_3O_{6.8}$ single-crystal samples as given in Fig. 8 indicates that the effects of radiation damage after 3.2×10^{28} electrons m^{-2} irradiation are, within experimental error, fairly independent of the electron-beam energy, in particular for thin films. For $YBa_2Cu_3O_{6.8}$ single crystals it was found that electrons of 15 keV are slightly more effective than low-energy (ca. 5-keV) electrons in inducing radiation damage, as indicated for copper and barium.

Oxygen decomposition in irradiated $YBa_2Cu_3O_{6.8}$ single crystals

Generally, the superconducting properties of $YBa_2Cu_3O_{7-x}$ superconducting systems are extremely sensitive to stoichiometric changes and in particular to the oxygen content. For example, T_c decreases with increasing x to nearly 60 K for $0.3 < x < 0.5$, and near the composition with $x \approx$ 0.65 the superconductivity disappears completely at the transition from orthorhombic to tetragonal phase symmetry. For these reasons, it seemed reasonable to study the influence of 10-keV electron irradiation on known $YBa_2Cu_3O_{6.8}$ single crystals.

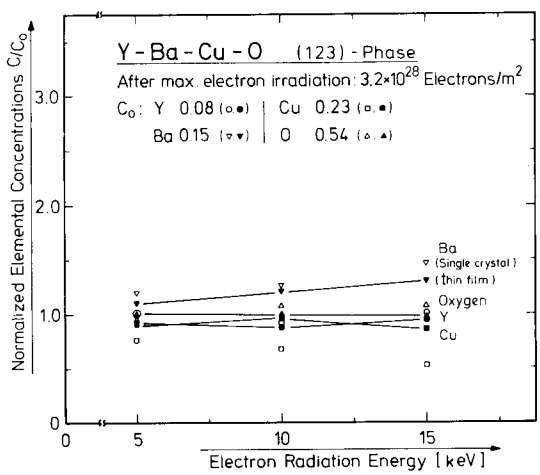

Fig. 8. Normalized surface elemental concentration values, C/C_0, of $YBa_2Cu_3O_{7-x}$–$SrTiO_3$ thin-film (solid symbols) and $YBa_2Cu_3O_{6.8}$ single-crystal (open symbols) samples vs. electron radiation energy after exposure to a maximum radiation dose of 3.2×10^{28} electrons m^{-2} (C_0 is defined as the preirradiation value).

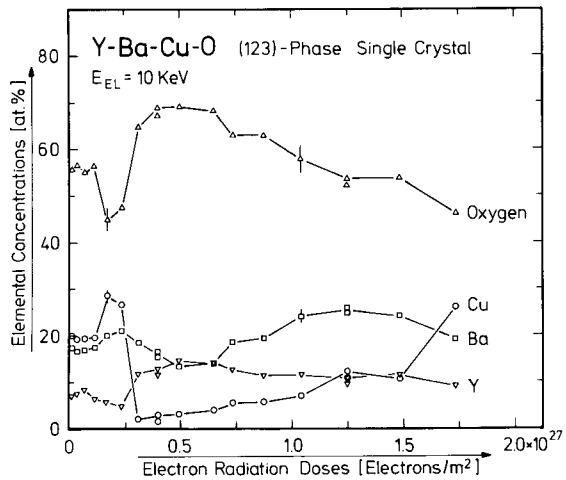

Fig. 9. Surface elemental concentrations of a $YBa_2Cu_3O_{6.8}$ single crystal vs. electron-beam radiation doses for 10-keV electrons.

Before irradiation, the state of the $YBa_2Cu_3O_{6.8}$ single-crystal sample (sample type No. 3) is characterized by a specific resistivity ρ(100 K; a–b plane) ≈ 110 $\mu\Omega$ cm, a transition temperature T_c(midpoint) = 90 K, transition widths $\Delta T_c \leqslant 2$ K and a residual resistance ratio of about 4. During electron irradiation periods, beam rastering with a raster size of 10×8 μm^2 was used to ensure the same homogeneous irradiation conditions as for the other sample types.

The radiation-induced changes in surface composition of a $YBa_2Cu_3O_{6.8}$ single crystal which were found for oxygen and other components are summarized in Fig. 9 up to a maximum radiation dose of about 1.5×10^{27} electrons m^{-2}. Electron irradiation was performed on an unsputtered a–b plane (parallel to the c-axis) to avoid surface damage by argon ions. It should be noted that because of surface contamination the starting surface composition values were slightly different from the values found in bulk measurements. Two remarkable effects which occur during irradiation are indicated in the concentration plot for

oxygen: strong changes in oxygen concentration in the low-radiation field and the tendency towards a radiation-induced annealing effect of damage at considerably higher doses ($> 1.5 \times 10^{27}$ electrons m^{-2}). As such, the oxygen concentration jumps from 55 at.% (preirradiation value at the surface) to 45 at.% at low radiation doses between about 1×10^{26} and 2×10^{26} electrons m^{-2}, followed by a rapid increase to a broad peak of oxygen concentration up to a maximum of about 68 at.%. It is interesting that after this fluctuation process the oxygen concentration decreases monotonously with increasing radiation doses to reach preirradiation values. Copper shows a similar behaviour in the opposite direction and reaches minimum concentrations of about 2 at.% at 3×10^{26} electrons m^{-2}. The components yttrium and barium also indicate fluctuations in concentrations, but with smaller amplitudes of about 6 at.%. However, all constituents of $YBa_2Cu_3O_{6.8}$ single crystals show the same tendency of an explicit damage recovery effect in the high-radiation field comparable to oxygen, that means the surface composition values reach approximately the same values as before irradiation. For an exact explanation of this observed damage recovery behaviour, further irradiation measurements are necessary to reach higher electron radiation doses.

The reason for this drastic oxygen decomposition effects presumably lies in a considerable disordering effect of Cu–O chains in the single-crystal lattice caused by a radiation-induced heating effect. Additionally, a significant increase in microcracks was observed with increasing radiation dose (see Fig. 10). This additional effect of microcracking contributes to facilitate movements of oxygen through the crystal lattice, which leads to relatively strong deviations of the oxygen stoichiometry.

The change in the oxygen content in the bulk composition was measured by depth profiling using a single-crystal sample irradiated up to a radiation dose of about 9×10^{26} electrons m^{-2}, i.e., reaching the saturation damage for oxygen. As illustrated in Fig. 11, in the case of electron-beam induced bulk damage, diffusion of liberated oxygen (and to a smaller extent also Ba and Y) to

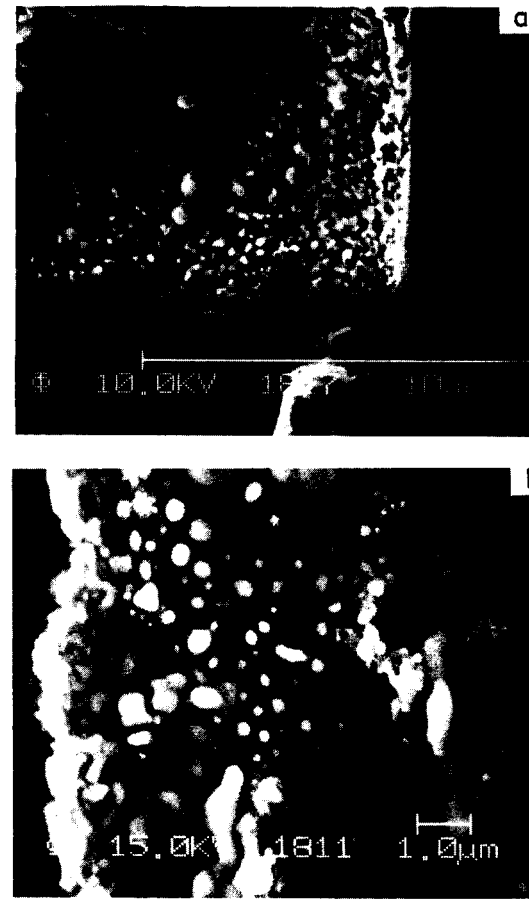

Fig. 10. SEM images of a $YBa_2Cu_3O_{6.8}$ single crystal surface after scanning 10-keV electron-beam irradiation of about 1×10^{27} electrons m^{-2} with magnifications of (a) 7500× and (b) 10000×. Typical radiation-induced microcracks are visible in detail.

near-surface regions occurs from the whole damage range due to electron-beam heating and leads to non-superconducting minor phases of Ba–O or Y–O at the single-crystal surface. In contrast, copper is driven more into the interior of the crystal. Compared with the Bi(2223)-phase superconductors, the bulk damage behaviour seems to be similar but less pronounced for $YBa_2Cu_3O_{6.8}$ single crystals.

Conclusion

The decomposition phenomena of Bi–Pb–Sr–Ca–Cu–O and Y–Ba–Cu–O superconducting

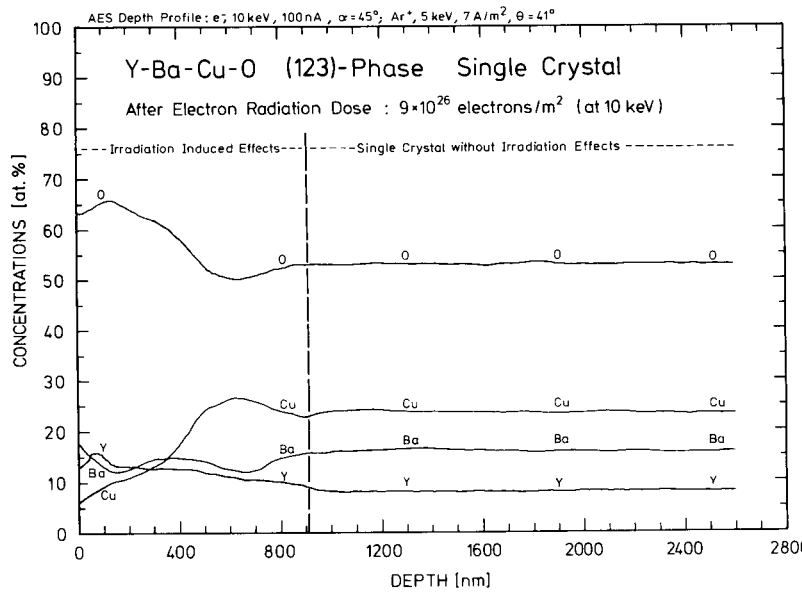

Fig. 11. Bulk decomposition effects of a $YBa_2Cu_3O_{6.8}$ single crystal after 10-keV electron-beam irradiation of about 9×10^{26} electrons m^{-2} as a function of sample depth.

systems during electron-beam irradiation have been investigated by SEM and AES. It can be concluded that Bi(2223)-phase superconductors are fairly sensitive to electron irradiation and exhibit surface and bulk decomposition effects after exposure to critical electron doses of about 5×10^{27} electrons m^{-2}. For Y–Ba–Cu–O systems, there is a significant difference in the degree of radiation damage between epitaxially grown thin films and single crystals, with larger changes induced in elemental surface and bulk concentrations in single-crystal superconductors after relatively low critical doses of about 2×10^{26} electrons m^{-2}.

The rates of elemental decomposition produced by electron-beam irradiation of both high-T_c superconducting systems depend to different extents on the electron energy, which ranges from 5 to 15 keV. Stoichiometric Bi(2223)-phase superconductors are significantly more sensitive when exposed to electron-beam irradiation with increasing electron energy than $YBa_2Cu_3O_{7-x}$–$SrTiO_3$ thin-film and, to a lesser extent, $YBa_2Cu_3O_{6.8}$ single-crystal superconductors.

Electron radiation-induced oxygen decomposition in $YBa_2Cu_3O_{6.8}$ single crystals occurs both near the surface and in the whole irradiated crystal volume. A remarkable recovery effect of the radiation surface damage is stimulated by higher electron radiation doses.

This investigation was performed as part of the Incentive Programme on High-Temperature Superconductors supported by the Belgian State–Prime Minister's Service–Science Policy Office. The authors thank Professor Dr. R. Flükiger (University of Geneva, Switzerland) and Dr. Th. Wolf for supplying some samples and for discussions. They also thank Mr. J. Pytlik for technical assistance.

References

[1] A.C. Bódi, J. Crikai, R. Pepelnik, I. Halász, I. Kirchner, Gy. Kovács, T. Porjesz and T. Träger, Physica C, 165 (1990) 83.

[2] P.H. Hor, Z.J. Huang, L. Gao, R.L. Meng, Y.Y. Xue, C.W. Chu, Y.C. Jean and J. Farmer, Mod. Phys. Lett. B, 4 (1990) 703.

[3] B. Hensel, B. Roas, S. Henke, R. Hopfengärtner, M. Lippert, J.P. Ströbel, M. Vildić and G. Saemann-Ischenko, Phys. Rev. B 42 (1990) 4135.

[4] V.F. Elesin, I.A. Esin, N.Yu. Bezrukova, M.A. Bondarenko, P.V. Brathukin, P.B. Zhilin, V.E. Zhuchkov, A.A. Ivanov, A.V. Kuznetsov, A.P. Menushenkov, A.A. Mikhailov, I.A. Rudnev and S.V. Shavkin, Supercond. Phys. Chem. Technol., 5 (1992) 515.
[5] T. Kutsukake, H. Somei, Y. Ohki, K. Nagasawa and F. Kaneko, Jpn. J. Appl. Phys., 28 (1989) L 1393.
[6] H. Küpfer, I. Apfelstedt, W. Schauer, R. Flükiger, R. Meier-Hirmer, H. Wühl and H. Scheurer, Z. Phys. B, 69 (1987) 167.
[7] A. Wisniewski, M. Baran, P. Przyslupski, P. Szymczak, A. Pajaczkowska, B. Pytel and K. Pytel, Solid State Commun., 65 (1988) 577.
[8] F.W. Clinard Jr., E.M. Foltyn, R.J. Livak, D.E. Peterson, W.A. Coghlan and L.W. Hobbs, J. Appl. Phys., 65 (1989) 5057.
[9] D.M. Parkin, Metall. Trans. A, 21 (1990) 1015.
[10] J.D. Jorgensen, B.W. Veal, A.P. Paulikas, L.J. Nowicki, G.W. Crabtree, H. Claus and W.K. Kwok, Phys. Rev. B, 41 (1990) 1863.
[11] R. Flükiger, A. Jeremie, B. Hensel, E.W. Seibt, J.Q. Xu and Y. Yamada, Adv. Cryog. Eng. (Mater.), 38 (1992) 1073.
[12] R. Flükiger, B. Hensel, A. Jeremie, M. Decroux, H. Küpfer, W. Jahn, E.W. Seibt, W. Goldacker, Y. Yamada and J.Q. Xu, Supercond. Sci. Technol., 5 (1992) S 61.
[13] E.W. Seibt, A. Jeremie and R. Flükiger, Thin Solid Films, 228 (1993) 196.
[14] Th. Wolf, W. Goldacker, B. Obst, G. Roth and R. Flükiger, J. Cryst. Growth, 96 (1989) 1010.
[15] E.W. Seibt and A. Zalar, Vuoto, 20 (1990) 399.
[16] E.W. Seibt and A. Zalar, Mater. Lett., 11 (1991) 1.
[17] L.W. Reimer, Scanning Electron Microscopy, Springer, Berlin, 1985.
[18] S. Matsui, T. Ichihashi, T. Yoshitake, S. Miura, T. Satoh and M. Mito, J. Vac. Sci. Technol. B, 8 (1990) 1771.

ELSEVIER

Analytica Chimica Acta 297 (1994) 165–178

ANALYTICA CHIMICA ACTA

Characterization of grain boundary segregation in an Fe–Si alloy

Pavel Lejček

Institute of Physics, Academy of Sciences, Na Slovance 2, 180 40 Prague 8 (Czech Republic)

Received 15th February 1993; revised manuscript received 2nd July 1993

Abstract

In studying grain boundary segregation by Auger electron spectroscopy, several questions arise during data evaluation. The most important ones are: (1) How are segregants distributed between the two fracture surfaces which expose the boundary for measurements? (2) What is the best way to extract information about chemical composition from Auger spectra? (3) Is chemical composition the relevant characteristic of grain boundary segregation? These issues are discussed in detail, using solute segregation at numerous well-characterized grain boundaries in Fe–Si alloy bicrystals as a model system. It is shown that segregants are equally distributed between the two fracture surfaces for symmetrical grain boundaries whereas uneven distribution is observed for asymmetrical grain boundaries. Both types of segregant distribution can be described on the basis of a zig-zag intergranular fracturing. The atomic composition of the grain boundary is evaluated from measured Auger spectra using a method which accounts for the solute depth distribution, Auger electron attenuation and primary electron backscattering. Contradictory solute concentration dependences on orientation suggest that the chemical composition of grain boundaries in multicomponent systems may not be representative of interfacial segregation. It is shown that the grain boundary segregation anisotropy can be clearly and directly characterized by segregation enthalpies.

Keywords: Surface techniques; Auger electron spectroscopy; Bicrystals; Grain boundary segregation; Metal alloys

Grain boundaries (GBs) in polycrystalline materials are interfaces between mutually misoriented crystals, connected by low-energy arrangements of atoms. From the viewpoint of the crystal lattice, they can be considered as planar defects which behave differently when compared to the bulk crystal. Since GBs usually form a three-dimensional network, their behaviour strongly affects material properties as a whole. One important phenomenon in this respect is GB segregation. Chemical composition differences between these regions and the bulk change the type and strength of chemical bonds at GBs and therefore control the mechanical properties of materials such as creep rupture life and brittleness [1]. Thus, with respect to materials properties and technological applications, it is very important to be aware of the nature and extent of GB segregation. Since GB segregation represents the interaction between point defects (solute atoms) and

Correspondence to: P. Lejček, Institute of Physics, Academy of Sciences, Na Slovance 2, 180 40 Prague 8 (Czech Republic).

SSDI 0003-2670(93)E0388-N

planar defects (GBs) [2], the interaction (i.e. segregation) energy for a chosen binary system will depend on the actual position of the solute atom in the GB as proposed by Hashimoto et al. [3]. Due to differences in atomic structure, this energy will also vary between individual GBs, leading to GB segregation anisotropy (for a review see e.g. [4]). In multicomponent systems, however, the interaction between chemically distinct atoms and not only the GB but also each other must be taken into account. As a result, segregation of a solute at a chosen GB can be qualitatively different from that in the pure binary alloy (e.g. [5,6]). Thus the orientation dependence of GB concentration for the solute in a multicomponent system can be modified to such an extent that it does not represent realistically the behaviour of individual GBs [7,8].

Consistent with the GB structure, equilibrium segregation is confined to one or a few atomic layers parallel to the GB [9]. These strongly localized differences in chemical composition can be measured using techniques with "atomic" resolution in at least one dimension. A review of methods used to study GB segregation is given, e.g. by Joshi [10].

Auger electron spectroscopy has been widely used to analyse GB segregation both qualitatively and quantitatively. Due to its high depth resolution (several atomic layers), it has been used to study fresh fracture surfaces (FSs) obtained by in situ intergranular fracture. In this case, the question arises of how the species, originally segregated at the GB, are distributed between the two FSs. Since usually one part of a broken sample is retained for measurements, there are only few experiments which compare segregant concentration on both specimen halves [11–14]. However, for quantitative determination of GB segregation it is necessary to know how the segregants are distributed between the FSs after intergranular separation.

To determine the chemical composition of a GB, it is necessary to evaluate atomic concentrations from the Auger spectra. However, there is presently no standard procedure for this conversion. The best way to calibrate the concentration scale is using similar standards of known composition and then interpolating between the results, as described, e.g. by Grabke et al. [15]. If no suitable standards are available, GB composition can be determined from Auger spectra by accounting for the process of Auger electron emission and assuming a particular solute depth distribution below the FS [16].

The aim of the present paper is to characterize

Table 1
Enthalpies (ΔH_i°) and entropies (ΔS_i) of segregation of Si, P and C at various symmetrical and asymmetrical tilt GBs in an Fe–3.5 at% Si alloy [7,8,17,18] (model 1 [36])

Grain boundary	ΔH_i° (kJ mol^{-1})			ΔS_i (J mol^{-1} K^{-1})		
	Si	P	C	Si	P	C
70.5°[100],{112}	−3.0	−7.9		−3.8	+42.7	
18.9°[100],{016}	−21	−28	−51	−20	+20	0
22.6°[100],{015}	−14	−15	−43	−11	+39	+7
28.1°[100],{014}	−14	−33	−51	−9	+20	+2
36.9°[100],{013}	−8.2	−12.5	−41	−3	+45.9	+12
36.9°[100],(018)/(04$\bar{7}$)	−14	−30	−50	−11	+21	+3
36.9°[100],(001/03$\bar{4}$)	−11	−23	−45	−5	+31	+7
36.9°[100],(0$\bar{1}$7)/(01$\bar{1}$)	−8.0	−13.5	−36	−3.6	+40.1	+14
36.9°[100],(0 $\bar{3}$ 11)/(09$\bar{7}$)	−12	−30	−48	−5	+23	+3
45.2°[100],{0 5 12}	−17	−34	−50	−13	+20	+7
50.0°[100],{0 7 15}	−11	−29	−45	−3	+26	+7
53.1°[100],{012}	−5.5	−10.3	−35.2	−0.9	+43.0	+12
58.1°[100],{059}	−13	−32	−48	−6	+21	+4
64.0°[100],{058}	−17	−35	−53	−12	+18	−1

GB segregation in multicomponent systems. By way of illustration, the following questions will be considered for well-characterized GBs in an Fe–Si alloy containing traces of phosphorus and carbon [7,8,17,18]: (1) How are segregated species distributed between the two FSs? (2) How are Auger spectra related to chemical composition? (3) Is the chemical composition the relevant characteristic of GB segregation?

1. Experimental

A study of solute segregation at selected GBs was performed using carefully oriented bicrystalline samples. The bicrystals of an Fe–Si model alloy (3.55 at% Si, 0.0089 at% P, 0.014 at% C and 0.007 at% O) were grown by the floating-zone technique. To establish the GB orientation and the desired misorientation between the crystals, two semicylindrical single-crystalline pieces were joined together as to form the bicrystal seed for growth [19]. The bicrystals were cylinders with a diameter of 13 mm and a length of 50 mm. The planar GBs were parallel to the cylinder axis. All bicrystals were of tilt character with the crystallography described by the nominal angles and corresponding GB orientations given in Table 1. The deviation of the real GB orientation, checked by the Laue x-ray back-reflection technique, was less than $\pm 1°$ with respect to the nominal orientation.

From the bicrystals, cylindrical samples for Auger electron spectroscopy were machined such that the GB plane was perpendicular to the sample axis. To facilitate the fracture necessary to expose the GB for Auger electron spectroscopy analysis, a circular notch was made at the GB position. Notched samples were chemically polished in a mixture of HF (40%)–H_2O_2 (30%)–H_2O (8:100:17, v/v/v) to remove the layer damaged by machining. The samples were then annealed in vacuum ($\approx 10^{-3}$ Pa of Ar) at a constant temperature of 773, 873, 873, 1073 or 1173 K for 168, 96, 48, 24 or 24 h, respectively. These times are sufficient to reach equilibrium segregation at those temperatures [5,17]. To preserve the equilibrium state corresponding to each temperature, the samples were water-quenched after annealing.

Individual samples were fractured in situ under ultra high vacuum ($< 10^{-7}$ Pa) by impact bending in a PHI 600 Multiprobe (Perkin-Elmer) at a temperature of about 170 K, at which the material is brittle. Immediately after fracture, Auger spectra of the FS were collected. A primary electron beam (energy of 10 keV and current of 350 nA) with a diameter of 1 μm was used for point analysis. To check the extent of segregation, depth profiles were measured during Ar^+ ion sputtering (voltage 3 kV, sputtered area

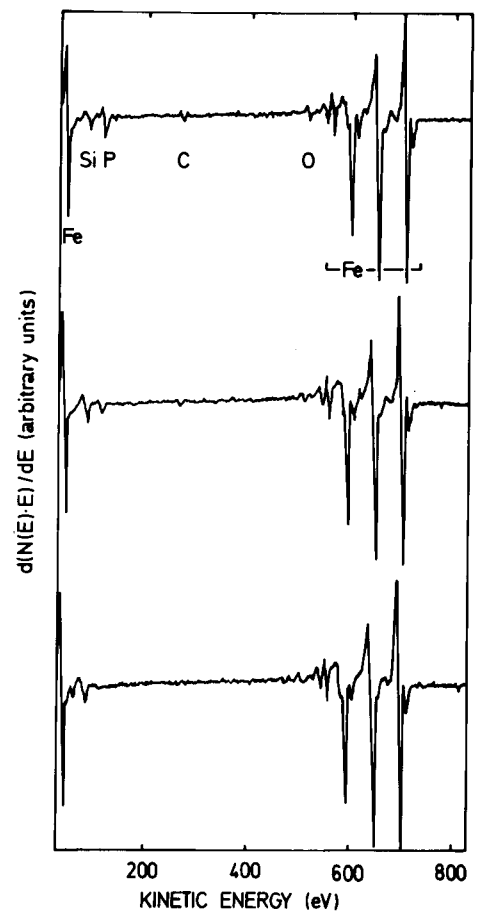

Fig. 1. Typical Auger spectra from a fracture surface of the {013} symmetrical grain boundary in [100] tilt bicrystal of an Fe–3.5 at% Si for temperatures of 773 K (upper spectrum) and 973 K (middle spectrum). For comparison, the Auger spectrum of a transcrystalline cleavage surface is also shown (lower spectrum).

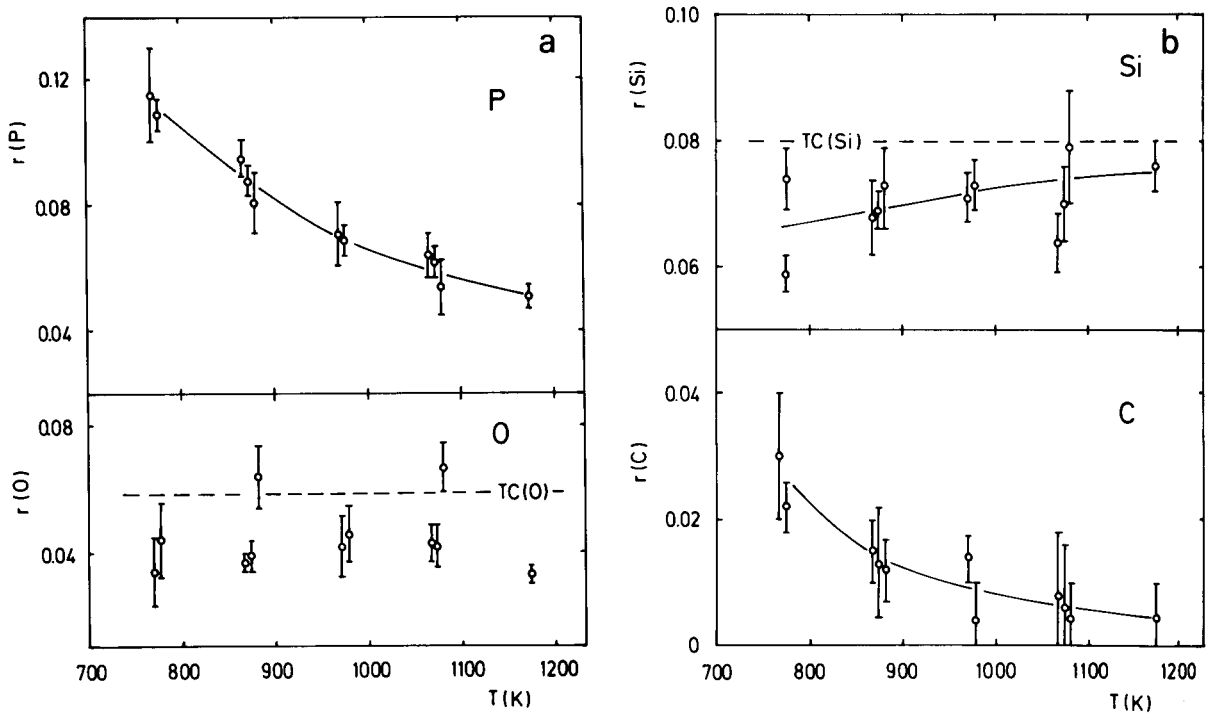

Fig. 2. Temperature dependence of relative peak height $r(i)$ for (a) phosphorus and oxygen and (b) silicon and carbon measured at the {013} symmetrical tilt grain boundary. The average values of TC(Si) and TC(O) found at transcrystalline cleavage surfaces are also shown.

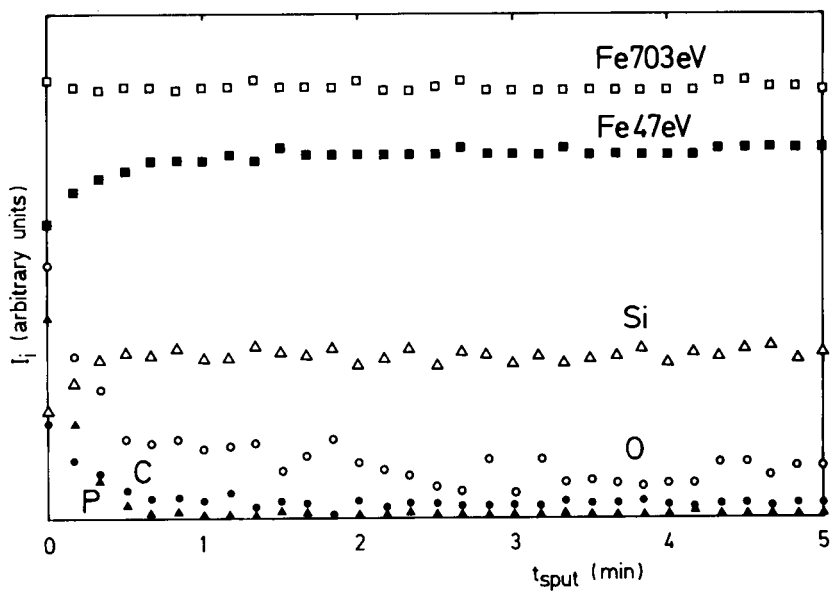

Fig. 3. Depth distribution of individual solutes in the vicinity of the {013} grain boundary measured by Auger electron spectroscopy during Ar^+ ion sputtering (sputtering rate 1 nm min^{-1}).

about 3×3 mm^2, analysed area 7×7 μm^2). The sputtering rate was referenced to Ta_2O_5 samples of known thickness.

2. Results and discussion

The Auger electron spectroscopy measurements revealed the presence of silicon, phosphorus, carbon and oxygen at individual FSs. As seen in Fig. 1, the peaks of Si (92), P (120), C (272) and O (510 eV) are distinct from the peaks of the matrix iron (47, 598, 651 and 703 eV) in derivative Auger electron spectra. From Fig. 1 it is also apparent that the Auger peak-to-peak heights (APPHs) of individual elements which reflect their concentrations at the fracture surface, change with temperature. From the spectra, the APPHs of individual elements i were measured and the relative peak heights r(i) were determined as

$$r(\mathrm{i}) = \mathrm{APPH(i)}/\mathrm{APPH(Fe\ 703\ eV)} \quad (1)$$

For each sample and element, average values of r(i) were calculated. An example of the temperature dependence of r(i) is shown in Fig. 2. It is apparent that silicon, phosphorus and carbon segregate at the GBs, as shown by the clear temperature dependence of the corresponding r(i). On the other hand, values of r(O) are widely scattered and exhibit no temperature dependence. Comparison of r(O) with the values measured at transcrystalline cleavage surfaces [TC(O) in Fig. 2] confirms that the presence of oxygen at FSs is mainly caused by contamination from residual gases in the apparatus (Fig. 1). The solute depth distribution shows that segregation effects are confined to a narrow zone parallel to the FS (Fig. 3). Usually, the segregation effects completely disappear after removing a layer of the thickness ranging between 0.4 and 0.6 nm as calibrated by means of Ta_2O_5 standards. The oxygen signal decreases more slowly due to simultaneous contamination during sputtering.

Grain boundary fracture

A low-temperature brittle intercrystalline fracture separates a bicrystal into two single-crystalline parts and produces two FSs from the original GB. Simultaneously, the solute atoms segregated at the GB are distributed between these FSs. Since only one part of the bicrystal (i.e. one FS) is usually available for Auger electron spectroscopy measurements, a model has to be selected which describes the distribution of segregants during fracture. A theoretical analysis of the bond strength in the case of phosphorus segregation in α-iron shows that the existence of strong Fe–P bonds weakens the neighboring Fe–Fe bonds where the separation takes place [20–22]. Therefore it is assumed that the fracture path zig-zags across the boundary and that the segregated species are distributed equally on both FSs [20]. This assumption seems quite reasonable for the case of symmetrical GBs. In the case of asymmetrical GBs, however, weaker bonds may be unevenly spread between the two sides of the boundary core [23]. Thus, different amounts of segregation would be measured at individual FSs.

Only rarely is it possible to compare the results of Auger electron spectroscopy measurements on matching FSs. By measuring phosphorus segregation at numerous pairs of corresponding facets on matching FSs of polycrystalline tungsten, Hofmann [4] proved that phosphorus is equally distributed between both FSs. A similar conclusion was drawn from the results reported by Viefhaus et al. [11] for phosphorus segregation in α-iron. On the other hand, Menyhard and McMahon [12] found markedly different phosphorus concentrations on matching FSs of polycrystalline iron and also on the two sides of a separated symmetrical {013} tilt GB in an Fe–Si alloy [13,14]. Simultaneously, a very inhomogeneous distribution of phosphorus over relatively large areas of one FS was detected [13,14]. Model calculation suggested that the fracture path did not zig-zag through the GB core but passed parallel to the GB at a distance of 1–2 atomic layers from the core over a relatively large area. After meeting a defect at the GB, such as deformation twin from plastic deformation before cracking, the fracture can jump onto the corresponding path on the other side of this symmetrical {013} GB [13,14]. However, the samples in this study were not brought to equilibrium and therefore the region of increased phosphorus concentration was extremely wide.

In the case of equilibrium segregation, the layer with altered chemical composition was found to be very narrow. As shown by sputter depth profiling of present samples, the segregation width is one atomic layer in the GB (Fig. 3). Comparative measurements of chemical composition at FSs in numerous samples containing the same GB after identical heat treatment revealed differences between symmetrical and asymmetrical GBs. In the case of symmetrical GBs, the values of APPHs were statistically very similar (scatter usually less than 10%; Fig. 2). As documented and discussed by Briant [24] in more detail, such scatter can be expected in Auger electron spectroscopy studies of single GB segregation. Therefore, the model of zig-zag fracture at these GBs [20,21] with equal distribution of segregated atoms on the two FSs is appropriate for quantifying data in this case. On the other hand, systematic differences between the two FSs of asymmetrical GBs were found (Fig. 4). This suggests asymmetrical fracturing with uneven distribution of solutes between the FSs. These findings will be described and discussed in more detail elsewhere [25]. In this case we can also employ a generalized model of zig-zag fracturing which allows uneven solute distribution.

In principle, some differences of r(i) can arise from the electron channeling effect. According to Bennett and Viefhaus [26], an increase in all APPHs can be expected if the incident electron beam is parallel to the ⟨100⟩ crystallographic direction of the target as compared to other crystallographic directions ⟨hkl⟩. This increase is substantially higher for high-energy Fe APPH as compared to the low-energy peaks of Si, P and C (Fig. 3 in Ref. 26). As a result, lower r(i) should be expected in the former case than in the latter case as proved also by Rothman and Menyhard [27]. Such differences can reach exceptionally a value of almost 100% [26] although the scatter of about 10–16% can be usually expected as caused by the channeling effect on flat FSs [27]. In the present case, the Auger electron spectra were measured on FSs of different crystallography with the primary electron beam inclined 30° from the surface normal. Under special circumstances, the incident electron beam could be nearly parallel to

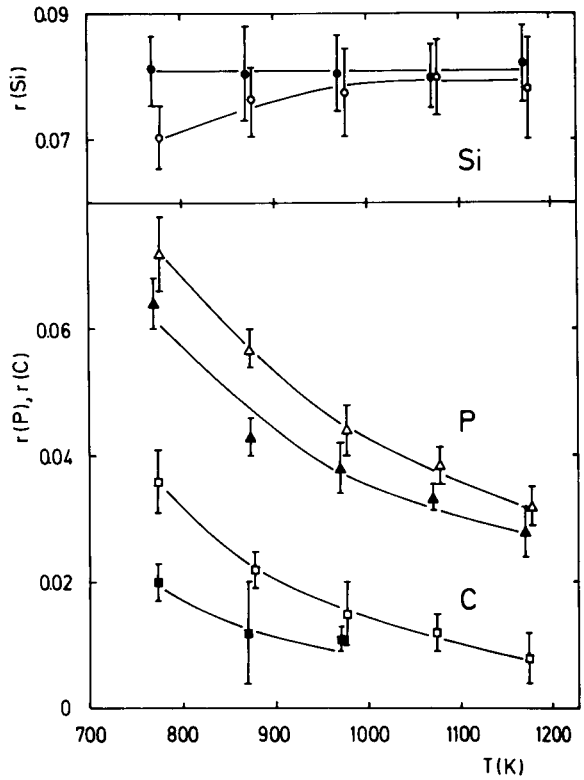

Fig. 4. Temperature dependence of relative peak height r(i) for phosphorus, silicon and carbon measured at the $(0\bar{1}7)/(01\bar{1})$ asymmetrical tilt grain boundary. Open symbols correspond to the $(01\bar{1})$ fracture surface, solid symbols to the $(0\bar{1}7)$ fracture surface.

the ⟨100⟩ crystallographic direction of our samples in the case of the {012}, {059} and {058} symmetrical GBs, and the {018}/{047} asymmetrical GB. Since the samples were mounted randomly into the Auger electron spectroscopy sample holder, different crystallographic directions were parallel to the incident beam in individual cases. Nevertheless, the scatter of the data corresponding to a given FS at a given temperature was always less than 10% considered as a limiting scatter for single surface measurements [24]. As mentioned above, large differences exist between different FSs of asymmetrical GBs. If the electron channeling would be responsible for the differences of r(i), not only r(P) and r(C) but even r(Si) have to be higher for one fracture surface as compared to the other one. However, an opposite behaviour was found experimentally

(e.g. Fig. 4). Therefore, we can conclude that electron channeling was not effective in our measurements and the differences found at different FSs of asymmetrical GBs can be fully ascribed to an uneven segregant distribution during the fracture.

Let us consider a bicrystal with a segregated GB, one atomic monolayer thick between crystals I and II (Fig. 5a). During intergranular separation, the fracture path is assumed to zig-zag through the GB and segregated species are assumed to be distributed between both FSs. In general, the fracture path will oscillate between both sides of the GB layer so that $\delta_i \cdot 100\%$ of segregated solute i will remain at the FS(I) of the grain I and the rest $(1-\delta_i)\cdot 100\%$ at the other FS(II). Then the atomic densities $N_i^{FS(I)}$ and $N_i^{FS(II)}$ of an element i at the FS(I) and FS(II), respectively, are combinations of atomic densities at the GB and in the bulk, N_i^{GB} and N_i^{B}, respectively (Fig. 5b), as

$$N_i^{FS(I)} = \delta_i N_i^{GB} + (1-\delta_i) N_i^{B} \quad (2a)$$

and

$$N_i^{FS(II)} = (1-\delta_i) N_i^{GB} + \delta_i N_i^{B} \quad (2b)$$

Thus, the real atomic density of i at the GB can be determined from the values $N_i^{FS(I)}$, $N_i^{FS(II)}$ and N_i^{B} as

$$N_i^{GB} = \left(N_i^{FS(I)} + N_i^{FS(II)}\right) - N_i^{B} \quad (3a)$$

In the case of symmetrical GB, $N_i^{FS(I)} = N_i^{FS(II)} = N_i^{FS}$ and Eq. 3a can be simplified to

$$N_i^{GB} = 2N_i^{FS} - N_i^{B} \quad (3b)$$

Eqs. 3a and b serve as the basis for determining the composition of asymmetrical and symmetrical GBs, respectively, from the data measured at FSs.

Grain boundary chemical composition

Recently, methods which have been used to determine chemical composition from individual APPHs in derivative Auger electron spectroscopy spectra were reviewed [16]. An analysis of the Auger electron emission process showed that it is possible to express the Auger electron current I_i at the surface by means of the current $I_i(d)$ measured at another surface parallel to the original one in the distance d as [16]

$$I_i = K_i R(E_i, \alpha) \int_0^d N_i(z) \exp[-z/\lambda(E_i, \phi)]\, dz + I_i(d) \exp[-d/\lambda(E_i, \phi)] \quad (4)$$

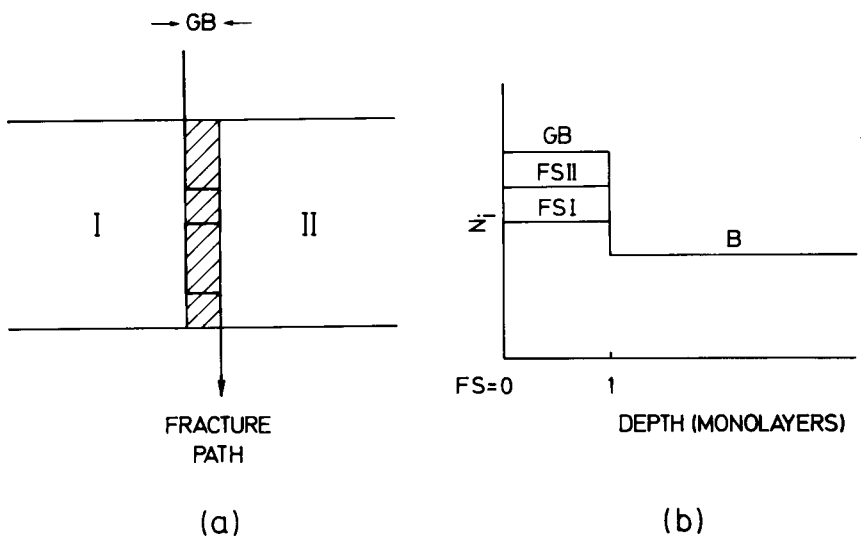

Fig. 5. Schematic representation of (a) intergranular separation of a bicrystal by a zig-zag fracture path and (b) atomic density of a solute N_i below the fracture surface FS and the grain boundary GB (see text for details).

In Eq. 4, K_i is a factor containing the ionization cross section of primary electrons with the energy E_p, the primary electron beam current and the parameters of the spectrometer. $R(E_i, \alpha)$ is the backscattering term which depends on both the matrix M and the energy E_i of Auger electrons of element i, with the angle α between the surface normal and the primary electron beam. $N_i(z)$ is the atomic density of element i at depth z from the surface. $\lambda(E_i, \phi)$ denotes the product $\lambda(E_i) \cdot \cos \phi$ where $\lambda(E_i)$ is the attenuation length of Auger electrons in the matrix M and ϕ is the angle of emission of Auger electrons to the surface normal. Assuming a homogeneous distribution of i in individual monolayers, i.e. $N_i(z) =$ constant for $0 \le z \le d$, we can express the atomic density N_i of element i in the top atomic layer of matrix M as

$$N_i = \frac{1}{K_i \lambda(E_i, \phi) R(E_i, \alpha)} \cdot \frac{I_i - I_i(d) \exp[-d/\lambda(E_i, \phi)]}{1 - \exp[-d/\lambda(E_i, \phi)]} \quad (5)$$

Since for a bulk standard s (pure element i), $N_i^s(z) = N_i^s =$ constant for each z we can write

$$N_i^s = I_i^s / [K_i^s \lambda^s(E_i, \phi) R^s(E_i, \alpha)] \quad (6)$$

Supposing $K_i^s \approx K_i$ we can rewrite Eq. 5 as

$$N_i = F_i \frac{I_i - I_i(d) \exp[-d/\lambda(E_i, \phi)]}{1 - \exp[-d/\lambda(E_i, \phi)]} \quad (7)$$

where [16]

$$F_i = [N_i^s \lambda^s(E_i, \phi) R^s(E_i, \alpha)] / [I_i^s \lambda(E_i, \phi) R(E_i, \alpha)] \quad (8)$$

Using Eqs. 3a and b we can determine the atomic density of i at a symmetrical GB as

$$N_i^{GB} = F_i \frac{2I_i^{FS} - I_i^B\{1 + \exp[-d/\lambda(E_i, \phi)]\}}{1 - \exp[-d/\lambda(E_i, \phi)]} \quad (9a)$$

assuming $I_i = I_i^{FS}$ and $I_i(d) = I_i(2d) = I_i^B$. For an asymmetrical GB,

$$N_i^{GB} = F_i\left(I_i^{FS(I)} + I_i^{FS(II)} - I_i^B\{1 + \exp[-d/\lambda(E_i, \phi)]\}\right) / (1 - \exp[-d/\lambda(E_i, \phi)]) \quad (9b)$$

which includes the different Auger electron currents at FS(I) and FS(II). The atomic fraction of the element i at the GB of the alloy M is defined as

$$X_i^{GB} = N_i^{GB} / \sum_j N_j^{GB} \quad (10)$$

In practice, the measured APPHs and relative sensitivity factors [28] can be substituted directly by the currents I_i and I_i^s, respectively, in Eqs. 8–10 to determine the composition of individual grain boundaries. The attenuation lengths of individual elements in matrix M and standard s can be estimated by [29]

$$\lambda(E_i) = a\left[538/E_i^2 + 0.41(aE_i)^{1/2}\right] \quad (11)$$

where a (in nm) is the average atom size in matrix M or the atom size of standard s.

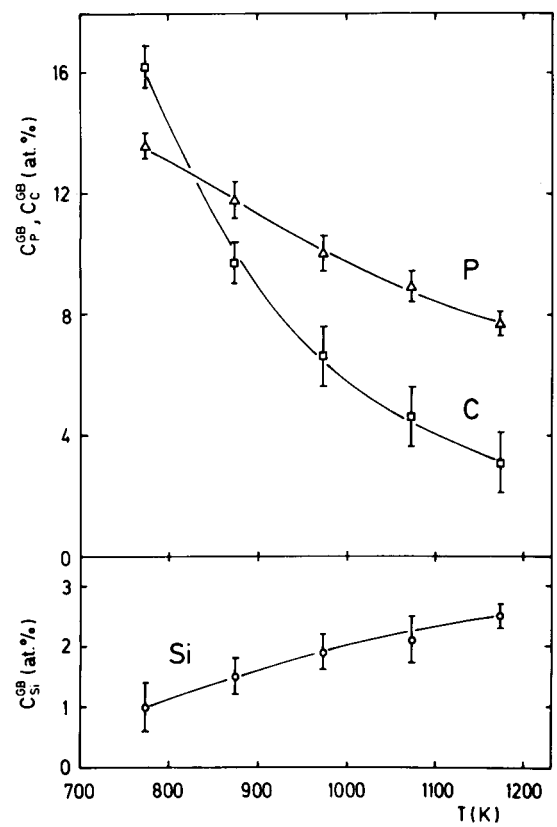

Fig. 6. Chemical composition ($C_i^{GB} = 100 X_i^{GB}$) of the 36.9°[100], {013} symmetrical grain boundary at different temperatures.

Backscattering factors $R(E_i, \alpha)$ can be evaluated by [30]

$$R(E_i, \alpha = 30°) = \left[0.462 - 0.777(Z)^{0.2}\right](E_p/E_i)^{-0.32} + 1.15(Z)^{0.2} - 0.05 \quad (12)$$

where Z is the mean atomic number of matrix M or the atomic number of standard s.

According to Eqs. 8–10 the GB composition can be determined. Since the Si 92 eV peak, which is used for determining the GB concentration of Si, overlaps with a small Fe peak at 86 eV, a calibration was applied in this case. The value $r(\mathrm{Si}) \simeq 0.080$ has been measured at both transcrystalline cleavage surfaces and FSs after sufficient sputtering to completely remove all segregation effects. Both cases represent the bulk material. However, the value $r(\mathrm{Si}) = 0.054$ applied in Eqs. 8–10 for the bulk material ($I_i^{FS} = I_i^B$) corresponds to the silicon bulk atomic fraction $X_{Si} = 0.0355$. Thus, the measured values of r(Si) were reduced for quantification of the Auger data on the basis of this difference. Moreover, corrections of carbon peaks on FS contamination were made in individual cases in comparison to its content at transcrystalline cleavage areas. In the case of very small measured APPHs (P or C) the average value of the background level was taken into account [17]. In this way, the composition of individual GBs was determined. For example, the temperature dependence of the chemical composition of the 36.9°[100], {013} symmetrical GB is shown in Fig. 6.

Thermodynamic parameters of grain boundary segregation

The chemical composition of GBs is usually employed to characterize GB segregation in particular systems (e.g. [1]). Many phenomena influencing the GB composition in various systems have been studied [31], e.g. the effect of the solid solubility limit [1], the effect of an additional element and of temperature [32], and the effect of GB orientation [4,9]. Nevertheless, some contradictory results have been obtained. For example, a practically constant oxygen concentration was found at all high angle [100] symmetrical tilt

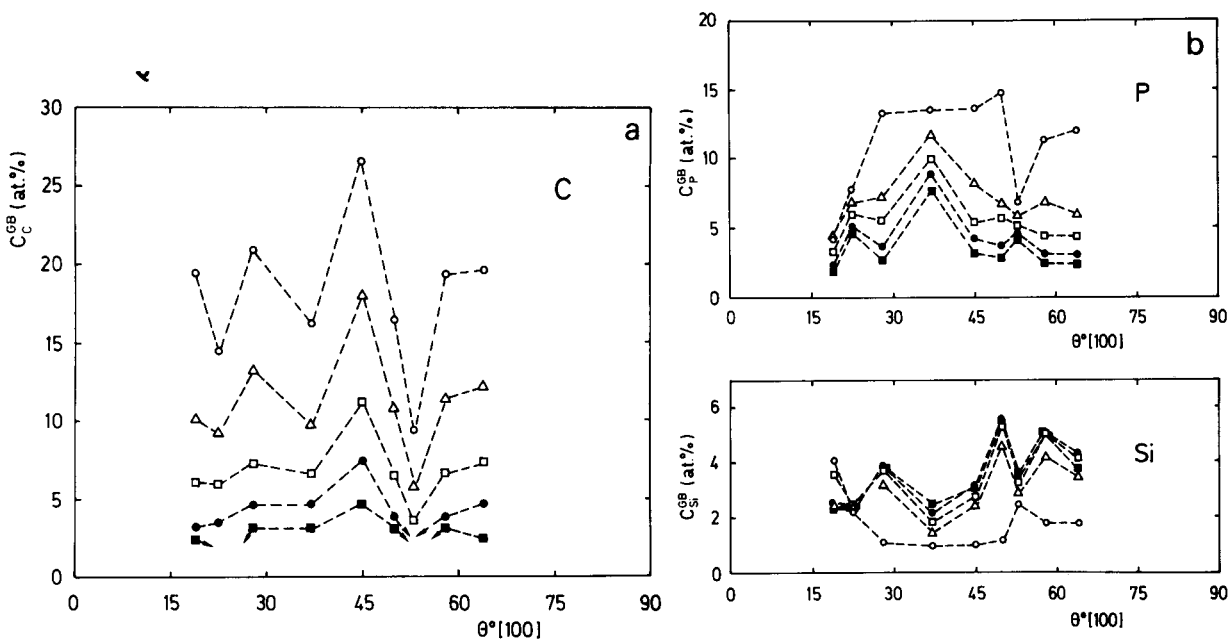

Fig. 7. Grain boundary concentration dependence for (a) carbon and (b) phosphorus and silicon on the misorientation angle θ of both crystals in [100] symmetrical tilt bicrystals of an Fe–3.5 at% Si alloy. (○) 773, (△) 873, (□) 973, (●) 1073 and (■) 1173 K.

GBs of molybdenum [33] whereas crystal misorientations in the range 37°–50° exhibited a broad minimum of Bi segregation at [100] tilt GBs of Cu [34]. On the other hand, maxima of Si segregation were recently observed at the 36.9°[100], {013}, 53.1°[100], {012} and 67.4°[100], {023} symmetrical tilt GBs of a Cr–Ni stainless steel [35]. Obviously, it is not possible to drawn any general conclusions about the anisotropy of GB segregation from these findings [33–35].

The orientation-dependent chemical composition of various [100] symmetrical tilt GBs in the Fe–Si alloy under consideration is also complex (Fig. 7). We can see in Fig. 7 that the GB segregation is anisotropic. In the case of carbon, the minima of segregation correspond to the 22.6°[100], {015}, 36.9°[100], {013}, and 53.1°[100], {012} GBs. The carbon content at GBs generally decreases with temperature and the differences between individual GBs also decrease. In the case of phosporus, the only minimum appears at the {102} GB at 773 K, but the character of the orientation dependence changes qualitatively with increasing temperature. The silicon GB concentration dependence on orientation is more complicated. The amount of silicon at GBs generally increases with increasing temperature, albeit not monotonically. Since the bulk content of silicon in the alloy was 3.55 at%, in many cases a depletion of silicon occurs. This has also been confirmed in the depth distribution of the solute (Fig. 3). The behaviour of individual segregants at the GBs results from the complex effects of site competition and mutual interaction between individual solutes in the multicomponent system [6,36].

From the experimental evidence it is obvious that the orientation dependence of GB composition at a fixed temperature is not sufficient to describe the GB segregation anisotropy. Such a representation may be misleading, particularly in the case of high solute concentrations (i.e. near to the solubility limit) and/or in multicomponent systems. From this perspective, the segregation enthalpy is clearly the fundamental parameter for describing GB segregation anisotropy.

To determine the values of thermodynamic parameters of GB segregation, Guttmann's theory of segregation in multicomponent systems [36] was employed. The simplest model is based on regular behaviour of all components (model 1 in [36]) with the GB atomic fraction X_i^{GB} of segregant i given by

$$\frac{X_i^{GB}}{X^\circ - \sum_{j \neq Fe} X_j^{GB}} = \frac{X_i}{1 - \sum_{j \neq Fe} X_j} \exp[-\Delta G_i/RT] \tag{13}$$

where

$$\Delta G_i = \Delta H_i^\circ - T\Delta S_i - 2\alpha_{Fe-i}\left(X_i^{GB} - X_i\right) + \sum_{j \neq Fe,i} \alpha'_{ij}\left(X_j^{GB} - X_j\right) \tag{14}$$

X° is the segregant atom fraction in the GB layer at saturation, X_i is the bulk atomic fraction of element i, ΔH_i° is the molar segregation enthalpy in the binary Fe–i system and ΔS_i is the segregation entropy term, α_{Fe-i} and α'_{ij} are the Fe–i interaction coefficient in the binary regular solution (Fowler term) and the i–j interaction coefficient in an Fe matrix, respectively.

One of the assumptions in this model is that the components only occupy lattice sites. In the system Fe–Si(P, C) this assumption is not valid because carbon occupies interstitial positions. However, an extended model which includes two "sublattices" can be used (model 2 in [36]). According to this model, Eq. 13 is still valid for the substitutional solutes P and Si, but it is modified for interstitial carbon as

$$\frac{X_C^{GB}}{a_I - X_C^{GB}} = \frac{X_C}{a_I - X_C} \exp[-\Delta G_C/RT] \tag{15}$$

where a_I is the interstitial site ratio in the lattice. For the *bcc* lattice in which C atoms occupy octahedral interstitial sites, the value of a_I is 0.6. Similarly, Eq. 13 can be rewritten in model 2 as

$$\Delta G_i = \Delta H_i^\circ - T\Delta S_i - 2q_{Fe-i} \times \left(\frac{X_i^{GB}}{1 - X_C^{GB}} - \frac{X_i}{1 - X_C}\right) + \sum q'_{ij}\left(\frac{X_j^{GB}}{1 - X_C^{GB}} - \frac{X_j}{1 - X_C}\right) \tag{16}$$

Here, the interaction coefficients α_{Fe-i} and α'_{ij} of Eq. 14 are replaced by q_{Fe-i} and q'_{ij}, respectively.

The evaluation of segregation parameters (i.e. ΔH_i°, ΔS_i and interaction coefficients) is described in more detail in [17,18]. Assuming Fe–Si and Fe–P interactions to be negligible [37] and $X^\circ = 1$, the value $\alpha'_{SiP} = +92 \pm 6$ kJ mol^{-1} was determined by a least-squares fit to results for the {112} coherent twin GB at temperature where no C segregation was detected [17]. From measurements at the {013} and {012} symmetrical GBs, the values $\alpha_{FeC} = -5 \pm 5$ kJ mol^{-1}, $\alpha'_{SiC} = -3 \pm 9$ kJ mol^{-1} and $\alpha'_{PC} = +7 \pm 2.5$ kJ mol^{-1} were obtained from model 1, and $q_{FeC} = -2 \pm 3$ kJ mol^{-1}, $q'_{SiC} = -15 \pm 5$ kJ mol^{-1} and $q'_{PC} = +7 \pm 1.5$ kJ mol^{-1} from model 2 [18]. Using these parameters, the segregation enthalpies and entropies of numerous tilt GBs were determined. These values are listed in Tables 1 and 2. Comparison of corresponding values of ΔH_i° and ΔS_i determined by models 1 and 2 (Tables 1 and 2, respectively) shows only small differences of the order of measurement errors.

The values of the thermodynamic parameters of GB segregation listed in Tables 1 and 2 were determined according to Eqs. 13 and 14, and Eqs. 13, 15 and 16, respectively, with a saturation coverage $X^\circ = 1$. Realistically this value, corresponding to a complete monolayer of segregant(s) at the boundary, seems improbable. Unfortunately, it is not possible to determine the saturation coverage for each GB experimentally, e.g. by low-energy electron diffraction (LEED), as on free surfaces [37]. During intergranular fracture plastic deformation occurs and therefore some strain remains at the FSs after separation which would distort the LEED measurements. Some model calculations were done for values of $X^\circ < 1$ in Eq. 13. The results were tested by the sum of squares σ_G of differences between calculated and experimental values of segregation free energies ΔG_{ij}^{calc} and ΔG_{ij}^{exp}, respectively, for all three elements i in various samples j

$$\sigma_G = \left\{ \left[\sum_i \sum_j^N \left(\Delta G_{ij}^{calc} - \Delta G_{ij}^{exp} \right)^2 \right] / (3N - 1) \right\} \quad (17)$$

where N is the number of experimental data. The results show that the lowest value of σ_G is achieved for $X^\circ = 1$ [18].

Although an agreement can be found between the value $\Delta S_P^\circ = 21.5$ J mol^{-1} K^{-1} [38] and values of segregation entropy for general GBs (Tables 1 and 2), ΔS_i in Eqs. 14 and 16 may not

Table 2
Enthalpies (ΔH_i°) and entropies (ΔS_i) of segregation of Si, P and C at various symmetrical and asymmetrical tilt GBs in an Fe–3.5 at% Si alloy [7,8,17,18] (model 2 [36])

Grain boundary	ΔH_i° (kJ mol^{-1})			ΔS_i (J mol^{-1} K^{-1})		
	Si	P	C	Si	P	C
70.5°[100],{112}	−3.0	−7.9		−3.8	+42.7	
18.9°[100],{016}	−16	−31	−49	−15	−17	+1
22.6°[100],{015}	−12	−16	−43	−9	+38	+7
28.1°[100],{014}	−14	−35	−50	−9	+19	+2
36.9°[100],{013}	−8.5	−13.3	−40	−3	+45.2	+12
36.9°[100],(018)/(04$\bar{7}$)	−10	−32	−50	−8	+19	+3
36.9°[100],(001)/(03$\bar{4}$)	−9	−25	−44	−3	+29	+6
36.9°[100],(0$\bar{1}$7)/(01$\bar{1}$)	−6.1	−14.5	−36	−2.2	+39.3	+14
36.9°[100],(0 $\bar{3}$ 11)/(09$\bar{7}$)	−11	−32	−48	−5	+21	+3
45.2°[100],{0 5 12}	−17	−37	−51	−13	+18	+6
50.0°[100],{0 7 15}	−12	−31	−45	−3	+25	+6
53.1°[100],{012}	−4.1	−10.9	−35.0	+0.2	+42.5	+12
58.1°[100],{059}	−12	−34	−48	−5	+20	+4
64.0°[100],{058}	−16	−37	−53	−11	+16	−1

represent segregation entropy in pure binary system Fe–i. Eqs. 14 and 16 were derived assuming only ideal segregation entropy [36]. Nevertheless, the entropy term in a real system should also contain an excess contribution $\Delta\bar{S}_i^E$ which may be responsible for substantial differences of ΔS_i from that measured in pure binary system Fe–i. Unfortunately, no theory of $\Delta\bar{S}_i^E$ has been developed till now and thus, it is not possible to assess the excess contribution to ΔS_i in the present quaternary system. From this point of view, ΔS_i given in Tables 1 and 2 can serve only as fitting parameters with little information concerning Fe–i binary systems.

On the other hand, an excess contribution was clearly extracted from the enthalpy term in Eqs. 14 and 16 [36] and therefore ΔH_i° represent segregation enthalpies for Fe–i binary alloys. Some values of ΔH_i° in iron alloys are available in the literature. However, these data were obtained from measurements of the chemical composition at various GBs with unknown orientation parameters in fractured polycrystalline materials. Therefore, they do not represent segregation enthalpies for specific grain boundaries, but only average values determined from the temperature dependence for all GBs present [39,40]. Nevertheless, it may be interesting to compare these data with those determined in our work, since the general GBs are most susceptible to intergranular fracture [39,41,42]. Therefore, these GBs should dominate contributions to the values in the literature. For example, three very different values of ΔH_C° have been reported: -37 kJ mol^{-1} [43], -57 kJ mol^{-1} [37] and -76 kJ mol^{-1} [38]. Among general GBs the maximum negative value for ΔH_C° in Tables 1 and 2 is -53 kJ mol^{-1}, which corresponds to the most recent value -57 kJ mol^{-1} [37]. The value $\Delta H_{Si}^\circ = -17$ kJ mol^{-1} used as a best fit for segregation data in [44], and the values $\Delta H_P^\circ = -34.3$ kJ mol^{-1} [38] as well $\Delta H_P^\circ = -38$ kJ mol^{-1} [39] are also in good agreement with our results.

Recently, attempts have been made to calculate the solute segregation energy at specific GBs using computer simulations. Based on molecular dynamics, Hashimoto et al. [3] calculated the energy of phosphorus segregation for various sites at the {013} symmetrical tilt GB of α-Fe and obtained -2.15 eV per atom (i.e. -208 kJ mol^{-1}), -2.25 eV per atom (-217 kJ mol^{-1}), $+0.02$ eV per atom ($+1.19$ kJ mol^{-1}) and -0.81 eV per atom (-78 kJ mol^{-1}). Apart from the positive value $+1.19$ kJ mol^{-1}, which excludes

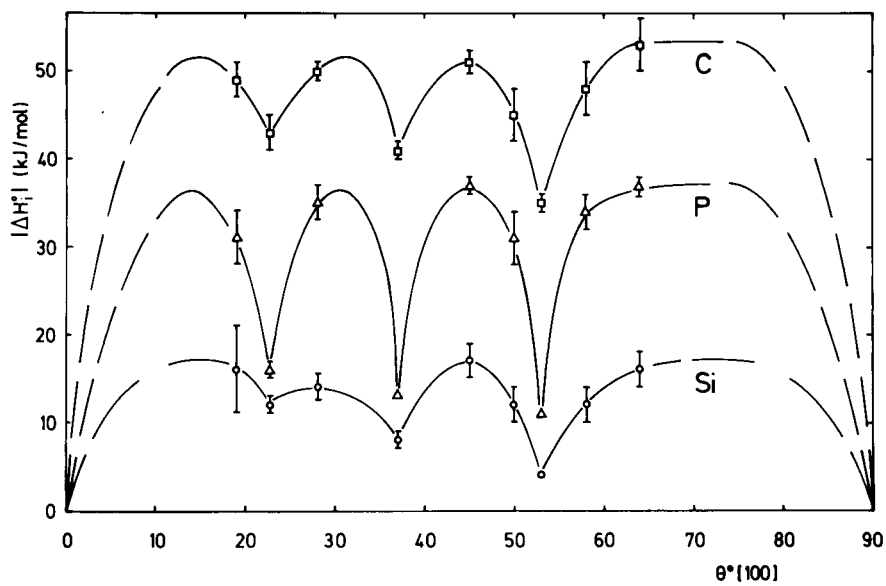

Fig. 8. Dependence of the segregation enthalpy ΔH_i° on the misorientation angle θ of both adjacent lattices in [100] symmetrical tilt bicrystals of an Fe–3.5 at% Si alloy.

this position from segregation, the absolute values for the other sites are much higher than either the present results or literature values which, in addition, represent general GBs. On the other hand, Masuda-Jindo [45] used the tight-binding approximation to examine solute segregation at the same {013} GB. The segregation energies of Si (−0.10 eV per atom, i.e. −9.8 kJ mol^{-1}) and P (0.15 eV per atom, i.e. −14.6 kJ mol^{-1}) resulting from these calculations [45] are in excellent agreement with our results for the same boundary [−8.5 kJ mol^{-1} and −13.3 kJ mol^{-1}, respectively (Table 2)].

Like the GB composition dependence on orientation (Fig. 7) the segregation enthalpy can be plotted as a function of orientation (Fig. 8) [8]. There are three pronounced cusps in the orientation-dependent absolute values of segregation enthalpy for all three elements at the 22.6°[100], {015}, 36.9°[100], {013} and 53.1°[100], {012} symmetrical GBs. These cusps indicate special GBs whose behaviour differs from that of the other general GBs which form the majority [9]. Special properties of the {012}, {013} and {015} symmetrical tilt GBs have been described from various points of view [9]. The segregation behaviour of individual GBs was correlated with the classification scheme proposed by Paidar [46]. In this approach, the symmetrical tilt GBs are classified according to their structure, represented by the interplanar spacing. It was shown that GBs exhibiting special behaviour belong to low classification levels and have large interplanar spacing [46]. Correlation with the orientation dependence of the segregation enthalpy showed that the {013} GB belongs to the 1st classification level and that the {012} and {015} GBs are the only GBs occupying the 2nd level [46]. These GBs also exhibit exceptional segregation behaviour, and can be considered special. The GBs which belong to higher levels exhibit much higher values of $|\Delta H_i^\circ|$, and their behaviour is characterized as general.

The GB segregation enthalpies in bicrystals with the same 36.9°[100] orientation relationship for both crystals can be represented in a similar way [7,47,48]. In this case, which involves both symmetrical and asymmetrical GBs, an anisotropy in GB segregation also exists (Tables 1 and 2). Cusps in the $|\Delta H_i^\circ|$ dependence on the deviation angle of the GB from the symmetrical position [48] were observed for the (001)/(03$\bar{4}$) and (0$\bar{1}$7)/(01$\bar{1}$) GBs. These dependences which indicate the existence of special behaviour in the case of asymmetrical GBs, are discussed in more detail elsewhere [7,47,48].

Conclusions

An Auger electron spectroscopy study of GB segregation differs from those of surface segregation due to the need to expose the GB by intergranular brittle fracture. Questions arise in connection with the fracture process and with segregation in multicomponent systems as discussed in the introduction. This study of solute segregation at well-characterized GBs in tilt bicrystals of an Fe–Si(P, C) alloy was performed with these considerations in mind. From this study the following conclusions can be drawn:

(i) During brittle intercrystalline fracture, the segregated atoms are distributed between the two FSs. Their distribution is equal in the case of symmetrical GBs, but uneven for asymmetrical ones. In both cases, the zig-zag fracture model can be used for quantification.

(ii) The best way to extract the chemical composition of GBs from Auger spectra is to use well-characterized standards of the similar composition. If standards are not available, the recommended method accounts for the depth distribution of solutes and considers corrections for attenuation and backscattering of Auger electrons.

(iii) As demonstrated for segregation at symmetrical tilt GBs in an Fe–Si alloy, concentration can fail to fully describe segregation in a complex alloy. To characterize the segregation, an intensive thermodynamic parameter which is independent of both the temperature and the presence of other solutes in the matrix would be more suitable. From this point of view, it appears that the molar segregation enthalpy is the fundamental parameter for describing GB segregation. This is clearly the case for the anisotropy in the segregation enthalpy dependence on orientation for silicon, phosphorus and carbon in α-iron.

This work summarizes results obtained during my stay at the Max-Planck-Institut für Metallforschung, Institut für Werkstoffwissenschaft in Stuttgart (Germany). I would like to acknowledge gratefully the support of the Alexander von Humboldt-Stiftung and the Max-Planck-Gesellschaft during these stays. I also deeply appreciate the cooperation with Prof. Dr. Siegfried Hofmann in the experiments and valuable discussions, and Dr. Lucia Markert for critically reading the manuscript.

References

[1] E.D. Hondros and M.P. Seah, Int. Metall. Rev., 22 (1977) 262.
[2] S. Hofmann, in P.A. Dowben and A. Miller (Eds.), Surface Segregation Phenomena, CRC Press, Boca Raton, FL, 1990, p. 107.
[3] M. Hashimoto, Y. Ishida, R. Yamamoto and M. Doyama, Acta Metall., 32 (1984) 1.
[4] S. Hofmann, Scanning Electron Microsc. III (1985) 1071.
[5] S. Hofmann and P. Lejček, J. Phys. (Paris), 51 (1990) C1–179.
[6] P. Lejček, Prog. Surf. Sci., 35 (1990) 203.
[7] P. Lejček, J. Adámek and S. Hofmann, Surf. Sci., 264 (1992) 449.
[8] S. Hofmann, P. Lejček and J. Adámek, Surf. Interface Anal., 19 (1992) 601.
[9] R.W. Balluffi, in W.C. Johnson and J.M. Blakely (Eds.), Interfacial Segregation, ASM, Metals Park, OH, 1979, p. 193.
[10] A. Joshi, in W.C. Johnson and J.M. Blakely (Eds.), Interfacial Segregation, ASM, Metals Park, OH, 1979, p. 39.
[11] H. Viefhaus, R. Möller, H. Erhart and H.J. Grabke, Scripta Metall., 17 (1983) 165.
[12] M. Menyhard and C.J. McMahon, Jr., Scripta Metall. Mater., 25 (1991) 935.
[13] M. Menyhard, C.J. McMahon, P. Lejček and V. Paidar, in M.H. Yoo, C.L. Briant and W.A.T. Clark (Eds.), Interfacial Structure, Properties and Design (Proc. MRS Symp., Vol. 122), Materials Research Society, Pittsburgh, PA, 1989, p. 255.
[14] M. Menyhard, B. Rothman, C.J. McMahon, Jr., P. Lejček and V. Paidar, Acta Metall. Mater., 39 (1991) 1289.
[15] H.J. Grabke, H. Erhart and R. Möller, Mikrochim. Acta Suppl., 10 (1983) 119.
[16] P. Lejček, Surface Sci., 202 (1988) 493.
[17] P. Lejček and S. Hofmann, Surf. Interface Anal., 16 (1990) 546.
[18] P. Lejček and S. Hofmann, Acta Metall. Mater., 39 (1991) 2469.
[19] S. Kadečková, P. Toula and J. Adámek, J. Cryst. Growth, 83 (1987) 410.
[20] C.L. Briant and R.P. Messmer, Acta Metall., 32 (1984) 2043.
[21] W. Losch, in R.M. Latanision and R.H. Jones (Eds.), Chemistry and Physics of Fracture, Martinus Nijhoff, Dordrecht, 1987, p. 461.
[22] R. Wu, A.J. Freeman and G.B. Olson, J. Mater. Res., 7 (1992) 2403.
[23] S. Suzuki, K. Abiko and H. Kimura, Scripta Metall., 15 (1981) 1139.
[24] C.L. Briant, Acta Metall., 31 (1983) 257.
[25] P. Lejček and S. Hofmann, Surf. Sci., submitted for publication.
[26] B. Bennett and H. Viefhaus, Surf. Interface Sci., 8 (1986) 127.
[27] B. Rothman and M. Menyhard, Scripta Metall., 23 (1989) 1169.
[28] L.E. Davies, N.C. McDonald, P.W. Palmberg, G.E. Riach and R.E. Weber, Handbook of Auger Electron Spectroscopy, Phys. Electr. Ind., Eden Prairie, MN, 2nd ed., 1976.
[29] M.P. Seah and W.A. Dench, Surf. Interface Anal., 1 (1979) 2.
[30] S. Ichimura and R. Shimizu, Surface Sci., 112 (1982) 386.
[31] M.P. Seah, in D. Briggs and M.P. Seah (Eds.), Practical Surface Analysis, Vol. 1, Wiley Chichester, 2nd ed., 1990, p. 311.
[32] C.L. Briant and H.J. Grabke, Mater. Sci. Forum, 46 (1989) 253.
[33] M. Biscondi, J. Phys. (Paris), 43 (1982) C6–293.
[34] A. Fraczkiewicz and M. Biscondi, J. Phys. (Paris), 46 (1985) C4–497.
[35] J. Stolarz and J. LeCoze, J. Phys. (Paris), 51 (1990) C1–641.
[36] M. Guttmann and D. McLean, in W.C. Johnson and J.M. Blakely (Eds.), Interfacial Segregation, ASM, Metals Park, OH, 1979, p. 261.
[37] H.J. Grabke, Steel Res., 57 (1986) 178.
[38] H. Erhart and H.J. Grabke, Metal Sci., 15 (1981) 401.
[39] K. Tatsumi, N. Okumura and S. Funaki, in Grain Boundary Structure and Related Phenomena, Proc. JIMIS-4, Trans JIM (Suppl.), Japan Inst. of Metals, Sendai, 1986, p. 427.
[40] M. Menyhard and C.J. McMahon, Jr., Acta Metall., 37 (1989) 2287.
[41] G.S. Was and S.M. Bruemmer (Eds.), Grain Boundary Chemistry and Intergranular Fracture, Mater. Sci. Forum, 46 (1989).
[42] P. Lejček, Mater. Sci. Eng., submitted for publication.
[43] H. Hänsel and H.J. Grabke, Scripta Metall., 20 (1986) 1641.
[44] C.M. Liu, K. Abiko and H. Kimura, in P.O. Kettunen, T.K. Lepistö and M.E. Lehtonen (Eds.), Strength of Metals and Alloys (Proc. 8th Int. Conf. ICSMA), Vol. 2, Pergamon Press, Oxford, 1988, p. 1101.
[45] K. Masuda-Jindo, Phys. Stat. Sol. B, 134 (1986) 545.
[46] V. Paidar, Acta Metall., 35 (1987) 2035.
[47] S. Hofmann and P. Lejček, Scripta Metall. Mater., 25 (1991) 2259.
[48] P. Lejček and S. Hofmann, Mater. Sci. Forum, 126–128 (1993) 157.

ELSEVIER

Analytica Chimica Acta 297 (1994) 179–186

ANALYTICA CHIMICA ACTA

X-ray photoelectron spectroscopic study of the oxidation of polycrystalline rhenium by exposure to O_2 and low energy O_2^+ ions

C. Morant, L. Galán, J.M. Sanz

Dpto Física Aplicada C-XII, Universidad Autónoma de Madrid, Cantoblanco, E-28049 Madrid (Spain)

Received 1st April 1993; revised manuscript received 10th August 1993

Abstract

X-ray photoelectron spectroscopy has been used to study the interaction of O_2 and low energy O_2^+ ions with polycrystalline rhenium. The results indicate that rhenium oxides cannot be obtained at temperatures below 630 K even for very high O_2 exposures at low pressures or by low energy O_2^+ implantation. It has been observed that upon exposure to oxygen the oxygen atoms incorporate into the near surface region of the metal up to 17 atom% (i.e., $ReO_{0.2}$) by a non-thermally activated process, at least for temperatures below 630 K. At higher exposures and more markedly at high temperatures a suboxide labelled as ReO forms at the surface up to coverages of ≈ 0.7 monolayers (ML). Bombardment with low energy O_2^+ ions caused a higher incorporation of oxygen atoms up to 30 atom% ($ReO_{0.45}$), but in no case an oxidation state higher than Re^{2+} was detected. In addition it is shown that the full width at half maximum (FWHM) of the Re 4f peak can be used to determine the oxygen incorporated into the Re (i.e., ReO_x) during the initial steps of the oxidation process, where no appreciable chemical shifts are observed.

Keywords: Oxygen; Polycrystalline rhenium; Rhenium; Surface analysis

During the last two decades the interaction of oxygen with a clean metal surface has become one of the most intensive applications of the, since then developed, surface sensitive techniques such as x-ray photoelectron spectroscopy (XPS) and Auger electron spectroscopy (AES) [1]. In particular XPS used in a dynamic mode has been fruitfully applied to many oxygen/metal systems providing unique quantitative information on the chemistry of the metal–oxygen interaction as well as on the species and oxidation states which are formed during the process of oxidation [1–4].

In most cases, a simple analysis and quantification of the XPS spectra in terms of overlapping peaks associated to different oxidation states, has enabled important contributions to a better knowledge of the chemistry of metal surfaces, especially from the moment the computer was incorporated into the analysis of the spectra [1–4].

Correspondence to: J.M. Sanz, Dpto Física Aplicada C-XII, Universidad Autónoma de Madrid, Cantoblanco, E-28049 Madrid (Spain).

SSDI 0003-2670(93)E0482-M

However, in the case of the early stages of oxidation, where the situation is complicated by the fact that the XPS spectra remain almost unchanged, the lineshape analysis of the XPS spectra becomes difficult and in general it has been very scarcely performed or even neglected. This has been the case with the interaction of oxygen with Re, for which only little information is available [5–11]. Previous work [5–11] has mainly focussed on the adsorption of several oxygen containing molecules on rhenium single crystals. The studies indicate that oxygen dissociates forming a surface layer which has been controversially proposed as a superficial oxide of composition ReO [5–8]. None of these studies, however attempted a quantitative analysis of the spectra. In fact the initial step of incorporation of oxygen into the near surface region of the metal before ReO is formed has still not been analyzed for Re and only very scarcely for other metals [12–14].

The present study reports a detailed and quantitative study of the interaction of oxygen with polycrystalline Re at different temperatures in order to monitor the initial steps of the interaction as well as the oxidation state of Re and the thickness and composition of the resulting overlayer. The question on the oxidation state of Re and whether suboxide formation occurs will also

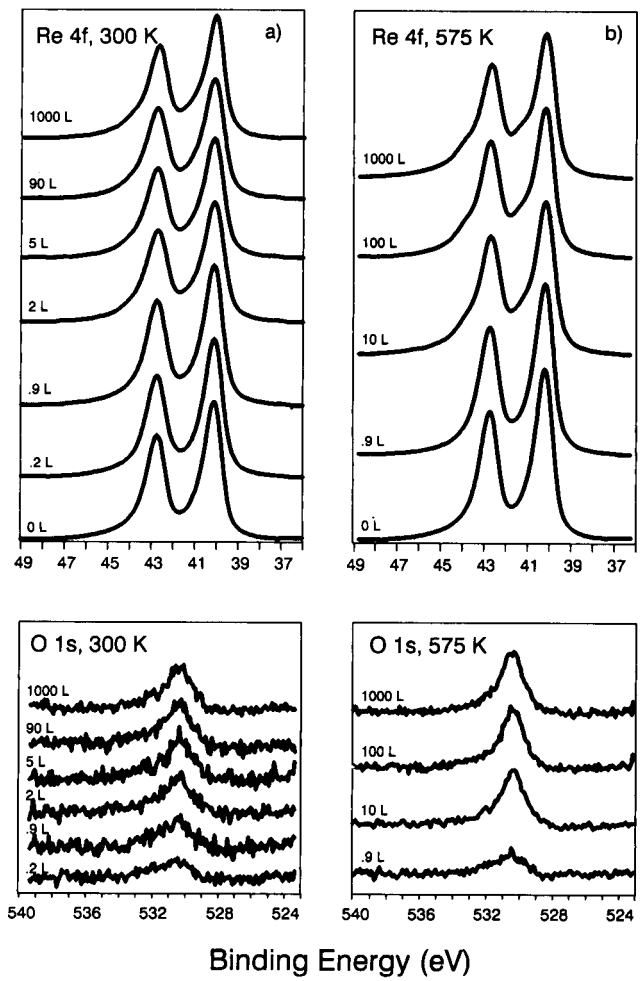

Fig. 1. XPS Re 4f and O 1s spectra obtained after the exposure of Re to O_2 at (a) 300 K and (b) 575 K.

be addressed. In addition, the interaction of low energy O_2^+ ions with Re has been studied in order to determine the products of the chemically modified near surface region. This is an important issue in plasma and ion processing of oxides, however our main purpose was to complete the information obtained from the interaction with O_2, with respect to the observed broadening of the Re 4f XPS line.

1. Experimental

Polycrystalline rhenium of 99.99% nominal purity from Goodfellow Metals was used throughout this work. The samples were degreased in acetone and alcohol, immersed in deionized water and dried before they were introduced into the spectrometer. The samples were resistively heated up to 1200 K for 5 min in a preparation chamber with a residual pressure of ca. 10^{-10} Torr. After that, small amounts of Fe, C and O were detected at the surface, but they could be easily removed by several cycles of Ar^+ sputtering and annealing, except for a small quantity of subsurface oxygen which persisted even at high Ar^+ doses. Exposures to oxygen were then performed by introducing high purity oxygen through a leak valve at low pressures 10^{-8}–10^{-6} Torr, keeping the samples at different temperatures between 300 and 630 K.

Low energy O_2^+ implantation in rhenium was realized with an ion source of the Penning type producing an O_2^+ current of 4–7 μA on an area of 3.5 cm^2. The XPS analysis was performed with a commercial LHS-10 ESCA spectrometer (Leybold-Heraeus) using Mg $K\alpha$ radiation as excitation source. The analyzer was operated in the constant pass energy mode (E_{pass} = 20 eV) with a Gaussian resolution function of full width at half maximum (FWHM) = 0.25 eV. Photoelectrons were usually collected perpendicular to the surface except in some cases where the take off angle was changed to make the analysis more surface sensitive.

2. Results

O_2 exposure

XPS spectra of Re 4f and O 1s taken as a function of the oxygen exposure for two different temperatures (i.e., 300 and 575 K) are shown in Fig. 1. Similar data obtained at 630 K have not been included. The spectra are presented after background subtraction [15,16] and correspond to the clean metal and after several exposures to oxygen as labelled (1 L = 10^{-6} Torr s).

For Re metal, each component of the Re $4f_{7/2,5/2}$ doublet was fitted by a mixed asymmetrical Gaussian/Lorentzian function of total FWHM of 1 eV, weighted by an intensity ratio of 0.72 and separated in energy by 2.43 eV due to the spin-orbit splitting [17].

Fig. 1 shows that upon exposure to oxygen, it is only at high exposures (> 10 L) and in a more marked manner at high temperatures that a shoulder at the high energy side of the Re 4f peak is clearly distinguished. At lower exposures one simply notes a decrease in the height of the peaks and a symmetric broadening of the line (for example, at oxygen exposures of 10 L the FWHM value increases from 1.00 eV (Re metal) up to 1.05, 1.10, 1.12 at 300, 575 and 630 K, respectively). Parallel to that behaviour the intensity of the O 1s peak increases monotonously until saturation is reached. This saturation region is reached at exposures around 100 L when the oxidation temperature is lower than 600 K (Fig. 2).

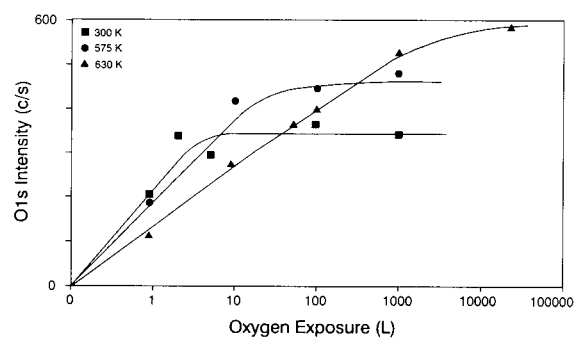

Fig. 2. Intensities of the O 1s as a function of the oxygen exposure for three different temperatures.

The spectra were first analyzed in terms of two components associated to the pure metal and to the extra feature observed at high exposures. However the results of subtracting a suitably scaled clean metal spectrum (0 L) from the other experimental spectra was not satisfactory. The procedure was unable to account for the symmetrical broadening of the line. In order to get a satisfactory analysis at all exposures, the spectra were analyzed by a non linear least-squares procedure [18] taking into account the two contributions mentioned above. The component assigned to the metal was allowed to increase its FWHM monotonously between 1 and 1.3 eV with the oxygen exposure. In fact this was the only manner to account for the observed symmetric broadening of the peak upon O_2 exposure. On the other hand, the fitting parameters for this new structure were difficult to estimate because this signal overlaps with the metal contribution. Therefore, assuming this structure corresponds to an oxide state, the symmetrical line shape and the FWHM were fixed in the least-square procedure with the same values obtained for the stable rhenium oxides (ReO_3, Re_2O_7) analyzed in a different study [19] with the same system. By means of this fitting procedure the binding energy of this feature could be calculated as 41.4 eV, i.e., 1.1 ± 0.1 eV above the binding energy of the metal Re 4f peak. The line shape and fitting parameters of the different components are summarized in Table 1. Typical results of the lineshape fitting in terms of those two components are shown in Fig. 3 by a continuous line through the experimental points. The individual components are shown by the dashed lines.

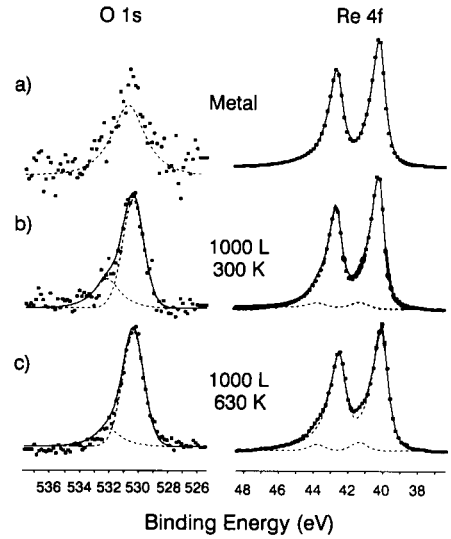

Fig. 3. Analysis of the XPS Re 4f and O 1s spectra as labelled on the figure. Square dots: experimental data. Continuous line: least-squares synthesis. Dashed lines: components used in the analysis.

Table 1
Best-fit parameters for Re 4f XPS spectra [a]

	Clean metal	ReO
Binding energy $4f_{7/2}$	40.3	41.4
Spin-orbit splitting	2.43	2.43
Spin-orbit intensity ratio	0.72	0.72
Intrinsic Gaussian width	0.35	0.40
Intrinsic Lorentzian width	0.39	0.20
Doniach-Sunjic asymmetry	0.16	0.00
Experimental FWHM	1.00	1.24
Reference binding energy Ag 3d 368.21		

values are given in eV; energy errors are 0.05 eV.

Fig. 3 also shows that the O 1s spectra consist of at least two components, as observed in many other metals. The main peak at 530.3 eV is due to the incipient oxidation and oxygen incorporation into the metal, whereas the broad shoulder at 532 eV is consistent with some form of adsorbed oxygen with a lower effective charge [1,3,9].

Low energy O_2^+ bombardment

In order to complete the above study, the chemical interaction of low energy O_2^+ ions with Re was also studied by XPS. O_2^+ ions of 0.5 and 5 keV were used indistinctly to change the implantation depth of the ions. The results of such implantation are shown in Fig. 4 for the Re 4f. The spectra correspond to the metal and to different accumulative O_2^+ doses at 5 and 0.5 keV as indicated on the figure. The O 1s line corresponding to the initial and final states are also shown.

The data of Fig. 4 for O_2^+ implantation correlate very well with those obtained during the

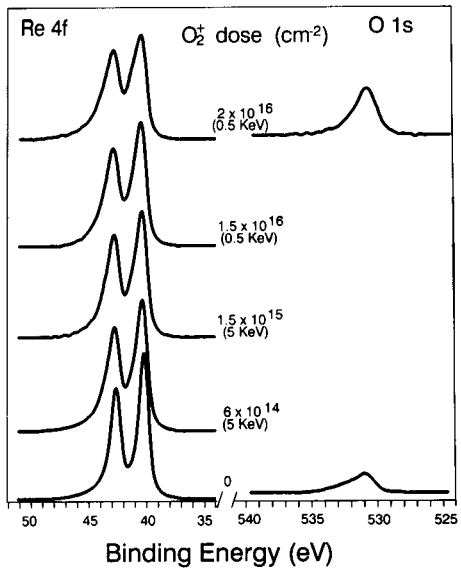

Fig. 4. XPS Re 4f and O 1s spectra obtained after O_2^+ bombardment of Re.

thermal oxidation. They show that even when oxygen is being implanted into the rhenium the lineshape of the Re 4f line remains nearly unchanged. In fact it broadens with respect to the initial spectrum, and shows a small shift of up to 0.3 eV to higher binding energies at very high doses. In this case the FWHM of the Re 4f peak increased up to 1.5 eV at the highest doses. No direct evidence of the formation of oxide is revealed.

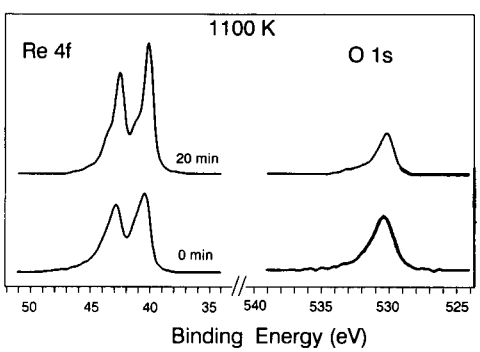

Fig. 5. XPS Re 4f and O 1s spectra of the O_2^+ bombarded sample from Fig. 4 (0 min) and after annealing at 1100 K for 20 min.

The effect of annealing the sample at 1100 K after the highest O_2^+ doses is shown in Fig. 5. Apart from a decrease of the oxygen signal the Re 4f shows the appearance of the shoulder assigned to ReO as well as a sharpening of the metal peak. All results suggest that annealing causes a redistribution of the oxygen atoms which oversaturate the selvedge of the sample in the form of a metastable state to form a ReO monolayer at the surface whereas the excess of oxygen is dissolved deeper in the sample.

3. Discussion

The broadening of the metal peak upon oxygen adsorption has been observed in other transition metals [12–14], however, no clear interpretation can be found in the literature.

We propose that the broadening of the Re 4f line is due to the incorporation of the dissociatively adsorbed oxygen into the near surface region of the metal without causing any observable chemical shift of the Re 4f peak, which could be assigned to a change in the oxidation state of the metal atoms. This interpretation of the broadening effect is further supported by the experiments with low energy O_2^+ ions. These show that the implantation of oxygen causes similar effects as those mentioned above for the exposure to O_2. The data suggest that the incorporated oxygen atoms are bound to the Re atoms in the O^{2-} formal oxidation state, with a certain charge transfer and some hybridization with the Re valence electrons. This causes a very small chemical shift in the Re 4f levels, which is hardly observable when the oxygen content is low, as well as a broadening of the peaks due to the increase of the ionicity.

Re 4f and O 1s spectra were also measured at 30° with respect to the surface perpendicular in order to make them more surface sensitive (not shown here). We were unable to separate the contributions of pure Re and Re with dissolved oxygen [i.e., Re(O)] even by changing the take off angle of the photoelectrons. We did not obtain more information with the O 1s spectra taken at 30° either, only that the shoulder at 532 eV is a

surface contribution. Thus, we can only conclude that the incorporation of oxygen is on the first layers. Although this incorporation is likely inhomogeneous, we assumed an homogeneous distribution within the analysis depth of the technique (i.e., 20–30 Å) in order to make a quantitative analysis.

The incipient oxidation of the rhenium surface is characterized by the appearance at high exposures and/or high temperatures of the discrete feature at 41.4 eV, which has been assigned to the formation of ReO at the outermost layer in agreement with data from the literature [5–8]. Therefore, it appears that as the oxygen concentration in the near surface region builds up the oxidation process terminates with the formation of a monolayer of ReO at the surface.

In order to draw more quantitative conclusions from the results discussed above the Re 4f and O 1s peaks were quantitatively analyzed in terms of Re(O) with oxygen dissolved and ReO, assuming that the species are distributed according to the scheme included in the inset of Fig. 6b. Oxygen is assumed to be incorporated homogeneously within the information depth of the measured photoelectrons (i.e., 20–30 Å) whereas ReO grows at the outermost layer.

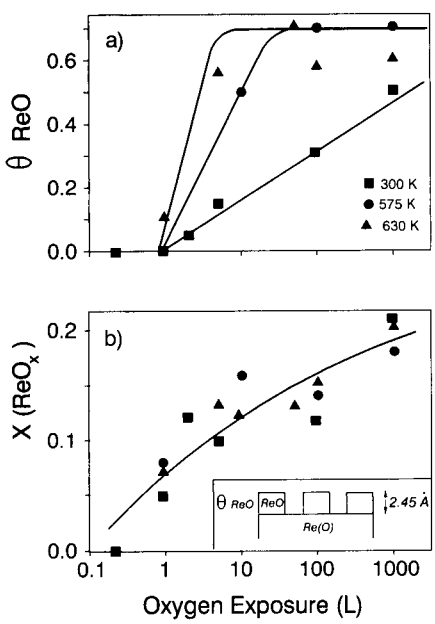

Fig. 6. Coverage (θ) of (a) ReO and atomic fraction x in (b) ReO_x as a function of the oxygen exposure for three different temperatures. A scheme of the assumed model is included in (b).

According to this model a quantification of the O 1s peak assigned to ReO or to Re(O) can also be done easily [3,4,20]. If ReO is located in the outermost layer its intensity is proportional to the fractional monolayer θ and the rest of oxygen is in the form of Re(O) homogeneously distributed in depth. Using the intensities of both Re species [i.e., Re(O) and Re^{2+}] and of oxygen, the atomic proportion x of dissolved oxygen (i.e., ReO_x) and the fraction θ of monolayer of ReO grown at the surface were determined as a function of the oxygen exposure by the usual methods of quantitative XPS [3,4,17]. The quantification of the O 1s peak at 532 eV (i.e., adsorbed oxygen) indicates the presence of some adsorbed oxygen during the whole process reaching a saturation value of 0.4 ML at exposures > 100 L. The attenuation lengths $\lambda_{Re} = 22.3$ Å and $\lambda_O = 16.4$ Å were estimated from the empirical relation given by Seah and Dench [21] and the sensitivity factors were taken from the corresponding tables supplied by Leybold-Heraeus with the spectrometer.

The results of θ and x are shown in Fig. 6a and b, respectively, as a function of the oxygen exposure for three different temperatures. They clearly indicate that oxygen atoms incorporate into the metal lattice at the very initial stage of adsorption whereas ReO is detected only at exposures higher than 1 L. The onset of ReO formation is established from the emergence of the feature at 41.4 eV assigned to the Re^{2+} species.

It is interesting to observe that whereas x is independent of the substrate temperature within the range of temperatures studied here (i.e., 300–630 K), the formation of ReO is clearly accelerated by an increase of temperature. That is a clear indication that the process of oxygen incorporation is not a thermally activated process. This fact neglects diffusion as the possible mechanism and suggests that a place exchange mechanism [22] could be responsible. In fact, it appears that for small exposures of oxygen the incorporation of the very electronegative oxygen adsorbed atoms dominates the oxidation process.

In addition, it is observed that the growth of ReO is approximately linear with oxygen exposure, until a coverage of ca. 0.7 ML is reached and the rate begins to level off. Whereas the slope increases with temperature the coverage at saturation appears to be independent of it. The coverage of ReO at saturation is also compatible with data for monocrystals from other authors [5–7], which led to the conclusion that ReO corresponds to an oxygen coverage $\Theta \geqslant 0.5$ at the surface.

By gathering up all the data from both the exposure to O_2 and low energy O_2^+ the dependence of the binding energy and FWHM of the Re 4f XPS peak as a function of the oxygen atomic fraction x (i.e., ReO_x) could be determined for $0 \leqslant x \leqslant 0.5$. The results have been collected in Fig. 7 so that they can be used for analytical purposes. They confirm the idea that the observed broadening of the XPS peaks for $x \leqslant 0.2$ during exposure to O_2, was caused by the incorporation of the oxygen atoms below the surface. Furthermore, in the case of O_2^+ implantation the concentration of oxygen incorporated into the substrate could be increased up to $x \approx 0.45$, i.e., well above the limit observed in the above section for exposure to O_2. However, this state is obviously not stable and annealing causes significant changes in the spectrum towards a state which is equivalent to that obtained by exposure to O_2 (i.e., $ReO_{0.2}$ and ReO), as it was shown in Fig. 5.

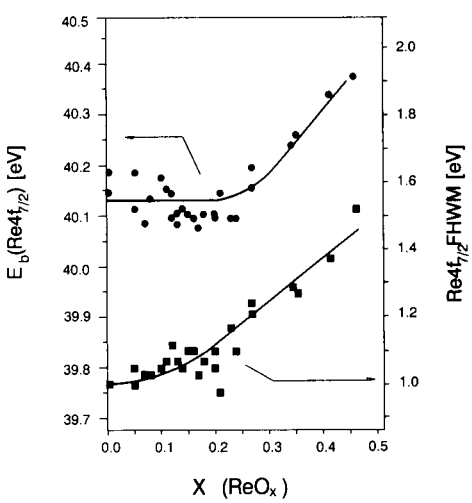

Fig. 7. Binding energy E_b and FWHM of the Re $4f_{7/2}$ level as a function of the composition x (ReO_x).

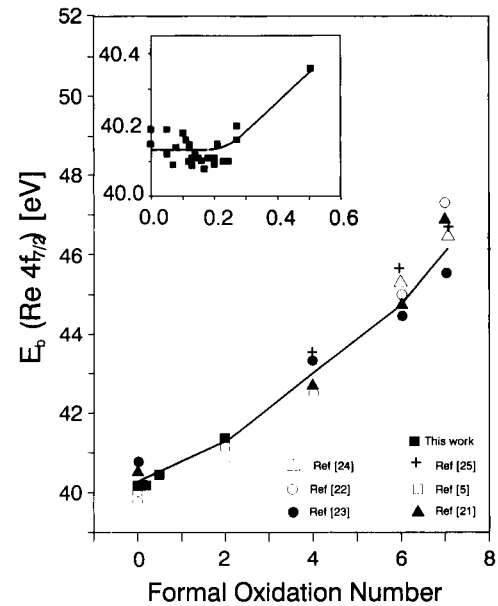

Fig. 8. Binding energy of the Re $4f_{7/2}$ level as a function of the oxidation number of Re as obtained from the literature in comparison with results of Fig. 7.

The data in Fig. 7 clearly show that the FWHM of the Re 4f peak is more sensitive than the binding energy to determine the average composition of ReO_x within the range $0 \leqslant x \leqslant 0.3$, where the binding energy of the level remains almost constant. However, for higher oxygen concentrations (i.e., $x \geqslant 0.3$) and obviously for the rhenium oxides, the binding energy depends very strongly on the oxidation state of Re. For completeness, data reported in the literature [5,19,23–26] for the different oxidation states of Re have been represented in Fig. 8 in comparison to those determined in this work for the initial stages of oxidation.

Conclusions

By summarizing the results we can conclude that in the early stages of the oxygen interaction with rhenium, at low oxygen pressures and temperatures below 630 K, the incorporation of the oxygen atoms into the near surface region of the

sample dominates the oxidation process. That incorporation causes a broadening of the Re 4f XPS peaks without inducing any observable chemical shift in their binding energy. The incorporation process is a non thermally activated process, and saturates at concentrations of ca. 17–24 atom%. Increasing the oxygen exposure, and especially at higher temperatures the adsorbed oxygen reacts with the Re atoms to form ReO up to coverages of ca. 0.7 ML. By bombardment with low energy O_2^+ ions the amount of oxygen incorporated into the selvedge could be increased up to 31 atom%. However annealing at 1120 K caused the formation of ReO at the surface and Re metal with dissolved oxygen, in good agreement with the phases observed for O_2 exposure under the conditions studied here. In addition it has also been shown that both the FWHM and the binding energy of the Re 4f XPS peak can be used to determine both the oxygen atomic concentrations of ReO_x for $x \leqslant 0.5$ during the initial stages of the oxidation of Re.

References

[1] K. Wandelt, Surf. Sci. Reports, 2 (1982) 1.
[2] A.F. Carley, P.R. Chalker, J.C. Riviere and M.W. Roberts, J. Chem. Soc., Faraday Trans. 1, 83 (1987) 351.
[3] C. Morant, J.M. Sanz, L. Galán, L. Soriano and F. Rueda, Surf. Sci., 218 (1989) 331.
[4] C. Morant, L. Galán and J.M. Sanz, Surf. Interface Anal., 16 (1990) 304.
[5] R. Ducros, M. Alnot, J.J. Ehrhardt, M. Housley, G. Piquard and A. Cassuto, Surf. Sci., 94 (1980) 154.
[6] M. Alnot and J.J. Ehrhardt, J. Chim. Phys., 79 (1982) 735.
[7] F. Zaera and G.A. Somorjai, Surf. Sci., 154 (1985) 303.
[8] R. Ducros and J. Fusy, J. Electron Spectrosc. Relat. Phenom., 42 (1987) 305.
[9] S. Tatarenko, P. Dolle, R. Morancho, M. Alnot, J.J. Ehrhardt and R. Ducros, Surf. Sci., 134 (1983) L505.
[10] D.R. Baer, R.L. Gordon and C.W. Hubbard, Appl. Surf. Sci., 45 (1990) 71.
[11] J.A. Rodriguez, R.A. Campbell and D.W. Goodman, Surf. Sci., 244 (1991) 211.
[12] P. Sen, M.S. Hedge and C.N. Rao, Appl. Surf. Sci., 19 (1982) 63.
[13] G. Gewinner, J.C. Peruchetti, A. Jaegle and A. Kalt, Surf. Sci., 78 (1978) 439.
[14] J.C. Peruchetti, G. Gewinner and A. Jaegle, Surf. Sci., 88 (1979) 479.
[15] D.A. Shirley, Phys. Rev. B, 5 (1972) 4709.
[16] H.E. Bishop, Surf. Interface Anal., 3 (1981) 272.
[17] M.P. Seah, in D. Briggs and M.P. Seah (Eds.), Practical Surface Analysis, Vol. 1, Auger and X-ray Photoelectron Spectroscopy, Wiley, Chichester, 1990, Chap. 5.
[18] W.J. Dixon (Ed.), Non-linear regression in BMDP Statistical Software, University of California Press, Berkeley, CA, 1983, p. 289.
[19] C. Horaut, L. Soriano and L. Galan, Surface Interface Anal., submitted for publication.
[20] P.M.A. Sherwood, in D. Briggs and M.P. Seah (Ed.), Practical Surface Analysis, Vol. 1, Auger and X-ray Photoelectron Spectroscopy, Wiley, Chichester, 1990, App. 3
[21] M.P. Seah and W.A. Dench, Surf. Interface Anal., 1 (1979) 2.
[22] M.A.H. Lanyon and B.M.W. Trapnell, Proc. R. Soc. A, 227 (1955) 387.
[23] A. Cimino, B.A. de Angelis, D. Gazzoli and M. Valigi, Z. Anorg. Allg. Chem., 460 (1980) 86.
[24] W.T. Tysoe, F. Zaera and G.A. Somorjai, Surf. Sci., 200 (1988) 1.
[25] E.S. Shapiro, V.I. Avaev, G.V. Antoshin, M.A. Ryashentseva and Kh.M. Minachev, J. Catal., 55 (1978) 402.
[26] M. Komiyama, Y. Ogino, Y. Akai and M. Goto, J. Chem. Soc. Faraday Trans. 2, 79 (1983) 1719.

ELSEVIER

Analytica Chimica Acta 297 (1994) 187–195

ANALYTICA CHIMICA ACTA

Application of factor analysis in electron spectroscopic depth profiling on copper oxide

Henning Bubert [a,*], Monika Korte [a], Rainer P.H. Garten [b], Erhard Grallath Marek Wielunski [c]

[a] *Institut für Spektrochemie und angewandte Spektroskopie (ISAS), Bunsen-Kirchhoff-Strasse 11, D-44139 Dortmund, Germany,*
[b] *Max-Planck-Institut für Metallforschung Stuttgart, Laboratorium für Reinststoffanalytik, Bunsen-Kirchhoff-Strasse 13, D-44139 Dortmund, Germany,*
[c] *Dynamitron-Tandem-Laboratorium, Ruhr-Universität Bochum, Universitätsstrasse 150, D-44801 Bochum, Germany*

(Received 27th November 1993; revised manuscript received 10th January 1994)

Abstract

Depth profiles were taken by x-ray photoelectron spectrometry/Ar-ion sputtering from copper sheets oxidized during 30 min in air at 200 or 300°C, respectively. The data of the depth profiles were subjected to factor analysis in order to determine the relevant components of the copper oxide layers. Factor analysis shows the existence of a cuprous oxide layer (Cu_2O) on both specimens under bombardment with 2 keV argon ions during depth profiling. Rutherford backscattering measurements and carrier gas fusion analysis were successfully applied to determine the oxygen content of the oxide layers. Results corroborate the identification of Cu_2O in both layers.

Keywords: X-Ray photoelectron spectrometry; Copper oxide; Depth profiling; Factor analysis

1. Introduction

X-ray photoelectron spectrometry (XPS) is widely accepted as a technique to study the oxidation state of elements in thin oxide layers [1–3]. The superposition of signals from several oxidation states of the same element in a thin film may require deconvolution procedures, or may sometimes even lead to ambiguous contributing signals. More sophisticated deconvolution procedures, including least-squares fitting methods and factor analysis [4] can help to improve the selectivity and reliability by means of common utilization of separated information from several independent spectra. Therefore, factor analysis was applied to the elucidation of different species on oxide layers deliberately prepared on copper foil.

The knowledge of the oxidation state of copper in thin copper oxide layers plays an important role in different fields of materials technology and analysis. Thus, the need exists to have at disposal calibration standards, e.g., for the analysis of high-T_C superconductors [5,6] or for the characterisation of oxides on circuit boards [7].

* Corresponding author.

SSDI 0003-2670(94)00053-O

2. Experimental

2.1. Sample preparation

Strips of 100×8 mm^2 were cut from 0.1 mm polycrystalline Cu foil of 99.7% purity (Merck, metallic impurities according to the supplier in wt.-%: Ag: 0.002, Pb: 0.05, Sn, Fe, Mn, Sb: 0.005, As: 0.0002). The surface was cleaned by immersing the samples successively several times in: (1) acetone, (2) mixture of HCl (2 M) and H_2O_2 (30%), (3) HCl (2 M), followed by thorough rinsing with distilled H_2O and acetone. In order to reduce the oxygen content, the samples were annealed at 700°C for 30 min in flowing H_2 (atmospheric pressure) and left cooling to room temperature in N_2. From the Cu strips thus purified, one was left untreated (specimen 1), and two were oxidized by moving them during 30 min through an air-purged tube furnace at 200 or 300°C, respectively (specimen 2 and 3). Finished samples were stored in dry air for several days until analysis.

2.2. XPS

Photoelectron spectra and depth profiles were recorded on an x-ray photoelectron spectrometer, AXIS-HS (Kratos), using the following conditions. Excitation: non-monochromatic Mg K_α radiation ($h\nu = 1253.6$ eV) was used, the anode operated at 20 mA and 15 kV; analysis: take-off angle for the electrons 0° with respect to the surface normal, diameter of the analyzed area 135 μm, fixed analyser transmission (FAT) mode, pass energy of the concentric hemispherical analyser (CHA) 10 eV, data acquisition with 0.2 eV per step; sputtering ions for depth profiling: Ar^+, energy 2 keV, current 390 nA, angle of incidence 45° with respect to the surface normal, scanned area approx. 2.5×2.5 mm^2. Alternating sputtering with a cycle time of 5 min was used normally. The system base pressure was 4×10^{-7} Pa.

Depth profiles were taken for the spectral ranges of the photoelectron lines Cu $2p_{3/2}$, O 1s, C 1s and the Auger line Cu LVV. The Cu $2p_{3/2}$ peak of the sputter exposed copper target base was used to calibrate the binding energy scale (932.7 eV) [8]; a very small carbon peak could only be observed in the uppermost layer. A background correction was not necessary due to the applied factor analysis as evaluation procedure of the acquired data of the depth profiles.

2.3. Rutherford backscattering (RBS)

RBS investigations were carried out by using a standard RBS arrangement [9] (cf. also the review by L.J. van IJzendoorn in this special issue of Anal. Chim. Acta). The analyzing beam of 2.3 MeV $^4He^{2+}$ was generated by a 4-MV Dynamitron Tandem accelerator at Bochum (Germany). The incident angle of the ion beam was normal to the specimen surface. The backscattering angle was 160°. The measured area was 0.5×2 mm^2 due to the aperture selected. The total energy resolution amounted to about 15 keV. The ion beam current was 10 nA at a measuring time of 600 s to avoid beam heating and an excessive dead time in the detection channel. The system base pressure in the RBS chamber was about 2×10^{-5} Pa.

2.4. Chemical analysis

The oxygen contents of the samples were determined by two different methods: (1) the total amount of oxygen by carrier-gas fusion analysis (CGFA), and (2) the surface oxygen by selective dissolution of Cu_2O/CuO. The latter method is based on the fact that, protected from the oxygen of the atmosphere, only Cu oxides react with NH_4OH–NH_4Cl mixture, forming ammine complexes, leaving the metallic Cu surface unattacked [10,11]. The dissolved Cu is determined by spectrophotometry, and the mass and the thickness of the oxide layer can then be calculated, if the stoichiometry of the Cu_xO is known.

3. Theoretical

Factor analysis has become a powerful multivariate statistical method for data handling and spectral interpretation in Auger electron spectroscopy and in photoelectron spectroscopy, too

[12–16]. Physical and/or chemical requirements for the application of factor analysis are that (1) the individual components are independent and (2) the measured spectra can be attained by linear combination of the spectra of these components. Here, the term 'component' denotes such a state the spectra of which cannot be generated by any linear combination of other components. Thus, components in a physical or chemical sense can be elements, chemical compounds, intermediate (non-stoichiometric) states or even states that were produced by physical processes (e.g., charging of the specimen) owing to the analysis, provided that spectra differ significantly.

A depth profile recorded at L sputter cycles comprises L spectra, each spectrum is related to one sputter cycle. Such a spectrum can consist of several single spectra, i.e., energy regions joint together contiguously. The data of these spectra form L columns of the data matrix **D**. If the number of data of a spectrum consist of N intensity values, then the data matrix **D** contains N rows. The aim of the factor analysis is now to determine the two matrices **R** and **C** which by multiplication reproduce the data matrix that means

$$\mathbf{D} = \mathbf{R} \cdot \mathbf{C} \tag{1}$$

The mathematical procedure to solve the mentioned problem results in the generation of two matrices $\mathbf{R}^*$ and $\mathbf{C}^*$ which normally have no physical significance and are therefore termed the 'abstract spectra' and the 'abstract concentration' matrices, respectively. (Details of this procedure can be found in [16]). Since the data matrix **D** cannot be directly subjected to factor analysis, the solution of the mentioned problem can be managed by forming the covariance matrix

$$\mathbf{Z} = \mathbf{D}^{\mathrm{T}} \cdot \mathbf{D} \tag{2}$$

where $\mathbf{D}^{\mathrm{T}}$ is the transposed data matrix. The covariance matrix is diagonalized, i.e., that the eigenvalue problem

$$\mathbf{Q}^{-1} \cdot \mathbf{Z} \cdot \mathbf{Q} = \lambda \tag{3}$$

has to be solved. It should be mentioned that the calculation of eigenvalues of the covariance matrix **Z** is a central step of the mathematical procedure, because the two 'abstract' matrices $\mathbf{R}^*$ and $\mathbf{C}^*$ can be obtained from

$$\mathbf{R}^* = \mathbf{D} \cdot \mathbf{Q} \tag{4}$$

and

$$\mathbf{C}^* = \mathbf{Q}^{\mathrm{T}} \tag{5}$$

The 'abstract spectra' matrix $\mathbf{R}^*$ is composed of the same number of spectra as there exist sputter cycles, namely L. Not all of these spectra are required to reproduce the original spectra satisfactorily; only those spectra of which the corresponding eigenvalues λ exceed a statistical criterion are necessary for the reproduction. Hugus and El-Awady [17] have derived a suitable criterion which has the advantage that different magnitude of the statistical errors in the single spectra can individually be taken into account in the mathematical procedure. (A simplified approach is described elsewhere [18], that uses a more vague criterion based on the so-called imbedded error, instead of using any measured spectral noise.) If K is the number of the remaining significant spectra, the dimension of the 'abstract spectra' matrix is reduced to $N \times K$, and that of the 'abstract concentration' matrix is to $K \times L$. In order to proceed from the 'abstract spectra' to chemically and/or physically meaningful spectra, both 'abstract' matrices have to be transformed. An often applied procedure of this so-called target transformation starts from the proved or hypothetical case that the molar fractions of all components in K sputter cycles are known. Then, a transformation matrix can be constructed that transfers the 'abstract' matrices into 'real' matrices. If the molar fractions are known from too few sputter cycles only, the data matrix must be extended by suitable reference spectra with known molar fractions. As final result one obtains a concentration matrix that contains the molar fractions of the K significant components in its L columns, so that a 'component depth profile' for these components can be derived.

4. Results and discussion

4.1. Preparation

Temperatures, T, and oxygen pressure, p, for heat treatment of Cu foil were deliberately adjusted to form, under equilibrium conditions, two different types of oxides, viz. Cu_2O on specimen 2 ($T = 200°C$), and CuO on specimen 3 ($T = 300°C$), according to the respective regions of thermodynamic stability in the phase diagram Cu–O [19].

4.2. XPS

XPS investigations have been carried out to determine the composition, the chemical species present and the thicknesses of the oxide layers formed on copper foil by annealing in air. As can be seen from the Cu 2p signal in Fig. 1(2) and 1(3), the uppermost surface compositions of both specimens show the existence of CuO. This finding is not surprising, because, after sample preparation, the specimens have been stored in dry air before XPS investigations, so that any Cu_2O initially formed on the uppermost surface layer, can be oxidized to CuO during storage time of several days. In contrast, the Cu 2p signal of the untreated surface of specimen 1 mainly represents the spectrum of metallic Cu (Fig. 1, curve 1).

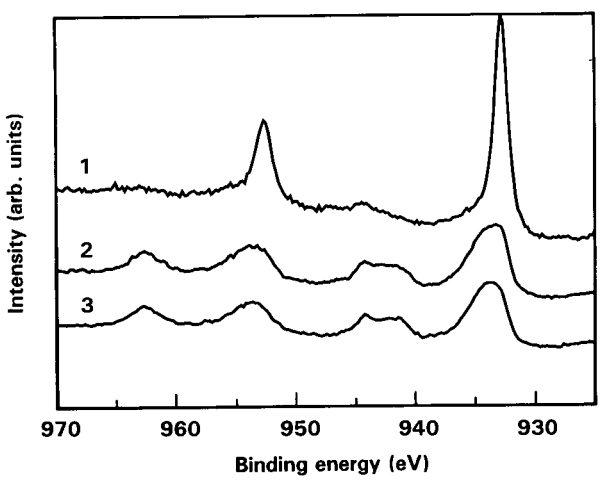

Fig. 1. Normalized Auger electron spectra of the Cu LVV region by excitation with Mg K_α radiation. (1) Untreated Cu sheet (specimen 1), (2) specimen 2 and (3) specimen 3: Cu sheets oxidized at 200°C and 300°C, respectively, for 30 min.

Table 1
Kinetic energy regions (eV) used for evaluation, factor analysis and noise determination

Element	Level/ transition	Region (eV) for analysis	Region (eV) for noise
Cu	$2p_{3/2}$	314–325	285–290
O	1s	717–727	715–725
C[a]	1s	962–972	960–966
Cu	LVV	908–926	900–904

[a] Not used for factor analysis.

The data of the depth profiles of the specimens 2 and 3 have been subjected to factor analysis. The energy regions used for factor analysis and for noise determinations are listed in Table 1. The C 1s line has not been included into the factor analysis. If the carbon line would have been included, factor analysis would have revealed in any case a surface-near component, because carbon was only present in the uppermost layer. The first result of the factor analysis is that three components are present, i.e., $K = 3$. This is deduced from the comparison of the eigenvalues λ_i with the standard deviations σ_i derived from the noise determination of the respective region (Table 1): only the first three eigenvalues are greater than $3\sigma_i$. As an example, Table 2 gives the eigenvalues λ_i and the standard deviations σ_i for specimen 3. The data matrix can satisfactorily be reproduced with these three eigenvectors. Fig. 2 shows the three energy regions of Cu $2p_{3/2}$, Cu LVV and O 1s obtained after factor-analyzing from specimen 3, in a

Table 2
Eigenvalues λ_i and standard deviations σ_i of the intensity measurements

i	λ_i	σ_i
1	2.87×10^{10}	4.15×10^{6}
2	2.18×10^{8}	2.72×10^{6}
3	1.03×10^{8}	2.77×10^{6}
4	1.36×10^{6}	2.85×10^{6}
5	0.61×10^{6}	2.74×10^{6}
6	0.53×10^{6}	2.80×10^{6}
....		
21	0.16×10^{6}	2.77×10^{6}

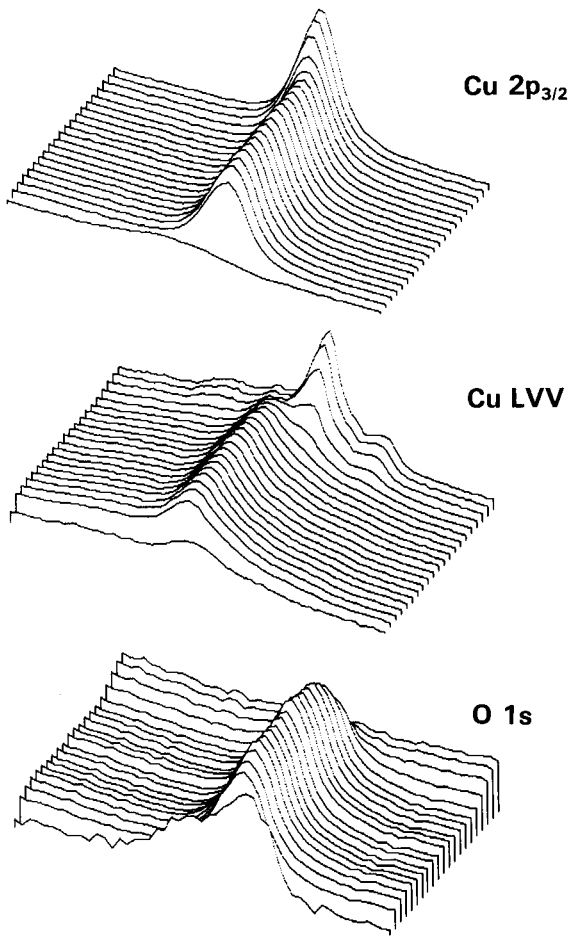

Fig. 2. Three-dimensional plot of the energy regions Cu $2p_{3/2}$, Cu LVV and O 1s for the specimen 3, as reproduced from factor analysis. The consecutive depths of the displayed cycles are 0, 1.25, 8 nm, and then plus 12.7 nm per cycle.

three-dimensional plot. The depth of each sputter cycle is indicated in figure caption 2, the depth scale calibration being based on a constant sputter rate for the oxide layer of specimen 3. The course in depth for the three components is presented in Fig. 3. It is presumed that only the first component exists at the first cycle, only the second component at the 13th cycle and only the third component at the last (21st) cycle. These components need not correspond with unique chemical states, as mentioned in the Theoretical section, but in this case the second component has to be attributed to the Cu_2O state, and the

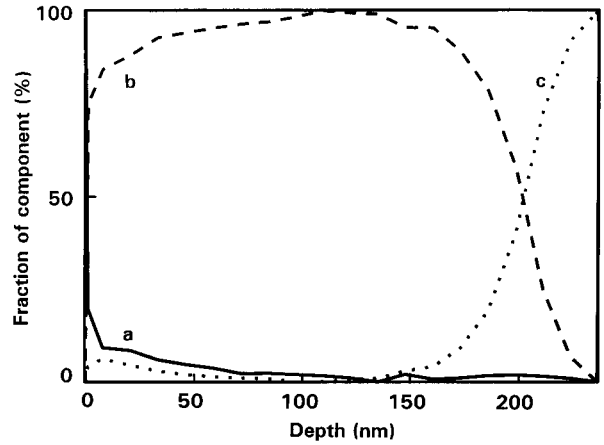

Fig. 3. 'Component depth profile' of the Cu sheet oxidized at 300°C for 30 min (specimen 3).

third component to the metallic Cu state. Proper assignment of the first component is more difficult, as is outlined below. The energetic positions of the maxima of the regarded lines are listed in Table 3. In Fig. 4, the Cu $2p_{3/2}$, the Cu LVV and the O 1s lines are presented for specimen 3. Analogous results are obtained for specimen 2. The XP spectra of both specimens show that, besides the uppermost layers, the oxide layers should consist of Cu_2O. This finding is in sharp contrast to the implication of the formation of two different oxides on specimens 2 or 3, by choosing oxidation temperatures, T, adjusted to the stability regions of Cu_2O or CuO, respectively.

This discrepancy could be accounted either for (a) incomplete reaction to the stable oxide CuO

Table 3
Energy position of Auger and photoelectron lines as a result of factor analysis

Specimen	Cycle	Sputter time (min)	Cu $2p_{3/2}$ BE [a] (eV)	Position Cu LVV KE [a] (eV)	O 1s BE [a] (eV)
2	1	0	932.6	917.2	529.7
	4	6	932.1	916.8	530.1
	18	34	932.4	918.7	–
3	1	0	933.7	917.3	529.8
	13	319	932.0	916.9	530.1
	21	559	932.3	918.7	–

[a] BE = binding energy, KE = kinetic energy.

during preparation of specimen 3 (e.g., compare conditions used in [20]), or for (b) an alteration of the layer composition CuO during depth profiling by preferential sputtering of oxygen, e.g., [1,3,21, 22].

In the last case, under ion bombardment, a reduction of CuO takes place which can be written as

$$2CuO \longrightarrow Cu_2O + O$$

This argument is in accordance with the criterion that oxides should lose preferentially oxygen under ion bombardment, if the decomposition pressure is greater than 100 bar at approximately 3000 K [20]. In general, the deviations of the energy positions between specimen 2 and 3, as well as small variations in the line shapes, can be explained by uncertainties of measurement.

Deviant from this, the difference of the Cu $2p_{3/2}$ line from the uppermost layer (i.e., non-sputtered) between specimen 2 and 3 is significant with regard to the line position and the FWHM, as can be seen in Fig. 5. Therefore, superposition of Cu lines from different chemical states is suggested and curve fitting with three lines is applied to the measured Cu $2p_{3/2}$ lines. The results are given in Table 4. Some contribution from superficial carbonaceous copper compounds may cause additional line shift, thus complicating the interpretation of these results. Comparison with reference spectra indicates that only the uppermost layers of the two specimens consist of a mixture of Cu_2O, CuO and $Cu(OH)_2$, and that the contribution of bivalent Cu in this uppermost layer is roughly double in specimen 3 compared to specimen 2. In contrast, the Cu $2p_{3/2}$ signal of the untreated surface of specimen 1 represents the spectrum of metallic Cu.

In order to check the argument that a reduction of CuO appears during ion sputtering, the

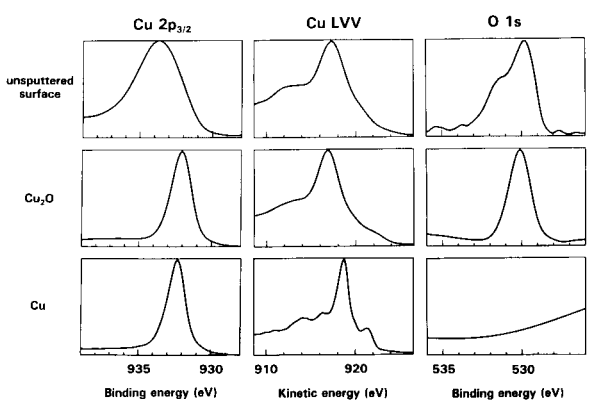

Fig. 4. Normalized intensities (arbitrary units) of the Cu $2p_{3/2}$, Cu LVV and O 1s lines obtained from the unsputtered surface, from the middle of the oxide layer (Cu_2O) and from the Cu base of specimen 3.

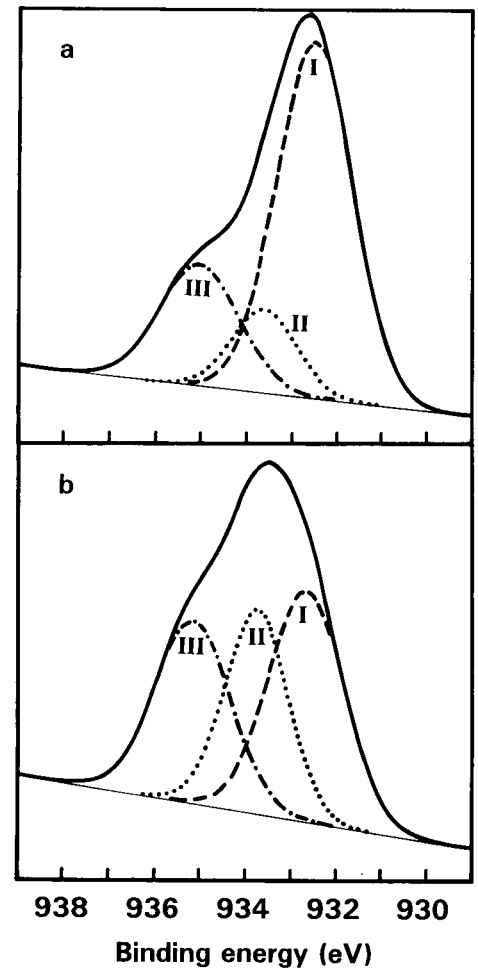

Fig. 5. Cu $2p_{3/2}$ line obtained from the surface of (a) specimen 2 and (b) specimen 3, respectively. Gaussian curve fitting with three lines is applied. The dashed line (I) represents the portion of Cu_2O, the dotted line (II) the portion of CuO, and the dash-dotted line (III) the portion of $Cu(OH)_2$. (Roman figures correspond with those given in Table 4.)

Table 4
Spectral position (binding energy), FWHM and portion of intensity relative to the total line for Cu $2p_{3/2}$ at the surface of specimen 2 and 3. Model: Gaussian curve fitting

Specimen	Line label [a]	Position (eV)	FWHM (eV)	Intensity (%)	
2	I	932.5	1.95	64	
	II	933.6	1.60	15	
	III	935.0	1.95	21	
3	I	932.7	1.95	37	
	II	933.8	1.61	33	
	III	935.2	1.95	30	
RD [b]		932.5	–	100	Cu_2O
		932.6	–	100	Cu
		933.7	–	100	CuO
		935.1	–	100	$Cu(OH)_2$

[a] Line label, see Fig. 5.
[b] RD = Reference data from handbook [8].

composition of the oxide layers has been determined independently by Rutherford backscattering spectrometry (RBS) and by chemical analysis.

4.3. RBS

RBS experiments have been run on specimen 3 to analyze the composition of the oxide layer by depth profiling without any ion sputtering [9]. The RBS spectrum taken from specimen 3 is reproduced in Fig. 6. As can be seen, the best computer simulation of the measured RBS spectrum is obtained assuming Cu_2O for the oxide layer. A comparison with the spectrum of CuO powder ($\geqslant 99\%$ purity, Merck, Darmstadt) is given in Fig. 7. It verifies that decomposition of CuO powder did not take place under $^4He^{2+}$ bombardment of 2 MeV. Therefore, the oxide layer of specimen 3 does not change under ion bombardment in RBS. The oxide layer of specimen 3 is unequivocally found to consist of Cu_2O, with a certain broadening of the interface region to the base metal, which can be attributed to the surface and interface roughness. The Cu_2O layer thickness is determined from RBS to $(2.5 \pm 0.2) \times 10^{18}$ Cu atoms/cm^2, corresponding to an oxygen content of 2.1 μmol/cm^2. The layer thickness is found to be 500 ± 40 nm. This result is in clear contrast to the intended formation of CuO in specimen 3 (see preparation), but is in complete agreement with the depth profile analysis by XPS of this specimen. Therefore, no assumption of preferential sputtering of oxygen is required to interpret the XPS profiles obtained using Ar^+ ion sputtering. From that result, the preparation conditions of specimen 3 have to be judged as being insufficient for the preparation of CuO layers. Further preparation experiments will require higher temperatures, higher oxygen pressure, or longer duration of oxidation annealing.

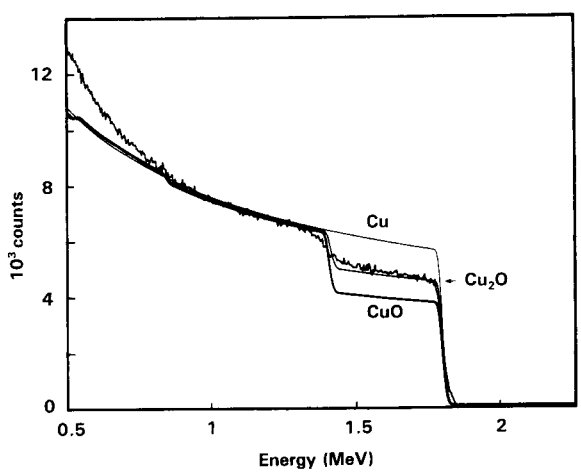

Fig. 6. RBS spectrum of specimen 3, together with computer simulations for Cu, Cu_2O and CuO.

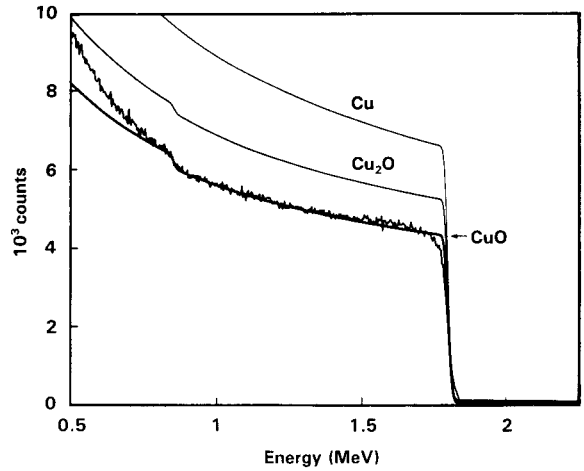

Fig. 7. RBS spectrum of powdered CuO, together with computer simulations for Cu, Cu_2O and CuO.

Table 5
Values from chemical analysis and RBS of the specimens prepared (measured data are printed in bold)

Specimen	Carrier gas fusion			Dissolution		Thickness (nm)	Cu/O ratio (mol/mol)
	Total oxygen ($\mu g/cm^2$)	Surface oxygen ($\mu g/cm^2$)	($\mu mol/cm^2$)	Surface copper ($\mu g/cm^2$)	($\mu mol/cm^2$)		
1	**2.1 ± 0.1**	–	–	**2.4 ± 0.8**	–	–	
2	**3.5 ± 0.15**	1.7 [a]	0.106	**14.8 ± 0.8**	0.233	27.5	2.2
3	**27.4 ± 0.6**	25.6 [a]	1.60	**111.6 ± 16** [b],	1.756 [b]	211.7 [b]	1.1 [b]
		RBS					
3		33.7 ± 2.7	2.11	268.0 ± 21	4.22	**500 ± 40**	**2**

[a] Calculated from the total oxygen diminished by (2.1–0.3) $\mu g/cm^2$.
[b] Dependent on the assumed mechanism of dissolution.

4.4. Sputtering yield

With the knowledge of the layer thickness, the sputtering yield for Cu_2O is obtained according to

$$Y = \frac{F\rho qd}{iMt}$$

Here, F is Faraday's constant, ρ is the density, q (≈ 0.06 cm^2) is the sputtered area, d is the layer thickness, i (= 390 nA) is the sputtering ion current, M is the molecular weight, and t (= 8 h) is the time to erode the oxide layer. With the thickness d = 500 nm determined from RBS, the sputtering yield is determined to $Y(Cu_2O) = 3.4$ atoms/ion. Based on the CGFA data (see below), this yield would result to 2.5 atom/ion.

4.5. Chemical analysis

As a less sophisticated approach, chemical analysis by CGFA and by selective dissolution of oxidized copper/photometry was used. The raw data obtained from CGFA and from the dissolution of the copper oxides are listed in Table 5, together with the respective RBS results. The total oxygen determined by CGFA, is composed of the oxygen forming the oxide layer and of the oxygen dissolved in the Cu bulk [a]. This last portion has to be substracted from the amount of the total oxygen of specimen 2 and 3 in order to obtain the oxygen amount of the oxide layer. It is determined from the total oxygen of specimen 1 diminished by the surface oxygen (0.3 $\mu g/cm^2$ as determined by Cu dissolution). This is calculated from the amount of copper (2.4 ± 0.8 $\mu g/cm^2$) assuming cuprous oxide (Cu_2O) as natural layer. Based on the ratios of copper to oxygen in the oxide layer, quoted in $\mu mol/cm^2$ (specimen 2: 0.233/0.106 = 2.2; specimen 3: 1.76/1.6 = 1.1), it must be concluded that an oxide layer is formed on the sample surface consisting of cuprous oxide Cu_2O in the case of specimen 2, and of cupric oxide CuO in the case of specimen 3. The deviations of the Cu/O ratios from the expected values is approximately 10% and can be explained by measuring uncertainties. However, the process of chemical dissolution of the oxide layers under the condition applied [11] is not verified in sufficient detail as yet. Dependent on the possible mechanisms of dissolution, the resulting Cu contents and, subsequently, the thicknesses and Cu/O ratios may differ from each other up to a factor of 2. Therefore, further experiments are required to explore the valid mechanism.

The results of the oxygen determination by CGFA are ca. 25% below the results for the integrated oxygen coverage as determined from RBS depth profiling. In view of the low coverage and the corresponding uncertainty of both values, this agreement appears to be acceptable. Thus, CGFA is considered to corroborate the RBS results, and also the conclusion drawn from XPS/factor analysis.

[a] This bulk oxygen has been checked not to increase during air annealing at 300°C. Annealed samples were treated to dissolve the surface oxide, and subjected to CGFA afterwards. The bulk oxygen was found at the same level as for the non-annealed samples.

5. Conclusion

XPS data from depth profiling analysis using Ar ion sputtering are subjected to factor analysis. This technique is found to be appropriate to obtain component depth profiles from the copper oxide layers prepared. The components identified can be attributed to Cu, Cu_2O, and a surface layer composed of cuprous and cupric oxides, the portions of which depend on the preparation conditions.

Therefore, XPS/factor analysis is successful in identification and determining the course of chemical species in these thin oxide layers. However, the problem of possible artifacts in depth profiling analysis due to sputter-induced alteration of the layers cannot be solved solely from XPS/sputtering data. Using RBS depth profiling, the stoichiometry of the oxide layer in question is unequivocally determined. From that result, the influence of sputter induced artifacts in this layer can be excluded, and the association to Cu_2O by XPS is verified.

Determination of oxide layer thickness by chemical analysis is also found to be feasible, using CGFA, which has proved to be a reliable method [23]. Results from CGFA agree with the result from the specimen investigated by RBS. Further experiments will be performed on high purity copper foil to discover the applicable mechanism in selective dissolution. Further experiments are also needed to prepare stoichiometric CuO layers, using higher temperatures, higher oxygen pressure, or longer oxidation time to prepare these thin oxide layers.

Acknowledgements

This work was supported financially by the 'Bundesminister für Forschung und Technologie' and by the 'Minister für Wissenschaft und Forschung des Landes Nordrhein-Westfalen'. Thanks are due to S. Karcz for technical assistance.

References

[1] J.M. Sanz and S. Hofmann, J. Electron Spectrosc. Relat. Phenom., 34 (1984) 149; Thin Solid Films, 120 (1984) 185.
[2] R. Holm and S. Storp, Appl. Phys., 9 (1976) 217; Appl. Phys., 12 (1977) 101.
[3] N.S. McIntyre and T.C. Chan, in D. Briggs and M.P. Seah (Ed.), Practical Surface Analysis, Wiley, Chichester, 2nd edn., 1990.
[4] H.J. Steffen and S. Hofmann, Surf. Interface Anal., 19 (1992) 157.
[5] T. Shimizu, H. Nonaka and K. Arai, Surf. Interface Anal., 19 (1992) 365.
[6] H. Nonaka, T. Shimizu and K. Arai, Appl. Phys. Lett., 57 (1990) 2850.
[7] A. Manara, V. Sirtori and L. Mammarella, Surf. Interface Anal., 18 (1992) 32.
[8] J.F. Moulder, W.F. Stickle, P.E. Sobol and K.D. Bomben, Handbook of X-ray Photoelectron Spectroscopy, Perkin-Elmer, Eden Prairie, MN, 1992.
[9] H. Bubert, L. Palmetshofer, G. Stingeder and M. Wielunski, Anal. Chem., 63 (1991) 1562.
[10] J.S. Powell and P.C. Joy, Anal. Chem., 21 (1949) 296.
[11] E. Grallath, Max-Planck-Institut für Metallforschung, Laboratorium für Reinststoffanalytik, Dortmund, unpublished results, 1993.
[12] S.W. Gaarenstroom, J. Vac. Sci. Technol., 16 (1979) 600.
[13] V. Atzrodt and H. Lange, Phys. Status Solidi, 79A (1983) 489.
[14] J.S. Solomon, Thin Solid Films, 154 (1987) 11.
[15] H.J. Steffen and S. Hofmann, Surf. Interface Anal., 14 (1989) 59.
[16] H. Bubert and H. Jenett, Fresenius' Z. Anal. Chem., 335 (1989) 643.
[17] Z.Z. Hugus Jr. and A.A. El-Awady, J. Phys. Chem., 75 (1971) 2954.
[18] E.R. Malinowski and D.G. Howery, Factor Analysis in Chemistry, Wiley, New York, 1980.
[19] A. Rönnquist and H. Fischmeister, J. Inst. Metals, 89 (1960–61) 65.
[20] L. Pedocchi, A. Billi, E. Marinelli, J.X. Wu and G. Rovida, Surf. Interface Anal., 19 (1992) 414.
[21] R. Kelly, Mater. Sci. Eng., 115A (1989) 11.
[22] G. Betz and G.K. Wehner, in R. Behrisch (Ed.), Sputtering by Particle Bombardment II (Topics in Applied Physics, Vol. 52), Springer-Verlag, Berlin, Heidelberg, New York, 1983, pp. 11–90.
[23] T.F. Chen, R.P.H. Garten, E. Grallath, H. Bubert and H. Jenett, Fresenius' Z. Anal. Chem., 329 (1987) 174.

ELSEVIER

Analytica Chimica Acta 297 (1994) 197–230

ANALYTICA CHIMICA ACTA

Review

Spatially multidimensional secondary ion mass spectrometry analysis

F.G. Rüdenauer

Austrian Research Ctr. Seibersdorf, A-2444 Seibersdorf, Austria

(Received 21st November 1993)

Abstract

This article gives a survey on recent technical developments in imaging secondary ion mass spectrometry (SIMS) analysis. In the first section, the three instrumental imaging principles (scanning ion microprobe, ion microscope, image dissector) are shortly described and their capabilities are compared. In the second section, data acquisition and data handling techniques are treated, with particular emphasis on 2-dimensional imaging and its natural extension to 3 spatial dimensions via image stacking. The potential of retrospective analytical evaluation of 3D image stacks is demonstrated. The third section concentrates on quantification techniques for mass spectra and ion images. The state of the art of image quantification is described and the limitations of the standard method, sensitivity factor correction, are demonstrated. In the fourth section the concept of "imaging" of an analytical sample is treated as a process of (imperfect) information transfer, transforming the spatially 3-dimensional elemental atomic density in the sample into an "ion image" stored in a computer. This view offers a natural mathematical concept of "resolution" and its dependence on instrumental as well as sample parameters. This concept can be naturally extended to statistically limited imaging where spatial resolution is not limited by instrumental parameters but rather by the number of atoms available for analysis.

Keywords: Mass spectrometry; Spatially multidimensional SIMS; Technical developments in SIMS

1. 2D-Imaging principles in SIMS

"Imaging" in secondary ion mass spectrometry (SIMS) can be considered as the process of *reconstruction* of the spatially 2-dimensional ion emission density at the sample surface from the spatial or temporal distribution of secondary ions arriving at the mass spectrometer detector. Three different imaging principles have been technically realized (a) the scanning ion microprobe, (b) the ion microscope, (c) the image dissector ion microscope.

1.1. Scanning ion microprobe

In the scanning ion microprobe the spatial information is *impressed* onto the primary ion beam: a focused beam with small diameter is scanned across the sample surface by applying certain time-dependent voltage patterns onto X/Y deflection plates. Secondary ions emitted in

* Corresponding author.

SSDI 0003-2670(93)E0661-P

close vicinity of the impinging primary ions, are mass analyzed and detected time-sequentially at the mass spectrometer detector (Fig. 1). The spatial information contained in the primary beam is used to decode the time series of detector pulses and reconstruct the spatial distribution of ion emission at the sample surface. An essential requirement in this process is, that secondary ions are emitted in close spatial and temporal vicinity of the impinging primary ions. Thus, physical properties of the emission process, i.e. the spatial and temporal extent of the collision cascade are essential to the 3-dimensional localization of the point of origin of emitted secondary ions. Computer simulations yield typical values of 10^{-12} s and 30 nm for lifetime and spatial extent respectively of a collision cascade released by a 50 keV Ga ion on Si [1,2]. Modern ion microprobes equipped with a liquid metal primary ion source actually are approaching this "cascade" resolution limit.

The first commercial scanning ion microprobe was developed by Liebl [3]. This instrument used a Duoplasmatron primary ion source, a two-stage electrostatic primary lens system and a double focusing mass spectrometer for analysis of secondary ions. The smallest resolvable distance was of the order of 1–2 μm and all three conventional analytical SIMS modes: bulk analysis, profile analysis and imaging analysis were successfully performed. The instrument was known as the IMMA (ion microprobe mass analyzer) and marketed by Applied Research Labs. at Sunland, CA.

The next major step forward occurred when high brightness liquid metal primary ion sources were introduced [4–6]. Smallest resolvable distances below 0.1 μm now became available in commercial SIMS instruments. The new instrument generation was equipped with an ultra high vacuum (UHV) sample chamber, automated target manipulation and computerized beam scan-

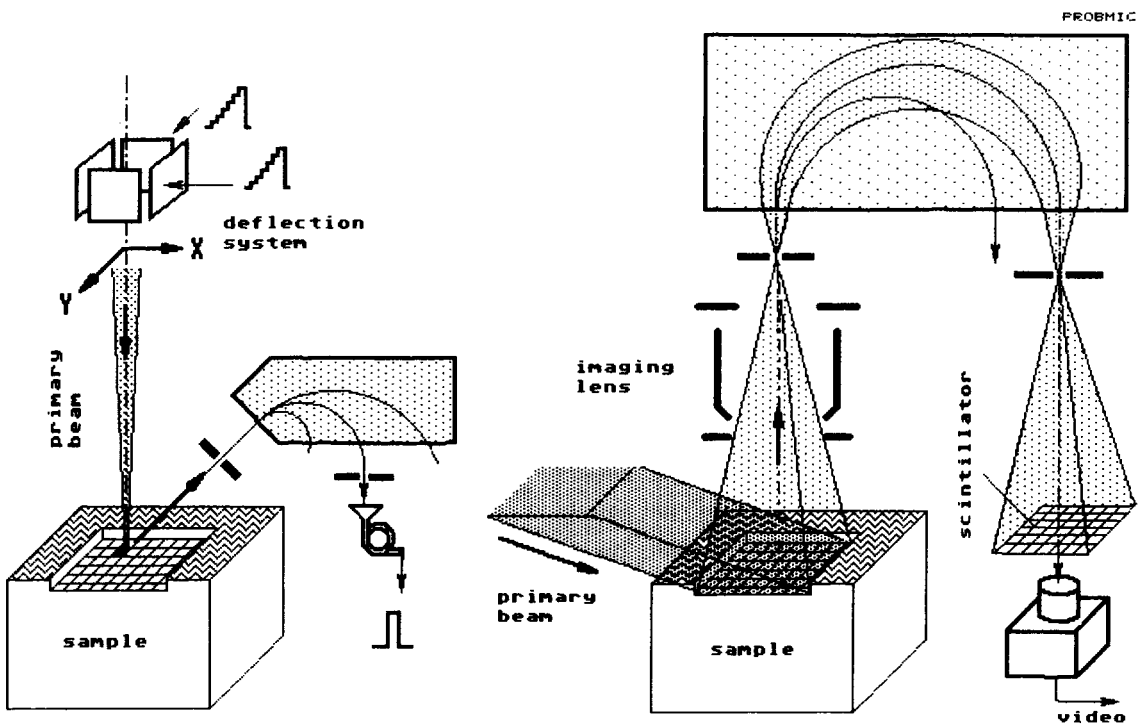

Fig. 1. Image formation in scanning ion microprobe (left) and ion microscope (right), schematic.

ning and digital image storage capability. VG IONEX at Burgess Hill (formerly VG Instruments) was pioneering the commercial introduction of this instrument type. Many remarkable results were obtained.

A scanning ion microprobe with very high spatial resolution was designed and built at the university of Chicago, in cooperation with Hughes Res. Labs. [7,8] (UC-HRL-ion probe). A schematic of this system is shown in Fig. 2. The primary ion gun consists of a Ga liquid metal ion source (LMIS) similar to that described by Seliger et al. [9] and a three-element asymmetric electrostatic lens [10] forming an intermediary source crossover in the plane of a differential pumping aperture. A pre-objective electrostatic dual octupole assembly is used for beam adjustment and scanning. An electrostatic "einzel-lens" objective produces the final beam spot with perpendicular incidence at the target surface. Positive or negative secondary ions leaving the target in perpendicular direction are accelerated by a voltage of the order of ± 100 V, applied to the target and energy analyzed by a small, 8 mm radius cylindrical electrostatic deflector fitting into the space between target and objective lens (total height 1.2 cm). The deflected secondary ions are focused by a multielement transport optics into a quadrupole mass analyzer. Mass selected secondary ions are detected by a channeltron multiplier operating in the pulse counting mode. Imaging information can be obtained either from the quadrupole detector (SIMS mode) or a second channeltron detecting either ion induced non-mass filtered secondary ions ("ISI"-mode) or ion induced secondary electrons ("ISE"- or "SIM"-mode, "scanning ion microscopy"), respectively. Beam positioning and scanning is controlled by a digital image acquisition and processing system [11]. This system also takes over image storage, display and processing tasks. Table 1 lists some of the characteristic data of the instrument.

Smallest resolvable distances down to 20 nm have been determined in SIMS images (Fig. 3).

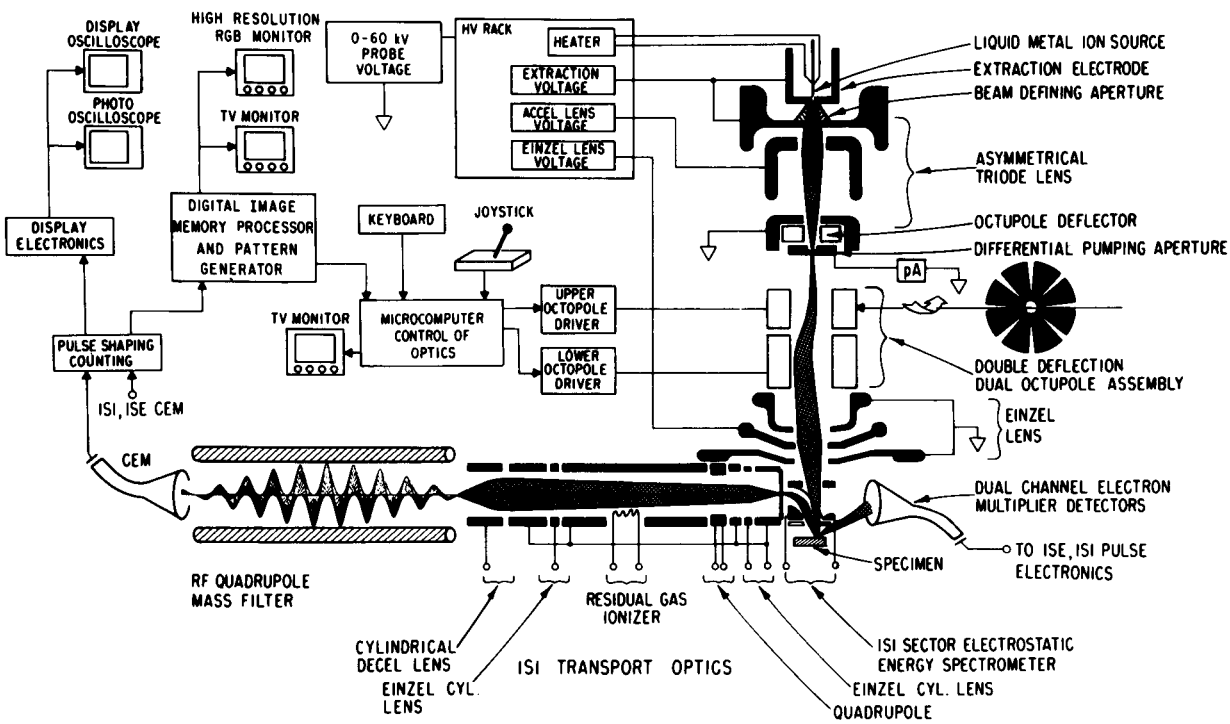

Fig. 2. Schematic of the UC/HRL submicron ion microprobe; courtesy R. Levi-Setti.

Table 1
Typical operating data of the UC-HRL scanning ion microprobe

Primary ion energy	20–60 keV primary
Spot diameter	20–100 nm
Primary beam current	2–50
Pixel number	1024×1024
Image recording time	256 s (typ.)
Secondary ion transmission	= 0.2% for Al^+
Mass resolution	$M/\Delta M = 300$
Base pressure in chamber	5×10^{-10} Torr

This is close to the limit set up by the spatial extent of the sputtering cascade [1]. With a beam current of 2 pA into a 20 nm primary spot counting rates of the order of 10^5 counts/s are obtained from oxygenated surfaces for many elements. This translates into useful yields (see 3.1.) between 1×10^{-4} (for Si^+) and 0.1 (for Li^+) detected ions/sputtered atom [12]. For the low-mass range this is of the same order, for heavier masses it seems to be lower than what is achievable in high sensitivity double focusing mass spectrometers [13]. The destructive nature of SIMS however is setting up an interdependency between spatial resolution (in three dimensions) and detection limit [14,15]. Curves representing a theoretical estimate for this relation are shown in Fig. 4 together with some experimentally determined values. Obviously, at 20 nm resolution, detection limits are in the 10 at.% range. This is of the same order of magnitude than estimated for Auger microprobes in this resolution range. In SIMS however, an image of such spatial resolution can be recorded in about 256 s, whereas an

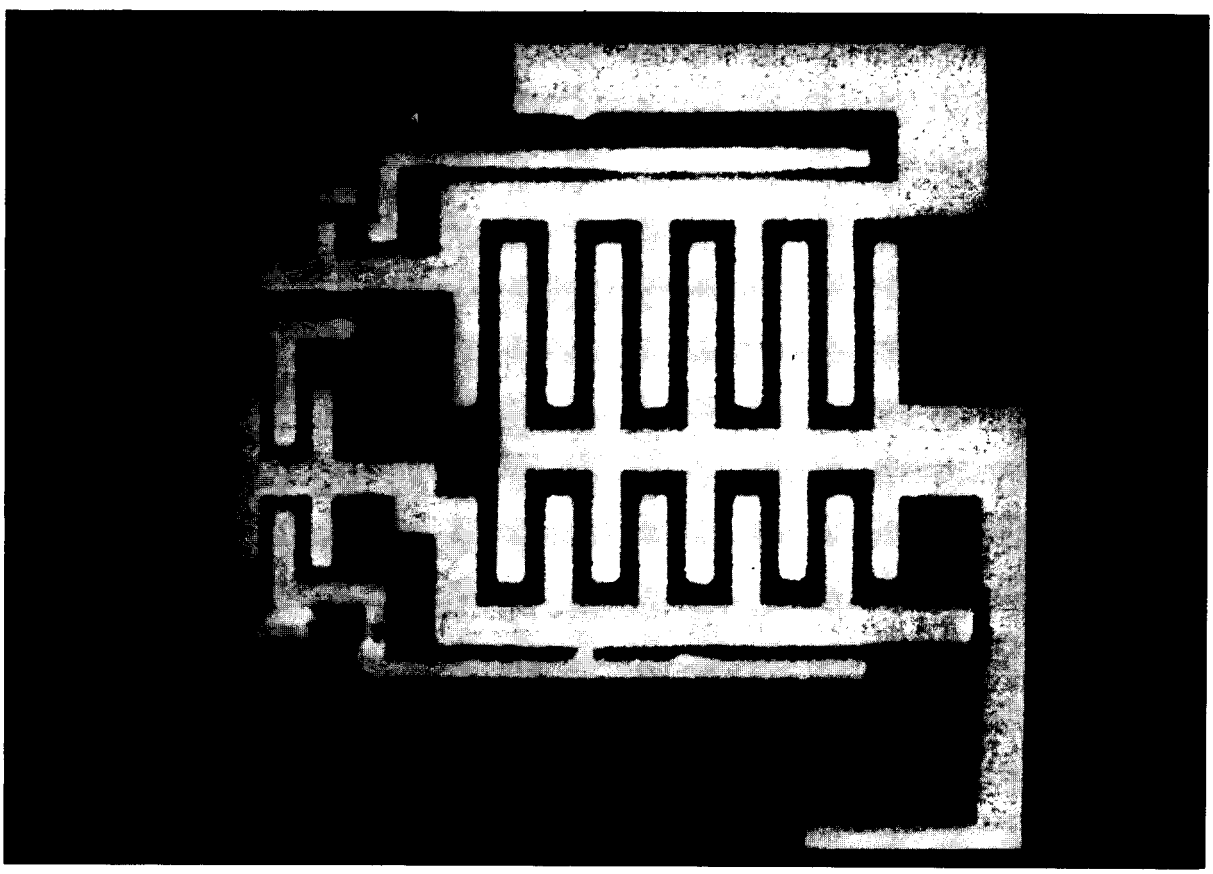

Fig. 3. High resolution Al^+ ion image obtained with the UC/HRl ion microprobe. Scale bar 1 μm. Courtesy R. Levi-Setti.

Auger probe requires image recording times of the order of 30 min.

1.2. Ion microscope

In an ion microscope the sample is bombarded ("illuminated") by a broad primary ion beam. (Fig. 1). Secondary ions are accelerated by an electrostatic emission lens forming a virtual image of the secondary ion emission density distribution by virtue of the imaging properties of a homogeneous electrostatic acceleration field [16]. This image then is transported through a stigmatic focusing mass spectrometer and projected in a magnified scale on a scintillator screen or equivalent detector equipment. The lateral resolution of this imaging process is limited by the energy spread of the secondary ions and the chromatic aberration of the emission lens.

The commercial standard of an ion microscope instrument is the CAMECA IMS 3F [17]. In the IMS 4F version, the microscope and microprobe modes are incorporated in a single instrument (Fig. 5). Two ion sources (1) and (2) can be operated alternately. A magnetic mass selector (3) selects ions with the appropriate mass number and deflects them into a 3-lens primary focusing gun. A scanning system deflects the focused beam across the sample (5). Secondary ions from the sample are focused by an immersion lens (4) and an electrostatic transfer system (7) so that a virtual image of the sample emission intensity distribution is generated inside the double focusing mass spectrometer (8–14). A dynamic emittance matching system is incorporated in the transfer optics which guarantees high ion transmittance from a large field of view in the scanning probe mode of operation. A projection lens system (15) projects the mass selected virtual sample image onto a multichannel-plate/scintillator combination where a magnified image of the element distribution is displayed. This image can be viewed

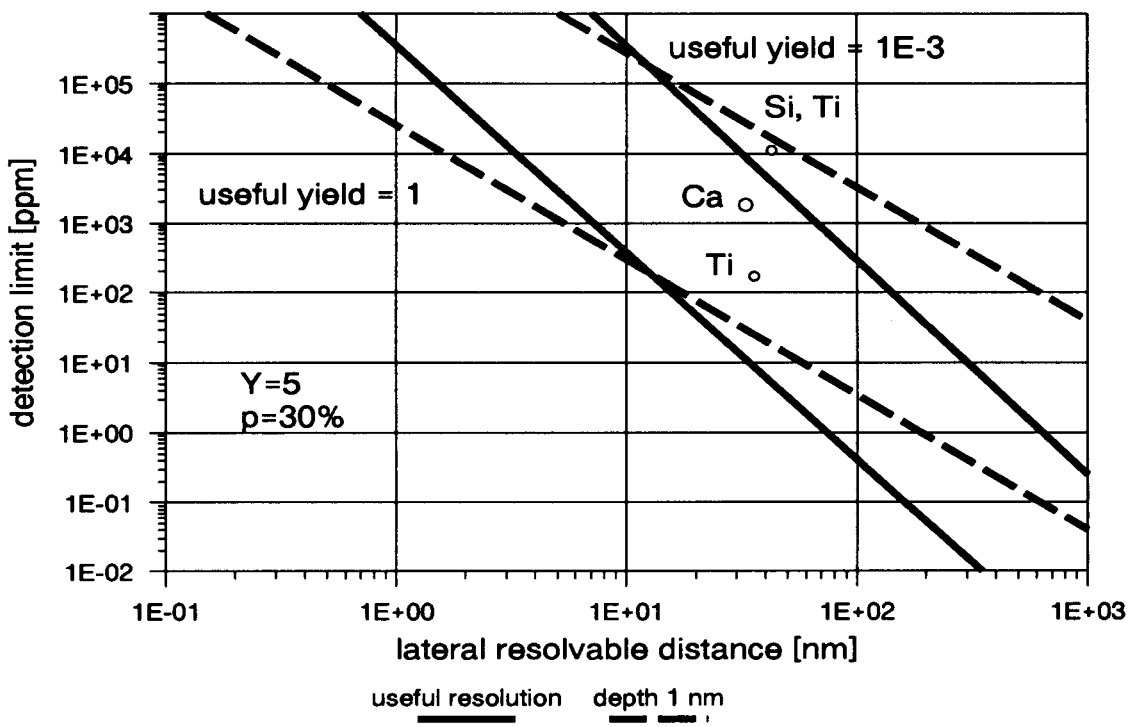

Fig. 4. Connection between detection limit and lateral resolvable distance in SIMS. δ_{10}, sputtering depth 10 nm; δ_u, depth equal to spot diameter (useful resolution). Assumptions: sputter yield = 5, $\tau_u = 10^{-3}$ (curves 1,2); $\tau_u = 1$ (perfect postionization and transmission, curves 3,4). Marks: experimental points (lower limits) according to Chabala et al. [12].

by a microscope or TV-camera. TV images can be digitized and stored in an image processing system. Alternately, the mass selected secondary ions can be deflected electrostatically (9) onto a Faraday detector/multiplier combination (21), (22) where they can be detected in DC or ion counting mode. The signal from the multiplier is used in the ion microprobe mode to generate scanning ion images with high sensitivity. The mass spectrometer can be operated in a high

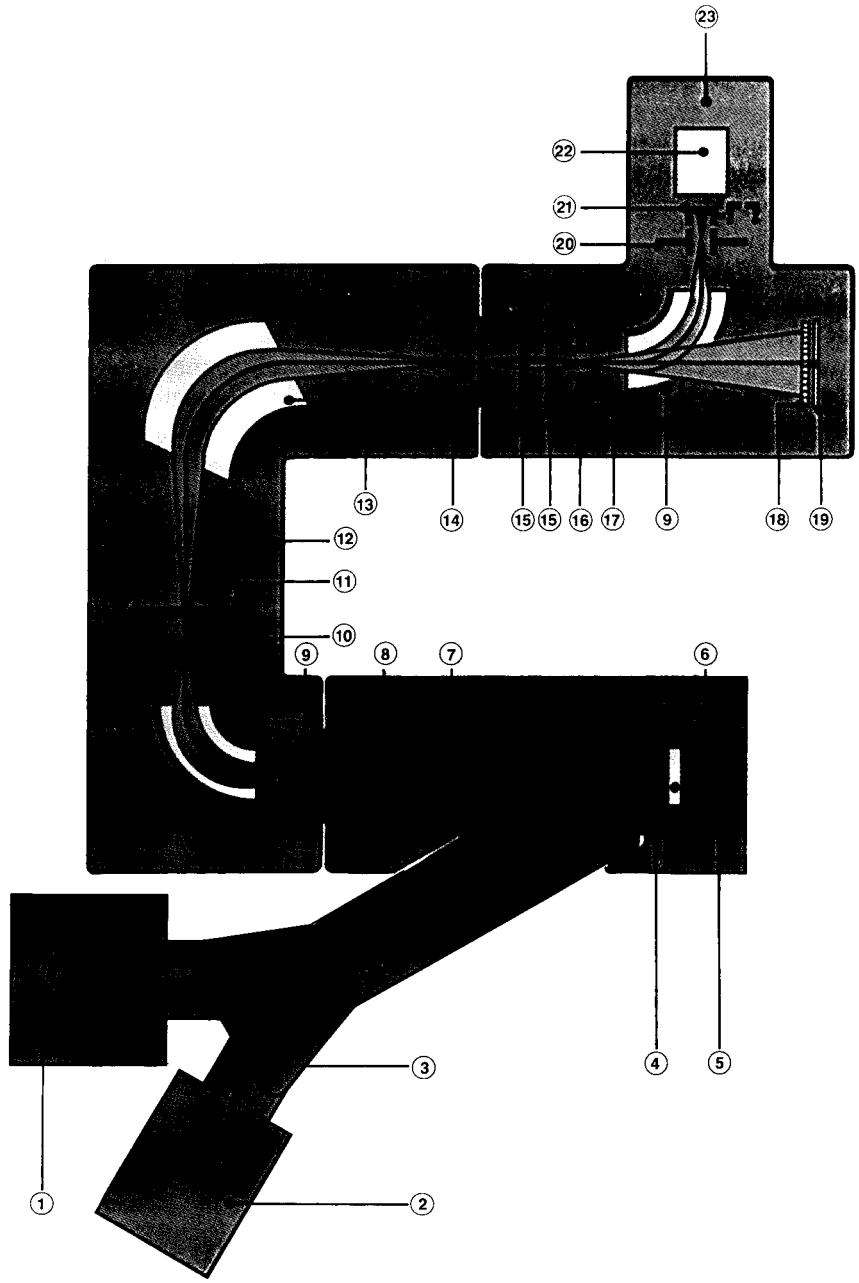

Fig. 5. Schematic of IMS 3f ion microscope [17].

mass resolution mode ($M/\Delta M > 12\,000$) for separation of isobaric masses.

1.3. The image dissector ion microscope

The image dissector ion microscope is a hybrid between ion microscope and scanning probe. Similar as in the ion microscope, the sample is illuminated by a broad primary ion beam (see Fig. 6). An emission lens produces a virtual image of the ion emission density at the sample surface. A magnified real image of this first virtual image is projected onto an aperture plane. A pair of X/Y-deflection plates is scanning the whole image across a small central aperture in this plane so that only that part of the ion image corresponding to the central resolution element can pass through the mass spectrometer. Detection and decoding of the image information from the time series of detector currents is identical to the scanning probe. As in the ion microscope, the spatial resolution and the secondary ion transmission in the dissector is determined by the properties of the emission lens.

The first image dissector ion microscope was built by McHugh (as reported in [14]) who combined an immersion lens system with deflector and a magnetic mass spectrometer. Another image dissector microscope has been built at Kiev, Ukrainian Republic by Cherepin [19] (see Fig. 6). The primary beam is generated in a cold cathode duoplasmatron (19), shaped by two condenser lenses (20,21) and is hitting the target (1). An immersion lens (2) accelerates and focuses the secondary ions into an unfiltered intermediary image of the surface, much as in the ion microscope. The contrast diaphragm (3) limits lateral energy spread of transmitted ions and therefore determines spatial resolution. The unfiltered intermediary image is projected in variable magnification to the surface electrode of an ion/electron image converter (7–9) with the help of the transfer lens (5). Secondary electrons from the converter electrode are accelerated back into the direction of the incoming ion beam and focused by the immersion lens (9–7) onto the scintillator screen (18) where a magnified electron image (ca. 200×) corresponding to the total ion emission

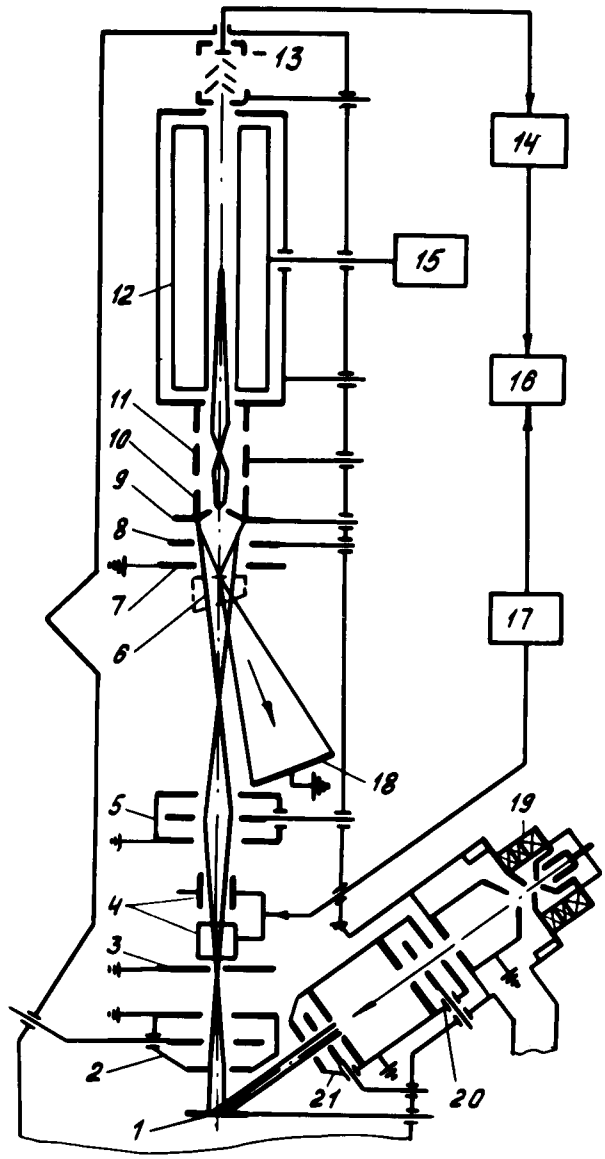

Fig. 6. Schematic of Kiev monopole image dissector ion microprobe; further explanations see text; courtesy V.T. Cherepin.

density in the sample plane can be observed. A small permanent magnet (6) is used to deflect the electron image out of the axis of the secondary ion beam. This observation system for the unfiltered image is similar to that used in early ion microscopes [16]. Ions passing the hole in the converter electrode (9) are decelerated by the

immersion lens system (9–11) into the quadrupole mass analyzer (12). Mass-filtered ions hit the conversion dynode of the electron multiplier (13) producing ion pulses which are amplified (14) and recorded in the central processing unit.

The unfiltered image observed on the scintillator screen is mainly used to place the area of interest into the dissector aperture in (9). By varying the optical power of the immersion/transfer lens system (2,5) and by feeding appropriate voltages to the deflection system (4) it is possible to vary size and location of the area of interest from which mass spectra or depth profiles are to be obtained. If the crossover of the transfer lens (5) is placed into the dissecting aperture, the secondary ion beam passes completely and an average analysis of the full illuminated sample area is obtained. By setting the quadrupole to a certain mass number and scanning the unfiltered image across the dissecting diaphragm, using the deflection system (4), a "scanning" elemental distribution image of the selected element can be obtained.

1.4. Comparison

Spatial resolution is actually limited by physical properties of the secondary ion emission process in all three imaging modes. Whereas in the scanning probe the limit is set up by the spatial extent of the collision cascade, the essential factor in the microscope and the image dissector is the energy distribution of the secondary ions. Whereas the cascade width contribution is fundamental in the microprobe, the resolution in the microscopic mode can, in principle at least, be improved by narrowing down the acceptance windows for emission energy and beam divergence at the cost of signal intensity. Note also, that in the microscope the lateral extent of the collision cascade is not a factor limiting lateral resolution.

Information flow, as expressed e.g. by the total number of detected ions/s, irrespective of the point of origin, at high spatial resolution is higher in the microscope than in the microprobe since it is spot limited in the former and acceptance limited in the latter case. In a given time interval we obtain high information from a small number of pixels in the microprobe and little information from a large number of pixels in the microscope. Therefore, the image recording time generally is lower in the microscope since all pixels within the field of view are processed in parallel. On the basis of equal total count numbers/image the ratio of image recording times for the scanning microprobe (SP) and the microscope (MS) mode can be calculated by multiplying the pixel recording times t_{pix} by the number of pixels in an image of diameter d_f [μ] [20]:

$$\frac{t_{im,SP}}{t_{im,MS}} = \left(\frac{t_{pix,SP}}{t_{pix,MS}}\right)\cdot\left(\frac{d_f}{\delta}\right)^2$$

$$= \left(\frac{J_{MS}}{J_{SP}}\right)\cdot\left(\frac{T_{MS}}{T_{SP}}\right)\cdot\left(\frac{d_f}{\delta}\right)^2 =$$

$$= 7\times 10^{-3}\cdot\left(\frac{J_{MS}}{J_{SP}}\right)\cdot\left(\frac{E}{\epsilon}\right)^{2/3}$$

$$\cdot\delta[\mu]^{2/3}\cdot\left(\frac{d_f}{\delta}\right)^2 \qquad (1)$$

Here, T_{MS}, T_{SP} are the transmissions and J_{MS}, J_{SP} the local primary current densities for microscope and microprobe respectively; $T_{SP} = 1$ has been assumed and $\delta[\mu]$ is the lateral resolution measured in micrometers. Assuming standard values $J_{SP} = 1$ A/cm^2 (chromatically limited liquid metal primary source), $J_{MS} = 5$ mA/cm^2, $E = 10^4$ V/cm, $\epsilon = 10$V, $d_f/\delta = 256$ we obtain

$$\frac{t_{im,SP}}{t_{im,MS}} \cong 46\cdot\delta[\mu]^{2/3} \qquad (1a)$$

i.e. approx. 50 times faster image recording in the microscope at 1 μm spatial resolution and comparable image recording times at a hypothetical 3.2 nm resolution. A slightly different relation has been derived for spherically limited primary ion beams [14].

The useful yield (see Section 3.1.) actually determines the amount of information (detected ions) which can be obtained from a given sample volume. It therefore is the essential parameter determining detection efficiency in the reconstruction of 3-dimensional element distributions.

The ratio of useful yields for microprobe and microscope can be calculated as [20]:

$$\frac{\tau_{SP}}{\tau_{MS}} = \frac{T_{SP}}{T_{MS}} = 2^{-5/3} \cdot \frac{(\epsilon/E)^{2/3}}{\delta^{2/3}}$$

$$\cong 1.46 \times 10^2 \cdot \frac{(\epsilon/E)^{2/3}}{\delta[\mu]^{2/3}} \quad (2)$$

For the same numerical assumptions as above we estimate

$$\frac{\tau_{SP}}{\tau_{MS}} \cong \frac{1.46}{\delta[\mu]^{2/3}} \quad (2a)$$

i.e. a definite advantage for the microprobe at resolvable distances below 1 μm.

The ratio of useful yields also determines the ratio of sputter depths Δ required to acquire images with the same total pixelcount numbers in the microscope and the microprobe [19]:

$$\frac{\Delta_{MS}}{\Delta_{SP}} = \frac{\tau_{SP}}{\tau_{MS}} \cong \frac{1.46}{\delta[\mu]^{2/3}} \quad (3)$$

Again, a slightly different expression holds for spherically limited primary beams.

A comparative assessment of the two imaging principles which today are employed in commercial instruments must consider the following facts:

(i) all pixels are processed parallel in the microscope.
(ii) instrument transmission is lower in the microscope.
(iii) generally image recording time is shorter in the microscope.
(iv) sputter depth/image is higher in the microscope.
(v) useful yield is higher in the scanning probe.

Note that the terms "ion probe" and "ion microscope" refer to particular primary beam illumination modes [21] of the sample and not necessarily to physically different instruments. In fact, the CAMECA 4F-instrument (see Section 1.2.) incorporates both the primary beam scanning ion microprobe and the direct imaging ion microscope modes.

2. 3D-Imaging and image processing

Ion microprobe mass spectrometry, by virtue of its ion optical imaging capability, is a well-known method for investigation of 2-dimensional element distributions at solid surfaces. This property can be combined with the continuous sputter-removal of atomic surface layers, inherent to all ion beam methods, to perform spatially 3-dimensional microanalysis of solids. The technique can be implemented on scanning ion microprobes and ion microscopes. A microcomputer is required to control acquisition of secondary ion intensity data which are stored as pixel intensities in a stack of 2-dimensional ion images obtained from the same lateral field of view during continued beam sputtering [22]. This image stack contains the spatially 3-dimensional element distribution in the analyzed microvolume of the solid (Fig. 7). From this 3D-data set all conventional analytical modes (local analysis, line scan analysis, depth profile analysis, image analysis) of ion probe analysis can be reconstructed retrospectively using numerical methods [15,23]. Additional display modes, e.g. animated image series, surface reconstruction of inclusions or grain boundaries can be implemented by suitable selection and rearrangement of 3D image elements ("voxels"). Spatial resolution limits of the technique in the lateral dimension are determined by ion optical properties of the microprobe used, depth resolution is limited by physical properties of the sputtering process. State-of-the-art values are < 20 nm and < 0.3 nm respectively under favourable sample conditions [6,7,14]. A superseding resolution limit may be set up by the destructive nature of SIMS [15]: since a sputtered microvolume (voxel volume) contains a limited number of atoms, of which a generally small ionized fraction is recorded at the detector, the detected ion count depends on voxel volume, instrument transmission and element concentration. For a voxel count with desired statistical significance, the voxel volume therefore must exceed a minimum size (Fig. 4).

Retrospective point analysis now is performed by selecting single correlated voxels in each elemental 3D-stack and displaying voxel intensity in

the form of a "mass spectrum". 1-Dimensional line analysis can be performed by selecting voxels along an arbitrary line in the stack and displaying voxel intensity as "line scan". Depth profiling is realized by summing voxel intensities over identical arbitrary subareas in surface-parallel stack-planes and displaying the voxel sum versus depth from the original surface. Conventional 2D image analysis is performed by selecting an arbitrary surface-parallel stack-plane and displaying voxel intensity distribution in the form of an intensity modulated "ion image". These images are usually addressed as "coaxial" images since the direction of observation is coaxial with the sputtering direction.

Digital storage and processing of 3D data sets allows to generalize and extend these "conventional" modes and also to create qualitatively new analytical modes. In line scan analysis, for example, the line along which voxel intensities are displayed can be arbitrarily oriented in 3D space, and may even be an arbitrary 3D-curve. In addition, spatial averaging can be performed along the line in order to improve statistics of data. In image analysis, the 3D stack can be intersected by arbitrarily oriented planes and the voxel intensities in the intersection plane can be displayed as 2D image. A special case here are "transaxial" images obtained for intersection planes oriented perpendicularly to the original macroscopic sample surface. Similar to a CT (computer tomographic) image, a transaxial image offers a view into the interior of the sample. Contrary to tomographic imaging however, transaxial images can be obtained in SIMS, in principle at least, by simple rearrangement of raw voxel data so that complicated image reconstruction algorithms are not required [22,24]. A qualitatively new analytical mode is the reconstruction of 3D feature shapes in the form of 2D surfaces in 3D space [18] which turns out to be particularly useful for morphologic analysis of microstructures such as

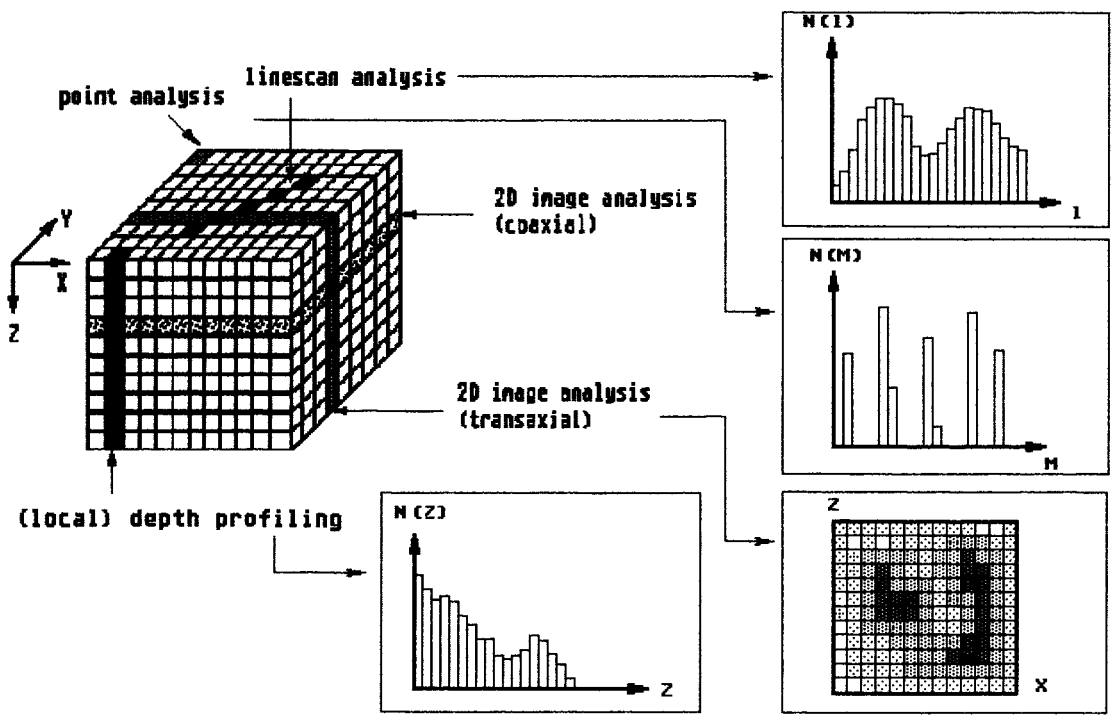

Fig. 7. Retrospective evaluation modes from 3D image stack.

grain boundaries, precipitates or lithographic structures. Examples for practical application of these techniques will be described below.

2.1. Display of 3D-distributions

Series of coaxial images

The simplest way to visualize a 3D elemental distribution is to simultaneously display a number of coaxial images, directly acquired and stored during a 3D analysis session, on the screen of the image storage unit. Rough comparison of image features at different sputtering depth is possible in this way. Fig. 8 shows such a "static" image series obtained during sputtering through a lithographically produced Al-microdot of 50 μm diameter and 0.2 μm height on a Si-substrate (Fig. 9). A series of 64 Al-images with 256 × 256 pixels each was obtained in this way. Starting from the image obtained immediately at the microdot surface (upper left), image shape and intensity seem to remain approximately constant through rows 1–4; this is to be expected due to the cylindrical shape of the microdot. Starting from row 5, however, the image appears to shrink gradually until almost no Al signal is present after image no. 62. The images also seem to move off centre somewhat in the lower rows, the degree of this shift cannot however be easily determined in such a display mode.

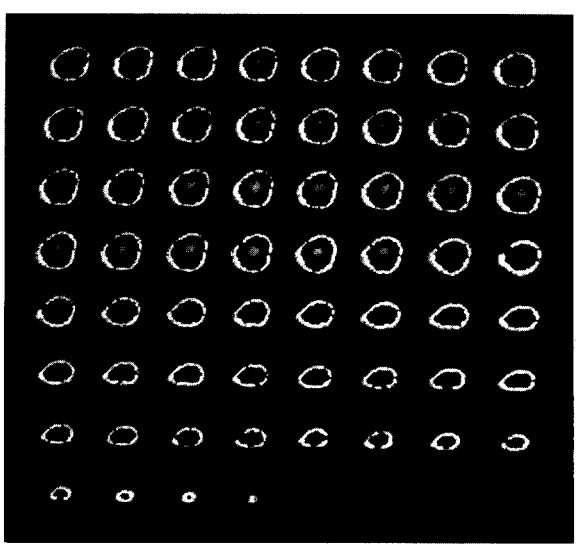

Fig. 8. Series of coaxial Al^+ images obtained during sputtering of microdot shown in Fig. 17. Original in pseudocolours.

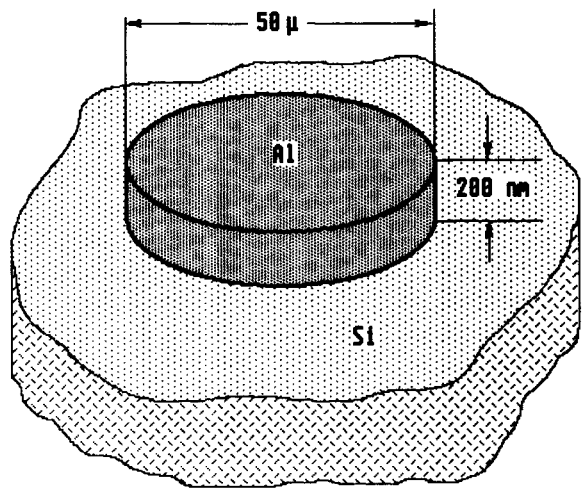

Fig. 9. Sample geometry of lithographically produced Al microdot.

Animated image series

Another possibility of presenting the complete 3-dimensional distribution of one or more elements to the observer is to replay, in an accelerated timescale, the surface distribution as it changes in the course of the original data-taking sputtering process. The observing analyst then can stop the replay at any desired time and evaluate in detail the "frozen" image corresponding to the lateral distribution at a certain depth below the original surface. In our terminology such an animation sequence would consist of a time-sequential display of consecutive coaxial elemental distribution images. The problem to overcome here is the frequently small number of individual elemental frames acquired during sputtering through the sample; even if fast storage capacity for say 50 frames per element is available, a replay of these data, at the usual TV-standard would take only about 2 s. Various methods are available to extend this to a timescale more adapted to human perception capabilities, e.g. frame-jump, linear interpolation [20] and random updating [25].

Coaxial and transaxial sections

An example illustrating the capabilities of transaxial sectioning is given in Fig. 10. The sample is a structured implant of boron in Si consisting of 4 μm wide implanted stripes and 6 μm wide spaces. The depth of the implanted regions is about 0.6 μm. The sample was sputtered in an ion microscope until the full implanted depth was sputtered through. Coaxial images were taken continuously during sputtering using a reactive anode encoder (RAE) in the image plane of the microscope (see Fig. 5). The resulting coaxial image stack was sectioned along a line perpendicular to the implant stripes, giving the transaxial 2D-image shown in Fig. 10. In this "cross section" through the sample it can be seen that the B-intensity in the implanted stripes peaks at a depth lying somewhat below the surface. This is a known property of the implant-range distribution. What is however peculiar is the fact that B also can be detected in the "unimplanted" regions. This may be either an instrumental artifact or an incomplete shielding by the photoresist mask used in the fabrication of the patterned implant (see Fig. 10). Another example for transaxial sectioning is shown in Fig. 11. This is a retrospective vertical slice from a stack of images acquired during sputtering through a AlGaAs/GaAs multi-quantum-well of 70 Å repeat layers. The image demonstrates the excellent depth resolution capability of the method. Since the microvolume, sputtered during a 3D analysis usually does not extend to more than a few μm in depth but covers a few tens of μm laterally, the display depth scale usually is extended in order to utilize the full display area.

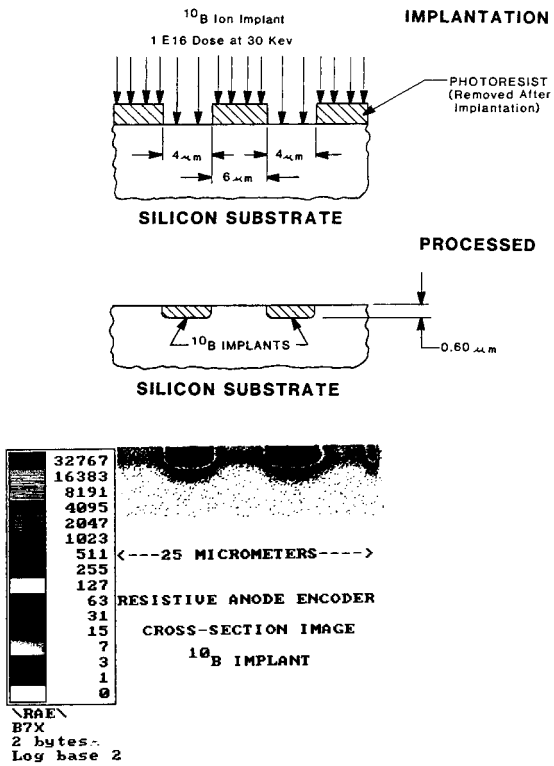

Fig. 10. Upper half: production steps for structured boron-implant in Si. Lower half: transaxial image of $^{10}B^{+}$. Original colour coded. Courtesy C.A. Evans and Associates.

Pie sections

A very informative method for display of 3D-distributions is "Pie"-sectioning. From the 3D data set a piece, defined by two transaxial sectioning planes, is "cut out" like a piece is cut out from a pie. The cut out piece (or the remaining piece, according to visibility) of the 3D data set is drawn in perspective onto the display screen. The distribution of a selected element on the surfaces of the cut out piece is displayed using standard 2D-display techniques (intensity modulation, colour coding or iso-intensity contours). The visible surface consists of spatially connected parts from one coax section and from two transax sections through the 3D data set. Thus, the chemical structure of the interior of the sample can be observed and spatially correlated to the structure at the surface [26,27].

The usefulness of the Pie-sectioning technique is demonstrated in the analysis of a boron-double implant (50 kV, $2 \times 10^{16}/cm^2$) in Si. The first implant zone is in the shape of a vertical (with respect to the field of view of the instrument) strip of 200 μm width. It has been annealed for 2 h at 1000°C. The second implant (horizontal strip of same dimension) is not annealed (Fig. 12). Analysis was performed in the intersection area of the implants by sputtering to a depth of approximately 2 projected ranges and recording a stack of 18 coaxial images during this process.

Intersecting this data volume with two perpendicular transaxial planes parallel to the implanted stripes would obviously show transax distribution images through the diffused and the undiffused stripes in the front and right view of the cutout Pie piece respectively and an additional coax distribution in the top view. Fig. 13 shows an actually measured Pie-section through the analytical volume. The top plane of this section is the coaxial image directly at the sample surface. The dimensions of the imaged volume are 350×350 μm laterally and 0.6 μm in depth. The different distributions of boron in the diffused (vertical) and the undiffused stripe are clearly visible: (a) B has diffused to the surface so that the vertical stripe is clearly visible in the top plane, whereas almost no intensity is visible in the horizontal stripe; (b) B has also diffused laterally as visible from the widths of the intersections through the two implanted zones; (c) the depth positions and intensities of the concentration maxima in the two stripes are almost identical; diffusion mainly has occurred in the low-concentration regions of the profile.

A more quantitative comparison of the B diffusion in the unannealed and the annealed stripes is possible by constructing retrospective local depth profiles and local lines scans, indicated schematically in Fig. 12.

2.2. Local depth profiles

Once a 3D image stack has been stored in the computer, depth profiling can be performed ret-

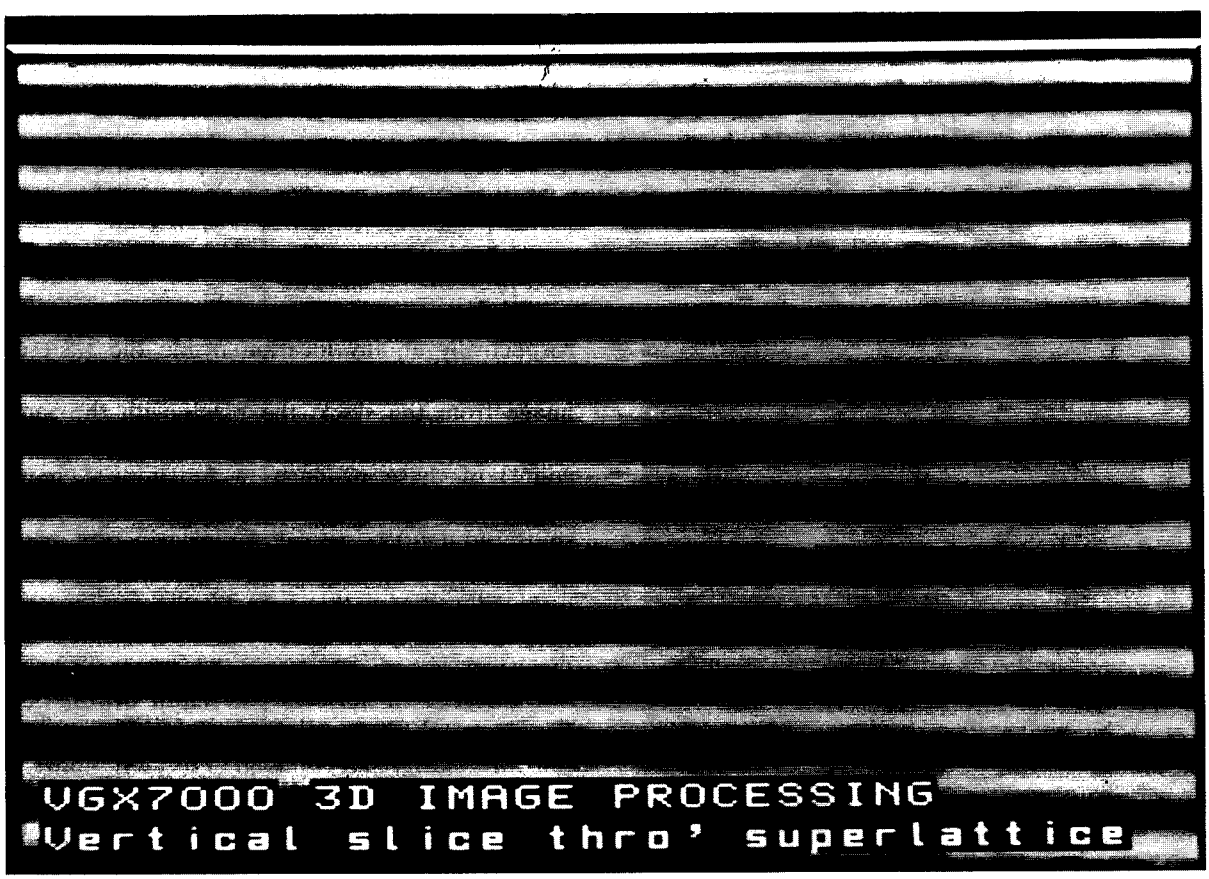

Fig. 11. Transaxial image (Al_2^+) of AlGaAs/GaAs multi-quantum-well device with 70 Å repeat layers. Courtesy VG Ionex, Burgess Hill, UK.

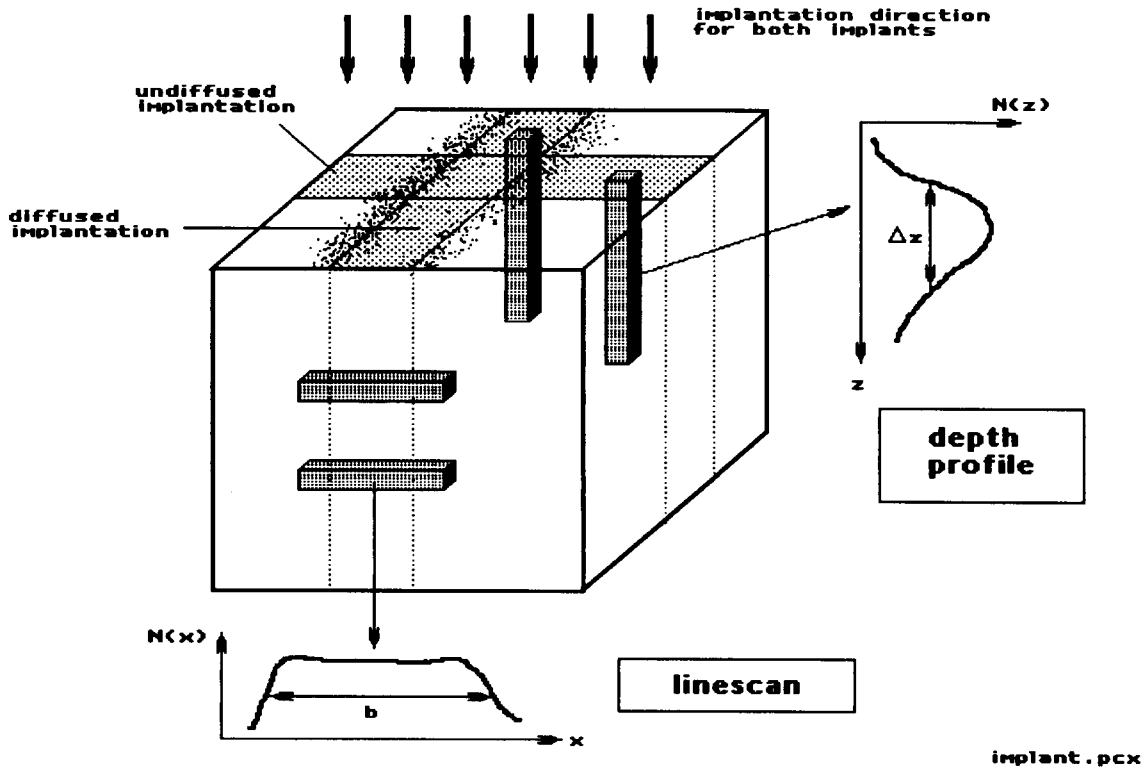

Fig. 12. Possibilities for retrospective quantitative 3D evaluation of double implant; further explanations, see text.

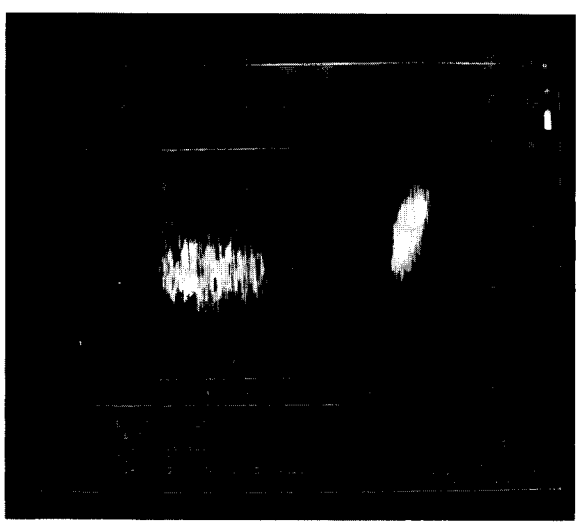

Fig. 13. Pie section through structured double implant of ^{11}B described in Fig. 12. Diffusion of annealed vertical stripe is clearly visible. Original colour coded.

rospectively at any location inside the rastered sample area (see Fig. 7) by selecting, in each coax image from the stack, the pixels with the same X/Y-coordinates and displaying the content (ion count) of these pixels as a function of frame number (frame number can be easily coded in sputtered depth). Instead of displaying the intensity of a single pixel in each frame, the sum of pixel intensities within a certain region, centred around the selected pixel, can be calculated and displayed as a depth profile. This procedure reduces statistical noise in the depth distribution, approximately proportional to the diameter of the averaging surrounding. Fig. 14 shows a boron-profile, computed from the 3D data set of the structured implant already shown in Fig. 10. The averaging zone was a 4×4 μm area centred in one of the implanted stripes. Also shown in Fig. 14 is a second boron profile, computed from

the full field of view shown in Fig. 10 (25 μm diam.). It can be seen that both profiles are almost identical, with exception of the higher "background" level for the 4×4 μm local profile. The increased background in the latter case is due to worse counting statistics, since less ions contribute to the selected-area profile than to the full-field profile.

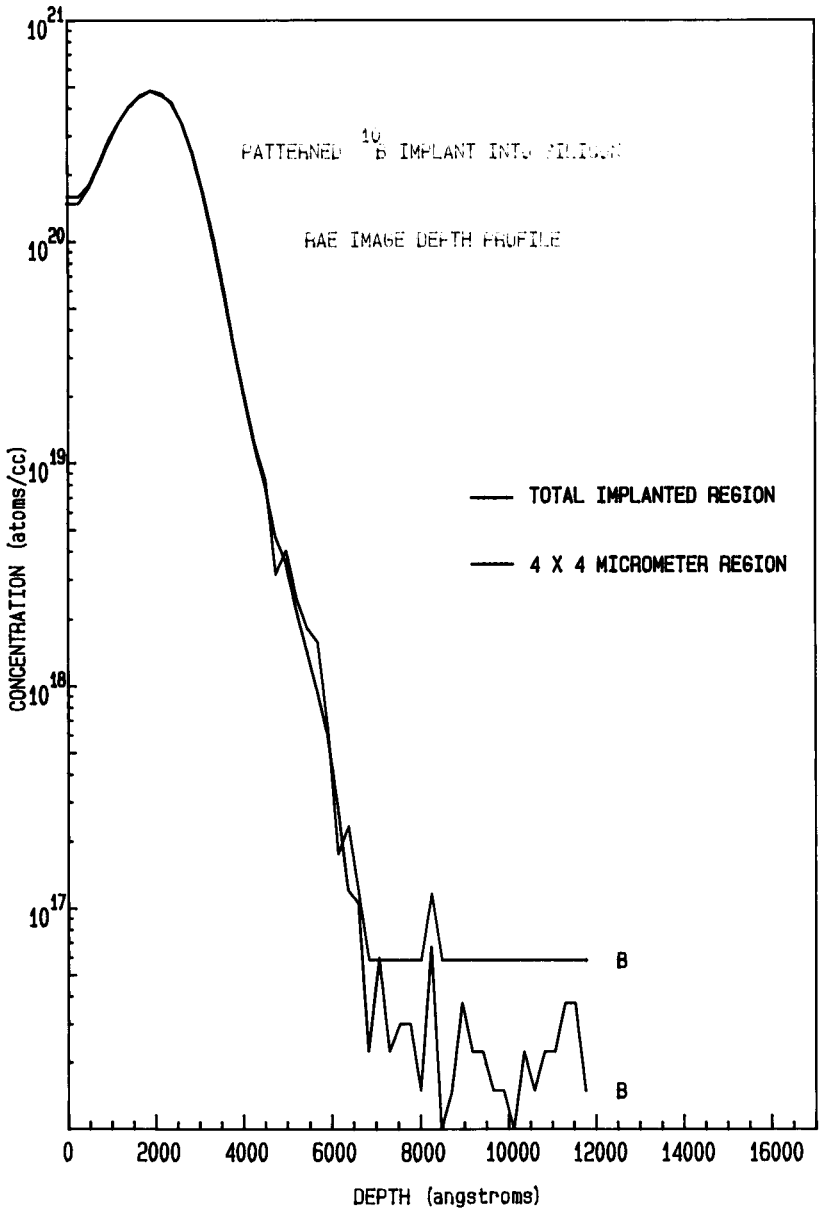

Fig. 14. Local depth profiles of ^{10}B in device shown in Fig. 10 reconstructed from 3D image stack. Lower curve, reconstructed from full field of view (25 μm diam.); upper curve, reconstructed from 4×4 μm subfield, centred in one of the implanted stripes. Courtesy C.A. Evans and Associates. Sputter time: 697 s.

2.3. Surface reconstructions

Another analytical question often is to reconstruct the morphological shape of a more or less homogeneous chemical structure (e.g. a grain boundary or an artificially fabricated structure). Again, this analytical mode may be performed a posteriori by numerical operations on a 3D stack of images obtained during SIMS analysis. Fig. 15 shows, in 2 different views, the analytical reconstruction of a small aluminum microdot structure, already described in Fig. 9. The analysis was performed by sputtering completely through the microdot and simultaneous recording of 36 coaxial Al-images. These coax images are linearly interpolated for better visibility to a stack of 64 coax images (see Fig. 8). The surface of the 3D-structure was defined as that surface in 3D-space consisting of all voxels with 90% of maximum voxel intensity. For a given direction of observation this surface was located and shaded by a ray-tracing algorithm for each pixel of the display screen. Thereby, a plastic impression of the topography of the microdot structure is obtained. It can be seen that the reconstructed surface is not cylindrical as expected, but has an asymmetric protrusion in the axial direction. This indicates a fault in one of the processing steps during manufacture of the microdot. Reconstruction of the surface from different viewing angles allows to set up image series which can be replayed as animated image sequences (displaying e.g. rotation of the microdot around its axis). Thus, a convenient quick survey of the complete shape of the structure is possible and interpretation capability of 3D data is considerably improved.

3. Quantification

3.1. The linear postulate or "fundamental" SIMS formula

The physical phenomena leading to emission of secondary ions from an ion bombarded solid, are not fully understood yet. Presently discussed physical models of the ion emission process at best allow a semiquantitative calculation of element concentrations from first principles and measured ion intensities [14]. In practical analysis therefore, phenomenological algorithms are applied almost exclusively. SIMS quantification usually is based on the linear "fundamental" SIMS equation (FSE) relating the detected ion current $\dot{N}^{+\prime}(\mathrm{X})$ (ions/s) of the analytical atomic ion species X to the fractional atomic concentration $c(\mathrm{X})$ of that species in the sample [14]:

$$\dot{N}^{+\prime}(\mathrm{X}) = \dot{N}_{\mathrm{p}} \cdot Y_{\mathrm{tot}} \cdot c(\mathrm{X}) \cdot \alpha^{+}(\mathrm{X}) \cdot T(\mathrm{X}) \qquad (4)$$

Here, $\dot{N}_{\mathrm{p}}$ is the primary ion current, $\alpha^{+}(\mathrm{X})$ is the degree of ionization (number of emitted X^{+} ions/number of total emitted X atoms), and $T(\mathrm{X})$ is the transmission of the mass spectrometer for element X. Eq. 4 has been written down for

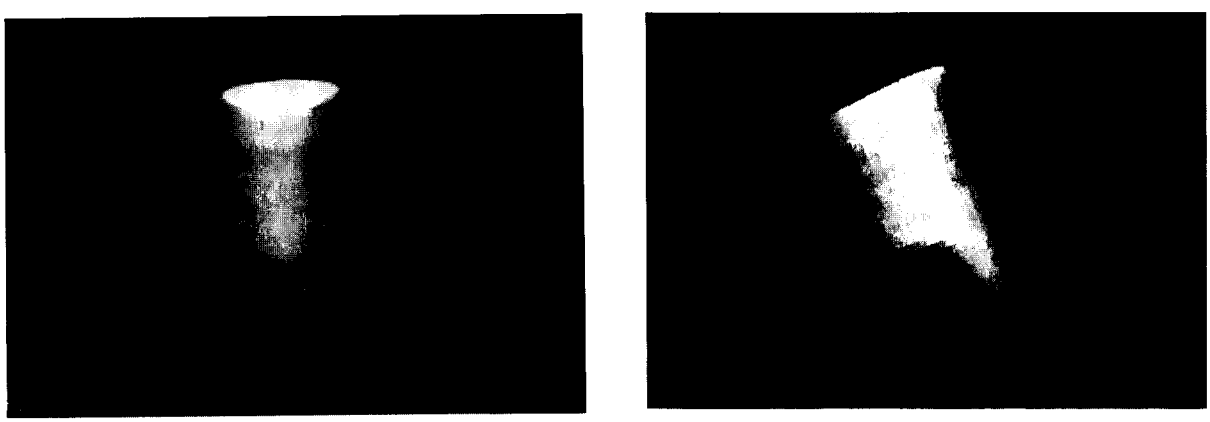

Fig. 15. Reconstruction of 3D surface of microdot (schematically shown in Fig. 9) from 3D image stack shown in Fig. 8. Two views from different directions shown.

singly charged positive atomic ions; analogous equations can be formulated for molecular analytical species of different charge state. At first sight the formula seems to be self-evident, because, on the right hand side, the first two terms $\dot{N}_p \cdot Y_{tot}$ designate the total number of sputtered atoms/s; the first three terms, including $c(X)$, designate the total number of atoms of kind X emitted/s; the first 4 terms, including $\alpha^+(X)$, represent the total number of ionized atoms of kind X emitted/s; and the full right hand side, including $T(X)$ represent the total number of detected ions/s of kind X.

The following derivation of Eq. 4 may shed a different light on the actual meaning of the "fundamental" formula. The derivation starts from an identity and is repeatedly expanded by various factors identically equal to unity. Regrouping and renaming of these factors gives the desired equation.

$$\dot{N}^{+\prime}(X) = \dot{N}^{+\prime}(X) \cdot \frac{\dot{N}^+(X)}{\dot{N}^+(X)} \cdot \frac{\dot{N}(X)}{\dot{N}(X)} \cdot \frac{\dot{N}_{tot}}{N_{tot}} \cdot \frac{\dot{N}_P}{\dot{N}_P} \tag{4a}$$

The following variables and abbreviations have been introduced in this equality:

$\dot{N}^+(X)$ total emitted number of X^+ ions/s

$\dot{N}(X)$ total number of X atoms (irrespective of charge state) emitted/s

$\dot{N}_{tot}$ total number of target atoms (irrespective of element and charge state) emitted/s

$$Y_{tot} = \frac{\dot{N}_{tot}}{\dot{N}_p}$$ total sputtering yield

$$c(X) = \frac{\dot{N}(X)}{\dot{N}_{tot}}$$ fractional atomic concentration of X atoms in sample

$$\alpha^+(X) = \frac{\dot{N}^+(X)}{\dot{N}(X)}$$ degree of (positive) ionization of sputtered X atoms

$$T(X) = \frac{\dot{N}^{+\prime}(X)}{\dot{N}^+(X)}$$ transmission for X^+ ions

Obviously, in a derivation like Eq. 4a virtually any variable (pressure, temperature, etc.) might have been introduced without formally falsifying the equation. We therefore must come to the conclusion, that a "fundamental" equation such as Eq. 4 may have, in a minimal interpretation, a very limited physical content. In a maximum interpretation the FSE tells us the following facts:

(a) detected secondary ion current depends on the 5 physical and instrumental parameters contained in Eq. 4; (b) it does not depend on any other parameters; (c) the dependence on the listed parameters is linear; (d) the listed parameters are mutually independent.

Only statement (a) has been demonstrated experimentally; statements (b–d) on the contrary have been shown wrong in one or the other instance. In particular, the interdependence of Y_{tot}, $\alpha^+(X)$ on $c(X)$, known as the "*matrix effect*" has been demonstrated in many instances.

An interdependence of parameters however greatly reduces the practical usefulness of the "fundamental" Eq. 4. In the SIMS literature, it appears as a self-evident postulate without any attempt of theoretical foundation. It has been shown however, that the essential feature of the FSE, the proportionality between elemental concentration and analytical signal (at least in the small-concentration approximation) can be put on a sound theoretical foundation [28].

It is acknowledged that it is generally impossible to predict or calculate the other factors appearing in Eq. 4 with an accuracy sufficient for accurate prediction of the analytical signal from elemental concentration $c(X)$ or vice versa. Therefore, those factors which are known experimentally, are explicitly retained in addition to the elemental concentration $c(X)$, and the remaining factors are combined into a factors of proportionality which have to be determined experimentally. These factors generally depend on properties of the sample and the analytical instrument. According to the particular analytical situation, various factors may be explicitly retained so that Eq. 4 may be alternatively written as:

$$\dot{N}^{+\prime} = S_a(X) \cdot c(X)$$

$$\dot{N}^{+\prime} = S_p(X) \cdot c(X) \cdot I_p$$

$$\dot{N}^{+\prime} = \tau_u(X) \cdot c(X) \cdot I_p \cdot Y_{tot} \tag{5}$$

The factors of proportionality $S_a(X)$, $S_p(X)$, $\tau_u(X)$ can be considered "sensitivities" since for a given elemental concentration the analytical signals increase with increasing numerical value of these factors. They are named "absolute sensitivity", "practical sensitivity" and "useful sensitivity" respectively. Since these factors also increase with instrument transmission T, they can be considered figures of merit for a particular SIMS instrument.

The sensitivities in Eq. 5 have to be determined under controlled experimental conditions from samples of known concentrations (and known sputtering yield). Inversion of Eq. 5 forms the basis for a phenomenological interpretation as well as the experimental determination of sensitivities:

$$S_a(X) = \frac{\dot{N}^{+\prime}(X)}{c(X)} \left(\frac{\text{detected X ions s}^{-1}}{\text{concentration}} \right)$$

$$S_p(X) = \frac{\dot{N}^{+\prime}(X)}{\dot{N}_p \cdot c(X)} \left(\frac{\text{detected X ions s}^{-1}}{\text{primary ions} \cdot \text{concentration}} \right) \quad (6)$$

$$\tau_u(X) = \frac{\dot{N}^{+\prime}(X)}{Y_{tot} \cdot \dot{N}_p \cdot c(X)} \left(\frac{\text{detected X ions s}^{-1}}{\text{sputtered X atoms}} \right)$$

3.2. Relative sensitivity factor quantification

The ratio of sensitivities for two elements X and Y from the same sample is called the relative sensitivity factor $S_r(X)$ of element X with respect to reference element Y:

$$S_r(X) = \frac{S_a(X)}{S_a(Y)} = \frac{S_p(X)}{S_p(Y)} = \frac{\tau_u(X)}{\tau_u(Y)} \quad (7)$$

From the phenomenological interpretation of sensitivities follows a phenomenological interpretation of the relative sensitivity factor (RSF):

$$S_r(X) = \frac{I(X)/c(X)}{I(Y)/c(Y)} \quad (8)$$

Since an RSF is a ratio of two empirical constants, it may itself be determined empirically from standard samples with a known concentration ratio for elements X and Y. Eq. 8 is the basis for two similar quantification algorithms by which relative concentration figures of an unknown element X, $c(X)$, can be computed from measured secondary ion intensities of elements E_i, $I(E_i)$ contained in the sample:

(a) internal standard available

If an internal standard, i.e. an element (Y) with known fractional concentration $c(Y)$ is available in the sample, the concentration of the unknown can be calculated from Eq. 8.

$$c(X) = \frac{1}{S_r(X)} \cdot \frac{I(X)}{I(Y)} \cdot c(Y) \quad (9)$$

Obviously, a single ratio of two secondary ion intensities, (from the unknown and from the internal standard) has to be measured during analysis.

(b) no internal standard available

In this case, RSF quantification starts from the identity

$$c(X) = \frac{c(X)}{\sum_{i=1}^{N} c(E_i)}$$

where N is the total number of elements contained in the sample. In this equation, $c(X)$ and $c(E_i)$ are calculated from Eq. 9 for all elements X and E_i and substituted in the right side of the last equation. Obviously, intensity and concentration of the reference element Y can be eliminated, finally giving

$$c(X) = \frac{I(X)/S_r(X)}{\sum_{i=1}^{N} I(E_i)/S_r(E_i)} \quad (10)$$

In this case, ion currents of all elements contained in the sample have to be measured and relative sensitivity factors of all these elements have to be known for quantification of a single element X. Algorithm (a) requires less analytical and computation time than algorithm (b). In addition, the concentration of an internal standard

element and the RSF of the unknown with respect to the standard have to be known a priori. Algorithm (b) requires more analytical time and the knowledge of more RSFs; no internal standard however is required. Which of these algorithms is to be preferred, depends on the particular analytical situation. In quantification of implant profiles, algorithm (a) is frequently used. The unknown X here is the implanted species, the reference element frequently is the matrix species and the RSF usually is obtained from a knowledge of the total implanted dose [14]. Note that relative sensitivity factors are purely empirical constants. RSF quantification algorithms therefore can only give accurate and correct results

(a) if RSFs are determined from calibration samples with similar composition as the unknown sample, and

(b) if experimental conditions are similar during determination of RSFs and analysis of the unknown sample.

According to condition (b), transfer of RSFs between different SIMS instruments generally is not an allowed procedure. Only under very special standardised instrument tuning conditions ("cross calibration" [28]) is it possible to achieve semiquantitative analytical results (error factor < 2) using "transferred" relative sensitivity factors.

3.3. Image quantification

One of the main goals of multidimensional SIMS analysis is the determination of the spatial distribution of element concentrations (elemental maps) inside a solid. Two-dimensional ion images (ion micrographs), as acquired during SIMS analysis, actually show the spatial distribution of local secondary ion emission intensities. The transfer from ion micrographs to quantitative elemental maps generally is known as "image quantification". This, by no means, is a straightforward process and presently can be performed rigorously for a very limited class of samples only. It should however be pointed out that in many analytical situations useful information can also be extracted from unprocessed ion micrographs.

Image artifacts

It is known [14] that in SIMS the proportionality between concentration and ion count is not always guaranteed. In the general case therefore, a number of artifacts are contained in an ion image as acquired directly from the instrument [14]. "Artifacts" in 3D analysis of solids can be understood as effects which cause a deviation of the measured concentration $c_m(x,y,z)_m$ at a measured sample location $(x,y,z)_m$ from the actual concentration $c_o(x,y,z)$ which was present at location (x,y,z) before the analysis was performed. It is possible that the location (x,y,z) of the analytical pixel is correctly determined although the measured concentration value $c_m(x,y,z)$ is incorrect. In this case, one is observing "*artifact contrast*":

$$c_m(x,y,z) \neq c_o(x,y,z)$$

This type of artifact may e.g. be caused by matrix effects and crystallographic, topographic or chromatic contrast [14]. It can also happen, that concentration is correctly determined, but the corresponding voxel is incorrectly placed in space; in this case, one is speaking of "*misregistration*":

$$(x,y,z)_m \neq (x,y,z)_o$$

This type of artifact can be caused by e.g. differential sputtering effects, causing locally variable sputtering speed. A third class of artifact is *atomic relocation*, in the sense that spatial elemental distribution at the time of analysis differs from that prior to analysis. This phenomenon can be caused by atomic mixing [29], radiation enhanced diffusion and redeposition [26] and appears in particular at high spatial resolution analysis of nonplanar samples [30,31]. There are, however, a large number of application areas, where artifacts can be neglected, e.g. ion implantation (see Fig. 12) or topographic reconstruction of homogeneous structures (Fig. 15). In addition, selected artifacts may be removed from the images by pixelwise application of correction algorithms [32,33].

On a planar surface ion transmission is approximately constant across the full field of view

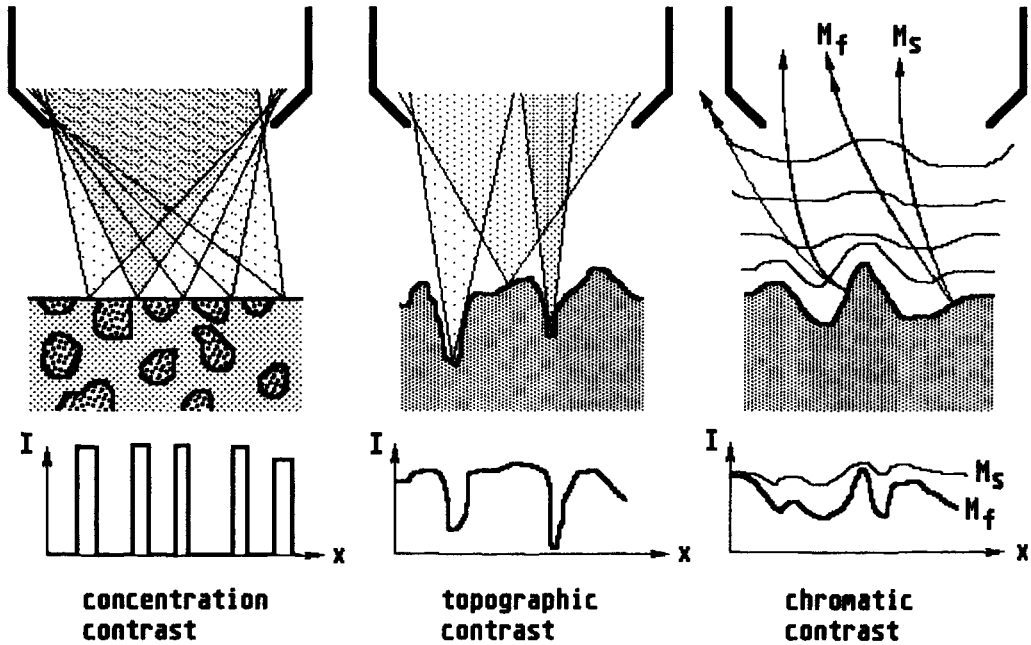

Fig. 16. Artifact contrast on nonplanar surfaces compared to ideal concentration contrast (left). Bottom row: SIMS matrix signal along sample sections shown in upper half.

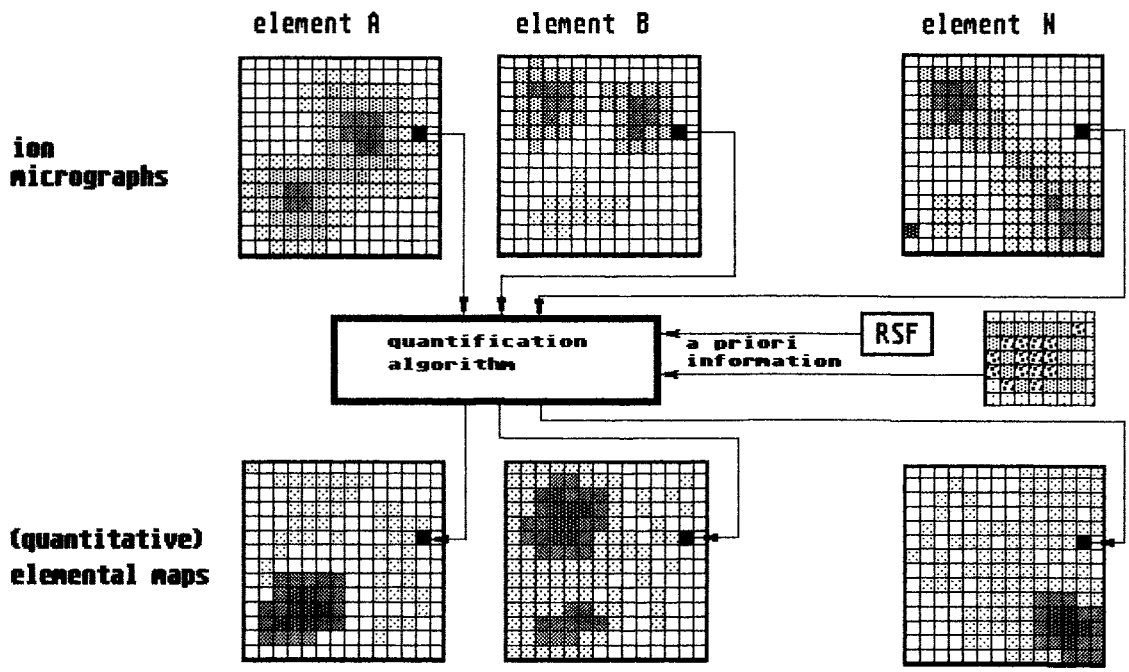

Fig. 17. Image quantification in SIMS, schematic. "Raw" ion micrographs are corrected pixelwise and thus transformed into quantitative elemental maps.

with a possible transmission decrease at the field edges ("vignetting"). The spatial dependence of the matrix signal from a sample with a homogeneous matrix containing a few inclusions (Fig. 16, left) will therefore reflect the local concentration of the matrix element. On a rough surface the signal from a homogeneous matrix will show modulation according to the local topographic structure. When the secondary ion extraction field is small, the main contrast effect will be due to the different solid angles of ions reaching the extraction optics from deep crevices and high ridges respectively (Fig. 16, centre): we have "*topographic contrast*". In this case the intensity distribution in the ion micrograph reflects the topographic structure of the surface and not the concentration distribution of the matrix element. When the extraction field is stronger, the electrostatic field distribution near topographic microstructures introduces transmission discrimination between ion species with different mean emission energies (Fig. 16, right). Since faster ions (M_f) are less deflected by an electrostatic field than slow ions (M_s), the topographically introduced signal modulation will be stronger for fast and less pronounced for slow ions "*chromatic contrast*".

Image correction and quantification algorithms

An ion image (micrograph) with N_l lines and N_c columns consists of $N_l \times N_c$ pixels with pixel intensities which must be considered to be independent from each other. Quantification of an ion image then is equivalent to performing $N_l \times N_c$ independent pixel quantifications. Quantification algorithms which are available for single point quantification can, in principle at least, also be applied for quantification of images. Fig. 17 shows the schematic procedure. The input data here are the raw elemental ion micrographs from corresponding analytical volumes in the sample. From each of these micrographs the pixel intensities in corresponding locations (X_i,Y_i) are used as input to a quantification algorithm. Most quantification algorithms need additional a priori knowledge for computation of elemental concentrations (see Section 3.2.). This information may consist of a set of appropriate relative sensitivity factors and/or an internal standard. In the case of image quantification of course this standard must be available in each pixel, thus constituting a "standard image". Using all this input, the quantification algorithm computes concentration figures for all input elements. This procedure is repeated for all input pixels (X_i/Y_i), thus building up a set of quantified elemental maps for all input elements.

The realization of this scheme is difficult due to the following facts: (a) the accuracy of quantification algorithms in SIMS is not very high (b) for the most precise algorithm, the RSF quantification, it is difficult to obtain proper RSFs which, in the most general case, must be considered as locally dependent. (c) it is difficult to obtain local internal standards for each pixel in the image. As a consequence, acceptable solutions have been found so far only for special cases. In one case [34] a "homogeneous" internal standard (i.e. an element for which there was reason to assume homogeneous distribution in the sample) has been used as a basis for a locally adaptive image quantification based on the LTE algorithm [14]. In another case reported locally invariant RSFs were used for quantification of the distribution of an ion implant [33]. In other cases, the use of spatially invariant RSFs seems to be less appropriate due to the locally variable matrix composition.

Contrary to full image quantification, removal of selected artifact contrast effects, has been tried with good success. Topographic contrast in particular can be partially removed by ratioing of ion intensities in each pixel. This procedure is suggested by the consideration that local surface structure influences the accepted solid angle of each ionic species in the same way. Ratioing of ion intensities (or referencing a specific elemental intensity to the sum of elemental intensities) in each pixel therefore produces images which are not fully corrected, but which at least contain less influence of local or global topography. Such a partial correction has been done in hardware [35] and software.

An example for an analytical problem which requires artifact correction is the analysis of contamination elements on the surface of a liquid metal ion emitter. The emitter consists of a stain-

less steel reservoir (4 mm diam.) and a tungsten needle (200 μm diam.), wetted with indium metal. During operation of the emitter sputtered material from the stainless steel extraction electrode is deposited on the liquid indium surface. The peculiar situation here is the macroscopic, rotationally symmetric sample, with a surface of locally variable inclination and therefore locally variable extraction efficiency. Fig. 18 shows, in the left column, the ion micrographs of In and Cr obtained on our scanning ion microprobe. The field of view here is 1.5 mm! The images obviously are strongly influenced by topographic contrast. The distribution of In, e.g., should be roughly homogeneous along the needle and the meniscus. Local referencing the In and Cr images to the sum of elemental intensities (In, Cr, Fe, Ni were measured) gives the images displayed in the right column of Fig. 18. The In-intensity here is much more homogeneous along needle and meniscus, in the Cr-image the structure of the emitter becomes more clearly visible. Note that Cr seems to be almost homogeneously distributed on the meniscus with decreasing intensity along the needle in the tip direction. This is interpreted as a "self cleaning" effect on the In-surface of the

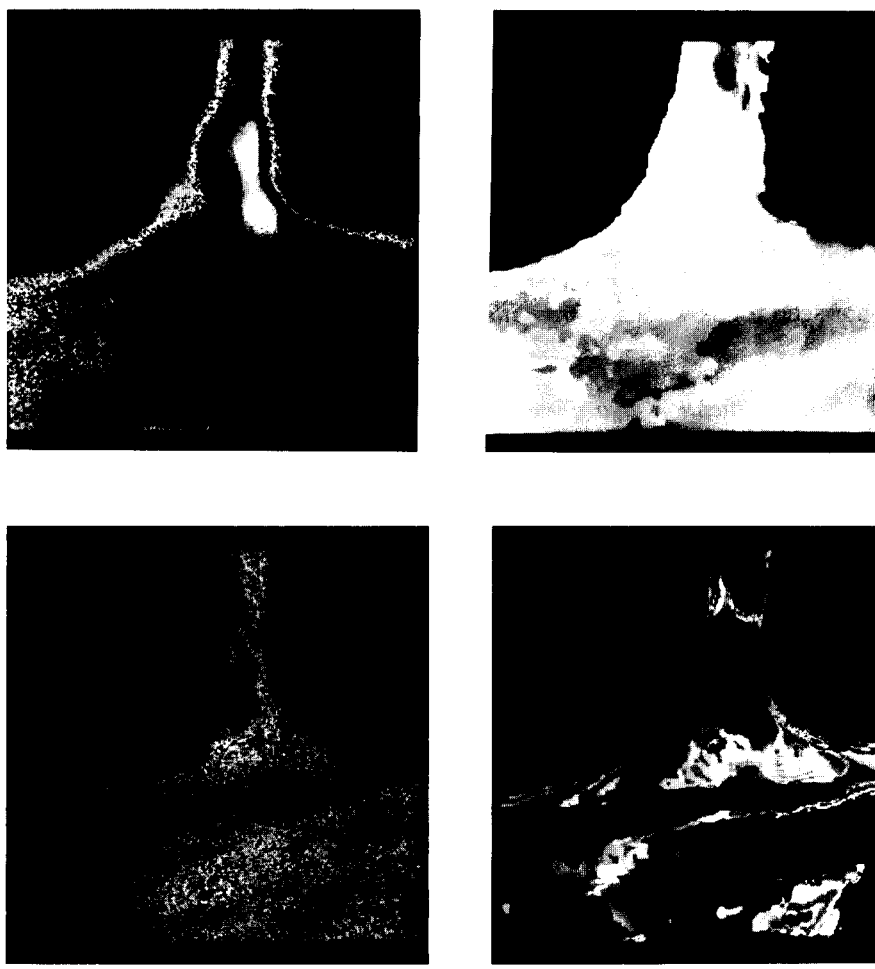

Fig. 18. Analysis of contamination on liquid metal In ion emitter. Left column: ion micrographs of In and Cr (contamination). Right column: topographic contrast removed by local ratioing algorithm. Originals colour coded.

needle which is moving faster during operation than the stagnant meniscus area. The local referencing process described above was performed on a fast pipeline processor. Total running time was < 10 s.

4. Concepts and limits of spatial resolution

4.1. Image formation as an information transfer process

The situation in imaging SIMS analysis of "flat" samples can be schematically described as shown in Fig. 19: we have an object (sample), characterized by the distribution of element E, $n_E(X,Y)$ in the coordinate system $\{X,Y\}$, referred to as the object plane (= sample surface). The SIMS instrument is considered as an image formation system which acts upon the sample (via the primary beam), stimulates emission of particle radiation (via the sputtering process), intercepts part of this radiation, transports it through space and transforms it in such a manner that in the coordinate system $\{X',Y'\}$, referred to as the image plane, an image $N_E(X',Y')$ is formed. $n_E(X,Y)$ may be given as the (locally averaged) number of E atoms/cm^3 in the sample and $N_E(X',Y')$ as the number of ion counts collected at position (X',Y') of the final image. SIMS images can be considered as representations of objects (samples) that are sensed by direct interaction of the image formation system with the object. These considerations are easily generalized to 3-dimensional objects and object representations.

Neighbourhood processes

The image formation system creates the image point (X',Y') by acting upon and transporting the particles sputtered from the object. However, due to imperfections in the system, the image point (X',Y') may receive ions not only from the object point (X,Y) but from all other points (x,y) of the object or their respective image points (x',y'). It can be expected that, as the distance from the object point (X,Y) to other points in the object plane increases, the particle contributions from these other points to the measured intensity

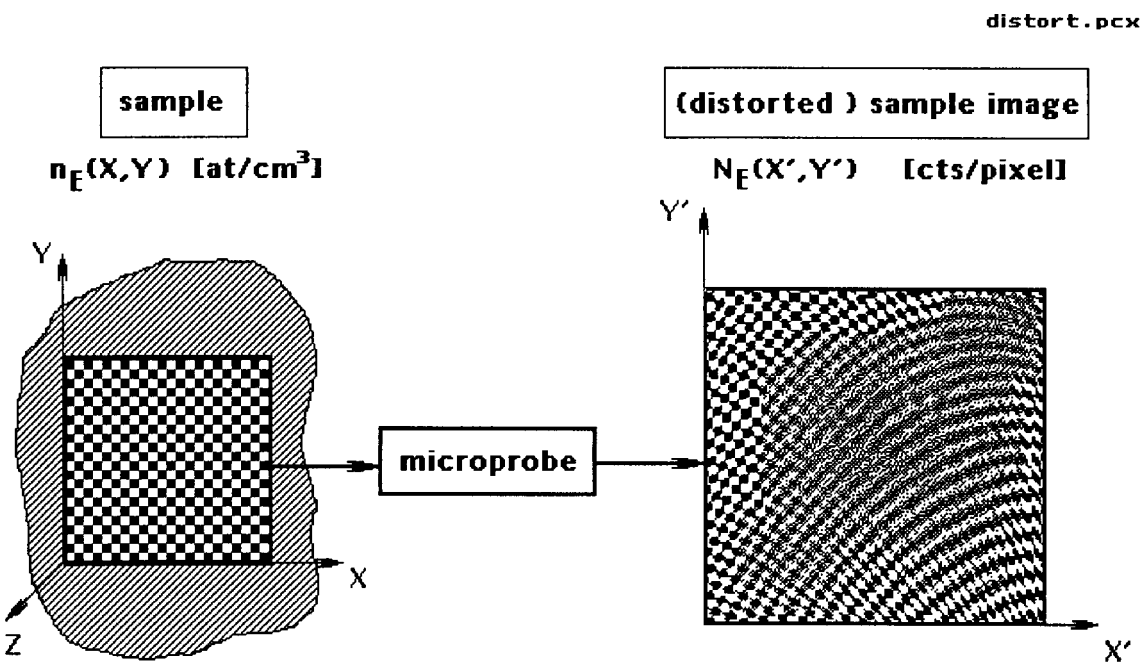

Fig. 19. Symbolic description of imaging microanalysis as imperfect information channel between elemental distribution in sample and distribution image.

$N_E(X',Y')$ in the image point will decrease. Basically however, we must recognize the image formation process as a neighbourhood process, i.e. (in the SIMS case) the ion count in an image point may depend on the atomic density in the object point and on points in a (possibly infinite) neighbourhood surrounding the object point. For the different physical processes causing neighbourhood effects in ion microprobes and ion microscopes (see also Section 1).

In effect, these neighbourhood processes are causing a blurring action in the final image. This blurring action is characterized by the point spread function (PSF) $h(x',y';\ X',Y')$ which is the output image for a unit-intensity object point at (X,Y) (see Fig. 19). Mathematically, the blurred image $N_E(X',Y')$ is the convolution of the unblurred image $N(X',Y')$ with the point spread function $h(x',y';\ X',Y')$ [20,36]. In other words, the object is "blurred" by the PSF to give the image:

$$N_E(X',Y') = \int_{-\infty}^{\infty}\int_{-\infty}^{\infty} h(x',y';X',Y') \cdot N(x',y') \cdot dx'dy' \tag{11}$$

The convolution interpretation is valid only for linear systems with "space invariant" point spread function [20]. In Fourier space, the convolution can be expressed as a multiplication

$$\underline{N}(U,V) = \underline{h}(U,V) \cdot \underline{n}(U,V) \tag{12}$$

where the underlined functions are the Fourier transforms of the corresponding spatial functions and (U,V) the spatial frequencies (in cm^{-1}) in the X',Y' directions of image space. This shows, that each spatial frequency in the object appears in the image, modulated by $\underline{h}(U,V)$, the transform of the PSF. $\underline{h}(U,V)$ therefore is called the optical transfer function (OTF) of the imaging system. In non-optical applications the OTF is frequently called the transfer function of the system.

In the case of SIMS, object and image functions are real valued, positive definite functions. The Fourier transforms of object, image and PSF generally are complex functions. The transfer function 12 can be written as the product of a real amplitude and a complex phase factor:

$$\underline{h}(U,V) = \mathrm{MTF}(U,V) \cdot e^{i \cdot \mathrm{PTF}(U,V)} \tag{13}$$

MTF(U,V) and PTF(U,V) are called the modulation transfer function and the phase transfer function (PTF) respectively [36,37]. According to Eqs. 12 and 13 therefore, each spatial frequency component in the object is damped by the MTF and shifted in phase by the PTF to give the corresponding frequency component in the image.

Gaussian point spread functions

In ion and electron optics it is frequently assumed that the PSF is space-invariant and has the functional form of a 2-dimensional Gaussian

$$\mathrm{PSF}(x',y') = \frac{N}{2\pi\sigma^2} \cdot e^{-(x'^2+y'^2)/(2\sigma^2)} \tag{14}$$

where, without loss of generality, $X' = Y' = 0$, σ^2 is the variance of the Gaussian and N is its integral. In SIMS, N can be considered the total number of detected ion counts contained in the image of a quasi-point source. In ion microprobe imaging such a Gaussian PSF might be the result of a primary ion beam with Gaussian current density distribution, in ion microscope imaging of a gaussian current density distribution in the virtual image spot produced by the emission lens [38].

Further properties of the gaussian PSF are [20]: (a) it has rotational symmetry and decreases to a fraction of 0.607 of its central maximum at a central distance equal to σ; (b) a homogeneous PSF ("top hat" cross section) with equal central height and total intensity has a radius of $\sqrt{2}\sigma$; (c) 50% of the total intensity of the gaussian are contained within a circle of radius 1.18σ, 90% within a circle of radius 2.15σ.

Obviously, the spatial extent of the blurring action of the PSF is connected to the notion of "spatial resolution" (for a more accurate definition see below). The blurring action of a gaussian PSF can be expressed by a single parameter, viz. its standard deviation σ. This fact makes it well suited for simple modelling of resolution behaviour in imaging systems.

4.2. Basic problems in imaging analysis

Realizing that any SIMS image contains distortions with respect to the true elemental distribution, the central problem in spatially resolved SIMS analysis is the reconstruction of the true elemental distribution from a measured SIMS image ("*restoration problem*"). It is obvious that for this purpose the distorting properties of the image formation system (SIMS instrument) must be known (Fig. 20c); the case that distortions may also depend on the object itself is not considered at the moment. The distortion properties of the image formation system itself may be determined a posteriori by comparison of a suitable object with known distribution (resolution test sample) with its image as produced at the output of the image formation system ("*determination problem*", see Fig. 20b). It is obvious that we cannot determine resolution in an image without additional a priori information because we have defined "resolution" as a measure of distortion which the true image signal is suffering in the process of analysis and image recording. A low contrast image may represent a perfectly transmitted, close to homogeneous, true object distribution or a heavily blurred true distribution with strong local concentration variations. We therefore must clearly separate between the property of an image which can be expressed as contrast, acutance [36], etc. and the property of the imaging and recording process, expressed as distortion, resolution, resolving power, etc.

The expected quality of the images representing a suitably given "true" object distribution may also be estimated a priori (without actually performing a SIMS analysis). In this case the distorting properties are estimated from a (usually imperfect) knowledge of the experimental conditions and physical principles involved in a SIMS analysis; mathematical simulation of the action of the distortions on the known object distribution allows to predict the image distribution ("*a priori prediction problem*", see Fig. 20a). A priori prediction is typically applied when the basic solvability of an analytical problem requiring high

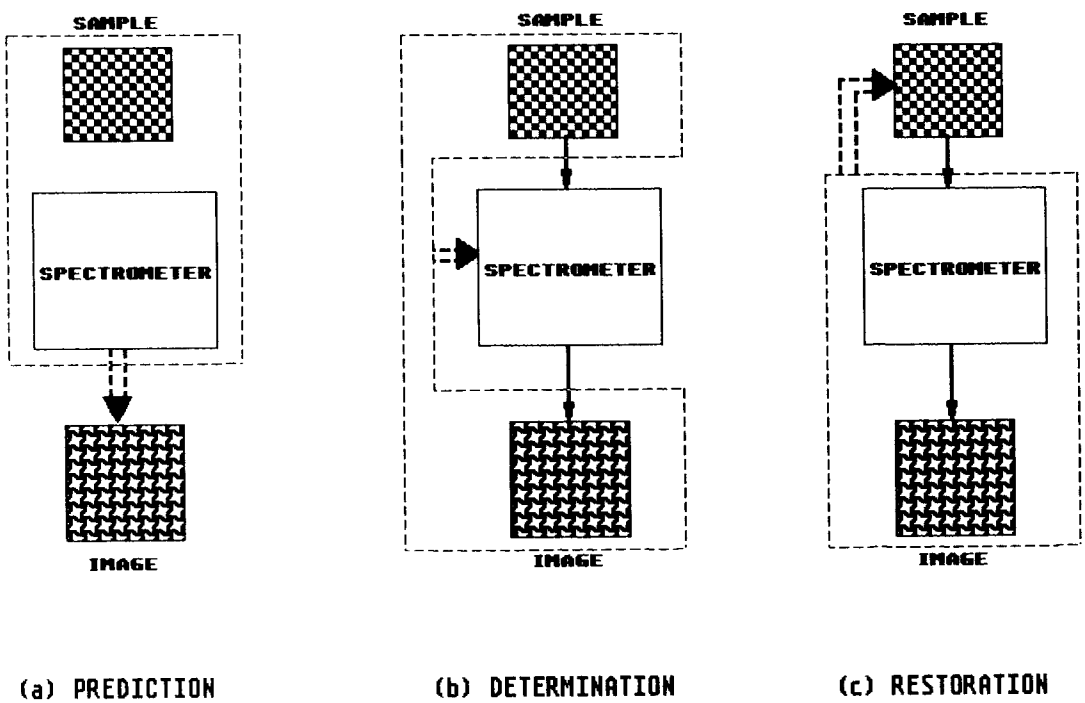

Fig. 20. Three fundamental problems in imaging analysis.

spatial resolution has to be decided; when the ultimate theoretical resolution limits of the method have to be estimated; or in the pre-development and development phase of a new analytical technique when design and operating parameters have to be optimized. Fig. 20 shows schematically, that the prediction problem, the determination problem and the reconstruction problem can be considered complementary processes of information flow.

The determination problem

We have seen in Section 4.1. that the blurring effect which the image formation system introduces into the representation of an object can be fully characterized by the point spread function $h(x',y';X',Y')$. The a posteriori determination problem therefore can be considered solved, when the PSF can be determined from the measured image and the corresponding true object distribution. In the case of a general object and a space invariant PSF, the problem can be solved in Fourier space using the convolution theorem 12. The Fourier transform of the PSF (i.e., the OTF) is given by

$$\underline{h}(u,v) = \frac{\underline{N}(U,V)}{\underline{n}(u,v)} \tag{15}$$

When the object is a periodic function, the image consequently is also a periodic function. In this case, the modulation function 15 is real [20] and can be expressed by the ratio of the modulations M of image and object respectively:

$$\mathrm{MTF} = \frac{M_i}{M_o} \tag{16}$$

where the modulations M are defined as simple functions of maximum values I_M and minimum values I_m in the images respectively [36]:

$$M = \frac{I_M - I_m}{I_M + I_m} \tag{17}$$

When, in addition, the object is binary, i.e. it consists of periodic "black" and "white" areas only, the object modulation obviously is equal to unity and the MTF then is equal to the modulation in the image

$$\mathrm{MTF} = M_i \tag{18}$$

The determination of the point spread function from an ion image is considerably simplified when special "resolution test patterns" are used. Frequently used test patterns are binary point, line, edge, slit and bar patterns. The width of the PSF (which is connected to the concept of "spatial resolution", see below) can be determined from the modulation in the image of a pattern of known dimensions. In scanning probe instruments an alternative method to obtain image resolution is to connect all "black" and "white" pattern sections to a pair of contacts and to measure the current flowing to these contacts as the beam is scanned across the pattern. The resulting current/beam position curve is equivalent to an image intensity profile along the same scanning line. In the sections below we assume a Gaussian PSF. The pattern shapes discussed are essentially 1-dimensional and therefore allow to determine projections of the PSF onto the scan direction only. The 2D shape of the PSF may be obtained by rotation of the patterns.

Point and line test patterns. Let us consider a test pattern consisting of two "points" situated at $x = +d/2$ on the x-axis (Fig. 21, right). When such a pattern is imaged, both point images will be blurred by the gaussian PSF and the image intensity between the point images at $x = 0$ will rise to a nonzero value. When the point sources move closer, the depth of the intensity dip at $x = 0$ will decrease until, at a certain critical distance, the bimodal distribution changes into a monomodal one. The distance between the point sources, at which their images can just be visually resolved is called the "smallest resolvable distance" (SRD). Of course the criterion for separability of the overlapping images is, to a large degree, arbitrary. Frequently, it is defined in analogy to the *Rayleigh-criterion* as a drop to 73.46% of maximum intensity between the blurred point images. This condition, derived from optical diffraction theory, is fulfilled when the first diffraction minimum of one source coincides with

the central maximum of the other source. In this case the intensity ratio $f = I_{1/2}/I_o$ halfway between the point images is given by the Airy function $I_{1/2}/I_o = 2.178J_1^2(0.61\pi) = 0.73463$ [39], where J_1 is the Bessel function of first order [40]. In ion optics, diffraction effects usually play a minor role so that the intensity distribution in a scanning beam or a virtual point source image generally is (e.g., in the gaussian case above) different from the Airy-function [39]. The 74% criterion therefore can only be based on an analogy to optics. Other authors have defined the SRD as that distance between the point sources, where the dip between the images just disappears, i.e. where the curvature at the median point disappears [41,42]. This of course would be a less arbitrary criterion, however it may seem somewhat overstating the resolution capabilities of an imaging system because at such a SRD point sources actually may not be separated visually.

The intensity distribution $N(X)$ along a line through the centers of two blurred point images corresponding to the images of two point objects, separated by a distance d, is given by the superposition of the two Gaussian PSFs of the two object points. This function has been calculated [20] and is shown graphically in Fig. 21. Rayleigh modulation ($f = 0.735 = 1 - 0.27$ or $M = 0.153$, respectively) is obtained when the points have a distance SRDP

$$\mathrm{SRD_P} \approx 2.80\sigma \tag{19}$$

Similarly, the smallest resolvable distances for the line, slit and periodic bar test patterns shown in Fig. 21 are given by

$$\begin{aligned} \mathrm{SRD_L} &= 2.80\sigma \\ \mathrm{SRD_S} &= 0.68\sigma \\ \mathrm{SRD_B} &= 1.56\sigma \end{aligned} \tag{19a}$$

The corresponding "modulation curves" (M vs. σ/d) are shown in Fig. 22. The modulation

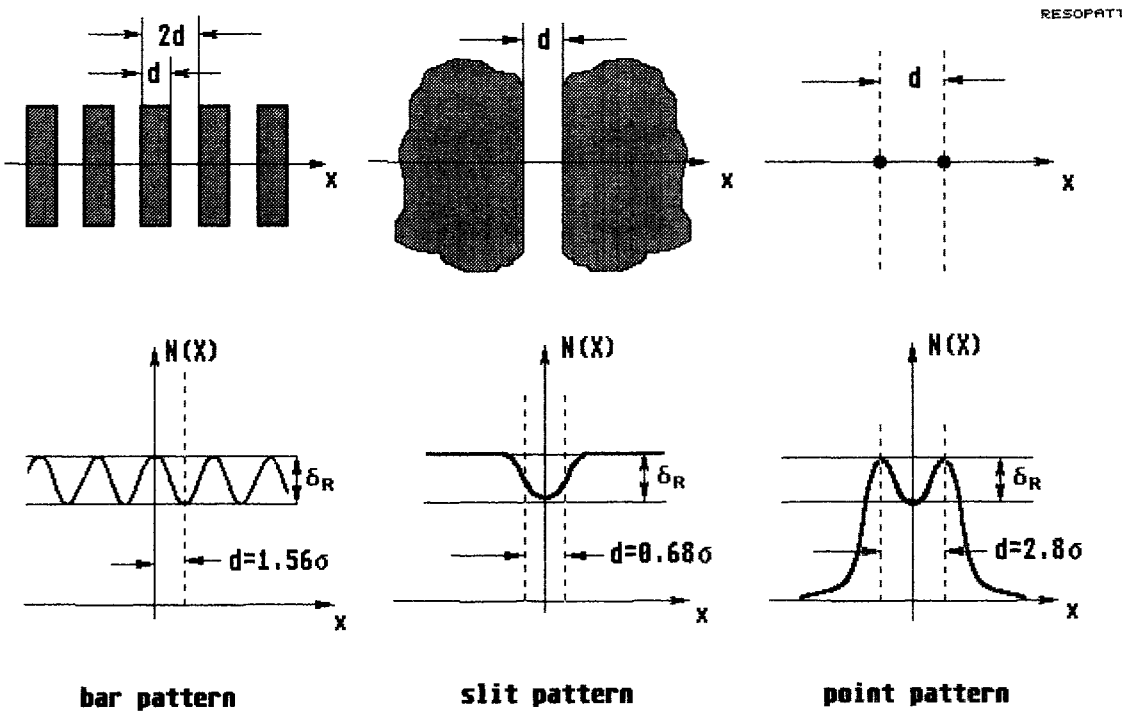

Fig. 21. Widths d of point, slit and bar test patterns producing Rayleigh modulation ($M = 0.153$) when imaged by Gaussian PSF with width σ.

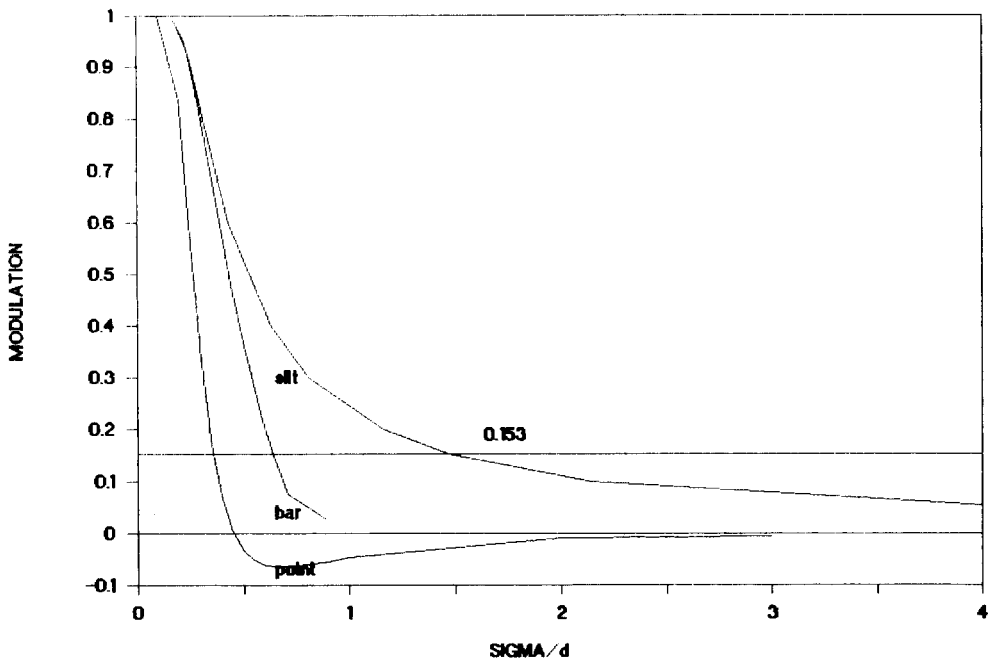

Fig. 22. Modulation curves from point, slit and bar test patterns imaged with Gaussian PSF. sigma, width of PSF; d, characteristic pattern width; horizontal line, Rayleigh modulation ($M = 0.153$).

curves offer a convenient method for determination of the width σ of the blurring PSF. A suitable test pattern with known feature width d is chosen and imaged by the instrument. In the image, the modulation M is determined, following Eq. 17. The corresponding value of $\sigma/d = r$ is taken from the appropriate curve in Fig. 22. The width σ of the PSF simply is calculated according to

$$\sigma = r \cdot d \tag{20}$$

The periodic bar pattern shown in Fig. 21 has the fundamental spatial frequency

$$n = \frac{1}{2d} \text{ (line pairs/mm)} \tag{21}$$

The pattern is considered to be just resolved when the image modulation is equal to the Rayleigh value. The spatial frequency u_c of this critical dimension test pattern is called the *spatial resolution* R of the imaging system:

$$R = u_c = \frac{1}{2d_c} = \frac{1}{2\text{SRD}} \text{ (lp/mm)} \tag{22}$$

Spatial resolution and smallest resolvable distance obviously are indirectly proportional.

Terminology. The terminology expressing concepts of "spatial resolution" is often used in a confusing and ambiguous way. The fundamental desire obviously is to give a figure on how well distinct features or distances between features in an object can be resolved by a microscopic instrument. This leads to the concept of a "smallest resolvable distance" which is often thought to be an unambiguous property of the instrument itself. Obviously a microscopic instrument is considered of better quality, the smaller this smallest resolvable distance is. A figure of merit which assumes a higher numerical value with "better" quality of the instrument is "resolution" or "resolving power" as defined above. Often, the terms "resolution" and "smallest resolvable distance" are used synonymously which of course is sloppy language. From the discussions in the previous sections it should however be clear that (a) "smallest resolvable distance" is not a property of an in-

strument alone, but a combined quality of instrument and sample. (b) The only figure of merit related to spatial resolving capability which is independent of the sample under test and only a property of the instrument is the point spread function (which may be represented by one or more parameters describing its spatial extent).

Prediction problem

The prediction problem comes into effect in SIMS, when it has to be decided, if a structure of given shape can be spatially resolved in a SIMS instrument with a known point spread function. We have seen above that this problem cannot be uniquely decided by knowledge of the smallest feature dimension in the sample and a "resolution" figure of the instrument, at least when feature size and "resolution" of the instrument are of the same order. The way to proceed in this case would be to numerically convolve (blur) the known sample structure with the known PSF of the instrument (see Eq. 11) and to decide if in the "blurred" image the feature of interest is separated well enough. Such a procedure is however seldom applied because the actual experiment may decide the issue faster and more reliable. The situation is different, when special situations are expected to appear in actual analysis, e.g when the image signal is noisy due to low beam intensity or low concentration of the analytical

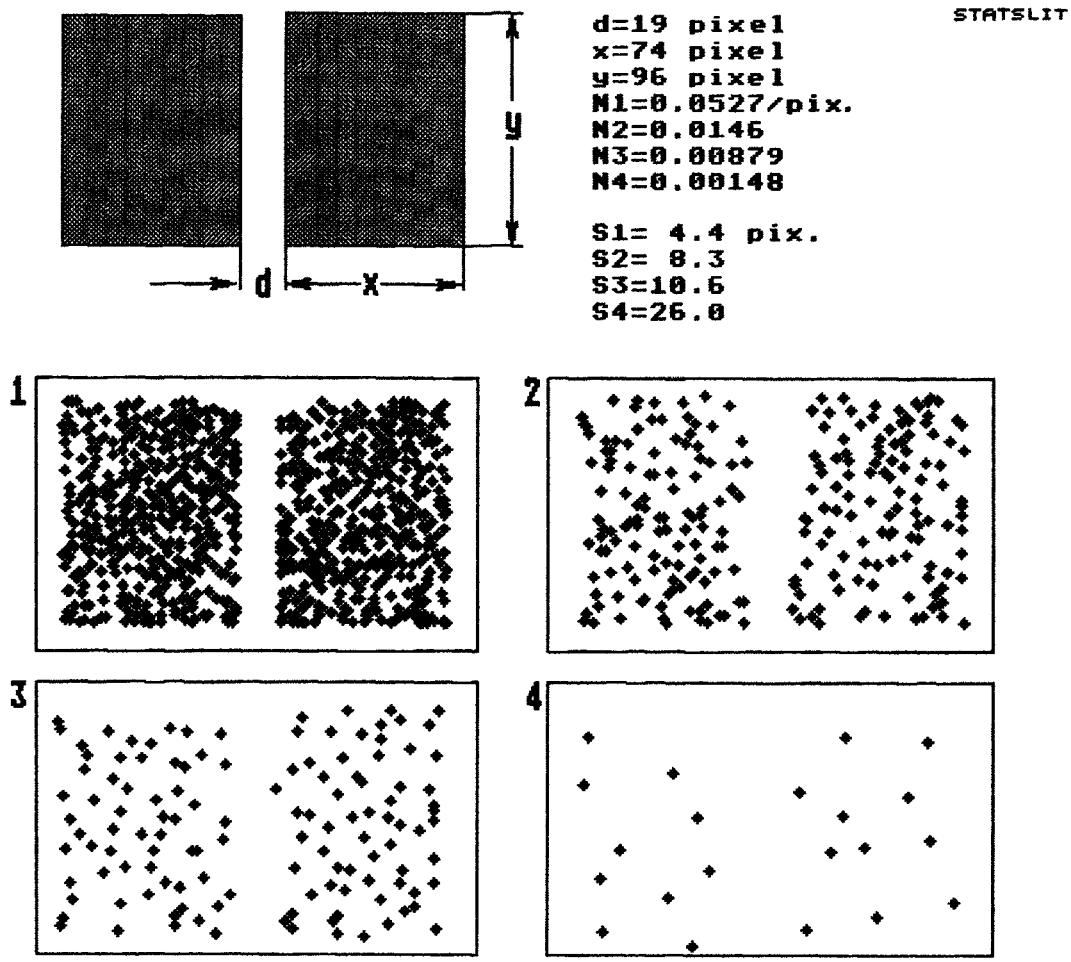

Fig. 23. Degradation of slit image recorded with progressively fewer average ion counts/pixel. Ni, ion counts/pixel; Si, mean distance between occupied pixels.

element. Methods for estimation of image resolution in these cases are given in the sections below.

Consideration of count rate statistics. At small secondary ion counting rates (e.g. for trace elements or for sub-0.1 μm primary beams), a new limit to spatial resolution appears. Due to the statistical nature of secondary ion emission, an image will consist basically of single-ion count pixels separated by empty pixels. Structures in the image (such as the slit feature in Fig. 23) will become unrecognizable if the average distance between occupied pixels is larger than the characteristic dimension of the object.

Levi-Setti [8] has introduced the concept of "mean signal distance", d_s, along a digitally scanned image line, i.e. the mean linear distance between occupied pixels:

$$d_s = \frac{d_r}{N} \tag{23}$$

where d_r is the scanning step-width (= pixel distance) and N the average ion count/pixel. The smallest resolvable distance d_i which can be expected in a low-ion count image, recorded by a digitally scanned ion microprobe, then is calculated as a convolution of probe diameter d_p, scanning stepwidth d_r, mean signal distance ds and the width of the sputtering cascade, d_c [1,2]:

$$d_i^2 = d_p^2 + d_r^2 + d_s^2 + d_c^2 = d_p^2 + d_r^2\left(1 + \frac{1}{N}\right)^2 + d_c^2 \tag{24}$$

For very small counting rates, the mean signal distance d_s obviously becomes the limiting resolution parameter and

$d_i \rightarrow d_r/N$

A different concept is the use of the same detectability criteria for image features (modulation limits) as in the large-signal case described in Section 4.2. above. Image statistics is taken into account by additionally requiring certain precision limits on all modulation measurements. Let us consider a test pattern consisting of a slit of width δ in an otherwise homogeneous sample. The image is assumed to be sampled with a step width of δ, the average count number in each bin (pixel) of width δ is N. If N is small, the statistical fluctuations in the count number/bin will cause graininess in the image which may prevent detection of the slit pattern. In order to reduce statistical fluctuations, the image may be low-pass filtered (averaged) by a filter of width Δ. Such a filter however is smearing out the image of the slit pattern so that the intensity in the slit centre may not be sufficiently depressed for an unambiguous identification of the slit. Let us consider the intensity N_{min} in the centre of the averaged slit image and N_{max} in large distance from the slit centre:

$$N_{min} = (\Delta - d) \cdot \frac{N}{\delta}$$

$$N_{max} = \Delta \cdot \frac{N}{\delta} \tag{25}$$

We use the same detectability criterion for the slit image as in Section 4.2., namely that the intensity ratio $R = N_{min}/N_{max}$ should be below the Rayleigh-limit ("*modulation criterion*"):

$$R = \frac{N_{min}}{N_{max}} < 1 - \sigma_R \tag{26}$$

where $\sigma_R = 0.27$. In a statistically dominated image this condition is however not sufficient for unambiguous identification, because R may exceed the upper limit Eq. 26, just due to statistical fluctuations. Therefore, a second condition is necessary, limiting somehow the allowed extent of statistical fluctuations of R. It seems reasonable to require that, once Rayleigh modulation has been determined from the image, the expected statistical uncertainty δR of this determination is smaller than σ_R (image modulation always < 1). This leads to a second detectability requirement ("*precision criterion*"):

$$\delta R = \sigma_R \approx 0.27 \tag{27}$$

For low pixel count ($N/\delta \ll 13.7/d$) the two criteria (Eqs. 26 and 27) lead to a smallest, safely detectable width d of a "black" slit in a "white" plane at given pixel size δ and pixel count N [20]

$$d \approx 4.70\frac{\delta}{N} \tag{28}$$

The minimum required integration interval Δ (minimum statistical resolution) then follows from Eq. 25 as

$$\Delta \approx 17.70 \frac{\delta}{N} \quad (28a)$$

Example: for a mean count rate of $N = 1$ count/pixel, the minimum detectable slit width is about 5 pixel widths (see Eq. 28). In order to measure under these circumstances the intensity depression corresponding to the slit with sufficient precision, we have to integrate counts along a distance Δ of about 18 pixels. For the more heuristic "mean signal-distance"-concept a slit would already appear detectable at a count rate of 1/pixel, if its width is larger than about 1.4 pixel widths.

Smallest resolvable volume and detection limit. Counting rate statistics, as described in the previous section, may e.g. become dominant when the concentration of the analytical element is low. This obviously means, that element concentration, i.e. a sample property, is setting a limit to spatial resolution. In contrast to the previous section, where the statistical limitations to 2D-resolution were treated, it is shown in this section, that the element concentration actually sets a limit to the size of the microvolume which can be uniquely discriminated from the neighbouring microvolume. In other words, element concentration is setting a limit to 3D-spatial resolution. Let us consider a microvolume with lateral extensions $\delta \times \delta$ and depth extension δz which is sputtered in the course of an analysis. We want to know the smallest concentration c_{min} which we can detect in this microvolume. Obviously, this microvolume contains a limited number of atoms, among them some of the analytical species X. In the process of SIMS analysis, these analytic atoms are removed from the sample by the sputtering effect, some of them in ionized state. A fraction of these analytic ions is collected by the mass spectrometer, mass analyzed and detected, usually in a counting arrangement. Since the sputtering process is destructive, these ion counts are the only opportunity to obtain information on the composition of the selected microvolume. Counting

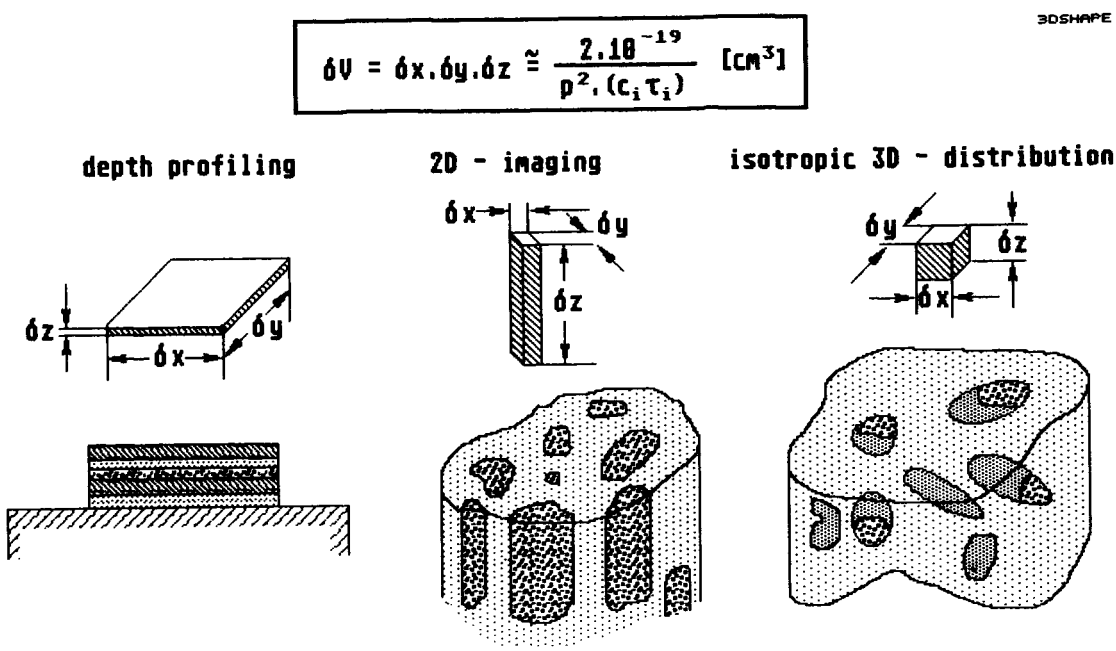

Fig. 24. Optimal shaping of analytical microvolume in different analytical modes.

statistics therefore dictates, that we must collect a minimum number of

$$N^{+\prime}(\mathrm{X}) = \frac{10^4}{p^2} \text{ (ions)} \tag{29}$$

ions of the analytic species for our intensity measurement to be precise to within p (%) [16]. Assuming unit detector efficiency, the number of X ions detected relates to the total number N_{tot} of atoms contained in the microvolume considered (see Section 3.1.):

$$\begin{aligned} N^{+\prime}(\mathrm{X}) &= N_{\mathrm{tot}} \cdot c(\mathrm{X}) \cdot \alpha^{+}(\mathrm{X}) \cdot T \\ &= n \cdot \delta V \cdot c(\mathrm{X}) \cdot \alpha^{+}(\mathrm{X}) \cdot T \end{aligned} \tag{30}$$

The last equality in Eq. 30 has been obtained by relating the microvolume, δV, to the number N_{tot} of atoms contained in it by $N_{\mathrm{tot}} = \delta V \cdot n$ (n is the total number of sample atoms/cm^3). Combining Eqs. 29 and 30 yields a relation for the minimum sampling volume required for the detection of an element of concentration c(X) with a precision of p (%):

$$\begin{aligned} \delta V > \delta^2 \cdot \delta z &= \frac{10^4}{n \cdot p^2 \cdot c(X) \cdot \alpha^{+}(\mathrm{X}) \cdot T} \\ &\approx \frac{2 \times 10^{-19}}{p^2 \cdot c(\mathrm{X}) \cdot \tau_{\mathrm{u}}(\mathrm{X})} \end{aligned} \tag{31}$$

where in the last approximate equality an average atomic density of $n = 5 \times 10^{22}$ has been assumed and the useful sensitivity of element X, τ_{u}(X) has been introduced (see Section 3.1.). The useful sensitivity therefore is the relevant sensitivity parameter in 3D-analysis where we are dealing with a sampling volume of limited size.

Note that Eq. 31 determines the minimum size of the sampling volume required for detection of a given analyte concentration, but not its shape. The sampling volume now might be shaped according to the particular analytical requirement (see Fig. 24). In depth profiling we usually are interested in a small resolved depth interval δz and might ask what limitations on the analyzed area are imposed by the minimum sampling volume required for accurate measurement of an element with concentration c(X). From Eq. 31 we can calculate the required lateral extension δ of the analyzed area:

$$\delta(\mathrm{X}) > \frac{5 \times 10^{-10}}{p \cdot \sqrt{c(\mathrm{X}) \cdot \tau_{\mathrm{u}}(\mathrm{X}) \cdot \delta z}} \tag{32}$$

In (lateral) imaging analysis the problem is to estimate the minimum sputter depth δz required for imaging an element X with concentration c(X) with a desired lateral resolution δ. The respective relation again is derived from Eq. 31 as

$$\delta z(\mathrm{X}) > \frac{5 \times 10^{-19}}{p^2 \cdot c(\mathrm{X}) \cdot \tau_{\mathrm{u}}(\mathrm{X}) \cdot \delta^2} \tag{32a}$$

In 3D analysis of isotropic samples it might be useful to define a resolution element of equal extent δ_{u} in all three spatial coordinate directions. In this case the volume $\delta V = \delta_{\mathrm{u}}^3$ and Eq. 31 yields for the minimum lateral extension δ_{u} of the isotropic resolution volume

$$\delta_{\mathrm{u}}(\mathrm{X}) > \frac{6 \times 10^{-7}}{p^{2/3} \cdot \left(c(\mathrm{X}) \cdot \tau_{\mathrm{u}}(\mathrm{X})\right)^{1/3}} \tag{32b}$$

Note that these resolution measures depend on the analytical element X. The element dependent factor in all these equations is the product $c(\mathrm{X}) \cdot \tau_{\mathrm{u}}(\mathrm{X})$. Therefore, in the same sample, the spatial resolution limit for a matrix (or high yield) element is better than for a trace (or low sensitivity) element.

Naturally, Eqs. 32–32b can be reversed to give expressions for the lowest detectable concentration in a spatial resolution element of given dimensions. Note that in all analytical modes the lowest detectable concentration c(X) of an element X in a given analytical volume is indirectly proportional to the useful yield.

Note also that postionisation of the sputtered particles effectively changes the numerical value of the useful yield τ_{u}. In the ultimate case of a technique with 100% ionization efficiency, 100% overlap between ionization volume and sputtering plume and 100% spectrometer transmission, the effective useful sensitivity is 1. Eqs. 31–32b then can be used to estimate the respective spatial resolution limits for this "ultimate" sputtering technique.

Fig. 4 shows graphically the relationship between spatial resolution and lowest detectable concentration, as given by Eqs. 32 and 32b. The solid lines represent the "useful resolution" δ_u (equal spatial resolution in all directions); the broken lines give the estimated dependence of detection limit on lateral resolution for the case where the sputtering depth is limited to 10 nm. The right pair of lines are calculated for $\tau_u = 10^{-3}$ (average value for a good SIMS instrument, the left pair of lines represent the case $\tau_u = 1$ (perfect postionization)). Obviously, in this case the "sputtering limit" to spatial resolution is close to atomic dimension.

Reconstruction problem

There have been very few attempts to tackle the problem of image reconstruction, i.e. the reconstruction of the spatially true local element distribution from the measured ion micrograph and an assumedly known point spread function (see Section 4.1.). The reasons are that artifact contrast, which is a true pixel property, must be completely removed before the geometric "deblurring", which affects a local vicinity, can be attempted. Since artifact removal is only partially possible in SIMS, new artifacts may be induced when deblurring is attempted on an incompletely "precleaned" image. It is hoped, however, that successful application of reconstruction algorithms allows to increase image resolution beyond that available in the raw ion micrograph. Deblurring actually may be implemented in Fourier space by calculating the Fourier transform of the deblurred image, $\underline{n}(U,V)$, from the transforms of the blurred image and the point spread function respectively (see Eq. 12). This procedure does not always lead to success since there may be infinities and negative values in the output. Other filtering routines are available [36,37] which guarantee a non-negative finite output function. In one case reported in the literature [43], 1-dimensional linescans obtained on a scanning ion microprobe, were deblurred and an apparent resolution increase by a factor of 1.5–2 was obtained. The point spread function was obtained by imaging an edge structure of known shape and reconstructing the PSF from this image. Using this reconstructed PSF, reconstruction of the (linescan) image was performed. The smallest resolvable distance in the original image (2 μm) was improved to about 1 μm by this process.

Acknowledgements

This work was performed with support from TSP-program of the Austrian Ministry of Science and Research and the Austrian Society for Microelectronics (GME). Many fruitful discussions with W. Steiger and M. Alff are acknowledged.

References

[1] R. Levi-Setti, J. Chabala and Y.L. Wang, Scanning Microscopy, Suppl. 1 (1987) 13.
[2] G. Betz and F. Rüdenauer, Appl. Surf. Sci., 51 (1991) 103.
[3] H.J. Liebl, J. Appl. Phys., 38 (1967) 5277.
[4] P.D. Prewett and D.K. Jefferies, Inst. Phys. Conf. Ser., 54 (1980) 316.
[5] H. Gnaser, F.G. Rüdenauer, H. Studnicka and P. Pollinger, in H.O. Andren and H. Norden (Eds.), Proc. 29th Int. Field Emission Symposium, Almqvist and Wiksell, Stockholm, 1982, p. 401.
[6] A.R. Bayly, D.J. Fathers, P. Vohralik, M.J. Walls, A.R. Waugh and J. Wolstenholme, in A. Benninghoven et al. (Eds.), Secondary Ion Mass Spectrometry; SIMS V, Springer, Berlin, 1986, p. 253.
[7] R. Levi-Setti, G. Crow and Y.L. Wang, in A. Benninghoven et al. (Eds.), Secondary Ion Mass Spectrometry; SIMS V, Springer, Berlin, 1986, p. 132.
[8] R. Levi-Setti, in Scanning Electron Microscopy, 1983, SEM Inc., O'Hare, 1983, p. 1.
[9] R.L. Seliger, R.L. Kubena, R.D. Olney, J.W. Ward and V. Wang, J. Vac. Sci. Technol., 16 (1979) 1610.
[10] J. Orloff and L.W. Swanson, J. Vac. Sci. Technol., 19 (1981) 1149.
[11] M. Alff, in J.D. Brown and R.H. Packwood (Eds.), Proc. 11th Int. Congr. X-Ray Optics and Microanalysis, Univ. W. Ontario, 1986, p. 451.
[12] J.M. Chabala, R. Levi-Setti and Y.L. Wang, J. Vac. Sci. Technol., B6 (1988) 910.
[13] G. Slodzian, in A. Septier (Ed.), Applied Charged Particle Optics, Part B, Academic Press, New York, 1980, p. 1.
[14] A. Benninghoven, F.G. Rüdenauer and H.W. Werner, Secondary Ion Mass Spectrometry, Wiley, New York, 1987.
[15] F.G. Rüdenauer, Surf. Int. Anal., 6 (1984) 132.
[16] R. Castaing and G. Slodzian, J. Microsc. (Paris), 1 (1962) 395.

[17] "IMS 3f"-brochure, CAMECA, Courbevoie, France (1984).
[18] S.R. Bryan, W.S. Larkin, J.H. Gibson and G.G. Leininger, in A. Benninghoven et al. (Eds.), Secondary Ion Mass Spectrometry; SIMS VI, Wiley, New York, 1988, p. 369.
[19] V.T. Cherepin, in A. Benninghoven et al. (Eds.), Secondary Ion Mass Spectrometry; SIMS III, Springer, Berlin, 1982, p. 77.
[20] F.G. Rüdenauer, OEFZS-A-2358, Sept. 1992, Austrian Res. Ctr. Seibersdorf, Seibersdorf
[21] G. Slodzian, NBS Spec. Publ., 427 (1975) 33.
[22] F.G. Rüdenauer, P. Pollinger, H. Studnicka, H. Gnaser, W. Steiger and M.J. Higatsberger, in A. Benninghoven et al. (Eds.), Secondary Ion Mass Spectrometry; SIMS III, Springer, Berlin, 1982, p. 43.
[23] F.G. Rüdenauer, Fresenius Z. Anal. Chem., 333 (1989) 308.
[24] F.G. Rüdenauer and W. Steiger, Mikrochim. Acta (Wien), Suppl. II (1981) 375.
[25] W. Steiger, F.G. Rüdenauer and G. Ernst, Anal. Chem., 58 (1986) 2037.
[26] F.G. Rüdenauer, Beitr. Elektron. Mikrosk. Direktabb. Oberfl., 18 (1985) 25.
[27] S.R. Bryan, W.S. Woodward and R.W. Linton, J. Vac. Sci. Technol., A3 (1985) 2102.
[28] F.G. Rüdenauer, M. Riedel, F. Adams, H.E. Beske, H. Düsterhöft, M. Gericke, J. Giber, R. Gijbels, H. Holzbrecher, A. Lodding, H. Mai, F. Michiels, S. Oswald, C.-E. Richter, U. Södervall, A. Solyom, R. Stahlberg, W. Steiger, M. Trapp, G. Stingeder and R. Voigtmann, OEFZS-Report No. A-1441 (May 1989); Austrian Res. Ctr. Seibersdorf, Seibersdorf, Austria.
[29] U. Littmark and W.O. Hofer, Nucl. Instrum. Meth., 168 (1980) 329.
[30] F.G. Rüdenauer and W. Steiger, Ultramicroscopy, 24 (1988) 115.
[31] J.M. Chabala, R. Levi-Setti and Y.L. Wang, Appl. Surf. Sci., 32 (1988) 10.
[32] W. Steiger and F.G. Rüdenauer, Anal. Chem., 51 (1979) 2107.
[33] A.J. Patkin and G.H. Morrison, Anal. Chem., 54 (1982) 2.
[34] W. Steiger and F.G. Rüdenauer, Anal. Chem., 51 (1979) 2107.
[35] H. Kobayashi, K. Suzuki, K. Yukawa, H. Tamura and T. Ishitani, Rev. Sci. Instrum., 48 (1977) 1298.
[36] A. Rosenfeld and A.C. Kak, Digital Picture Processing, Academic Press, New York, 1976.
[37] H.C. Andrews and B.R. Hunt, Digital Image Restoration, Prentice-Hall, Englewood Cliffs, 1977.
[38] A. Septier, J. Phys. Rad., 15 (1954) 573.
[39] M. Born, Optik, Springer, Berlin, 1985.
[40] E.A. Chistova, Tables of Bessel Functions of the True Argument and of Integrals derived from them, Pergamon, New York, 1959, p. 78.
[41] M.D. Giley, R.K. Watts and E. Labate, J. Vac. Sci. Technol., B5 (1987) 1588.
[42] M.T. Bernius, Y.-C. Ling and G.H. Morrison, Anal. Chem., 58 (1986) 94.
[43] M. Bitterlich, B. Koch, H. Mai, F.K. Nähring, U. Seidenkranz, R. Syhre and R. Voigtmann, in K. Hohmuth (Ed.), Proc. Int. Conf. on Ion Implantation in Semicond., Part II, ZfK-360 (1978), ZfK Rossendorf, Dresden.

ELSEVIER

Analytica Chimica Acta 297 (1994) 231–251

ANALYTICA CHIMICA ACTA

Review

Optimization of secondary ion mass spectrometry for quantitative trace analysis [1]

G. Stingeder *,[2]

Institute for Analytical Chemistry, University of Technology Vienna, Getreidemarkt 9 / 151, A-1060 Vienna, Austria

(Received 14th December 1993; revised manuscript received 14th January 1994)

Abstract

The potential of *dynamic* secondary ion mass spectrometry (SIMS) for quantitative trace analysis is evaluated from the basic equations of signal formation and instrumental detection. The key factors are sputtering yield and ionization probability. The aim of optimization of measurement technique for problem solving is to gain *maximum relevant quantitative information*. In qualitative analysis elemental ions have to be identified and interfering molecular ions are separated by differences in kinetic energy distribution (energy discrimination) or mass (high mass resolution). Due to the complex signal formation process, quantification of intensities is performed by relative sensitivity factors obtained by calibration samples. Practically no *certified* reference materials are available. Calibration samples can be produced by chemical doping of substances, but routinely ion implantation is applied. Transfer of sensitivity factors between different laboratories respectively utilization of compiled values from the literature leads only to semiquantitative results. The prerequisite for accurate quantitative analysis are low random errors and reduction, preferably elimination of systematic errors. In an empirical problem oriented approach, variation of measurement parameters, use of different calibration methods and analytical techniques are combined to achieve optimum or maximum accuracy or information. For homogeneous samples a reproducibility of typically $\pm 2\%$rel. and an accuracy of $\pm 5\%$rel. can be obtained. Matrix and charging effects can severely limit SIMS analysis. Our experiences to control these effects are discussed. The course of the surface charge during depth profiling of a layer system can yield additional information on the quality of insulating layers. Examples for elimination of the matrix effect by flooding the surface with oxygen and by utilizing the energy distribution of the secondary ions are presented. Some references are given for the combination of SIMS depth profiling with imaging methods like electron probe micro analysis (EMPA), scanning tunneling microscopy (STM), atomic force microscopy (AFM), and transmission electron microscopy (TEM) to gain additional information.

Keywords: Mass spectrometry; Secondary ion MS; Trace analysis

1. Introduction

Since the early 1970s, secondary ion mass spectrometry (SIMS) has developed from the ion

* Corresponding author.

[1] Dedicated to the memory of Hans Pötzl, Professor of Physical Electronics, University of Technology Vienna.

[2] Permanent address: Institute for Chemistry, University of Agriculture, Gregor-Mendel-Strasse 33, A-1180 Vienna, Austria.

SSDI 0003-2670(94)00054-P

probe, primarily used for the bulk analysis of solids, into a number of sophisticated techniques for surface and near-surface analysis [1–3]. *Static SIMS* using gentle bombardment conditions has provided the analyst with a technique able to extensively characterize the chemistry of the top surface of almost all types of materials whilst causing negligible surface damage [3,4]. *Dynamic SIMS*, the successor of ion probe, has become the most sensitive elemental analysis technique applicable to solid state analysis, able to provide concentration–depth profiles with depth resolutions of a few nanometers and elemental detection limits down to typically 1 part per billion atomic (1 ppba = 1 atom per 10^9 atoms). Concurrent with these developments, *imaging SIMS* using highly focused ion beams or an ion microscope has been able to provide detailed chemical images in the static and dynamic mode of operation with a lateral resolution of approx. 1 μm for ion microscopes and approx. 100 nm for scanning ion probes [5].

SIMS is based on the fact that charged atomic and molecular species are ejected from the surface of a condensed phase (liquid or solid) under particle bombardment. The primary particle beam usually consists of ions (O^-, O_2^+, Cs^+, Ar^+, Xe^+ or Ga^+) or sometimes of neutral noble gas atoms. O_2^+ is typically used for the detection of electropositive species, Cs^+ for electronegative species, Ga^+ for improved lateral resolution and O^- or neutral noble gas atoms for analysis of poorly conducting materials. The sample can intercept the primary beam at different angles of incidence, with a typical range from normal to 60° from normal. The sputtering process is not just a surface layer phenomenon but consists of the implantation of the primary species into the sample and removal of surface atoms by the energy loss of the primary species via a collision cascade. Many species are formed by the interaction of the beam with the sample but the positive and negative secondary ions are the species of interest for SIMS. Most of the secondary particles are neutrals and can be detected by post ionization (secondary neutral mass spectrometry or SNMS). The secondary ions are extracted by electrical fields and then energy and mass analyzed. Detection is performed by an electron multiplier, Faraday cup, or an ion sensitive image amplifier for imaging.

Virtually all secondary ions originate from the uppermost atomic layers of the bombarded surface. This results in one of the most important features of SIMS – its surface sensitivity. Other advantages are the ability to detect all elements and their isotopes, the high spatial resolution and the sensitivity mentioned above. Chemical information can be obtained from relative molecular ion abundances. The major limitations are determined by the complexity of the mass spectra, the large variation of the secondary ion yields for different elements, and also for a particular element in different matrices (chemical matrix effect), and by the mixing of atoms and chemical changes in the altered layer formed by the sputtering process.

SIMS has been applied in all fields of material science, geology, organics, and biology. Examples are provided in the proceedings of past SIMS international conferences [6–11]. In this paper problems of dynamic SIMS in quantitative trace analysis are discussed by the basic equations of SIMS and by examples from our laboratory. Our main task has been to develop measurement techniques and strategies which should be generally applicable for other analytical problems and show the potential and limitation of the method. Quantitative information has to be gained on technical materials which should be: (1) relevant to material properties and, (2) of appropriate accuracy. Because SIMS is a very complex method and often unique information can be obtained, the definition of the analytical problem is, maybe more than with other analytical methods, a key point. As much as possible pre-information should be collected and other methods with lower expenditure have to be taken into account. If other analytical methods cannot give full appropriate information, SIMS should be utilized in addition. In quantitative depth profiling inaccuracies of concentration and depth scale are frequently of equal importance. In our work "optimization of SIMS for quantitative trace analysis" stands for gaining *maximum relevant quantitative information*. The expenditure depends on the definition of the problem and on the experience of the

analyst. The main advantage of SIMS for the analyst is that it is scarcely ever routine, but mostly challenging.

2. Potential of SIMS for quantitative trace analysis

In this chapter the basics of SIMS are reviewed by using mainly three excellent books as sources [1–3]. The potential of dynamic SIMS for quantitative analysis can be evaluated from the following basic equations:

$$I^{+(-)}_{(^{n}A)} = I_p Y \alpha^{+(-)}_{(A)} C_{(^{n}A)} T_{(A)} \quad (1)$$

$$Y_{(A)} = Y C_{(A)} \quad (2)$$

$$C_{(^{n}A)} = C_{(A)} f_{(^{n}A)} \quad (3)$$

$$T_{(A)} = f(\Delta E) f(\Delta \Omega) T_{m,(A)} \beta_{(A)} \quad (4)$$

$I^{+(-)}_{(^{n}A)}$, (usually in ions s^{-1}) is the measured (positive or negative) secondary ion (SI) intensity of the isotope ^{n}A of the chemical element A. I_p (in μA or ions s^{-1}; 1 $\mu A = 6.25 \times 10^{12}$ ions s^{-1}) is the primary ion (PI) current delivered to the area sampled by the secondary ion optics (="detected" or "analyzed area"). Y, the total (or global) sputtering yield of the sample (in number of SA/number of PI) is the total number of (secondary) atoms (SA) sputtered for each incident primary ion. It should not be confused with the sputtering rate, which is the erosion rate of the sample usually in (nm/s). $Y_{(A)}$, is the partial sputtering yield of the chemical element A. $\alpha^{+(-)}_{(A)}$, the (positive or negative) ionization probability (or efficiency; in number of SI/number of SA) is the fraction of the flux of a sputtered species that is ionized. $C_{(A)}$ (in atoms of element A/atoms total), is the fractional atomic concentration. $f_{(^{n}A)}$ is the isotopic abundance of ^{n}A. $T_{(A)}$ (in number of SI generated/number of SI detected), the instrumental efficiency (overall instrumental transmission) of the secondary ion mass analyzer, is proportional to the fraction of ionized particle flux that falls in the energy ($f(\Delta E)$) and solid angle ($f(\Delta\Omega)$) acceptance windows of the mass spectrometer, the transmission of the mass spectrometer, $T_{m,(A)}$, and the yield of the ion detector, $\beta_{(A)}$.

The *sputtering yield, Y*, in general has values between 0.5 and 10. For a given PI and PI conditions (energy, angle of incidence, etc.) and for different elements through the Periodic Table it varies by a factor of about 5. Since the energy of the primary beam is transferred to the atoms in the solid by a collision (a billard-ball-type process), Y depends on the mass, energy and angle of incidence of the bombarding species and on the masses of the sample atoms. Furthermore it shows a dependence on crystal orientation, crystal type (amorphous, polycrystalline, or single crystal), topography, sample temperature and chemistry of the surface. The chemistry is related to the surface binding energy, which is related to the sublimation energy. Y can be calculated for chemical elements by models [12], but for chemical compounds results are scarce [1,3].

During sputtering there is a competition between ion implantation of PI and sputtering of the implemented PI element. Thus the concentration of the PI element at the momentary surface (altered layer in the crater bottom, analyzed by SIMS) will vary with time in the initial stage of the implantation process, but finally arrives at a steady-state saturation value when the sputter front has caught up with the original implantation front. This occurs when a depth of approximately $R_p + 2\Delta R_p$ has been sputtered away. R_p is the projected range and ΔR_p is the "straggling" of the implantation distribution of the PI. The equilibrium concentration of the PI element is inversely proportional to Y [13].

Other important phenomena which are related to the sputtering process and complicate quantification (of the depth scale) are [1–3,6–13]: formation of clusters or molecular ions, preferential sputtering, (isotropic and anisotropic) beam induced mixing (cascade mixing and recoil implantation), microtopography (roughening of originally smooth surfaces, selective sputtering of phases or crystal orientations), chemical effects (sputtering induced (radiation enhanced) diffusion of elements at the surface and in the bulk, segregation of trace elements between altered layer and bulk), electrical effects (surface charg-

ing of insulators – migration (charge driven diffusion) of trace elements).

The *ionization probability* $\alpha_{(A)}^{+(-)}$, is the crucial factor for quantification of the SI intensities to concentrations. For positive SI it depends inversely on the ionization potential and for negative SI on the electron affinity. This means (like Y) it follows the change of the properties in the Periodic System of Elements (compare Figs. 1 and 2 [14]). Furthermore it depends on the electronic state of the target material (matrix). As the PI are implanted into the sample, the matrix is changed. If the PI are reactive (in principle all elements, except the noble gases), the electronic state of the analyzed surface is changed, and thus the ionization probability differs from that of the virgin sample. This is also the case for adsorption of reactive species from the residual gas at the crater bottom and in the sputtering induced transition zone of interfaces between layers of different chemical composition. It has to be emphasized, that the SIMS signal is generated mainly from the two uppermost monolayers of the altered zone.

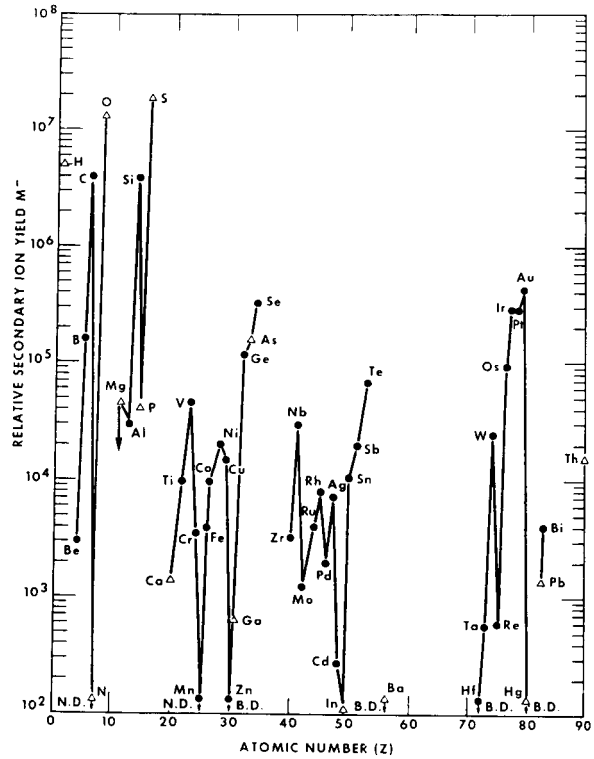

Fig. 2. Relative negative ion yields for 16.5 keV Cs^+ at normal angle of incidence. N.D. signifies not detected [14].

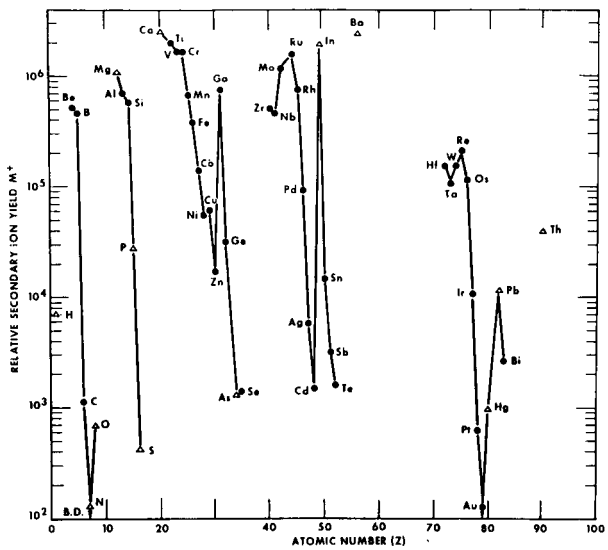

Fig. 1. Relative positive ion yields for 13.5 keV O^- at normal angle of incidence. D signifies that a compound sample was used, while B.D. means barely detectable [14].

As shown in Eq. 1, the SI intensity measured is always proportional to the product of $Y\alpha_{(A)}^{+(-)}$. Because none of both factors can be obtained independently from experiments, in praxis

$$Y_{(A)}^{+(-)} = Y_{(A)}\alpha_{(A)}^{+(-)} \tag{5}$$

the secondary ion yield, is used to compare sensitivities of different chemical elements. $Y_{(A)}^{+(-)}$ (in number of SI/number of PI), is defined as the number of sputtered secondary ions of the chemical element A, for each primary ion impact.

Because the overall transmission, $T_{(A)}$, depends on the element, and its value is usually not known, another possibility to compare relative ionization yields of pure elements (or instruments or analyses) is the practical sensitivity, Sp, in (ions s^{-1}/nA) [1]:

$$Sp = I_{(A)}^{+(-)}/I_p \tag{6}$$

with the SI intensity of the element A

$$I^{+(-)}_{(A)} = I^{+(-)}_{(^nA)}/f_{(^nA)} \quad (7)$$

The absolute values of $Y^{+(-)}_{(A)}$ for pure elements bombarded with noble gas ions given in the literature show a large scatter, because of the difference in experimental conditions (e.g., instrumental conditions, purity of the elements, residual gas background, etc. [1]), but over the Periodic Table both $Y^{+}_{(A)}$ and $Y^{-}_{(A)}$ span a range of typically 4–5 (–8) orders of magnitude (compare Figs. 1 and 2). The combination of both values, $Y^{+(-)}_{(A)}$, still varies by 6 (–8) orders of magnitude. As Y varies typically by a factor of 5, $\alpha^{+(-)}_{(A)}$ shows practically the same variation like $Y^{+(-)}_{(A)}$.

The influence of the chemistry of the emitting surface (electronic state) makes the understanding and theoretical calculation of $\alpha^{+(-)}_{(A)}$, respectively $Y^{+(-)}_{(A)}$, even more complicated. During the ionization process the atoms "feel" their chemical environment. Positive ion yields are greatly enhanced in the presence of electronegative species at the surface. e.g., If a metal surface is oxidized the increase is often of the order of 10^2 (-10^4). The extent of increase varies from element to element and this fact complicates quantification. There is evidence that the effect is related to the increase in work function, thus there is an increased probability of ion escape from the surface [3]. Analogously to this, negative ion yields are enhanced in the presence of electropositive elements (e.g., Cs). A comprehensive review on SI emission is given in [1].

The effects discussed above are called the (chemical) matrix effects. It is a general term used to describe differences in ion yield for a given element in samples with different compositions [2]. Differences in trace element contents do not change the composition of the "matrix", but the chemical environment of an atom is changed if there are differences above the 0.1–1% level. Thus below ca. 0.1at.%, down to the limit of detection (< ppba) sensitivities are constant and working curves are linear over many orders of magnitude, as long as the composition of the matrix is kept constant.

All the facts listed above have led to the use of oxygen (O_2^+ or O^-) and cesium (Cs^+) as primary ions in dynamic SIMS analyses. For a "true surface analysis" (static SIMS) mainly noble gas ions (e.g., Ar^+) are used [3].

It was mentioned above, that in sputtering equilibrium the surface concentration of the PI element is inversely proportional to Y. In general, ionization probabilities vary strongly with oxygen or cesium atom density:

$$\alpha^{+(-)}_{(A)} = k(\rho_O)^n \quad (8)$$

where ρ_O is the oxygen or cesium atom density (= volume concentration in atoms cm^{-3}), k is a proportionality factor and n is a number between 2 and 3 [2,15]. Therefore $\alpha^{+(-)}_{(A)}$ is also proportional to the 2nd to 3rd power of $(1/Y)$ and all factors influencing Y will strongly change $\alpha^{+(-)}_{(A)}$.

In practical dynamic SIMS analysis $Y^{+(-)}_{(A)}$ is of primary importance, because the more ions are emitted, the easier it is to perform an accurate and sensitive analysis of a sample. For selection of the polarity of the secondary ions and the application of O_2^+ or Cs^+ Fig. 3 [14] can be used. It gives the ratio of $Y^{-}_{(A)}$ under Cs^+ bombard-

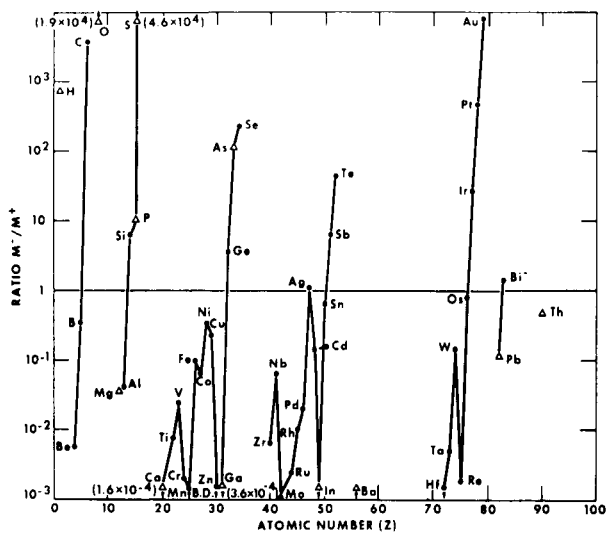

Fig. 3. Secondary ion yield ratios M^-/M^+ for Cs^+ and O^- bombardment from Figs. 1 and 2, respectively. Instrument used for measurements was the IMMA from Applied Research Laboratories [14].

ment to $Y^+_{(A)}$ under O^- bombardment. Hence where it has a value > 1, Cs^+ should be used.

In sputtered neutral mass spectrometry (SNMS) [16–20] the sputtering and the ionization process are decoupled. The SI formed in the SIMS process are separated by an electric field and the remaining neutrals are postionized in the gas phase by an electron beam, an electron or Ar plasma or by means of lasers (resonant or nonresonant). The matrix effects are practically eliminated and the variation of sensitivity over the periodic table of elements by a factor of ca. 10 is negligible compared to SIMS. Quantification can be performed by elemental reference standards, but the sputtering yield has to be known. By use of lasers, SNMS is very sensitive (ppb of monolayers), but restricted to surface analysis with a maximum depth of typically 10 nm. The other techniques are utilized successfully, e.g., for analysis of contaminants at interfaces, but their sensitivity is by 3 orders of magnitude lower than SIMS. Glow discharge mass spectrometry (GDMS) applying an Ar plasma is mainly used for ultra trace bulk analysis. Combination with SIMS is the best approach in solving of analytical problems [1,3,6–11,18,19].

The *instrumental efficiency* $T_{(A)}$, (or overall instrumental transmission), of the secondary ion mass analyzer, (see Eq. 4) depends on the type of the instrument and on the (optimized) adjustment for the distinct analytical problem. The aspects concerning the instrumental design will not be discussed here (for a comprehensive review, see e.g. [1]). Rough numbers of commercial, routine instruments for T_m are 0.005 for quadrupole mass spectrometers, 0.1 for magnetic sector instruments and ca. 1 for time-of-flight (TOF) mass spectrometers. β usually has a value close to unity. $f(\Delta\Omega)$ corresponds to the quality of the SI extraction and transfer (into the mass spectrometer) optics. For instance in magnetic sector instruments it has to be optimized to obtain high mass resolution for separation of interfering species and in direct imaging instruments to optimize lateral resolution. It is also influenced by the emission characteristics of a given species and is therefore matrix dependent.

Much attention should be given to $f(\Delta E)$. It is significantly higher for magnetic sector instruments than for quadrupole instruments, and within these groups of spectrometers it has different characteristics. This can lead to systematic errors by more than a factor of 20 in transfers of the relative sensitivity factors from one instrument to another [1,21]. The energy distributions of the SI vary for distinct chemical elements and in addition, for a given element it is influenced by the matrix, thus $f(\Delta E)$ is element and matrix dependent. Surface charging of insulators changes the kinetic energy of the SI and can lead to artifacts by signal drops or can result in a complete signal loss.

Setting of an energy window is frequently used to optimize analytical conditions. Like $f(\Delta\Omega)$, also $f(\Delta E)$ has to be reduced to separate interfering species and optimize lateral resolution.

The transmission shows mass discrimination effects not only for different chemical elements, but also for isotopes of a defined element. Isotopic effects are usually low and only of significance for highly precise isotope ratio measurements in geology with an accuracy in the 0.1% range [1,22,33].

Another characteristic number used in praxis is the useful yield, $\tau_{u(A)}$, (in number of SI/number of SA):

$$\tau_{u(A)} = \alpha^{+(-)}_{(A)} T_{(A)} \tag{9}$$

It is defined as the ratio of total ions of a species detected to the atoms of that species sputtered (within the detected or analyzed area) and includes contributions of both ion yield and transmission. It is a figure of merit for an analysis and it is used to compare different analyses with a distinct combination of analytical (trace) element and matrix (e.g,. analyses of B in Si). The variables in this comparison can be different (types) of instruments and analytical conditions as: kind of PI (e.g., O^+_2/Cs^+), energy filtering/high mass resolution, positive SI/negative SI, atomic SI/molecular SI, energy and angle of incidence of PI, even different adjustment of the instrument, etc. Usually it is determined by means of implanted standard materials (see chapter on quantification).

3. Optimization of measurement technique

3.1. Qualitative analysis – interferences

Which ions are formed?

The fundamental equation of SIMS (Eq. 1) was discussed only for singly charged atomic ions. But in the sputtering/ionization process a variety of other ions is formed. The corresponding more complex equations are discussed thoroughly in [1]. In addition there are different sources for the formation of ions containing elements which are not originally present in the sample.

The sample is in a clean environment in the instrument. This we can regard as a closed system. Ions can be formed by elements from the

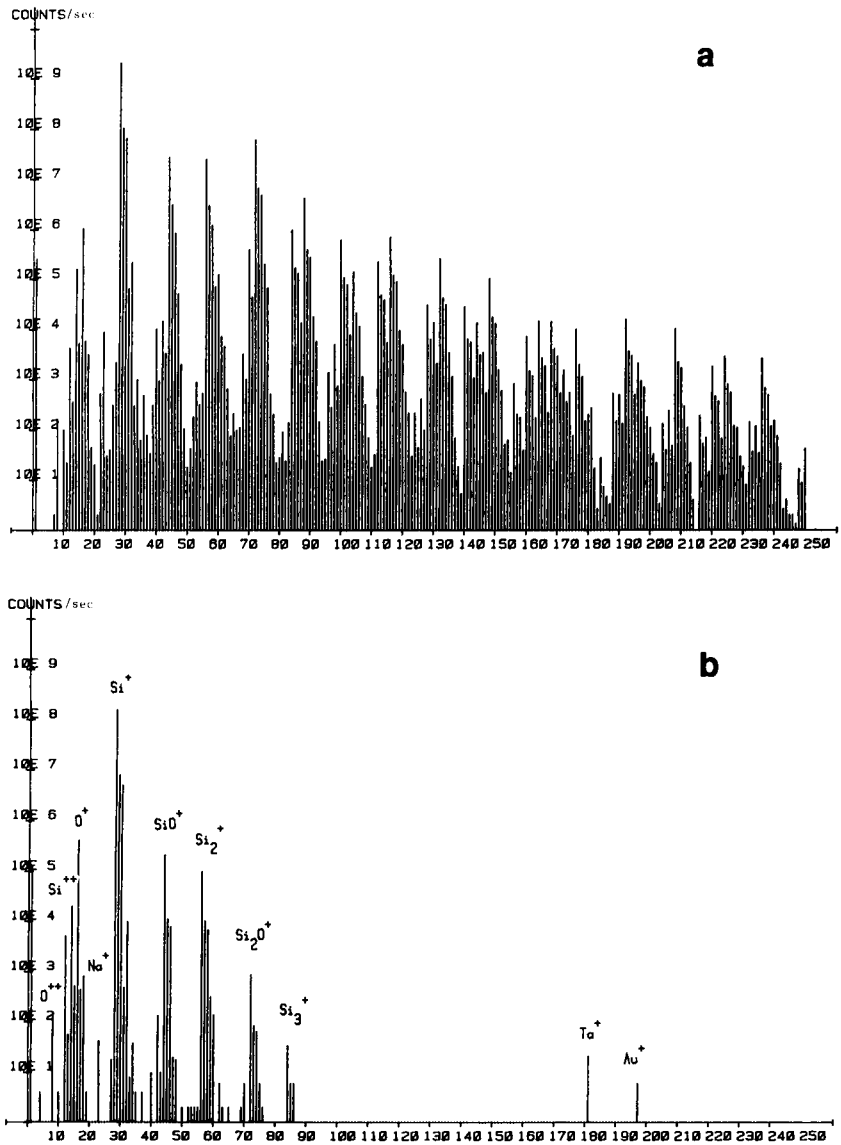

Fig. 4. Mass spectra of silicon bombarded with 5.5 keV O_2^+ (2 μA, rastered area = 500 × 500 μm^2, diameter of analyzed area = 150 μm). (a) SI with an initial energy range of 0–75 eV detected. (b) SI with an initial energy range of 50–180 eV detected.

sample, the primary ions, residual gas adsorbed at the freshly sputtered, often very reactive sample surface, sputtered parts of the primary and secondary ion column (especially apertures) and of the sample chamber, or by instrument contamination from prior analyses deposited by sputtering.

Usually the primary beam is purified by a primary ion beam mass filter. If this is not the case, an instrumental background of, e.g., O and N will occur. The residual gas molecules mainly consist of H, C, O and N. This can lead to a constant adsorption rate of these elements at the sputtered surface. Instrumental parts often consist of Fe, Cr, Ni and Ta. In magnetic sector field instruments the extraction lens is close to the sample surface (e.g., for the CAMECA ims 3/4f the distance is 5 mm), thus resputtering of prior deposited sample material will lead to a background. Impurity memory can limit the dynamic range in a depth profile as heteromemory or homomemory [2]. Heteromemory is a contamination from a prior analysis of a sample that has a high atom density of the species of interest (e.g., As in Si after GaAs). Homomemory is contamination from a high level of the species of interest in the sample being analyzed. For the CAMECA instrument this limits the dynamic range of profiles with a steep gradient to 5 orders of magnitude.

The variety of the different ions formed can be seen in a mass spectrum. The spectra of positive SI contain the following: (1) elemental atomic ions, singly or multiply charged. The mass spectrometers separate after the mass to charge ratio (m/e), thus $^{28}Si^{2+}$ will be detected at 14 Daltons and $^{28}Si^{3+}$ at 9.33 Daltons. (2) Molecular or cluster ions (e.g., $A_xB_yC_z^+$), which can contain all elements of the "closed system" discussed above. Note, that at an interface the matrix is changing and peaks of unexpected ions can form. For example at a C/Si interface $^{40}(SiC)^+$ could be confused with contamination of Ca.

The possible combination of isotopes of the different elements creates ion abundance patterns. Molecular ion abundances can be calculated from the natural abundances by using a binomial expansion (mass discrimination effects are neglected), but one has to keep in mind, that the relative intensity (ion yield) between different patterns cannot be calculated. Consequently this patterns are not affected by the method of excitation (PI) or by matrix effects.

The main differences of negative SI spectra are: (1) virtually no multiply charged ions, (2) the yield of molecular ions is, especially with Cs^+ PI, higher (absolute and relative to atomic ions).

Separation of interfering molecular ions

Usually the main composition of the samples (matrix elements) are known from their production process or from analyses by other, less complex or time consuming methods (e.g., electron probe microanalysis). Thus qualitative analysis is focused on minor and trace elements. The procedure applied is also necessary for recognition of interferences, sources of background and selection of "analytical ions" for trace analysis and depth profiling.

Fig. 4a shows a typical positive SI mass spectrum of pure silicon bombarded with oxygen PI. It is a monoelemental matrix, but nevertheless the spectrum is very complex. All combinations of $Si_xO_y^+$ with the silicon ($f(^{28}Si) = 92.2\%$, $f(^{29}Si) = 4.7\%$, $f(^{30}Si) = 3.1\%$,) and oxygen isotopes ($f(^{16}O) = 99.8\%$, $f(^{17}O) = 0.04\%$, $f(^{18}O) = 0.20\%$) are observable and some of the molecular abundance patterns are overlapping (e.g., $^{60}(Si_2$ and $SiO_2)$). At "mass" (exactly "m/e") number 75, arsenic could occur, but $^{75}(Si_2O)^+$ yields a background intensity of ca. 10^5. Except for the doubly charged matrix ions, at masses lower than the matrix (Si and implanted O), trace element peaks are not interfered and can be detected (^1H, ^{12}C, ^{23}Na).

To obtain maximum information for qualitative analysis, signals of many masses have to be detected. Mass spectra and, if the signals are not constant, depth profiles have to be measured. Contributions of residual gas adsorption and memory effects can be assessed by changing the PI density. At equilibrium pressure, adsorption rate of residual gas (main elements C, H and O) is constant, accordingly the signal is constant and does not follow PI density changes. Memory effects are proportional to the PI current. At con-

stant PI current they are not influenced by changes of the rastered area (PI density is changed). But they increase with higher PI currents. With this approach in quantitative analysis of oxygen in silicon we could determine residual gas contributions with an accuracy of better than ±10%rel. [24].

The chemical elements are identified via isotopic ratios. Intensities of polyatomic or cluster ions have to be minimized. One approach to remove the interferences is the peak stripping method. The characteristic intensity patterns are subtracted and the resulting intensities are used for identification. This method is limited by the signal/noise ratio and therefore rarely successful. But it can be used for background subtraction in depth profiling. For example the background of $^{27}(BO^+)$ to $^{27}Al^+$ is proportional to the signal of $^{11}B^+$ [2]. Another approach is to use different properties of atomic and molecular ions, namely differences in energy distributions and mass.

Energy discrimination

Due to the statistical sputtering process the SI have an energy distribution. Fig. 5 shows normalized energy distributions of different Si_x^+ clusters [25]. In general the molecular ions have a narrower energy distribution than the atomic ions. As more atoms a molecular SI consists of, the narrower is the energy distribution. By setting of an energy window (and reduction of $f(\Delta E)$) to discriminate against low energy ions, the intensity of molecular ions is much more reduced than that of atomic ions. This approach is called "energy filtering" or "voltage offset". Fig. 4b shows a mass spectrum measured with the identical PI conditions as in Fig. 4a, only the SI with an initial energy of < 50 eV were discriminated. The intensity of clusters containing more than 3 atoms is reduced to zero, that of 3 atoms by 5 orders of magnitude and that of 2 atoms by ca. 100, whereas the intensity of Si is reduced by only a factor of ca. 10. Arsenic is not present, but signals at the nominal masses of Ta and Au are observed. In this case Ta is a background from the PI apertures and Au a memory effect from a gold coated sample measured prior to the pure silicon.

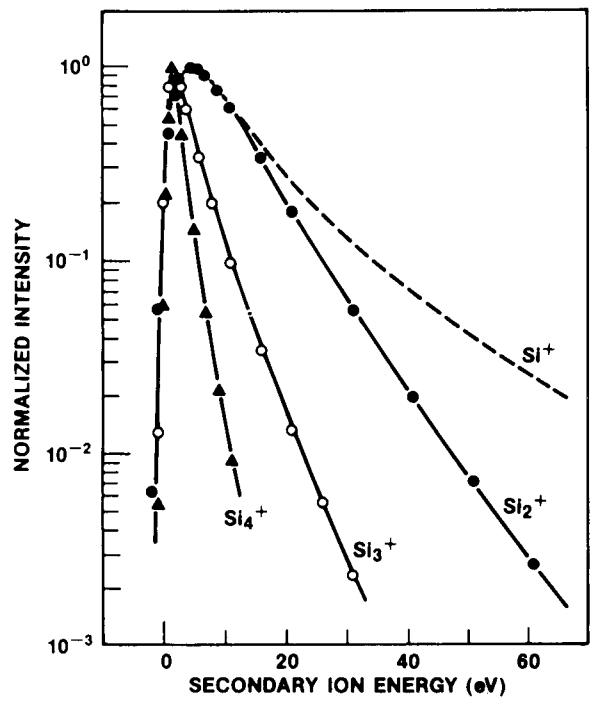

Fig. 5. Normalized energy distributions of sputtered Si and Si molecular ions. Specimen, silicon. PI, Ar^+ from K. Wittmaack [25]. Analyzed using a quadrupole instrument.

The energy distribution of atomic ions differs from element to element. It is also dependent on the matrix. For example Na^+ has a relatively narrow energy distribution, comparable to diatomic molecular ions. This means, that unequivocal identification is not possible by the energy filtering approach.

High resolution mass spectra

Due to the mass defect ($\Delta m = \Delta E c^2$) corresponding to the high binding forces in atomic nuclei, usually the atomic ions have a slightly lower mass than the molecular ions. For example the mass difference (ΔM) between $^{75}As^+$ and $^{75}(^{29}Si^{30}Si^{16}O)$ is 0.0235 u and a mass resolution of $M/\Delta M = 3200$ is necessary to separate both species. The absolute mass of a given species can be used for unambiguous identification. This depends, of course, on the accuracy of absolute mass determination. In praxis often the mass difference of species at a given mass number is

used. In this case the identity of at least one species (frequently a hydrocarbon molecule, which has the lowest mass) has to be known or assumed. With a mass resolution $M/\Delta M$ between 2000 and 7000 most of the overlapping peaks can be separated.

This mass resolution can be achieved using double focusing magnetic sector field and time of flight instruments, but not by quadrupoles. Fig. 6a [26] shows the low mass resolution ($M/\Delta M = 300$) mass spectrum of a hard metal (WC–TiC–NbC–TaC–Co) in which phosphorus should be determined. While there is a pronounced peak at $M = 31$ (P^+), investigation with high mass resolution (Fig. 6b, $M/\Delta M = 2300$) shows that there are strong interferences of the phosphorus peak by CO^+, NO^+ and CH_3O^+, which, if not eliminated, would have caused a significant analytical error (qualitatively and quantitatively). To achieve high mass resolution $f(\Delta E)$ has to be reduced.

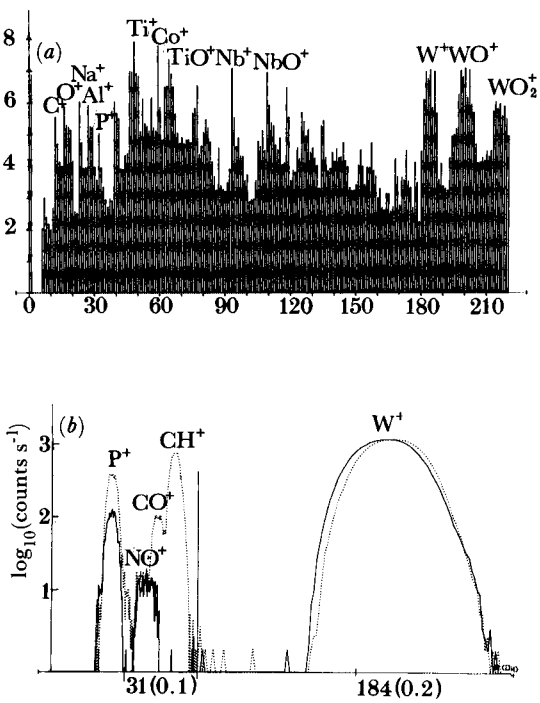

Fig. 6. Low (a) and high (b) mass resolution spectra of a hard metal specimen (88% WC, 6% TiC–TaC–NbC, 6% Co) showing the complexity of secondary ion mass spectra at the trace element level: (a) masses 1–220; (b) mass 31 ± 0.05 u and mass 184 ± 0.1 u, (· · · · · ·) presintered material, 8 $\mu g\ g^{-1}$ phosphorus; (– – –) sintered metal, 2 $\mu g\ g^{-1}$ phosphorus. Measurement: PI = O_2^+, 5.5 keV, 2.5 μA [26].

This can change the relative sensitivity factors for quantification.

3.2. Quantitative analysis

Quantification is the major problem of SIMS. This was one reason that until the mid 1980s the potential of SIMS was not realized by material scientists and also by many analytical chemists. The time consuming but sensitive and accurate neutron activation analysis (NAA) was utilized for (distribution) analysis of trace elements. But due to comprehensive developments by the SIMS community, SIMS has become a routine method in many fields and NAA now is used almost exclusively as a reference method. The stability and sensitivity of the instruments has been improved considerably and quantitative results have been confirmed by interlaboratory comparison, calibration samples and measurement by independent methods. Since the mid 1980s in semiconductor industry SIMS is used for in-line process control.

Strategies have to be adapted for each given analytical problem, and if necessary new methodological developments have to be performed. But this is common practice for all (complex) analytical methods with high information content.

To use the full potential of SIMS, the sputtering time scale has to be converted to a depth scale and intensities have to be quantified to concentrations.

Depth scale

Quantification of the depth scale is directly related to all phenomena and problems discussed for the sputtering yield, Y. These problems can lead to systematic errors in the depth scale. For example, it has to be emphasized that at an interface between two layers the situation is very complex. A transition zone of changing chemical composition is created due to the sputtering process.

In praxis the depth of each sputtered crater is measured by surface profilometry (in our laboratory by a SLOAN–DEKTAK IIA instrument). The accuracy of these instruments is in the range of $\pm 5\%$rel. for a depth of > 100 nm.

Usually a series of samples is measured with constant PI conditions (energy and current density), thus the sputtering rate in (nm/s) should be constant. The stability of the PI current density can be better than 1%rel. for the duration of one measurement (ca. 30 min). After each depth profile the PI current can be readjusted. Therefore the crater measurements of all samples can be used to find outliers, to quantify flat craters and to obtain a *relative* error between different depth profiles which is in the range of ±1.5%rel. via the average sputtering rate.

For multilayer samples the sputtering rate differs from layer to layer. The boundary between the layers has to be defined on the raw data depth profile. Usually the signal of a main element of each layer is detected and the interface is established in an arbitrary manner by using a 50% valley criterion. In most cases the thicknesses of the individual layers are known from the production process of the samples or they are measured by other methods (e.g., ellipsometry). If this is not the case, they can be calculated by using other samples consisting of the respective materials or by sputtering individual craters until the end of each layer and measuring the total depth.

If the sample is laterally inhomogeneous within the analyzed area, only 3-dimensional depth profiling [5,27–32] yields meaningful results. Imaging SIMS can also be used to expose uneven craters or sputtering induced roughness [33]. For quantification, the individual sputtering rate of each phase (e.g., precipitate or grain boundary) should be taken into account. With high experimental effort this on principle possible, but until now only semiquantitative results were presented [34]. Usually the sputtering rate of the matrix is used to convert the time scale into depth. The error of the depth scale (size) of, e.g., precipitates corresponds to the ratio of the sputtering rates of precipitate/matrix and can be a factor of 2.

Concentration scale

If SIMS is used for solving technological problems, three different levels of information concerning the concentration scale are commonly used. The lowest level after the raw data ("shape of a depth profile or intensity for a chemical element") is *relative comparison* of a "good" and a "bad" sample. This maybe sounds trivial, but in homogeneous samples the reproducibility of measurements is very high (typically < 10%rel.) and because SIMS measurements often yield unique information (all elements, low concentrations, good lateral and excellent depth resolution) for the *majority of problems* this approach is adequate. The next level is *semiquantitative analysis*. Here we try to obtain an accuracy by a factor of 2 (±100%rel.), but also the correct order of magnitude belongs to this level. *Quantitative analysis* should be better than typically ±30%rel. The upper limit for the inaccuracy of precision measurements is ±5% rel.

The most impressive SIMS data concerning precision and accuracy (but of relative concentrations) were achieved in isotopic ratio measurements of extraterrestrial materials, e.g., [22,23]. The accuracy of the isotopic ratios has to be better than 0.1%, because from such small deviations significant conclusions are drawn. This is a particular field of SIMS and instruments have to be adapted for these special requirements (e.g., counting system and stability of power supplies).

The main problems for quantification were discussed with Eqs. 1, 5 and 8. The key factor is the secondary ion yield, $Y^{+(-)}_{(A)}$, in particular the ionization probability $\alpha^{+(-)}_{(A)}$. The matrix effects are so significant that quantitative analysis is only possible empirically by sensitivity factors obtained from standard samples consisting of the "same" matrix. The concentrations of elements at a level of roughly > 1at.% (better 0.1at.%) have to be identical in sample and standard. Then the working curves of the trace elements are linear over many orders of magnitude. SIMS is used mainly for concentrations below 0.01at.%. At higher concentrations other methods like AES (Auger electron spectroscopy), XPS (x-ray photoelectron spectroscopy) or EMPA (electron microprobe analysis) should be used. Only in special cases measurements of concentrations of > 0.1at.% are useful. For example, we have published recently measurements of high dose Cr and Co implanted Si [35,36]. Depth profiles of implants should be quantified from > 10at.% to the limit of detec-

tion (ppba). In such a case it is possible to use two methods (e.g., AES and SIMS), but, if the SIMS matrix effect can be eliminated, it is more efficient and economical to measure the profile only by SIMS.

Calibration by reference materials

As pointed out above, SIMS is, like all instrumental methods of analysis, a relative method. The inaccuracy of the results is limited by the quality of the reference materials (RMs). Production of such RMs involves a great expense, because trace and ultratrace levels of many elements have to be incorporated into a solid matrix. They should be distributed laterally homogeneously and their chemical state respectively their chemical environment has to be defined. To eliminate systematic errors, the concentrations of the trace elements have to be verified by independent calibration methods.

Round robin analysis were performed for some elements in semiconductor materials (Si [37,38] and GaAs [39,40]). Many companies sell calibration samples, but *practically no certified reference materials are available.* Each laboratory has its own calibration samples.

Calibration samples can be produced by chemical doping of substances or by ion implantation. Chemical doping is in principle a powerful means to produce multielement calibration samples. To achieve the same chemical state of the trace elements, the calibration samples should be produced by the same process as the specimens under investigation. For example for *bulk* ultra trace analysis of refractory metals (W, Mo, Nb and Ta) used as sputter targets for electrode lines in VLSI devices, materials containing 30 elements in the $\mu g/g$ region could be produced by doping the starting materials of the refractory metals, the corresponding oxides, with aqueous solutions of the trace components [41]. The concentrations of the trace elements were determined in a round robin experiment using chemical bulk analysis methods, yielding the average concentration. A major drawback of such materials is their inherent inhomogeneity, thus elaborate measurement and statistical data evaluation techniques had to be used which allow to characterize the inhomogeneity of the material. After development of an imaging system, a 3-dimensional representation of the trace elements distributed in form of precipitates could be obtained [28,29]. An estimate of the accuracy achievable with these materials which includes the sampling error yields a value of $\pm 30\%$ for relative homogeneously distributed elements, up to a typical error factor of 2 for other elements. This inaccuracy is acceptable since changes in trace element content encompass up to five orders of magnitude. The sensitivity factors obtained by the calibration samples were used to quantify ultrapure materials. The detection limits of SIMS for bulk analysis are in the order of pg/g–ng/g [41,42].

Another example for homogeneously doped calibration samples is semiconductor technology. The major trace elements used in Si technology are the electrically active dopant elements B, P, As and Sb and the contamination element O (from SiO_2 crucibles used in the Czochralski process for single crystal production). All these elements can be incorporated homogeneously in Si wafers. The homogeneity over the major part of the wafer is much smaller than the reproducibility of the SIMS measurements ($< 1\%$). They are routinely characterized by electrical resistance measurements, from which elemental concentrations can be derived. These samples are doped with only one element (single element reference samples). In depth profiling for semiconductor industry, the total depth for a profile is typically between 10 nm for surface analysis, 500 nm for implantation profiles and 2 mm for diffusion profiles. To obtain a sufficient depth resolution (data points/depth) the sputtering rate is usually adjusted for a total analysis time of 30 min. This means that the sputter rate can vary by a factor of 100. The main advantage of homogeneous reference samples for SIMS is the independence of the accuracy of the sensitivity factors on the sputtering rate. At each sputtering rate the resulting profile should be a horizontal line and, in contrast to implanted reference samples, depth resolution has no influence.

Ion implantation is routinely used for the preparation of calibration samples, with the major drawback that the samples contain mostly one

and sometimes only a few elements. The technique is used in production of semiconductor devices. Mass separated ions are implanted with an energy of typically 100 keV into a solid material. The depth distribution has a near-Gaussian shape. Fluences (doses) are determined from the product of target current and time; backscatter or sputter effects can be corrected. In careful experiments the fluence (atoms cm^{-2}) can be determined with an inaccuracy of ca. $< \pm 3\%$rel., but rather frequently we observed systematic errors of $> 10\%$rel. It has the key advantage that laterally homogeneous samples of almost any combinations of chemical elements can be produced. Because the sample is not in thermal equilibrium also otherwise nonmiscible solid state solutions can be obtained. The fluences can be varied over many orders of magnitude. To eliminate systematic errors, samples containing high fluences can be calibrated with in situ methods less sensitive as SIMS (e.g.: RBS, Rutherford backscattering spectroscopy [36]; AES, Auger electron spectroscpy [36]; NAA, neutron activation analysis [43,44] or XRFA, x-ray fluorescence analysis [45]), or after dissolution by chemical methods like AAS (atomic absorption spectrometry) [45]. Low fluence samples are produced by reducing only the implantation time. With this approach SIMS matrix effects can be studied systematically [35,36]. Another advantage is that isotopes (not elements) are implanted and so "solid state standard addition" [46] can be performed, e.g., by implanting ^{18}O, if the element oxygen is investigated. Some groups also used the SIMS instrument as an implanter to produce in situ implants directly into the altered layer of the sputter crater.

Sensitivity factors are calculated by the "integration method", namely by the relation of the integrated SI intensity/analyzed area to the fluence (implanted atoms/area) [1,2,46,47]. It has to be emphasized that this integration is performed over the crater depth and relative errors of the depth scale are directly transferred (added) to the concentration scale. This is of course not the case for homogeneous standards. Furthermore the sputter rate, respectively the depth resolution (in data points/depth), has to be optimized for sample and standard. This has the disadvantage that in routine analysis of a series of samples the current density has to be changed.

The relative sensitivity factor approach

By normalization of Eq. 1 for an "analytical ion", A, to a "reference mass, matrix mass resp. ion", M, a relative sensitivity factor, $RSF_{A/M}$ is derived as [48]:

$$I_{(A)}^{+(-)}/I_{(M)}^{+(-)} \cdot RSF_{A/M} = C_{(A)}/C_{(M)} \quad (10)$$

The intensities, $I_{(A)}^{+(-)}$ and $I_{(M)}^{+(-)}$, are corrected for background signals and isotopic abundances. They are the intensities of the elements A and M (compare Eq. 7). $RSF_{A/M}$ includes the secondary ion yields and the instrumental efficiencies of A and M. For the concentrations, C, the fractional atomic concentrations should be used.

The aim of the use of RSFs is to eliminate, respectively reduce the influence of different, often unknown and very complex sources of error (instrumental and from the process of signal generation) by normalization. For diffusion studies and semiconductor analysis, concentrations in atoms/cm^3 are used and the concentration of M is included in the RSF. Most values for RFSs listed in the SIMS literature correspond to this definition. RSFs for many matrices are compiled in [2]. Rüdenauer et al. [21] have published an approach to transfer RSFs between different instruments. Because of the great expense in production of reference samples mentioned above, the use of compiled RSFs is of essential significance to the SIMS community. But up to now only semiquantitative results can be obtained. One reason is that the secondary ion yields are influenced by many factors. The other source of errors is the instrumental efficiency, optimized by the operator. Here the key factor is $f(\Delta E)$ [20]. *Compiled RSFs should only be used for analysis with full transmission* (low mass resolution and maximum energy acceptance).

For quantitative analysis with high precision ($< 5\%$rel.) all experimental conditions between sample and "standard" (reference sample) should be constant. In routine analysis of a series of samples after each two samples a standard is measured and all RSFs are compared to eliminate systematic errors. In magnetic sector field

instruments even the geometric position of the crater is of importance. The reference mass has to be selected carefully in this normalization approach. To reduce errors of the measured intensity, both signals (A and M) should be measured by the identical detector. The ions should be of the same type (atomic or molecular) and charge (e.g., singly or doubly).

Examples for assessment of precision and accuracy

Random errors. The prerequisite for high accuracy in trace analysis with SIMS is a low random error [26]. Basically the contributions to the random error are counting statistics and reproducibility of the measurement. Since the error introduced by counting statistics is negligible – except near the limit of detection – due to the high ion intensities encountered, the reproducibility of measurement determines the random error.

A measure for the random error is the reproducibility of the RSF. In SIMS it is limited by instrumental variations and the homogeneity of the reference samples. Due to the small volume analyzed, precision measurements can only be performed with single crystalline semiconductor samples (Si, GaAs). Semiconductor samples are used for performance check of instruments and for the first training of new operators.

The maximum reproducibility depends on the analytical problem. Standard depth profiling conditions are: no surface charging, conducting sample; no matrix effect, low concentrations, no interfaces; no instrumental background to subtract (adsorption from the residual gas, memory effects). If under these conditions no interfering ion has to be separated (e.g., B in Si), we obtain a reproducibility of typically $\pm 2\%$rel. [49] in our CAMECA ims3f instrument for measurements with homogeneous samples. To obtain this value, most of the high voltage power supplies of this more than 10 years old instrument had to be replaced by high stability (5×10^{-5}) supplies [50]. In using energy filtering to separate an interference (e.g., As in Si), the reproducibility is typically $\pm 5\%$rel. Depth profiling with high mass resolution (e.g., P in Si) can only be performed by a skilled operator. To achieve a reproducibility of typically 10–15%rel., we developed a new magnetic field control [50] and a peak centring computer routine to control the magnetic field in each cycle of the high mass resolution depth profile [51,52].

Analysis of oxygen in Czochralski silicon is of high significance in electronic industry. The main problem for analysis by SIMS is background induced by adsorption of oxygen-containing species from the residual gas of the sample chamber. We also observed a random matrix effect originating from this adsorption and/or surface contamination. It turned out that this effect changes the distribution of the ions with an initial kinetic energy of typically < 40 eV. By energy filtering the one-day reproducibility could be improved from typically ± 5–10%rel. to $\pm 2\%$rel. When all RSFs from a 5 month period were regarded, the relative standard deviation could be improved from 7.4% to only 3.5% [53].

Systematic errors. The key to accurate quantitative analysis is reduction, preferably elimination as well as assessment of systematic errors [26]. In a problem oriented approach we empirically combine the variation of measurement parameters, the use of different calibration methods and analytical techniques. This is limited by the instrument and by physical principles (e.g., atomic mixing due to sputtering). Then the only way is correction by mathematical simulation of the basic processes (e.g., analysis of sub-monoatomic layers, so called delta-layers or transient signals at interfaces (compare contribution of M.G. Dowsett and R.D. Barlow in this issue, and, e.g., [1,2,6–11]).

The most important *variations of the measurement parameters* concern: (1) primary and secondary ion species, (2) surface chemistry (through primary ion implantation and chemical saturation by oxygen flooding) and (3) energy filtering to study matrix effects (see next chapter), (4) primary ion energy and angle of incidence for detection of energy dependent artifacts, like profile distortion by recoil implantation, and (5) change of primary ion density to check for contamination effects from the residual gas or (re)sputtering

from instrumental parts. For analysis of metals (polycrystalline materials), crater bottom roughness induced by selective sputtering of different crystal orientations in some cases can be strongly reduced by flooding with oxygen [54]. It must be considered as a great advantage of SIMS that many parameters can be varied and thus various influences on the signal can be made evident.

Different calibration techniques: a first estimate of the accuracy can be obtained and should always be applied – e.g., for semiconductor analysis the comparison of RSFs determined from homogeneous and implanted external standards with those received from internal calibration by the fluence of implanted trace elements assigned from the production process. Implanted and homogeneously doped calibration samples were used for the above mentioned determination of oxygen in silicon in the $\mu g/g$ range. Agreement between the independently determined RSFs is better than 10%, differences being obviously caused by the analytical error of the oxygen determination [55] of both reference materials.

If the bulk concentration is known for distribution analysis of an arbitrary sample (metal, glass, etc.), an analogous approach can be used. A "dose or fluence" in atoms cm^{-2} can be calculated and used for quantification by the integration method [1,2,46,47]. For example, we applied this for the investigation of the surface reaction of a FeAlSi alloy with CO and the difference of the RSFs of carbon was only $< 10\%$rel. [54]. Semiquantitative analysis can be performed by evaluation of the relation of signals of the matrix (known concentration of main elements) and trace elements, and comparison with the relative intensities of Storms et al. [14] for pure elements or compounds and/or by compiled RSFs [2].

The *application of different analytical techniques* each exhibiting a different principle of signal generation and consequently different sources for systematic errors is the common way in analytical chemistry. It is the most important, but equally the most challenging and difficult task, in the assessment of accuracy. In general, the evaluation of the accuracy of solid state mass spectrometry, particularly SIMS, is severely limited by the lack of reference techniques and reference materials. There is an intrinsic connection between the two problems; without suitable reference techniques it is impossible to characterize reference materials to the desired degree of accuracy. Even for rather simple problems like the characterization of the distribution of dopant elements in silicon severe problems exist. While detection limits can be determined with a high degree of reliability (see Table 1), the accuracy can only be really determined for boron for which an excellent reference method (neutron depth profiling) [56] exists. For all other dopant elements a combination of activation analysis (with chemical etching), RBS, and electrical measurements like spreading resistance or C/V (capacitance/voltage) has to be applied [57–59]. These methods may exhibit substantial error, of the local concentration, on the 10% level or even more, if not carefully optimized in an interlaboratory comparison. Therefore inaccuracies of SIMS can *efficiently* be only estimated to the values listed in Table 1. Considerable efforts are made to characterize reference materials in a kind of an iterative procedure with a detailed study of systematic errors encountered with the various techniques used for calibration.

Table 1
Analytical figures of merit for depth profiling of dopant elements in silicon with SIMS (data of University of Technology Vienna) [26]

Dopant	Primary ion	Secondary ions species	Detection limit (cm^{-3})	Detection limit (ppba)	Inaccuracy (%)
B	O_2^+	$^{11}B^+$	1×10^{14}	2	±5–10
P	Cs^+	$^{31}P^-$	1×10^{15}	20	±20
As	Cs^+	$^{75}As^{28}Si$	1×10^{14}	2	±10
Sb	Cs^+	$^{121}Sb^{28}Si$	4×10^{13}	1	±20
		$^{123}Sb^{28}Si$	3×10^{14}	5	±5–10

3.3. Optimization of measurement technique to reduce matrix and charging effects

Because matrix and charging effects limit severely SIMS analysis, they are discussed in this separate paragraph. In the literature many approaches to tackle these effects are given [1–3,10,11]. As mentioned above, we try to observe

information by variation of measurement parameters and comparing the resulting profiles. Our approach is to find signals – "indicators" – which are more sensitive to the effects than the signal of the element – "analytical ion" – under consideration. From the behaviour of these indicators we can assess the quality of our approach to compensate or eliminate the disturbing effects.

Charging effects

Bombardment of an insulator – or better of a poorly conducting material – with energetic ions leads to surface charging. The total kinetic energy of an SI is the sum of the initial energy transferred in the sputtering process and the energy due to the extraction lens of the instrument. If charging occurs, the surface potential, respectively the total energy of the SI is changed. This leads to a shift of the detected energy window ($f(\Delta E)$) and subsequently to partial or total signal loss. To reduce these effects, the surface charge has to be minimized, and/or the potential at the surface has to be corrected to achieve constant total kinetic energy of the SI, respectively constant $f(\Delta E)$. There are many approaches to reduce surface charging [1–3], e.g., sputtering with neutrals (Ar), negative PI (O^-), low PI current density, conductive surface layers and bombardment or flooding with electrons. In analysis of insulating bulk samples and layer systems of changing conductivity usually a basic difference is observed. Bulk samples exhibit a relatively constant charging shortly after starting the analysis, whereas for layer systems surface charging is corresponding to the total resistivity of the system, which is changed by sputtering. Only in flooding the surface with low energy electrons (ca. 1 eV), positive surface charging can be fully compensated. Coating of the samples with, e.g., gold creates a new interface and can lead to contamination.

To control residual charging in each cycle of a depth profile we developed a computer routine [60] and we implemented a power supply for the extraction lens which is computer controlled over its full range. Depth profiling can be performed in CVD (chemical vapour deposition) diamond layers on silicon substrates exhibiting surface

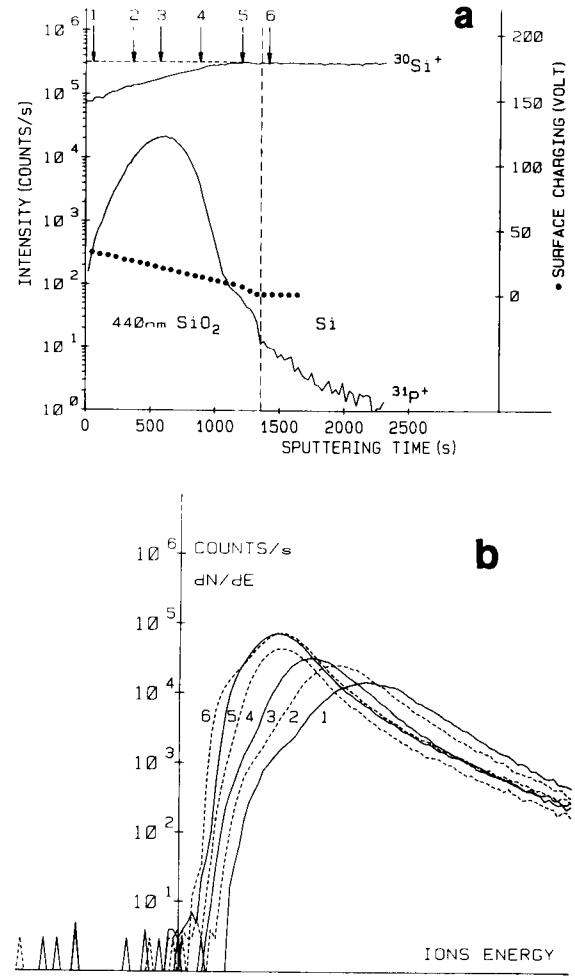

Fig. 7. SIMS depth profile of P in highly insulating thermal SiO_2 (a) and energy distribution of $^{30}Si^+$ at various amounts of charging (b). Implantation: 150 keV P, 1×10^{16} cm^{-2} into 440 nm SiO_2. Measurement: PI = O_2^+, 5.5 keV, partial charge compensation by electron bombardement [60].

charging of ca. 700 V [61]. Usually surface charging is not constant over the crater area, in addition the extraction field is distorted. This broadens the measured (integrated over different lateral positions) energy distribution and changes the instrumental efficiency ($f(\Delta E)$ and $f(\Delta\Omega)$). Fig. 7 shows this effect for analysis of phosphorus in a SiO_2 layer. By normalization to the reference signal in this case a reproducibility of $\pm10\%$ and an inaccuracy of $\pm30\%$ could be achieved for depth profiling with a mass resolution of 4500

[60]. Quadrupole mass spectrometers accept a much smaller energy window ($f(\Delta E)$) than magnetic sector instruments. In this case the integrated energy distribution of both analytical ion and reference ion have to be normalized in each cycle of the depth profile [62].

To control the quality of charge compensation, the reference signal (atomic ion of the matrix) can be used. To amplify the effect, we use molecular SI with a narrow energy distribution as indicators. The steep slope of their energy distribution has to be positioned at the edge of the energy window accepted by the analyser of the instrument. For example in analysis of the SiO_2/Si layer system we utilized $Si_2O^{+,-}$. A shift of only 10 V causes a signal change for $Si^{+,-}$ by a factor of 1.3, but $Si_2O^{+,-}$ is changed by one order of magnitude, thus errors in charge compensation of 1 V can be made visible [63].

Because the course of surface charge is registered, frequently additional, often unexpected information on the production process and on the electrical conductivity of samples is obtained. This is illustrated in Fig. 8. Layers of ZnS on $Hg_{1-x}Cd_xTe$ which can be used for production of infrared detectors had to be investigated. In quality tests the samples showed good and poor electrical resistivity. In Fig. 8 depth profiles of the contaminants B, C and Na are depicted. The signal at "mass 130" is corresponding to $^{130}(Zn_2)^+$ and $^{130}Te^+$. The signal at "mass 36" should be sulphur, but this was not verified. Fig. 8a shows the expected behaviour. Surface charging is continuously decreasing towards the interface and contamination is constant. The sample of the bad quality exhibits a higher contamination with Na and lower charging at the surface (see Fig. 8b). In addition, the peaks of Na, C and B indicate that it was produced in two steps. The contaminants form a conducting interlayer and reduce the resistivity of the ZnS layer. It could be shown, that the profile of Na is correlated to the course of temperature during the production process.

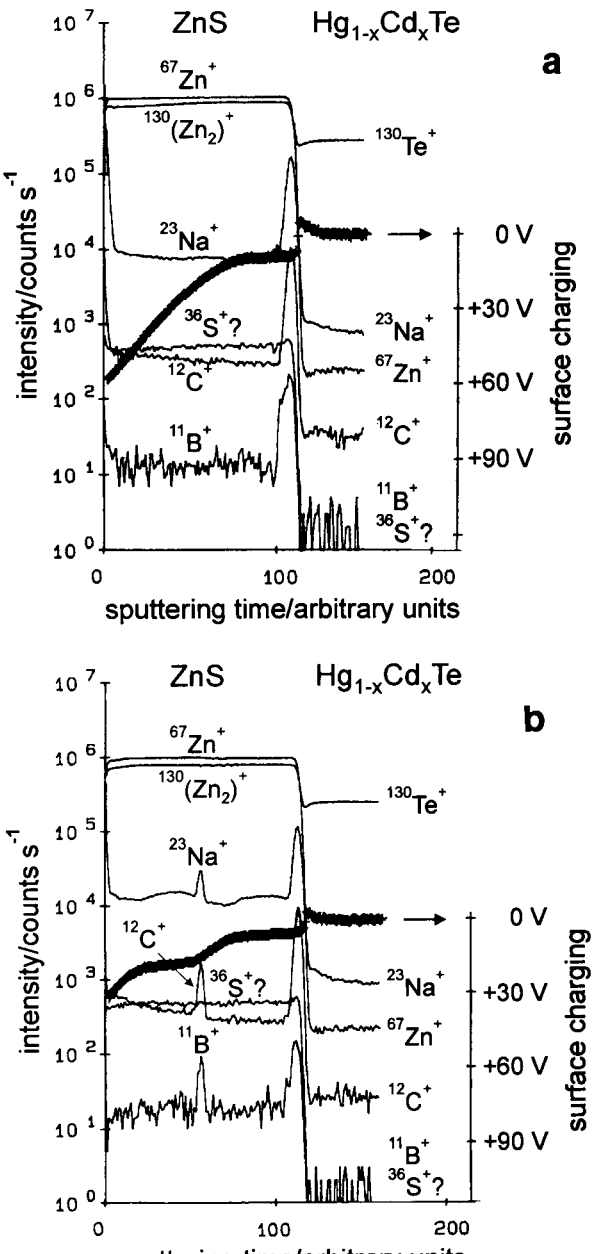

Fig. 8. Depth profiles in a ZnS layer on $Hg_{1-x}Cd_xTe$. Signals of the contaminants B, C and Na and the matrix elements Zn, S and Te were detected. Surface charging (thick full line) was measured in each cylce of the profile. (a) "Good" layer with high resistivity. (b) "Bad" sample with a decreased resistivity.

Chemical matrix effects

The term chemical matrix effect was defined in the discussion of the basic equation of SIMS (secondary ion yield, $Y^{+(-)}_{(A)}$). SNMS (sputtered neutral mass spectrometry) [16–20] was developed to overcome this problem. It has been applied successfully in many cases, but it exhibits

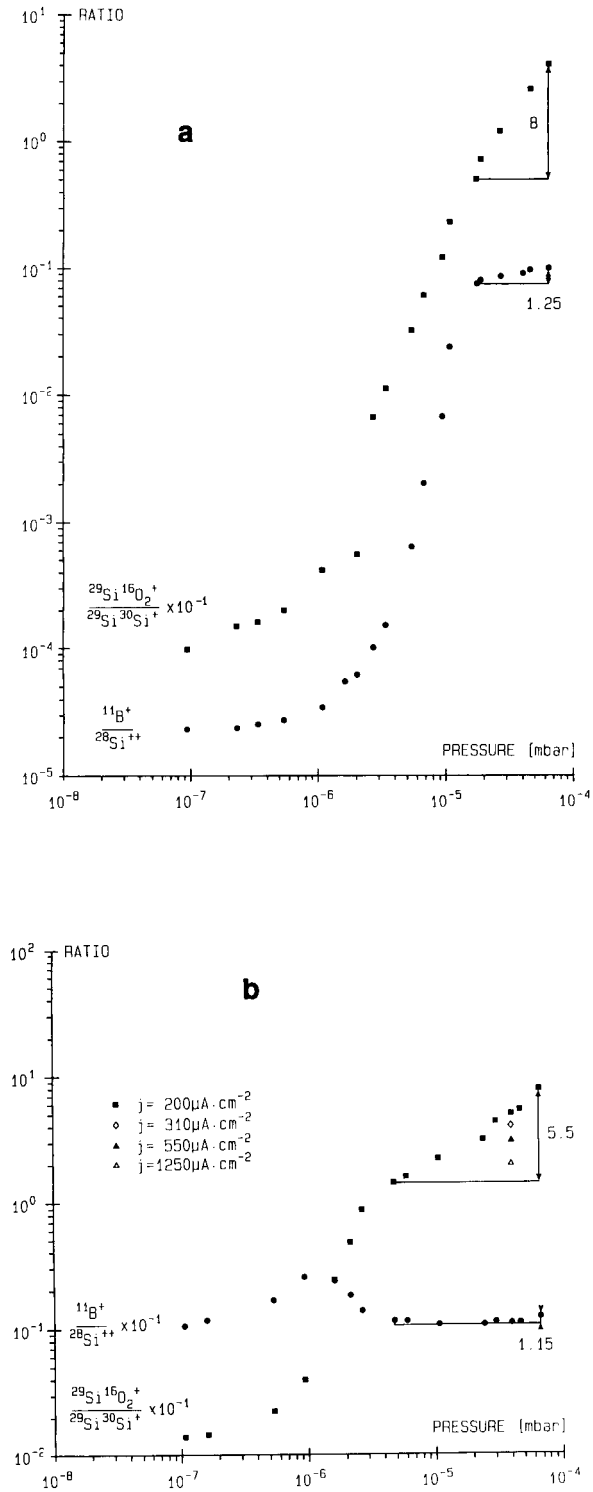

Fig. 9. Intensity ratios of $^{11}B^+/^{28}Si^{2+}$, $^{29}Si^{16}O_2^+/^{29}Si^{30}Si^+$ [59] from a target homogeneously doped with 5×10^{18} at cm^{-3} B versus the oxygen pressure in the sample chamber. Analytical conditions: (a) 5.5 keV Ar^+, 400 nA, rastered area = 500× 500 μm^2, diameter of analyzed area = 150 μm. (b) 5.5 keV O_2^+, 500 nA, rastered area = 500×500 μm^2, diameter of analyzed area = 150 μm. The current density, j, was varied at a pressure of $4X10^{-5}$ mbar.

detection limits in the range of μg/g which are approximately 3 orders of magnitude higher than the values of SIMS. One effective approach in SIMS is to use Cs^+ PI and to detect MCs^+ ions [1–3,10,11] and, e.g., [64–66]. In the present paper it is not possible to discuss the chemical matrix effect thoroughly, but some of our experiences for reduction respectively elimination will be discussed. The analysis of contaminants at interfaces would be the subject for a separate review. Here we have to refer to [1–3,6–11].

The first example is the investigation of dopant elements at the interface SiO_2/Si. The segregation coefficients resulting during thermal oxidation of silicon are important for process simulation. Charging effects occurring in this layer system were discussed in the previous paragraph. In sputtering with O_2^+ we observed enhancements of the ion yield in SiO_2 by 3 for B, by 8 for As and by 27 for Sb [63], and by 30 for P [60]. The larger sensitivity in SiO_2 means that SiO_2 was not formed during sputtering with O_2^+. The formation of oxide depends critically on the angle of incidence of the primary ions. At small angles (relative to normal incidence) SiO_2 is formed. In our case, however, the angle was larger than 30°, which resulted in incomplete oxidation of the sputtered surface. Generally electronegative elements like oxygen enhance the yield of positive SI and can be used to reduce matrix effects by compensating sensitivities in different matrices. In the particular system, SiO_2/Si the matrix effect can be eliminated by flooding the sputtered surface with oxygen during analysis. The local supply of oxygen (corresponding to the pressure gauge reading) necessary to saturate the surface with oxygen depends on the sputter rate respectively the sputtered volume of Si per unit of time. In order to verify that saturation, we recorded the

ratio of the signals SiO_2^+/Si_2^+ [60,63]. The intensity of SiO_2^+ of course increases with oxygen supply. The intensity of Si_2^+ decreases because two Si atoms are necessary for its formation and the silicon lattice is "diluted" with oxygen atoms. This indicator is in the pressure range of 5×10^{-5}–5×10^{-6} mbar by a factor of 5–8.5 more sensitive to changes of the oxygen supply than the signals of the four elements mentioned above. Therefore we conclude if this ratio is nearly constant in sputtering across the interface, then the matrix effect is eliminated. This can be proven by comparing the RSFs obtained by reference implants in SiO_2 and Si [60]. Fig. 9 shows the dependence of the corresponding intensity ratios for a homogeneously doped boron sample sputtered with Ar^+ and with O_2^+ [59]. In Fig. 9b also the influence of the PI current density is obvious.

A similar approach was applied for investigation of the surface reaction of a FeAlSi alloy with CO [54]. The depth distributions of C and O were measured with Ar^+ and detection of negative SI. The alloy was polycrystalline and contained precipitates of SiO_2 and Al_2O_3. Due to selective sputtering very rugged craters were obtained. The matrix effect of Si and Al induced by a local high concentration of carbon and oxygen was minimized by an optimized surface reaction with oxygen. Positive and negative ions of FeO, AlO and SiO were used as indicators. In Ar^+ sputtering without oxygen supply the signals were enhanced by following factors: Fe^+: 8, Si^+: 40, Al^+: 100, FeO^+: 1400, SiO^+: 5000, AlO^+: 40000; and Fe^-: 3, Si^-: 9, Al^-: 20, FeO^-: 500, SiO^-: 20, AlO^-: 850. For the atomic ions this was reduced to less than 20% by oxygen supply. An important side effect was that the craters became very flat, because of crystallinity loss of the Fe matrix by formation of an amorphous oxide.

The energy distribution of the SI shows a maximum at 5–20 eV, which is related to the surface binding energy of the atoms. These low energy ions have a low velocity and "feel" the chemistry of the surface. In the literature the connection between matrix effect and energy distribution is reported [67–70]. We systematically studied the reduction of matrix effects by energy filtering for high dose chromium and cobalt implanted silicon [35,36]. The concentrations had values up to 15at.%. By separation of ions with an initial energy of < 60 eV the matrix effect can be eliminated or at least substantially reduced, depending on the concentration. This is in accordance with the threshold found for analysis of oxygen in silicon [53]. The ratios of signals of different energy windows ($f(\Delta E)$) were used as indicators for elimination of the matrix effect [36]. If the ratio is not dependent on the concentration, the matrix effect is minimized for both energy windows. For assessment of systematic errors the samples were measured with AES, RBS, XRF [36,45] and NAA [39,40].

3.4. Combination of SIMS depth profiling with imaging methods to gain additional information

SIMS has a lateral resolution in the mm and a depth resolution in the nm range. A review of imaging SIMS is presented in this issue [5]. A combination of high synergistic power is SIMS plus electron probe micro analysis (EMPA) [29,32,71], since EMPA is the most important method for quantitative microanalysis and high resolution microstructural imaging of solid specimens, but suffers from rather poor detection power (typically 0.01–0.1% within the analyzed volume).

Methods exhibiting a resolution in the atomic scale yield additional information for the investigation of interfaces, ultrathin layer systems and for investigation of disturbing SIMS effects like altered layer and sputter induced surface roughening. Scanning probe microscopy in form of STM (scanning tunneling microscopy) and AFM (atomic force microscopy) are used to study SIMS craters [10] and, e.g., [71,72].

The combination of SIMS and TEM (transmission electron microscopy) is routinely used for semiconductor characterization, e.g., [58,59,73]. Because sample preparation for TEM involves a great expense, in the first step usually SIMS is utilized to determine the elemental distribution after different processes. SIMS enables to characterize effects like segregation or precipitation in a certain zone or enhanced diffusion at high concentrations. This information enables purposeful

preparation of selected specimens for TEM. The kind of defects, their spatial distribution and the form of enrichments at interfaces can then be studied. Cross section TEM is also used to study the altered layer in SIMS craters [74].

Acknowledgements

Support by the Austrian Scientific Research Council (Project Nos. S43/10, P 7495, S59/02 and S62/05) is gratefully acknowledged. The author wants to thank M. Grasserbauer and K. Piplits for cooperation on which this paper is based.

References

[1] A. Benninghoven, F.G. Rüdenauer and H.W. Werner, Secondary Ion Mass Spectrometry. Basic Concepts, Instrumental Aspects, Applications and Trends, Wiley, New York, 1987.
[2] R.G. Wilson, F.A. Stevie and C.W. Magee, Secondary Ion Mass Spectrometry: A Practical Handbook for Depth Profiling and Bulk Impurity Analysis, Wiley, New York, 1989.
[3] J.C. Vickerman, A. Brown and N. Reed, Secondary Ion Mass Spectrometry: Principles and Applications, Oxford University Press, New York, 1989.
[4] E. Niehuis, in preparation.
[5] F.G. Rüdenauer, Anal. Chim. Acta, 297 (1994) 197.
[6] A. Benninghoven, J. Okano, R. Shimizu and H.W. Werner (Eds.), Secondary Ion Mass Spectrometry, SIMS IV, Springer, Berlin, 1984.
[7] A. Benninghoven, R.J. Colton, D.S. Simons and H.W. Werner (Eds.), Secondary Ion Mass Spectrometry, SIMS V, Springer, Berlin, 1986.
[8] A. Benninghoven, A.M. Huber and H.W. Werner (Eds.), Secondary Ion Mass Spectrometry, SIMS VI, Wiley, New York, 1988.
[9] A. Benninghoven, C.A. Evans, K.D. McKeegan, H.A. Storms and H.W. Werner (Eds.), Secondary Ion Mass Spectrometry, SIMS VII, Wiley, New York, 1990.
[10] A. Benninghoven, K.T.F. Janssen, J. Tümpner and H.W. Werner (Eds.), Secondary Ion Mass Spectrometry, SIMS VIII, Wiley, New York, 1992.
[11] A. Benninghoven, Y. Nihei, R. Shimizu and H.W. Werner (Eds.), Secondary Ion Mass Spectrometry, SIMS IX, Wiley, New York, 1994, to be published.
[12] P. Sigmund, in R. Behrisch (Ed.), Topics in Applied Physics, Vol. 47, Sputtering by Particle Bombardment I, Springer Verlag, Berlin, 1981, p.9.
[13] P. Williams, in S. Datz (Ed.), Applied Atomic Collision Physics, Vol. 4, Academic Press, New York, 1983.
[14] H.A. Storms, K.F. Brown and J.D. Stein, Anal. Chem., 49 (1977) 2023.
[15] K. Wittmaack, Vacuum, 34 (1984) 119.
[16] W. Reuter, Trends Anal. Chem., 8 (1989) 203.
[17] H. Oechsner, Appl. Surf. Sci., 70/71 (1993) 250.
[18] C.H. Becker, C.R. Ayre and L. Moro, in Ref. 11, to be published.
[19] W. Bock, H. Gnaser and H. Oechsner, Anal. Chim. Acta, 297 (1994) 277.
[20] H. Jenett, et al., Anal. Chim. Acta, 297 (1994) 285.
[21] F.G. Rüdenauer, W. Steiger, M. Riedel, H.E. Beske, H. Holzbrecher, H. Düsterhöft, M. Gericke, C.E. Richter, M. Rieth, M. Trapp, J. Giber, A. Solyom, H. Mai and G. Stingeder, Anal.Chem., 57 (1985) 1636.
[22] E. Zinner and G. Crozaz, Int. J. Mass Spectrom. Ion Proc., 69 (1986) 17.
[23] E. Zinner, Proc. Workshop on New Frontiers in Stable Iosotope Research, USGS Bulletin 1890, 1989, p. 145.
[24] S. Gara, G. Stingeder, S. Pahlke, H. Schwenk, E. Guerrero and M. Grasserbauer, in Ref. 9, p. 267.
[25] K. Wittmaack, Phys. Lett., 69A (1979) 322.
[26] M. Grasserbauer, G. Stingeder, G. Friedbacher and A. Virag, Surf. Interface Anal., 14 (1989) 623.
[27] H. Hutter and M. Grasserbauer, in Ref. 10, p. 533.
[28] H. Hutter and M. Grasserbauer, Mikrochim. Acta, 107 (1992) 137.
[29] H. Hutter, P. Wilhartitz and M. Grasserbauer, Fresenius' Z. Anal. Chem., 346 (1993) 66.
[30] S. Gara, H. Hutter, G. Stingeder, C. Tian, H. Führer and M. Grasserbauer, Mikrochim. Acta, 107 (1992) 149.
[31] H. Hutter and M. Grasserbauer, Chemom. Intell. Lab. Syst., in press.
[32] M. Grasserbauer and H. Hutter, in Ref. 11, in press.
[33] K. Miethe, D. Schwarzbach, W. Betz, H. Nickel, R. Lösch, W. Schlapp, G. Stingeder and M. Grasserbauer, in Ref. 10, p. 395.
[34] R. Steiner, G. Stingeder, H. Hutter, M. Grasserbauer, R. Haubner and B. Lux, Fresenius' Z. Anal. Chem., in press.
[35] C. Tian, G. Stingeder and H. Bubert, Anal. Chem., 65 (1993) 1035.
[36] H. Bubert, L. Palmetshofer, G. Stingeder and M. Wielunski, Anal. Chem., 63 (1991) 1562.
[37] P. Roitman, D.S. Simons, P.H. Chi, R.M. Lindstrom, G.E. Lux, S. Baumann, S.W. Novak, R.G. Wilson, D. Farrington, J. Keenan, F.A. Stevie, J.L. Moore, R.B. Irwin, A.J. Filo, C.W. Magee, R. Alcorn and D. File, in Ref. 9, p. 115.
[38] R. v. Criegern, in Ref. 10, p. 403.
[39] Y. Homma, S. Kurosawa, Y. Kubota, N. Nakamura, K. Nomura, M. Shibata, H. Shichi, J. Takahashi, Y. Yoshioka and T. Ogawa, in Ref. 9, p. 119.
[40] K. Miethe, in Ref. 10, p. 399.
[41] P. Wilhartitz, A. Virag, G. Friedbacher, M. Grasserbauer and H.M. Ortner, Fresenius' Z. Anal. Chem., 329 (1987) 228.

[42] A. Virag, G. Friedbacher and M. Grasserbauer, in Ref. 8, p. 561.
[43] R.P.H. Garten, H. Bubert and L. Palmetshofer, Anal. Chem., 64 (1992) 1100.
[44] R.P.H. Garten, H. Bubert and L. Palmetshofer, Surf. Interface Anal., 19 (1992) 211.
[45] R. Klockenkämper, M. Becker, H. Bubert, P. Burba and L. Palmetshofer, Anal. Chem., 62 (1992) 1674.
[46] D.P. Leta and G.H. Morrison, Anal. Chem., 52 (1980) 277.
[47] P. Williams, in Ref. 8, p. 261.
[48] J.A. Mc Hugh, in K.F.J. Heinrich, D.E. Newbury (Eds.), Secondary Ion Mass Spectrometry, National Bureau of Standards (US), SP 427, 1975, p. 129.
[49] C. Tian, S. Gara, G. Hobler and G. Stingeder, in Ref. 10, p. 845.
[50] K. Piplits, W. Tomischko, G. Stingeder and. H. Hutter, in Ref. 10, p. 199.
[51] G. Stingeder, M. Grasserbauer, U. Traxlmayr, E. Guerrero and H. Pötzl, Mikrochim. Acta, Suppl., 11 (1985) 171.
[52] G. Stingeder, K. Piplits, S. Gara, M. Grasserbauer, M. Budil and H. Pötzl, Anal. Chem., 61 (1989) 412.
[53] G. Stingeder, S. Gara, S. Pahlke, H. Schwenk, E. Guerrero and M. Grasserbauer, Fresenius' Z. Anal. Chem., 333 (1989) 576.
[54] G. Stingeder, P. Wilhartitz, M. Schreiner and M. Grasserbauer, Fresenius' Z. Anal. Chem., 319 (1984) 787.
[55] DIN 50438/1, Beuth Verlag, Berlin.
[56] D.S. Simons, P. Chi, R.G. Downing, J.R. Ehrstein and J.F.Knudsen, in Ref. 8, p. 433.
[57] M. Grasserbauer and G. Stingeder, Trends Anal. Chem., 35 (1984) 133.
[58] M. Grasserbauer and G. Stingeder, Vacuum, 39 (1989) 1077.
[59] M. Grasserbauer and G. Stingeder, Fresenius' Z. Anal. Chem., 337 (1990) 701.
[60] G. Stingeder, Anal. Chem., 60 (1988) 1524.
[61] M. Grießer, G. Stingeder, M. Grasserbauer, H. Baumann, F. Link, R. Wurzinger, H. Lux, R. Haubner and B. Lux, Diamond and Related Materials, in press.
[62] W. Reuter, M.L. Yu, M.A. Frisch and M.B. Small, J. Appl. Phys., 51 (1980) 850.
[63] G. Stingeder, Fresenius' Z. Anal. Chem., 327 (1987) 225.
[64] Y. Gao, J. Appl. Phys., 64 (1988) 3760.
[65] K. Wittmaack, in Ref. 10, p. 91.
[66] H. Gnaser and H. Oechsner, in Ref. 10, p. 95.
[67] G. Slodzian and J.F. Hennequin, C.R. Acad. Sci., 263B (1966) 1246.
[68] L.M. Yu and W. Reuter, J. Appl. Phys., 52 (1981) 1489.
[69] E.V. Engström, A. Lodding, H. Odelius and V. Södervall, Mikrochim. Acta, I (1987) 387.
[70] C.E. Richter, M. Trapp and M. Gericke, Vacuum, 40 (1990) 499.
[71] M. Grasserbauer, G. Friedbacher, H. Hutter and G. Stingeder, Fresenius' Z. Anal. Chem., 346 (1993) 594.
[72] A. Ishitani, A. Karen, Y. Nakagawa, M. Uchida, M. Hatada, K. Okuno and F. Soeda, in Ref. 10, p. 315.
[73] G. Stingeder, P. Pongratz, W. Kuhnert, T. Brabec and M. Budil, Fresenius' Z. Anal. Chem., 333 (1989) 191.
[74] R. Treichler, H. Cerva, W. Hösler and R. v. Criegern, in Ref. 9, p. 259.

ELSEVIER

Analytica Chimica Acta 297 (1994) 253–275

ANALYTICA CHIMICA ACTA

Review

Characterization of sharp interfaces and delta doped layers in semiconductors using secondary ion mass spectrometry

M.G. Dowsett [a], R.D. Barlow

ASP Research, Department of Physics, University of Warwick, Coventry CV4 7AL (UK)

Received 22nd June 1993; revised manuscript received 14th October 1993

Abstract

Methods for the quantitative analysis of very thin (delta) layers and sharp interfaces in semiconductors, differentiating between features close to or consisting of changes in matrix composition, and dilute features are reviewed. Although it is shown that no method currently exists for accurate quantification in the former case, a number of experimental techniques for obtaining the best estimate of the true concentration profile are described, in particular the use of XCs^+ secondary ions. For dilute features, it is shown that deconvolution of the chemical profile using a correctly defined response function gives complete quantification, and the formal framework of the method is given. Depth resolution, and the difficulties inherent in defining and measuring consistent parameters, related to particular mechanisms are discussed within this context.

Keywords: Mass spectrometry; Surface techniques; Delta layers; Semiconductors

The technique of depth profiling using secondary ion mass spectrometry (SIMS) is based on the experimental observation that when certain homogeneous solid materials are bombarded by a beam of ions in the low keV energy range, *under ideal conditions* the processes leading to modification of the physical structure and chemistry of the top 10–30 nm reach a steady state for a probe dose density $\leqslant 10^{17}$ ions cm^{-2}. If the accumulated dose is increased beyond this, the surface of the material recedes at a constant rate due to sputtering. The composition profile of the near surface region is modified from that of the underlying material by the effects of preferential sputtering, the incorporation of probe atoms, and mass transport caused by energy deposition from the probe; and is known as the altered layer [1–3]. The top ≈ 1 nm of the altered layer acts as the source of sputtered secondary particles, but because this is maintained in equilibrium, the efficiencies with which ions and neutrals are emitted are constant. If a dilute impurity with a slowly varying concentration, is present in the

Correspondence to: M.G. Dowsett, ASP Research, Department of Physics, University of Warwick, Coventry CV4 7AL (UK).

SSDI 0003-2670(93)E0568-R

system, the ion yield for the impurity is expected to be proportional to the concentration at the eroded depth which is itself taken as proportional to the accumulated ion dose (ions cm^{-2}). Almost all SIMS profiles are quantified on the basis of this simple argument. Despite the fact that such ideal behaviour is rarely obtained in practice, the results from this process have been sufficiently good to establish the technique for semiconductor analysis and a wide range of other applications. Indeed, the quantification of most sputter profiling techniques, for example Auger profiling, is similarly derived.

This paper explores the extent to which, and by what means, quantitative analysis is possible in material systems where the above arguments do not apply exactly or at all – those containing sharp interfaces or thin buried layers. In these samples any steady state is lost, at least temporarily, in the vicinity of the interface(s) and the measured secondary ion signals are transient responses. Without being specific about its definition for the time being, we identify a depth resolution δz such that two features on the *true concentration profile* separated by a depth $z < \delta z$ are not distinguishable in a SIMS profile. We also define for some impurity species X_i, present in a true concentration profile $C_{Xi}(z)$ a dilute limit in concentration $C_{X_i}^{\lim}$ where for $C_{X_i}(z) > C_{X_i}^{\lim}$ the measured ion yield for X_i or some other species of interest X_j is no longer proportional to its concentration. (i.e. The presence of X_i influences the ionization coefficient and sputtering characteristics of X_j. This is known as a matrix effect [4–7].) For the purposes of this paper, we then classify six basic structures according to how seriously they deviate from the simple picture and whether or not they are *resolvable* (rather than whether $C_{Xi}(z)$ is supposed to be a single atomic plane for example). These are as follows:

(i) A slowly varying impurity profile $C_X(z) < C_X^{\lim}$ everywhere, in an homogeneous matrix which is well behaved during ion bombardment. The simplest case of a *dilute system*, included for completeness.

(ii) An impurity profile $C_X(z)$ which rises or falls in a depth interval $< \delta z$, whilst remaining below $C_X^{\lim}$. This we describe as a *dilute step*.

(iii) A $C_X(z)$ which rises *and* falls in a depth interval $< \delta z$, whilst remaining below $C_X^{\lim}$. This we describe as a *dilute delta*.

(iv) $C_{X_i}(z) > C_{X_i}^{\lim}$ in some part of the profile, but the slopes $\partial C/\partial z$ are small. This is a *slow matrix variation*.

(v) $C_{X_i}(z)$ changes between two levels at least one of which is above $C_{X_i}^{\lim}$ in a depth interval $< \delta z$. This is a *matrix step*.

(vi) $C_{X_i}(z)$ rises and falls between two levels the higher of which at least is $> C_{X_i}^{\lim}$ in a depth interval $< \delta z$. This is a *matrix delta*.

In the last three cases

$$\alpha_{X_j}^c = f\left(C_{X_i}(z)\right)\big|_{j=i \text{ or } j \neq i} \tag{1}$$

where $\alpha_{X_j}^c$ is the ionization coefficient of X_j – the number of ions of X_j sputtered in charge state c per total sputtered X_j.

The true concentration profile in a real sample may consist of a combination of the descriptions above. For example, (iii) with (v) gives a dilute delta in the vicinity of a matrix interface – a situation frequently encountered in practice. However, it cannot be assumed that the measured ion yields from a real sample can be deduced from a linear superposition of ion yields from the individual cases, except under very restricted (but useful) circumstances.

1. Quantification

Quantification is often assumed in SIMS to be *just* the conversion of a measured secondary ion intensity to a concentration. Here, we use the term in the sense of a complete process: the transformation or mapping of a secondary ion yield $Y_X(\phi)$ for species X measured as a function of primary ion dose ϕ (or for practical purposes $Y_X(t)$ measured as a function of elapsed time, t) to a concentration profile $C_X(z)$ – i.e. in this paper quantification refers to the combination of intensity and depth calibration. The SIMS measurement process may be formally written [8]

$$Y_X(\phi) = \mathbf{R}C_X(z) + n \tag{2}$$

where $\mathbf{R}$ is a non-linear operator which describes the physics of the process including a complete

description of ion beam induced mass transport (random cascade mixing, radiation enhanced diffusion and segregation etc.), and the effects of the composition of the top nm or so of the altered layer on the degree of ionization (see also the review by G. Stingeder in this issue), and n is additive noise produced by processes outside the influence of **R** (e.g. statistical fluctuations in the primary beam current). Quantification is the inversion of Eq. 2. Several partial mathematical descriptions of **R** exist, of which probably the most complete are the IMPETUS code developed at the University of Salford [9–11] and the model of Littmark and Hofer [12,13]. IMPETUS simulates the effects of random cascade mixing, probe incorporation, and sputtering in a compound sample with dilute or bulk compositional changes, and can output the partial sputter yield of neutrals, and predict the instantaneous surface composition. In effect, it is a simulation of sputtered *neutral* mass spectrometry (SNMS). (For a review of other models see [14]) What is completely lacking in general at present is any quantitatively accurate method for modelling secondary ion emission given a particular surface chemistry.

Quantification of dilute impurities and matrix species at matrix steps and deltas

Given that some more complete form for **R** may be developed in future, an ideal quantification process for samples containing matrix steps and deltas would be the inversion of Eq. 2 using a *forward* method as follows. Some initial estimate of the true concentration profile $C_X^{\text{trial}}(z)$ is constructed, and a corresponding $Y_X^{\text{trial}}(\phi)$ obtained from

$$Y_X^{\text{trial}}(\phi) = \mathbf{R}C_X^{\text{trial}}(z) \tag{3}$$

Using standard optimization techniques, an iterative process for comparing $Y_X^{\text{trial}}(\phi)$ with $Y_X(\phi)$ and refining the estimate of $C_X^{\text{trial}}(z)$ correspondingly is then followed, until an acceptable match is obtained between measured and simulated yields. Both the presence of n in Eq. 2 and the fact that the experimental data set is *underdetermined* (i.e. a finite set of ordinates) preclude a unique solution to the inversion problem (true of any experimental data), and some means (for example maximum entropy (MaxEnt) methods [15,16]), is required to guide the refinement of $C_X^{\text{trial}}(z)$ towards a solution which represents the best (least biased) estimate.

At present, however, there are broadly three approaches to the treatment of SIMS data from samples containing matrix steps and deltas.

It is still quite common for SIMS data to be taken at face value, ignoring the changes in ionization coefficient and erosion rate which accompany changes of matrix. This is acceptable where independent experiments have established that such changes are small in the materials system and under the SIMS conditions used. However, evidence is rarely presented to this effect. Consequently, one suspects that SIMS data are used and published when they (fortuitously) confirm prior knowledge, and discarded otherwise. This approach has done much to impede the development of the technique.

A more satisfactory method for application to matrix steps is to calibrate the changes which occur in α and erosion rate $\dot{z} = \mathrm{d}z/\mathrm{d}t$ or $\mathrm{d}z/\mathrm{d}\phi$, either side of the step, after selecting experimental conditions which minimize them if possible. The ion yield in the transient region itself is quantified by obtaining some local functional relationship between α and ϕ, using measurements made on a transient from a known concentration profile [1]. The transient condition of $\dot{z}$ may be similarly treated, or two appropriate values applied either side of some (defined) position of the interface. By this means one can improve the estimate of the true profile in the vicinity of an interface, and keep track of changes in erosion rate so that depth registration is maintained in profiles with several steps. However, because of the non-linear character of **R** this process cannot really quantify the transient region. (Therefore, because the signals from a matrix delta are all transient, such samples cannot be quantified this

[1] One might expect a relationship between α and $C(z)$ to be required. However, $C(z)$ is by definition unknown in the transient region (at the least because of atomic mixing effects), and measurements on a standard transient actually establish α as a function of ϕ.

way – indeed, there is no method of accurately quantifying the transient region other than a full inversion of Eq. 2.) Dowsett et al. [17] used this method to extract boron profiles from thin gate oxides on thermally processed silicon-on-sapphire material (SOS) as follows. Samples were analysed using O_2^+ bombardment at normal incidence which reduced the ratio of the ionisation coefficients for boron from SiO_2 and Si, $\alpha^+_{B(SiO_2)}/\alpha^+_{B(Si)}$, from a possible several orders of magnitude to 1.1. (At the same time it maximizes the ratio of the erosion rates $\dot{z}_{SiO_2}/\dot{z}_{Si}$, but this only involves a change from ≈ 1 to 2.0.) Standards were constructed by implanting boron into wafers where half the wafer was covered in a thick oxide, similar in character to the gate oxide so that $\alpha^+_{B(SiO_2)}/\alpha^+_{B(Si)}$ and $\dot{z}_{SiO_2}/\dot{z}_{Si}$ could be measured accurately. When quantified, these profiles also established that the stopping characteristics of the oxide and silicon matrices were nearly identical, except for slight channelling in the latter, permitting the assumption that the true boron concentration across the interface in an as-implanted sample would be continuous. A calibration function was extracted from these data which forced the transient signal to continuity with the rest of the profile. A further standard consisted of an implant through the gate oxide, where half the wafer was stripped of oxide *after* implantation. Registration of deep regions in the profiles from either half of this wafer indicated the true position of the oxide/silicon interface in the transient region of the profile from the oxidized half, so that the relative erosion rates could be applied across the correct dose range. (A similar procedure was adopted for the thermally processed samples.) The calibration function was used to quantify the transient regions in a range of implanted and thermally processed samples. It produced continuous interfaces irrespective of implant dose and energy in as-implanted samples, whilst isolating segregation of boron at the interface in those that had been thermally processed. Fig. 1a and b shows the results for 5×10^{14} cm^{-2} implants into SOS at 25 keV and 160 keV, and for 25 keV implants into SOS and oxidised bulk silicon with identical thermal processing. It is clear that the boron profile through most of the oxide is identical in all the 25 keV samples. The thermally processed samples show slight segregation at the interface, and rather different diffusion behaviour between the bulk and epitaxial layers. A similar approach was reported recently for extracting Mg profiles from the Si_3N_4/InGaAs interface [18]. These methods generalize a technique proposed by Wittmaack and Wach [19] for quantifying the SIMS surface transient for a particular species X by normalizing it to that from an otherwise identical sample with a uniform concentration of X up to the surface. This has been successfully applied by Bryan et al. [20]. In contrast, Morgan and Maillot [21] used an

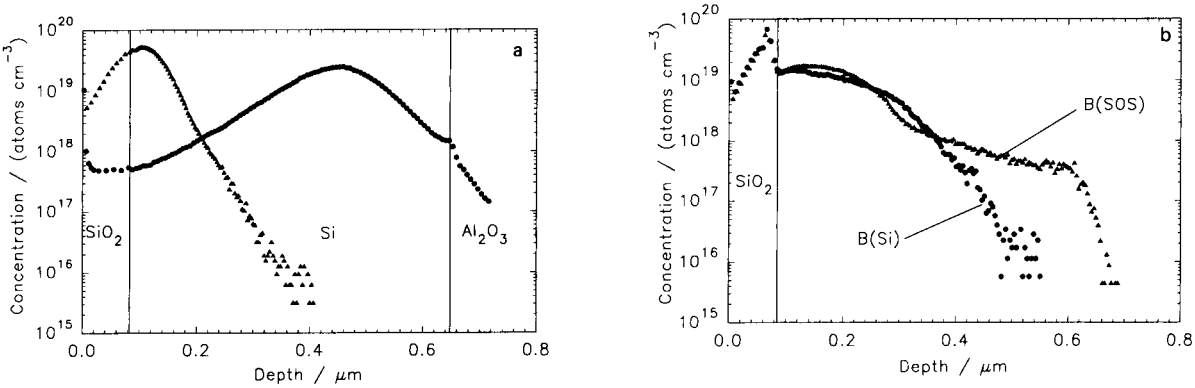

Fig. 1. (a) Quantified data from 25 (▲) and 160 (●) keV 5×10^{14} cm^{-2} ^{11}B implanted through 70 nm gate oxide on SOS. (b) Profiles from thermally processed (900°C, 20 min) 25 keV implants through gate oxide on bulk silicon (●) and SOS (▲). The profile from the oxide remains unchanged, except for slight segregation at the interface.

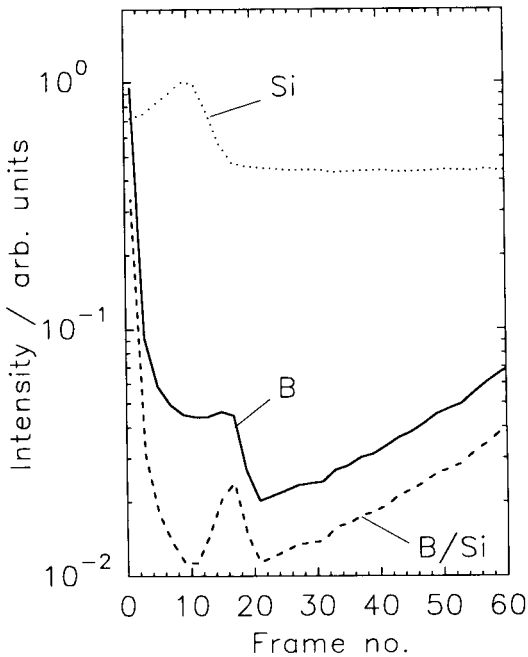

Fig. 2. The boron channel from the raw data in Fig. 1a, normalised to the silicon channel. A spurious boron peak is introduced because the mechanisms determining the shapes of the interfacial transients are different.

exponential correction across the SiO_2/Si interface for both erosion rate and ion yield in the case of arsenic implanted through the oxide. They reduced the magnitude of the As^+ transient by normalizing to the Si^+ (matrix) signal. This procedure is a common method of guarding against changes in primary current and other instrumental settings when using relative sensitivity factors for quantification [22]. However, it can be misleading when used across an interface, because the yield variation for the matrix and the analyte are *dis*similar functions of dose, and normalization can result in the development of spurious spikes and troughs in the signal as demonstrated in Fig. 2.

Potentially the best SIMS-related method for the quantitative analysis of matrix steps and deltas is to use some form of SNMS. In this technique, secondary ions emitted directly from the sample are ignored, and neutral species are post ionized and assayed using one of a large variety of different methods. The matrix retains some influence on the ionization coefficients because it controls such parameters as the relative numbers of neutral species sputtered into atomic and molecular channels and the population of excited and ground states. However, the effects are usually several orders of magnitude lower than in SIMS, and with careful choice of experimental conditions their influence on the data can be made negligible. (For a recent review of SNMS techniques see [23].) Under these circumstances, the shapes of the transient signals will be characteristic of ion beam induced mass transport processes, and the development of a general model for **R** enabling as complete a quantification as possible seems feasible. Ionization methods include electron impact from an electron beam [24,25] or a low density plasma containing hot electrons [26,27]; and laser-based methods such as resonant and non-resonant multi-photon ionization [28–31]. Recently, Sykes [32] has reported high depth resolution analyses in multi-layer structures using glow discharge mass spectrometry (GDMS).

Here, we discuss results from two different methods – resonant ionization mass spectrometry (RIMS) [33,34], and a technique which may be applied on almost any SIMS instrument – the detection of XCs^+ clusters whilst using a cæsium primary ion beam. (The latter process is believed to be a form of post-ionization where a sputtered neutral X combines with a Cs^+ over the surface [35–37])

RIMS uses multiple photon absorption to excite and then ionize neutrals sputtered from the surface. The photon energies used are specific to the electronic structure of the neutral species sought, so the process can be highly selective. An additional advantage of RIMS is that molecules can be ionized in principle without the dissociation which accompanies electron impact [33]. To achieve a constant sensitivity for species X_j from one matrix to another, it is necessary to find experimental conditions where the ratio of sputtered X_j^0 to all other emitted species (including ions) containing X_j stays constant, as should the ratio of populations in the excitation state for which the ionization scheme is designed (not necessarily the ground state [38]) to all other states. For example, Downey et al. have investigated the

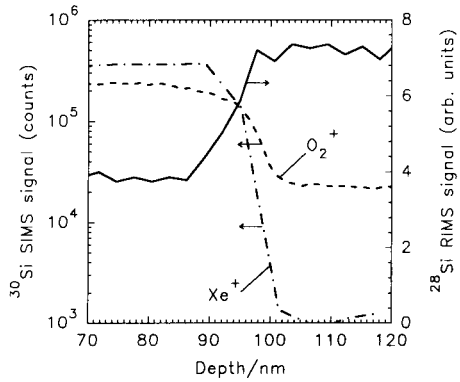

Fig. 3. SIMS and RIMS data across the SiO_2/Si interface after Downey and Emerson [39]. RIMS data show an approximately correct increase in the silicon signal at the interface whereas O_2^+ and Xe^+ SIMS data show large matrix effects.

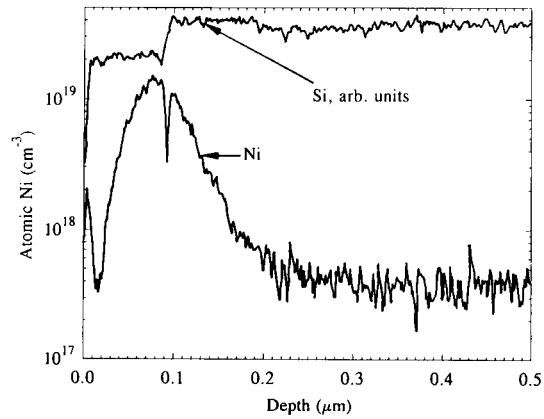

Fig. 4. Quantified RIMS data from a Ni implant across the SiO_2/Si interface after Downey and Emerson [39]. The depletion in the Ni signal at the interface is believed to be due to a silicide formation which modified the yield into the low energy state in the ionization scheme.

ratios of molecular to atomic species formed, and its effect on the RIMS signal for the atomic species for the GaAlAs system [38] and SiO_2/Si [39]. For primary ion conditions intended to optimize depth resolution (2 keV, 60° to normal) they find a strong reduction with increasing x in $Al_xGa_{1-x}As$ in the fraction of Al sputtered as ground state neutral free atoms for Xe^+ primaries, with a similar but weaker behaviour for Ar^+. For SiO_2 they find that the production of molecular ions rises steeply as Xe^+ energy is reduced below 4 keV, whereas Ar^+ gives a more or less constant ratio of 2 between the Si^+ RIMS signal from bulk Si and SiO_2 across an energy range of 2–14 keV. They demonstrate that the greatest quantitative accuracy is achieved using Ar^+. Fig. 3 shows their comparison between SIMS and RIMS data for Si from the SiO_2/Si interface, for 6 keV bombardment at approximately 40° incidence. Fig. 4 shows quantitative RIMS data for a Ni implant straddling the interface, compared with the SIMS equivalent. Both profiles were obtained using 6 keV Xe^+ bombardment. The authors attribute the interfacial transient in the Ni RIMS signal to silicide formation. Elsewhere [40] the same group has demonstrated the ability of RIMS to obtain data on impurity profiles at interfaces free from the gross distortion which occurs in SIMS. Fig. 5 shows their comparison between SIMS and RIMS data for Be across the GaAlAs/GaAs interface. The Be^+ SIMS signal shows a large spike at the interface which the RIMS data demonstrate is non-existent.

In 1977, Storms et al. [41] developed and tested one of the first practical caesium ion sources for SIMS, and measured the secondary ion yields for a large number of elemental and compound targets across the Periodic Table in the ARL ion microprobe. They observed high yields for ions such as $ZnCs^+$, $CuCs^+$, $GaCs^+$, $CdCs^+$ and

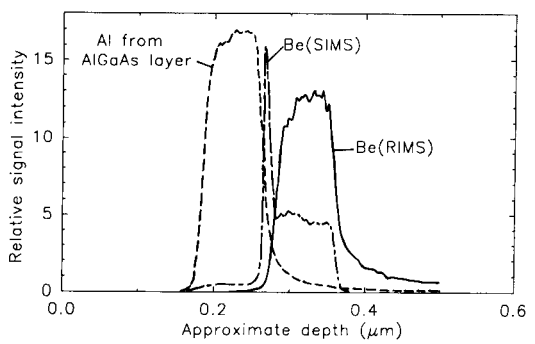

Fig. 5. SIMS and RIMS Be profiles from the GaAlAs/GaAs interface after Downey et al. [40]. The SIMS signal shows a spurious Be spike, which is absent from the RIMS profile. SIMS would indicate that most of the Be has segregated to the interface whereas RIMS demonstrates that this is a SIMS matrix effect.

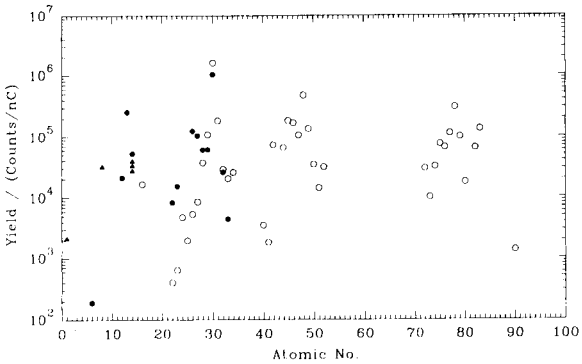

Fig. 6. Yield data for XCs^+ where X runs across the Periodic Table. First results for normal incidence Cs^+ beam (after Storms et al. [41]) show that the amplitude of the SIMS matrix effect has been reduced by over 3 orders of magnitude compared to that for the same set of elements using normal positive and negative ion detection. Recent results from Wittmaack [36] at 60–65° compress the amplitude to less than two orders of magnitude. Yields calculated from the work of Gnaser and Oechsner, extending the range of elements [47,49] are also included.

$PtCs^+$, and the ratio of minimum to maximum yields ($ZnCs^+/TiCs^+$) was a little over 3 orders of magnitude for normal incidence bombardment. The spans of X^+ and X^- yields for O_2^+ and Cs^+ bombardment respectively are at least 1000 times worse [41]. Their data are reproduced in Fig. 6. Some years later, the sputtering of XCs^+ ions was used for rare gas analysis [35], and then relative independence from matrix effects for the main constituents in III–V semiconductors was demonstrated by Gao [42]. Gao was the first of several authors to show that whilst yields for different X in general varied by an order of magnitude or so, yields for the same X in different III–V matrices only varied by a few percent. After Garrison et al. [43,44], Ray et al. [35] argued that where X was a rare gas, a the XCs^+ ion was formed by combination of a sputtered Cs^+ ions and a rare neutral close enough to the surface for the latter to act as the momentum conserving body. They ruled out the post-ionization of an excited XCs neutral both because electron exchange with the solid would lead to strong matrix dependence, and because primary beam impact post-ionization would dissociate the molecule. (They showed that the $KrCs^+$ intensity varied linearly with Cs^+ primary ion current density, whereas the relationship between Kr^+ emission and O_2^+ current density was parabolic, thereby demonstrating that the $KrCs^+$ emission was due to ionization at the surface, whilst the Kr^+ emission was due to gas phase collisions between sputtered neutrals and incoming primaries.) Other authors have proposed a similar mechanism for XCs^+ for general X [36,37,42], and there is experimental evidence to support this [45]. In a systematic study of the dependence of XCs^+ emission on energy and angle of the primary beam, Wittmaack has shown [36] that bombardment conditions leading to a high stationary surface concentration of Cs can result in the suppression of XCs^+ emission, possibly through reduction in the work function. Bombardment angles between 60° and 65° to normal give the highest XCs^+ yields in general, and a smaller nett variation in ion yield across the periodic table. His data are overlaid on the early work of Storms et al. in Fig. 6, together with some other yields from the literature.. Valizadeh et al. [46] using in situ Rutherford backscattering (RBS) and medium energy ion scattering (MEIS) measurements on 5 keV, 45° Cs^+ implants into Si have shown that a stationary total retained areal dose of 1.7×10^{15} ions cm^{-2} is achieved for a total areal dose of 7×10^{15} ions cm^{-2} and as much as 10% of this may be within 20 Å of the surface.

Several authors have now demonstrated the practical use of XCs^+ analysis for quantitative profiling across matrix steps, for example in III–V materials [37,42,47,48], SiO_2/Si [47,49] and metal layers [47,50]. Some of their data are shown in Figs. 7 and 8. Fig. 7 shows OCs^+ and $SiCs^+$ profiles through a 100 nm thick SiO_2 layer buried under a 50 nm Si cap from the work of Gnaser and Oechsner [47]. The signal ratio $OCs^+/SiCs^+$ of 2:1 directly reflects the oxide stoichiometry (although the authors note that this may be fortuitious) and the $SiCs^+$ signal decreases by a factor of 2.5 in the oxide after correcting for changes in erosion rate. By comparison, the Si^+ RIMS data in Fig. 3 show a decrease of 1.9. The correct ratio would lie in the range 2.1–2.3 depending on the density of the oxide. Both techniques are quite

accurately quantitative in a matrix where the Si^+ yield would have changed by several orders of magnitude under the bombardment conditions used. Magee [48] reports a 5–10% quantitative accuracy. for matrix elements across interfaces in ternary and quaternary III–V materials. Fig. 8 shows his data for a 10 nm thick GaAs layer buried at a depth of 1.6 μm in AlGaAs with compositional steps. The $CsAl^+/CsGa^+$ ratio, also shown, is approximately constant. Because it is sited at a depth which is 160 times its own thickness, the GaAs layer is an example of a matrix delta – i.e. the signals in this region are transients whose shape is determined by the main depth resolution limiting factors (probably crater macro-topography at this depth [51]) since matrix effects are almost absent in the ion species monitored. For this reason, the atomic fractions of Ga and Al do not reach 0.5 and 0 respectively.

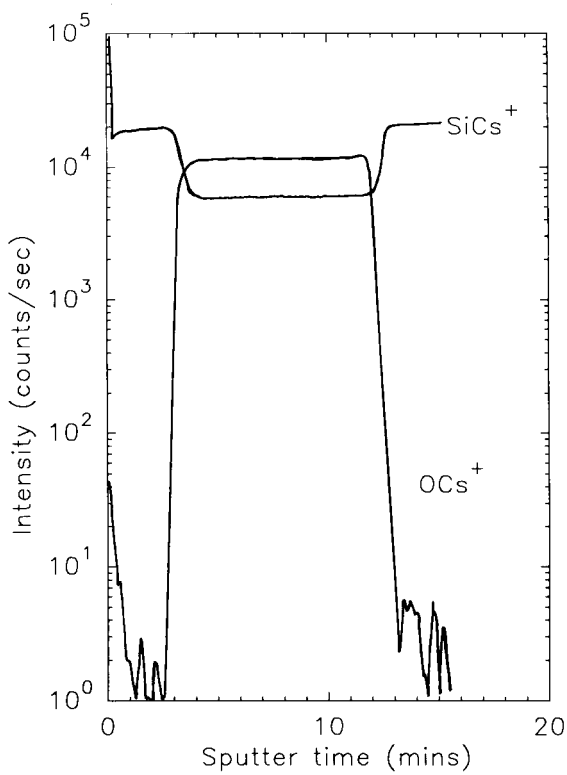

Fig. 7. Oxygen and silicon profiles from an $Si/SiO_2/Si$ structure, monitoring OCs^+ and $SiCs^+$ ions after Gnaser and Oechsner [47]. There is good agreement between the Si channel and the RIMS data in Fig. 3.

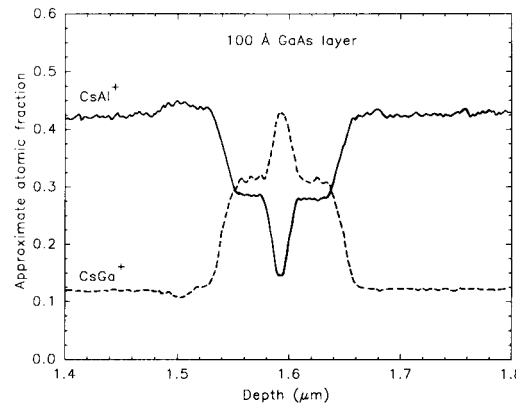

Fig. 8. SIMS data from a deeply situated 10 nm GaAs layer in an AlGaAs matrix. These data are a small section from a very detailed profile extending from the surface. Primary ions: Cs^+ at 60° to normal. After Magee [48]

Bleiler and Huneke [50] have applied the principle to the analysis of oxygen and nitrogen in polycrystalline metals, where the presence of local matrix effects at the (varying) grain boundary pattern intersected by the sampled area in the depth profile normally result in unstable signals.

Slow matrix variation

The SNMS and XCs^+ techniques described above are directly applicable in samples where there is a slow matrix variation. SIMS data are also quantifiable using ion yields measured from standards across the concentration range of interest to deduce a functional relationship between α_{X_j}, $\dot{z}$ and $C_{X_i}(z)$. This is inherently different from the method of treating a matrix step (see first footnote). The relationship may for example approximate to a power law dependence [6,52]. Ion yield ratios do not necessarily increase or decrease monotonically with concentration [53–55], so that ratioing to matrix signals can be misleading. Yield measurements must be carefully matched to the analytical conditions used. In a magnetic sector instrument (where the angle of bombardment is coupled to the primary beam energy) Clark [55] showed that measured Al^+/Ga^+ signal ratios measured from $Al_xGa_{1-x}As$ using O_2^+ and Ar^+ were almost proportional to $x/(1-x)$ for $x \leqslant 0.5$, but saturated thereafter. Moreover, the proportionality constant showed a

strong inverse dependence on primary beam energy below 3 keV/O_2^+ which became more pronounced as x increased. In contrast, Schwartz et al. [56] working with 6 keV O_2^+ at normal incidence found proportionality over the full range of aluminium stoichiometry.

Smith and Harris [57] found it necessary to combine both the SNMS-like technique of monitoring XCs^+ emission and subsequent correction for the (reduced) matrix effects. They evaluated the use of Co^+, Co_2^+, $CoSi_2^+$, Cs^+ and $SiCs^+$ signals from the $CoSi_2$/Si system to correct the $AsCs^+$ signal produced using 5.5 keV Cs^+ primaries incident at 42° for a matrix effect due to a progressive transition from silicide to silicon across a rough interface. Their intrinsic (beam limited) depth resolution was small compared to the interface roughness, and so the analysis behaved somewhat as if the interfacial composition was graded (provided the crater bottom had not developed a topography comparable in height with that of the interfacial roughness). Some of their data are shown in Fig. 9. They found that the most accurate correction was achieved using a Cs containing ion.

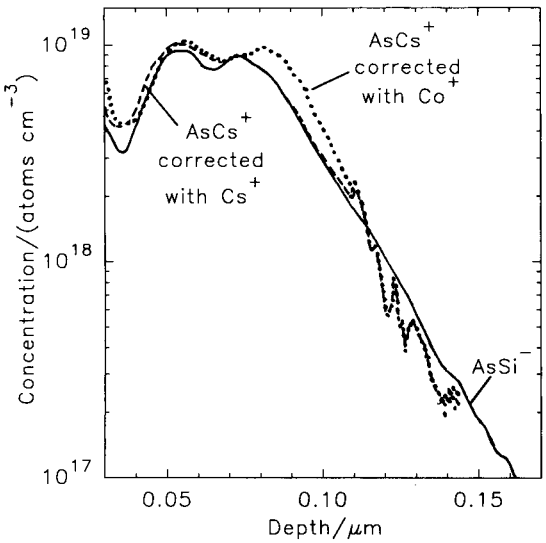

Fig. 9. Arsenic profiles extracted from across a rough $CoSi_2$/Si interface after Smith and Harris [57]. Original As implant: 7×10^{13} cm^{-3}. SIMS conditions: 5.5 keV Cs^+ 42°. The $AsSi^-$ signal (solid line) is believed to be relatively free from matrix effects across this interface. The $AsCs^+$ signal has been corrected for matrix effects using Co^+ as a measure of matrix stoichiometry to correct the useful yield (·····) and Cs^+ to correct for differences in the cæsium emission across the interface (— — —).

Dilute features

A dilute concentration profile $C_{X_i}(z)$ is not expected to influence $\dot{z}$ or $\alpha_{X_{ij}}$ significantly, so one only need consider the quantification of $Y_{X_i}(\phi)$ itself. The $Y_{X_i}(\phi)$ from a dilute step or delta is still a transient signal, but its shape will be determined by depth resolution limiting effects such as ion beam induced mass transport and the development of surface topography. Since by definition the species X_j are too widely separated in the matrix to modify their own mixing in a concentration dependent manner, **R** is approximately linear, and the measurement process may be described by a convolution-like equation and a mapping:

$$Y_X(\phi) = \int_0^\infty\int_0^\infty R_r(\phi'',\phi)R_m(\phi-\phi'-\phi'') \times Y_X^{\text{perfect}}(\phi')\mathrm{d}\phi''\mathrm{d}\phi' + n \quad (4)$$

where it has been assumed that surface topography and mass transport effects may be decoupled, and $R_r(\phi)$ is a dose dependent response function whose convolution with $Y_X^{\text{perfect}}(\phi)$ describes the effects of progressive surface topography development [2], $R_m(\phi)$ similarly describes probe induced mass transport and

$$Y_X^{\text{perfect}}(\phi) = \mathbf{M}C_X(z) \quad (5)$$

is the SIMS profile which would be obtained if the measuring process were perfect. **M** is a linear mapping operation. For example, if $C_X(z)$ and $Y_X^{\text{perfect}}(\phi)$ are written as coordinate sets then

$$\begin{pmatrix} Y^{\text{perfect}} \\ \phi \end{pmatrix} = \begin{pmatrix} K & 0 \\ 0 & \dfrac{d\phi}{dz} \end{pmatrix}\begin{pmatrix} C \\ z \end{pmatrix} \quad (6)$$

[2] It is most important to note this is only valid where development of surface roughness is not accompanied by a matrix effect due to a change in the surface retention of an ion yield enhancing species. Where this is the case one is back to a non-linear **R** and convolution is an inappropriate model.

It is exactly Eq. 6 which is inverted in conventional SIMS depth profile quantification. It is then easy to see that if Y is measured in counts per unit dose (or per unit time) and C is measured in atoms cm^{-3},

$$K = \tau A \Delta z \tag{7}$$

where τ is the steady state useful yield, A is the analysed area and Δz is the depth eroded per unit dose (or per unit time), and $d\phi/dz$ is the inverse of the true erosion rate of the matrix at steady state. As we have shown elsewhere $R_m(\phi)$ can then be defined in a rigorous manner so as to contain both profile broadening and profile shifting effects [8,58,59]. If the effects of surface topography are negligible, then Eq. 6 reduces to a simple convolution:

$$Y_X(\phi) = \int_0^\infty R_m(\phi - \phi') Y_X^{perfect}(\phi') d\phi' + n \tag{8}$$

The inversion of Eqs. 4 or 8 including the mapping Eq. 6 constitutes a formally correct and complete quantification scheme. Note that the definition of the response functions in terms of ϕ rather than z is intrinsic to this process. Elsewhere, we have described MaxEnt-based deconvolution techniques for the inversion of Eq. 8, and demonstrated that they give superior, albeit computationally slower performance to Fourier transform (FT) methods [8,59,60]. Fig. 10a and b shows a comparison between MaxEnt and FT methods for a SIMS profile of a silicon doped layer in GaAs obtained using 6 keV 45° Cs^+ primary ions. Fig. 10a on semi-log plot shows the quantification overall, and in the low concentration regions, whilst Fig. 10b on a linear scale shows the effect in the vicinity of the peak.

Additive noise, n, is still present in Eq. 8 which imposes the need for smoothing on inverse FT and equivalent methods which were naturally the first attempted [61–63]. It contributes to their tendency to develop large negative concentrations. If matrix effects are minimal, and the mixing can be shown to be approximately linear (for example from *very* good agreement between profiles synthesized by superposition and measured data from thick layers [64,65]) Eq. 8 may be applied with caution and inverted in the case of a

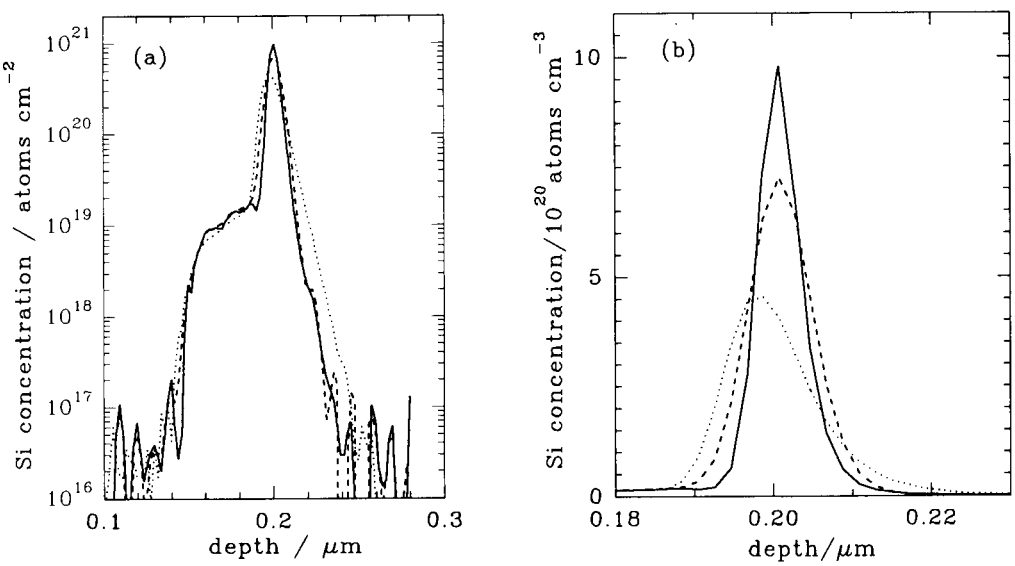

Fig. 10. A comparison of MaxEnt (———), smoothed, inverse Fourier transform (— — —), and conventional (· · · · · ·) methods for the quantification of a thin diffused Si layer in GaAs. Data courtesy of M. Maier, Fraunhofer Institut für Angewandte Festkorperphysik. MaxEnt and Fourier transform software, Mr P.N. Allen, ASP, University of Warwick. (a) Semi-log plot showing recovery of detail in low intensity regions. (b) Linear plot demonstrating superior performance of MaxEnt in the peak region.

matrix step or delta. Considering a delta of matrix A in matrix B or a step between A and B, if the effect of material B on the mixing of material A is identical with the effects of material A on itself, then the system will be approximately linear. An obvious example is where A and B are different isotopes of the same element with only a small mass difference [66,67].

2. Depth resolution

Defining the depth resolution

Any description of depth resolution implies that the profile has been quantified, at least using the inversion of Eq. 6. In general, the shape of the transient signal from a step or delta is determined by matrix effects (modified by intermixing of the matrices), radiation enhanced diffusion and segregation, development of surface macro- and micro-topography, recoil implantation, Kirkendall effects [11] and random cascade mixing. One of these processes, particularly one of the first three may dominate. Consideration of Eq. 2 will show that in the *non-dilute* case it is meaningless mathematically to define the depth resolution using a single parameter, even where appropriate experimental technique has reduced the content of the transient to random cascade mixing only. In a particular case it may be *pragmatic* to do so, but it is dangerous to develop a simple functional form around the parameter and attempt a deconvolution, except under limited circumstances discussed at the end of the last section. It is also evident that where matrix effects determine the transient from a non-dilute system (such as the popular GaAs/GaAlAs combination), the information on random cascade mixing, for example, is concealed.

When discussing depth resolution, it is more convenient to map the ϕ axis of the response functions onto z using $R(z) = \mathbf{M}^{-1}R(\phi)$ (the inverse of Eq. 5). This operation will produce a response function correctly scaled to depth, but generally with some shift [58]. For a dilute system, the parameters used to give a figure of merit for the depth resolution δz will necessarily depend on the nett shape of the response function $R_{\text{nett}}(z)$. For example, from Eq. 4:

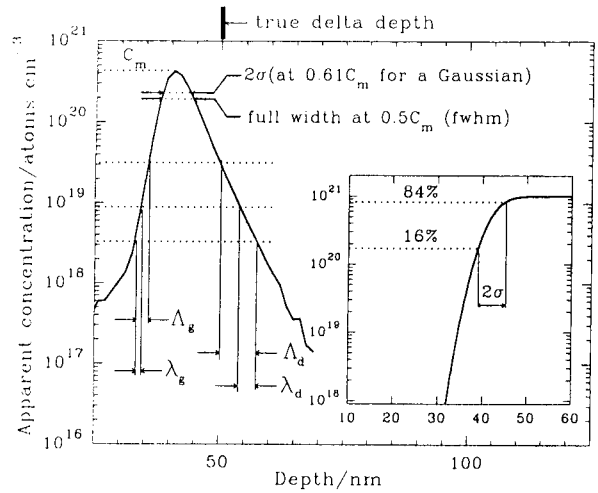

Fig. 11. Definitions of commonly used resolution parameters: growth and decay lengths, λ_g, λ_d, inverse growth and decay slopes, Λ_g, Λ_d, standard deviation, σ, and full width at half maximum (fwhm). In general, the parameters should be measured from the transient response to a delta, not the response to a step (see text). The transient response should be describable using a function containing the parameter(s). Note that if Eq. 11 is accurately representative of the response, neither λ_g nor σ are defined as shown [71]. Inset: For the convolution of a Gaussian response with a step, the 16–84% interval is 2σ.

$$R_{\text{nett}}(z) = \int_0^\infty R_r(z - \xi_r, z) R_m(\xi_r) d\xi_r \qquad (9)$$

If $R_{\text{nett}}(z)$ were dominated by surface roughness with a Gaussian distribution, then it would be appropriate to characterize depth resolution using the standard deviation σ. There are particular instances in the literature where the leading edge behaviour in a delta or step profile is Gaussian-like, whereas the trailing edge is not [66,68]. Here, an appropriate leading edge resolution parameter may be a width (e.g. σ or 16–84% respectively). Leading and trailing edges in SIMS profiles often display an exponential behaviour, and in particular SIMS response functions from dilute deltas are sometimes close to the form

$$R(z) = \begin{cases} \exp[(z - z_0)/\lambda_g], & z \le z_0 \\ \exp[-(z - z_0)/\lambda_d], & z > z_0 \end{cases} \qquad (10)$$

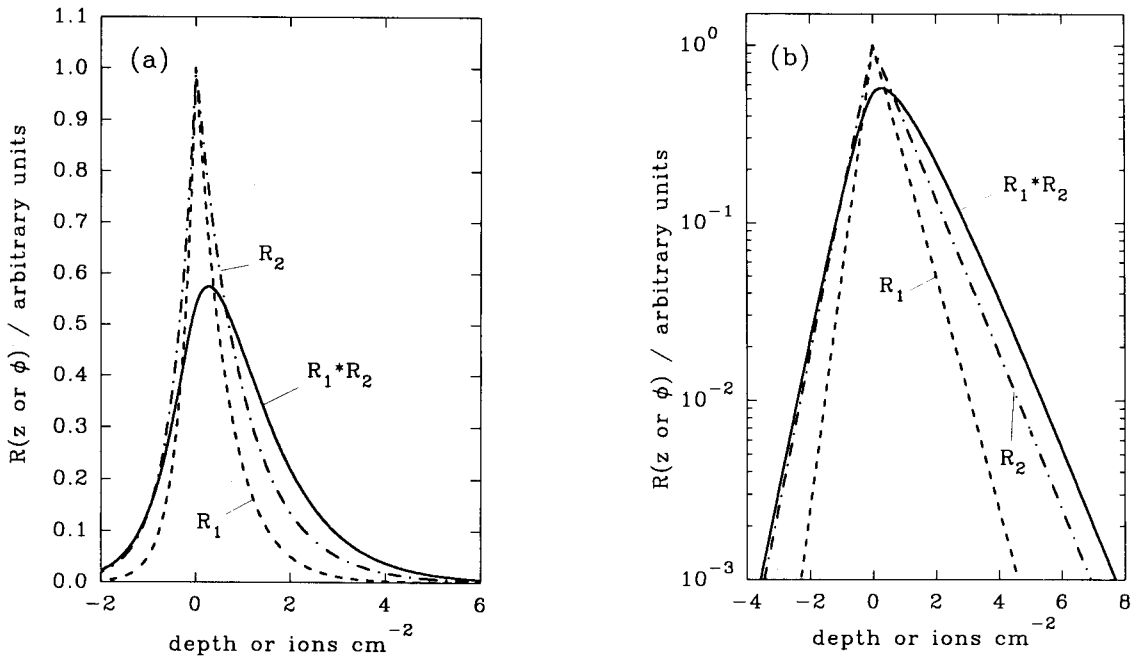

Fig. 12. Example of the analytic convolution of two double exponential response functions according to Eq. 10 and 13. Note the standard deviation is *not* a parameter of the system. (a) Linear scale, (b) semi-log plot.

where λ_g and λ_d are growth and decay lengths and z_0 is the apparent peak depth. Either the λs (with units of length), or a growth (leading edge) or decay (trailing edge) *inverse slope* (in units of length per decade of signal), Λ_g or Λ_d, are used to characterize the depth resolution in such cases. These and a width parameter σ are shown in Fig. 11. Note that the 16–84% definition for edge width in common use applies not to a response function, but the convolution of a Gaussian with a step. Eq. 10 is itself physically unrealistic because it is cusped. Zalm and de Kruif [69] have shown recently that it is also incomplete in the sense that the primary beam energy dependence in the λs alone cannot account for the energy dependent widths of measured responses. Zalm [70] has found that the convolution of Eq. 10 with a function such as $\gamma^{-1}\cos^2(z\pi/2\gamma)$ where γ is a width parameter is a good fit to several measured responses. We have found that the convolution of Eq. 10 with a Gaussian of standard deviation σ:

$$R_{\text{nett}}(z) = \frac{B(\lambda_g+\lambda_d)}{2} \times \left\{(1-\text{erf}\,\xi_1)\exp\left[\frac{z}{\lambda_g}+\frac{1}{2}\left(\frac{\sigma}{\lambda_g}\right)^2\right] + (1+\text{erf}\,\xi_2)\exp-\left[\frac{z}{\lambda_d}-\frac{1}{2}\left(\frac{\sigma}{\lambda_d}\right)^2\right]\right\} \quad (11)$$

where z_0 is taken as the origin, $\xi_1 = (z/\sigma + \sigma/\lambda_g)/\sqrt{2}$ and $\xi_2 = (z/\lambda_d)/\sqrt{2}$ is also an excellent fit for several impurities in gallium arsenide and silicon [60,71], and enables the energy dependence of the three parameters to be extracted.

It is frequently stated that depth resolution parameters δz_i due to different processes may be added in quadrature to obtain a nett parameter δz_{nett}:

$$\delta z_{nett} = \sqrt{\Sigma \delta z_i^2} \tag{12}$$

This property arises because the convolution of a set of Gaussians is itself a Gaussian. It is straightforward to show that it is generally *inapplicable*. Consider the analytic convolution [3] of two response functions R_1 and R_2 where both are of the form in Eq. 10. R_1 has growth and decay lengths written for convenience as $1/a$ and $1/b$ respectively. Corresponding parameters for R_2 are $1/p$ and $1/q$. The convolution is:

$$R_{nett}(z) = \begin{cases} [(a+q)^{-1} - (a-p)^{-1}] \exp[a(z-z_0)] \\ \quad + [(a-p)^{-1} + (b+p)^{-1}] \exp[p(z-z_0)], \\ \quad z \le z_0 \\ [(b+p)^{-1} - (b-q)^{-1}] \exp[-b(z-z_0)] \\ \quad + [(a+q)^{-1} + (b-q)^{-1}] \exp[-q(z-z_0)], \\ \quad z > z_0 \end{cases} \tag{13}$$

This is illustrated in Fig. 12a and b which shows linear and semi-log plots respectively with $a = 3$, $b = 1.5$, $p = 2$ and $q = 1$. Unlike the convolution of two Gaussians, $R_{nett}(z)$ differs in form its progenitors. The full widths at half maximum (fwhm) for R_1 and R_2 are given by $(a^{-1} + b^{-1})\ln 0.5$ and $(p^{-1} + q^{-1})\ln 0.5$, respectively. There is no simple expression for the fwhm of $R_{nett}(z)$ which is generally the root of a trancendental equation. However, where $a = p = b = q$, i.e. $R_1 \equiv R_2 \equiv R$, it is easy to show that the fwhm of $R_{nett}(z)$ is $3.357/a$, i.e. 1.7 times larger than addition in quadrature would suggest. Most plausible response functions deviate significantly from Eq. 12. Zalm and de Kruif [69] have shown that for two processes producing exponential growth or decay lengths λ_1 and λ_2 remote from the maximum, an approximate parameter λ_{nett} is given by:

$$\lambda_{nett} = \left(\lambda_1^4 + \lambda_2^4\right)^{1/4} \tag{14}$$

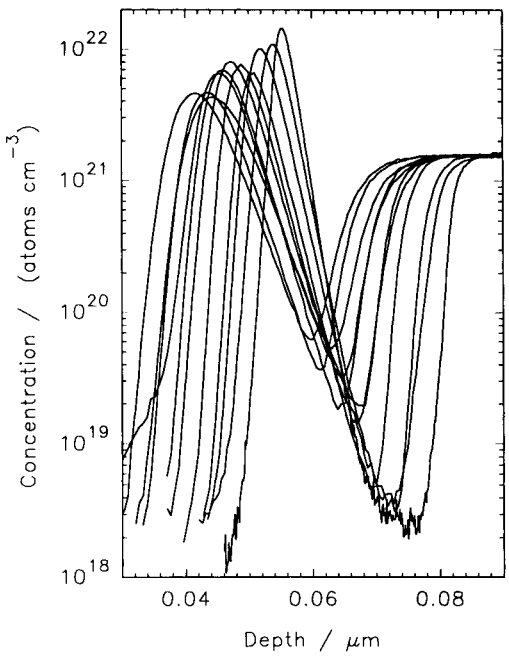

Fig. 13. Response functions for a ^{30}Si delta in a ^{28}Si matrix obtained using normal incidence O_2^+ bombardment from energies of 1–11 keV per ion. Note the progressive departure from the double exponential form and the peak shift towards the surface with increasing energy. The sample was produced by IBD at University of Salford, UK and analysed using the authors' EVA 2000 instrument.

Suitability of a sample for resolution measurements

It is difficult to produce samples so as to isolate a particular broadening phenomenon for study. Fig. 13 shows what one might hope is an ideal case: A set of response functions measured from a ≈ 2 mono-layer ^{30}Si delta on a 30 nm ^{28}Si buffer layer with a 55 nm ^{28}Si cap. The sample was produced by ion beam deposition (IBD) at Salford University [67], and the data were measured using normally incident $^{16}O_2^+$ ions from 1

[3] Having measured a response function, it is a useful exercise (if possible) to find an analytic function or set of functions which give a good fit and which may themselves be analytically convolved with simple features. The convolutions reveal dependencies on the parameters of the feature and the response function which are not obvious from numerical convolution (see for example [69] and [108]).

to 11 keV. The data should be free from segregation and matrix effects, and characteristic of physical mixing with perhaps a small contribution from roughening due to the statistical nature of sputtering, intrinsic surface roughness, and intrinsic roughness at the delta interfaces. Since the data were quantified from the isotopic abundance of ^{30}Si in the substrate, the small departure of the delta shapes from a systematic energy dependence gives a measure of the total experimental error (both sample and measurement related). It is evident that the response function departs progressively from the double exponential form (Eq. 10) especially in the leading edge as probe energy E_p is increased, and $R_{nett}(E_p, z)$ is the result of competition between at least two energy dependent processes. The data are well described by Eq. 11 with a strong energy dependence in σ and λ_d. Perhaps λ_u is intrinsic to the sample and dominated by random cascade mixing and probe incorporation at higher E_p.

One might think that depth resolution information could be extracted equally well from a dilute delta or a dilute step. Recently, Wittmaack and Poker [66] measured depth resolution data from 100 nm thick isotopically pure Si/Si layers also grown by IBD. They could extract decay lengths from the trailing edges, but found it necessary to characterize the leading edges by a width parameter δ measured between 1% and 50% of the plateau level. Before discussing their data further, we make the following observation: Neglecting the fact that our data (Fig. 13) show that the double exponential form is only a good approximation at low energy, we can extract limiting growth and decay lengths from Ref. [66], and construct a double exponential $R(z)$ for 8 keV $^{16}O_2^+$ bombardment. With reference to Fig. 14, the analytic convolution of Eq. 10 with an ideal 100 nm layer (chain dotted line, $C(z)$) situated between depths z_1 and z_2 is given by:

$$Y(z) = K\begin{cases} p^{-1}\{\exp[p(z-z_1)] - \exp[p(z-z_2)]\}, & z < z_1 \\ p^{-1} + q^{-1} - p^{-1}\exp[p(z-z_2)] - q^{-1} \times \exp[-q(z-z_1)], & z_1 \le z \le z_2 \\ q^{-1}\{\exp[-q(z-z_2)] - \exp[-q(z-z_1)]\}, & z > z_2 \end{cases} \quad (15)$$

where K is a constant, and p and q are the inverse growth and decay lengths as in Eq. 13. This result is the solid line $R * C$. The scale of $R(z)$ is chosen to give equal areas under $C(z)$ and $R * C$, and the relative positions of $C(z)$ and $R * C$ are as dictated by the convolution. Note that even though the response function is cusped, the leading edge of the convolution could reasonably be characterized by a width parameter *or* an exponential (tending towards $\exp(pz)$), whereas the trailing edge is almost exponential (tending towards $\exp(-qz)$). This general asymmetry in the measured profile of a thick layer was pointed

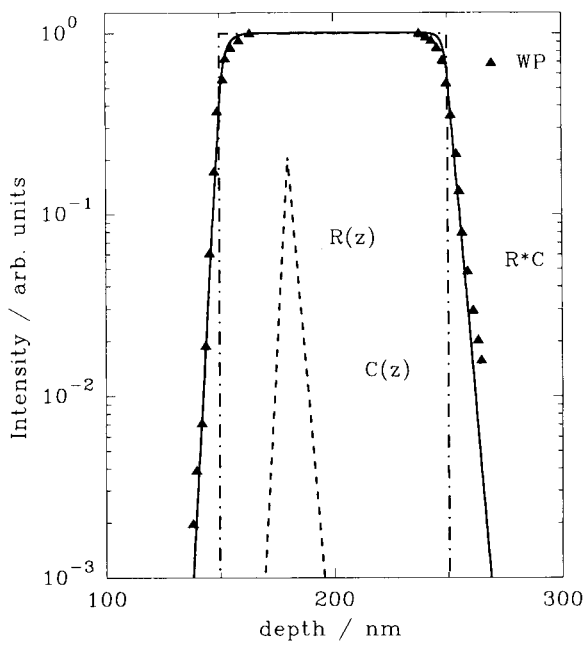

Fig. 14. Analytic convolution of a double exponential response function for 8 keV O_2^+, $R(z,)$ with $\lambda_g = 1.99$, and $\lambda_d = 2.95$ (calculated from Wittmaack and Poker [66]) with a perfect thick layer $C(z)$ to give an asymmetric simulated profile $R * C$ (Eqn. 15). Measured data from [66] are superimposed (▲). $R(z)$ is shown at the correct scale to give equal areas under $C(z)$ and $R * C$.

out by Littmaack and Hofer [12]. We have superimposed the measured data (filled triangles) from [66] on the convolution. The δ measurements, and growth and decay lengths for the convolution and the experimental data are identical, and the overall agreement is good despite the fact that the response function constructed is extremely artificial for 8 keV beam energy (cf. Fig. 12). This exercise demonstrates the following:

(i) Since the wrong response function convolved with the $C(z)$ for a step up followed by a step down gives good agreement with $Y(z) = R * C$, one cannot from measurements on a step uniquely identify the right response function [4] (obviously this is a deconvolution problem with no unique solution – see also [58]).

(ii) It is the response function from a delta which contains the fundamental resolution related parameters. It is difficult to extract corresponding parameters from its convolution with a step (if that is the only information available); i.e., measurements on thick layers do not necessarily yield depth resolution parameters which are directly dependent on the physical process, and it is not immediately clear from which part of the yield curve of a thick layer the resolution information should be extracted.

Decay lengths measured from the data in Fig. 13 are in excellent agreement with those from [66] across the whole energy range. As we have already implied, it would be necessary to convolve real response functions such as those in Fig. 13 with their true chemical profile to extract directly comparable δ values. We can, however, measure this parameter directly from the ^{30}Si channel at the ^{28}Si buffer/substrate interface. (At higher energies it was necessary to extrapolate the signal by $\approx \frac{1}{2}$ order of magnitude as consistent with the trend in Eq. 15) Our values

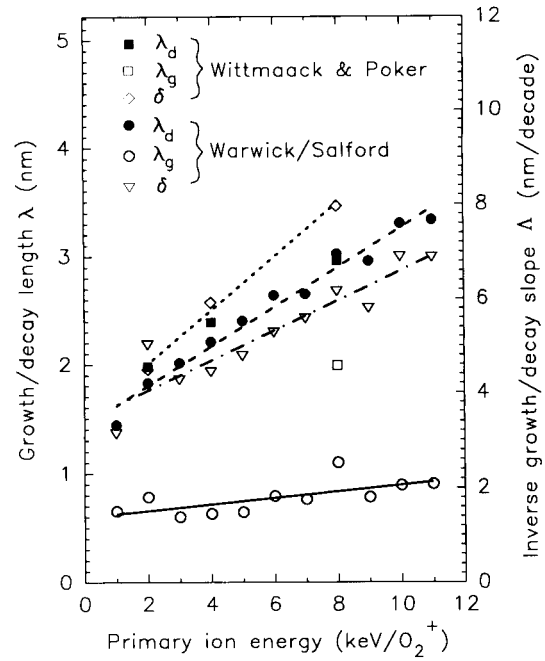

Fig. 15. Resolution parameters for the ^{30}Si delta in a ^{28}Si matrix of Fig. 13 and from the data of Wittmaack and Poker [66].

for δ, λ_g and λ_d are compared with theirs in Fig. 15. We find a significantly lower δ value – with a weaker energy dependence. This suggests that δ is partly determined by energy dependent interaction between the beam and some material parameter. For example, the intrinsic point defect density in the material at the periphery of individual collision cascades may determine radiation enhanced diffusion. Given both data sets one might suspect that neither has reached the fundamental limit imposed by random cascade mixing, Kirkendall effects, and sputter-related statistical roughening.

A system which has been studied more frequently is that of boron layers or deltas in silicon. Fig. 16 shows a summary of literature growth and decay values for $^{16}O_2^+$ primary probes as a function of energy. Firstly we discuss the decay lengths (filled symbols). The data of Turner et al. [72], show both the largest values and the strongest energy dependence. Their data are almost continuous with our early data [73,74]. A sample of our more recent data from a shallow delta [58], and

[4] Analytically, one can differentiate the step data and retrieve the response function. In the real case, differentiation will amplify noise, so one must either smooth the data or fit a function and differentiate that. Both processes will impose a bias depending on the method used – indeed the latter is just a forced definition of the response function. It is better to measure the response function directly where possible.

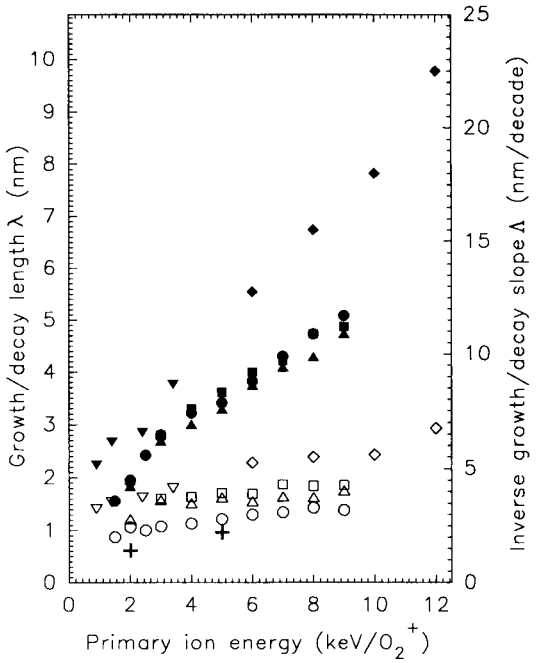

Fig. 16. Resolution parameters λ_g and λ_d for $^{16}O_2^+$ analysis of boron deltas and thicker layers in silicon. ♦◇, 50 nm thick, 50 nm deep 5×10^{18} cm^{-3} layer grown by limited reaction processing (LRP), analysed at 20° to normal, from Turner et al. [72]. +, λ_g from MBE delta, 9×10^{12} cm^{-2}, 195 nm cap, normal incidence, from Wittmaack [76]. ▼▽, MBE delta, 10^{13} cm^{-2}; 80 nm cap, normal incidence [73,74]. ▲△, MBE delta, 3×10^{14} cm^{-2}, 50 nm cap, normal incidence [58]. △▲, MBE delta, 3×10^{14} cm^{-2}, 500 nm cap, normal incidence [75]. □■, MBE delta, 3×10^{14} cm^{-2}, 500 nm cap, 45° incidence [75]. (The cap is the top layer of silicon.)

one at 10 times the depth analysed at both normal incidence and 45° [75] show shorter decay lengths, and those from the deep delta (most recent material/measurement) are shortest of all. There is a distinct change of slope in the energy dependence for these data at 3–4 keV which we have previously ascribed to the overlap between the delta and the extreme limit of the SIMS pre-equilibrium region [75]. Since the deep and shallow deltas exhibit similar behaviour, this explanation is wrong. We suggest that the phenomenon is either associated with an intrinsically non-linear energy dependence in the decay length, or with the high concentration in these layers – the mass transport is entering the non-dilute regime. In this case, above a certain threshold energy there is sufficient cascade dilution [4] to move the behaviour to the linear regime. Recent data presented by Wittmaack [76] on more dilute deltas (omitted for clarity) is in precise agreement with the 4–10 keV region of our data. The 45° data from the deep delta have marginally larger decay lengths than those measured at normal incidence. Growth lengths (open symbols) are far weaker in their energy dependence, but the trend in magnitude from one data set to another is the same as for the decay lengths. The data from [76] show especially small values. Each data set is characteristic of a particular balance of mass transport processes in the sample measured and, as for the silicon in silicon case, there is evidently some material quality interacting with the probe to produce different magnitudes and parameter dependencies. Elsewhere, we have given an example of such an interaction for the case of Si/SiGe alloy layers [60,77]. Normal incidence analysis of a system of thick unstrained layers showed very pronounced heels on the leading edge of each SiGe alloy layer indicative of surface segregation of Ge during growth. However, in a 45° profile of the same sample, the heels were completely absent. SEM examination of the profiled regions showed that the interaction between the probe and the sample had produced large voids in the analysed surface at normal incidence, distorting the profile shape according to the resulting macrotopography. (Note that Zalm and co-workers [78,79] investigated superficially similar heels in SiGe material, but were able to attribute them to surface segregation during growth.)

It would be fortuitious if any set of growth and decay length measurements were characteristic of a single broadening effect with a single energy dependence. The data in Fig. 15, together with much other data in the literature [e.g. 80,81] superficially suggest a probe energy dependence of the form

$$\delta z = \delta z_0 + kE_p \qquad (16)$$

Following the arguments of Badheka et al. [68,82] one expects δz_0 to be characteristic of the true feature shape combined with several sources of roughness-like behaviour (e.g. intrinsic surface or

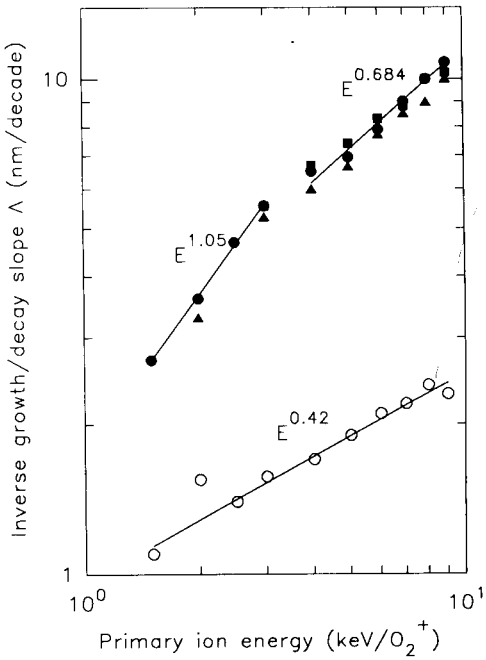

Fig. 17. Log–log plot for our boron growth and decay length data from Fig. 16 corrected for a non-energy dependent broadening assumed to be ≈ 1 nm. Note an $E_p^{1/2}$ dependence is nowhere to be seen. Symbols as in Fig. 16.

interface roughness, statistical effects of sputtering, statistical roughness at the altered layer/sample interface [83]) which are not or may not be energy dependent. (Incidentally, it is these effects which will probably limit the ultimate depth resolution in SIMS.) In the limit of low energy, and *assuming* that the nett effect of all these processes is Gaussian (or at least symmetric), the growth and decay lengths should tend to the same value. In Fig. 16 for example this value lies in the range 1–1.5 nm. Using our data alone, we have subtracted a mean value for λ_0 from the growth and decay length data, and sought a power law dependence using Marquardt-Levenberg non-linear regression [5]. The result is shown in Fig. 17. The low energy decay lengths are linearly dependent on energy. Above 4 keV we find an $E_p^{0.7}$ behaviour for both normal incidence and 45° bombardment. The growth length goes as $E_p^{0.4}$. Before these (or any other) dependencies can be ascribed to a particular mechanism the behaviour of the impurity in the altered layer needs to be established.

Dependence of depth resolution on primary ion parameters

In 1979 H.H. Andersen published a simple model for estimating the depth resolution of sputter profiling where the determining process was random cascade mixing [84]. He found a symmetrical (Gaussian) form for the observed profile of a delta, neglecting the movement of the surface across the problem due to sputtering [85]. In fact, the model predicts the standard deviation, σ, of a pseudo-internal profile produced as if the integrated energy deposited from the beam had been dumped in the vicinity of the delta:

$$\sigma = 2R\sqrt{E_p/(4E_{d,min}S)} \quad (17)$$

where R is the mean range of the recoils in the cascade, $E_{d,min}$ is the minimum displacement energy, and S is the sputter yield. In numerous subsequent publications this has been used to justify the assumption of a form $\lambda = kE_p^{1/2}$ for the dependence of depth resolution on probe energy *despite* the complex energy dependence of S. Andersen makes no such claim. His modelled data do not show a power law dependence, but extracting approximate power laws $\lambda = kE_p^n$ from his data in the range 1–10 keV one obtains values for n of 0.37 and 0.87 for Ar^+ bombardment of silicon and copper for example. More recently, Zalm and Vriezema [86] developed a simple model for the energy and angular dependence of depth resolution based on earlier work for high energy mixing by Cheng [87]. This predicts an $E_p^{1/2}\cos\theta$ dependence where θ is the angle to the surface normal, and was intended to give an explanation of the *relative* insensitivity of depth resolution on bombarding species (in the absence of strong chemical effects) and impurity mass, as well as a rapid method for estimating likely achievable resolution. It was not intended limit the search for the resolution dependence to an $E_p^{1/2}$ form [70]. In recent articles Petravi et al.

[5] In SigmaPlot 5.0, Jandel Scientific.

[88,89] claim to have substantiated the model across rather a large range of matrix/impurity types. Fig. 18a shows their decay length data for O_2^+, Ar^+ and Cs^+ bombardment of a Ge delta layer [88]. (We have re-measured their published Ar^+ profiles as their plotted decay lengths do not correspond with these.) The solid lines in Fig. 18a show a non-linear regression (see footnote on p. 267) of the form $\lambda = kE_p^n$, whereas the dashed lines show a forced best-fit $E_p^{1/2}$ dependence. None of the data is a good fit to the latter. However, it is also certain that there will be a

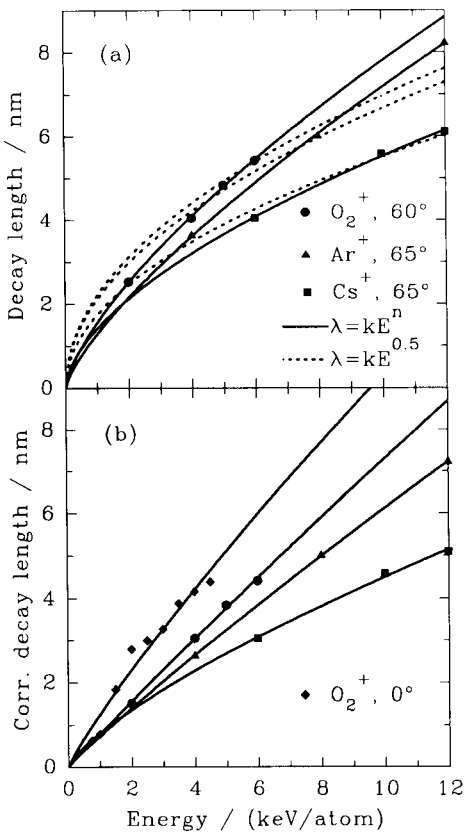

Fig. 18. Decay lengths for a germanium delta in silicon [88,89] analysed using a variety of primary ions. (a) Fitted power law dependence $\lambda_d = kE_p^n$ (———) using data as measured. See Table 1 for values of k and n. A forced $E_p^{1/2}$ dependence (— — —) is not a good fit. (b) The same data with an intercept ≈ 1 nm subtracted to correct for non-energy dependent sources of broadening. An $E_p^{1/2}$ fit (not shown) is even less appropriate. Data obtained at normal incidence [58] where the SiGe alloy altered layer behaviour is complex [3] is included for comparison (◆).

Table 1
Result of fitting $\lambda = kE_p^n$ to Ge decay lengths from Ref. 88

Species	As published		Forced $n = \frac{1}{2}$		Intercept subtracted		Normal Inc. [58]	
	k	n	k	n	k	n	k	n
O_2^+	1.55	0.70	2.10	0.5	0.81	0.96	1.26	0.87
Ar^+	1.27	0.74	2.20	0.5	0.75	0.91	–	–
Cs^+	1.40	0.59	1.73	0.5	0.81	0.74	–	–

non-energy dependent contribution to the data as already discussed. The data *must* therefore exhibit an intercept [6]. This cannot be added to the energy dependent resolution in quadrature (see Eq. (13) and (14) with the associated discussion) nor set to zero [89]. The data in Fig. 18a are consistent with an intercept in the vicinity of 1 nm. Fig. 18b shows the data replotted with this value subtracted from the decay lengths. The solid lines are again fits to $\lambda = kE^n$. The power n varies between 1 and 0.8. Our normal incidence data from Ref. [58] are also shown (with an intercept of 2.7 nm subtracted). The fitting parameters are summarised in Table 1. Both the corrected results, and those in Fig. 17 agree well in magnitude with a model for the decay length based on the behaviour of the internal mixing profile for the impurity suggested by Wittmaack and co-workers [85,90,91]. They found that

$$\lambda_d = R/rq_0 \tag{18}$$

where R is a depth parameter related to the range of the primary ions, r is the ratio of the sputter yield of the impurity to that of the matrix, and q_0 is a constant within limitations given in [91]. If r is independent of E_p, and R is closely correlated with the primary ion projected range then

$$\lambda_d \approx kE_p^n \tag{19}$$

[6] However, note that if the resolution function must be characterized by two or more parameters, e.g. Eqs. 10 and 11, *which* parameters exhibit an intercept cannot be deduced unless the true $C_X(z)$ is known apriori.

where n lies in the range 0.8 to 1.0 under typical analytical conditions.

In general, the dependence of decay length on angle of bombardment is found to take the form [92]

$$\lambda_d = \lambda_{min} + \lambda' cos^n \theta \quad (20)$$

where n is close to 1 and λ_{min} is present for reasons already discussed. λ_{min} and λ' are both dependent on the analyte species. An important exception to this behaviour occurs where the dilution of the matrix by incorporated probe atoms buffers the effects of the cascade mixing [19], producing a smaller decay length than expected. This occurs for example for oxygen bombardment of silicon for θ between 0° and 27° when the near surface is converted to stoichiometric SiO_2 [2,77,83]. The effect on the decay length has been modelled by Meuris et al. [93], showing it to be nearly constant across this range of angles, then increasing to a maximum at 45°, and decreasing thereafter to achieve a similar magnitude to 0° at 60°.

There is no obvious dependence of decay length on the mass of the analyte, although there are local dependencies on atomic number [85], and chemical species [58,64,81,82] especially where radiation enhanced diffusion and segregation are believed to occur [94–96]. Meuris et al. [97] also found no obvious relationship between the decay length and the mass of the probe atoms. Finally, it should be mentioned that Vandervorst and Clarysse have recently produced an extensive survey of decay lengths and corresponding analytical conditions in a review article [98].

The ion bombardment of a surface in general produces a dose dependent roughening which may cause progressive loss of depth resolution even from a depth of a few nm [99] or a rather sudden loss of depth resolution accompanied by changes in erosion rate and ion yield at depths from ≈ 1 μm onwards [e.g. 99–103]. This type of effect has been modelled by Carter et al. [104]. Although this problem is potentially serious for SIMS, especially as devices such as lasers can have very deeply buried interfaces, it can be solved by using near normal incidence bombardment (at least for silicon and gallium arsenide) [100], or by sample rotation [99,105,106].

Conclusions

Accurate quantification of features close to matrix steps and deltas will have to await fuller forward models of the SIMS process. In the mean time, better estimates of the true profile can be obtained by a variety of practical means, especially SNMS and XCs^+ profiles. Such methods are not free from matrix effects, but these may be reduced to a few percent for certain experimental conditions. For RIMS, probe species, bombardment angle, and energy need to be optimised to the ionization scheme selected, to ensure a constant emission coefficient for the low energy state. For XCs^+ the bombardment angle should be in the range 60–65° in many cases. A model for SNMS profiles for specific matrix/matrix and impurity/matrix combinations is currently available (IMPETUS) [9–11,68,82]. A SIMS forward model requires the addition of a method for the prediction of ionization coefficient from a knowledge of the instantaneous surface chemistry. Accurate modelling of this problem may become possible in the next few years.

Quantification of dilute systems containing transient signals may, of course utilise some of the methods appropriate to matrix deltas and steps. However, the full quantification of systems of dilute deltas and/or steps is by definition a deconvolution problem. This method is practical where the response function from a single delta can be measured. Even with very accurately measured data, the deconvolution has no unique solution, and care must be taken to ensure that the deconvolution algorithm used does not impose a bias. There is little point in deconvolving the concentration profile using a modelled or assumed response function (unless the model fits measured data and predicts correct behaviour with variations in probe parameters). Considering deconvolution as division of the Fourier transform of the measured data by the Fourier transform of the response function, one can see that if the measured data had been produced by convolution of the concentration profile with a different response, the transform of the measured data

could contain finite intensity where the transform of the assumed response was zero, or very small. The division would then produce high fictitious amplitudes, distorting the deconvolved data and introducing noise.

Depth resolution parameters need to be closely related to the form of the response function if they are to be useful in the development of forward models, and the estimation of the dependence on probe parameters. There is evidence to show that unsuspected interaction between aspects of the sample quality and the probe is responsible for sometimes large variations in resolution parameters observed from the same sample types.

There exist a large number of novel approaches to the analysis of sharp features at high depth resolution which are not covered here. These include various bevelling and sectioning methods, and reverse side profiling. These are briefly reviewed in [77]. A technique for correcting transients due to rapid changes in surface potential at interfaces is described in [83].

Because of the relative insensitivity of depth resolution to the mass of the bombarding beam, and given a finite useful working range in angle of incidence, one can only reduce E_p to gain further improvements. The limiting factor will be roughness both inherent in the sample and related to the statistical nature of the ion solid interaction. Perhaps, with the advent of atomic layer epitaxy (ALE) and its inverse technique atomic layer etching [107] which could form the basis of a depth profiling mass spectrometry technique we may ultimately see these problems reduced to near zero.

MGD is grateful to the Royal Society Industrial Fellowship Scheme and Kratos Analytical Ltd for their support. RDB is currently funded by ESPRIT III project ADEQUAT. The authors are fortunate in having a large supply of MBE grown material from Prof. E.H.C. Parker's Advanced Semiconductor Group to concentrate their minds on the subject matter of this paper. We are grateful to colleagues in the UK IED 1559 and 1540 projects who provided some of the material presented here, and and everyone whose data we have used (sometimes in ways they might not have wished – if so, our appologies). Thanks are due to Mr. P.N. Allen, SERC CASE student for discussions on convolution and sharp MaxEnt deconvolution software, and to Dr. R. Collins (York) without whom our work in MaxEnt would not have come about.

References

[1] R. Treichler, H. Cerva, W. Hösler and R. v. Criegern, in A. Benninghoven, C.A. Evans, K.D. McKeegan, H.A. Storms and H.W. Werner (Eds.), Secondary Ion Mass Spectrometry SIMS VII, Wiley, Chichester, 1990, p. 259.

[2] S.D. Littlewood and J.A. Kilner, J. Appl. Phys., 63 (1988) 2173.

[3] M.G. Dowsett, D.M. James, I.W. Drummond, M.M. El Gomati, T.A. El Bakush, F.J. Street and R.D. Barlow, in A. Benninghoven, K.T.F. Janssen, J. Tümpner and H.W. Werner (Eds.), Secondary Ion Mass Spectrometry SIMS VIII, Wiley, Chichester, 1990, p 359.

[4] P. Williams, in D. Briggs and M.P. Sheah (Eds.), Practical Surface Analysis, Vol. 2, Wiley, Chichester, 1990, Chap. 4.

[5] K. Wittmaack, Nucl. Instrum. Meth., 168 (1980) 343.

[6] K. Wittmaack, Appl. Surf. Sci., 9 (1981) 315.

[7] Y. Gao, Appl. Surf. Sci., 32 (1988) 420.

[8] R. Collins, M.G. Dowsett and P.N. Allen, in A. Benninghoven, K.T.F. Janssen, J. Tümpner and H.W. Werner (Eds.), Secondary Ion Mass Spectrometry SIMS VIII, Wiley, Chichester, 1990, p. 111.

[9] D.G. Armour, M. Wadsworth, R. Badheka, J.A. Van den Berg, G. Blackmore, S. Courtney, C.R. Whitehouse, E.A. Clark, D.E. Sykes and R. Collins, in A. Benninghoven, A.M. Huber and H.W. Werner (Eds.), Secondary Ion Mass Spectrometry SIMS VI, Wiley, Chichester, 1988, p. 399.

[10] M. Wadsworth, D.G. Armour, R. Badheka and R. Collins, Int. J. Numer. Modelling, 3 (1990) 157.

[11] R. Collins, J.J. Jimenez-Rodriguez, M. Wadsworth and R. Badheka, J. Appl. Phys., 64 (1988) 1120.

[12] U. Littmark and W.O. Hofer, Nucl. Instrum. Meth., 168 (1980) 329.

[13] U. Littmark, Nucl. Instrum. Meth. Phys. Res., B7 (1985) 684.

[14] R.P. Webb, in D. Briggs and M.P. Seah (Eds.), Practical Surface Analysis, Vol. 2, Wiley, Chichester, 1990, Appendix 3.

[15] J. Skilling, in J.H. Justice (Ed.), Maximum Entropy and Bayesian Methods in Applied Statistics, Cambridge Univ. Press, 1986.

[16] J. Skilling and S.F. Gull, in J. Skilling (Ed.), Maximum Entropy and Bayesian Methods, Kluwer, Dordrecht, 1989.
[17] M.G. Dowsett, P.J. Mole, and E.H.C. Parker, J. Appl. Phys., 54 (1983) 6340.
[18] D.S. McPhail and S.D. Littlewood, in A. Benninghoven, K.T.F. Janssen, J. Tümpner and H.W. Werner (Eds.), Secondary Ion Mass Spectrometry SIMS VIII, Wiley, Chichester, 1990, p. 407.
[19] K. Witmaack and W. Wach, Nucl. Instrum. Methods, 191 (1981) 327.
[20] S.R. Bryan, R.W. Linton and D.P. Griffis, J. Vac. Sci. Technol., A5 (1987) 9.
[21] A.E. Morgan and P. Maillot, Appl. Phys. Lett., 50 (1987) 959.
[22] R.G. Wilson, C.L. Kirschbaum, G.E. Lux, S.P. Smith and C.J. Hitzman, in A. Benninghoven, K.T.F. Janssen, J. Tümpner, and H.W. Werner (Eds.), Secondary Ion Mass Spectrometry SIMS VIII, Wiley, Chichester, 1990, p. 151.
[23] R. Jede, O. Ganschow, U. Kaiser, in D. Briggs and M.P. Seah (Eds.), Practical Surface Analysis, Vol. 2, Wiley, Chichester, 1990, Chap. 8.
[24] J. Tümpner, in A. Benninghoven, A.M. Huber and H.W. Werner (Eds.), Secondary Ion Mass Spectrometry SIMS VI, Wiley, Chichester, 1988, p. 797.
[25] O. Ganschow, in A. Benninghoven, R.J. Colton, D.S. Simons and H.W. Werner (Eds.), Secondary Ion Mass Spectrometry SIMS V, Springer-Verlag, Berlin, 1986, p. 79.
[26] J.R. Woodyard and C.B. Cooper, J. Appl. Phys., 35 (1964) 1107.
[27] H. Oechsner, H. Paulus and P. Beckmann, J. Vac. Sci. Technol., A3 (1985) 1403.
[28] N. Winograd, J.P. Baxter and F.M. Kimock, Chem. Phys. Lett., 88 (1981) 581.
[29] D.M. Gruen, M.J. Pellin, C.E. Young and W.F. Calaway, J. Vac. Sci. Technol., A4 (1986) 1779.
[30] C.H. Becker, Fesenius' Z. Anal. Chem., 341 (1991) 3.
[31] S.R. Bryan, M. Nicholas and G.J. Havrilla, in A. Benninghoven, K.T.F. Janssen, J. Tümpner and H.W. Werner (Eds.), Secondary Ion Mass Spectrometry SIMS VIII, Wiley, Chichester, 1990, p. 571.
[32] D.E. Sykes, ISST, personal communication.
[33] R.C. Beavis, J. Lindner, J. Grotemeyer and E.W. Schlag, Ber. Bunsenges. Phys. Chem., 93 (1989) 365.
[34] S.W. Downey and R.S. Hozack, J. Vac. Sci. Technol., A8 (1990) 791.
[35] M.A. Ray, J.E. Baker, C.M. Loxton and J.E. Greene, J. Vac. Sci. Technol., A6 (1988) 44.
[36] K. Wittmaack, Nucl. Instrum. Meth. Phys. Res., B64 (1992) 621.
[37] E.W. Thomas and Abbas Torabi, Nucl. Instrum. Meth. Phys. Res., B73 (1993) 214.
[38] S.W. Downey, A.B. Emerson and R. Kopf, Nucl. Inst. Meth. Phys. Res., B62 (1992) 456.
[39] S.W. Downey and A.B. Emerson, Surf. Interface Anal., 20 (1993) 53.
[40] S.W. Downey, A.B. Emerson and R.W. Kopf, Proc. 1st International Workshop on the Measurement and Characterization of Ultra Shallow Doping Profiles in Semiconductors, C. Osburn and G. McGuire (Eds.), Microelectronics Centre of North Carolina, 1991, p. 172.
[41] H.A. Storms, K.F. Brown and J.D. Stein, Anal. Chem., 49 (1977) 2023
[42] Y. Gao, J. Appl. Phys., 64 (1988) 3760.
[43] B.J. Garrison, N. Winograd and D.E. Harrison Jr., J. Vac. Sci. Technol., 16, (1979) 789.
[44] B.J. Garrison, N. Winograd and D.E. Harrison Jr., Surf. Sci., 78 (1978) 467.
[45] H. Gnaser and H. Oechsner, in A. Benninghoven, K.T.F. Janssen, J. Tümpner and H.W. Werner (Eds.), Secondary Ion Mass Spectrometry SIMS VIII, Wiley, Chichester, 1990, p. 95.
[46] R. Valizadeh, J.A. van den Berg, R. Badheka, A. Al Bayati and D.G. Armour, Nucl. Instrum. Meth. Phys. Res., B64 (1992) 609
[47] H. Gnaser and H. Oechsner, Fresenius' J. Anal. Chem., 341 (1991) 54
[48] C.W. Magee, in A. Benninghoven, C.A. Evans, K.D. McKeegan, H.A. Storms and H.W. Werner (Eds.), Secondary Ion Mass Spectrometry SIMS VII, Wiley, Chichester, 1990, p. 543
[49] H. Gnaser and H. Oechsner, Nucl. Instrum. Meth. Phys Res, B64 (1992) 646
[50] R.J. Beiler and J.C. Huneke, in A. Benninghoven, K.T.F. Janssen, J. Tümpner and H.W. Werner (Eds.), Secondary Ion Mass Spectrometry SIMS VIII, Wiley, Chichester, 1990, p. 103.
[51] D.S. McPhail, M.G. Dowsett and E.H. C Parker, Vacuum, 36 (1986) 997.
[52] K. Wittmaack, Surf. Sci., 112 (1981) 168.
[53] G.D.T. Spiller and J.R. Davis, in A. Benninghoven, A.M. Huber and H.W. Werner (Eds.), Secondary Ion Mass Spectrometry SIMS VI, Wiley, Chichester, 1988, p. 705.
[54] J.A. Kilner, R.J. Chater, P.L.F. Hemment, R.F. Peart, E.A. Maydell-Ondrusz, M.R. Taylor and R.P. Arrowsmith, Nucl. Instrum. Meth. Phys. Res., B7/8 (1985) 293.
[55] E.A. Clark, Vacuum, 36 (1986) 861.
[56] S.A. Schwarz, C.L. Schwartz, J.P. Harbison and L.T. Florez, in A. Benninghoven, C.A. Evans, K.D. McKeegan, H.A. Storms, H.W. Werner (Eds.), Secondary Ion Mass Spectrometry SIMS VII, Wiley, Chichester, 1990, p. 467.
[57] H.E. Smith and W.C. Harris, in A. Benninghoven, K.T.F. Janssen, J. Tümpner and H.W. Werner (Eds.), Secondary Ion Mass Spectrometry VIII, Wiley, Chichester, 1990, p. 99.
[58] M.G. Dowsett, R.D. Barlow, H.S. Fox, R.A.A. Kubiak and R. Collins, J. Vac. Sci. Technol., B10 (1992) 336.

[59] P.N. Allen, M.G. Dowsett and R. Collins, Surf. Interface Anal., 20 (1993) 696.
[60] M.G. Dowsett, R.D. Barlow and P.N. Allen, J. Vac. Sci. Technol. B, in press.
[61] J.B. Clegg and R.B. Beall, in A. Benninghoven, C.A. Evans, K.D. McKeegan, H.A. Storms and H.W. Werner (Eds.), Secondary Ion Mass Spectrometry VII, Wiley, Chichester, 1990, p. 99.
[62] P.S. Ho and J.E. Lewis, Surf. Sci., 55 (1976) 335.
[63] B.V. King and I.S.T. Tsong, Nucl. Instrum. Meth. Phys. Res., B7 (1985) 793.
[64] J.B. Clegg and I.G. Gale, Surf. Interface Anal., 17 (1991) 190.
[65] D.S. Mcphail, M.G. Dowsett, R.A.A. Kubiak, S.M. Newstead, S. Biswas and S.D. Littlewood, in A. Benninghoven, C.A. Evans, K.D. McKeegan, H.A. Storms and H.W. Werner (Eds.), Secondary Ion Mass Spectrometry VII, Wiley, Chichester, 1990, p. 103.
[66] K. Wittmaack and D.B. Poker, Nucl. Instrum. Meth. Phys. Res., B47 (1990) 224.
[67] R.D. Barlow, M.G. Dowsett, R. Valizadeh and J.A. Van den Berg, unpublished results.
[68] R. Badheka, M. Wadsworth, D.G. Armour, J.A. van den Berg and J.B. Clegg, Surf. Interface Anal., 15 (1990) 550.
[69] P.C. Zalm and R.C.M. de Kruif, Appl. Surf. Sci., 70 (1993) 73.
[70] P.C. Zalm, personal communication.
[71] M.G. Dowsett, P.N. Allen and G. Rowlands, Surf. Interface Anal., in press.
[72] J.E. Turner, Jun Amano, C.M. Gronet and J.F. Gibbons, Appl. Phys. Lett., 50 (1987) 1601.
[73] N.L. Mattey, M. Hopkinson, R.F. Houghton, M.G. Dowsett, D.S. Mcphail, T.E. Whall, E.H.C. Parker, G.R. Booker and J. Whitehurst, Thin Solid Films, 184 (1990) 1648.
[74] N.L. Mattey, M.G. Dowsett, E.H.C. Parker, T.E. Whall, S. Taylor and J.F. Zhang, Appl. Phys. Lett., 57 (1990) 1648.
[75] R.D. Barlow, M.G. Dowsett, H.S. Fox R.A.A. Kubiak and S.M. Newstead, Nucl. Instrum. Methods, B72 (1992) 442.
[76] K. Wittmaack, J. Vac. Sci. Technol. B, in press.
[77] M.G. Dowsett and E.A. Clark, in D. Briggs and M.P. Seah (Eds.), Practical Surface Analysis, Vol. 2, Wiley, Chichester, 1990, Chap. 5.
[78] P.C. Zalm, G.F.A. van de Walle, D.J. Gravesteijn and A.A. van Gorkum, Appl. Phys. Lett., 55 (1989) 2520.
[79] D.J. Gravesteijn, P.C. Zalm, G.F.A. van de Walle, C.J. Vriezema, A.A. van Gorkum and L.J. van IJzendoorn, Thin Solid Films, 183 (1989) 191.
[80] M. Meuris, P. De Bisschop, W. Vandervorst, J.A. Jackman, T.E. Jackman, in A. Benninghoven, C.A. Evans, K.D. McKeegan, H.A. Storms and H.W. Werner (Eds.), Secondary Ion Mass Spectrometry SIMS VII, Wiley, Chichester, 1990, p. 623.
[81] J.B. Clegg and R.B. Beall, Surf. Interface Anal., 14 (1989) 307.
[82] R. Badheka, J.A. van den Berg and D.G. Armour, Vacuum, 44 (1993) 331.
[83] M.G. Dowsett, Fresenius' J. Anal. Chem., 341 (1991) 224.
[84] H.H. Andersen, Appl. Phys., 18 (1979) 131.
[85] K. Wittmaack, Vacuum, 34 (1984) 119.
[86] P.C. Zalm and C.J. Vriezema, Nucl. Instrum. Meth. Phys. Res., B67 (1992) 495.
[87] Y.T. Cheng, Mater. Sci. Rep., 5 (1990) 495.
[88] M. Petravic, R.G. Elliman and J.S. Williams, in A. Benninghoven, K.T.F. Janssen, J. Tümpner and H.W. Werner (Eds.), Secondary Ion Mass Spectrometry SIMS VIII, Wiley, Chichester, 1990, p. 367.
[89] M. Petravic, B.G. Svensson and J.S. Williams, Appl. Phys. Lett., 62 (1993) 278.
[90] K. Wittmaack, J. Appl. Phys., 53 (1982) 4817.
[91] Y. Homma and K. Wittmaack, Appl. Phys., A50 (1990) 417.
[92] K. Wittmaack, J. Vac. Sci. Technol., A3 (1985) 1350.
[93] M. Meuris, W. Vandervorst and J. Jackman, J. Vac. Sci. Technol., A9 (1991) 1482.
[94] P.R. Boudewijn, H.W.P. Ackerboom and M.N.C. Kemperers, Spectrochim. Acta, 39b (1984) 1567.
[95] K. Wittmaack and N. Menzel, Appl. Phys. Lett., 50 (1987) 815.
[96] J.A. Kilner, D.S. McPhail and S.D. Littlewood, Nucl. Instrum. Meth. Phys. Res., B64 (1992) 632.
[97] M. Meuris, W. Vandervorst, P. De Bisschop and D. Avau, Appl. Phys. Lett., 54 (1989) 1531.
[98] W. Vandervorst and T. Clarysse, J. Vac. Sci. Technol., B10 (1992) 302.
[99] E.-H. Cirlin, J.J. Vajo and T.C. Hasenberg, in Proc. Second International Workshop on the Measurement and Characterization of Ultra-Shallow Doping Profiles in Semiconductors, R. Subrahmanyan, C.M. Osburn and P. Rai-Choudhury (Eds.), Microelectronics Centre of North Carolina, 1993, p. 171.
[100] K. Wittmaack, J. Vac. Sci. Technol., A8 (1990) 2246.
[101] S. Duncan, R. Smith, D.E. Sykes and J.M. Walls, Vacuum, 34 (1984) 145.
[102] F.A. Stevie, P.M. Kahora, D.S. Simons and P. Chi, J. Vac. Sci. Technol., A6 (1987) 76.
[103] A. Benninghoven, K.T.F. Janssen, J. Tümpner and H.W. Werner (Eds.), Secondary Ion Mass Spectrometry SIMS VIII, Wiley, Chichester, 1990, pp. 323–358.
[104] G. Carter, M.J. Nobes, G.W. Lewis and C.R. Brown, Surf. Interface Anal., 7 (1985) 35.
[105] C.W.T. Bulle-Lieuwma and P.C. Zalm, Surf. Interface Anal., 10 (1987) 210.
[106] A.D. Buonaquisti, D. Ricks, Y. Ryabov, D.P. Griffis and

J.L. Hunter Jr., in Proc. Second International Workshop on the Measurement and Characterization of Ultra-Shallow Doping Profiles in Semiconductors, R. Subrahmanyan, C.M. Osburn and P. Rai-Choudhury (Eds.), Microelectronics Centre of North Carolina, 1993, p. 245.

[107] S.M. Bedair, in Proc. Second International Workshop on the Measurement and Characterization of Ultra-Shallow Doping Profiles in Semiconductors, R. Subrahmanyan, C.M. Osburn and P. Rai-Choudhury (Eds.), Microelectronics Centre of North Carolina, 1993, p. 16.

[108] V.V. Makarov, Surf. Interface Anal., 20 (1993) 821.

ELSEVIER

Analytica Chimica Acta 297 (1994) 277–283

ANALYTICA CHIMICA ACTA

Secondary-neutral and secondary-ion mass spectrometry analysis of TiN-based hard coatings: an assessment of quantification procedures

W. Bock, H. Gnaser *, H. Oechsner

Fachbereich Physik and Institut für Oberflächen- und Schichtanalytik, Universität Kaiserslautern, D-67663 Kaiserslautern, Germany

(Received 29th September 1993; revised manuscript received 1st November 1993)

Abstract

Secondary-neutral mass spectrometry (SNMS) utilizing electron-gas post-ionization and secondary-ion mass spectrometry (SIMS) monitoring MCs^+ ion species (M stands for a sample component) were used to characterize TiN-based film structures, namely TiCN and TiAlN/TiN. It is shown that for both techniques a quantitative evaluation of the depth-dependent composition is possible employing relative sensitivity factors. While the latter were derived from various standard materials, the corresponding factor for C/N could be determined from a correlation of the respective intensities in the TiCN specimen and rendered a standard superfluous for those elements; this approach was found to work for both SNMS and SIMS. The sample compositions determined by these techniques exhibit generally a good agreement with respect to the absolute concentration values and their depth dependence; a possible exception is the Ti/N ratio in the TiAlN sample which appears larger in SNMS than in SIMS. The general concepts of quantification using relative sensitivity factors and their transferability among different specimens are discussed.

Keywords: Mass spectrometry; Caesium; Coatings; Secondary-neutral and secondary-ion MS; Thin films; Titanium

1. Introduction

Secondary-neutral mass spectrometry (SNMS) is, by now, a mature technique for the analysis of solid surfaces and thin films [1]. In particular, post-ionization by means of the electron component of a low-pressure plasma (electron-gas SNMS [2]) has been developed to a high degree of sophistication and reliability. Among the advantages of this method is the comparatively simple quantification scheme based on the use of sensitivity factors. The latter appear largely independent of sample composition and are mostly element-specific (a minor influence of the specimen may occur at low bombarding energies due to variations of the angular and energy distributions of sputtered particles [3,4]). Thus, a quantitative evaluation of very different specimens using one and the same set of sensitivity factors is possible. This insensitivity of calibration factors towards sample composition is due to the decou-

* Corresponding author.

SSDI 0003-2670(93)E0626-I

pling of the emission process (sputtering by ion bombardment) from the ionization step of the sputtered neutrals in the plasma [2]. This kind of separation is not found in the emission of secondary ions and, not surprisingly, the ionization probabilities of those species generally exhibit an extreme sensitivity towards variations of sample composition [5]. This so-called matrix effect, in fact, severely complicates quantification procedures in secondary-ion mass spectrometry (SIMS) and prevented a more general application of this technique to quantitative analysis, despite its inherently high detection sensitivity [6]. Recently, however, it was demonstrated that the quantification of SIMS data can be improved considerably by monitoring MCs^+ secondary ions (where M stands for an element contained in the sample) which are emitted under Cs^+ primary ion bombardment. The existence of these species is well established for quite some time [7] and they have been used for the sensitive detection of selected elements (e.g. the rare gases [8]). A much wider application [9–14] came with the observation that matrix effects which are common for atomic secondary ions, are strongly reduced or even absent for MCs^+ ions. Under these conditions sensitivity factors can be used for the quantitative evaluation of SIMS intensities and the viability of this approach has been shown for various binary and ternary alloys [15,16]. It is formally equivalent to the one employed in SNMS.

It was the scope of the present study to compare these quantification procedures for SNMS and SIMS and to highlight the respective advantages and limitations. These investigations were carried out for two TiN-based thin film structures (TiCN and TiAlN). While these types of hard coatings are of increasing technological importance their analytical characterization with respect to depth-dependent composition is often difficult. First, these layers tend to exhibit very low erosion rates in sputtering and therefore high current densities are required; second, the detection of nitrogen in TiN poses problems in Auger electron spectroscopy (AES) due to the overlapping with a Ti peak; also, the analysis of these light elements is generally demanding due to interferences from residual gas adsorption on the surface. It will be shown that both electron-gas SNMS and SIMS utilizing MCs^+ are suited to circumvent those and related problems and to provide a quantitative characterization of such TiN-based thin film structures.

2. Experimental

The SNMS measurements were performed in a Leybold INA-3 secondary neutral mass spectrometer described in detail elsewhere [17]. In brief, the electron component (density ca. 10^{10} cm^{-3}) of a low-pressure (1.5×10^{-3} mbar) rf (Argon)-plasma sustained by electron cyclotron wave resonance [18] is employed for post-ionizing sputtered neutral species. To effect sputtering, ions are extracted from this plasma and accelerated onto the target which is biased negatively. For the current measurements an impact energy of 500 eV was chosen; the current density was about 1.2 mA/cm^2. Leaving the plasma, post-ionized neutral species are guided into the quadrupole mass spectrometer by means of two sets of electrostatic lenses and a 90° energy analyzer.

The SIMS measurements were carried out in a Cameca IMS-4f ion microscope [19]. A Cs^+ primary ion beam with an impact energy of 5.5 keV was used, resulting in an incidence angle of 42° with respect to the surface normal. Typical beam currents were 25 nA and the focused ion beam was scanned across a sample area of 65×80 μm^2. Positive secondary ions were accepted from a circular area limited to a diameter of 33 μm by ion optical means. The instrument was operated at a mass resolution of 300 and an energy window of 130 eV. The working pressure in the sample chamber amounted to about 1.5×10^{-9} mbar.

The samples were TiCN and TiAlN films (thickness 3–4 μm) deposited on WC substrates. For TiCN the deposition was performed keeping Ti roughly constant and varying C and N. Thus the stoichiometry of the film is close to TiC_xN_{1-x} with a varying value x. TiAlN was deposited with constant composition, with an additional TiN buffer layer sandwiched between the substrate and the film.

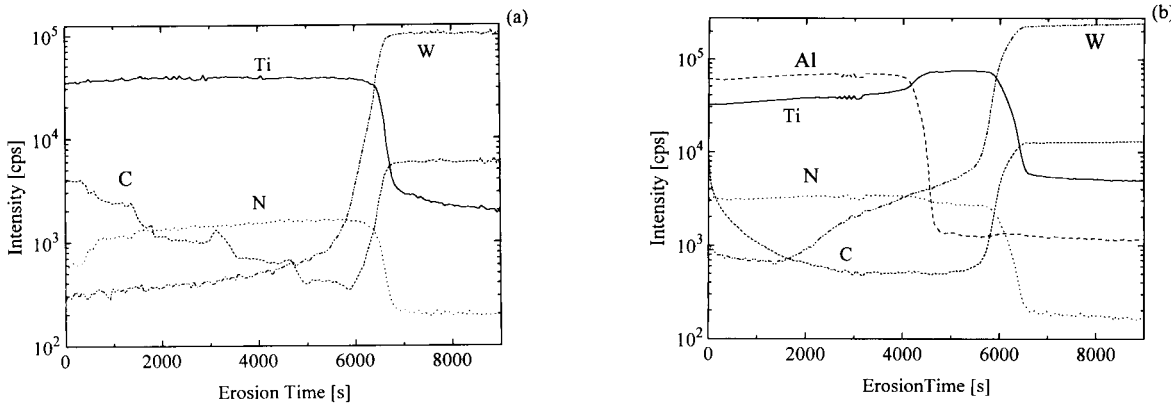

Fig. 1. SNMS depth profiles of the (a) TiCN and of the (b) TiAlN/TiN specimens. 500 eV Ar^+ bombardment at a current density of 1.2 mA/cm^2.

3. Results and discussion

Fig. 1a and b shows the SNMS sputter depth profiles of the TiCN and TiAlN films, respectively. The intensities of the post-ionized sputtered neutrals are plotted versus the erosion time of the samples. The predicted film compositions are reproduced. In the TiCN film the concentrations of C and N vary while the Ti signal remains constant. The TiAlN film shows a constant elemental stoichiometry and the TiN buffer layer.

SIMS depth profiles of the TiCN and the TiAlN specimen are depicted in Fig. 2a and b, respectively. MCs^+ secondary ions of all the sample components were recorded with the exception of WCs^+ which falls beyond the mass range of the instrument (< 280 amu). In addition, the signal of resputtered Cs^+ ions was monitored. This species exhibits quite pronounced intensity variations, in particular between the TiN-containing layers and the WC substrates. Changes of Cs^+ ion yields among different matrices have

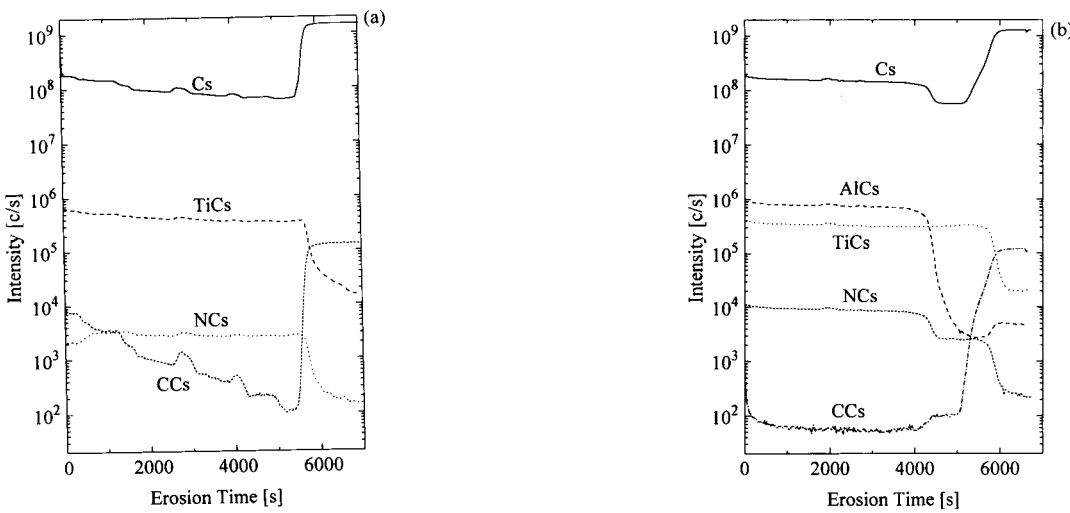

Fig. 2. SIMS depth profiles of the (a) TiCN and of the (b) TiAlN sample monitoring Cs^+ and the MCs^+ secondary ions indicated. A 5.5 keV Cs^+ primary ion beam with a current density of 0.5 mA/cm^2 was used.

been observed before [13,20] but they were usually rather moderate (a factor of 5 at the most). While the origin of this difference is not clear yet, they exemplify the extreme and well-documented dependence of atomic secondary ion yields on sample composition. Not surprisingly, this variation of Cs^+ intensity is also reflected in corresponding variations of the MCs^+ intensities (see the discussion below).

4. Quantification procedures

The quantification of SNMS data is usually done via (relative) sensitivity factors. The intensity of a post-ionized sputtered neutral atom is then given by

$$I_A = I_p Y c_A S_A \quad (1)$$

where I_p is the primary ion flux (ions/s), Y the sample's sputtering yield (sputtered atoms/ion), c_A the concentration of element A and S_A the sensitivity factor for A (detected atoms A/sputtered atom A). In this simple form Eq. 1 is valid if element A is sputtered predominantly as a neutral atom, that is to say, other emission channels (e.g., molecules or secondary ions) are negligible, a condition that is most often fulfilled. The sensitivity factor for a given species depends on the post-ionization efficiency and on some geometrical and transmission parameters determined by the specific instrumental arrangement. Provided they are independent of the sample composition, a set of $(n-1)$ *relative* sensitivity factors (derived e.g. from a standard) suffices for the quantification of a specimen with n components; this approach has been employed rather extensively in electron-gas SNMS. Nevertheless, this concentration evaluation is sometimes impossible due to the lack of appropriate standards. Especially in the case of the N containing hard coatings of concern in the present work, suitable standards with sufficiently well known compositions are hardly accessible. In these cases the sensitivity factors may be taken from a standard with a different matrix or estimated as a rough approximation according to the sputtered particles ionization potential and flight time through the plasma [1,21]. If samples with different stoichiometry are available, there is another way to get the sensitivity factors for the system under consideration: In binary systems correlations like Eq. 1 for components A and B can be combined to

$$I_A = Y I_p S_A - (S_A/S_B) I_B \quad (2)$$

Thus, a linear dependence between I_A and I_B results if I_p, Y and the sensitivity factors are constant; the slope yields S_A/S_B. With this rather general approach (frequently used for example in AES [22]) a quantitative evaluation is possible without resorting to a standard [16]. From an independent determination of Y also the absolute sensitivity factors can be derived, see Eq. 2. The advantage of this method is not only to get a sensitivity factor at all, its value for sure is valid for the very system to be analyzed and one does not have to consider influences of the aforementioned matrix effects.

The arguments outlined above should apply also for the quantification of SIMS and, in fact, have been used in some selected cases [9–11,15,16]. A major difference, however, results from the molecular nature of the detected species. Current experimental observations [12,13] and theoretical concepts [23] indicate that MCs^+ ions form by the combinative association of a Cs^+ ion and a neutral M atom. This emission model is well suited to rationalize the apparent lack of matrix effects: resputtered cesium atoms exhibit a high degree of ionization (close to 100% in many cases) while the flux of M atoms depends, as in SNMS (cf. Eq.1), only on the sputtering yield Y and the concentration c. For SIMS, therefore, the intensity of an MCs^+ ion should depend on I_{Cs^+} and Eq. 1 has to be extended by this quantity (strictly speaking, the above-mentioned MCs^+ formation scheme implies a dependence on the particle densities rather than the fluxes; energy distributions indicate, however, that those differences are negligible). While for the quantification via Eq. 1 employing relative sensitivity factors the I_{Cs^+} contribution will cancel out, in an evaluation according to Eq. 2 they probably are important (formally they might be equivalent to a sputter yield variation) and have to be considered.

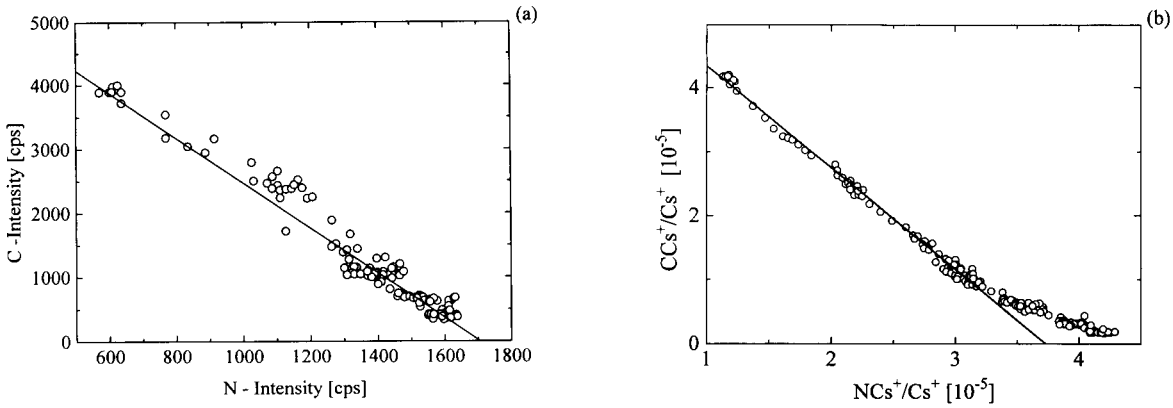

Fig. 3. (a) Correlation between the SNMS intensities of C and N atoms sputtered from the TiCN layer (see Fig. 1a). The straight line is a least-squares fit to the data and yields the relative sensitivity factor for these elements; (b) as in (a) but for the SIMS signals of CCs^+ and NCs^+ normalized to the Cs^+ intensity.

In the following a quantitative evaluation of the depth profiles presented in Figs. 1 and 2 using relative sensitivity factors will be given. For the TiCN sample a correlation between C- and N-specific signals in accordance with Eq. 2 could be established both by SNMS and by SIMS. These data are shown in Fig. 3. In both cases only data points from the TiCN layer were employed while those from the interface region and the substrate were omitted; in that range drastic sputter yield changes do occur and the assumption of a binary system underlying Eq. 2 will break down. Indications of such deviations are observed probably in the SIMS plot for low CCs^+ values, see Fig. 3b. From the respective slopes relative sensitivity factors $S_C/S_N = 3.5$ for SNMS and $S_{CCs}/S_{NCs} = 1.6$ for SIMS were derived. The latter compares quite favourably with a value of $S_{CCs}/S_{NCs} = 1.74$ obtained by SIMS from a different set of specimens, namely nitrogenated amorphous carbon layers [16]. This close agreement clearly demonstrates the robustness of MCs^+-derived sensitivity factors against sample composition changes.

Complete concentration plots for the TiCN specimen are shown in Fig. 4. To create these data for SNMS the following additional sensitivity factors were used: $S_{Ti}/S_N = 18$ was taken from a TiN sample of known composition and $S_{Ti}/S_W = 3.6$ was derived from metallic samples. For SIMS the value $S_{TiCs}/S_{NCs} = 119$ was determined from

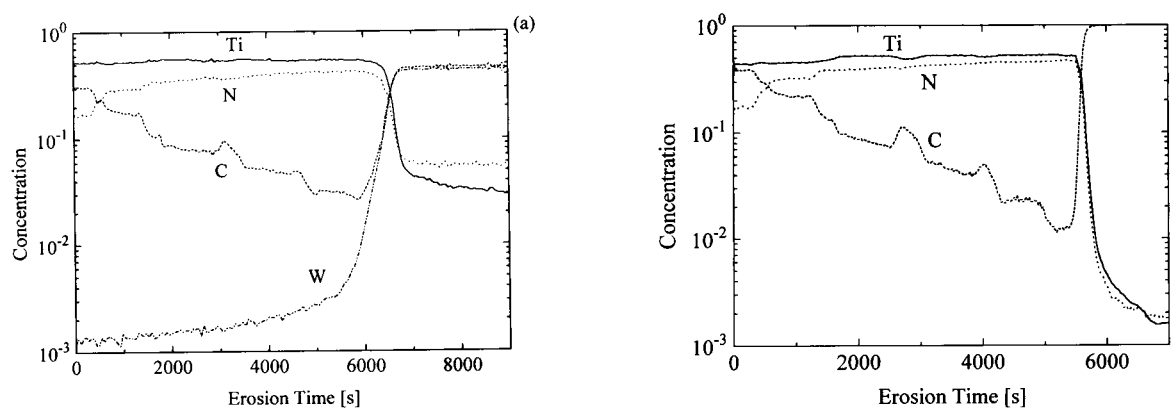

Fig. 4. Depth-dependent concentrations of the elements in the TiCN film derived by SNMS (a) and SIMS (b) using the data shown in Figs. 1 and 2, respectively, and relative sensitivity factors for quantification (see text).

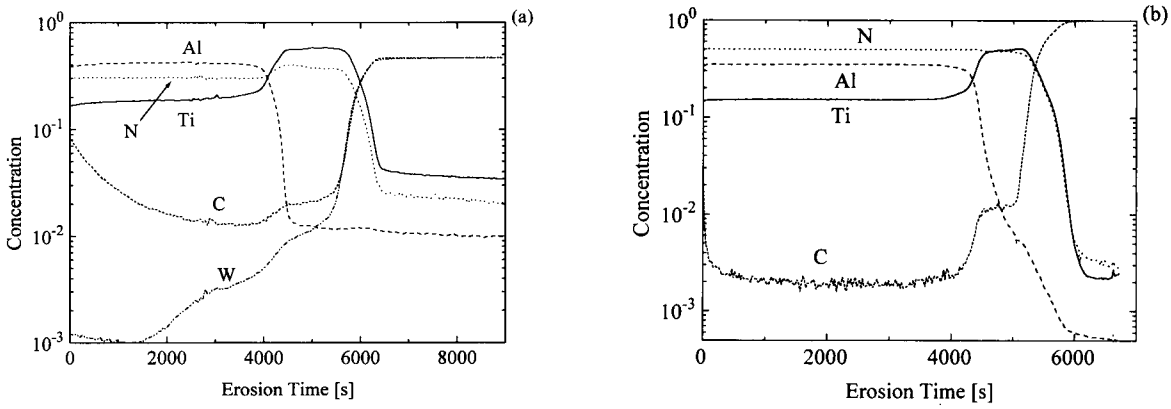

Fig. 5. As in Fig. 4, but for the TiAlN specimen.

the same TiN standard. A comparison of SNMS and SIMS results indicates that both techniques produce depth-dependent composition profiles which agree rather closely. Detailed scrutiny of the data reveals a somewhat higher N/Ti ratio towards the interface in SIMS and a lower near-surface concentration of carbon in SNMS. Both techniques confirm a roughly constant Ti concentration throughout the film, although the SIMS data indicate a slightly lower Ti content near the surface. With c_{Ti} constant the remaining components form essentially a binary system and that is apparently the reason why correlations in agreement with Eq. 2 could be observed, see Fig. 3. Furthermore, the sputtering yield as evaluated from Eq. 1 exhibits little variation with film composition. This constitutes yet another condition for the applicability of Eq. 2.

By contrast, the constant concentrations of the major components in the TiAlN specimen (cf. Fig. 5) did not provide the possibility to establish those intensity correlation plots. For a quantitative evaluation relative sensitivity factors derived from standards ($S_{Ti}/S_{Al} = 1.43$ in SNMS and $S_{TiCs}/S_{AlCs} = 0.99$ for the SIMS data) were used in addition to those already utilized for the TiCN layer (see above). The corresponding depth-dependent concentrations are shown in Fig. 5a and b for SNMS and SIMS, respectively. Here, these techniques produce somewhat different results; while the Ti concentration is roughly identical for both methods, the stoichiometry of the TiN buffer layer is essentially one-to-one in SIMS, but $c_{TI}/c_N \approx 1.5$ in SNMS. The same difference in the Ti/N concentration ratio is also observed in the TiAlN layer. As a consequence, the Al content as determined by SNMS is about 42 at% while it is roughly 35% according to the SIMS evaluation. The reason for this discrepancy is not quite clear, but the relative sensitivity factors Ti/N were expected to be sensitive towards changes in sample composition for both techniques. To clarify this problem the value S_{TiCs}/S_{NCs} for SIMS was determined also from a metallic reference material; the value derived in that case (ca. 114) is very close to what was used in the evaluation of Fig. 5b, namely 119. Clearly, the accuracy of the quantitative data evaluation depends on the determination of the relative sensitivity factors and their transferability between different samples. The analyses shown in Figs. 4 and 5 indicate that the latter might limit the accuracy of quantification to a factor of 1.5 in extreme cases (e.g. for elements like carbon and nitrogen). A better accuracy (ca. 20%) can be expected for metallic elements, an anticipation supported by the concentration data of Al and Ti depicted in Figs. 4 and 5.

5. Conclusions

The quantitative characterization of TiN-based hard coating layers by SNMS and SIMS shows

good agreement between these techniques. While in electron-gas SNMS the application of relative sensitivity factors and their independence for different samples is well established, this approach is apparently valid also for SIMS and is largely due to the use of MCs^+ secondary ions which are rather insensitive against specimen composition. Clearly, for those species the Cs^+ ion yield may influence the intensity of MCs^+ ions; the Cs^+ yields exhibit generally some matrix-dependent variations (cf. Fig. 2) which probably are governed by the work-function of the specimen. The latter is modified by the amount of cesium incorporated into the near-surface region of the sample. This Cs saturation concentration, in turn, will be determined by parameters like the sputtering yield, the primary-ion impact angle [13] and various material-specific quantities. Unfortunately, the understanding of these processes and their influence on MCs^+ ion yields is still limited. To fully exploit MCs^+ species for SIMS quantification those effects deserve thus further scrutiny.

The accurate determination of the sensitivity factors for light elements (C and N in the present case) may constitute a special problem for both techniques. In SNMS light species tend to exhibit different angular emission distributions relative to heavier species at the low bombarding energies typically used. Conceivably, this effect might depend on the elements contained in the specimen and might cause some shift of the relative sensitivity factors. In SIMS MCs^+ ions of these light elements have comparatively low intensities; furthermore, other molecular ions carrying those elements are observed (e.g. $TiNCs^+$, $TiCCs^+$ or CCs_2^+ in the present experiments) and the possible interplay between those emission channels has not been established as yet. Despite these limitations the present study demonstrates the applicability of MCs^+ ions for a quantitative evaluation of SIMS data. Of particular interest for both techniques is the possibility to derive relative sensitivity factors directly from intensity correlations rendering external standards superfluous.

References

[1] H. Oechsner, Nucl. Instrum. Methods, B33 (1988) 918.
[2] H. Oechsner, in H. Oechsner (Ed.), Thin Film and Depth Profile Analysis, Springer, Berlin, 1984, p. 63.
[3] A. Wucher, F. Novak and W. Reuter, J. Vac. Sci. Technol., A6 (1988) 2265.
[4] A. Wucher and W. Reuter, J. Vac. Sci. Technol., A6 (1988) 2316.
[5] A. Benninghoven, F.G. Rüdenauer and H.W. Werner, Secondary Ion Mass Spectrometry, Wiley, New York, 1987.
[6] R.G. Wilson, F.A. Stevie and C.W. Magee, Secondary Ion Mass Spectrometry, Wiley, New York, 1989.
[7] H.A. Storms, K.F. Brown and J.D. Stein, Anal. Chem., 49 (1977) 2023.
[8] M.A. Ray, J.E. Baker, C.M. Loxton and J.E. Greene, J. Vac. Sci. Technol., A6 (1988) 44.
[9] Y. Gao, J. Appl. Phys., 64 (1988) 3760.
[10] C.W. Magee, W.L. Harrington and E.M. Botnick, Int. J. Mass Spectrom. Ion Proc., 103 (1990) 45.
[11] H. Gnaser and H. Oechsner, Surf. Interface Anal., 17 (1991) 646.
[12] H. Gnaser and H. Oechsner, Fresenius, J. Anal. Chem., 341 (1991) 54.
[13] K. Wittmaack, Nucl. Instrum. Methods, B64 (1992) 621.
[14] H. Gnaser and H. Oechsner, Nucl. Instrum. Methods, B64 (1992) 646.
[15] H. Gnaser, W. Bock, H. Oechsner and T.K. Bhattacharyya, Appl. Surf. Sci., 70/71 (1993) 44.
[16] M. Haag, H. Gnaser and H. Oechsner, in A. Benninghoven et al. (Eds.), Secondary Ion Mass Spectrometry SIMS IX, Wiley, Chichester, 1994, in press.
[17] R. Jede, H. Peters, G. Dünnebier, O. Ganschow, U. Kaiser and K. Seifert, J. Vac. Sci. Technol., A6 (1988) 2271.
[18] H. Oechsner, Plasma Phys., 16 (1974) 835.
[19] H.N. Migeon, C. Le Pipec and J.J. Le Goux, in A. Benninghoven et al. (Eds.), Secondary Ion Mass Spectrometry SIMS V, Springer, Berlin, 1986, p. 155.
[20] H. Gnaser and H. Oechsner, Surf. Interface Anal., in press.
[21] A. Wucher, J. Vac. Sci. Technol., A6 (1988) 2287.
[22] P.M. Hall, J.M. Morabito, and D.K. Conley, Surf. Sci., 62 (1977) 1.
[23] H. Gnaser and H. Oechsner, Surf. Sci. Lett., in press.

ELSEVIER

Analytica Chimica Acta 297 (1994) 285–300

ANALYTICA CHIMICA ACTA

Plasma secondary-neutral and secondary-ion mass spectrometry investigations on ceramic/copper powder pellets

Holger Jenett[a,1,*], Matthias Luczak[b], Olivier Dessenne [c]

[a] *Institut für Spektrochemie und angewandte Spektroskopie (ISAS), Bunsen-Kirchhoff-Str. 11, Postfach 101352, D-44013 Dortmund, Germany*

[b] *Fachhochschule Münster, Abt. Steinfurt, Fachbereich Chemieingenieurwesen, Stegerwaldstraße 62, D-48565 Steinfurt, Germany*

[c] *Pechiney Centre de Recherche de Voreppe (CRV), B.P. 27, F-38340 Voreppe, France*

(Received 5th October 1993; revised manuscript received 30th November 1993)

Abstract

As a preliminary quantification study on ceramic materials using electron gas (or plasma) secondary-neutral mass spectrometry, matrix effects are demonstrated in terms of relative element sensitivity factors which are obtained from Cu pellets containing the ceramic powders AlN, BN, TiN, $Si_9N_4O_6$, B_4C and SiC. Additionally, measurement conditions are varied within the range of typical practical conditions. Matrix and instrumental effects are discussed on the background of "usual", energy, negative secondary ion and negatively post-ionized sputtered neutral spectra yielding evidence that the emission of not only molecular, but also thermal and negative particles has to be included into the evaluation of matrix effects. The negative mode using direct Ar^+ bombardment from the plasma is introduced into plasma secondary-neutral and secondary-ion mass spectrometry.

Keywords: Mass spectrometry; Ceramics; Copper; Carbides; Nitrides

1. Introduction

In principle, plasma secondary-neutral mass spectrometry (SNMS) signals are matrix independent, and quantification is straightforward, because atomization (sputtering) and excitation (ionization) processes are decoupled [1]. As a consequence of this, the simple equation [2]

$$I_X = I_P \cdot Y_{tot} \cdot c_X \cdot D_X \quad (1)$$

(where I_x = measured intensity of positively post-ionized secondary neutral atoms (SN^+) of element X, I_p = primary ion current, Y_{tot} = total sputter yield of the sample material, c_X = concentration (mole fraction), D_X = detection (sensitivity) factor or useful yield) can be applied – if the emission of positive and negative secondary ions ($SI^{\pm}$) and neutral clusters are negligible, and if D_X is not matrix dependent. The

* Corresponding author.

[1] Major parts of this work have been presented on the 7. Tagung Festkörperanalytik, June 22–25, 1993, Chemnitz, Germany, and on the 3rd Int. Workshop on Postionization Techniques in Surface Analysis (PITSA 3), Nov. 2–5, 1993, Kawaguchi-ko, Japan, minor parts also on the 9th Int. Conf. on Secondary Ion Mass Spectrometry (SIMS IX), Nov. 7–12, 1993, Yokohama, Japan.

SSDI 0003-2670(93)E0675-W

detection factor D_X can be written as [2]

$$D_X = \frac{Y_X}{c_X \cdot Y_{tot}} \beta_X^0 \cdot \alpha_X^+ \cdot W_X \cdot T_X \quad (2)$$

(where Y_X = sputter yield of X atoms, being $c_X \cdot Y_{tot}$ in the simplest case (i.e., proportional sputtering of X atoms only), β_X^0 = fraction of X atoms emitted in charge state 0, α_X^+ = probability of positive post-ionization of X atoms, W_X = fraction of X^+ particles reaching the ion optics, T_X = optics transmission and detector sensitivity for X^+ particles). For simplicity and practical reasons, only one type of primary particles (Ar^+), a homogeneous ion beam and one ionization type of the secondaries ($0 \rightarrow +1$) are regarded. Therefore, the remaining parameters to be considered are the emission angle and the energy of the sputtered X atoms.

D_X can be related to the detection factor D_{ref} of a reference element [3]:

$$D_{ref,X} = \frac{D_X}{D_{ref}} = \frac{I_X}{I_{ref}} \cdot \frac{c_{ref}}{c_X} \quad (3)$$

This definition is inverse to $D_{X,ref} = D_{ref}/D_X$, which has been more common in SNMS (see, e.g. [2,4]), but it makes more sense and has also in part been used in inorganic mass spectrometry, e.g. [5,6].

Cluster [7–9] and $SI^{\pm}$ emissions [2,3] as well as variations in energy [10] and angular [3] distributions do not play an important role with metals, apart from larger mass differences in alloys which may change angular distributions especially at low energies [11]. On the whole, this allows the straightforward application of Eq. 3 for metals in nearly every case. This might be different for ceramic materials which typically are electrically nonconductive and have, at least in part, covalent chemical bonds, as is the case with B and Si compounds. Furthermore, they contain the light elements B, C, N and/or O, the latter two belonging to the most electronegative ones and being gaseous in elementary form. In fact, first SNMS studies on oxide powders pressed in Fe/Cu pellets [12] and on various oxyanion salts [5] show, at least in part, large deviations for O. Therefore, in the present work attention is focused on the relative deviation between maximum and minimum $D_{ref,X}$ and on the chemical and physical context of these extremes in order to step into the direction of better SNMS quantification even for "difficult", but important, materials such as technological ceramics. Therefore, as one of the first steps in this direction [5,12], some μm fine ceramic powders, pressed into Cu in order to circumvent the charging problem, are investigated with respect to severe deviation of sensitivity factors. Then energy and SN/SI^- spectra are recorded under some typical experimental conditions and discussed especially in the cases with reproducible extreme deviations of $D_{Cu,X}$.

2. Experimental

The investigated powders are listed in Table 1. Except $Si_9N_4O_6$, all ceramic powders had been manufactured by H.C. Starck, Goslar, Germany. $Si_9N_4O_6$ was a laboratory production (MPI für Metallforschung, PML, Stuttgart, Germany) ready for sintering and therefore contained also 3.3 wt-% Y_2O_3 and 1.7 wt-% Al_2O_3, the O contents of which being included in the gross stoichiometric formula.

First, a series of varying BN concentrations in Cu was prepared as follows: 0.4, 0.2, 0.1 and 0.05 g of BN powder, respectively, were homogenized

Table 1
Powders

Material	Type/ manufacturer [a]	Mean diameter (μm)	Max. deviation from stoichiometry (%) [b]
Cu	r.g./Merck	< 63	0.4 (CuO)
BN	A01/HCSt	1.5	1.1
AlN	A/HCSt	4	5.6
TiN	C/HCSt	0.8	4.4
$Si_9N_4O_6$	(Lab.)/MPI S	3	1.3
B_4C	F1200–3/HCSt	0.8	2.3 (B_2O_3)
SiC	B10/HCSt	< 0.7	1.6 (SiO_2)

[a] HCSt: H.C.Starck, MPI S: MPI für Metallforschung, IWW-PML Stuttgart.

[b] According to N and O bulk analyses, either derived from O content and given as the indicated oxide species derived or from deviating N content.

with 1.6, 1.8, 1.9 and 1.95 g of reagent grade (r.g.) Cu powder by shaking it for 10 min in a closed plexiglass vessel of 1 cm diameter and 5 cm length together with a plexiglass ball of 9 mm diameter. This yielded a concentration series 1:5, 1:10, 1:20 and 1:40 (w:w) in order to check for concentration effects. Second, two (BN: three) 1:20 specimens of each ceramic powder were prepared in the same way. About 0.5 g of every mixture were pressed to a pellet with 60 kN/cm^2. For comparison, r.g. Cu pellets without ceramic powder were pressed. It should be already realized at this point that the residual O content of Cu of 0.1% (w:w), if diffused and bound to the less noble metal components M of the ceramic compounds, would yield molar O:M ratios between 3 and 7%. This is the reason why the thickness ratio between the Cu and the ceramic particles was left relatively high, although it is known from [13] that this may prolong the time to reach a relative sputter equilibrium.

SNMS/SIMS$^-$ measurements were performed using a Leybold INA-3 type instrument (Leybold, Köln, now SPECS, Berlin) in the direct bombardment mode (DBM; attraction of sputtering Ar^+ ions from the plasma by a $U_{DBM} \approx -10^{-1}$ kV bias voltage).

At *first*, the three BN pellets were measured under the conditions given in Table 2 for series A, but with $D = 3$ mm. *Second*, an *asymmetric* sputtering experiment was carried out in order to check for severe angular effects caused by combined emission and optics acceptance functions,

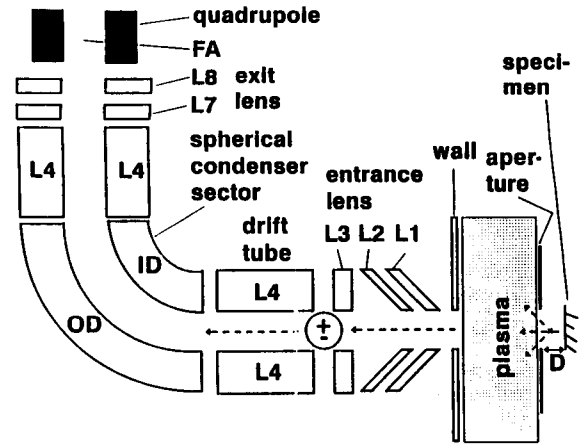

Fig. 1. Schematic of the INA-3 ion optics. The potentials of the different parts shown are given in the text; the metal wall between the plasma chamber and the optics is fixed to earth potential (0 V).

both of them being unknown: One and the same spot of 2 mm diameter (contrary to the general 5 mm, see below) on a 1:20 BN pellet being framed by a mask and a plasma aperture of the same diameters was, with regard to this size, exactly sputtered using $U_{DBM} = -330$ V for $D = 3$ mm (see Fig. 1) until static intensity ratios were reached. The specimen was remounted after every measurement, first centric around the axis of the entrance lens of the optics ($d_e = 0$ mm), then at $d_e = 2$, 4 and 6 mm off axis and then centric again. This procedure was performed once in vertical and once in horizontal direction. *Third*,

Table 2
Measurement conditions

Series	Sample			Plasma				Energy analyzer	
	D (mm)	T (K)	$-U_{DBM}$ (V)	I_M (A)	P_{HF} (W)	I_p (mA)	$-U_p$ (V)	E (eV)	C_{Perf}
Asymmetric	3	328 ± 3	330	5.6	160–40	0.24	5.0	49	0.47
c_{BN} variation	3	330 ± 1	270	5.8	190–60	0.28	3.5 ± 0.2	46	0.50
A	2	150 ± 20	260	5.5	180–30	0.25	2.2–4.0	47–58	0.47–0.52
B	3	330 ± 10	390	5.8	185–55	0.28	3.2	56	0.46
Energy spectra	3	330 ± 1	270	5.8	180–55	0.28	3.7 ± 0.2	var.	0.47
DBM-SI$^-$,SN$^-$	3	324	270	5.7	155–48	0.23	5.8	270	0.47

D = distance between surface and plasma aperture, T = sample temperature, U_{DBM} = DBM voltage, P_{HF} = RF power (input-reflected), I_M = magnet coil current, $C_{Perf} = (U_{L4} - U_{ID})/(U_{OD} - U_{ID})$ performance constant (spherical condenser condition: $C_{Perf} \approx 0.45$).

the series with varying BN concentration ("c_{BN} *variation*", see also Table 2) was measured. *Fourth*, two SNMS measurement *series A* (subdivided into a and b because of plasma and optics variations) *and B* were performed on all powder specimens in the range of typical practical measurement conditions. *Fifth*, a series of energy spectra was taken under the conditions specified below. *Finally*, negative ion spectra were obtained after first experiments with energy spectra and inverse polarity had revealed a good performance of the spectrometer for SI^- even in the energy range between 200 and 300 eV.

The instrumental conditions which differed between the series are listed in Tab. 2. The common conditions for all investigations were:

Specimen: Water cooled apart from series A (LN_2). DBM sputtered area 0.2 cm^2 (5 mm diameter).

U_{DBM}: In order to obtain $D_{Cu,X}$ data which would be applicable to future depth profiles, U_{DBM} was adjusted to optimum depth resolution under the given plasma conditions [14] in series A and B. For comparability, especially the energy and negative ion mass spectra were taken under $U_{DBM} = -270$ V. The absolute value of this voltage could not be increased, since U_{FA} (see Fig. 1) has to be adjusted to the ion energy of eU_{DBM} for DBM generated Si^- spectra and is limited to ± 300 V on the commercially available INA-3 instrument at present.

Plasma: Ar pressure (plasma ion gauge reading): 5×10^{-3} mbar, corresponding to about 7 eV plasma electron energy [15]; Ar^+ current to the sample: 0.28 ± 0.01 mA (not corrected for secondary electrons). Probably because of a long-time used Ta foil covering the inner metal walls of the plasma chamber, the amount of previously gettered and now re-emitted O species was considerable, yielding an estimated adsorption rate of $\frac{1}{4}$ O monolayer/s. This is less than 5% of the sputter rate for Cu under the given experimental conditions (5.7 Cu monolayers/s), but it probably forms the most important source of contamination.

Optics (see Fig. 1 and [16]): For "usual" use in the series c_{BN} *variation*, *A* and *B*, all electrode potentials U_{Li} were tuned to maximum peak intensity and optimum (Gaussian) peak shape as well as to plasma gas suppression. Pass energy E and resolution ΔE of the energy filter, calculated according to [17]

$$E/e = 0.909(U_{OD} - U_{ID}) + U_{L4}$$
$$\Delta E/e = 0.0375 \cdot 0.909(U_{OD} - U_{ID}) \quad (4)$$

were adjusted to the actual plasma conditions (see Table 2: "energy analyzer") and set to 8.4 ± 0.1 eV, respectively. The ion optics have not been tuned to the actual plasma conditions in the case of a slowly and moderately changing plasma arising upon prolonged sputtering of Cu. For the *energy spectra*, U_{L1-3} were kept constant as optimized in the "usual" mode; the potentials of the energy filter (U_{L4}, U_{ID} and U_{OD}) as well as the potentials of the focusing system behind (U_{L7}, U_{L8}, U_{FA}) were scanned using a PC connected to the INA-3 computer and suitable computer programs. ΔE was kept constant at 1 eV, thus leaving a constant energy of 26.7 eV to the ions passing the ID/OD deflection system and probably causing a $T_X \propto E_X^{-2}$ transmission because of the two-dimensional suppression of particles with lateral velocity components. For DBM generated *negative SIMS and SNMS*, U_{L1-3} were approximately set to plasma potential $U_{pl} \approx +40$ V. The energy filter was set to $E = e \cdot U_{DBM}$ (SI^-) or 47 (and 9) eV (SN^-) [2], $\Delta E = 2$ eV (SI^-) or 1 eV (SN^-). With respect to SN^- detection it is important to note that the metal wall between the plasma chamber and the ion optics is fixed to ground potential (± 0 V).

Quadrupole: The field axis potential U_{FA} was always kept about 10 V above the potential of ion formation (U_{pl} or, for SI^- spectra, U_{DBM}) so that no energy dependence of the transmisson was to be expected [16]. The typical mass resolution $\Delta m/z$ was near 1 across the mass range 0–100 amu.

[2] As discussed below, parts of the negative ions with $E = 47$ eV also stem from electrically charged residual agglomerations. The mass spectra at this energy show peaks and intensities being similar to the "true" SN^- spectra at $E \approx 9$ eV which are less stable because of yet unknown reasons.

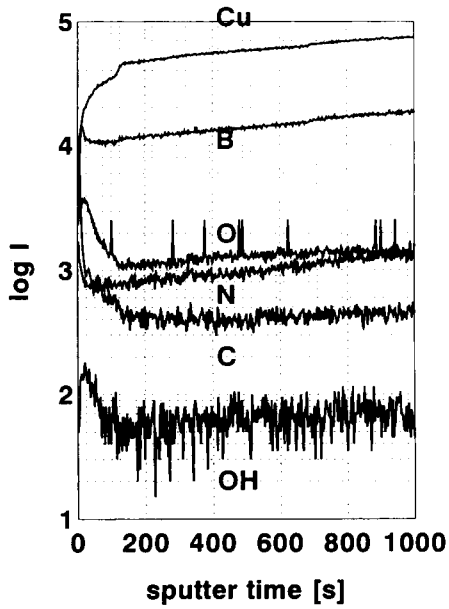

Fig. 2. SN^+ time profile on a freshly prepared BN/Cu pellet.

Multiplier: $-/+2.0$ kV (ion to electron conversion)/ $+2.0$ kV (electrons, start of the plateau region).

SI^- spectra were reproduced using the Ar^+ gun being part of the INA-3 at 5 kV acceleration voltage with the plasma being off, the plasma chamber pumped down to the 10^{-7} level (thus without strict exclusion of residual O contamination) and the specimen sputtered to constant relative intensities.

For each of the series c_{BN} variation, A and B, a new powder pellet was introduced into the plasma chamber of the instrument and sputtered for $\frac{1}{4}$ to 2 h until relative intensities were constant (see Fig. 2). Then 3 repetitive spectra with a "usual" energy window were taken immediately after each other. Blind values of the elements under concern were taken from spectra on the pure, presputtered Cu pellets before and after each sequence.

After the measurements, a pellet of each type was inspected in a scanning electron microscope (SEM) without any further treatment (e.g. gold coating).

3. Results and discussion

3.1. General

The sputtered surfaces exhibit typical cones (Fig. 3), the ceramic tops of which look well connected to the copper below and show no charging effects in the SEM. This finding is independent of the ceramic compound, which is more (TiN) or less (e.g. BN) conductive. Therefore in the following charging effects will only be discussed with respect to the BN pellets of higher concentrations than 1:20. The 1:5 and 1:10 BN pellets, in fact, show larger areas of ceramic agglomerations, thus suggesting doubts that all ceramic material has effectively been sputtered.

Because of the similar surface morphology of all sputtered specimens, differences in the angular distribution of the emitted particles, especially between the light elements C and N and the heavy Cu, are assumed to be the same for all kinds of pellets after sputtering to equilibrium.

From the series asymmetric sputtering, c_{BN} variation, A and B, net element intensities I_X were calculated from the peak heights of all isotopes and molecular species minus the blank values of the pure Cu pellets. It has to be emphasized that no nitride clusters were detectable. Other molecular peaks like M_2^+ (M = metal or semiconductor), C_2^+ and N_2^+ dimers (the latter, in part, not being discernible from Si^+ and CO^+),

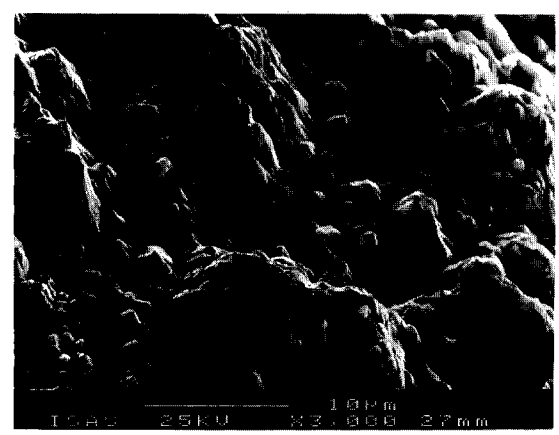

Fig. 3. SEM image of a BN/Cu pellet after about 2 h sputtering.

BO^+ (from the O contaminations), CuO^+, and SiO^+ (from $Si_9N_4O_6$) showed intensity ratios between 10^{-4} and 10^{-2} with respect to the monomer intensity. Blank intensities did not exceed 10^3 cps, apart from mainly (about 70%) "implanted" Ar with an intensity of about 1×10^5 cps. Although that blank level applies also for O^+, neither quantitative evaluation of O signals nor qualitative conclusions from O^+ energy spectra will be drawn. Only the effect of chemical sputtering induced by plasma O will be discussed.

Relative standard deviations (RSDs) of repetitive immediate spectra on one and the same pellet under identical conditions typically lie between 1 and 5%. Using Eq. 3, net element intensities I_X (X = B,C,N,Al,Si,Ti) are related to Cu intensities $I_{ref} = I_{Cu}$ ($\approx 3 \times 10^5$ cps) thus yielding the $D_{Cu,X}$ data in Table 3 and 4. Unless otherwise stated, e.g. using "±" for the RSD of a defined entity, a $D_{Cu,X}$ "deviation" will be given as the ratio of the maximum over minimum data of an entity, if equal to or larger than a factor of 2 (100%), and in percent, if smaller than this value.

The measurements on the three different BN pellets yielded $D_{Cu,N} = 0.034 \pm 0.002$ thus excluding preparation effects from the major topic in the subsequent discussions.

3.2. Asymmetric sputtering (Table 3)

Out of the results of the asymmetric sputtering experiment given in Table 3, the 0, 2 and 4 mm positions are relevant for the typical analyzed area of 5 mm diameter. It becomes visible that combined angular effects of emission and optics acceptance may change $D_{Cu,X}$ by less than 30%. This holds for either direction (v and h) even for the given type of inhomogeneous sample and large mass differences between the elements to be determined (B,N) and the reference element (Cu). From the $D_{Cu,X}$ values decreasing with increasing d_e, one finds that, expectedly [11], the lighter elements are predominantly sputtered in forward direction. Since this happens with exactly the same I_B/I_N ratio irrespective of the direction and the sputtering spot position (RSD ≈ 10% without the d_e = 6 mm (h) data), one might even use the $I_X(d_e)$ intensities of X = B,N for a rough and relative T_X determination with $I_X(d_e = 0) =$ 100%: For d_e = 2, 4 and 6 mm one obtains 94 ± 1, 52 ± 1 and 34 ± 1% in vertical and 34 ± 7, 10 ± 2 and 3 ± 1% in horizontal direction, respectively. These data possibly hold for masses in the 10 to 15 amu range only.

3.3. c_{BN} variation (Table 3)

The results of the c_{BN} variation in Table 3 show that relative B as well as N intensities grow with the BN dilution in the pellet increasing from 1:5 to 1:20. This probably means that at higher BN concentrations (1:5, 1:10), larger areas of ceramic agglomerations are not sputtered because of charging effects. This finding is in conformity with the SEM observations. Interestingly,

Table 3
Results of the (i) asymmetric sputtering and (ii) c_{BN} variation series

(i) Excentric position d_e/mm [a]		0 [b]	2	4	6
$D_{Cu,B}$	v	0.34 ± 0.01	0.27	0.27	0.18
	h	0.32 ± 0.06	0.27	0.25	0.28
$D_{Cu,N}$	v	0.037 ± 0.001	0.031	0.029	0.021
	h	0.036 ± 0.001	0.037	0.034	0.023
$D_{Cu,B}/D_{Cu,N} = I_B/I_N$	v	9.2	8.7	9.3	8.6
	h	8.9	7.3	7.4	12.2
(ii) Mass ratio BN:mixture		1:5	1:10	1:20	1:40
$D_{Cu,B}$		0.40	0.59	0.91	0.89
$D_{Cu,N}$		0.026	0.042	0.080	0.071
$D_{Cu,B}/D_{Cu,N} = I_B/I_N$		15	14	11	13

[a] v = vertical, h = horizontal direction. [b] n = 2.

Table 4
Sensitivity factors $D_{Cu,M\ or\ X}$, observed effects, intensity ratios

Series		A			B	$I(E)$		DBM-SNMS$^-$/SIMS$^-$ [b]			
					matrix effects only						
Material	M	a	b	significant				SI$^-$		SN$^-$ [c]	
	X	$D_{Cu,M\ or\ X}$	$D_{Cu,M\ or\ X}$	effects of... on [a]	$D_{Cu,M\ or\ X}$	$D_{Cu,M\ or\ X}$ from $\int I(E)T^{E,G}dE$	$I^{max}_{M\ or\ X}(E)$	$I_{MN\ or\ C2}/I_{MO2}$	I_{MO2}/I_O	$I_{MN\ or\ C2}/I_{MO2}$	I_{MO2}/I_O
BN	B	0.75	–	matrix on N	0.60	0.67	0.46	0.1	8.5	0.2	1
	N	0.036	–		0.048	0.061	0.14				
AlN	Al	5.0	–		3.0	1.33	0.94	0.003	0.15	n.d.	0.015
	N	0.056	–		0.063	0.16	0.26				
TiN	Ti	2.3	2.3	plasma on N	2.0	2.3	2.4	0.03	0.07	n.d.	n.d.
	N	0.14	0.18		0.11	0.18	0.50				
$Si_9N_4O_6$	Si	1.82	1.92	plasma + optics	1.39	0.78	0.61	0.1	0.2	0.015	0.02
	N	0.14	0.12	on none	0.11	0.28	0.41				
B_4C	B	0.67	0.85	plasma on B	0.58	0.42	0.28	0.02	10	0.01	1.6
	C	0.42	0.53	and C	0.40	0.34	0.99				
SiC	Si	1.85	2.2	plasma on C	2.13	1.73	1.46	3.5	0.5	2	0.01
	C	0.36	0.44	and Si	0.33	0.33	0.19				

[a] Compare a with b, apart from BN with AlN. [b] Hydride intensities included; I_{MN} for the nitrides, I_{C2} for the carbides; n.d. = not detected. [c] $E = 47$ eV

the "normal" emission/post-ionization/detection process seems to be more suppressed for N than for B with higher concentration in Cu, thus enhancing the obvious matrix effect for N to be discussed below. For the following discussions it can be stated that concentration effects may be disregarded for all 1:20 (w:w) concentrations of all ceramic powder pellets, since all concentrations are in the range of the BN 1:20 and 1:40 samples even if recalculated to mole fractions. The differences of the 1:20 value to the results of the asymmetric sputtering series as well as to the $D_{Cu,N}$ data in Table 4 have to be attributed to the differing experimental conditions listed in Table 2 and, maybe more important, to the badly controlled O contamination of the plasma differing between the series.

3.4. Series A, B (Table 4)

The comparison of the $D_{Cu,M}$ data (M = Ti, Si, Al) between the different series in Table 4 and with the theoretical α_M/α_{Cu} of Table 5 shows that the reliability of SNMS quantification is clearly given even for the inhomogeneous matrix under concern as long as typical metals and low mass differences to the reference element are regarded: for M = Ti, a maximum relative difference of "only" 13% is given, whereas this data increases to factors of about 2.5 and 4 for Si and Al, respectively. Instrumental effects as discussed in [18] may be responsible for this to a large extent, because increasing mass differences obviously cause increasing deviations for the individual W_X and T_X (see Eq. 2).

Series A shows a clear matrix effect for N in BN and AlN of about 60%. As the instrumental conditions in series A deviated for the TiN measurements, a further matrix effect cannot be stated at this point. Plasma variations between subseries a and b, in these cases deliberately not followed by optics readjustments, cause $D_{Cu,X}$ deviations between 0 (X = Ti) and nearly 30% (X = N).

Since it was possible to keep all instrumental parameters nearly constant in series B, clear matrix effects can be stated for C (about 20%), N (factor 2) and Si (about 20%), whereas B is unaffected in this case. The matrix effect for C is accompanied by a typical I_{C2}/I_C ratio being twice as high for SiC ($\approx 1\%$) than for B_4C ($\approx 0.5\%$). This, by itself, is far from quantitatively balancing the matrix effect, but it might point to a hidden "parasitic" C emission/ionization channel. The same may be true for the Si compounds with an I_{SiO}/I_{Si} ratio of about 2% for $Si_9N_4O_6$ (massive, but hidden loss of substrate SiO_x?) and 0.3% for SiC (small hidden loss of SiO_x formed with O contamination?).

Table 5
Data to be compared with $D_{Cu,X}$

X	B	C	N	Al	Si	Ti
α_X/α_{Cu} [a]	0.34	0.18	0.082	1.25	0.83	2.3
$D_{Cu,X}$ [b]	–	0.34	0.045	–	1.32	–

[a] Calculated theoretical α_X/α_{Cu} for $T_e = 8.7 \cdot 10^4$ K (7.4 eV) from [27]. [b] Experimental $D_{Cu,X}$ from [5].

However, the most prominent matrix effect having become evident is the $D_{Cu,N}$ variation in series B. After the results discussed above it cannot be attributed to preparation and concentration effects. Since the asymmetric sputtering experiment has not been carried out on other nitrides than BN, enhanced forward N sputtering from AlN, TiN and $Si_9N_4O_6$ cannot be excluded as the reason for the stated matrix effect at this point, although it looks less probable since AlN and $Si_9N_4O_6$ contain metal constituents with approximately the same masses but yield clearly different $D_{Cu,N}$ values. In the following, additional possible contributions are discussed.

From the general findings (see above) it can be concluded that cluster emission according to Oechsner's direct emission model [7] which predominantly holds for high mass differences between the metal and the nonmetal partner in a cluster like TiN can probably be excluded because no TiN^+ signals were obtained in the spectra. The same is true for the atom combination model [8] being applicable to the BN molecule because of its low internal mass difference [7], since no BN^+ clusters were detected in the "usual" SN^+ spectra. So the reproducibly low $D_{Cu,N}$ values derived from BN (abbreviation for

such as used in the following: $D_{Cu,N}$(BN)) point to a yet unexplained N emission.

3.5. SN^+ energy spectra (Figs. 1 and 4–6; Table 4)

With regard to the energy distributions discussed in the following, it has to be noted that the E^{-2} transmission as probably caused by the retardation by L4 to the ID/OD pass energy of 26.7 eV does not change their typical shapes to a large extent: The ^{63}Cu intensities from the sputtered r.g. Cu pellet (Fig. 4) have to be multiplied by factors of 1.2 and 3 at 50 and 80 eV, respectively, if the maximum intensity is left unchanged for reasons of comparability.

The ion energy distributions of the plasma gas itself are considered first, since under the present conditions they lie in the 10 meV range [2], if any overlayed plasma potential is disregarded. But since the variation of the latter between the sheath edge and the bulk is [2]

$$\Delta U_{pl} = U_{pl} \cdot \left[1 - \ln\left(\frac{2\pi m_e}{m_i}\right)\right]^{-1} \quad (5)$$

(where $m_{e,i}$ = electron and ion (Ar^+, in this case) masses, respectively) one has to expect a variation of 4 V for the formation potential of plasma gas ions ($m_i = 40$ amu and $U_{pl} \approx 42$ V, see the onset of the spectra in Fig. 4). The corresponding difference to the Ar^+ peak width of 6 eV may be explained by energy analyzer broadening so that the energy window is probably somewhat larger than the calculated 1 eV.

After prolonged sputtering of the Cu powder pellets, the plasma gas contains also some Cu contamination, the energy spectrum of which is shown in Fig. 4, too. All contamination intensities decrease to background within about 13 eV. The narrow energy distributions of the contamination elements C, N and Cu can be taken as representing typical thermal ones, because no sputtering has occurred upon their generation. A tentative explanation for their narrower peak width compared to that of Ar may be that upon collisions with the Ar neutrals forming the overwhelming part of the plasma, contamination ions transfer kinetic energy, but no charge because of the higher ionization potential of Ar. This is probably different for Ar^+–Ar^0 collisions so that the average Ar^+ ion has "seen" more of the total ΔU_{pl} drop than the average contamination ion. This may be added to the initial energy E_0 of several eV of resputtered particles from the walls of the plasma chamber.

As shown exemplarily in Fig. 4, all energy distributions $I_X(E)$ found in this work are nar-

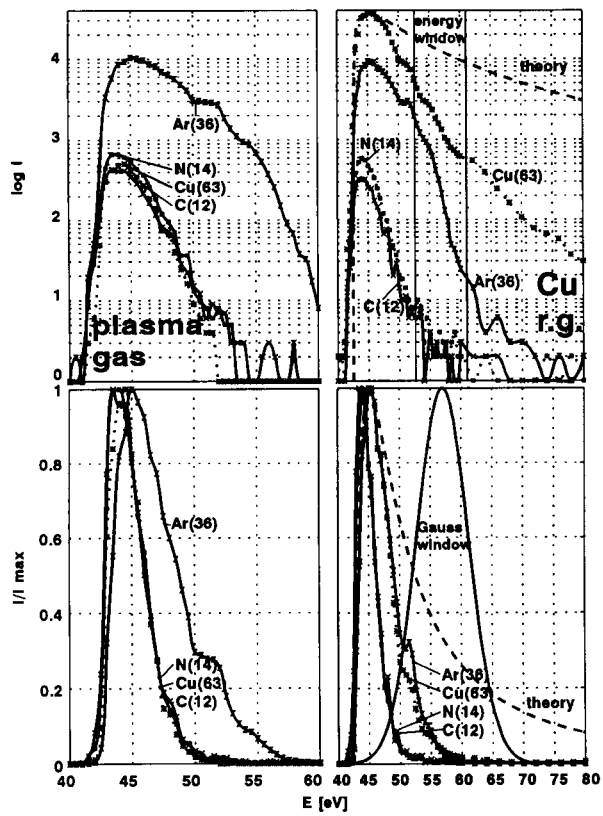

Fig. 4. Absolute (above) and normalized (below) positive ion energy spectra of the plasma gas (left, $U_{DBM} = 0$ V) and a pure Cu pellet (right, $U_{DBM} = -270$ V). The plasma gas spectra are taken immediately after prolonged sputtering of a pellet; therefore, the contamination peaks do not represent typical background values. The theoretical distribution is calculated according to Eqs. 6, 7 with $U_0 = 5$ eV and $U_{pl} = 42$ V. The energy window setting corresponds to the typical experimental values of the series asymmetric, c_{BN} variation, A and B.

rower than the theoretical distribution calculated according to [10]

$$\frac{dN^*}{dE'} = \frac{27}{4} \cdot \frac{E'}{(E'+1)^3} \quad (6)$$

(where $E' = E_0/U_0$, and U_0 = surface binding (sublimation) energy,

$$E = E_0 \pm e \cdot U_{pl} \quad (7)$$

which is valid for $SN^{\pm}$. U_{pl} shifted $I(E_0)/I^{max}(E_0)$ distributions as measured in this work are assumed to be equivalent to dN^*/dE'. $U_0 = 2 \cdot E_0(I^{max}) = 5$ eV [19] is taken for the theoretical curves in Fig. 4. Apart from angular effects which cannot be excluded as yet, the reason for the narrower experimental distributions may lie in effects induced by a "compound" surface layer of resputtered Cu and/or ceramic material causing additional energy reduction on the escaping atoms from the "pure" local ceramic material or Cu. Such an effect is described in [20] for Rh{111} with a benzene overlayer.

Despite such ambiguities, certain qualitative and even quantitative conclusions from the energy spectra can be drawn. The first one regards the "usual" energy window which is always placed some eV higher than the maxima of the energy distributions (see Fig. 4) in order to suppress the transport of plasma gas ions into the detection system. In order to estimate the effect of the position of the energy window, the distributions are folded with the assumed $T_X \propto E^{-2}$ dependency and with a Gauss function with a half width of 8.4 eV (see Experimental section). This is supposed to represent the ion optics transmission now named $T^{E,G}$, the resulting $D_{Cu,X}$ data being given in column 7 of Table 4. (Using a rectangular shape of the energy window with $2\Delta E$ around 56 eV yields, within a deviation of 20%, the same $D_{Cu,X}$. Especially the $D_{Cu,N}$(BN, AlN, TiN) values are the same within 5%. Neglecting the E^{-2} proportionality yields deviations of $\leqslant 3\%$ rel. only.) Furthermore, simply the maximum intensities from the energy spectra were recalculated to the $D_{Cu,X}$ data in column 8 of Table 4. These calculations qualitatively result in the same sequence of $D_{Cu,X}$ as found in both series A and B. On the other hand, even quantitative reproducibility is achieved for $D_{Cu,Ti}$ irrespective of the part of the energy spectrum from which $D_{Cu,Ti}$ has been taken. On the whole, the first conclusion is that combined effects of energy distribution and window cannot be made responsible for the observed matrix effects having been reproduced in the $I_X(E)$ series for a third time at least, since instrumental parameters could be kept constant within this series again.

The second conclusion concerns the reproducibly narrow shape and a 1–2 eV shift of the peak maxima towards lower energies being visible in all N distributions and in the C peak of B_4C. Comparison with the plasma gas energy spectra (Fig. 4) suggests that in these cases most of the detected C^+ and N^+ monatomic ions are thermalized, apart from a small fraction being visible above about 52 eV, where the tails of the N and C spectra approach more typical SN distributions. Thermalization is easily explained on the background of Kelly's discussion of thermal effects in sputtering [21]: If one can calculate a vapour pressure of 1–10 MPa, resulting from decomposition of the sample, for $T \approx 3000$–4000 K, which is the about 10^{-11} s long lasting elevated temperature estimated for a sputter cascade region, the energy distribution of the sputtered particles accordingly contains a "prompt thermal spike" component in the 0.1 eV range. As is known from the materials data in [22,23], all the nitrides investigated in the present work except BN but including Si_3N_4, which is taken as one component of $Si_9N_4O_6$, and SiC decompose below 3000°C. Simple application of the ideal gas law for the released N_2 then yields pressures in the MPa range. SiC decomposes to solids, which is reflected by the cascade type energy distribution also for C. On the other hand, BN, B_4C, B_2O_3 (from substrate B and contamination O) and SiO_2 sublime or boil, respectively, in or below the thermal spike temperature range with 3000 K vapour pressures in the 10^3 (B_2O_3, SiO_2), 10^2 (BN) or lower Pa range (estimated for B_4C for which no applicable $\Delta_f G^\circ = -RT \cdot \ln(p/\text{bar})$ data could be found in [24]). The presence of thermal N and C atomic ions in the BN and B_4C spectra, respectively, which is not accompanied

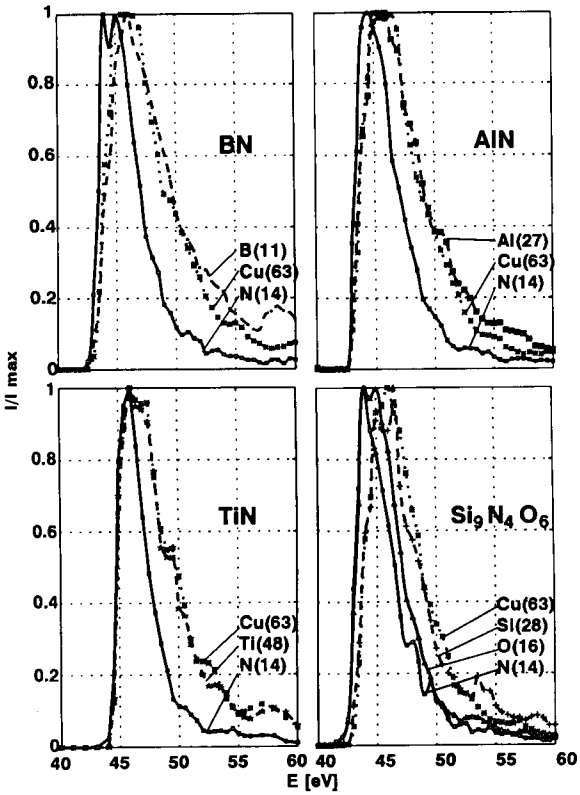

Fig. 5. Normalized SN^+ energy spectra of BN, AlN, TiN and $Si_9N_4O_6$.

by thermal B^+ energy distributions can therefore not be explained at this point in terms of B–X bond breaking (X = N,C) by the 7 eV plasma electrons.

Thirdly, $D_{Cu,X}$ (X = N,C) values derived from the $I_X^{max}(E)$ of the nitrides and of B_4C are typically 3 times higher than the means of series A and B and also much higher than the corresponding theoretical post-ionization probabilities (Table 5). The reason probably lies in the longer interaction time of thermalized particles with the plasma which also might enable Penning ionization [2]. On the other hand, B, Al and Si as well as C from SiC show, in part, drastic reductions in that comparison. This might be due to enhanced emission of (oxide?) clusters the energy distributions of which are known to cover the lower part of the atomic ones [3,25,26]. Saidoh et al. [25] already argued that metal oxide desorption processes are not superimposed on the cascade spectrum but replace it. In order to prove a "low energy depletion" of the SN^+ atom signal, at least some spectral evidence for a strong molecular emission should be found.

Fourth, an explanation of the high-energy B^+ distribution is required which is extended up to about 120 eV and is found for BN as well as for B_4C in the 10^{1-2} cps or 0.1 $I_B^{max}(E)$ range. An interpretation will be tried below.

3.6. SI / SN^- energy spectra (Fig. 7)

BN^- energy spectra giving evidence for the formation of DBM generated negative secondary ions (SI^-) as well as of negatively post-ionized secondary neutrals (SN^-) are shown in Fig. 7. The former are easily identified because of their direct dependence on U_{DBM} and will be discussed

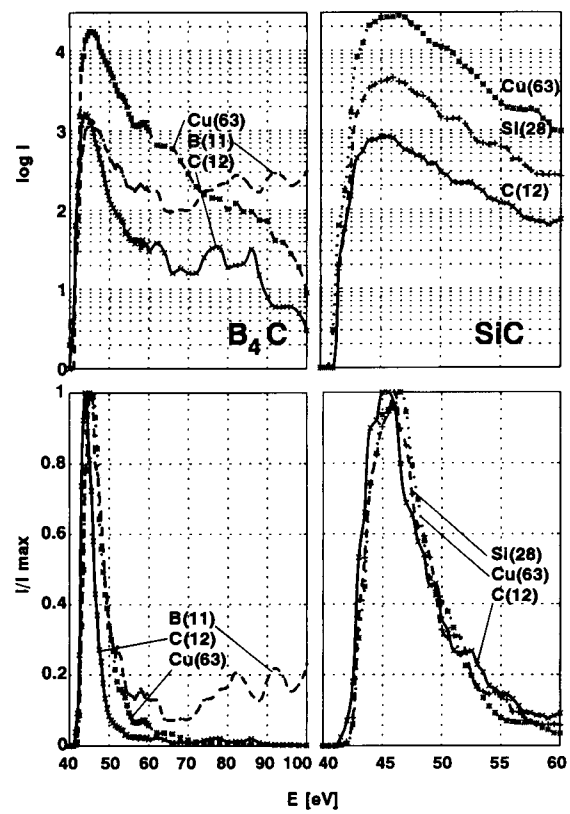

Fig. 6. Absolute (above) and normalized (below) SN^+ energy spectra of B_4C and SiC.

first in the next section. Similarly to the "true" SI^- peaks at $e \cdot U_{DBM}$, the small peaks and shoulders visible between 10 and 150 eV are shifted with varying U_{DBM} the more the higher their positions in the energy spectrum are. A peak at 66 eV, e.g., is shifted to 44 eV, if U_{DBM} is lowered by 40 V. This probably comes from SI^- emission from residual, less conductive ceramic powder agglomerations which are positively charged by the sputtering ions.

On the other hand, a peak near 9 eV (comprised in a more detailed spectrum not shown) stays static upon U_{DBM} variation. This finding suggests that the low energetic negative ions are part of the high-energy tail of negatively post-ionized sputtered neutrals (SN^-) generated in the positive space charge ($U_{pl} \approx +40$ V) of the plasma. Together with the grounded chamber wall (Fig. 1), the plasma forms a trap for SN^- particles with energies below 40 eV so that the "true" maxima between 1 and 5 eV cannot be made visible with the given INA-3 construction. The negative ionization mechanism cannot clearly be stated at this point; charge transfer from

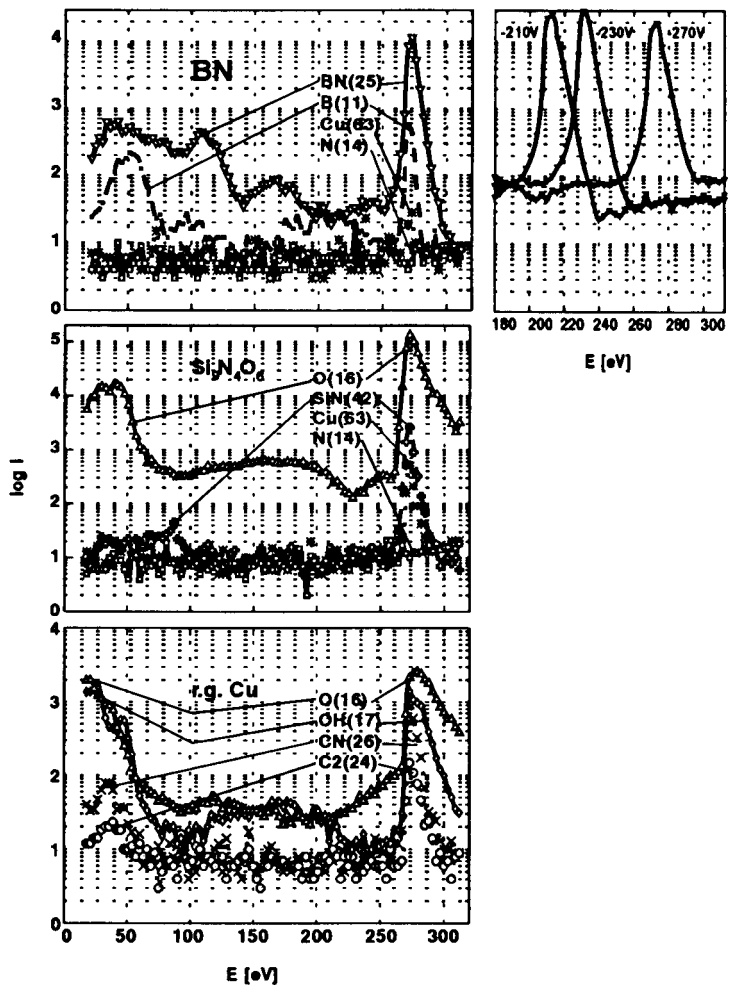

Fig. 7. Negative ion energy spectra of BN, $Si_9N_4O_6$ and r.g. Cu powder pellets. For BN^- (mass 25), also the peak shift with varying U_{DBM} is shown.

plasma enriched O^- cannot be excluded. Further investigations under better defined experimental conditions are clearly required.

3.7. SI^- mass spectra (Fig. 8, Table 4)

Some typical DBM generated SI^- mass spectra are shown in Fig. 8. It has to be pointed out that the patterns of the spectra are entirely reproducible using the ion gun with the plasma being off and the O contamination reduced to a large extent, apart from somewhat (factor 2) higher intensities of the oxide clusters in the plasma DBM case, which is probably due to additional O contamination causing chemical sputtering as, e.g., discussed in [25]. The intensity reduction induced by the L4 deceleration from 270 to 54 eV ($\Delta E = 2$ eV in this case) may be estimated to a factor of 25. Clearly, the SI^- spectra are governed by electron affinity lying between 3.1 and 3.8 eV for F, Cl, BO, BO_2, C_2 and CN [23], but near −0.07 eV [24] for N, which is consequently not visible in the SI^- spectra. For semiquantitative comparisons in the following discussion, the most intense MO_2^- and O^- peaks generated by virtually the same O flux to all specimens will be taken for internal reference.

Since the BO_2^- signal is even one or more than

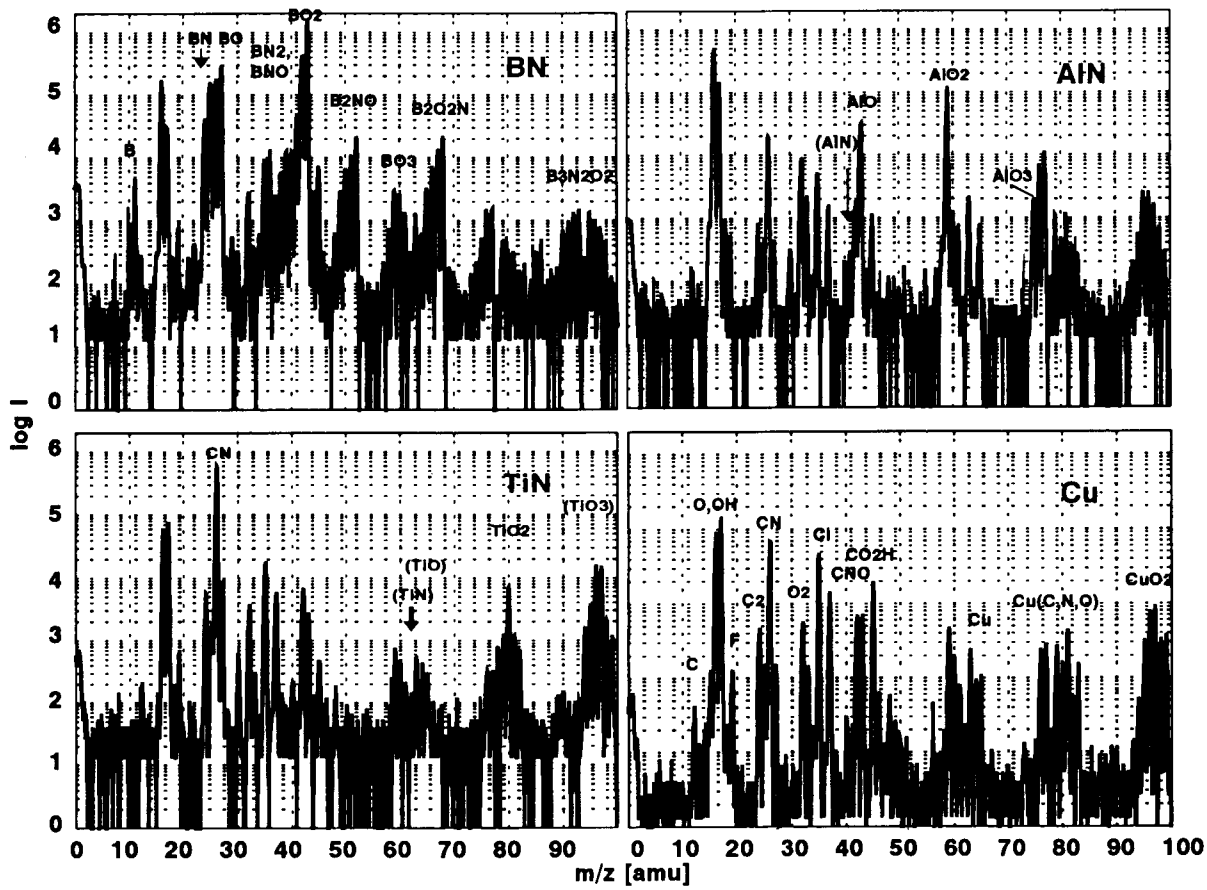

Fig. 8. Plasma generated SI^- spectra ($E = 270$ eV) of 1:20 (w/w) BN, AlN and TiN in Cu powder pellets. For comparison, also an SI^- spectrum of a pure Cu pellet is shown. For simplicity, the peaks of the latter are not assigned in the other spectra; the same holds for most hydrogen containing fragments. In brackets: positions of missing or ambiguous peaks.

two orders of magnitude more intense than BN^- or BC^-, respectively, and since its energy distribution is assumed to be similar to the BN^- distribution given in Fig. 7, it can be concluded that the extraordinarily high energies found in the tails of the B^+ distributions of BN as well as of B_4C (Figs. 5 and 6) stem from processes like

$$BO_2^- + e^- \rightarrow B^+ + 2O^- \quad (8)$$

by which the kinetic energies of the precursor cluster ions are approximately shared by the atomic fragments. Since corresponding energies for O^- can be found, too, Eq. 8 can be taken to describe the formation of positive as well as negative "tertiary" ions.

Another striking feature of the negative BN spectra is a certain amount of negatively ionized B being visible neither with B_4C nor with any other metal component of the other ceramics. B^- can be regarded as the residue of molecular ions fractured according to

$$BN^- \rightarrow B^- + N^0 \quad (9)$$

The difference of this formulation to Eq. 8 arises from the negative electron affinity of N. A formulation similar to Eq. 8 would describe the much more probable positive ionization of B which then contributes to the high-energy B^+ region discussed above. Probably because of their high ionization potential (14.53 eV), N atoms thus formed will remain neutral upon BN fracture and leave the ionization volume "seen" by the optics faster than positive ionization could occur.

The most interesting point is that nitride clusters clearly appear with BN and $Si_9N_4O_6$, but they are hardly detectable on the AlN and TiN specimens, see column 9 in Table 4 and also the "background" spectrum obtained on the pure Cu pellet (Fig. 8). In spite of the unknown emission probabilities β_X^- of the different negative clusters, this strong emission is clearly "parasitic" for N. The reduction of $D_{Cu,B}$ by BO_2^- and BN^- emissions is counterbalanced by the high position of the "usual" energy window accepting a part of the B^+ high-energy tail. Unfortunately, a comparative measurement on a Cu pellet containing elemental B was not feasible within this work.

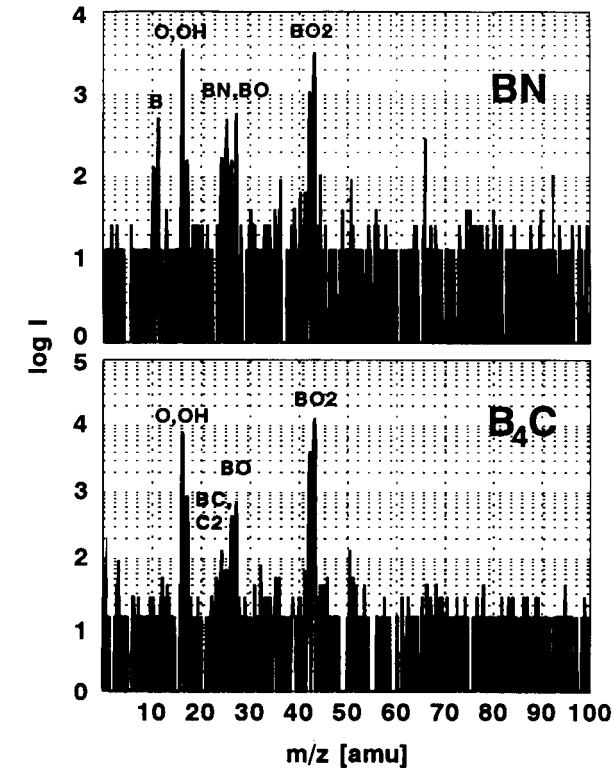

Fig. 9. Plasma generated SN^- spectra ($E = 47$ eV) of 1:20 (w/w) BN and B_4C, respectively, in Cu powder pellets.

With respect to the carbides and the oxide component in $Si_9N_4O_6$, the clearly higher and typical [26] strong C_2^- emission from SiC can be made responsible for the C matrix effect discussed above. The SI^- spectrum of $Si_9N_4O_6$ (not shown) exhibits high $SiO_{2,3}^-$ intensities being comparable to the AlO_2^- emission from AlN. By this, the molecule emission channels suspected to deplete the low-energy amount of atomic metal SN^+ and being "hidden" from the SN^+ point of view (see section "SN^+ energy spectra") can be regarded as identified in the contamination enhanced MO_X^- emission. This is not contradictory to the relatively high $D_{Cu,Ti}(I_{Ti}^{max}(E)) = 2.4$ value in Table 4, col. 8 since the $SI\text{–}TiO_{2,3}^-$ intensities are relatively low.

3.8. SN^- mass spectra (Fig. 9 and Table 4)

Mass spectra recorded at energies around 47 eV standing for the "true" SN^- spectra with

$E = 9$ eV are comparable to the corresponding SI^- spectra but with much lower intensities of typical contamination peaks like CN^- and Cl^-. Dominant, again, are the relatively high MO_2^- intensities especially for the B containing ceramic powders.

From the presence of BO_x^- cluster ions in both the SI^- and SN^- regimes, it can be concluded that also chemical sputtering with O from the plasma contamination occurs on both B compounds investigated. If a kind of superficial B_2O_3 formation can be assumed, this compound would easily be evaporated upon thermal spikes because of its low boiling point (b.p., 1860°C) which is more than 1000 or 1500°C lower than the sublimation or boiling temperatures of the respective original compounds BN and B_4C as well as 400°C lower than the b.p. of SiO_2. This combined chemical/thermal sputtering process occurring to a lesser extent on SiC is suspected to cause the formation of thermal N^+ and C^+ atomic ions (see Figs. 5 and 6) from the respective B compounds by a kind of co-evaporation. Apart from some oxide also formed on SiC, possibly amorphous C formed upon thermal spike decomposition (see above) is made responsible for the relatively high emission of C_2^- (see also Table 4, col. 9, 11).

Contrary to the "pure" SI^- case at $E = 270$ eV, I_{MN}/I_{MO2} in the SN^- spectra is significantly higher for BN than for all other nitrides including $Si_9N_4O_6$. This is probably due to a strong molecular thermal BN emission: At the estimated thermal spike temperature of 3000 K (see above), the BN sublimation pressure to be calculated from [24] is in the 10^2 Pa range. As mentioned in the section "SN^+ energy spectra", the other nitrides decompose. Together with SI^- formation, thermal BN emission is suspected to be another major reason for the low $D_{Cu,N}(BN)$ values: The BN^- intensity above the threshold of 0 eV at about 25 eV should be compared to a typical SN^+ intensity near 100 eV (difference $\approx 2 \cdot e \cdot U_{pl}$) which lies 2–3 orders of magnitude below the maximum intensity (compare Figs. 6 and 7). From this, a comparatively high "hidden" $I_{BN}^{max}(E) \approx 10^{5-6}$ cps range might be estimated. This, however, would be a value for a trapped species possibly enriched in the plasma. On the other hand, it shows that in the case of strong emission of probably thermal molecules, this sputtering channel might deplete the atomic SN^+ formation channel to an extent which could even affect SN^+ sensitivity factors.

4. Conclusion

As a first and preliminary study on sensitivity factors $D_{Cu,X}$ as derived from technological ceramic powders embedded into conducting Cu powder pellets, the following effects have been observed and are discussed with respect to $D_{Cu,X}$ variations amounting up to half an order of magnitude and more:

(i) Thermal atomic N and, in part, C emission from nitrides and carbides, respectively.
(ii) Negative secondary ion emission, typically as clusters being only marginally visible in the SN^+ spectra.
(iii) Evidence for the negative post-ionization of probably thermal spike emitted neutral clusters, the main part probably being trapped in the positive space charge of the plasma.

As a plausible hypothesis especially based on negative ion energy and mass spectra, low $D_{Cu,N}$ values if derived from BN are mainly explained in terms of strong SI^- and thermal BN emission and fracture into N^0 and $B^\pm$ upon a further collision. Further detailed investigations under more favourable experimental conditions, especially under exclusion of O contamination giving rise to chemical sputtering, are required for the quantification of these processes.

Acknowledgements

This work was supported by the Bundesminister für Forschung und Technologie and the Minister für Wissenschaft und Forschung des Landes Nordrhein-Westfalen. Thanks are due to Dr. R. Jede for valuable discussions and advices with regard to ion energy spectroscopy, Dr. E. Grallath for the bulk analyses of N and O, Prof. Dr. R. Riedel for the $Si_9N_4O_6$ powder, Mrs. A.

Kauenberg, Mr. R. Giese and Mr. M. Hein for technical assistance, Mrs. M. Becker for the SEM pictures and Dr. H. Gnaser, Dr. J. Goschnick, Prof. Dr. R.W. Schmutzler and Prof. Dr. P. Williams for interesting suggestions and references.

References

[1] H. Oechsner, in H. Oechsner (Ed.), Thin Film and Depth Profile Analysis, Topics Curr. Phys. 37, Springer, Berlin, 1984, Chap. 4.
[2] R. Jede, O. Ganschow and U. Kaiser, in D. Briggs and M.P. Sheah (Eds.), Practical Surface Analysis, Vol 2: Ion and Neutral Spectroscopy, Wiley, Chichester, 2nd edn., 1992, Chap. 8.
[3] A. Benninghoven, F.G. Rüdenauer and H.W. Werner, in P.J. Elving, J.D. Winefordner and I.M. Kolthoff (Eds.), Secondary Ion Mass Spectrometry, Chem. Anal. 86, Wiley-Interscience, New York 1987, Chaps. 2 and 3.
[4] H. Jenett, S. Bredendiek-Kämper and J. Sunderkötter, Mikrochim. Acta, 110 (1993) 13.
[5] M. Fichtner, J. Goschnick, U.C. Schmidt, A. Schweiker and H.J. Ache, J. Vac. Sci. Technol. A, 10 (1992) 362.
[6] N. Jakubowski, D. Stuewer and W. Vieth, Anal. Chem., 59 (1987) 1825.
[7] H. Oechsner, in A. Benninghoven, J. Giber, J. László, M. Riedel and H.W. Werner (Eds.), SIMS III, Chem. Phys. Series 19, Springer, Berlin, 1982, 106–114.
[8] W. Gerhard and H. Oechsner, Z. Phys. B, 22 (1975) 41.
[9] H. Gnaser and H. Oechsner, Nucl. Instrum. Meth. Phys. Res. B, 58 (1991) 438.
[10] H. Oechsner, Z. Phys., 238 (1970) 433.
[11] A. Wucher and W. Reuter, J. Vac. Sci. Technol. A, 6 (1988) 2316.
[12] K.H. Koch, D. Sommer and D. Grunenberg, Mikrochim. Acta [Wien], II (1990) 101.
[13] D. Grunenberg, lecture on the 7th INA-3 Anwendertreffen, Dortmund, Dec. 12, 1991.
[14] H. Jenett and Y. Kikuta, Spectrochim. Acta B, 47 (1992) 143.
[15] A. Wucher, J. Vac. Sci. Technol. A, 6 (1988) 2293.
[16] R. Jede, O. Ganschow and U. Kaiser, in D. Briggs and M.P. Sheah (Eds.), Practical Surface Analysis, Vol 2: Ion and Neutral Spectroscopy, Wiley, Chichester, 2nd edn., 1992, Chap. 2.
[17] Leybold AG: INA-3 manual.
[18] Y. Kikuta and H. Jenett, Anal. Sci., 7 (1991) 757.
[19] P. Sigmund, in R. Behrisch (Ed.), Sputtering by Particle Bombardment I, Topics Appl. Phys. 47, Springer, Berlin, 1981, Chap. 2.
[20] N. Winograd and B.J. Garrison, in A.W. Czanderna and D.M. Hercules (Eds.), Ion Spectroscopies for Surface Analysis, Meth. Surf. Characteriz. 1 (C.J. Powell, A.W. Czanderna, D.M. Hercules, T.E. Madey and J.T. Yates (Eds.)), Plenum, New York, 1991, Chap. 2.
[21] R. Kelly, Surf. Sci., 90 (1979) 280.
[22] J. Falbe and M. Regitz (Eds.), Römpp Chemie Lexikon, Thieme Verlag, Stuttgart, 1989–1992.
[23] D.R. Lide (Ed.), Handbook of Chemistry and Physics, 73rd edn., CRC Press, Boca Raton, FL, 1992.
[24] M.W. Chase, C.A. Davies, J.R. Downey, D.J. Frurip, R.A. McDonald and A.N. Syverud (Eds.), JANAF Thermochemical Tables (3rd edn.), J. Phys. Chem. Ref. Data 14 Suppl. 1 (1985).
[25] M. Saidoh, H. Gnaser and W.O. Hofer, Appl. Phys. A, 40 (1986) 197.
[26] H. Morikawa et al., in A. Benninghoven et al. (Eds.), SIMS IX, Wiley, New York, submitted for publication.
[27] A. Wucher, J. Vac. Sci. Technol. A, 6 (1988) 2287.

ELSEVIER

Analytica Chimica Acta 297 (1994) 301–311

ANALYTICA CHIMICA ACTA

Time-of-flight secondary ion mass spectrometry of poly(alkyl acrylates): comparison with poly(alkyl methacrylates)

Paul A. Zimmerman, David M. Hercules

Department of Chemistry, University of Pittsburgh, Pittsburgh, PA 15260 (USA)

Received 23rd June 1993; revised manuscript received 19th October 1993

Abstract

Time-of-flight secondary ion mass spectrometry (TOF-SIMS) has been used to examine a series of poly(alkyl acrylate) (PAA) homopolymers containing a variety of ester groups. Reproducible spectra for the PAAs are obtained up to 3500 Da. The spectra are composed of clusters arranged in a series of repeating patterns. These clusters are silver cationized neutral fragments of the main polymer chain. Free radical fragmentation mechanisms are proposed for PAAs under ion beam bombardment. The effect of the nature of the ester group on the fragmentation patterns of PAAs is discussed. The PAA spectra are also compared with spectra obtained from a previous TOF-SIMS study of poly(alkyl methacrylates).

Keywords: Mass spectrometry; Poly(alkyl methacrylates); Poly(alkyl acrylates); Time-of-flight secondary ion MS

Time-of-flight secondary ion mass spectrometry (TOF-SIMS) has shown great utility in the analysis of different types of polymers [1–4]. A TOF-SIMS study was recently completed on a series of poly(alkyl methacrylates) (PAMAs) [5]. This work offers insights into possible fragmentation pathways, as well as giving unique and reproducible spectra for a series of PAMAs. The present study is intended to analyze in more detail another important branch of the acrylic family, the poly(alkyl acrylates)(PAAs).

PAAs are an industrially important class of polymers used in paint and plastic manufacturing to improve flexibility and extensibility [6–8]. To date no comprehensive study of the fragmentation of PAAs has been completed by non-thermal methods. Only a few selected PAAs have been analyzed using quadrupole-SIMS [9–11]. Using the TOF-SIMS, peaks can be seen in PAA spectra up to 3500 daltons. This is comparable to the mass range obtained for PAMA spectra, facilitating comparison between the spectra for PAAs and PAMAs. TOF-SIMS offers an alternative to thermal analysis of PAAs by using a primary ion beam to sputter large fragments characteristic of a polymer.

Correspondence to: P.A. Zimmerman, Department of Chemistry, University of Pittsburgh, Pittsburgh, PA 15260 (USA).

SSDI 0003-2670(93)E0594-W

1. Experimental

The atactic PAAs ($M_w = 75\ 000$) were obtained from Scientific Polymer Products (Ontario, New York). The generic structures for the PAMAs and PAAs are shown in Fig. 1. TOF-SIMS spectra were obtained for the following poly(R acrylates): R = methyl (PMA), ethyl (PEA), *n*-propyl (PnPA), isopropyl (PiPA), *n*-butyl (PnBA), isobutyl (PiBA), *n*-hexyl (PnHA), cyclohexyl (PcHA), benzyl (PBzA), decyl (PDA), lauryl (PLA), and octadecyl (PoDA).

The instrument used was a time-of-flight mass spectrometer, TOF III (Ion Tof, Münster). The instrument is described in greater detail elsewhere [12]. During the measurement a target is bombarded by 10 keV argon ions with an average current of 0.4 pA for approximately 200 s. The total primary ion dose is less than 10^{13} ions/cm^2 which corresponds to the static SIMS mode. The samples were prepared for analysis by dissolving the polymers in toluene. Typical solutions had a concentration of 1–10 mg/ml. 1–5 μl of the samples were deposited on an etched silver target that had an area of approximately 0.12 cm^2. To obtain high quality spectra it was necessary to scratch the silver targets with the tip of a sharpened micro-spatula after polymer deposition so that the surface appeared to be shiny.

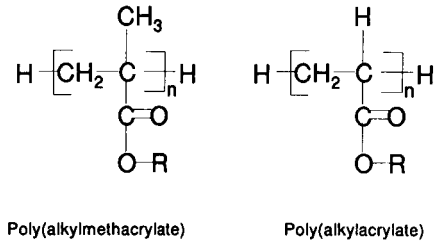

Fig. 1. Structure of poly(alkyl acrylates) and poly(alkyl methacrylates).

2. Results and discussion

Spectral interpretation of the acrylate polymer patterns

Fig. 2 shows the TOF-SIMS spectrum of poly(isobutyl acrylate) (PiBA) which is typical of spectra for PAAs. As with the methacrylates, the spectra can be divided into three regions: 10–100 Da; 100–800 Da; and above 800 Da. The mass range below 100 Da is dominated by peaks arising from side chain and backbone fragments. These characteristics are similar to those observed for the comparable methacrylates (i.e. CH_3^+, $C_2H_3^+$, $C_2H_5^+$, $C_3H_5^+$, $C_3H_7^+$, $C_2H_3O^+$, $C_3H_5O^+$, and $C_4H_9^+$). However, one difference is that the acrylate backbone gives an intense peak at 55 Da due to the acryloyl ion CH_2=CH–C≡O$^+$, [11,13] whereas PAMAs give an intense peak at 69 Da corresponding to the methacryloyl ion [10] (CH_2=C(CH_3)–C≡O$^+$). The region of the spectrum between 200 and 800 Da is dominated by silver clusters and silver cationized fragments. Unfortunately, this region offers little information about the structure of the polymer.

This study will concentrate on the spectrum above 800 Da which offers information about the mass of the polymer repeat unit and characteristics of the ester group. The terminology that will be used to describe the TOF-SIMS spectra is identical to that used previously for the PAMAs and is as follows: *fragment* will refer to a segment from the polymer chain; *pattern* will refer to a repeat sequence of peaks; *cluster* will refer to a group of peaks corresponding to a particular fragment. A cluster and a pattern are illustrated in Fig. 2. Each pattern contains a number of clusters equal to the number of carbons + oxygens in the repeat unit of the polymer. Within the patterns an integral number of polymer repeat units will be defined as nM. The fine structure varies between clusters, so we will use Δ to represent the approximate spacing between clusters (12–16 amu). All PAA spectra show clusters in each pattern at nM, nM + Δ, nM + 2Δ, nM + 3Δ, and nM − Δ. These clusters will be referred to as the *main chain fragments* and will be listed as Δ, 2Δ, 3Δ, nM, and −Δ. The most intense clusters in the PAA spectra are generally nM, −Δ, and Δ.

Table 1 shows the relative intensities for the poly(alkyl acrylates) with six or fewer carbons in their ester group. The table lists data for poly(methyl acrylate) (PMA), poly(ethyl acrylate)

(PEA), poly(*n*-propyl acrylate) (PnPA), poly(isopropyl acrylate) (PiPA), poly(*n*-butyl acrylate) (PnBA), poly(isobutyl acrylate) (PiBA), poly(*n*-hexyl acrylate) (PnHA) and poly(cyclohexyl acrylate) (PcHA). The numbers were compiled from the absolute intensities minus the background for each cluster in the spectra averaged for five consecutive patterns. The standard deviation (not shown) for the data in Table 1 was less than or equal to ± 0.08. The data in Table 1 show that the integral monomer peak (nM) is the most intense in the pattern for all of the poly(alkyl acrylates) (PAAs) studied. The intensities of the clusters decrease from nM to $+\Delta$ to 2Δ etc. An exception is the 5Δ clusters which show an increase in relative intensity compared to the 4Δ cluster in each case. Going down the Table from PMA to PcHMA the relative intensities of the clusters reach a maximum for the poly(propyl acrylates) and then decrease upon going further down the table. This indicates that as the size of the ester group is increased, the trend is towards decreasing intensities for most clusters relative to the nM cluster. Table 1 shows that there is some relationship between the relative intensities of clusters and branching in the ester group. PnBA

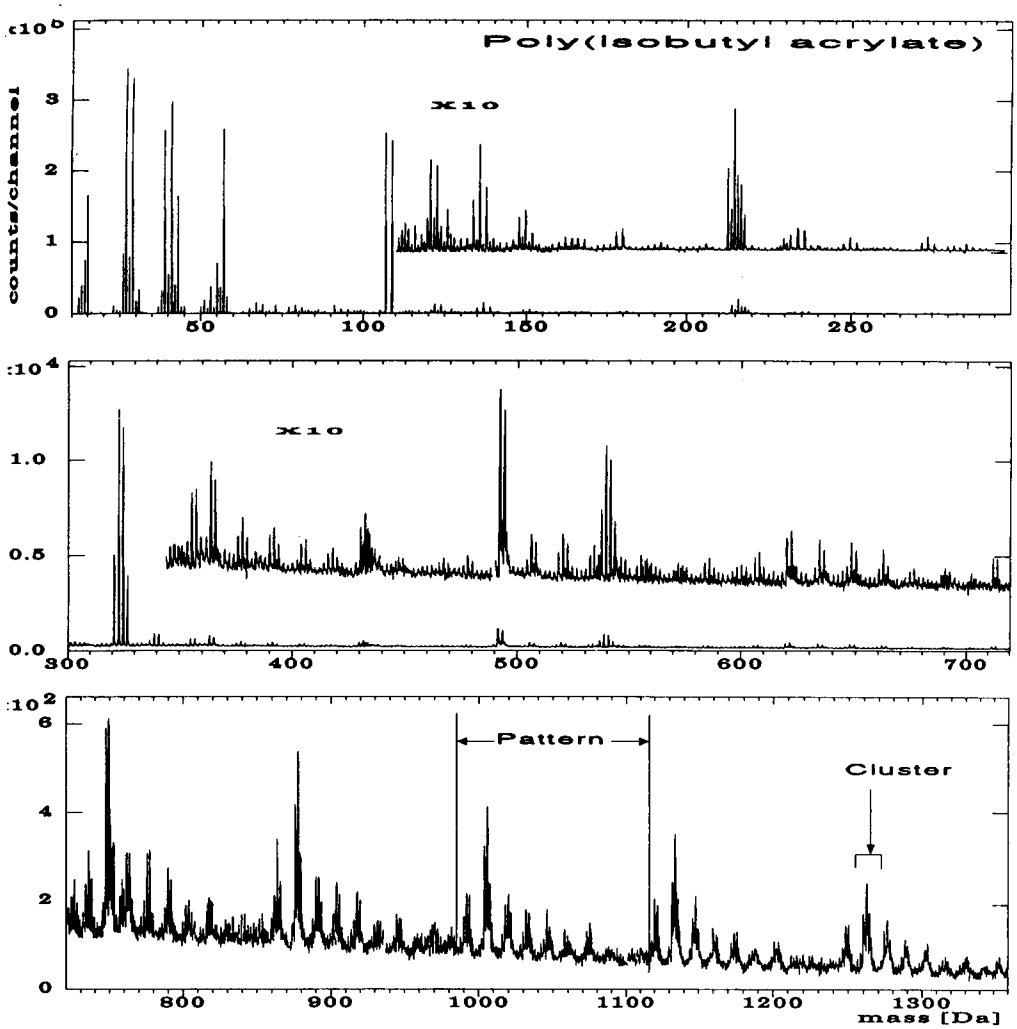

Fig. 2. TOF-SIMS spectrum of poly(isobutyl acrylate).

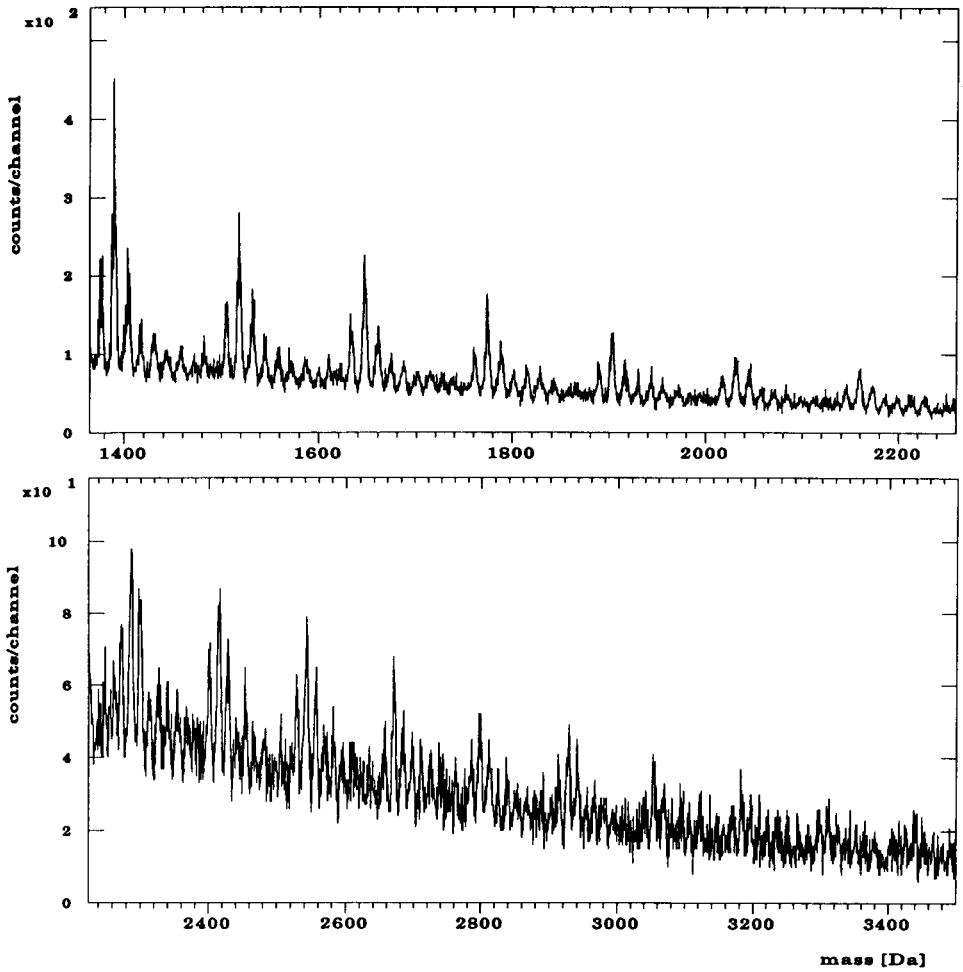

Fig. 2 (continued).

Table 1
Average relative intensities of five repeat patterns for ester groups containing 1–6 carbons

−Δ	nM	Δ	2Δ	3Δ	4Δ	5Δ	6Δ	7Δ	8Δ	9Δ
0.67	PMA	0.84	0.54	0.57	0.40					
0.88	PEA	0.78	0.58	0.45	0.43	0.50				
0.81	PnPA	0.81	0.66	0.67	0.57	0.73	0.71			
0.87	PiPA	0.82	0.62	0.61	0.56	0.73	0.60			
0.67	PnBA	0.51	0.56	0.41	0.42	0.54	0.22	0.29		
0.49	PiBA	0.48	0.29	0.23	0.28	0.32	0.23	0.12		
0.29	PnHA	0.27	0.21	0.17	0.14	0.25	0.12	0.22	0.13	0.08
0.52	PcHA	0.26	0.22	0.24	0.18	0.44	0.15	0.20	0.18	0.15

and PiBA show distinct differences between the relative intensities of their clusters. However, no difference is seen between PnPA and PiPA. Inclusion of a ring in the ester group causes distinct differences in relative intensities between PnHA and PcHA as shown in Table 1. The differences are most evident in the $-\Delta$ and 5Δ clusters.

Some of the clusters from the main chain fragments are not as intense in the PAA spectra as those observed in the methacrylate spectra. For example, the 3Δ cluster is of greater intensity than the 2Δ cluster for all of the methacrylates but for none of the acrylates. This is a distinguishing feature between all PAAs and PAMAs and offers an analytical means for differentiating between the two types of acrylics. Fig. 3 depicts the difference for PnBMA and PnBA.

Interpretation of some fragmentation pathways of PAAs can be accomplished using the same mechanisms as those proposed for the PAMAs. The two free radical mechanisms involve either direct main chain scission or ester group elimination leading to rearrangement of the radical which is then followed by main chain scission. An assumption is made that all desorption and transformation probabilities are the same. Scheme 1 shows the mechanism for main chain scission of PAAs. Initial fragmentation of the chain leads to two possible fragments, each of which undergoes subsequent fragmentation and subsequent addi-

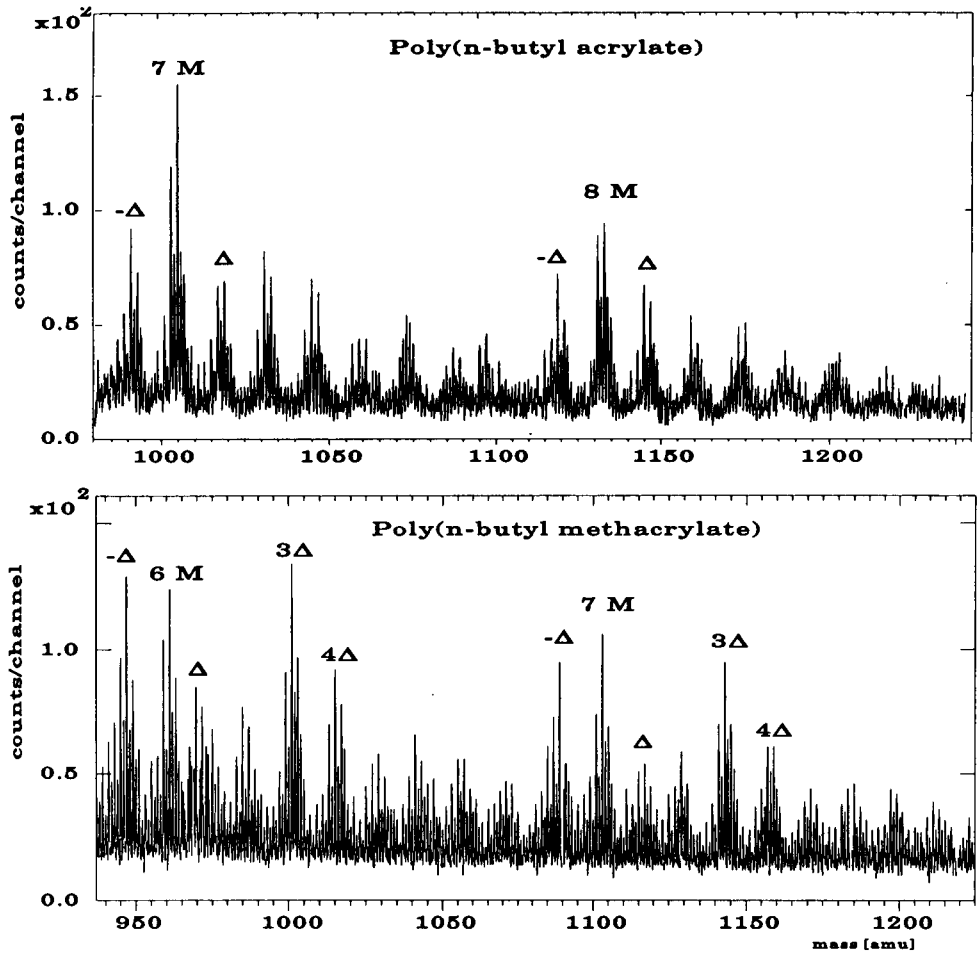

Fig. 3. A portion of the TOF-SIMS spectra of poly(*n*-butyl acrylate) and poly(*n*-butyl methacrylate).

tion of hydrogen to form a neutral molecule. This neutral fragment is cationized by a silver ion and detected. The end result of this process explains the formation of the nM, $+\Delta$, and $-\Delta$ fragments. This mechanism predicts that nM will be the most intense peak in the PAA spectra, as is observed for all but one of the PAAs studied.

Scheme 2 shows the proposed mechanism for ester group elimination leading to rearrangement and main chain scission. The initial event is the loss of –COOR moiety. Next, rearrangement leads to main chain fragmentation, producing a radical and an olefin terminus. The radical fragment undergoes subsequent scission to form nM and $-\Delta$ fragments. Ensuing scission of the olefin terminus fragment causes the formation of 3Δ and 2Δ fragments.

Overall the two schemes provide a reasonable picture for the fragmentation of PAAs that is consistent with the observed spectra. Based on the results of the present study, the best explanation for the fragmentation of PAAs is that both Scheme 1 and 2 are major mechanisms. Fragments corresponding to the most intense peaks in the spectrum (i.e. nM and $-\Delta$) are accounted for by both mechanisms. However, other clusters are seen which are not accounted for by Scheme 1 or 2. Additionally, if schemes 1 and 2 occur at a ratio of equal probability, the mechanisms predict that the 2Δ and 3Δ clusters will be as intense as the Δ cluster which is not observed. Clearly additional work is needed to give a complete picture of all the mechanisms involved in the formation of PAA fragments by ion beams.

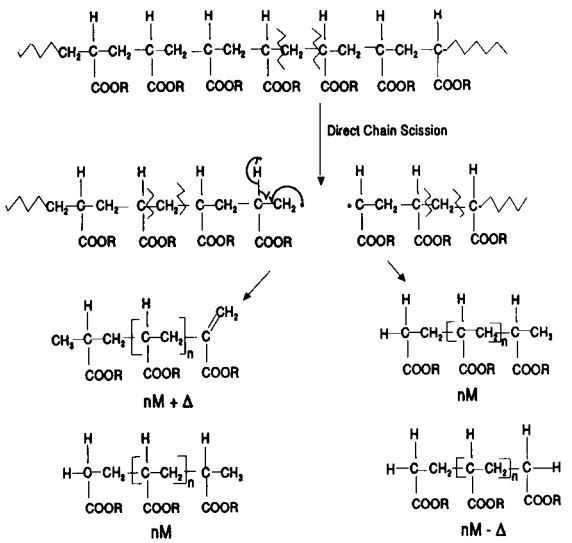

Scheme 1.

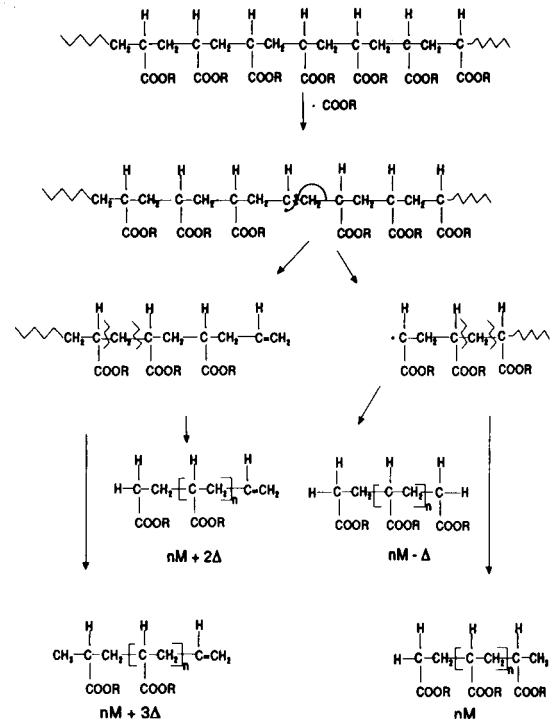

Scheme 2.

The proposed fragmentation mechanisms are based only on enthalpy considerations; a 10 keV ion beam has sufficient energy to break any bond within a polymer repeat unit. It is likely that the fragmentation products are at the end of a collision cascade and have energies of a few eV. Not considered in the proposed mechanism for either the PAAs or PAMAs, are the conformational forces which may be as important in some cases as the enthalpy considerations. For example, conformations that have orbitals that are antiperiplanar offer pathways for reactions that are of lower energy [14]. This may favor certain rearrangements or eliminations. This offers an avenue for further study of the mechanisms for acrylate and methacrylate polymers.

The suggested fragmentation of PAAs does not incorporate any use of ionic mechanisms to explain any of the clusters. Montaudo et al. [15,16] have suggested the presence of a number of ionic degradation pathways for multiple polymer systems. A concise explanation of all the clusters may require consideration of ionic mechanisms along with the free radical mechanisms discussed. However, more research is needed into these pathways which is beyond the present scope of this study.

Effect of the ester group on PAA fragmentation patterns

As seen previously in Table 1 there can be an influence on the TOF-SIMS spectrum arising from the nature of the ester group. Fig. 4 shows one pattern each for PnBA and PiBA. Branching of the ester group increases the intensity of the nM cluster relative to the other clusters in the pattern (i.e. PnBA < PiBA). However, no difference is seen between PnPA and PiPA (Table 1). It seems that the ester group must reach a critical length before a difference from branching is observed in the TOF-SIMS spectra.

Fig. 5 shows patterns for the C_6/C_7 esters: PnHA, PcHA, and PBzA. It is clear from the figure that changing the nature of the branching or aromaticity has an effect on the spectrum obtained for a PAA. The most intense cluster in each pattern is nM. Also there is an increase in the intensity of the 5Δ cluster relative to 4Δ

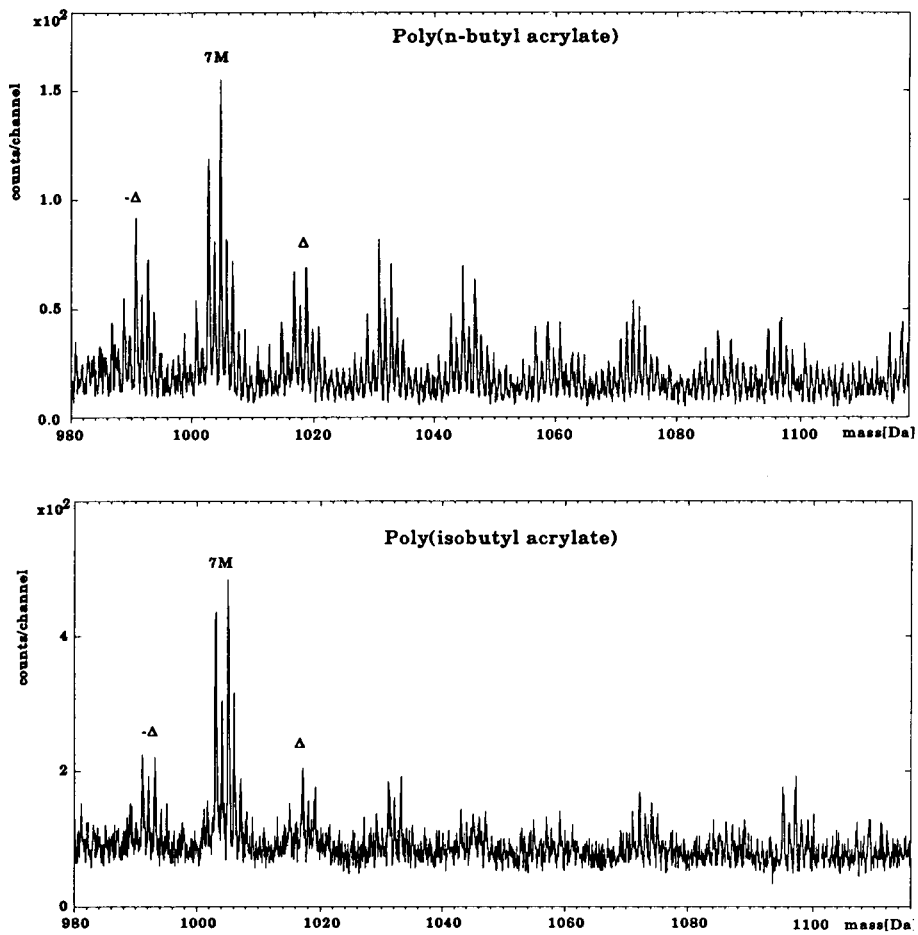

Fig. 4. A portion of the TOF-SIMS spectra of poly(*n*-butyl acrylate) and poly(isobutyl acrylate).

cluster throughout the spectrum for PcHA, PnHA and PBzA. However, PcHA shows a sharp decrease in intensity for Δ, 2Δ and 3Δ clusters relative to PnHA and PBzA. There is no clear explanation as to why these differences in intensity occur. Notwithstanding the explanation of the mechanism for the resulting differences, the data show that unique reproducible patterns in the high mass region are obtained for PnHA, PcHA and PBzA using TOF-SIMS

An interesting feature occurs for the PAAs with larger ester groups ($C \geqslant 6$) (Fig. 6) in that the 5Δ, 6Δ, 7Δ and the 8Δ all significantly increase in relative intensity as chain length is increased. This observation is unique to the PAAs, no such effect is observed for the PAMAs. Furthermore, as the number of carbons on the ester group is increased the relative intensity of the 5Δ–8Δ increases to a point where the 5Δ is nearly equal to the nM cluster as is the case for PLA. The 5Δ cluster corresponds to loss of the R group from one monomer in the fragmented chain. A possible explanation is a McLafferty rearrangement of an ester group to eliminate one of the R groups.

It is clear from data that changing the nature

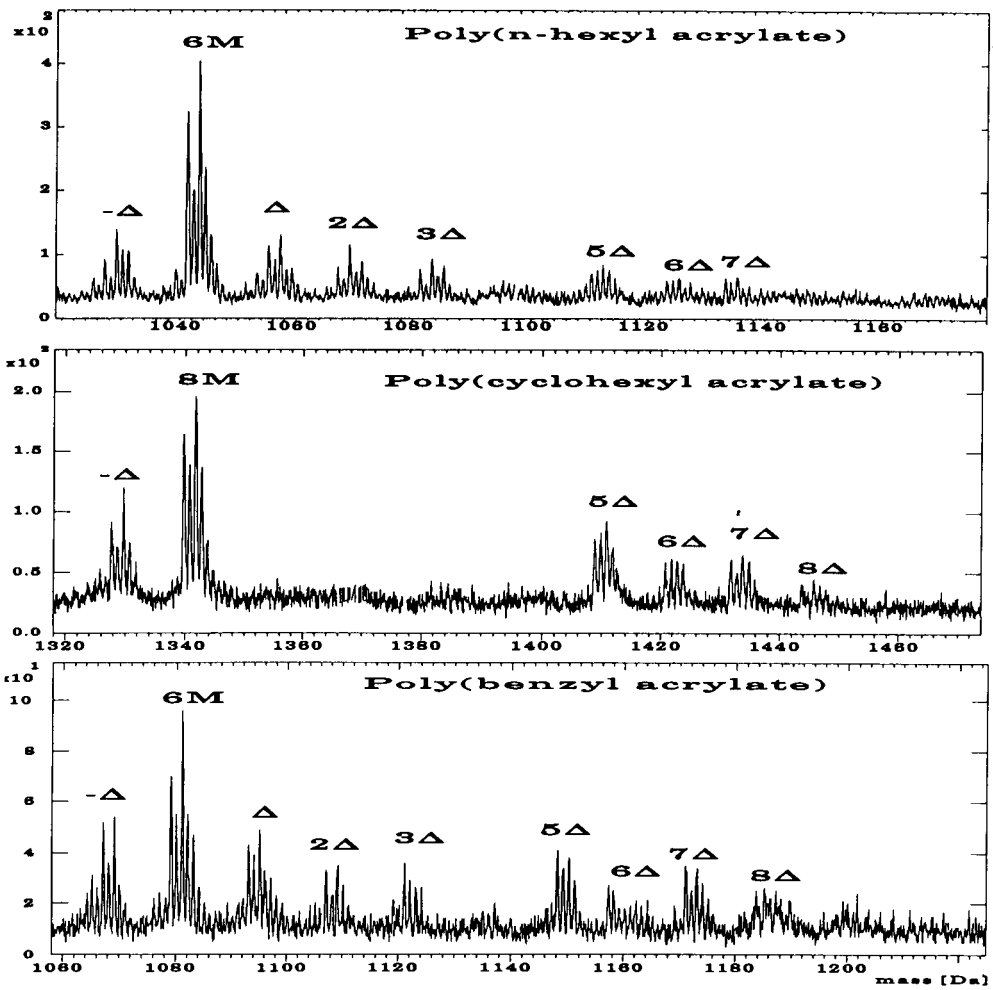

Fig. 5. One repeat pattern of poly(*n*-hexyl acrylate), poly(cyclohexyl acrylate) and poly(benzyl acrylate).

of the ester group can often affect the TOF-SIMS spectra. This offers a qualitative means of identifying particular PAAs using TOF-SIMS.

Fine structure of clusters

The clusters in the PAAs show more peaks than are to be expected for a single silver cationized species. Fig. 7 shows the fine structure of the nM cluster for PnBA. For a given cluster envelope several silver cationized species contribute to the overall structure. As with the clusters for the PAMAs, the PAAs show similar cluster structure from one pattern to the next. Using linear least-squares curve-fitting analysis it was found that the best fit was obtained using four components. It is assumed that similar transformation probabilities occur for each component. Three components were not enough to give satisfactory fit and five gave no better fit than four. Next the concentration of the components were calculated for the PAAs using a standard linear-least-squares program assuming 4 species which differ by 2 Da. Table 2 shows a tabulation for the concentration of components in the clusters for PnBA. The table reports the fragment involved and the four components listed as A–D; fragments correspond to differences of 0, 2, 4, and 6, Da, corresponding to 0, 1, 2, and 3 degrees of unsaturation, respectively.

Comparison of the relative concentration of components for different PAAs is hindered by large standard deviations for the concentration of

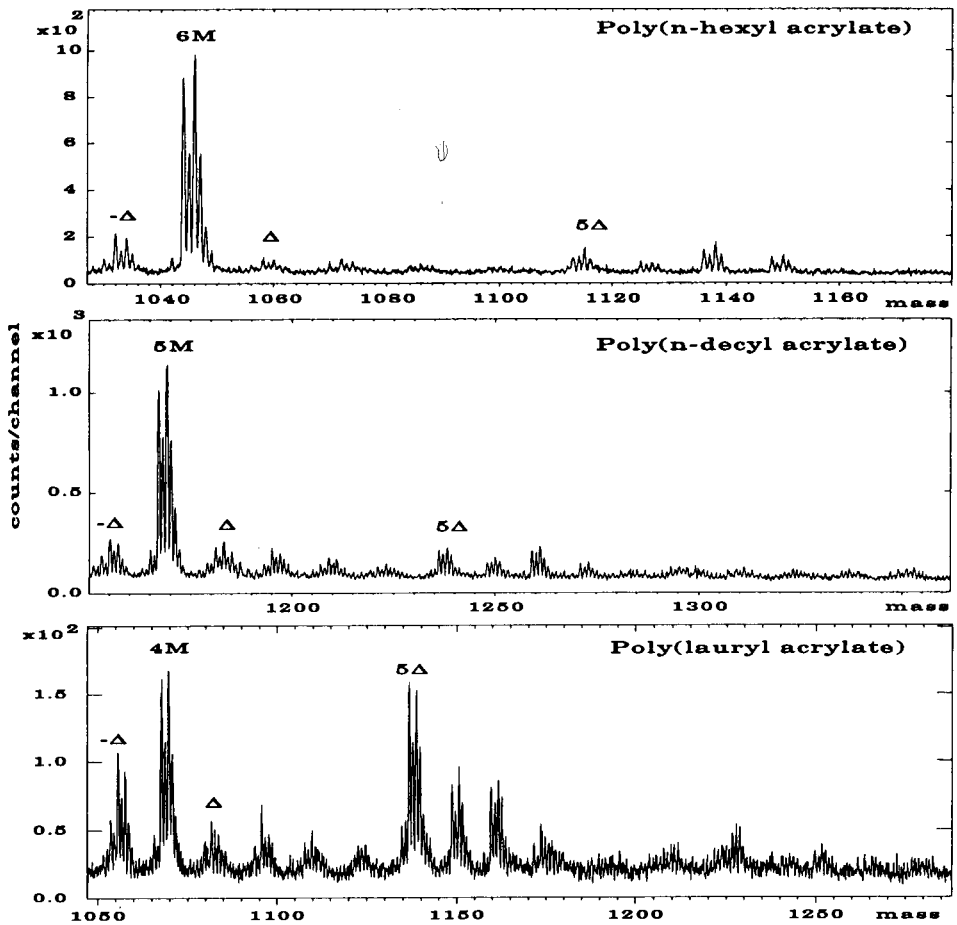

Fig. 6. One repeat pattern of poly(*n*-hexyl acrylate), poly(*n*-decyl acrylate) and poly(lauryl acrylate).

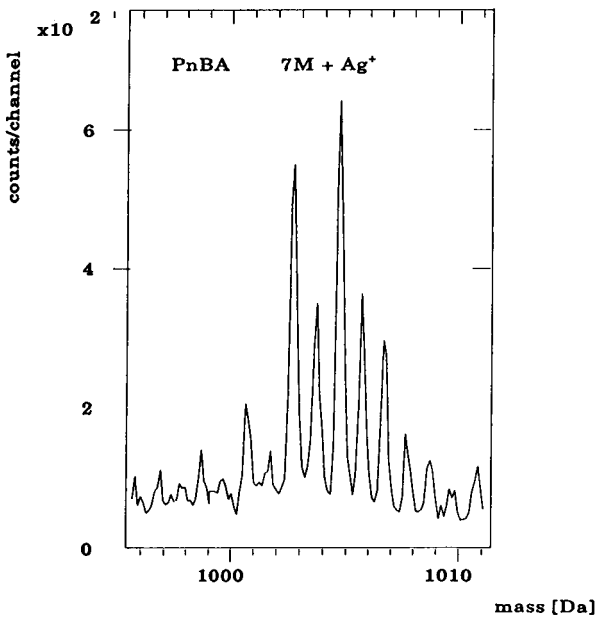

Fig. 7. Detail of the nM cluster for poly(*n*-butyl acrylate).

Table 2
Cluster structures for main chain fragments of poly(*n*-butyl acrylate)

Fragment	Degree of unsaturation	Relative intensity	Relative standard deviation
nM	0	19.5	7.5
	1	28.3	9.6
	2	37.2	9.6
	3	15.0	7.5
Δ	0	29.4	10.1
	1	27.4	13.1
	2	24.5	13.1
	3	18.7	10.1
2Δ	0	34.4	9.4
	1	29.1	12.1
	2	16.7	12.1
	3	19.8	9.4
3Δ	0	27.6	10.8
	1	30.4	14.0
	2	15.8	14.0
	3	26.2	10.8
−Δ	0	14.7	8.2
	1	41.3	10.5
	2	20.3	10.5
	3	23.7	8.2

the components of the clusters. It is still unclear how the individual species within the clusters in the PAA spectra originate. This is partially due to the complexity of the observed clusters. A possibility for obtaining additional information about the clusters is to used labelled PAAs. Using deuterium labelled species would show shifts, in the cluster pattern of 4 Da. if hydrogen is being lost as postulated previously [5].

Comparison of poly(alkyl methacrylate) and poly(alkyl acrylate) data

Previous analysis of PAAs and PAMAs focused on pyrolysis mass spectrometry data. However, the PAMAs for the most part undergo chain unzipping to form mainly methacrylate monomer while the PAAs tend to form much smaller fragments (i.e. CO, CO_2, CH_3OH etc.) [17]. This prevents direct comparison of PAAs with PAMAs. The PAA spectra obtained in this study allow for the first time a direct comparison with PAMA spectra obtained in a previous study [5]

Important similarities exist between the PAA and PAMA data not previously seen with any other method. For example, TOF-SIMS spectra are obtained for fragment ions from about 800–3500 Da. Additionally, spectra all consist of structured repeat patterns with spacing equal to the mass of the monomer units. A third similarity is found in the clusters of PAAs and PAMAs which are each made up of four species. A final similarity is that a change in the ester group (i.e. branching, rings, etc.) can affect the relative intensities of clusters in the spectra of both PAAs and PAMAs. Although the similarities offer a means for comparison between the acrylics, distinct differences are also observed.

Intuitively one would expect differences between spectra of PAAs and corresponding PAMAs on the basis of the thermal degradation data. In addition a previous study of substituted polystyrenes show significant differences between the spectra of the poly(α-methyl styrene) and the other polystyrenes [18].

Fig. 3, presented earlier in this paper, illustrates the most striking difference between the PAAs and PAMAs. This is an increase in relative

intensity going from the 2Δ to the 3Δ cluster for all PAMA spectra except for poly(octadecyl methacrylate), which is not seen in any of the PAA spectra. Similarly, the PAA spectra all show an increase in relative intensity from the 4Δ to the 5Δ cluster (Table 1) which is not seen for any of the PAMAs.

This work was supported by the National Science Foundation Grant CHE-9022135. Paul Zimmerman thanks BP for the fellowship which allowed him to complete this work.

References

[1] J. Lub and A. Benninghoven, Org. Mass Spectrom., 24 (1989) 164.
[2] I.V. Bletsos, D.M. Hercules, D. vanLeyen, A. Benninghoven, C.G. Karakatsanis and J.N. Rieck, Macromolecules, 23 (1990) 635.
[3] I.V. Bletsos, D.M. Hercules, D. Greifendorf, A. Benninghoven, Anal. Chem., 57 (1985) 2384.
[4] I.V. Blestsos, D.M. Hercules, D. vanLeyen, A. Benninghoven, C.G. Karakatsanis and J.N. Rieck, Anal. Chem., 61 (1989) 2142.
[5] P.A. Zimmerman, D.M. Hercules and A. Benninghoven, Anal. Chem., 65 (1993) 983.
[6] J.W. Nemec and W. Bauer, Jr., in M. Grayson (Ed.), Kirk-Othmer Encyclopedia of Chemical Technology, 3rd ed.n, Vol. 1, Wiley-Interscience, New York, 1978.
[7] B.B. Kine and R.W. Novak, in J. Kroschwitz (Ed.), Concise Encyclopedia of Polymer Science and Engineering, Wiley-Interscience, New York, 1989.
[8] N. Grassie and H.W. Melville, Proc. R. Soc. London, Ser. A, 199 (1949) 1.
[9] S. Straus and S.L. Madorsky, J. Res. Natl. Bur. Stand., 50 (1953) 165.
[10] D. Briggs, M.J. Hearn and B.D. Ratner, Surf. Interface Anal., 6 (1984) 189.
[11] D. Briggs and M.J. Hearn, Surf. Interface Anal., 11 (1988) 198.
[12] E. Niehuis, T. Heller, H. Feld and A. Benninghoven, J. Vac. Sci. Technol., 5 (1987) 1243.
[13] R.H.G. Brinkhuis and W.J. Van Ooij, Surf. Interface Anal., 11 (1988) 214.
[14] P.S. Kalsi, Sterochemistry; Conformation and Mechanism, Wiley, New York, 1990, pp. 160–163.
[15] G. Puglisi, G. Montaudo, D. Vitalini and Y. Morishma, J. Anal. Appl. Pyrol., 13 (1988) 161.
[16] G. Montaudo, C. Puglisi, D. Vitalini and Y. Morishma, Macromolecules, 21 (1988) 1594.
[17] N. Grassie and G. Scott, Polymer Degradation and Stabilization, Cambridge University Press, Cambridge, 1985.
[18] M.P. Chiarelli, A. Procter, I.V. Blestsos, D.M. Hercules, H. Feld, A. Leute and A. Benninghoven, Macromolecules, 25 (1989) 6970.

PUBLICATION SCHEDULE FOR 1995

	O'94	N'94	D'94	J	F	M	A	M	J	J	A	S
Anal. Chim. Acta	296/2 296/3 297/1–2	297/3 298/1 298/2	298/3 299/1 299/2	299/3 300/1–3 301/1–3	302/1 302/2–3 303/3							
Vib. Spec.		8/1		8/2		8/3		9/1		9/2		9/3

INFORMATION FOR AUTHORS

Detailed "Instructions to Authors" for *Analytica Chimica Acta* was published in Volume 289, No. 3, pp. 381–384. Free reprints of the "Instructions to Authors" of *Analytica Chimica Acta* and *Vibrational Spectroscopy* are available from the Editors or from: Elsevier Science B.V., P.O. Box 330, 1000 AH Amsterdam, The Netherlands. Telefax: (+31-20) 5862 459.

Manuscripts. The language of the journal is English. English linguistic improvement is provided as part of the normal editorial processing. Authors should submit three copies of the manuscript in clear double-spaced typing on one side of the paper only. *Vibrational Spectroscopy* also accepts papers in English only.

Rapid publication letters. *Letters* are short papers that describe innovative research. Criteria for letters are novelty, quality, significance, urgency and brevity. Submission data: max. of 2 printed pages (incl. Figs., Tables, Abstr., Refs.); short abstract (e.g., 3 lines); *no* proofs will be sent to the authors; submission on floppy disc; *no* revision will be possible.

Abstract. All papers, reviews and letters begin with an Abstract (50–250 words) which should comprise a factual account of the contents of the paper, with emphasis on new information.

Figures. Figures should be suitable for direct reproduction and as rich in contrast as possible. One original (or sharp glossy print) and two photostat (or other) copies are required. Attention should be given to line thickness, lettering (which should be kept to a minimum) and spacing on axes of graphs, to ensure suitability for reduction in size on printing. Axes of a graph should be clearly labelled, along the axes, outside the graph itself.

All figures should be numbered with Arabic numerals, and require descriptive legends which should be typed on a separate sheet of paper. Simple straight-line graphs are not acceptable, because they can readily be described in the text by means of an equation or a sentence. Claims of linearity should be supported by regression data that include slope, intercept, standard deviations of the slope and intercept, standard error and the number of data points; correlation coefficients are optional.

Photographs should be glossy prints and be as rich in contrast as possible; colour photographs cannot be accepted. Line diagrams are generally preferred to photographs of equipment. Computer outputs for reproduction as figures must be good quality on blank paper, and should preferably be submitted as glossy prints.

Nomenclature, abbreviations and symbols. In general, the recommendations of IUPAC should be followed, and attention should be given to the recommendations of the Analytical Chemistry Division in the journal *Pure and Applied Chemistry* (see also *IUPAC Compendium of Analytical Nomenclature, Definitive Rules*, 1987).

References. The references should be collected at the end of the paper, numbered in the order of their appearance in the text (*not* alphabetically) and typed on a separate sheet.

Reprints. Fifty reprints will be supplied free of charge. Additional reprints (minimum 100) can be ordered. An order form containing price quotations will be sent to the authors together with the proofs of their article.

Papers dealing with vibrational spectroscopy should be sent to: Dr J.G. Grasselli, 150 Greentree Road, Chagrin Falls, OH 44022, U.S.A. Telefax: (+1-216) 2473360 (Americas, Canada, Australia and New Zealand) or Dr J.H. van der Maas, Department of Analytical Molecular Spectrometry, Faculty of Chemistry, University of Utrecht, P.O. Box 80083, 3508 TB Utrecht, The Netherlands. Telefax: (+31-30) 518219 (all other countries).

0003-2670/94/$07.00

PRINTED IN THE NETHERLANDS

Environmental Analysis

Techniques, Applications and Quality Assurance

Edited by **D. Barceló**

Techniques and Instrumentation in Analytical Chemistry Volume 13

Three aspects of environmental analysis are treated in this book:

- the use of various analytical techniques
- their applications to trace analysis of pollutants, mainly organic compounds
- quality assurance aspects, including the use of certified reference materials for quality control of the entire analytical process.

The book will serve as a general reference for post-graduate students as well as a practical reference for environmental chemists who need to use the analytical techniques for environmental studies. Analytical chemists needing information on the complexity of environmental sample matrices and interferences will also find this an invaluable reference.

Contents: Part 1. Field Sampling Techniques and Sample Preparation. 1. Sampling techniques for air pollutants (R. Niessner). 2. Sample handling strategies for the analysis of organic contaminants from environmental samples (M.-C. Hennion, P. Scribe). 3. Extraction, clean-up and recoveries of persistent trace organic contaminants from sediment and biota samples (D.E. Wells).
Part 2. Application Areas. 4. Current developments in the analysis of polychlorinated biphenyls (PCBs) including planar and other toxic metabolites in environmental matrices (D.E. Wells). 5. Official methods of analysis of priority pesticides in water using gas chromatographic techniques (D. Barceló). 6. Coupled-column reversed phase liquid chromatography as a versatile technique for the determination of polar pesticides (E.A. Hogendoorn, P. van Zoonen). 7. Liquid chromatographic determination of phenols and substituted derivatives in water samples (G. Marko-Varga). 8. HPLC methods for the determination of mycotoxins and phycotoxins (J.F. Lawrence, P.M. Scott). 9. Determination of radionuclides in environmental samples (V. Valkovic).
Part 3. Quality Assurance and Reference Materials. 10. Quality assurance in environmental analysis (W.P. Cofino). 11. Certified reference materials for the quality control of measurements in environmental monitoring (E.A. Maier). 12. Standard reference materials for the determination of trace organic constituents in environmental samples (S.A. Wise).
Part 4. Emerging Techniques. 13. Application of fluorescence spectroscopic techniques in the determination of PAHs and PAH metabolites (F. Ariese, C. Gooijer, N.H. Velthorst). 14. Characterization of surfactants in water by desorption ionization methods (F. Ventura). 15. Utilization of various LC-MS interfacing systems in environmental analysis; application to polar pesticides (M.H. Lamoree, R.T. Ghijsen, U.A.Th. Brinkman). 16. Hyphenated techniques applied to the speciation of organometallic compounds in the environment (O.F.X. Donard, R. Ritsema). 17. The potential of capillary electrophoresis in environmental analysis (M.W.F. Nielen).
Subject index.

© 1993 660 pages Hardbound
Price: Dfl. 465.00 (US $ 265.75)
ISBN 0-444-89648-1

ORDER INFORMATION

For USA and Canada
ELSEVIER SCIENCE INC.
P.O. Box 945
Madison Square Station
New York, NY 10160-0757
Fax: (212) 633 3880

In all other countries
ELSEVIER SCIENCE B.V.
P.O. Box 330
1000 AH Amsterdam
The Netherlands
Fax: (+31-20) 5862 845

US$ prices are valid only for the USA & Canada and are subject to exchange rate fluctuations; in all other countries the Dutch guilder price (Dfl.) is definitive. Customers in the European Community should add the appropriate VAT rate applicable in their country to the price(s). Books are sent postfree if prepaid.

ELSEVIER SCIENCE B.V.

0003-2670(19941031)297:1/2;1-4